

Petrogenesis of granitoids in the northern sector of the Mineiro Belt : unraveling geodynamic processes of incipient subduction-collision orogenic cycles

Syro Gusthavo Lacerda

▶ **To cite this version:**

Syro Gusthavo Lacerda. Petrogenesis of granitoids in the northern sector of the Mineiro Belt : unraveling geodynamic processes of incipient subduction-collision orogenic cycles. Geochemistry. Université Clermont Auvergne; Universidade Federal de Ouro Preto, 2025. English. ⟨NNT : 2025UCFA0084⟩. ⟨tel-05576005⟩

HAL Id: tel-05576005

https://theses.hal.science/tel-05576005v1

Submitted on 1 Apr 2026

HAL is a multi-disciplinary open access archive for the deposit and dissemination of scientific research documents, whether they are published or not. The documents may come from teaching and research institutions in France or abroad, or from public or private research centers.

L'archive ouverte pluridisciplinaire **HAL**, est destinée au dépôt et à la diffusion de documents scientifiques de niveau recherche, publiés ou non, émanant des établissements d'enseignement et de recherche français ou étrangers, des laboratoires publics ou privés.



HAL Authorization

Petrogenesis of granitoids in the northern sector of the Mineiro Belt: unraveling geodynamic processes of incipient subduction-collision orogenic cycles

Pétrogenèse des granitoïdes dans le sector nord de la Ceinture Mineïro : mise en évidence des processus géodynamiques des anciens cycles orogéniques de subduction-collision

Petrogênese de granitoides do setor norte do Cinturão Mineiro: implicações para processos geodinâmicos de ciclos orogênicos antigos de subducção-colisão

Syro Gusthavo Lacerda

The thesis is submitted in fulfilment of the requirements for the degree of Doctor of Philosophy of the *Universidade Federal de Ouro Preto* and *Université Clermont-Auvergne*

Escola de Minas
Departamento de Geologia
Programa de Pós-graduação em Evolução Crustal e Recursos Naturais

École Doctorale Sciences Fondamentales
Observatoire de Physique du Globe de Clermont-Ferrand
Laboratoire Magmas et Volcans

The defense was made public on July 30, 2025, before the examination committee, which was composed of the following members:

Régis Doucelance	*Université Clermont-Auvergne*	Director
Pablo Samaniego	*Université Clermont-Auvergne*	Examiner
Hermínio Nalini Jr.	*Universidade Federal de Ouro Preto*	Examiner
Martin Guitreau	*Université Clermont-Auvergne*	Co-advisor
Leonardo Gonçalves	*Universidade Federal de Ouro Preto*	Director
Eliza Peixoto	*Universidade de Brasília*	President
Mahyra Tedeschi	*Geological Survey of Finland GTK*	Reporter
Rômulo Machado	*Universidade de São Paulo*	Reporter
Hugo Moreira	*University of Portsmouth*	Co-advisor
Marco Pinheiro	*Serviço Geológico do Brasil*	Co-advisor
Cristiane Gonçalves	*Universidade Federal de Ouro Preto*	Co-advisor

To my first geochemistry's professor *L. A. R. S.*

Un jour vient pourtant et l'homme constate ou dit qu'il a trente ans. Il affirme ainsi sa jeunesse. Mais du même coup, il se situe par rapport au temps. Il y prend sa place. Il reconnaît qu'il est à un certain moment d'une courbe qu'il confesse devoir parcourir. Il appartient au temps et, à cette horreur qui le saisit, il y reconnaît son pire ennemi. Demain, il souhaitait demain, quand tout lui-même aurait dû s'y refuser. Cette révolte de la chair, c'est l'absurde.

Alber Camus, Le Mythe de Sisyphe, 1942

Opening

A variety of interconnected factors have led to the unique evolution of Earth, setting it apart from other planets in the solar system and numerous other celestial bodies. This evolution has shaped our planet into the home we know today. One of the most significant and singular factor of the Earth is the existence, and ongoing formation, of a relatively thin and rigid layer that covers part of its surface and forms the continents: the continental crust. It consists mainly of granitic rocks, i.e. quartz-feldspar-rich plutonic igneous rocks, which have allowed it to survive several dynamic processes that could have recycled it into the underlying mantle. Since the Phanerozoic, their production is closely connected with the formation of mountain ranges, which is called orogenesis. But how far back in time can we extend the concept of orogenesis and its relationship to granite production and ultimately to continental crust formation? It is therefore essential to understand how these rocks have formed over time to reveal the evolution of the continental crust and compare primitive and current Earth's dynamic processes.

In this thesis, I focused on the genesis of granitic rocks exposed in southeast of Brazil, formed during the Paleoproterozoic era, 2.5 to 1.6 billion years ago. At that time, the Earth underwent important transformations in terms of igneous rock production, sedimentary rock deposition, metamorphic rock thermo-barometry, ore deposit formation, oceanic and atmospheric oxygen levels, and conditions for the emergence of life. This period is called the Archean-Paleoproterozoic Transition. In order to study how these granitic rocks were formed during this fascinating time interval, a series of geochemical analyses have been performed on accessory minerals (zircon, apatite, and titanite) and several proxies were applied based on their isotopic compositions. This approach allows the reconstruction of an ancient orogen and plausible Earth's dynamic processes involving newly formed and pre-existing continental crusts.

Abstract

Orogens build mountains and shape the Earth's surface. These key sites of internal and external geodynamic interactions are manifested by the generation, reworking, and recycling of continental crust. This process involves magmatism, metamorphism, and erosion. Recent models suggest that most of the continental crust (30-80%) formed early in Earth's history when orogens likely manifested differently due to hotter mantle-crust interactions. Understanding how ancient orogens operated, as well as how the continental crust grew and evolved, is crucial to defining its secular evolution and reconstructing plausible geodynamic scenarios. This thesis examines the geological record of ancient subduction-collision orogenic cycles and assesses how these cycles operated and shaped the continental crust during the Paleoproterozoic era.

The Mineiro Belt is part of a Paleoproterozoic orogenic system that was accreted by collision ca. 2.00 Ga to the Archean terrane of the Quadrilátero Ferrífero region. It remained tectonically stable during subsequent Neoproterozoic orogenic events. Prior to the collision, the orogen experienced a prolonged period of tonalite-trondhjemite-granodiorite (TTG) magma production from 2.15 to 2.11 Ga. The contrasting juvenile and reworked zircon $\varepsilon_{Hf(t)}$ signatures of these rocks suggest that they originated from the melting of Paleoproterozoic and Archean mafic protoliths. Additionally, their low zircon $\delta^{30}Si$ values compared to Archean TTGs suggest that hydrous secondary mineral formation was crucial in source alteration and fertilization, rather than silicification, which is more prevalent in the Archean. This shift in mechanisms is consistent with the reduced dissolved silicon composition of the oceans, as evidenced by the global deposition of silica-iron precipitates. The orogen's dynamics are accommodated by a passive margin-seafloor-arc system, in which subduction and the melting of oceanic crustal slabs produce TTG magmas under medium-pressure conditions (<10 kbar). Total consumption of the oceanic crust between the two terranes initiated final orogenic dynamics, which were accommodated by continental collision. This scenario is supported by anatexis and the partial mineral isotopic resetting (e.g., apatite and titanite) of TTG rocks around 2.05 Ga, followed by the formation of S-type granites of the Cupim pluton.

S-type granites formed between 2.01 and 1.98 Ga during the late orogenic phase via incongruent melting of sedimentary rocks tectonically transferred to the lower levels of upper plate. This process mirrors modern orogens like observed in the Himalayan mountain range. Their mineralogical and chemical heterogeneities coupled with the widespread and sub-chondritic zircon $\varepsilon_{Hf(t)}$ values reflect a complex mixture of Archean and Paleoproterozoic protoliths. Furthermore, low zircon $\delta^{30}Si$ values indicate sediment-derived melts involving highly fractionated materials such as clays. While some apatite grains show partial isotopic resetting, most preserve original signatures and track the parental magma composition.

Content

Opening ..... *i*

Abstract ..... *iii*

Content ..... *v*

Author's declaration ..... *ix*

List of figures ..... *xi*

List of tables ..... *xix*

Acknowledgements ..... *xxi*

Research dissemination ..... *xxv*

1. Introduction 1

1.1. Major concepts and definitions **1**

1.2. Rationale and geological issue **6**

1.3. A summary geological history of the Mineiro Belt **7**

1.4. Major topics, aims, goals and thesis's guidance **11**

1.5. Methodology **12**

1.5.1. Petrography and mineralogy 12

1.5.2. Whole-rock major and trace element analyses 13

1.5.3. U-Th-Pb geochronology 15

1.5.4. Zircon Hf and Silicon isotope measurements 19

1.5.5. Accessory mineral geochemical analyses 26

1.6. Outcomes and future prospects **28**

2. Unraveling the late orogenic stage of the studied area 31

2.1. Preface **31**

2.2. Paleoproterozoic sediment-derived magmas reveal a late orogenic stage in the southern São Francisco Craton, Brazil: evidence from petrogenesis of the 2.0 Ga Cupim Pluton leucogranites **31**

2.2.1. Introduction 33

2.2.2. Geological background 34

2.2.3. Material and Methods 38

2.2.4. Results 38

2.2.4.1. Petrography *38*

2.2.4.2.Mineral Chemistry *41*
2.2.4.3.Geochemistry *43*
2.2.4.4.U-Th-Pb Geochronology *46*
2.2.4.5.Zircon Lu-Hf isotopes *49*
2.2.4.6.Zircon Trace elements *52*
2.2.4.7.Zircon Si isotopes *52*
2.2.5.Discussion 54
2.2.5.1.Age of granite emplacement *54*
2.2.5.2.Sources *55*
2.2.5.3.Parental magma and magmatic processes *57*
2.2.5.4.Hf isotope variations in zircon *61*
2.2.5.5.Tectonic implications *62*
2.2.6.Conclusions 65
2.3. Supplementary material A 66
2.3.1.Methods 66
2.3.1.1.Sampling *66*
2.3.1.2.Mineral chemistry *66*
2.3.1.3.Whole-rock geochemistry *67*
2.3.1.4.Heavy mineral concentration and separation *67*
2.3.1.5.Zircon imaging *67*
2.3.1.6.Zircon U-Th-Pb geochronology *68*
2.3.1.7.Zircon Lu-Hf isotopes *71*
2.3.1.8.Zircon trace elements *72*
2.3.1.9.Zircon Si isotopes *73*

3. Surrounding rocks: the widespread TTG magma production in the studied area 75

3.1. Preface 75
3.2. Hafnium and Silicon isotope evidence for multiple unsilicified basaltic sources at the origin of Rhyacian TTG magmas in the Mineiro Belt (Brazil) 75
3.2.1.Introduction 77
3.2.2.Geological background 79
3.2.3.Materials and Methods 81
3.2.4.Results 83

3.2.4.1.Petrography and mineralogy 83
3.2.4.2.Mineral chemistry 86
3.2.4.3.Whole-rock Geochemistry 87
3.2.4.4.Zircon U-Pb dating 91
3.2.4.5.Zircon hafnium isotopes 94
3.2.4.6.Zircon trace elements 95
3.2.4.7.Zircon silicon isotopes 97
3.2.5.Discussions 97
3.2.5.1.Ages of TTG emplacement and melting 97
3.2.5.2.Sources and melting conditions 98
3.2.5.3.Parental magma 101
3.2.5.4.Magmatic processes 102
3.2.5.5.Surface implications 104
3.2.6.Conclusions 107

4. Tracking igneous and metamorphic processes using other accessory minerals 109

4.1. Preface 109
4.2. Accessory minerals unveil Paleoproterozoic igneous and metamorphic processes in Mineiro Belt, Brazil 109
4.2.1.Introduction 111
4.2.2.Geological background 112
4.2.3.Materials and Methods 114
4.2.4.Results 116
4.2.4.1.Texture and mineral phase equilibrium 116
4.2.4.2.Apatite major elements and volatiles 124
4.2.4.3.U-Pb dating 124
4.2.4.4.Mineral trace elements 128
4.2.5.Discussions 131
4.2.5.1.Apatite and titanite U-Th-Pb Ages 131
4.2.5.2.Tracking parental magma or liquid composition 131
4.2.5.3.Magmatic and metamorphic processes 134
4.2.6.Conclusions 137
4.3. Supplementary material C 138

5. Building an ancient orogen 139

5.1. 'Hot' or 'cold' orogen ? 139

5.2. Linking ages, crustal growth and reworking, tectonics, and geodynamics 141

6. Perspectives and future direction 147

6.1. Introduction 147

6.2. Rationale 147

6.3. Scientific issue 148

6.4. Proposed analyses 149

References 151

Appendix 179

Author's declaration

I hereby declare that this PhD thesis is the result of my original research. All findings, interpretations and conclusions are entirely my own. This material has not been previously published or disseminated and is numerically archived in university repositories and in HAL - a multidisciplinary open-access archive for sharing scientific research, published or unpublished. The ideas developed during the PhD were presented and discussed at conferences and in published, submitted, or in-preparation scientific publications. Furthermore, this work has not yet been submitted for consideration in any award or prize competition.

Word count: 65,284.

S.L.

List of figures

Figure 1.1: Schematic representation of distinct generations of juvenile (left) and reworked (right) crust in island arc and collisional tectonic scenarios, respectively. Common values of εHf and εNd for the geotectonic components (mantle, oceanic crust, continental crust, sediments) and magmatism of juvenile and reworked crust. δ18O values according to Roberts and Spencer (2014). δ30Si values according to Poitrasson et al., 2017. 3

Figure 1.2: Top: Map of Archean crustal exposures (in red) and Precambrian orogens (in gray) (mod. from Martin and Pinti, 2005). Bottom: Simplified age distribution of the four granitoid groups during the Archean-Paleoproterozoic Transition (modified from Laurent et al., 2014). 5

Figure 1.3: Geological and geotectonic context of the study area. (a) Main tectonic elements of South America modified from Cordani et al., (2016). Highlighted cratons: 1: Amazonas Craton, 1a: Guyana Shield, 1b:Central Brazil Shield; 2: São Luís Craton; 3: Parnaíba Block; 4: São Francisco Craton 5: Paranapanema Block; 6: Luiz Alves Craton; 7: Rio de la Plata Craton. Geological data from Gómes-Tapias et al., (2019). The white rectangle indicates the location of the study area shown in (b). Simplified geological unity of the South São Francisco Craton and its boundaries modified from Seixas et al. (2012). Highlighted are the regions of Quadrilátero Ferrífero and Mineiro Belt. Agn: Augen gneiss structures. The orange dashed line marks the interpreted boundaries of Neoproterozoic craton, while the white dashed rectangle defines the local study area shown in Figure 2.1.....8

Figure 1.4: Conceptual εHf space diagram of a magmatic rock and speculative interpretations of source material and processes. Arc and depleted mantle lines are delineated through recent compositions provided in Dhuime et al., 2011 and Chauvel and Blichert-Toft, 2001. CHUR line represents the 'Chondritic Uniform Reservoir' value (after Iizuka et al., 2015). Also displayed is the effect of mixing process between the depleted mantle and a hypothetical ancient crustal lithology. Values of 0.011 and 0.023 refer to 176Lu/177Hf characterizing the slopes of theoretical felsic and mafic precursor evolutions, respectively. TDM ages refer to the calculated model age for each source precursors, (FP) is a felsic precursors, and (MP) is a mafic precursor. 21

Figure 1.5: NBS28-normalized *δ*30Si values from whole-rock composition of high temperature rocks (after Savage et al., 2014; André et al., 2019; Deng et al., 2019). Zircon *δ*30Si values from different granitic rocks from Guitreau et al. (2022). Granulite xenolith and abyssal peridotite compositions from Savage et al. (2013a, 2013b). Dashed arrows indicate the effects of clay formation and sea-derived silica incorporation low-temperature process (see Poitrasson et al., 2017). 24

Figure 2.1: (a) São Francisco-Congo Craton in the west-Gondwana reconstruction. (b) The southern portion of the São Francisco Craton and the main lithostratigraphic and lithodemic unities, highlighted the northern portion of the Mineiro Belt. Adapted from Alkmim and Teixeira, (2017). (c) Simplified geology of the northern portion of the Mineiro Belt and the sample studied localities. Main granitic body limits from Seixas et al. (2012), Moreira et al., (2020); and Santos and Baltazar (2013). Meta-sedimentary rock locations came from Moreira et al., (2020); Cabral et al., (2019) and Teixeira et al., (2021). Qtz = quartzite. (To understand the colors in the figure(s), readers are directed to consult the online version of this article).....36

Figure 2.2: Main petrographic, mineral, and structural features of the sampled rocks. The left column is from Group 1 leucogranites, and the right column is from Group 2 leucogranites. (a) Two-mica leucogranite from GC1 sample highlighted the magmatic foliation marked by biotite and muscovite flakes. (b) Massive garnet-bearing leucogranite from GC7 sample highlighted a garnet grain. (c) Double-polarized microscope image from GC1 sample showing the intergranular textures between quartz, feldspars, and micas. Please note the presence of monazite grain at the center of the image. Single-polarized microscope image from GC6 sample

showing the main texture of garnet grain (see the text for details). (e) SEM image showing a common mantle-core texture displayed by monazite, apatite, and allanite from the GC5A sample. (f) SEM image details of a garnet grain from GC7 sample. Anhedral quartz inclusions and chlorite filling fractures are common. Note the sharp contact with locally Ca-rich rims. 40

Figure 2.3: Mineral chemistry of major phases from the leucogranite samples. (a) Feldspar composition plotted in ternary diagram of feldspar. (b) Biotite compositions of Al [IV] versus Fe#, and Mg-Al-Fe triangular diagram proposed by Abdel-Rahman (1994). (c) Garnet composition along a rim-rim profile. (d) Chemical ternary diagram of muscovite. A grey line separates the fields of primary plutonic muscovite composition from the field of secondary muscovite (after Miller et al., 1981). "Magmatic texture (core)", "Magmatic texture (rim)" and "metamorphic or alteration products" refer to textural criteria such as size distribution, association with minerals (feldspars), or association with shear zones. Mineral abbreviations from Warr (2021). 41

Figure 2.4: Major element geochemistry classification of the studied rocks. (a) CIPW-normative Ab-An-Or diagram of O'Connor (1965), with the fields defined by Barker (1979). To: tonalite, Gd: granodiorite, Tdj: trondhjemite, Gt: granite, qMz: quartz monzonite. (b) A-B milicationic diagram (Debon and Le Fort, 1983) with subdivisions according to Villaseca et al., (1998): l-P, m-P, and h-P are low-, medium-, and high-pressure peraluminous composition, and f-P is felsic-peraluminous. f-P field is partly defined by Tertiary High Himalaya granites (Villaseca et al., 1998), as well as Paleozoic collisional leucogranites (see Nabelek, 2020), Muscovite Peraluminous Granite (i.e. MPG Barbarin et al., 1999; Bonin et al., 2020; Moyen et al., 2017) and Archean-Paleoproterozoic Strong Peraluminous Granites (i.e., SPG, see Bucholz and Spencer, 2019; Poujol et al., 2021). (c) MALI diagram with classification limits defined by Frost et al., (2001). (d) A/CNK vs. A/NK proposed by Shand (1943) to define the alumina-alkalis composition. 'Altered rock' refers to the GC2 sample. 44

Figure 2.5: Trace element composition of the studied rocks from Cupim Pluton. (a) Rb/Sr vs. Eu/Eu* anomalies, Rb/Ba, and Sr/Y compositions of the leucogranites. (b) Zr (ppm) vs. Sr (ppm), Zr/Hf, and MgO (wt.%). Arrows in (b) and (d) suggest magmatic differentiation. 'Altered rock' refers to the GC2 sample. (c) Chondrite-normalized REE diagram (chondrite values from Taylor and McLennan, 1985). (d) Archean shale-normalized (Taylor and McLennan, 2009) multielement patterns from the leucogranites. Please note the non-normalized Rb/Sr ratio. 45

Figure 2.6: Representative SEM (BSE and CL) zircon images from the sampled rocks. The locations of laser spot analyses are indicated along with the spot name (e.g., z10). The corresponding 207Pb/206Pb dates are quoted with ±2SE uncertainty, in Ma. The calculated εHf(t) values are quoted with ±2SE uncertainty, while δ30Si values are with ±2SD uncertainty. ... 47

Figure 2.7: Concordia diagrams (206Pb/238U vs. 207Pb/235U) for zircon grains from the Cupim Pluton leucogranite samples. Error ellipses and dates are displayed at 2σ level of uncertainty. Analyses were not corrected from common Pb. Hollow ellipses are from inherited zircon domains. Small inserts illustrate the calculated ages of inherited zircon grains. The Mean Square Weighted Deviation (MSWD) is a measure of goodness of fit that considers the relative importance of both internal and external reproducibility. 47

Figure 2.8: Hf isotope composition of leucogranites of the Cupim Pluton. (a) Initial 176Hf/177Hf(t) vs. 207Pb/206Pb age. Grey vertical bars indicate the main magmatic stages in the southern São Francisco Craton. Dashed-arrow suggests a Pb-loss process. (b) εHf vs. age space for magmatic and inherited zircon domains showing possible Lu/Hf evolution lines. These evolution lines require 176Lu/177Hf values of 0.01 and 0.015 (typical of crustal reservoirs), anchored to the mainly Hf model ages (TDM) in the Mineiro Belt (2.50 Ga; Moreira et al., 2020) and Quadrilátero Ferrífero (3.20 Ga; Albert at al. 2016) regions; with respectively 176Hf/177Hf= 0.280850 and 176Hf/177Hf= 0.281385 compositions. (c) KDE distribution of the inherited cores and detrital zircon ages (Moreira et al., 2020). See details for Depleted Mantle (DM) and Chondritic Uniform Reservoir (CHUR) reservoirs in Supplementary Material A. 50

Figure 2.9: Zircon trace elements and silicon isotope composition from the Cupim Pluton leucogranites. Pink diamonds are pristine magmatic zircon grains, white diamonds are pristine inherited zircon grains. Altered magmatic and inherited zircon grains are tagged with square and diamond symbols in grey color. (a) Ti (ppm) vs. Hf (wt.%) zircon composition showing tectonic fields and trends according to Laurent et al. (2021). The orange star is the average composition of 3.46 Ga Barberton igneous zircon grains hosted in several granitic rocks (Laurent et al., 2021). The blue star represents the average zircon composition from S-type granites (Guitreau et al., 2022). (b) δ30Sicalc. vs. Y(ppm) composition. Vertical bars represent δ30Sicalc. values for zircon from the mantle (Trail et a., 2018) and S-type granites (Guitreau et al., 2022). (c) Chondrite normalized (Taylor and McLennan, 1985) patterns (full and colored lines) for zircon grains from the leucogranites. Patterns with diamond symbols refer to the respective average composition. (d) Calculated Ti-in-zircon temperatures vs. Δ30SiWR-Zrc for the analyzed zircon domains. Full and dashed lines indicate the related theoretic composition variation of rocks with 50%, 65%, and 100% of SiO2 (wt.%). Zircon composition from S-type granites is from Guitreau et al. (2022). 53

Figure 2.10: Source discrimination diagrams for the sampled leucogranites. (a) Na-K-Ca triangular diagram showing the relative composition of the leucogranites and the composition of experimental melts. Stars represent the source material composition, while ellipses represent the final products of melting. Dark grey symbols are TTG materials, and light grey and white symbols are meta-sedimentary materials. The abbreviations are the same as those used by Moyen (2011). (b) Al2O3 vs. CaO/Na2O composition for the studied samples and melts using different materials, and pressure and fluid activity. MS [Muscovite schist] and MBS [Muscovite–biotite schist] from Patiño Douce and Harris, 1998. Field of Strong Peraluminous Granites (SPG) defined by Sylvester et al., 1998. (c) Source diagram and classification proposed for Neoarchean granitoids (Laurent et al., 2014). The 2A/CNK pole suggests a sedimentary source. (d) Rb/Sr vs. Rb/Ba composition showing clay-rich and clay-poor heterogeneity of the produced melts (from Sylvester 1998). 57

Figure 2.11: Petrogenetic parameters of the magmatic process for the Cupim leucogranites. (a) Chondrite-normalized REE patterns of melts derived from the partial melting Archean shales (Taylor and McLennan, 2009) source and left behind K-feldspar cumulate residue. The modeled melts are compared with the proposed parental magma of the leucogranites (GC1). Details of the models are given in the text. (b) Sr vs. Ba variation for the leucogranites. The solid and the dashed lines are theoretical evolutions of a liquid throughout the fractionation of biotite, alkali feldspar, and plagioclase fractionation (Tartèse and Bouvais, 2010). (c) Distinct behavior of Rb/ Sr and Ba for different melting reactions (see Weinberg and Hasalová, 2015). Cupim leucogranites (from two-mica to garnet-bearing) mimic the muscovite dehydration reaction in the absence of aqueous fluids leading to an increase of Rb/Sr and a decrease in Ba. (d) Ternary projection of cotectic curves and minimum points (black squares) at various pressures and normative melt An contents, according to Tuttle and Bowen (1958). Shift from these minimum points to the right can indicate a decrease in water activity. 59

Figure 2.12: Detailed area in εHf vs. age space of magmatic zircon domains (excluding GC7 due to age uncertainty) showing variation between samples and on the same sample. Magmatic zircon grains are color-coded following Fig.8. Age (in Ma) refers to the upper intercept age calculated for each sample. The Lu/Hf evolution (grey lines) defines the two Hf radiogenic source end members, as shown in Fig.8b. Vertical dashed black arrows indicate variations in εHf values from the same sample (see text for details). 61

Figure 2.13: A proposed collisional tectonic scenario for the genesis of the Cupim Pluton leucogranites (not to scale). (a) Steepening of subducted oceanic slab generates TTG-sanukitoid magmas in the Mineiro Belt, which gradually approaches the rifted margin of the São Francisco Archean crust. From these two tectonic terrenes, forearc (Paleoproterozoic) and passive margin (Archean) sediments are deposited. (b) Consumption of oceanic crust promotes the onset of collision between the Mineiro Belt and the São Francisco rift margin. The soft collision heats the lower crust and generates migmatites and metamorphic fingerprints in both terranes.

Sediments of Archean and Palaeoproterozoic provenance are mixed and deposited within the orogen. (c) Compression of the orogen by Archean inliers and/or Paleoproterozoic belts promotes horizontal shortening and vertical thickening of the orogen. This results in the melting of crustal lithologies (mainly sedimentary rocks) and generates peraluminous magmas that form the Cupim Pluton leucogranites.....65

Figure 3.1: δ30Si values for different rock types, modified from Kleine et al. (2018). BSE = Bulk Silica Earth. OIB (recycled altered oceanic crust) from Pringle et al. (2016). Adakite data (n=4) from Deng et al. (2019). Silicified and unsilicified basalts and komatiites from Abraham et al. (2011) and André et al. (2022). Archean TTGs of the Barberton Greenstone Belt, Kaapvaal Craton, from André et al. (2019). Paleoproterozoic TTGs of the North China Craton (NCC) from Zhou et al. (2024). Paleoproterozoic TTGs (this study) are calculated from zircon values (see the text for details). 78

Figure 3.2: Simplified geological map of the northern part of the Mineiro Belt in the southern São Francisco Craton. Modified from published maps from Seixas (2000), Seixas et al. (2012, 2013), Moreira et al. (2018, 2020), Lacerda et al. (2024), and the Geological Survey of Brazil [Santos and Baltazar (2013)] based on this study. The inset shows the location of Archean, Proterozoic, and Phanerozoic crusts [from Tapias et al. (2019)] and the study area (indicated by the white arrow) on a map of Brazil in the South America geological context.....80

Figure 3.3: Petrographic features of the samples studied in this contribution. (a) Weakly-foliated Bt-Hbl-tonalite (CM49) from Caatinga-Lamim Complex. Plagioclase phenocrysts form shape-oriented cumulates surrounded by hornblende (and minor biotite) crystals. (b) Migmatitic Bt-gneiss from Caatinga-Lamim Complex. Its leucosome (CM44A) and melanosome parts exhibit lobate contacts, suggesting in-situ melt extraction. On the right is a detailed view of the partially melted gneiss, showing plagioclase cumulates embedded in biotite crystals. (c) Weakly-deformed tonalitic Bt-gneiss (CM47) from Caranaíba showing millimetric to centimetric dark bands mainly composed of biotite. Light bands are also milli- to centimetric but formed by plagioclase and quartz grains. Note a 17mm diameter coin to scale. (d) Weakly-deformed Bt-trondhjemite (CM46A) from Ressaquinha Complex with dark biotite presents as oriented flakes between unoriented plagioclase (whitish) and quartz (grayish to blueish) crystals. 84

Figure 3.4: Micro-petrography and micro-textures observed on the TTG rocks. The left column shows polarized-light microscope images, the middle column shows cross-polarized microscope images, and the right column shows detailed SEM images. The geologic unit and sample number/lithology are given on the left of each set of images. See the text for detailed descriptions. Dashed lines outline large (>1 mm) plagioclase phenocrysts. The mineral abbreviation used is after Warr (2021). Pls.: paleosome; Nes.: neosome. 85

Figure 3.5: Notable geochemical features of major minerals from TTG samples studied herein. Color-code symbols: CM49 (green), CM44A/B (dark/light blue), CM46A (yellow), and CM47 (purple). (a) Trigonal feldspar diagram showing the molar Or-An-Ab contents of analyzed crystals. The small inset shows their Al2O3 (wt.%) vs. An (%) composition. (b) Amphibole classification in terms of tetrahedral Si vs. Mg# after Leake et al. (1997). (c) Al[iv] vs. Fe# (top) and trigonal Mg-Al-Fe (bellow) composition of biotite grains. Fields of nature compositions are after Abdel-Rahman (1994) and mineral abbreviations after Warr (2021). (d) P-T crystallization conditions calculated from amphibole-plagioclase thermobarometers (Blundy and Holland, 1990; Schmidt, 1992). Arithmetic average and related square deviation (1SD) values are highlighted. 87

Figure 3.6: Major element geochemistry of the studied TTG rocks. (a) Normative Anorthite-Orthoclase-Albite triangular diagram (Barker, 1979; O'Connor, 1965) showing the different compositions of Archean TTG and modern continental crust (from Moyen and Martin, 2012). (b) A-B diagram (Debon and Le Fort, 1983; Villaseca et al., 1998). Arrows/fields represent the composition of TTG and modern granitoids based on the classification after Barbarin (1999): ACG - amphibole-rich calc-alkaline granitoids; KCG - K-rich and K-feldspar-porphyritic calc-

alkaline granitoids; CPG - cordierite-bearing, biotite-rich peraluminous granitoids; MPG - muscovite-bearing peraluminous granitoids (from Moyen et al., 2017). (c) SiO2 vs. Mg# [= 100 × molar Mg/(Mg + Fe)]. The reference line Mg#= 50 roughly divides the compositions of experimental melts derived from metabasalt, and adakites from Condie (2005). (d) A/CNK vs. A/NK diagram (Shand, 1943), molar [Al/(Ca + Na + K)] vs. molar [Al/(Na + K)], respectively. Arrows/fields indicate the composition of arc-related granitoids (e.g., Kohistan batholith), crustal-derived granitoids, and TTG (Moyen and Martin, 2012). 89

Figure 3.7: Incompatible element diagrams for the studied rocks [left column: Caatinga-Lamim complex (CM44A, CM44B, and CM49); right column: CM46A, and CM47]. The blueish line patterns represent average values for high-pressure 'Sodic-HP', medium-pressure 'Sodic-MP', and low-pressure 'Sodic-LP' TTG rocks from Moyen (2011). Small insets in (b) and (d) are (La/Yb)N vs. (Yb)N and Sr (ppm) vs. Y (ppm), respectively, with fields proposed in Moyen and Martin (2012) and Moyen (2011). In (a) and (b), REE concentrations are normalized to the chondrite values determined by Taylor and McLennan (1985). In (c) and (d), spider diagrams showing incompatible element concentrations (from Rb to Yb) are normalized to the primitive mantle values proposed by Sun and McDonough (1989). Note that Mg# [= 100 × molar (MgO / (MgO + 0.9 × Fe2O3(t)))] and Cr (ppm) are not normalized..... 91

Figure 3.8: Cathodoluminescence images of representative zircon grains from the studied TTG rocks, showing the location of each analysis. The age labels refer to 207Pb/206Pb ages, with their discordance percentage indicated within brackets. Values corresponding to Lu-Hf data refer to εHf units calculated according to interpreted sample ages, with quoted 2SE uncertainties. Silicon isotope data are reported as δ30Si normalized to quartz NBS 28 values with 2SD uncertainties. Th/U ratios correspond to semi-quantitative concentrations determined by external normalization to the reference material used or calculated directly from the trace element analyses, which are consistent with each other for all analyses. 91

Figure 3.9: Geochronological results of the studied TTG rocks from the Caatinga-Lamim complex [(a) and (b) from sample CM44A; (c) from CM44B; (d) from sample CM49]. In (a), the colored ellipses represent anatectic (phenocryst) zircons, while the colorless ellipses indicate inherited (xenocryst) zircons. In (b), the analysis of the inherited zircon reveals a Discordia line. In contrast, the more concordant analyses produce a concordant age, as shown in the small inset at the top left. In (c), the colored ellipses represent the analyses with negligible incorporation of common Pb, that define a Discordia line. In (d), all U-Th-Pb analyses form a well-defined Discordia line, while in the small inset, the age is calculated based on the most concordant analyses. Both approaches, using the discordant intercept and the Concordia method, yield similar ages for the sample. (e) CM46A, Ressaquinha trondhjemite. The colored ellipses represent all magmatic (phenocryst) zircons, while the colorless ellipses come from a single inherited zircon core (see zircon images in Figure 7). The more concordant analyses calculate a concordant age (small inset) consistent, within error, with the age calculated using the Discordia method. (f) CM47, Caranaíba gneiss. The colored ellipses represent all magmatic zircon grains, and the colorless ellipse likely indicates an inherited core. The small inset highlights the most concordant analysis, which calculates virtually the same age using all analyses with the Discordia method. 93

Figure 3.10: Zircon Lu-Hf isotopes of TTG rocks. The color code symbols for each sample are the sample used in Fig.5. Hollow symbols represent analyses performed on inherited zircon cores. Small gray diamonds refer to local TTG, sanukitoid, high Ba-Sr, and hybrid granitoids of Moreira et al. (2020). Depleted mantle curves were defined according to Dhuime (2011) and Ickert (2013) (full line), and Chauvel and Blichert-Toft (2001) (dashed line). CHUR values provided by Iizuka et al. (2015). (a) Initial 176Hf/177Hf composition vs. Pb-Pb apparent ages (Ma). Horizontal arrays define the average composition for each sample and suggest Pb-loss. (b) εHf vs. Pb-Pb apparent age (Ma) space showing plausible Lu/Hf evolution arrays (176Lu/177Hf= 0.01-0.015) anchored at apparent TDM (e.g., 2.35 Ga, 3.00 Ga) ages. 95

Figure 3.11: Trace elements and Si isotopes of zircon grains from TTG rocks. The color code symbols for each sample are the sample used in Fig.9. Gray pattern lines [in (a) and (b)] and

small gray diamonds [in (c) and (d)] refer to altered zircon compositions. Chondrite-normalized REE diagrams of (a) Caatinga-Lamim complex and (b) Rassaquinha trondhjemite and Caranaíba gneiss. (c) δ30Si vs. Th/U composition. The shaded field shows the typical δ30Si composition of zircon grains from Archean TTG rocks (Guitreau et al., 2022), whereas the horizontal line indicates the signature of mantle-derived zircons (Trail et al., 2018). Error bars indicate 2SD uncertainties. (d) U/Yb vs. Hf (ppm) composition. Fields of continental survey and MORB zircon grains, as well as arrows indicating melt fractionation, are from Grimes et al. (2015). Small blue crosses refer to zircon grains from Archean TTG rocks (Guitreau et al., 2022).....96

Figure 3.12: Plausible sources and melting conditions for TTG rocks. The color code and symbols for each sample are the same as those used in Fig. 9. (a) Trigonal source discrimination diagram for Neoarchean granitoids proposed by Laurent et al. (2014). Triangle vertices are: 2×A/CNK (molar [Al2O3/(CaO + K2O + Na2O)]; Na2O/K2O (wt.%) ratio; and 2×[FeOt + MgO + Sr + Ba] (wt.%) (FMSB). The TTG, Sk, Hyb and Gt fields designate TTG, sanukitoids, hybrid granitoids, and granitic (s.s.) suites respectively. (b) Na-K-Ca trigonal diagram shows several compositions of experimental melts (ellipses) and their starting material (stars), compiled by Moyen (2011). Dark grey: mafic sources; Light grey: sedimentary sources. Black diamonds represent local metabasalts (Teixeira et al., 2015), and the red star refers to the average composition of the mafic Archean crust (Taylor and McLennan, 2009). (c) Na2O/K2O vs. SiO2 composition of experimental melts from low-K andesite BL91(478), and (d) low-K calc-alkaline andesite BL91(557) performed by Beard and Lofgren (1991), compared with the studied samples. 99

Figure 3.13: Average modern MORB (Mo-MORB) normalized multi-element diagram showing partial melting model results for possible parental magmas CM47 Caranaíba gneiss (top) and CM46A Ressaquinha trondhjemite (bottom). Fine gray dashed lines indicate the percentage of melting (e.g. F= 10-30%). 'Residue' refers to the residual mineral assemblage proportions used in the model. The mineral abbreviation used is after Warr, 2021.....102

Figure 3.14: Magmatic process models for Caatinga-Lamim rocks. (a) CaO (wt.%) vs. SiO2 (wt.%) composition, amphibole (dark triangles), and plagioclase (colored triangles). For color code and symbology used, refer to Fig.9. Arrows indicate amphibole fractionation (black line) and plagioclase accumulation (gray line) trends. The percentage labels are based on the modal mineral assemblage of each sample. 'Anx' refers to the normative composition of plagioclase crystals from the Caatinga-Lamim rocks. (b) Ce/Sr ratio vs. Y (ppm). The Caatinga-Lamim rocks show a positive correlation that suggests plagioclase accumulation (Laurent et al., 2020a) from a plausible parental magma [Med.HREE-TTG (Moyen and Martin, 2012)]. The bluish fields represent high-pressure 'HP', medium-pressure 'MP', and low-pressure 'LP' TTG rocks from Moyen (2011). (c) Chondrite-normalized REE diagram showing fractionation model results considering a Med.HREE-TTG parental magma composition. 'Cumulate' refers to the fractionated mineral proportion. Dashed gray lines indicate the composition of the fractionated remaining liquids. The fractions of the remaining liquid are also shown.....103

Figure 3.15: Proposed geodynamic model for Paleoproterozoic TTG generation in the Mineiro Belt. Deposition of BIFs in the rifted passive margin of the Archean São Francisco continent scavenges the 30Si composition of the ocean. Coeval oceanic seafloor basalts interact with the Si-reduced seawater column and become unsilicified until recycled into the mantle during subduction in an island-arc scenario. Unsilicified basaltic subducted slabs underwent partial melting, producing low-Si TTG magmas. These melts locally interact with the metasomatized mantle wedge via oxidized sediments, which generate oxidized sanukitoid magmas (Moreira et al., 2023). 105

Figure 4.1: (a) Study area location in the South American continent context. Shadow areas represent Precambrian Cratons in the Brazilian shield: SFC – São Francisco; AM – Amazonas; PR – Paranapanema; SL – São Luís; DL – Rio de La Plata. (b) Geological map of the southern São Francisco Craton, modified from Campos et al. (2003), pointing to the Quadrilátero Ferrífero and Mineiro Belt regions (study area), available titanite ages, and sampling location (white star). Titanite ages were interpreted either as magmatic or metamorphic from (a) Machado and

Carneiro (1992); (b) Noce et al. (1998); (c) Aguilar et al. (2017); (d) Moreira et al. (2018); (e) Neves et al. (2022). 113

Figure 4.2: Optical microscope images [(a) double-cross polarized, (b-d) single-cross polarized] of apatite and titanite crystals from the studied rocks. (a) Apatite grains inclusions in a coarse K-feldspar crystal from two-mica Cupim leucogranites (Lacerda et al., 2024). (b) Prismatic to vermiform, colorless titanite and rounded apatite grains within biotite flakes from Caatinga-Lamim migmatitic gneiss (CM44B). (c) Rounded, brownish titanite grains associated with Fe-sulphide from Caatinga-Lamim migmatitic gneiss. (d) Prismatic, light brownish titanite grains between biotite, hornblende, and plagioclase crystals from Caatinga-Lamim tonalite (CM49).117

Figure 4.3: Cathodoluminescence (CL) images of apatite grains from Caatinga-Lamim migmatitic gneiss (CM44B; mosaic 1), and Cupim leucogranites (GC1, GC5a/B, and GC6; mosaic 2). Laser spot locations, the analysis number (e.g., ap#1), their respective U-Pb ages, and Y/Sr ratio values are also indicated.....118

Figure 4.4: Backscattering electron (BSE) images focused on titanite grains from Caatinga-Lamim migmatitc gneiss (CM44B; type i – mosaic 1, and type ii – mosaic 2) and tonalite (CM49, mosaic 3 and 4). Laser spot locations, the analysis number (e.g., Ttn#1), their respective U-Pb ages, and Y/Sr ratio values are highlighted.....120

Figure 4.5: Different methods to calculate apatite ages from Cupim leucogranite (GC1, left column) and Caatinga-Lamim migmatitic gneiss (CM44B, right column). (a-b) Tera-Wasserburg diagrams show the analyses before 208Pb correction; colored ellipses represent those used in the Discordia line discrimination, and hollow ones are the rejected analyses (see the text for details). The scale bar denotes the Pb (ppm) concentration. The stars represent the zircon age for each sample from Lacerda et al. (2024, submitted). (c-d) Analyses after 208Pb correction in the Tera-Wasserburg space. (e-f) Weighted mean 207Pb/206Pb ages. Hollow bars are rejected analyses. 126

Figure 4.6: Titanite ages. (a) Wetherill diagram shows all analyses of titanite grains from Caatinga-Lamim migmatitic gneiss (CM44B); greyish ellipses are type (i), and brownish type (ii) titanite (see the text for details). The color scale bar refers to Th/U ratio values of the analyses. On the right, the analyses are shown separately by type and nature (magmatic and metamorphic). (b) Tera-Wasserburg diagram shows analyses performed on titanite grains from Caatinga-Lamim tonalite (CM49). On the right, the analyses are separated following the nature of the domains (magmatic or metamorphic). The color scale bar defines U (ppm) concentration of the analyses.....127

Figure 4.7: Chondrite-normalized (after Boyton, 1974) REE patterns of selected apatite (left column) and titanite (right column) grains. (a and c) Caatinga-Lamim migmatitic gneiss (CM44B). (b) Cupim leucogranites (GC1, GC5A/B, GC6). (d) Caatinga-Lamim tonalite (CM49)..... 130

Figure 4.8: Host magma discrimination. (a) LREE-10*Y-100*Sr titanite discrimination diagram. Fields (TTG, sanukitoid, BARD) proposed by Bruand et al. 2020. The dashed arrow suggests the metamorphic trend. (b) LREE-10*Y-10*Sr apatite discrimination diagram. Fields (TTG, sanukitoid, BARD, I- and S-type) from Bruand et al. 2020. (c) Sr (ppm) vs. Y (ppm) concentration of titanite and apatite. The high Y concentration indicates igneous grains/domains, while low are mainly metamorphic. Sr enrichment could indicate the increase of crustal material into the host magma. (d) Sr (ppm) in apatite or titanite vs. Sr (ppm) whole-rock. The dashed line indicates the correlation trend suggested by Bruand et al. 2014. 133

Figure 4.9: REE composition of the parental magma back-calculated from the apatite and titanite composition. (a) Parental magma composition modeled from the average composition of magmatic titanite grains from Caatinga-Lamim gneiss (CM44B) compared with medium-pressure TTG composition and whole-rock composition. Note the effect of hornblende fractionation and plagioclase accumulation (dashed patterns). Average zircon composition from Lacerda et al. submitted (b) using the average composition of apatite grains. (c) Parental magma

composition obtained from the average composition of igneous titanite grains from Caatinga-Lamim tonalite (CM49). Note the effect of hornblende fractionation and plagioclase accumulation (dashed patterns). Average zircon composition from Lacerda et al. submitted (d) Parental magma calculated from the average composition of apatite grains from Cupim leucogranites compared to the whole-rock composition. Dashed patterns represent non-normalized partition coefficients of monazite and garnet.....135

Figure 4.10: Accessing igneous and metamorphic processes. Symbols used are the same as Fig.9. (a) Th/U vs. Zr-in-titanite temperature (°C) composition of titanite grains from Caatinga-Lamim rocks. Fields of igneous, recrystallized, and metamorphic titanite are proposed by Olierook et al., 2019. (b) Pb (ppm) vs. Th/U composition of titanite and apatite grains of the studied rocks. The arrow indicates the igneous-metamorphic trend. (d) Chondrite-normalized REE patterns of apatite grains from Cupim leucogranites compared with those from metagreywackes and pelite rocks (Biget et al., 2024). The whole-rock composition of two-mica and garnet-bearing leucogranites come from Lacerda et al. 2024. 137

Figure 5.1: Compilation of zircon, titanite and apatite U-Pb ages of magmatic bodies in the northern part of the Mineiro Belt and corresponding magmatism during orogenic evolution. Data from Noce (1995), Seixas et al. (2012; 2013), Moreira et al. (2018; 2020), and this thesis. All U-Pb analyses were performed by LA-ICP-MS or ID-TIMS. 145

List of tables

Table 1.1: Summary of ages obtained for reference materials (Standard zircon) using LA-ICP-MS system hosted in LMV. Details about equipments and analytical conditions are provided in the text. Weighted Mean Average refers to 207Pb/206Pb ages; n is the total of analyses performed for each reference material during each analytical session. 17

Table 1.2: Summary of ages obtained for reference materials (standard apatite) using LA-ICP-MS system hosted in LMV. Concordia age were calculated following Stacey-Kramers Concordia projection; n is the total of analyses performed for each reference material during each analytical sequences. 18

Table 1.3: Summary of ages obtained for reference materials (standard titanite) using LA-ICP-MS system hosted in LMV. 2SE refers to 2×standard error; n is the total of analyses performed for each reference material during each analytical session. 19

Table 1.4: Summary of average isotopic composition obtained for reference materials (standard zircon) using LA-MC-ICP-MS system hosted in LMV. 2SE and 2SD refers to 2×standard error and 2×standard deviation, respectively; n is the total of analysis performed for each reference material during all analytical sessions.....26

Table 2.1: Locality, modal composition, classification, and main textures of the collected samples of the Cupim Pluton leucogranites. 39

Table 2.2: Measured zircon Lu-Hf isotope compositions and calculated εHf(t) for Cupim leucogranite zircon crystals. Uncertainties correspond to 2σ confidential interval. 'm' and 'i' notations in Sample column refer to the number of analyses performed on magmatic and inherited domains, respectively. 50

Table 2.3: Summary of the main geochemical characteristics of Cupim leucogranite zircons. Si isotopes, calculated temperatures, Th/U ratios, and REE are from zircon crystals with pristine compositions. Uncertainties correspond to 2σ confidential interval. 55

Table 2.4: Petrogenetic parameters for the Cupim Pluton leucogranites. 60

Table S.1: Summary of calculated ages for zircon reference materials used in this study. Concordia ages using the algorithm of Ludwig (1998). 2σ notation refers to 2 × standard deviation (STD). MSWD is the Mean Square of the Weighted Deviations for age homogeneity. n refers to the number of analyses used for each calculated age. 70

Table S.2: Summary of Hf and Si isotope data for the analyzed zircon reference materials compared with equivalent data from the literature. 72

Table 3.1: Summary of analytical results obtained for zircon reference materials used in this study. Reported values for 176Hf/177Hf and δ30Si isotopic compositions correspond to averages. The value within brackets refers to the number of measurements considered to calculate averages. Errors are quoted as 2SE for ages and Hf isotopes, and 2SD for Si isotopes..82

Table 3.2: Summary of analytical results obtained on zircon crystals from the studied rock. 97

Table 4.1: Summary of calculated ages obtained for the apatite and titanite reference materials used. Into parenthesis are the number of analyses. Errors are quoted in 2SE for Discordia and 206Pb/238U Weighted Mean ages. 116

Table 4.2: Average composition of apatite and titanite grains from the studied rocks compared with TTG, sanukitoid (Bruand et al., 2020), and S-type granites (Belousova et al., 2001). Element concentrations are in ppm. 'n' is the number of analyses. 'Bdl' refers to 'below the detection limit'.....129

Table 5.1: Summary of petrogenetic parameters and implications for tectonics and geodynamics from several granitic unity in the northern part of the Mineiro Belt. εHf(t) are average values from zircon grains. εNd(t) are range values from whole-rock geochemistry. δ18O and δ30Si are average values from zircon grains. ΔFMQ refers to fayalite–magnetite–quartz buffer calculated via S6+/ΣSTOTAL oxybarometer on apatite grains. 142

Acknowledgements

Although I tend to doubt chance, I'm almost certain that I was in the right place during this journey, surrounded by remarkable people who, in their own ways, helped me reach the end of this important chapter in my life. Also, some of them gave me unique feelings and memories that I'll try to express below, even if I'm not quite sure how.

Martin, my geoscientist hero. You made me believe that I could fly even when I was just learning to crawl. You have provided me with an unparalleled opportunity for professional growth, allowing me to become personally involved in the field of Earth's science. Thank you for showing me a bit of the culture and geology of Auvergne, which lives between dormant volcanoes, red wine bottles, *Saint-Nectaire* cheese, *Fleur-de-pays* cigaret, and Michelin tires. Thank you so much for welcoming me into your home and introducing me to your beloved family. Thank you so much for being so kind and welcoming, Arthur, Léane, Éva, and Emilie: I'll always remember the French way of welcoming someone with a '*quiche aux poireaux*'. Thank you for letting me be part of your family Christmas — it meant a lot to me! You're all warmly invited to visit me in Brazil — I'd love to welcome you there! Thank you Inês Pereira for introducing me to Martin and to the LMV.

A heartfelt thank you to Léo and Cris, my advisors since 2018, when I started my first research project as an undergraduate in Geology. Since then, you've supported me and guided me along safer and more thoughtful paths, always with generosity and patience. Thank you for believing in me and for continuing to inspire new generations of geoscientists!

Thank you, Hugo—you are a true inspiration as a geoscientist! I've been following your work since 2018, and it has been a real privilege to have you as a co-advisor during my PhD. Our discussions about the "new data from the Mineiro Belt," where you've also dedicated so much of your PhD (and still do), have meant a lot to me. I truly admire the way you describe Earth science and your passion for sanukitoid rocks. I sincerely hope this bond of friendship and scientific collaboration will never fade!

A heartfelt thank you as well to Régis, for his kindness and patience during our many discussions on isotope geochemistry. I also truly appreciated our conversations about his journey in the Guianas and his fondness for Caetano Veloso's songs.

My deepest gratitude to the brilliant professors and researchers from LMV who guided and inspired me: Jean-François Moyen, Mickael Laumonier, and Nicolas Olivier. To the incredible technical and engineering team — Claire Fonquernie, Jean-Luc Piro, Abdelmouhcine Gannoun, Clara Gorce, Thierry Hamel, and Federica Schiavi — thank you for your constant support, patience, and expertise. To my fellow PhD candidates — Théo, Sid, Tristan (both), Julien, Quentin, Lukas, and Garance — what a joy it was to walk this path with you. And a very special thanks to my *marraine*, Julia Eychenne. I'll never forget the fieldwork in the Massif Central, a true highlight of this journey, where I had the honor of meeting icons of the geosciences: Bernard Barbarin,

Philippe Boulvais, Oscar Laurent, Simon Couzinié, Chris Yakymchuk, and Vojtech Janoušek. What an unforgettable privilege.

I'm grateful to DEGEO/UFOP team of professors—Isaac Rudnitzki, Gustavo Melo, Fernando Alkmim, Gláucia Queiroga, and Marco Paulo Castro—for their guidance, and to the technicians—Geraldo Magela, Adriana Trópia, Débora Vasconcelos, Sereno Chaves, Gustavo Filemon, and Gabriela Brito —for their constant support. Many thanks to the NEMIC research group for providing an inspiring and supportive environment. Special thanks to Isabela, Wilker, Carol, Pedro, Jéssica, and especially Stéphany—for sharing the fieldwork with me, collecting over 200 kg of granite samples!, and for all the chats about geochemistry, granites, and (hard) academic life.

I would also like to thank CPRM for the excellent laboratories, high-quality equipment, and the opportunity to work in such a professional environment. My sincere thanks to the teams at the Belo Horizonte and Caeté offices, especially Cassiano Costa and Marco Pinheiro. Cassiano, I'm especially grateful to you for patiently teaching me the entire heavy mineral separation process—your guidance was fundamental to this work. A big thank you to the entire LAMIN-Caeté team for their full support during lab work, and to the nigh-guards who kindly allowed me to extend my lab sessions when needed (haha). And a heartfelt hug to Wagner and his family, who generously hosted me in Caeté for several weeks.

A big hug to all my dear classmates who, throughout my PhD journey, patiently (and tirelessly!) listened to me talk endlessly about S-type granites, TTGs, the Archaean, and the Paleoproterozoic. Special thanks to Rafael and Luiza from DEGEO/UFOP, and to Baptiste, Steve, Shashank, Christy, Alexandra, and Jessi from LMV/UCA — you all made the ride so much more fun and meaningful. Luiza and Rafael, our car conversations were just as deep (if not deeper!) than the questions over English grammar during those intense writing sessions. Thank you so much for your daily friendship, our relaxed lunches, insane sunsets, and *French* goodbyes. And at LMV — how can I forget the late work sessions, where music became the soundtrack of our journey? Baptiste always brought the best taste (though I still insist: Radiohead is not good — haha), while Shashank kept the vibe light with the funniest picks. And of course, the perfect ending to so many days: climbing sessions that left our hands sore, our minds clear, and our spirits lifted.

Julie, '*ma Julye*', thank you to be my *thésard's* sister. I really appreciate you taking me in and introducing me to LMV and the other PhD candidates. We were a very efficient duo at the spectrometers. I remember when we did more than 250 analyses on your beloved apatites in a single day! Thanks for all the lunches on the terrace and the friendly *soirées*. I wish you all the best during the end of your thesis. I'm sure we'll meet more often in this world of geosciences. I'm excited to see you in Brazil!

I want to say a heartfelt thank you to my family. Thank you so much for believing in me from the very beginning, and for being by my side all the way to the end of this journey. Mom and Dad, your love, attention, and help in making the most difficult decisions were essential for everything

to happen most safely and profitably. Luana, my dear sister, I want to thank you from the bottom of my heart for being my best friend forever. I can't thank you enough for always being my confidant and knowing that I can always count on you. I know it wasn't easy being away from you all for over a year. The trip we took, unfortunately without my 'always busy father', was so heartwarming. We got to enjoy places together that we hadn't known before, and it was such a wonderful experience. I can't thank you enough for always letting us feel like 'my parents' house' was also 'our nest'.

Laís, my '*gatinha*'. You are the light of my cave's life. I can't imagine my days without you, my love, beloved companion, faithful friend, and my favorite partner in life. You make me smile every day, even when we're 10,000 Km apart. I can't thank you enough for making it possible for us to meet more often. I loved filling your head with stories of 'how granites are formed', and I really appreciate that you listened so patiently. I absolutely love it when you look me in the eye and leave me with the certainty of a long and happy future together. You turned my heart drunk in Santorini! Your fascination with tiny and curious cave-creatures during your PhD inspired me. Congratulations for this achievement! I'm sure you'll be successful in whatever you decide to do.

Bruno, thanks for being my best friend all these years, especially in the last two when we decided to share a place on Morro São Sebastião. Thanks for taking such good care of the dogs. Our humorous daily interaction left me 'comfortably numb', and Pearl Jam' songs will always make me remember you. Some days of 'liver pain' are sometimes casual in the underground. All the time we spent talking about Dostoevsky's books made me feel like life was pointless. It's like, what is the point of living if not to keep deciding not to end it all? Thank you for being part of my absurdity and good luck finishing your Master's - you can do it, brother!

Thank you all Rio Ipiranga' friends: Areda, Dyana, Maira, and Wendy. For all the great company, good humor, and dishes inspired by *MasterChef*. Thank you from the bottom of my heart.

I would like to thank my Paleoproterozoic research friends from Rio de Janeiro—Sandro, Charlys, Gisele, and Professor Ciro Ávila. I really enjoyed the fieldwork we did in 2020, and it was a pleasure working alongside all of you. I look forward to meeting you again at future events on the topic!

This thesis was supported by two main sources of funding: the Fundação Coordenação de Aperfeiçoamento de Pessoal de Nível Superior (CAPES, Brazil), which funded the research project and the international fellowship stage in France (PDSE/2022); and the French government initiative "Programme d'Investissements d'Avenir" managed by the Agence Nationale de la Recherche (ANR) under grant ANR-20-SFRI-0003, project CAP GS.

Additional expenses (including part of the field missions, geochemical analyses, and conference participation) were covered by the following organizations: the Minas Gerais Research Support Foundation (FAPEMIG), the Brazilian Research Council (CNPq), and Instituto Geoatlântico.

Research dissemination

Invited talk

Petrogênese de granitoides do setor setentrional do Cinturão Mineiro, sul do Cráton São Francisco, e seu significado tectônico. *In: Cafezin com prosa - Sua pesquisa em 30 minutos Cafezin com prosa, Departamento de Geologia, Universidade Federal de Ouro Preto.* Ouro Preto, Brazil. June 2022.

Les analyses multi-proxy dans des zircons élucide la genèse des granites paléoprotérozoïques au sud du Craton São Francisco, Brésil. *In: Journees scientifiques ClerVoc, Laboratoire Magmas et Volcans, Université Clermont-Auvergne*. Clermont-Ferrand, France. June 2023.

Conference attendance

Oral presentations

Petrology of Cupim Pluton leucogranites: implications for Paleoproterozoic orogeny in the São Francisco Craton, Brazil. *In: Granitoids, continents, life and puns: A workshop in tribute to Hervé Martin. Université Clermont-Auvergne*. Clermont-Ferrand, France. June 2023.

Leucogranitos do Pluton Cupim documentam o último estágio da orogenia Minas no sul do Cráton São Francisco, Brasil. *In: 17 Simpósio de Geologia do Sudeste*. Rio de Janeiro, Brazil. Sociedade Brasileira de Geologia. October 2023.

Tracing sources and melting processes: Hf isotope variability in zircons from the S-type Cupim pluton. *In: XIII South American Symposium on Isotope Geology.* Sociedade Brasileira de Geologia. Armação de Búzios, Brazil. May 2024.

Poster presentations

Paleoproterozoic Himalayan-type leucogranites disclose a late orogenic stage in the Southern São Francisco Craton (Brazil). *In: Goldschmidt 2023. France: European Association of Geochemistry.* Lyon, July 2023.

Petrogênese de granitoides do setor setentrional do Cinturão Mineiro, sul do Cráton São Francisco, e seu significado tectônico. *In: VIII Mostra dos Programas de Pós-graduação do Encontro de Saberes da UFOP. Universidade Federal de Ouro Preto*. Ouro Preto, Brazil, November 2023.

Co-authored papers during the PhD outside the scope of this thesis

Lopes S. R., Gonçalves L., Gonçalves C. C., Moreira H., **Lacerda S.**, Armond P. V. Diversity of Siderian magmatic pulses revealed by intracrustal melting of oceanic crust in the Mineiro Belt, southern São Francisco Craton. *Lithos, Volumes 488–489*, 2024.

Mauri S., Heilbron H., Bruno H., Bersan S., Almeida R., Marques R. A., **Lacerda S.**, Souza A. M., Paravidini G., Neto C., Valeriano C. M., Chapman G., Fowler M., Mottram C., Strachan R., Storey C. Coeval TTG and sanukitoid magmatism during the Rhyacian tectonic evolution of the Juiz de Fora Complex (São Francisco Paleocontinent, SE-Brazil). *Precambrian Research, Volume 414*, 2024.

1. Introduction

1.1. Major concepts and definitions

The Earth, like other rocky planets and asteroids in the Solar System, has undergone compositional differentiation since its formation about 4.566 billion years ago. The early stages of its differentiation (4.6-4.0 Ga) occurred through processes of condensation and accretion of particles. Subsequently, a substantial fraction of this accreted mass underwent partial melting, facilitated by potential and radioactive energy heat, combined with the influence of solar winds and intense meteoritic bombardment. These processes orchestrated the early segregation of the Earth into three distinct layers of different composition, arranged from interior to exterior: the core, the mantle, and the crust. The ongoing phase of differentiation, which began around 4.0 Ga, is attributed to the continuous differentiation of the mantle and the concomitant thickening of the crust. This phenomenon occurs through the internal transfer of matter and energy within the Earth, i.e., the process of magmatism, which is consistent with the gradual cooling of the planet (Bonin and Moyen, 2011).

Planetary crusts can be divided into three distinct types based on their characteristics: primary, secondary, and tertiary. Primary crusts are formed early in the planetary formation process, during the early stages of accretion, although they are rarely visible on Earth. In contrast, secondary and tertiary crusts, which are abundant on Earth, are the products of different geologic processes. Secondary crusts are formed by partial melting of the silicate mantle, whereas tertiary crusts are formed by dehydration and/or partial melting of pre-existing secondary crusts. The Earth's oceanic crust, composed mainly of gabbros and basalts, is a representative example of a secondary crust. On the other hand, the Earth's continental crust, which is dominated by granites (and granulites at depth), is the sole currently known example of tertiary crust in the entire Solar System (Taylor & McLennan, 2009).

Basalts and gabbros, characterized by a basic composition enriched in Fe and Mg silicate minerals such as olivine and pyroxene, and lacking in felsic minerals such as feldspars and quartz, exhibit high density. This high density of the Earth's modern oceanic crust makes it susceptible to subduction and recycling into the mantle when subject to thickening or forced by tectonic processes. Conversely, the continental crust, which consists of lower-density rocks composed primarily of quartz and feldspars, allows it to float on the mantle, thereby precluding the recycling process. As a result, continental crust is more susceptible to preservation over geologic time than oceanic crust. The importance of this is underscored by the observation that the oldest rocks on Earth, such as the Acasta Gneiss in Canada (4.03 Ga - Stern and Bleeker, 1998; Guitreau et al., 2014) and the Barberton TTG in South Africa (3.8 Ga - Moyen et al., 2019), are predominantly composed of continental crust (see Kranendonk et al., 2019). In contrast, oceanic crusts tend to have relatively younger ages (< 200 Ma), with rare older ophiolitic examples. As a result, the Earth's continental

crust serves as a "black box" that preserves important traces of the Earth's formation history, providing geologists with an optimal setting for studying the processes of the primitive Earth.

Granitic rocks, also known as granites *sensu lato* or more colloquially as granitoids, are the predominant component of the Earth's upper continental crust, primarily within the Precambrian and contemporary orogenic cratons. Characterized by their light color index and intermediate to acidic composition, granitic rocks are coarse-grained and composed predominantly of feldspars and quartz. Modal variations in the proportion of plagioclase (P) among the feldspars allow their classification into distinct subtypes according to Streckeisen (1976): tonalites and trondhjemites (P>90), granodiorites (P=65-90), granites (P=10-65), and alkali-feldspar granites (P<10). These rocks commonly contain minerals such as micas, amphiboles, and less commonly pyroxene and fayalite, along with accessory minerals such as garnet, apatite, zircon, titanite, tourmaline, and Fe-Ti oxides, although in lesser abundance. Significantly, granitoids serve as the primary host rock for zircon, a key mineral in long-term crustal evolution studies, particularly in the fields of U-Th-Pb geochronology and radioactive and stable isotopes. Therefore, understanding the origin of the granitoids that host these minerals is essential for elucidating the long-term evolution of the Earth's crust.

The origin of granitoids has been the subject of extensive debates since the early 20th century, supported mainly by local and regional studies involving field relations, petrology, major and trace element chemistry, and more recently isotopic analyses. In addition, experimental investigations using both natural and synthetic materials have contributed to this discourse (Moyen et al., 2021, and references therein). From a broad perspective, two main mechanisms have been proposed for the generation of differentiated magmas: (i) by the ultimate differentiation (fractional crystallization) of a basaltic fluid derived from mantle melting, and (ii) by partial melting of pre-existing crustal rocks. These mechanisms are intricately linked to various geodynamic processes involving the crust and mantle, which provide the temperature and pressure conditions necessary to initiate the magmatic processes (partial fusion/fractional crystallization) responsible for producing differentiated magmas. In addition, these processes create favorable conditions for their segregation from the source, ascent, and emplacement within the crust (Pitcher, 1987; Vigneresse, 2004; Jacob et al., 2021).

The first mechanism involves the authentic creation of new continental crust through high fractionation of mantle material. In contrast, the second mechanism, known as intracrustal, merely alters or transforms pre-existing crustal rocks and therefore does not contribute to an increase in crustal volume (Moyen et al., 2017). Crust produced by the first mechanism is referred to as 'juvenile' continental crust, whereas that produced by the second mechanism is referred to as 'reworked' continental crust (**Fig. 1.1**). Hybrid magmas add further complexity to the understanding of continental crust formation, as they are mixtures of mantle and crustal components that are difficult to distinguish. Consequently, several classifications of granitoids

have been proposed to distinguish potential source materials and magmatic processes, which either directly or indirectly provide insight into the likely geodynamic scenarios that prevailed during their formation (Chappell and White, 1974; Pearce et al., 1984; Barbarin, 1999; Bonin et al., 2020).

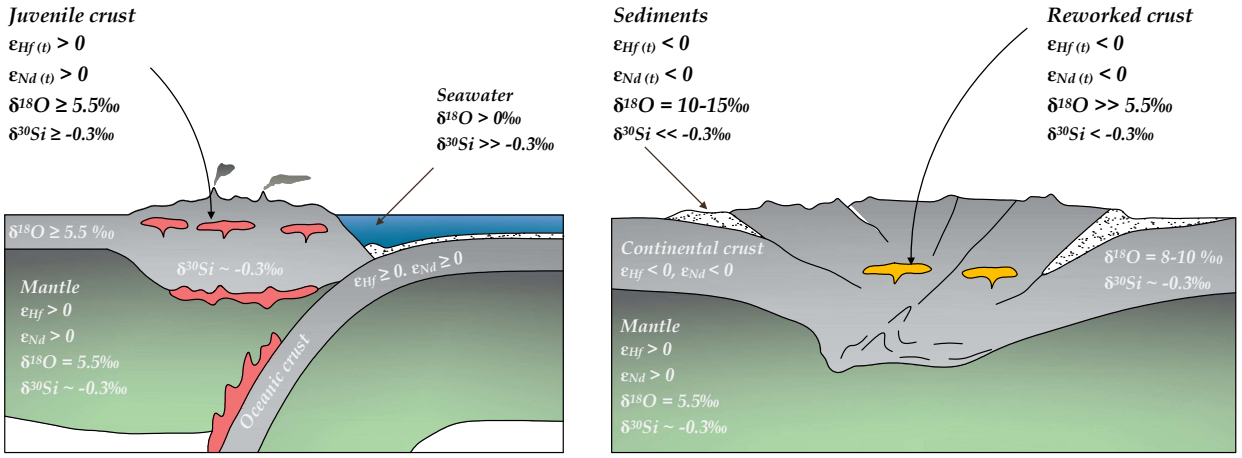


Figure 1.1: Schematic representation of distinct generations of juvenile (left) and reworked (right) crust in island arc and collisional tectonic scenarios, respectively. Common values of ε_{Hf} and ε_{Nd} for the geotectonic components (mantle, oceanic crust, continental crust, sediments) and magmatism of juvenile and reworked crust. $\delta^{18}O$ values according to Roberts and Spencer (2014). $\delta^{30}Si$ values according to Poitrasson et al., 2017.

Elucidating crustal evolution through an understanding of granitoid genesis involves delineating distinct intervals of magma production, specifying their characteristics (sources and magmatic processes), and discerning their spatial relationships. This effort requires envisioning plausible geodynamic scenarios and discerning how these scenarios have evolved during crustal evolution. At the forefront of this research are studies in petrology, geochronology, and, more recently, *in situ* isotopic analysis. Petrology is concerned with the formation of rocks, taking into account petrographic, mineralogical, microstructural, major and trace element chemical data. Meanwhile, geochronology allows the estimation of rock formation times based on the isotopic content of radioactive pairs (e.g., U-Pb, Sm-Nd, Rb-Sr) within specific minerals or the whole-rock, using known decay rates (Schoene, 2014). The incorporation of isotopic content of long-lived radiogenic pairs (e.g., Sm-Nd, Lu-Hf), as well as stable isotopes (e.g., O, Si, Mg, Ti, and S), provides a comprehensive framework for integrating diverse rock genesis information to define contributions from mantle or crustal sources, and surface condition implications.

On a global scale, several Precambrian cratons underwent significant changes in magma production during the Archean-Paleoproterozoic (APT) secular transition, resulting in shifts in the geodynamic behavior of the Earth's crust and mantle (Laurent et al., 2014, and references therein). Granitoids formed during the APT, which spanned 3.0 to 2.5 billion years ago, can be classified

into four distinct groups (**Fig. 1.2**): (i) tonalite-trondhjemite-granodiorite (TTG); (ii) sanukitoids sensu lato; (iii) granites rich in biotite and/or two micas; and (iv) hybrid granitoids.

TTG rocks are derived from the partial melting of hydrated (meta-)basalts at different depths (Moyen, 2011; Moyen and Martin, 2012). Sanukitoid sensu lato, which includes Mg+Fe and K-rich magmas (monzodiorites, monzogabbro and differentiation products), are formed by interactions between the peridotitic mantle and a component rich in incompatible elements, such as TTG and/or metasediments (Martin et al., 2009). Granites rich in biotite and/or two micas are peraluminous, potassium-rich rocks that result from the fusion of pre-existing crustal segments, such as ancient TTG and metasedimentary rocks (Sylvester, 1998; Watkins et al., 2007; Bucholz and Spencer, 2019). Hybrid granitoids, characterized by chemical and petrographic diversity, result from the interactions between magmas and/or source material of the other three groups, namely TTG, sanukitoid, and biotite-granite and/or two-mica granite (Laurent et al., 2014). The magmatic evolution during this particular time interval unfolds in two distinct phases, somewhat reflecting the ongoing tectonic processes (**Fig. 1.2**): (i) about 0.2-0.5 billion years, characterized by TTG generation within a subduction regime, followed by (ii) a subsequent period of about 0.02-0.15 Gy, characterized by the emergence of sanukitoids sensu lato and hybrid granitoids, along with derivatives of crustal reworking such as biotite granites and two-mica granites, within a collisional regime. The transition between these two magmatic phases is diachronous and has been documented across various cratons (**Fig. 1.2**) (e.g., Pilbara, Kaapvaal, Karelian, Amazon, Superior Province, Dharwar, North China, as reviewed in Laurent et al., 2014).

In the southern São Francisco Craton (SSFC), Moreira et al. (2018) meticulously documented the globally significant record of the magmatic transition within the Mineiro Belt. This transition is exemplified by the high-aluminum Lagoa Dourada TTG suite (~2.35 Ga) and the low-Ti Alto Maranhão sanukitoid suite, along with associated high-Ba and Sr granitoid plutons (São Brás and Bombaça plutons) and hybrids (Serra do Camapuã pluton, ~2.13 Ga) (Seixas et al., 2012; Seixas et al., 2013). Hafnium and oxygen isotopic studies on zircon characterize both episodes as involving crustal addition within an intra-oceanic proto-subduction regime. The second group of granitoids, the Alto Maranhão Suite and associated plutons, show evidence of sedimentary incorporation in their genesis (Moreira et al., 2020, 2023). Lacerda et al. (2020, 2021) present preliminary data on the geochemical, petrographic, mineralogical, and microstructural characteristics of the two-mica, peraluminous, and potassium-rich leucogranites that comprise the Cupim Pluton (Santos and Baltazar, 2013), located near Cristiano Otoni, Minas Gerais, Brazil. They postulate that this granitic body may represent direct evidence of crustal reworking. Peraluminous leucogranites, which are experimentally known to be produced by the fusion of metasedimentary rocks, are formed by the progressive thickening of the crust during collisional events. These collisional events impart specific mineralogical, geochemical, and isotopic signatures to the rocks (Hopkinson et al., 2017; Bucholz & Spencer, 2019; Nabelek, 2019).

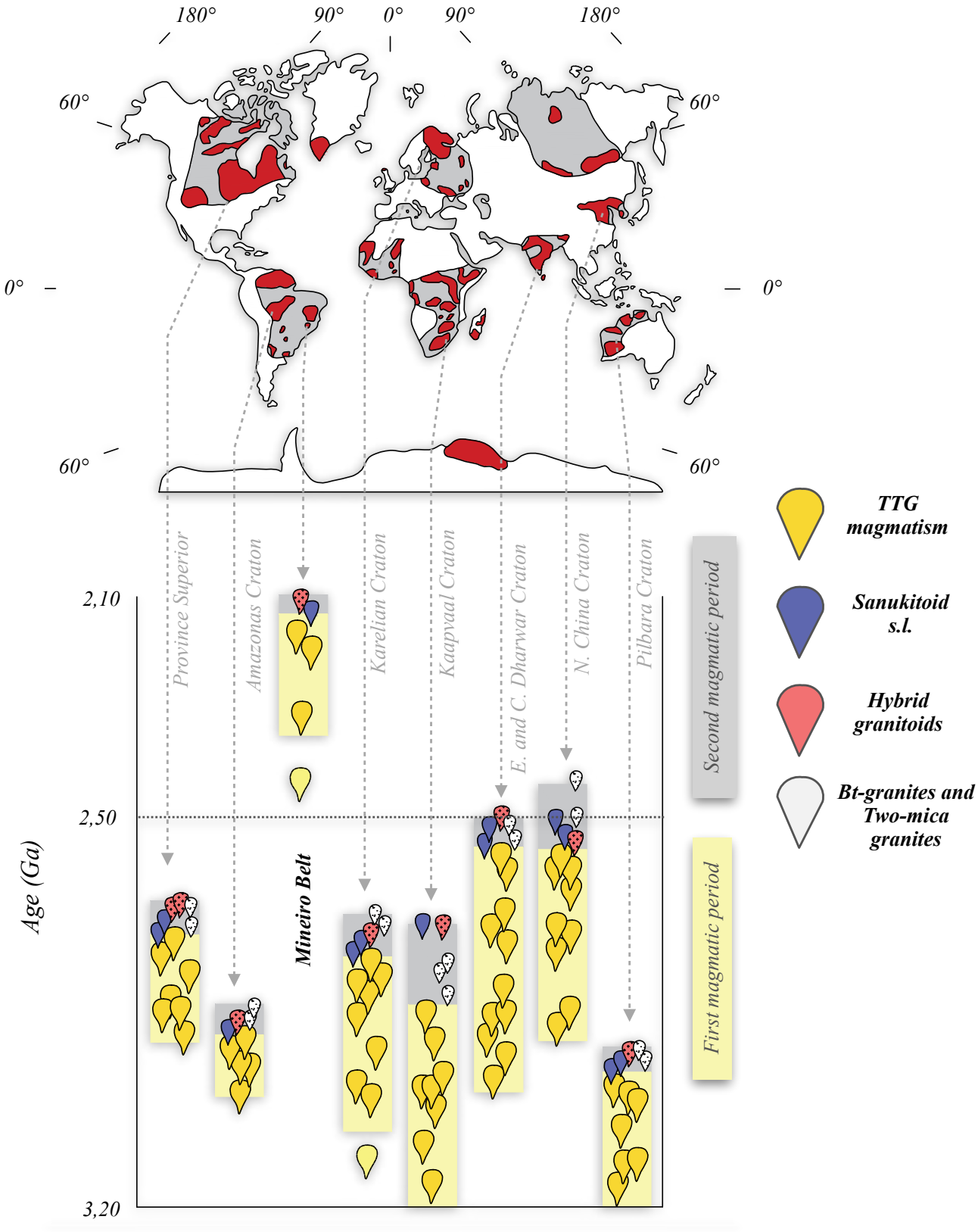


Figure 1.2: Top: Map of Archean crustal exposures (in red) and Precambrian orogens (in gray) (mod. from Martin and Pinti, 2005). Bottom: Simplified age distribution of the four granitoid groups during the Archean-Paleoproterozoic Transition (modified from Laurent et al., 2014).

This Ph.D. thesis aims to comprehensively characterize the crustal evolution by performing petrological analyses (mineralogy, major and trace element chemistry in whole rocks and mineral chemistry), geochronological studies (U-Pb in zircon, apatite and titanite) and isotopic studies (Si-Hf in zircon) on granitic rocks located in the northern part of the Mineiro Belt (**Fig. 1.2**) - south of the São Francisco Craton, in the state of Minas Gerais, Brazil. The overall objective is to identify the potential sources and magmatic processes responsible for their formation, and to correlate these findings with plausible geodynamic scenarios prevalent at this specific time. This will be followed by a comparative analysis with the evolutionary histories of other age-correlated cratons worldwide to identify both commonalities and differences. Remarkably, there is currently a paucity of isotopic studies of the Cupim Pluton and surrounding rocks. Consequently, this investigation seeks to improve our understanding of crustal evolution within the Mineiro Belt. This study is of particular importance because it explores the generation of peraluminous granitic magmas, exemplified by the Cupim Pluton. This exploration is crucial as it access mechanisms and processes that were less apparent during the APT, and sheds light on geodynamic scenarios that have received limited discussion within the geotectonic context of the Mineiro Belt, such as continental collision.

1.2. Rationale and geological issue

Recent studies identify significant changes in the geochemistry of magmas, particularly during the Archean-Paleoproterozoic transition, and attribute them to consequential changes in geodynamics, thereby influencing the evolution of the Earth's crust (Laurent et al., 2014). These magmatic and geochemical changes are indicative of terrestrial cooling and the maturation of continental crust over time and space (Keller and Schoene, 2012). Initially, low-K magmas are generated indirectly from mantle melting and contribute as new accretions to the continental crust. However, during the APT, the production of high-K magmas suggests a form of reworking of the continental crust (e.g., Bucholz and Spencer, 2019).

The Southern São Francisco Craton (SSFC) in the state of Minas Gerais, Brazil, preserves a segment of Archean-Paleoproterozoic crust of the granitoid-gneiss-greenstone belt type. This crust has undergone moderate to high degrees of metamorphism and is partially covered by younger sedimentary basins. A systematic study of different magmatic bodies initially proposed that the Archean rocks in the SSFC show an evolutionary trend from less evolved sodic magmas to K-enriched magmas (Lana et al., 2013; Farina et al., 2015). However, it has been highlighted that rocks indicative of subduction initiation processes, i.e. sanukitoid (Martin et al., 2005), are conspicuously absent in the Archean evolution of the SSFC.

One of the hypotheses considered is that the magmatic transition in the Southern São Francisco Craton may have occurred late in the Paleoproterozoic, as documented by petrological, geochronological, and isotopic analyses of granitic rocks in the Mineiro Belt (**Fig. 1.2**) (Moreira et al., 2018). Another hypothesis suggests the possibility of repetition (Bruno et al., 2020). Although the reasons for a possible geochemical and magmatic secular delay or repetition remain unclear in the literature, further investigations can shed light on this issue. In particular, sanukitoid magmas within the Mineiro Belt are thought to originate from a mantle enriched in higher K materials, indirectly indicating crustal reworking (Seixas et al., 2013; Moreira et al., 2020).

In addition, there is preliminary evidence for high-K magmatism resulting from more direct crustal reworking - by melting of pre-existing crustal rocks or their derived sediments - in granitoids within the Mineiro Belt around Cristiano Otoni (Lacerda et al., 2020, 2021). However, these findings require more comprehensive petrological, geochronological, and isotopic studies. The discovery and study of their petrogenesis can provide insights into the following points:

- *High-K magmatism resulting from sedimentary melting is less evident during the APT due to limited material available (e.g., large sedimentary basins) and/or insufficient temperature and pressure conditions for its formation. Consequently, details about the magmatic sources and processes leading to their formation can potentially classify them as pre- or post-APT events.*
- *The petrogenetic changes during the APT and their implications for the evolution of differentiation mechanisms in the continental crust remain poorly understood. The comprehensive study of the spatio-temporal evolution of magmatism within a craton, when extended and compared to other cratons on a global scale, has the potential to improve our understanding of the geodynamic changes that occurred during this specific period.*

1.3. A summary geological history of the Mineiro Belt

The Mineiro Belt (**Fig. 1.3**) denotes a geological terrane (>6000 Km^2) composed of low-grade Paleoproterozoic (~2.4-2.1 Ga) meta-igneous rocks emplaced as a result of orogenic accretionary evolution associated with the amalgamation of granite-gneiss-greenstone Archean nuclei (e.g., São Francisco and Congo cratons), coinciding in age with the Nuna/Columbia supercontinent (cf. Alkmim and Teixeira, 2017). Its orogenic evolution correlates in age with the Mantiqueira and Juiz de Fora complexes (Heilbron et al., 2010; Degler et al., 2018; Cutts et al., 2019; Bruno et al., 2020), now located east of the Mineiro Belt, which were metamorphosed to moderate and high degrees, respectively, during the Neoproterozoic to Ordovician Brasiliano-Pan African orogeny (Alkmim et al., 2017; Caxito and Alkmim, 2023).

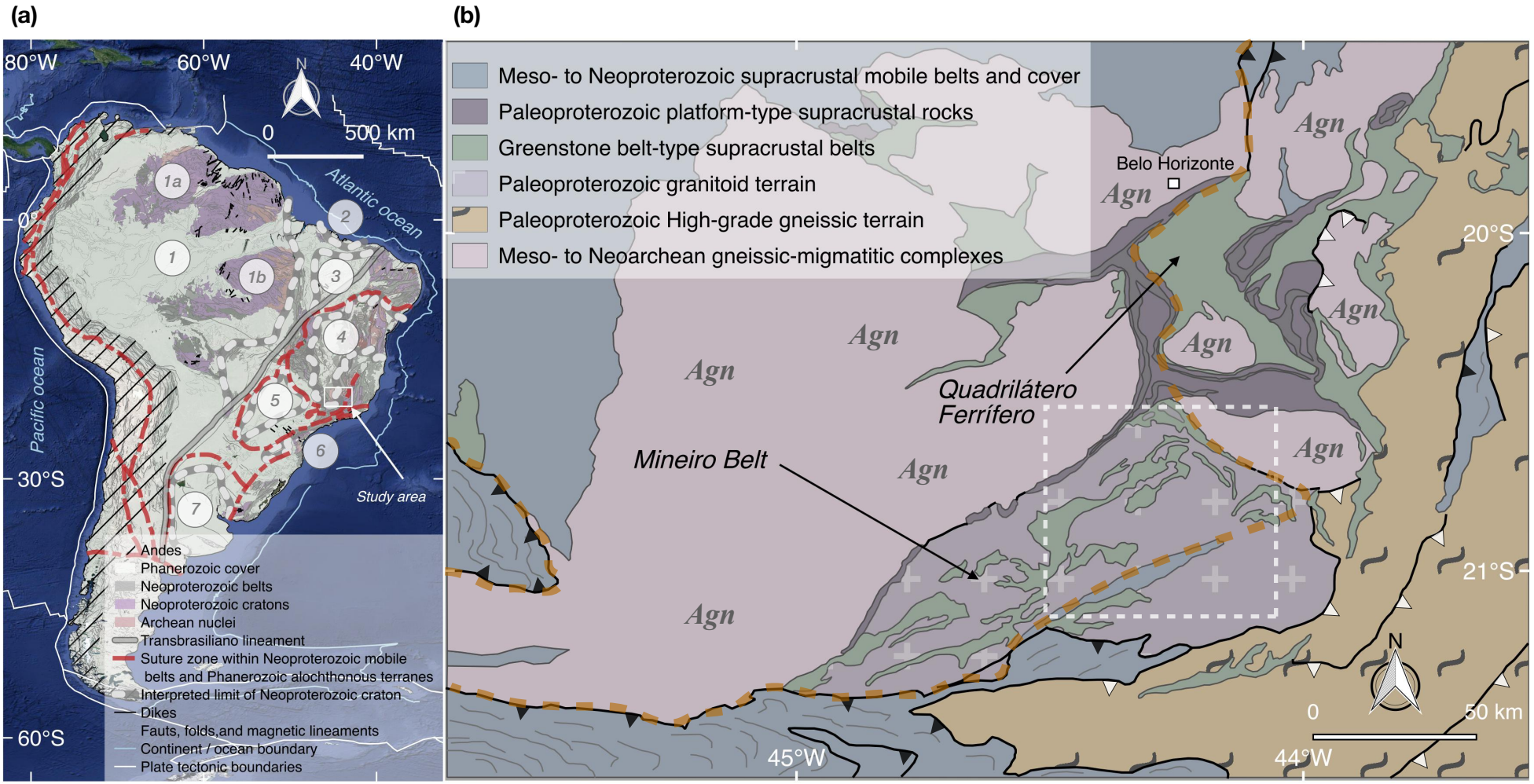


Figure 1.3: Geological and geotectonic context of the study area. (a) Main tectonic elements of South America modified from Cordani et al., (2016). Highlighted cratons*: 1: Amazonas Craton, 1a: Guyana Shield, 1b:Central Brazil Shield; 2: São Luís Craton; 3: Parnaíba Block; 4: São Francisco Craton 5: Paranapanema Block; 6: Luiz Alves Craton; 7: Rio de la Plata Craton*. Geological data from Gómes-Tapias et al., (2019). The white rectangle indicate the location of the study area shown in (b) Simplified geological unities of the South São Francisco Craton and its boundaries modified from Seixas et al., (2012). Highlighted the regions of Quadrilátero Ferrífero and Mineiro Belt. *Agn: Augen gneiss structures*. The orange dashed line marks the interpreted boundaries of Neoproterozoic craton, while the white dashed rectangle defines the local study area shown in the Figure 2.1.

Intermediate to acidic plutonic rocks gave rise to extensive magmatic bodies, known as plutons and suites, that intrude or correlate with Paleoproterozoic NE-SW trending greenstone metavolcanics and locally Mn-rich sedimentary rocks (Pinheiro et al., 2021). Within the northern sector of the Mineiro Belt, granitic rocks provide evidence for distinct episodes of crustal accretion. The 2.35 Ga TTG rocks of the Lagoa Dourada Suite, as documented by Seixas et al. (2012), represent a rare global example of juvenile crust formed during the magmatic quiescence interval (2.4-2.2 Ga). These magmas were formed by melting of 'proto' subducted (or basal-plateau), hydrated Na-rich basaltic rocks in an intra-oceanic environment, as proposed by Moreira et al. (2020). TTG magmas were intensely produced during the Archean, when geodynamics were not fully dominated by subduction-driven forces, limiting extensive plate mobility (Moyen and Laurent, 2018). Around 2.12 Ga, the occurrence of sanukitoid, high-Sr-Ba, and hybrid granitoids from the Alto Maranhão suite (Seixas et al., 2013) and the São Brás-Bombaça and Serra do Camapuã plutons (Moreira et al., 2018) represents a pivotal stage characterized by TTG melting + sediment input + mantle interaction, associated with the onset of "modern" plate tectonics (Moreira et al., 2020). The enriched radiogenic isotopic composition of these TTG, sanukitoid and correlated rocks rules out reworking of an ancient (Archean) crust. Instead, source extraction model (T_{DM}) ages suggest a short-lived crustal evolution with distinct melting episodes within 'ancient' to 'modern' geodynamic scenarios (Moreira et al., 2020; 2023). In addition, 2.20 to 2.18 Ga TTG rocks from the Água Limpa and Casa Grande plutons exhibit a middle radiogenic composition, suggesting melting of a long-lived Archean basaltic source during crustal thinning within a geodynamic scenario resembling a back-arc environment (Moreira et al., 2020).

Several granitic magmatic bodies (e.g., Rio Grande and Brumado, Lajedo, Fé, Gentil, and Macuco de Minas plutons; Cassiterita, Represa de Camargos, and Ritápolis batholiths; Resende Costa and Serrinha-Tiradentes suites) are recognized to the southwest of the above area and tentatively grouped into subsequent accretionary arcs (Cardoso et al., 2019; Teixeira et al., 2008; Silva et al., 2021; Neves et al., 2023; Barbosa et al., 2015, 2019; Teixeira et al., 2015; Ávila et al., 2010, 2014). The isotopic composition of these rocks suggests juvenile crustal inputs from a radiogenic-rich source, occasionally involving mantle/arc interactions and sometimes crustal assimilation processes. However, key structures and lithologies typical of modern arcs (e.g. paired low and high dT/dP metamorphic units, back-arc basins, ophiolites) have never been recognized or described in detail in the literature. In fact, the reconstruction of ancient arcs based only on correlated ages may not provide a reliable picture to visualize orogenic evolution and may lead to misinterpretations. Therefore, we decided not to use the term "arc" to categorize a specific period of magma production, despite the apparent manifestation of "arc-like" compositions [in many cases, such classifications are based solely on the presence of negative Nb-Ta anomalies in primitive mantle-normalized incompatible element diagrams (e.g., Barbosa et al., 2015)]. Instead, we have preferred

to use the term "stages" to refer to major orogenic periods of magma production, regardless of whether they are mantle- or crustal-derived magmas.

The early orogenic stages in the Minero Belt appear to be associated with an ancient tectonic style of TTG magma production by melting of a basaltic pile or stacked slab after its extraction from the mantle, without any interaction with an older crust or input of sediments. Tonalite, trondhjemite, and andesite rocks from the Lagoa Dourada [ca. 2.35 Ga, Seixas et al. (2012); Moreira et al. (2020)] and Serrinha-Tiradentes [2.20 Ga, Ávila et al. (2010, 2014)] suites better represent these magma production periods. Although trondhjemites from the Resende Costa suite have been tentatively correlated with this orogenic stage (Teixeira et al., 2015), their evolved geochemical composition, as well as the core-rim structures observed in zircon grains, rather suggest that these magmas were produced at 2.14 Ga by melting of a more mafic rock from the Lagoa Dourada suite (Moreira et al., 2018).

The subsequent orogenic stage appears to have been mainly shaped by interactions between mantle-derived magmas. Microgranular mafic enclaves and mixing/mingling structures observed in tonalite and diorite rocks from the Alto Maranhão suite [2.13 Ga, Noce et al. (2010); Seixas et al. (2012); Moreira et al. (2020)], São Brás-Bombaça and Serra do Camapuã [2.13 Ga, Moreira et al. (2018)]; Rio Grande and Brumado [2.14 Ga, Cardoso et al. (2019)]; and Macuco de Minas [2.14 Ga, Neves et al. (2023)] plutons are the main petrological witnesses of these mantle-derived magma interactions. These interactions indicate that the recently opened mantle wedge exerted a first-order control on granitic rock production during this period. These are hallmarks of a transitional style between 'ancient' and 'modern' tectonics (Moreira et al., 2020). At this point, occasional basaltic inputs into the lower continental crust may have induced crustal melting during this orogenic stage. Granites s.s. from the Ritápolis and Represa de Camargos batholiths [2.15 Ga (Barbosa et al., 2015), as well as from the Fé and Lajedo plutons [2.17 Ga, Teixeira et al. (2008)], are good candidates to represent crustal-derived magmatism, mainly due to their evolved geochemical compositions. However, the petrology and geochronology of these rocks are less constrained (e.g. Siqueira et al., 2023), and the involvement of sediments in their genesis may have been underestimated.

The final orogenic stages of the Mineiro Belt are not well constrained. While the sedimentary basin inversion of the Minas Supergroup in the Quadrilátero Ferrífero region suggests a soft collision of the Mineiro Belt against the Archean gneissic foreland [< 2.12 Ga, Barbosa et al. (2015); Moreira et al. (2019)], metamorphic overprinting and crystal growth [Moreira et al. (2018); Aguilar et al. (2017)] as well as crustal anatexis (Carvalho et al., 2018) around 2.05 Ga seem to prolong this final stage. The Cupim pluton (which is one of the focuses of this work) seems to be a potential record of this last orogenic stage, as its rocks show mineralogical and whole-rock geochemical affinities with 'modern' collisional sediment-derived leucogranites (e.g. Himalayan leucogranites, cf. Hopkinson et al., 2017; Nabelek, 2019). The petrology of the Cupim pluton and its surrounding

country rocks is the main interest of this thesis and will be detailed in the following chapters, with the aim of understanding and elaborating a comprehensive model that correlates geodynamics and magmatism.

1.4. Major topics, aims, goals and thesis's guidance

The main objective of this Ph.D. thesis is to delineate the crustal and geotectonic evolution during the Archean-Paleoproterozoic transition within the Southern São Francisco Craton by studying the petrogenesis of granitoids located in the northern part of the Mineiro Belt, Minas Gerais State, Brazil. In order to achieve this objective, our attention has been focused on the following main topics:

- *When and how crustal-derived magmas originated and crystallized to form the Cupim Pluton?*
- *Which tectonic model can explain the production of these crustal-derived magmas?*
- *What is the nature of the rocks surrounding the Cupim Pluton?*
- *Can they be related to the TTG-sanukitoid-hybrid suites previously described in the literature?*
- *What are the geodynamic implications of the interaction between the Mineiro Belt and the Archean to Paleoproterozoic terrane of the Quadrilátero Ferrífero region?*
- *How could the accretion of the Mineiro Belt have caused metamorphism and partial melting in both terranes?*

In summary, the specific aims of this thesis can be outlined as follows:

- *Evaluate the geochemical and isotopic composition of magmas in the northern part of the Mineiro Belt;*
- *Improve precision in determining the final period of the Minas Orogen and its accretion onto the Archean terrane.;*
- *Establish petrogenetic models and extend their implications to a global context;*
- *Make connections between geochemical variations and tectonic processes using accessory minerals.*

The forthcoming results are expected to contribute significantly to the understanding of the petrogenesis of granitic rocks during several stages of an orogenic event. Subsequent chapters will outline the development of ideas and the systematic methodology used to address key issues. These chapters will be consistent with the overarching methodology and will include at least three papers: the first is published, the second is submitted, and the last is in preparation for submission. Each paper (**Chapters 2, 3, and 4**) will provide a comprehensive account of the specific methodologies used. However, a general methodology is outlined in the following section. The study's findings are outlined in **Chapter 5**, and recommendations for future research are detailed in **Chapter 6**.

1.5. Methodology

Sample rocks (~3-10 Kg) were collected during two field campaigns (August 2021 and Mars 2022), and their precise location (UTM system) and field relationships are included in the Appendix material. 50 × 30mm polished thin sections were prepared at the Universidade Federal de Ouro Preto (UFOP) and the Université Clermont-Auvergne (UCA) for selected and lithologically representative samples using classical sawing, thinning and polishing techniques. Some rock fragments were mounted in epoxy resin and polished for further in situ mineral analysis. Twelve visually unaltered samples were prepared using crushing and grinding techniques (jaw crusher, tema mill) at the Universidade Federal de Ouro Preto for whole rock geochemical analyses. Heavy minerals were concentrated at the Laboratório de Análises Minerais LAMIN-Caeté of the Geological Survey of Brazil (CPRM) in Caeté (Brazil) and at the Université Clermont-Auvergne using panning, sieving and dense liquid (pure bromoform) and magnetic (Hand-imam and Frantz) separation techniques. In the final concentration process, we obtain three grain size fractions (60-80 #, 80-120 #, 120-200 #, i.e. 250-177 μm, 177-125 μm, 125-74 μm, respectively) for each sample. For each grain size fraction, five Frantz magnetic fractions (0.3, 0.5, 0.75, 1A, and nonmagnetic) were established. All thin sections and concentrated samples prepared in Brazil, as well as small rock fragments, were transported by air to France. All the following techniques, except the energy dispersive spectroscopy (EDS) analyses, were carried out at the *Laboratories Magmas et Volcans (LMV), Université Clermont-Auvergne*, in France.

Zircon, apatite, preferably from the non-magnetic sample fraction, and titanite grains were identified using a binocular and polarized microscope. Zircon and apatite grains were hand selected, embedded in epoxy resin, and carefully polished to reveal their intricate interiors. Subsequently, the zircon, apatite, and titanite grains were imaged [cathodoluminescence (CL) and backscattered electron (BSE)] using a scanning electron microscope (SEM) before (for zircon) and after (for apatite and titanite) the analytical sessions began. The following in situ analyses in titanite were performed on the polished thin sections.

We have used established and widely accepted methodologies, which are meticulously described in each chapter according to the required approach. Subsequent subchapters provide a comprehensive overview of the methodological limitations, laboratory reproducibility, and analytical nuances for each technique employed. In addition, the contribution of each method to the evaluation and geological interpretation of the samples analyzed is briefly outlined.

1.5.1. Petrography and mineralogy

Major and minor mineralogy and (micro)structural textures were observed macroscopically (hand specimens) and by transmitted and reflected light microscopy using different magnification objectives. Single and double polarized images of thin sections were obtained with the ZEN Digital Imaging for Light Microscopy (RRID:SCR_013672) and Leica Application Suite X

(RRID:SCR_013673) at the Universidade Federal de Ouro Preto and LMV, respectively. Observations were quantified in the form of modal analyses, an inventory of primary and secondary minerals, their microstructure, state of alteration and inter/intra crystal relations, and an inferred crystallization sequence, observing the order of growth and/or fractionation of solid phases. The classical QAPF diagram (Streckeisen, 1976) was used to classify plutonic rocks [M< 90, where M is an index of mafic and related minerals, e.g., mica, amphibole, pyroxene, olivine, opaque minerals, accessory minerals (e.g. zircon, apatite, titanite), epidote, allanite, garnet, melilite, monticellite, primary carbonate] according to the recommendations of the International Union of Geological Sciences, Subcommission on the Systematics of Igneous Rocks, provided in Le Maitre (2002).

Selected representative thin sections and rock fragment mounts were previously carbon coated prior to SEM/EDS analyses performed at the *Laboratório de Microanálises (Lmic)* of the *Universidade Federal de Ouro Preto*. Three analytical sections (August 24, 25, and 26, 2022) were performed using a SEM model JSM-6510 (JEOL) coupled with a Pentafex-INCA EDS detector (Oxford Instruments) and a SEM model JSM-6010 (JEOL) coupled with an EDS spectrometer designed by JEOL. The backscattered electron (BSE) images were obtained using a tungsten filament type apparatus under high vacuum conditions, 20 kV acceleration voltage, and maintaining a 15 mm or 11 mm working distance. Non-destructive EDS analyses were performed using Aztec software and a standard EDS software package on Oxford and JEOL instruments, respectively. Each analysis was completed within one minute, with manual identification of element spectra during data collection. Energy intensities of identified elemental spectra were converted to normalized percentages and reported in their oxide forms (SiO_2, TiO_2, Al_2O_3, CaO, MgO, FeO^t, MnO, Na_2O, K_2O, P_2O_5). Zr, REE and Y were semi-quantified in their oxide forms when element-rich (e.g. monazite, xenotime, zircon) minerals were analyzed. Mineral identification was based on oxide compositions within the ranges listed in Deer et al. (2013).

1.5.2.Whole-rock major and trace element analyses

The chemical compositions of homogenized rock powder samples were analyzed by X-ray fluorescence (XRF) and inductively coupled plasma spectrometry (ICP-OES and ICP-MS) at SGS Geosol Laboratórios Ltda., Vespasiano, Brazil, and at LMV and *Service d'Analyse des Roches et des Minéraux (SARM*) of the *Centre de Recherches Pétrographiques et Géochimiques (CRPG)*, Nancy, France. Using different techniques in different laboratories, the reproducibility of the analyses is certified for each (unknown) sample. A summary-comparative table for each analysis performed is provided in the Appendix.

SGS Labs (July 2022) used the lithium meta-borate ($LiBO_2$) and tetra-borate ($LiBO_4$) dissolution method as the analytical reference for ICP-OES (-MS) and XRF techniques, respectively. Loss on ignition (LOI) was determined by gravimetry (>1000 ^oC). Major elements (SiO_2, TiO_2, Al_2O_3, CaO, MgO, Fe_2O3, MnO, Na_2O, K_2O, P_2O_5) and LOI were reported as weight percentages (% wt.) with

detection limits of 0.01% for ICP-OES and XRF techniques (some oxides, such as Al_2O_3, MgO, and Na_2O, have detection limits of 0.1% for XRF technique). Trace elements (Ba, Co, Cs, Cu, Ga, Hf, Mo, Nb, Ni, Rb, Sn, Sr, Ta, Th, Tl, U, V, W, Y, Zn and Zr, and REE) are reported in parts per million (ppm) and often have detection limits below 0.1 ppm. Certified in-house standard reference materials (e.g. SG_142, SG_241, and SG-079) and duplicate unknown samples were used to ensure accuracy and reproducibility of analyses. The major and trace element compositions are within 5% and 10% of the reference values, respectively, and the reproducibility of the duplicate unknown samples is within 5%. Some HREE compositions (e.g. Tb, Tm) for some samples were not detected (<0.05 ppm).

Major elements (and Ba, Sr) were analyzed using the Agilent 5800 ICP-OES, at the LMV, during two sessions (September 2022 and November 2022). Samples were mixed in lithium meta-borate [~0.3 g (±10%)], heated (>1100 ^{o}C), diluted in HNO_3 (~7 $mol.L^{-1}$) and filtered with demineralized water (~18 $\Omega.cm^{-1}$). DR-N (diorite) and BHVO-1 (basalt) certified reference materials (Flanagan, 1986) were used to estimate the precision and accuracy of the analyses. Almost all major element concentrations are within 1.6% (RSD, n=3) of the reference materials; MnO (~4.5%) and P_2O_5 (~6.6%) concentrations vary more than the other elements due to their very low content (0.22 and 0.25, respectively). To certify the reproducibility, two unknown samples were analyzed twice during two separate sequences. The duplicated analyses do not differ more than 5%, except for CaO (~7%) to the first duplicated sample and MgO (~13%) and TiO_2 (~7%) to the second. However, CaO, MgO and TiO_2 have low concentrations (<1% by weight). All results are shown in the **Appendix**.

Trace element compositions [As, Ba, Be, Bi, Cd, Co, Cr, Cs, Cu, Ga, Ge, Hf, In, Mo, Nb, Ni, Pb, Rb, Sb, Sn, Sr, Ta, Th, U, V, W, Y, Zn, Zr, and REE (La, Ce, Pr, Nd, Sm, Eu, Gd, Tb, Dy, Ho, Er, Tm, Yb, Lu)] were determined by SARM using an ICP-MS iCapQ instrument. The analytical protocol is exactly the same as that used for the samples analyzed at LMV. The uncertainty (calculated for 200 mg of prepared sample) of the analyses for each element analyzed is a function of its concentration and is always less than 20%. The detection limits for each element and the detailed data are given in the **Appendix**. Contrary to the analyses carried out in Brazil, all HREE concentrations were detected in all samples.

In the following chapters, we have decided to use the main contents of the samples performed at the LMV and the trace element concentrations determined at the SARM, due to the higher precision and accuracy of the analyses. Nevertheless, SGS Lab analyses have been used wherever possible to certify and compare the selected analyses.

1.5.3.U-Th-Pb geochronology

The great advantage of using the U-Th-Pb over other geochronological methods (e.g., $^{40}Ar/^{39}Ar$ and K-Ar, Sm-Nd, Rb-Sr, Re-Os, U/Th-He) is that it is based on three different radiogenic clocks (^{238}U-^{206}Pb, ^{235}U-^{207}Pb, and ^{232}Th-^{208}Pb) that can be analyzed, and checked, simultaneously (Schoene, 2014; Spencer et al., 2016). The isotopic equations of the final parent-daughter decays (see Dickin, 2005; Faure and Mensing, 2005) are presented below:

$$^{238}U \rightarrow {}^{206}Pb + 8\alpha + 6\beta^- + Q;\ \lambda_{238} = 1.55125 \times 10^{-10}\ year^{-1} \quad (1.1)$$

$$^{235}U \rightarrow {}^{207}Pb + 7\alpha + 4\beta^- + Q;\ \lambda_{235} = 9.8485 \times 10^{-10}\ year^{-1} \quad (1.2)$$

$$^{232}Th \rightarrow {}^{208}Pb + 6\alpha + 4\beta^- + Q;\ \lambda_{232} = 4.9475 \times 10^{-11}\ year^{-1} \quad (1.3)$$

α is an alpha particle, β is a beta particle, and Q is energy released during the decay.

In addition, the advent and gradual improvement of inductively coupled plasma mass spectrometry techniques linked to a laser ablation systems (LA-ICP-MS) revolutionized the application of the method to the extent of that minor domains of accessory minerals could be analyzed in a short-time related and relatively less expensive analysis (Košler and Sylvester, 2003). Furthermore, the free access to good reference materials (mineral and synthetic standards) between different isotope laboratories around the world has improved the robustness of the geochronological method.

U-rich minerals (e.g., zircon, apatite, titanite) are particularly advantageous for geochronology due to the Pb detected being a consequence of radiogenic decay, distinguishing it from Pb integrated at the time of crystallization (common Pb). When common Pb is present, a viable correction for common Pb is feasible. For instance, the utilization of the non-radiogenic ^{204}Pb isotope based on a comprehensive bulk-Pb evolutionary model (Stacey and Kramers, 1975) allows for such corrections. However, zircon hardly incorporates Pb into its crystal lattice during crystallization (Hoskin and Schaltegger, 2003). Ages used for Pb corrections would have to be assumed, which could bias the interpretation, and so we decided not to apply this correction to the U-Th-Pb analyses on zircon.

In the context of this thesis, zircon grains investigated in the two papers (**Chapters 2, and 3**), employing LA-ICP-MS techniques, displayed ^{204}Pb counts consistent with background levels. Actually, when ^{204}Pb signals were detected above the background, the ablation was aborted at the beginning of the analysis so that another site could be investigated and the analysis time optimized. Moreover, analyses with ^{204}Pb signals above background levels were lately filtered and discarded using reduction data software (e.g. *Iolite4*; Petrus and Kamber, 2012; Paton et al., 2011).

In the third paper (**Chapter 4**), the U-Th-Pb geochronology of titanite and apatite, when influenced by common Pb, underwent corrections based on ^{207}Pb and ^{208}Pb contents using an in-

house spreadsheet developed by the PhD candidate at LMV, Julie Mallens. Julie Mallens, who will also contribute as a coauthor to this paper, conducted a comprehensive research during her PhD exploring diverse techniques (e.g., U-Th-Pb, Rb-Sr isotopes) applied to apatite grains from the Western Dharwar Craton, in India (Guitreau et al., 2017; Jayananda et al., 2023). Her thesis is also supported by Dr. Régis Doucelance and Dr. Martin Guitreau. Detailed tables used for the common Pb corrections are provided in the Appendix for reference.

The investigative approach encompassed high-quality imaging [via cathodoluminescence (CL) and back-scattered electrons (BSE) techniques] and spatial resolution (laser ablation system), crucial for in situ analyses targeting specific domain of the grains. Only zircon grains were imaged at the LMV during two sessions in October 2022 using a Jeol JSM-5910LV scanning electron microscope. All CL and BSE images for each sample are organized in the Appendix. Unfortunately, the LMV's SEM was broken in December 2022 until the end of the internship abroad in France and we couldn't image the apatite and titanite grains. This imaging has further carried out at the DEGEO facilities. LA-ICP-MS technique was performed at the LMV during several sessions (November and December 2022, February and June 2023) using a 193nm Resonetics Resolution M-50E laser ablation system coupled to a Thermo Scientific Element XR ICP-MS. Analytical conditions is provided in the **Appendix**. Details about precision and accuracy, as well as the used reference materials, for each session and for each accessory mineral chosen, is described in the following paragraphs.

This methodology proved instrumental in unveiling the intricate historical evolution of the samples under study. Textural evidence combined with age between several accessory minerals suggests that they denote crystallization and/or metamorphic ages pertinent to a complete petrochronology investigation of high-temperature rocks.

Zircon grains were carefully hand-picked using a binocular microscope, embedded in an epoxy resin, and polished until unveil theirs internal structures, before SEM imaging. SEM images allowed the characterization of the zircon textures and assisted to the location of 33µm spot analyses. During the LA-ICP-MS analytical sessions, 91500, Plešovice, and AS3 zircon reference materials (Wiedenbeck et al., 1995; Sláma et al., 2008; Schmitz et al., 2003) were used as primary and secondary standards, in order to correct the ablation inferences and equipment drift, and to double-check the age reproducibility, respectively. Calculated Concordia, Upper intercept, and Weighted Mean $^{207}Pb/^{206}Pb$ ages of reference materials yield standard errors (2SE) between 1 and 5% and are consistent with the accepted ages (Table 1.1). The use of the same reference materials during several analytical sessions proved the reproducibility of the analyses, in which the calculated ages did not vary by more than 3% (**Table 1.1**).

Table 1.1: Summary of ages obtained for reference materials (*Standard zircon*) using LA-ICP-MS system hosted in LMV. Details about equipments and analytical conditions are provided in the text. *Weighted Mean Average* refers to $^{207}Pb/^{206}Pb$ ages; *n* is the total of analyses performed for each reference material during each analytical session.

Standard zircon	Accepted age	November 24, 2022	November 28, 2022	December 8, 2022	December 12, 2022	December 15, 2022	February 16, 2023
91500	**1065 Ma Wiedenbeck et al., (1995)**	*As primary* Conc. Age 1063.63 ± 8.30 Ma (2SE, n=16) Conc. Age 1062.84 ± 4.46 Ma (2SE, n=27)	*As primary* Conc. Age 1062.58 ± 3.10 Ma (2SE, n=24) Conc. Age 1062.88 ± 2.94 Ma (2SE, n=12)	*As secondary* Conc. Age 1072.7 ± 12.8 Ma (2SE, n=5)	*As secondary* Weighted Mean Average 1067.9 ± 28.3 Ma (2SE, n=9)	*As secondary* Conc. Age 1059.1 ± 12.0 Ma (2SE, n=4)	*As secondary* Weighted Mean Average 1051.3 ± 21.9 Ma (2SE, n=5)
Plešovice	**337 Ma Sláma et al., (2008)**	*As secondary* Conc. Age 348.67 ± 8.24 Ma (2SE, n=3) Conc. Age 340.98 ± 3.82 Ma (n=5)	*As secondary* Weighted Mean Average *349.4 ± 24.9 Ma (6/6)* Weighted Mean Average *348.8 ± 22.1 Ma (2SE, n=2)*	*As primary* Conc. Age 337.18 ± 2.31 Ma (2SE, n=24)	*As primary* Conc. Age 337.22 ± 1.62 Ma (2SE, n=40)	*As primary* Conc. Age 337.23 ± 2.52 Ma (2SE, n=16)	*As primary* Conc. Age 337.07 ± 1.24 Ma (2SE, n=20)
AS3	**1099.1 ± 1.2 Ma Schmitz et al., (2003)**	*As secondary* Conc. Age 1105.5 ± 16.9 Ma (2SE, n=4) Conc. Age 1119.50 ± 9.90 (2SE, n=6)	*As secondary* Weighted Mean Average 1115.8 ± 22.4 Ma (2SE, n=5) Weighted Mean Average 1085.2 ± 14.8 Ma (2SE, n=3)	*As secondary* Weighted Mean Average 1084.6 ± 31.0 Ma (2SE, n=6)	*As secondary* Upper intercept Age 1105.0 ± 20.9 Ma (2SE, n=10)	*As secondary* Weighted Mean Average 1104.4 ± 36.6 Ma (2SE, n=4)	*As secondary* Weighted Mean Average 1087.0 ± 15.5 Ma (2SE, n=5)

Apatite grains were also hand-pick selected, mounted in epoxy resin, and well-polished to revel their internal structures at the LMV. For the LA-ICP-MS analysis at the LMV, a suite of apatite reference materials including MAD1, Kovdor, Sumé1, BRZ1, and Slyudyanka (Thompson et al., 2012; Amelin et al., 2002; Lana et al., 2022; Apen et al., 2022; Chew et al., 2011) was employed to calibrate the instrument's performance and verify analytical quality. Ablation spot analyses, using a 40 µm diameter, were conducted at several sites within the grains from the unknown samples, wherever spatially feasible. Moreover, the locus of U-Th-Pb spots was strategically done to reserve adequate space for subsequent LA-ICP-MS trace element analysis. Corrections for common lead were implemented based on the ^{208}Pb and ^{206}Pb contents, yielding better consistency in reproducing similar $^{206}Pb/^{238}U$ and $^{208}Pb/^{232}Th$ ages. This correction was uniformly applied across all unknown samples. The calculated ages for the apatite reference materials exhibit variations within 5% of the published values, except for Slyudyanka apatite (~18%), while aligning closely with the established uncertainties (see **Table 1.2**). Discrepancies between these calculated ages and the literature-accepted values likely stem from the chemical heterogeneity observed in the

reference materials. Preferentially, the calculated ages are presented in Tera–Wasserburg diagrams. Additionally, Stacey-Kramers Concordia projection ages are depicted for comparative analysis.

Table 1.2: Summary of ages obtained for reference materials (standard apatite) using LA-ICP-MS system hosted in LMV. *Concordia age* were calculated following Stacey-Kramers Concordia projection; *n* is the total of analyses performed for each reference material during each analytical sequences.

Standard apatite	Accepted age	February 17, 2023 Sequence 1	Sequence 2
MAD	**474.25 ± 0.41 Ma (Thomson et al., 2012)**	*As primary*	*As primary*
		Lower intercept age 470.8 ± 2.1 Ma (2SE, n=22)	Lower intercept age 476.4 ± 5.8 Ma (2SE, n=26)
		Concordia age 473.29 ± 0.76 Ma (2SE, n=22)	Concordia age 473.87 ± 0.70 Ma (2SE, n=26)
Kovdor	**377.5 ± 3.5 Ma (Amelin et al., 2002)**	*As secondary*	*As secondary*
		Lower intercept age 357 ± 15 Ma (2SE, n=5)	Lower intercept age 393.6 ± 8.5 Ma (2SE, n=6)
		Concordia age 397.63 ± 0.93 Ma (2SE, n=5)	Concordia age 383.02 ± 0.79 Ma (2SE, n=26)
Sumé 1	**568.0 ± 3.1 Ma (Lana et al., 2012)**	*As secondary*	*As secondary*
		Lower intercept age 544 ± 13 Ma (2SE, n=5)	Lower intercept age 586.9 ± 5.3 Ma (2SE, n=6)
		Concordia age 574.8 ± 1.3 Ma (2SE, n=5)	Concordia age 573.7 ± 1.2 Ma (2SE, n=6)
BRZ 1	**2078 ± 12 Ma (Apen et al., 2022)**	*As secondary*	*As secondary*
		Lower intercept age 2077 ± 49 Ma (2SE, n=6)	Lower intercept age 1885 ± 120 Ma (2SE, n=6)
		Concordia age 2044.3 ± 2.4 Ma (2SE, n=6)	Concordia age 2030.4 ± 2.1 Ma (2SE, n=6)
Slyudyanka	**450 ± 15 Ma (Chew et al., 2011)**	*As secondary*	*As secondary*
		Lower intercept age 482 ± 90 Ma (2SE, n=5)	Concordia age 413.86 ± 0.55 Ma (2SE, n=6)
		Concordia age 422.82 ± 0.58 Ma (2SE, n=5)	

Titanite grains were identified in the thin sections of some samples under microscope at the LMV, and were characterized for their textures and mineral-associations. The thin sections were polished before were taken directly into the LA-ICP-MS system. During the U-Th-Pb sessions we have used MKED1 (Spandler et al., 2016) as primary titanite reference material, and Khan , BLR1, and TH-Bear Lake as secondary standards (Ma et al., 2019; Aleinkoff et al., 2007; Fisher et al., 2020). MKED1 titanite reference material have negligible common Pb, therefore no common Pb correction

was applied nor propagated to the unknown samples. The obtained Concordia ages for reference materials agree within uncertainties (<2%) with the published values (**Table 1.3**). The ages obtained for TH-Bear Lake (as secondary standard) vary more than those presented in the literature, probably due to its chemical heterogeneity (Fisher et al., 2020). The reproducibility of the analyses was verified when similar ages (within uncertainties) were obtained during different sessions. Ages obtained for the unknown samples are preferentially plotted in Concordia and/or Tera–Wasserburg diagrams.

Table 1.3: Summary of ages obtained for reference materials (standard titanite) using LA-ICP-MS system hosted in LMV. *2SE* refers to 2×standard error; *n* is the total of analyses performed for each reference material during each analytical session.

Standard titanite	Accepted age	June 5, 2023 Sequence 1	Sequence 2	Sequence 3
MKED1	**1517.32 ± 0.32 Ma** **Spandler et al., (2016)**	*As primary* Conc. Age 1516.74 ± 6.93 Ma (2SE, n=16)	*As primary* Conc. Age 1516.86 ± 4.03 Ma (2SE, n=6)	*As primary* Conc. Age 1516.8 ± 14.0 Ma (2SE, n=14)
Khan	**518 ± 2 Ma** **Ma et al., (2019)**	*As secondary* Conc. Age 518.17 ± 3.82 Ma (2SE, n=8)	*As secondary* Conc. Age 527.20 ± 12.90 Ma (2SE, n=2)	*As secondary* Conc. Age 529.74 ± 8.59 Ma (2SE, n=6)
BLR1	**1047.1 ± 0.4 Ma** **Aleinikoff et al., (2007)**	*As secondary* Conc. Age 1047.1 ± 10.5 (2SE, n=4)	*As secondary* Conc. Age 1042.88 ± 3.90 Ma (n=1)	*As secondary* Conc. Age 1055.4 ± 22.4 Ma (2SE, n=3)
TH-Bear Lake	**1039 ± 23 Ma** **Fisher et al., (2020)**	*As secondary* Conc. Age 1057.9 ± 20.2 Ma (2SE, n=3)	*As secondary* Conc. Age 1093.09 ± 4.27 Ma (n=1)	*As secondary* Conc. Age 1081.7 ± 22.9 Ma (2SE, n=3)

1.5.4.Zircon Hf and Silicon isotope measurements

Combining radioactive and stable isotopes is the 'cutting-edge' method to trace the main sources of magmatic rocks and to constrain their tectonic environments of emplacement (e.g. Hawkesworth and Kemp, 2006; Kemp et al., 2007; Albert et al., 2016; Couzinié et al., 2016; Wang et al., 2016; Hopkinson et al., 2017; Moreira et al., 2020). While long-lived radioactive isotope pairs [e.g. ^{147}Sm-^{143}Nd (parent half-life ~106 billion years), ^{176}Lu-^{176}Hf] preserve the original composition of the source reservoir during magma extraction and crystallization, the composition of stable isotopes (e.g. O, Si, S, Mg and Ti) can restrict the nature of the source material, as long as the processes that generate its fractionation are well-understood and variations in concentration of the main known reservoirs are established. Although isotopic concentrations can be assessed from whole rock samples, advancements in dissolution and micro-sampling techniques (e.g., S- or LA-MC-ICP-MS and SIMS) for analyzing key minerals — particularly those abundant in radioactive or stable elements — have significantly bolstered detailed and precise investigations. This is

particularly notable in the granitic hosted accessory minerals, such as zircon, apatite, titanite, rutile, and garnet (see in Volante et al., 2022; Jung et al., 2022). In the second and third chapters of this thesis, Hf and Si isotopic concentrations of zircons from the selected samples were analyzed via LA-MC-ICP-MS at the LMV, Université Clermont Auvegne, France, during four analytical sessions (February and March 2023). The analytical conditions of the equipments used are provided in the **Appendix material**.

^{176}Hf is the product of the decay of ^{176}Lu with a half-life of ca. 37.2 Ga (Scherer et al., 2001; Söderlund et al., 2004). During the melting of spinel and garnet peridotite, Hf demonstrates higher incompatibility compared to Lu, resulting in its enrichment within crustal reservoirs. The process of crust extraction from the mantle consequently yields a continental crust with a low Lu/Hf ratio. This crustal composition evolves towards a lower ^{176}Hf/^{177}Hf ratio over time. Simultaneously, a depleted mantle with a high Lu/Hf ratio develops, showcasing a progressively more radiogenic Hf isotope signature, i.e., high ^{176}Hf/^{177}Hf (Kemp and Hawkesworth, 2014). The Hf isotope systematics present an analogous framework to the commonly employed whole-rock ^{147}Sm–^{143}Nd systematics, yet with Hf isotopes decaying three times faster, potentially offering enhanced resolution in tracing crust–mantle differentiation process. The Hf isotope compositions of significant crustal (Vervoort and Patchett, 1996; Vervoort and Blichert-Toft, 1999), and mantle (Chauvel and Blichert-Toft, 2001; Dhuime et al., 2011; Iizuka et al., 2013) reservoirs have been extensively characterized. While the Hf isotope composition of chondritic meteorites is well constrained (refer to Bouvier et al., 2009), the 'Chondritic Uniform Reservoir' (CHUR; Iizuka et al., 2015) is often used as a suitable reference for assessing bulk silicate Earth differentiation. Indeed, the ε_{Hf} notation is a deviation composition of a zircon grain from a chondritic reference (CHUR), calculated as follow in the **Equation 1.4**:

$$\varepsilon_{Hf(t)} = \{ [(^{176}Hf/^{177}Hf)_t{}^{zircon} / (^{176}Hf/^{177}Hf)_t{}^{CHUR}] - 1 \} \times 10^4 \qquad (1.4)$$

Whereas t is the assumed crystallization age of the magma. Positive $\varepsilon_{Hf(t)}$ values are more enriched in radiogenic Hf composition compared to CHUR, indicating juvenile additions to the crust. While negative $\varepsilon_{Hf(t)}$ values are less enriched in radiogenic Hf composition than CHUR and represents the crustal reworking of a long-lived old crust. Tentatively, $\varepsilon_{Hf(t)}$-time arrays indicate the Lu/Hf composition of the source material [e.g., mafic (Lu/Hf~0.02) and felsic (Lu/Hf~0.01) precursors], as well as crustal evolution process (Vervoort et al., 2000; Blichert-Toft and Albarède, 2008; Guitreau et al., 2012; Laurent et al., 2015). **Figure 1.4** illustrates a typical $\varepsilon_{Hf(t)}$ versus age diagram, showcasing the intricate nature of interpreting radiogenic Hf compositions.

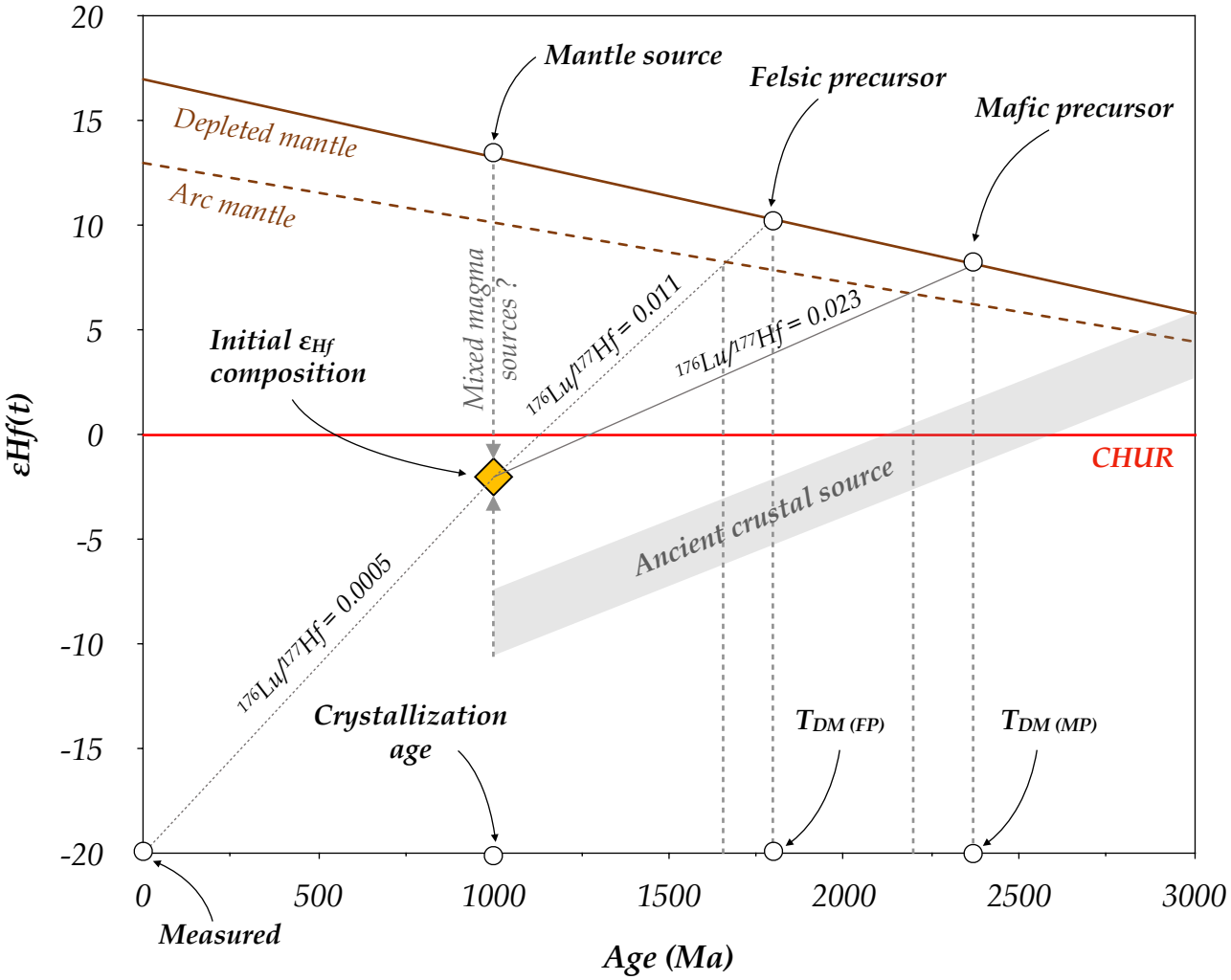


Figure 1.4: Conceptual ε_{Hf} space diagram of a magmatic rock and speculative interpretations of source material and processes. Arc and depleted mantle lines are delineated through recent compositions provided in Dhuime et al., 2011 and Chauvel and Blichert-Toft, 2001. CHUR line represents the 'Chondritic Uniform Reservoir' value (after Iizuka et al., 2015). Also displayed is the effect of mixing process between the depleted mantle and a hypothetical ancient crustal lithology. Values of 0.011 and 0.023 refer to $^{176}Lu/^{177}Hf$ characterizing the slopes of theoretical felsic and mafic precursor evolutions, respectively. T_{DM} ages refer to the calculated model age for each source precursors, (FP) is a felsic precursors, and (MP) is a mafic precursor.

Zircon stands out as a particularly advantageous mineral for assessing Hf compositions due to its elevated Hf concentrations (ranging between 0.5-2 wt%). This characteristic translates into low Lu/Hf ratios (typically <0.002), thereby safeguarding the original $^{176}Hf/^{177}Hf$ ratios established during the rock's crystallization time (Patchett, 1983; Kinny and Maas, 2003). Over recent years, various methodologies have been developed to enhance the precision of Hf isotope measurements. These techniques address concerns related to mass bias fractionation, isobaric interferences (primarily stemming from ^{176}Yb), and the identification of disturbances and artifacts within the signatures. These advancements aim to rectify misinterpretations and discrepancies in calculated model ages, thereby bolstering the reliability of interpretations (Stevenson and Patchett, 1990; Chu et al., 2002; Segal et al., 2003; Gerdes and Zeh, 2009; Ickert, 2013; Fisher et al., 2014; Guitreau and Blichert-Toft, 2014; Kemp and Hawkesworth, 2014; Vervoort and Kemp, 2016; Spencer et al., 2020).

We have performed Lu-Hf analyses in zircon crystals during two analytical sessions (February 2023) at LMV using the same laser ablation system used in U-Th-Pb analyses but coupled with a Thermo Scientific Neptune Plus MC-ICP-MS. To ensure precise correlation between U-Pb ages and the associated Hf isotope signatures, Lu-Hf analyses were conducted using 47μm spots strategically positioned on the top pits from prior U-Th-Pb analyses, or nevertheless in the same zircon domain. The analysis sequence was bounded by the synthetic REE-absent MUN zircon standard (MUN-0; Fisher et al., 2011). Among the zircon reference materials analyzed as unknowns were 91500, MudTank, and three synthetic MUN zircons (MUN-1, MUN-3, and MUN-4), exhibiting low, medium, and high Yb/Hf ratios, respectively. These standards served as benchmarks to oversee the fidelity of our data processing methodology. A recalibration of the $^{176}Hf/^{177}Hf$ ratios was undertaken by aligning them with the observed offset in the $^{178}Hf/^{177}Hf$ ratios in relation to natural values. The average $^{176}Hf/^{177}Hf$ composition obtained for all the zircon reference materials (**Table 1.4**) agrees with uncertainty with the published and accepted values in the literature (Blichert-Toft, 2008; Woodhead and Hergt, 2005; Fisher et al., 2011).

Silicon is the third most abundant element in the Earth [17.1 ± 0.2 wt.% Si; (Allègre et al. 2001)], and exhibits three naturally occurring stable isotopes, characterized by the subsequent mean abundances as documented by Debievre and Taylor (1993): ^{28}Si (92.23%), ^{29}Si (4.67%), and ^{30}Si (3.10%). Enhancements in precision and accuracy achieved through Gas Source, Solution or Laser Ablation Multi-collector Inductively Coupled Plasma Mass Spectrometry (GS-, S- or LA-MC-ICP-MS) and Secondary Ion Mass Spectrometry (SIMS) have significantly propelled progress in diverse applications of Si isotopes within planetary and Earth sciences, as well as in biological and environmental studies (see Poitrasson et al., 2017). Due to the higher precision in measuring isotopic ratios between samples compared to determining their absolute abundances through stable isotope mass spectrometry, silicon stable compositions are frequently expressed using the delta notation. The $\delta^{29}Si$ and $\delta^{30}Si$ values represent the deviation in per mil relative to standard $^{29}Si/^{28}Si$ and $^{30}Si/^{28}Si$ ratios in a sample concerning that of a standard as follow in the **Equations 1.5 and 1.6**:

$$\delta^{29}Si\ (‰) = \{ [(^{29}Si/^{28}Si)_{sample} / (^{29}Si/^{28}Si)_{standard}] - 1 \} \times 1000 \qquad (1.5)$$

$$\delta^{30}Si\ (‰) = \{ [(^{30}Si/^{28}Si)_{sample} / (^{30}Si/^{28}Si)_{standard}] - 1 \} \times 1000 \qquad (1.6)$$

The established reference material for reporting silicon isotopic data is the silica sand reference material RM 8546, distributed by the National Institute of Standards and Technology (NIST). Due to historical conventions, the equivalent name widely used in literature as well as in the following chapters of this thesis for this standard is NBS28.

Over the past decade, Paul S. Savage and his colleagues at Oxford University, United Kingdom, have undertaken substantial efforts to characterize and comprehend the composition and fractionation processes of terrestrial materials involving silicon isotopes at both low and high temperatures. Savage et al. (2010) established a δ^{30}Si value of the Bulk Silicate Earth (BSE) at -0.29 ± 0.08‰ (2SD) based on mafic and ultramafic rocks worldwide [samples varies from xenoliths from 'modern' continental rifts and arcs, to 'modern' Mid-Ocean Ridge Basalts (MORB) and Island-Arc Basalts (IAB)]. The primary insight is the precise measurement capability of silicon isotopes in Phanerozoic igneous materials, revealing predictable yet minor deviations primarily linked to increasing silica content during magmatic differentiation (Savage et al., 2011; Poitrasson and Zambardi, 2015). The silicon isotope values for the bulk Earth and the narrow, predictable range for 'modern' basalts and granites highlight these variations (Savage et al., 2012; 2014;). Although there are discernible patterns between silica content and Si isotopes (the 'igneous array' after Savage et al., 2011), the key takeaway is the subtle variability in Si isotopes within high-temperature igneous rocks (Savage et al., 2014).

The second significant observation underscores the resilience of silicon isotopes to metamorphism, as evidenced by data from granulite facies xenoliths in the Chudleigh and McBride suites in Queensland, Australia (Savage et al., 2013a). These xenoliths exhibit slight variations in Si isotopes, remaining nearly indistinguishable from their inferred protolith material and consistently aligning with the values for the Bulk Silicate Earth (BSE). This suggests that even in higher-grade facies, Si isotopes maintain resistance to metamorphism. Furthermore, the system displays resistance to hydration, supported by evidence from serpentinized abyssal peridotites (Savage et al., 2013b). The Si isotopes in these rocks closely resemble those in un-serpentinized lherzolites, both hovering around the BSE value, indicating the system's resistance to hydration processes.

The final noteworthy point is the contrasting impact of high-temperature versus surface processes on Si isotopes. While high-temperature processes induce subtle sub-per-mil impacts, surface processes (i.e., low-temperature processes) lead to significantly larger fractionations (see Poitrasson et al., 2017). Notably, two opposing effects dominate the isotope system: clay formation during weathering drives Si isotopes to highly negative values (Georg et al., 2009), while the incorporation of seawater-derived silica pushes values to strongly positive ones (Ziegler et a, 2005; Souza et al., 2014), like oxygen isotopes. This becomes particularly relevant when examining igneous materials, as the inclusion of 'non-igneous' inputs in melts records the Si isotope signatures of these processes. For instance, 'modern' S-type granites exhibit lighter silicon isotope signatures than I- and A-types, reflecting the incorporation of clay-rich sediments in the melt source (Savage et al., 2012). Therefore, the primary objective is to undertake Si isotope measurements in Precambrian igneous rocks with the aim of deciphering whether their signatures can yield valuable insights into the processes responsible for the formation of the ancient

continental crust (e.g., TTG from André et al., 2019; Deng et al., 2019). Additionally, the investigation seeks to draw parallels between these ancient processes and geodynamics and their modern counterparts. **Figure 1.5** visually presents a comprehensive overview of the key insights derived from Si isotope geochemistry.

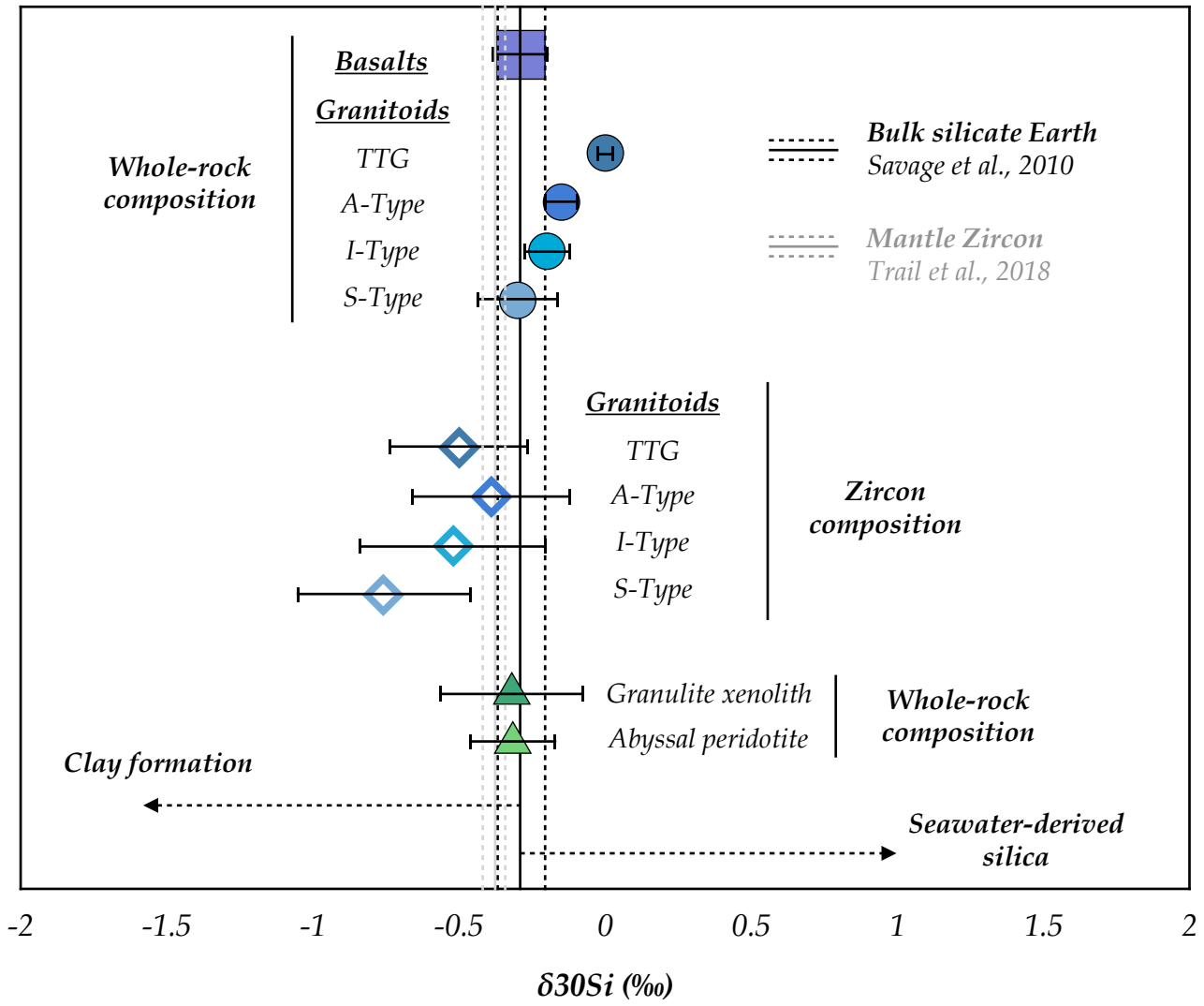


Figure 1.5: NBS28-normalized δ^{30}Si values from whole-rock composition of high temperature rocks (after Savage et al., 2014; André et al., 2019; Deng et al., 2019). Zircon δ^{30}Si values from different granitic rocks from Guitreau et al. (2022). Granulite xenolith and abyssal peridotite compositions from Savage et al. (2013a, 2013b). Dashed arrows indicate the effects of clay formation and sea-derived silica incorporation low-temperature process (see Poitrasson et al., 2017).

Recently, Guitreau et al. (2020) established a novel protocol for Si isotope measurements in zircon using LA-MC-ICP-MS techniques, providing a within-run error on zircon δ^{30}Si of approximately ~0.10–0.15‰ (2SE) and external precision of ~0.15–0.30‰ (2SD). This method aligns well with results obtained through S-MC-ICP-MS or SIMS (Trail et al., 2018). Furthermore, Guitreau et al. (2022) demonstrated that δ^{30}Si values in zircon can exhibit significant variations within a zircon population of a single sample and between granites of the same type or different types (e.g., TTG, A-type, I-type, and S-type, see **Fig. 1.5**). These variations arise from differences in zircon crystallization temperatures and parental magma SiO_2 contents, with the latter mirroring the fractionation observed in whole-rock compositions of granitic rocks (Savage et al., 2012). As a result, zircon δ^{30}Si serves also as a reliable proxy for magma evolution. It is important to note that secondary processes, such as metamorphism and alteration/weathering, may impact zircon δ^{30}Si values. However, these influences can be readily identified through examination of zircon internal textures using BSE/CL images and trace-element geochemistry, as delineated by Guitreau et al. (2022).

The Si isotope analyses conducted in this thesis during three analytical sessions in February 2023 at LMV using the same LA-MC-ICP-MS system used for Lu-Hf analyses, adhered to the protocols and instrument conditions as outlined by Guitreau et al. (2020, 2022), with the only deviation being the use of 47 μm of diameter ablation spots instead of ablation lines. Nevertheless, all analytical conditions are specified in the **Appendix**.

Unknown zircon samples were calibrated for instrumental fractionation using a standard-sample-standard bracketing protocol, using Plešovice zircon as the standard. MudTank and Mun-1 zircons were employed as quality control checks. The conducted measurements resulted in a within-run error on zircon δ^{30}Si ranging between 0.10 and 0.18‰ (2SE), with an average external precision of 0.23‰ (2SD). The δ^{30}Si values obtained for the zircon reference materials are in agreement within the associated uncertainty with those reported in the literature using S- or LA-MC-ICP-MS techniques (Trail et al., 2018; Guitreau et al., 2020, 2022; see **Table 1.4**). Additionally, the co-variation of δ^{29}Si and δ^{30}Si values for all analyzed zircons closely aligns with the equilibrium and kinetic mass-dependent fractionation lines (0.5178 and 0.5092, respectively).

Table 1.4: Summary of average isotopic composition obtained for reference materials (standard zircon) using LA-MC-ICP-MS system hosted in LMV. *2SE* and *2SD* refers to 2×standard error and 2×standard deviation, respectively; *n* is the total of analysis performed for each reference material during all analytical sessions.

Standard zircon	Accepted $^{176}Hf/^{177}Hf$ values	February 24 and 27, 2023	Accepted $\delta^{30}Si$ values	February 27, 28 and 29, 2023
91500	**0.282308 ± 0.000006 (Blichert-Toft, 2008)**	*As secondary* 0.282310 ± 0.000015 (2SE, n=8)		
MudTank	**0.282507 ± 0.000006 (Woodhead and Hergt, 2005)**	*As secondary* 0.282516 ± 0.000011 (2SE, n=8)	***LA-MC-ICP-MS*** **-0.38 ± 0.23‰ (Guitreau et al., 2022)** ***S-MC-ICP-MS*** **-0.34 ± 0.03 ‰ (Trail et al., 2018)** **-0.47 ± 0.17 ‰ (Guitreau et al., 2020)**	*As secondary* -0.38 ± 0.24‰ (2SD, n= 10)
Plešovice			***LA-MC-ICP-MS*** **-0.44 ± 0.21 ‰ (Guitreau et al., 2022)** ***S-MC-ICP-MS*** **-0.39 ± 0.06 ‰ (Guitreau et al., 2020)**	*As primary* -0.35 ± 0.23‰ (2SD, n= 93)
Mun-0	**0.282135 ± 0.000007 (Fisher et al., 2011)**	*As primary* 0.282135 ± 0.000005 (2SE, n=16)		
Mun-1	**0.282135 ± 0.000007 (Fisher et al., 2011)**	*As secondary* 0.282133 ± 0.000006 (2SE, n=16)	***LA-MC-ICP-MS*** **-2.02 ± 0.27 ‰ (Guitreau et al., 2022)** **S-MC-ICP-MS** **-2.08 ± 0.17 ‰ (Guitreau et al., 2020)**	*As secondary* -1.95 ± 0.23‰ (2SD, n= 9)
Mun-3	**0.282135 ± 0.000007 (Fisher et al., 2011)**	*As secondary* 0.282129 ± 0.000006 (2SE, n=8)		
Mun-4	**0.282135 ± 0.000007 (Fisher et al., 2011)**	*As secondary* 0.282129 ± 0.000015 (2SE, n=8)		

1.5.5. Accessory mineral geochemical analyses

The study of trace elements in accessory phases within igneous rocks is proving invaluable in elucidating processes such as assimilation, magma mixing and fractional crystallization. It also plays a crucial role in fields such as provenance determination and magma discrimination, thereby enriching our understanding of crustal evolution (Bruand et al., 2014, 2017, 2020; Antoine et al., 2020; Volante et al., 2022). Moreover, this methodology can be complemented with previous isotopic information (e.g., U-Th-Pb, Lu-Hf, O, and Si) from the same domains of the crystal. This integration provides a better understanding of magmatic changes and mineral crystallization sequence. All trace element analyses performed on zircon, apatite, and titanite crystals during this thesis were linked to the same domain previously ablated for U-Th-Pb analyses. This linkage

allows an examination of whether age anomalies are indicative of trace element diffusion or homogenization processes. In addition, trace element analysis spots within zircon crystals were strategically located near the pits previously ablated for Hf-Lu and Si isotopes, i.e. within the same domain, providing valuable insight to evaluate diffusion and fractionation processes. Trace element analyses were performed at LMV in May and September 2023 using the same LA-ICP-MS system used for the U-Th-Pb analyses. During these analytical sessions, we measured the following element-associated masses: ^{27}Al, ^{28}Si, ^{29}Si, ^{31}P, ^{39}K, ^{43}Ca, ^{44}Ca, ^{49}Ti, ^{51}V, ^{57}Fe, ^{66}Zn, ^{71}Ga, ^{85}Rb, ^{88}Sr, ^{89}Y, ^{90}Zr, ^{91}Zr, ^{96}Zr, ^{93}Nb, ^{137}Ba, ^{139}La, ^{140}Ce, ^{141}Pr, ^{146}Nd, ^{147}Sm, ^{153}Eu, ^{157}Gd, ^{159}Tb, ^{163}Dy, ^{165}Ho, ^{166}Er, ^{169}Tm, ^{172}Yb, ^{175}Lu, ^{178}Hf, ^{181}Ta, ^{206}Pb, ^{232}Th, ^{238}U. A comprehensive list of all analytical procedures is available in the **Appendix**. The analytical conditions closely adhered to the methodology outlined by Guitreau et al. (2022).

We used the synthetic glass standards SRM NIST 610 and NIST 612 (Jochum et al., 2011) as bracketing and secondary standards, respectively. 91500 (Wiedenbeck et al., 2004; Guitreau et al., 2022), MudTank (Gain et al., 2019; Guitreau et al., 2022), and AS3 (Takehara et al., 2018; Guitreau et al., 2022) zircon reference materials; Durango (Chew et al. 2016), Kovdor (Arzamastsev et al., 2009), and Sumé1 (Lana et al., 2022) apatite reference materials; Bear Lake River (BLR1, Ma et al., 2019), MKED1 (Ma et al., 2019) and CKHB (Cris Fisher's in-house standard) titanite reference materials, were also used for quality assurance purposes. Subsequent processing of trace element data employed *Iolite4 software* (Petrus and Kamber, 2012; Paton et al., 2011). For the analysis of trace elements in zircon, we employed the ^{28}Si concentration data as the internal standard, while for apatite and titanite, the internal standard was based on the ^{43}Ca concentration data. In cases where published ^{28}Si or ^{43}Ca concentration data were not available, stoichiometric values were employed to convert ICP-MS counts/second into concentrations, considering the structural formulas [zircon, $ZrSiO_4$], [fluorapatite, $Ca_5(PO_4)_3F$], and [titanite, $CaTiSiO_5$]. The elemental concentrations acquired for SRM NIST 610 and NIST 612 consistently exhibited a correlation with published values, displaying deviations of no more than 4% (Jochum et al., 2011). Regarding the zircon, apatite, and titanite standards, the obtained concentrations generally conformed to the available published values for most elements. However, certain elemental concentrations either fell within the established range of published values or were closely proximate. These deviations may be attributed to compositional differences among batches of reference materials or the influence of alteration effects. Nonetheless, the chondrite-normalized Rare Earth Element (REE) patterns of mineral standards closely resembled those reported in the literature (see in **Appendix**).

Electron microprobe analyses (EMPA) were conducted in December 2024 to determine the major and minor element compositions of apatite grains. The goal was to characterize the phase type and the content of fluids and halogens. The analyses were conducted at the Laboratory of Microscopy and Microanalysis (LMic) in the Department of Geology at the Universidade Federal de Ouro Preto in Brazil. The analyses were performed using a JEOL JXA-8230 Superprobe

equipped with five wavelength-dispersive spectrometers (WDS). Seven different analyzing crystals were employed: Thallium acid phthalate (TAP, WDS 2); lithium fluoride on an H-type spectrometer (LIFH, WDS 3); pentaerythritol on an H-type spectrometer (PETH, WDS 3); high-reflectivity pentaerythritol (PETJ, WDS 4); lithium fluoride (LIF, WDS 4); pentaerythritol (PETL, WDS 5); and lithium fluoride (LIFL, WDS 5). JEOL EMPA software version 3.0.1.16 was used for calibration, spectral overlap correction, and quantification. The analytical conditions included a 20 kV accelerating voltage, a 40 nA beam current, and a 5 μm beam diameter with a fixed working distance of 11 mm. Calibration was performed using a range of mineral and synthetic standards, including gold (Au), selenium (Se), indium arsenide (InAs), silver telluride (Ag_2Te), indium antimony (InSb), uranium glass (U-glass), cobalt (Co), magnetite, pyrite, rhyolitic glass (V), fluorapatite (F), copper (Cu), nickel (Ni), cadmium sulfide (CdS), bismuth (Bi), mercury sulfide (HgS), rutile, gahnite, tin dioxide (SnO_2), palladium (Pd), manganese (Mn), molybdenum (Mo), and platinum (Pt). The counting times were set to 30 seconds at the peak and 15 seconds at the background for Cr, Mn, and P; 10 seconds at the peak and 5 seconds at the background for Na, F, Si, Al, Mg, Fe, Cl, Ti, Ca, and K; and the Kα X-ray lines were used for all elements. Spectral interferences were corrected during standard analysis and quantification. Elemental standard deviations were consistently low, ranging from 0.08% (S) to 0.78% (U), ensuring analytical precision.

1.6. Outcomes and future prospects

The subsequent chapters encompass the main outcomes of this thesis. Afterwards, a conclusive chapter will constitute a synthesis of the investigations, that certainly will enhance the comprehension of continental crust evolution and plate tectonics. The following chapters can be succinctly encapsulated as follows, with corresponding to a manuscript:

- ***Chapter 2****, the first manuscript, introduces the petrogenesis of Cupim Pluton leucogranites and elucidates the final magmatic stage within the investigated region. These leucogranites documents a sediment-derived magma production during the final collisional to post-collisional orogenic stage. Utilizing U-Pb analyses of zircon, crystallization ages for the plutonic rocks are determined. Hf, Si and trace element analyses on zircon crystals advocate for a reworking process at 2.0 Ga.*
- ***Chapter 3,*** *the second manuscript, explores the petrogenesis of TTG rocks intruded by the Cupim Pluton. These rocks are divided into three units: 2.15 Ga Caranaíba gneiss, 2.13 Ga Caatinga-Lamim Complex, and 2.11 Ga Ressaquinha Complex. Their mineralogical and chemical variations indicate that TTG magmas were formed by dehydration melting at medium to high pressure, and hornblende fractionation and plagioclase accumulation. Zircon Hf-Si isotopic compositions indicate Archean and Paleoproterozoic unsilicified mafic protoliths. The low silicon isotopic composition is consistent with the depletion of the dissolved silicon (DSi) composition of the oceans attested by the global deposition of BIFs.*

• ***Chapter 4,*** *the third manuscript, investigates the textural relationships, chemical and isotopic (U-Th-Pb) compositions of apatite and titanite crystals from the TTG and S-type granites to access magmatic and metamorphic processes. Y/Sr- and LREE-rich phases retain their magmatic composition and calculates ages are in agreement with zircon geochronology. While Sr-rich phases suggest isotopic reseting at ca. 2.05 Ga. REE-based fractionation models of these minerals have been shown to be effective in tracing the original composition of primitive and anatectic magmas.*

• *The findings of this thesis are discussed in* ***Chapter 5*** *within the broader framework of orogenic evolution. This framework aims to address the long-standing debate on the timing and nature subduction-collision cycles. The study's findings, based on the integration of petrological, geochemical, and isotopic data from TTG and S-type granites, provide critical evidence supporting early Paleoproterozoic subduction-collision processes.*

• *The final chapter of this thesis (****Chapter 6****) outlines a potential avenue for future research focused on the magmatic implications of TTG genesis during the Paleoproterozoic. Given possible shifts in tectonic, orogenic, and sedimentation regimes during this period, it is likely that alteration processes affecting basaltic source rocks also evolved. I propose to analyze alteration proxies such as Ge/Si ratios and whole-rock silicon isotopes in TTG rocks and their potential basaltic precursors to investigate these changes. This approach may provide new constraints on alteration process, silicon isotopes, and Ge/Si secular evolution.*

2. Unraveling the late orogenic stage of the studied area

2.1. Preface

This chapter was published in December 2024 in the journal *Lithos*, volumes 490-491 (https://doi.org/10.1016/j.lithos.2024.107852). In this manuscript, we present novel data regarding the younger episode of magma production in the Mineiro Belt, situated in the southern São Francisco Craton (Brazil), which we have dated at 2000 Ma. These findings shed light on the final stages during the Paleoproterozoic Minas Orogen and offer insights into the reworking processes and geodynamics in this belt. Our study presents a detailed petrogenesis of two-mica and garnet-bearing leucogranites forming the Cupim Pluton. We conducted comprehensive petrography, mineral, and whole-rock geochemical analyses, coupled with combined U-Th-Pb, Lu-Hf, and Si isotope measurements in zircons. Our results indicate that the leucogranites of the Cupim Pluton were formed through crustal reworking via sediment melting. The zircon inheritance cargo attests to the provenance of these sediments from the subjacent Archean terrain, while chemical and isotopic variations confirm sedimentary source heterogeneity and minor magmatic differentiation. This younger episode of granite formation signifies the thickening of the Paleoproterozoic crust, due to a continent-collision event that marks the final of the orogenic system's evolution.

2.2. Paleoproterozoic sediment-derived magmas reveal a late orogenic stage in the southern São Francisco Craton, Brazil: evidence from petrogenesis of the 2.0 Ga Cupim Pluton leucogranites

The first author autonomously executed several research's steps under the guidance of Leonardo Gonçalves, Martin Guitreau, and Régis Doucelance, along with co-supervisors Hugo Moreira, Cristiane Gonçalves, Marco Pinheiro, and Cassiano Costa. Sample comminution and preparation for whole-rock geochemistry analysis were carried out at Universidade Federal de Ouro Preto (UFOP) in Brazil, utilizing UFOP facilities. EDS analyses were also conducted using UFOP facilities, while whole-rock geochemistry analyses were performed in laboratories in France. Heavy mineral separation techniques were collaboratively undertaken with Cassiano Costa at the Laboratório de Análises Minerais facilities in Brazil. Clara Gorce, at Laboratoire Magmas at Volcans (LMV), Université Clermont-Auvergne, France, supervised the heavy mineral separation.

SEM imaging and LA-ICP mass-spectrometry techniques were executed at LMV under the supervision of Martin Guitreau and Régis Doucelance. Zircon U-Th-Pb, Lu-Hf, and Silicon isotope data reduction were conducted by Syro Lacerda and Martin Guitreau. The conceptualization of main ideas and the manuscript writing were collaborative efforts involving all contributors.

Paleoproterozoic sediment-derived magmas reveal a late orogenic stage in the southern São Francisco Craton, Brazil: evidence from petrogenesis of the 2.0 Ga Cupim Pluton leucogranites

Syro Lacerda [a,b], Martin Guitreau [a], Leonardo Gonçalves [b], Hugo Moreira [c], Cristiane Castro [b], Marco Aurélio Pinheiro [d], Cassiano Costa [e], Régis Doucelance [a]

[a] Laboratoire Magmas et Volcans, CNRS-UMR6524, IRD-UMR163, OPGC, Université Clermont Auvergne, F-63178 Aubière, France

[b] Universidade Federal de Ouro Preto, Departamento de Geologia, Ouro Preto, Brazil

[c] Université de Montpellier, Géosciences Montpellier, Montpellier, France

[d] Center of apllied geosciences, Geological Survey of Brazil - CPRM, Av. Pasteur 404, Rio de Janeiro, Brazil

[e] Geological Survey of Brazil – CPRM, Av Brazil 1731, Belo Horizonte 30140-002, Brazil

Abstract

Sediment-derived granites (S-type) can provide detailed information about continental crust reworking processes and tectonic regimes through time. Their compositions reflect the nature of sedimentary rocks that melted to form them. Inherited accessory minerals in these granites can provide information regarding the age and nature of the crustal rocks that contributed to the formation of their sedimentary source rock. In addition, S-type granites typically form during collisional stages in modern orogens, and their Precambrian records can provide clues about ancient tectonics. In this contribution, we present a detailed petrogenesis of the Cupim Pluton, located in the Paleoproterozoic Mineiro Belt (Brazil). The Cupim pluton is composed of two-mica and garnet-bearing leucogranites that are strongly peraluminous (ASI>1.1), high-K (K_2O/Na_2O>1), low MgO+FeO+TiO_2 (<2 wt.%). Its composition is similar to that of melts experimentally produced by muscovite/biotite dehydration melting reactions. Rb/Sr and Rb/Ba ratios suggest that these leucogranites are formed by the melting of heterogeneous sedimentary source(s). Zircon crystals from the Cupim Pluton unveil a protracted crustal melting period (2.01-1.98 Ga) hitherto unknown in the Mineiro Belt, which itself discloses a late collisional orogenic stage in southern São Francisco Craton. Igneous zircon crystals exhibit $\varepsilon_{Hf(t)}$ between -16.4 and -0.6, and $\boldsymbol{\delta}^{30}Si$ between -1.16 and -0.26 ‰, which is typical for zircon from sediment-derived granites. Hafnium isotope variations reflect mixing between at least two crustal sources, which is in line with inherited zircon cores that evidence major Archean and minor Paleoproterozoic sediment contributions. The emplacement of the Cupim Pluton leucogranites ends a subduction-collision cycle, following a long period of TTG-sanukitoid magma production, and promoted the stabilization of the southern São Francisco Craton.

Keywords

S-type granites, Zircon Hf-Si isotopes, Collisional event, Paleoproterozoic, Mineiro Belt.

2.2.1.Introduction

Sediment-derived granites [aka., S-type, Strongly Peraluminous Granites (SPG), Muscovite/ Cordierite Peraluminous Granites (MPG/CPG)] represent the reworking products of highly evolved and weathered end-members of Earth's continental crust (Barbarin, 1999; Bonin et al., 2020; Bucholz and Spencer, 2019; Chappell and White, 1974; Sylvester, 1998). They form when sedimentary rocks are heated sufficiently to trigger water-present or dehydration melting reactions (see Weinberg and Hasalová, 2015) which produce melts that are subsequently extracted from their source, segregated, emplaced, and crystallized as magma bodies (Cashman et al., 2017; Moyen et al., 2021). Sediment-derived granites can be produced under several conditions and controlled by various parameters (Weinberg and Hasalová, 2015) such as the type(s) of sediment(s) in the source, fluid activity, temperature and pressure, melting reaction(s), and differentiation mechanisms of the produced melts (e.g., Tartèse and Boulvais, 2010). In 'modern' plate tectonic regime, they are commonly formed during continental collision stages of orogens (e.g., Himalayan Mountain range) where sedimentary rocks are transferred into anomalously hot thickened crust (Cao et al., 2022; Guo and Wilson, 2012; Hopkinson et al., 2017). Therefore, S-type granites can serve as markers for understanding the geological and tectonic history of continental collision zones (Yang et al., 2019).

Siliciclastic sedimentary rocks (e.g., conglomerate, arenite, greywackes, and pelites) result from weathering and erosion of local upper-continental crust lithologies, followed by transport and deposition, hence, forming an archive of local continental crust composition (Pereira et al., 2024). In this sense, detrital zircon grains could reveal the source material that contributed to the sedimentary basin, and the age distribution density can suggest its tectonic environment of deposition (Cawood et al., 2012, Gehrels, 2014). These zircon crystals can also survive their sedimentary host-rocks melting, thereby preserving them as inherited crystals in S-type granites. Therefore, studying inherited zircon grains from S-type granites can constrain the age and nature of the crustal material at the origin of the sedimentary source rock, even for portions of the crust that have now completely vanished (Bucholz and Spencer, 2019).

The Mineiro Belt is a Paleoproterozoic crustal segment accreted to the Archean continental margin at around 2.1 Ga (**Fig. 2.1**). The belt is located at the southernmost tip of the São Francisco Craton (Brazil), which is represented by the Quadrilátero Ferrífero region (Teixeira et al., 2015). The accretion promoted the stabilization of both Archaean and Paleoproterozoic terranes, however, the precise timing and mechanisms related to this accretionary event remain unclear. For example, there is no evidence of collisional-related magmatism is reported in the literature (e.g., S-type granites). Furthermore, well-documented granitic rocks in the Mineiro Belt record a delayed TTG-sanukitoid magmatism transition (Moreira et al., 2020), which is commonly followed by crustal-derived magmatism that resembles modern-like geodynamics (Laurent et al., 2014). The occurrence of S-type granites in the Mineiro Belt could contribute to debates regarding operating

tectonic regimes during Archean and Proterozoic Eons, and when a transition towards modern plate tectonics occurred (e.g., Hawkesworth et al., 2020).

In this study, we report the identification of a Paleoproterozoic two-mica to garnet-bearing granitic body, located in the Mineiro Belt, which is referred to as the Cupim Pluton. We present new data that document its mineral and whole-rock chemical composition, its corresponding zircon U-Th-Pb ages obtained by LA-ICP-MS, and zircon Hf and Si isotope compositions measured by LA-MC-ICP-MS. These data are used to describe and characterize the petrological variability of leucogranites in the Cupim Pluton, to determine their emplacement age and inheritance cargo, as well as to constrain their source-type and reworking mechanisms. Our study eventually contributes to the discussion of ancient collisional tectonics and their associated crustal-derived magmatism.

2.2.2. Geological background

The São Francisco Craton (SFC) is located in eastern Brazil, within the lowlands of the Atlantic shield on the South American platform. It comprises Archean and Paleoproterozoic nuclei with a protracted geodynamic evolution from ca. 3.5 to 1.8 Ga, that remained shielded from Neoproterozoic-Early Ordovician plutonism, metamorphism, and deformation (**Fig.2.1a**) (Heilbron et al., 2017 and references therein). These nuclei were partially overlain by Paleo/Mesoproterozoic rift-sag and Cryogenian-Ediacaran foreland basins (Reis et al., 2017). The best exposure of the basement rocks can be found in the southern and northeastern segments of the SFC (Barbosa and Sabaté, 2004; Teixeira and Figueiredo, 1991). The Quadrilátero Ferrífero (QF) (**Fig.2.1b**) is a dome and keel mineral province that is located in the southeastern part of the São Francisco Craton (Cutts et al., 2019). It includes Archean basement domes (~3.20 to 2.06 Ga), composed of TTG, high-K granites, and migmatites, associated with 2.70 Ga metavolcano-sedimentary keels - the Rio das Velhas Greenstone belt (Noce et al., 2005). Its Archean crustal evolution is related to four distinctive tectono-magmatic events: (i) Santa Bárbara (3.22-3.20 Ga); (ii) Rio das Velhas I (2.93-2.85 Ga); (iii) Rio das Velhas II (2.80-2.76 Ga); and (iv) Mamona (2.75-2.68 Ga) (Albert et al., 2016; Farina et al., 2015). These complexes are overlaid by the Paleoproterozoic Minas Supergroup, which contains one of the world-class iron deposits (e.g., Cauê Formation), and the Itacolomi Group (Alkmim and Martins-Neto, 2012). Towards the southern and eastern margins of the Quadrilátero Ferrífero, ~2.10 Ga Paleoproterozoic belts were accreted during the Minas accretionary orogeny event, previously known as the Transamazonian orogeny (Alkmim and Marshak, 1998). These Paleoproterozoic belts are interpreted as a diachronic system of juvenile island and continental arcs that formed due to the amalgamation of the Archean nuclei of the São Francisco and Congo paleo-cratons (Cutts et al., 2019). This study focuses on the Paleoproterozoic belt located at the southern end of the Quadrilátero Ferrífero region, known as the Mineiro Belt.

The Mineiro Belt (**Fig.2.1c**) is described as a juvenile terrane composed of ca. 2.40-2.10 Ga granitic plutons and suites tectonically associated with NE-SW well-oriented greenstone belt

segments (Moreira et al., 2018, 2020; Seixas et al., 2012, 2013). Towards the east of the Mineiro Belt, i.e., Mantiqueira and Juiz de Fora Complexes, were affected by a medium- to high-grade metamorphism and plutonism imposed by the Brasiliano-Pan African orogeny (Noce et al., 2007). The Mineiro Belt was only weakly affected by this event and, as such, represents a unique target to investigate magmatic and tectonic processes that occurred during the Paleoproterozoic. In its northern part, three main episodes of crust formation were described by Moreira et al. (2020) with respective tectonic environments of magma production. The first one corresponds to the formation of the ca. 2.35 Ga Lagoa Dourada Suite composed of high-Al biotite-hornblende tonalite to biotite-trondhjemite, with TTG-affinity, formed by melting of altered basaltic crust, rapidly after its extraction from the mantle, in an intra-oceanic environment (Moreira et al., 2020; Seixas et al., 2012). The following episode also produced TTG-magmas of ca. 2.18 Ga Água Limpa and Casa Grande plutons from the melting of ancient basaltic crust caught in the lower crust due to a lithospheric thinning and asthenosphere upwelling in a back-arc basin environment (Moreira et al., 2020). The latest described magmatic episode occurred around 2.13 Ga, when sanukitoid magmas of Alto Maranhão Suite and hybrids magmas of São Brás and Bombaça, and Serra do Camapuã plutons, were produced (Moreira et al., 2018; Seixas et al., 2013). In this episode, TTG magmas interacted with the mantle wedge metasomatized by sediments to produce sanukitoid magmas. Hybrid magmas formed from fractionation/magma evolution of similar sources and/or interaction with older sedimentary components. The transition from TTG to sanukitoid magmatism around 2.13 Ga, therefore, occurred later in the Mineiro Belt (Moreira et al., 2018) compared to worldwide distributed Archean cratons, for which the transition occurred mostly in the Meso-to Neoarchean (Laurent et al., 2014).

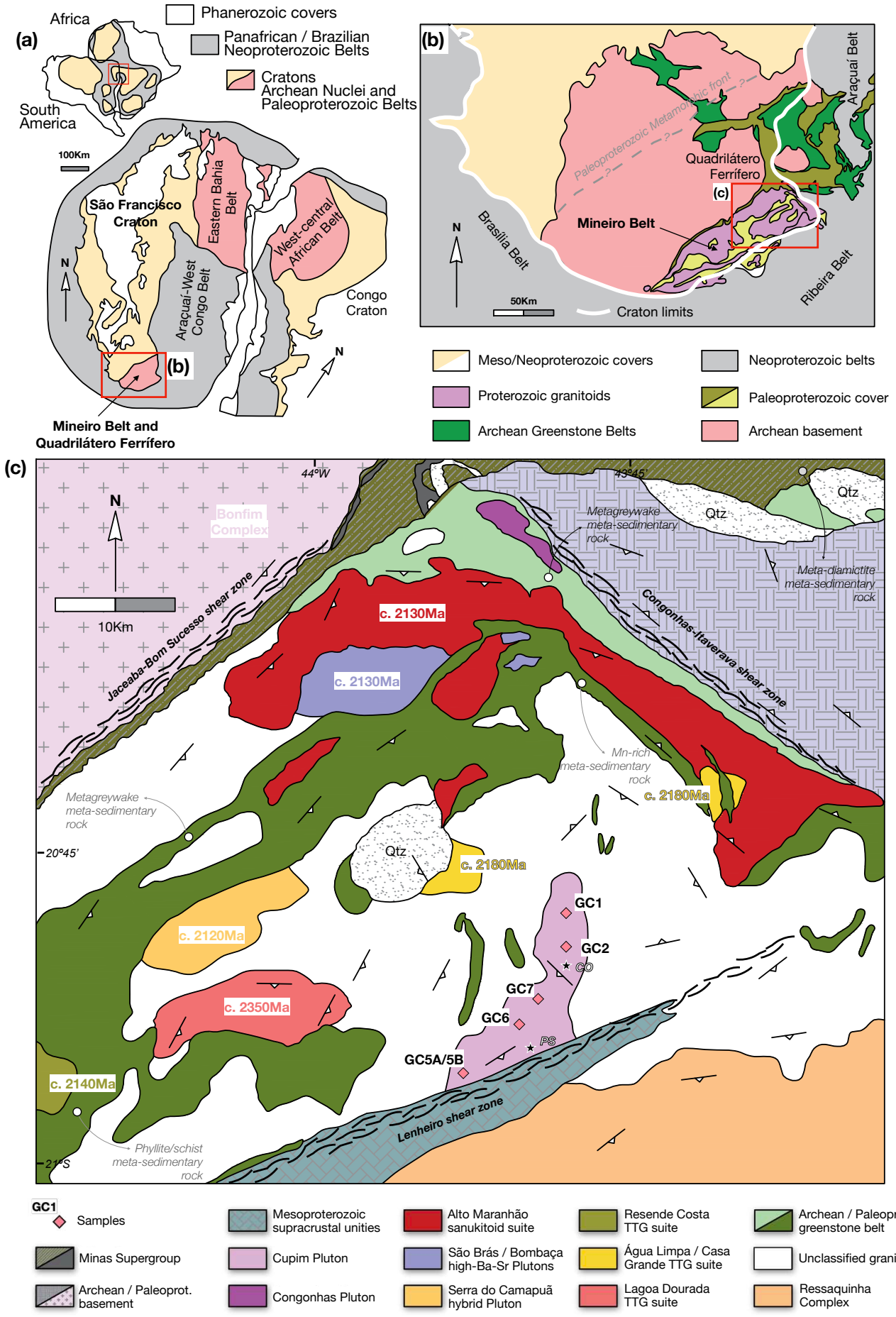
Metagreywacke rocks, located at the center and northeastern margins of the belt (**Fig.2.1c**), exhibit a higher proportion of Archean inheritance with a maximum depositional age of around 2.10 Ga, which was deduced from a detrital zircon age spectrum that includes 141 data (Moreira et al., 2020). The Paleoproterozoic inherited zircon grains found in these meta-sedimentary rocks display more negative $\varepsilon_{Hf(t)}$ values (as low as −7) compared to those of the main juvenile plutonic rocks of the Belt. Additionally, detrital and magmatic zircon crystals from Lafaiete Mn-deposits (Fig.2.1c) suggest that their deposition occurred between 2.07 and 1.86 Ga (Cabral et al., 2020). Detrital zircon crystals in quartzite intercalated within the Mn-rich sequence primarily exhibit a population age of around 2.19 Ga, with no Archean age identified. However, only a limited number of crystals were analyzed (n = 36). Furthermore, a compilation of detrital zircon grains from various meta-sedimentary units (Teixeira et al., 2021) reveals contributions from both Paleoproterozoic and Archean lithologies.

The understanding of magma production from continental crust reworking in the Mineiro Belt, as well as the continental collision with the Archean-Paleoproterozoic crust of the QF region, remains limited. The negative $\varepsilon_{Hf(t)}$ values observed in some plutonic rocks within the belt are

interpreted as evidence for assimilation and contamination processes during continental-arc activity (Barbosa et al., 2015). In contrast, the occurrence of Paleoproterozoic magmatism that affected the Archean domain is mainly restricted to minor intrusions of approximately 2.10 Ga, which crosscut the Archean-Paleoproterozoic crust in the southern border of the QF region (Moreira et al., 2019). Peraluminous (two-mica- and biotite-) granitoids marking continental collision events, when sediments are buried in the middle/lower crust and melted by heat imposed by radiogenic decay in thickened lithosphere (Bucholz and Spencer, 2019; Nabelek, 2020), have not been reported in the Mineiro Belt. Moreover, there is currently no evidence for a preserved Archean crust between the primary Paleoproterozoic greenstone belt and the granitic plutons in the Mineiro Belt. Nonetheless, the Sabará Group, located on top of the Minas Supergroup in the QF region, exhibits a detrital zircon age spectrum indicative of a foreland-type depositional environment, interpreted as the consequence of Paleoproterozoic belt continental collision (Moreira et al., 2020).

In this context, the Cupim Pluton plays a special role. It is composed of leucocratic to hololeucocratic granites s.s. that occupy an area of ca. 80 km² in the south-central part of the Mineiro Belt (**Fig.2.1c**). The origin of this pluton remains unknown and the present work addresses this issue by studying and discussing its source(s), melting conditions, segregation, ascent, emplacement and crystallization mechanisms, as well as its possible geodynamic setting, which are key questions to be addressed in order to better elucidate the geological history of the Mineiro Belt.

Figure 2.1: (a) São Francisco-Congo Craton in the west-Gondwana reconstruction. (b) The southern portion of the São Francisco Craton and the main lithostratigraphic and lithodemic unities, highlighted the northern portion of the Mineiro Belt. Adapted from Alkmim and Teixeira, (2017). (c) Simplified geology of the northern portion of the Mineiro Belt and the sample studied localities. Main granitic body limits from Seixas et al. (2012), Moreira et al., (2020); and Santos and Baltazar (2013). Meta-sedimentary rock locations came from Moreira et al., (2020); Cabral et al., (2019) and Teixeira et al., (2021). Qtz = quartzite. (To understand the colors in the figure(s), readers are directed to consult the online version of this article).


(a)
Africa
South America
Phanerozoic covers
Panafrican / Brazilian Neoproterozoic Belts
Cratons Archean Nuclei and Paleoproterozoic Belts
100Km
São Francisco Craton
Eastern Bahia Belt
West-central African Belt
Araçuaí-West Congo Belt
Congo Craton
N
(b)
Mineiro Belt and Quadrilátero Ferrífero
(b)
Araçuaí Belt
Paleoproterozoic Metamorphic front
Quadrilátero Ferrífero
(c)
Mineiro Belt
Brasília Belt
Ribeira Belt
50Km
Craton limits
Meso/Neoproterozoic covers
Neoproterozoic belts
Proterozoic granitoids
Paleoproterozoic cover
Archean Greenstone Belts
Archean basement
(c)
44°W
43°45'
20°45'
21°S
10Km
Bonfim Complex
Jaceaba-Bom Sucesso shear zone
Congonhas-Itaverava shear zone
Lenheiro shear zone
Metagreywake meta-sedimentary rock
Meta-diamictite meta-sedimentary rock
Mn-rich meta-sedimentary rock
Phyllite/schist meta-sedimentary rock
Qtz
c. 2130Ma
c. 2130Ma
c. 2180Ma
c. 2180Ma
c. 2120Ma
c. 2350Ma
c. 2140Ma
GC1
GC2
GC7
GC6
GC5A/5B
CO
PS
GC1 Samples
Minas Supergroup
Archean / Paleoprot. basement
Mesoproterozoic supracrustal unities
Cupim Pluton
Congonhas Pluton
Alto Maranhão sanukitoid suite
São Brás / Bombaça high-Ba-Sr Plutons
Serra do Camapuã hybrid Pluton
Resende Costa TTG suite
Água Limpa / Casa Grande TTG suite
Lagoa Dourada TTG suite
Archean / Paleoprot. greenstone belt
Unclassified granitoids
Ressaquinha Complex

2.2.3. Material and Methods

The fieldwork and analytical techniques applied include: (i) Sampling; (ii) Mineral chemistry; (iii) Whole-rock geochemistry; (iv) Heavy mineral concentration and separation; (v) Zircon imaging; (vi) Zircon U-Th-Pb geochronology; (vii) Zircon Lu-Hf isotopes; (viii) Zircon trace elements; and (ix) Zircon Si isotopes. A full and detailed description of the materials and methods is available in **Supplementary Material A**.

2.2.4.Results

2.2.4.1. Petrography

Six representative samples (GC1, GC2, GC5A, GC5B, GC6, and GC7) were collected across the Cupim Pluton (**Fig. 2.1c**) (see details in Supplementary Material A). They are leucogranites with similar mineralogical content often showing aluminous minerals and are medium- to coarse-grained, equigranular, isotropic to foliated (Fig. 2.2). Samples GC1 and GC5A/B exhibit magmatic foliation marked by biotite and muscovite micas. While GC5A/B samples exhibit well-developed structures of ductile deformation, in the localities of GC2, GC6, and GC7, the foliation is absent, and the isotropic texture is considered igneous (see Table 2.1; **Figs. 2.2a and 2.2b**). Equivalent proportions of modal quartz (25-30%), alkali-feldspar (25%), and plagioclase (25%) suggest the near-minimal composition of haplo-granitic systems, i.e., magmas close to eutectic or to cotectic (Barbarin, 1999; Bucholz and Spencer 2019).

Quartz is medium to fine-grained, subhedral to anhedral, usually among feldspar crystals. Undulatory extinction is a common feature and locally fine recrystallized or vermiform crystals as myrmekite are observed (**Fig. 2.2c**). Medium to coarse-grained K-feldspar crystals are generally subhedral and have cross-hatched twinning, typical of microcline, or simple orthoclase twinning. Very coarse (>5mm) porphyritic K-feldspar grains are observed in GC5A and GC5B samples. Feldspars commonly show perthite, microperthite, or flame-type unmixing. Plagioclase crystals are subhedral, medium to coarse-grained, often have polysynthetic twinning (occasionally deformed), sericite alterations, and sometimes occur as fine rounded inclusions into K-feldspar crystals. Biotite is the dominant ferromagnesian mineral in the leucogranites, with a low modal proportion (<10%). It occurs as fine tabular brownish-yellowish pleochroic crystals, among the feldspars and quartz crystals, defining the rock foliation, whenever apparent. Pleochroic halos due to zircon inclusions are common. Muscovite (<10% modal) occurs as tabular, colorless crystals, generally associated with biotite. They occur either as coarse tabular crystals or as fine crystals formed through feldspar alteration (sericitization) (**Fig. 2.2c**). Garnet forms subhedral, medium to coarse crystals. These are pinkish, commonly fractured (filled with chlorite), and often contain quartz inclusions (**Fig. 2.2d, f**).

Zircon, apatite, monazite, and allanite are ubiquitous accessory magmatic minerals and are found in all studied samples, but in variable proportions (**Table 2.1**). Fine isolated crystals of

xenotime also occur as accessory minerals in some samples (GC2) and/or are locally intergrown by allanite. Monazite crystals are commonly overgrown by apatite and/or allanite (**Fig. 2.2e**). These characteristics allow the Cupim Pluton to be subdivided into two main groups, according to the dominant peraluminous mineral. Group 1 refers to two-mica leucogranites, composed of GC1, GC2, GC5A, and GC5B samples; whereas Group 2 corresponds to garnet-bearing leucogranites, represented by GC6 and GC7 samples. Group 1 is located in the north and south of the Cupim pluton whereas Group 2 crops out in the center (**Fig. 2.1c**).

Table 2.1: Locality, modal composition, classification, and main textures of the collected samples of the Cupim Pluton leucogranites.

Sector	**North**		**South**		**Center**	
Lat	*20°48'10"S*	*20°48'40"S*	*20°54'45"S*	*20°54'46"S*	*20°51'49"S*	*20°50'57"S*
Long	*43°47'45"W*	*43°48'25"W*	*43°52'42"W*	*43°52'40"W*	*43°49'51"W*	*43°49'22"W*
Sample	GC1	GC2	GC5A	GC5B	GC6	GC7
Qz	32	24	28	33	36	34
Kfs	30	33	26	27	25	26
Pl	28	32	31	26	30	24
Bt	9	8	8	7	7	9
Ms	6	4	9	5	3	2
Grt					5	9
Class.	Ms-Bt-Mzg	Xtm-Ms-Bt-Mzg	Bt-Ms-Mzg	Ms-Bt-Mzg	Grt-Ms-Bt-Mzg	Grt-Ms-Bt-Mzg
Group	1	1	1	1	2	2
Accessory minerals						
Zrn*	0.04	0.05	0.06	0.04	0.02	0.02
Mnz*	0.02	0.01	0.02	0.02	0.01	0.01
Ap*	0.05	0.01	0.07	0.02	0.01	no
Aln*	0.02	no	0.02	0.03	no	no
Xtm-Y*	0.01	0.02	no	no	no	no
Secondary minerals						
Chl	C	no	C	C	P	P
Aln	P	no	P	P	P	P
Ep	P	no	P	P	no	no
Grt	P	no	no	P	no	no
Main textures						
	Equigr.	Equigr.	Equigr.	Equigr.	Equigr.	Equigr.
	Coarse gr.	Coarse gr.	Medium gr.	Medium gr.	Medium gr.	Coarse gr.
	Foliated	Massive	Foliated	Foliated	Massive	Massive

Mzg is the abbreviation for monzogranite. Zrn*, Mnz*, Ap*, Aln* and Xtm-Y* are estimated from the whole rock composition of Zr (ppm), La (ppm), P_2O_5 (%wt.), Ce (ppm) and Y (ppm), respectively, and observations in the thin section (50mm x 30mm). Qualitative estimative in the thin section: C, common (more than five crystals); P, present (less than five crystals); no, absent. Mineral abbreviations from Warr (2021).

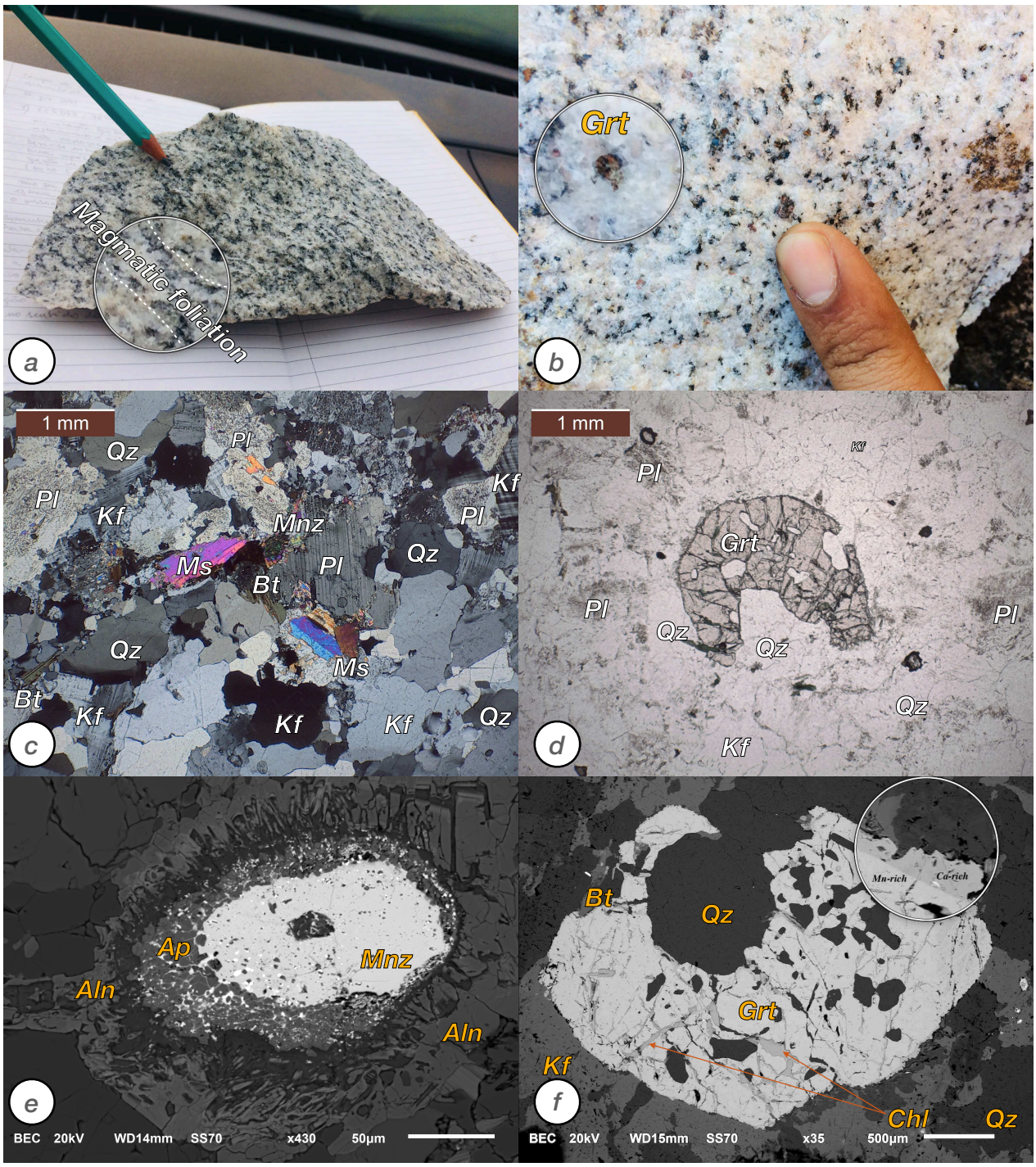
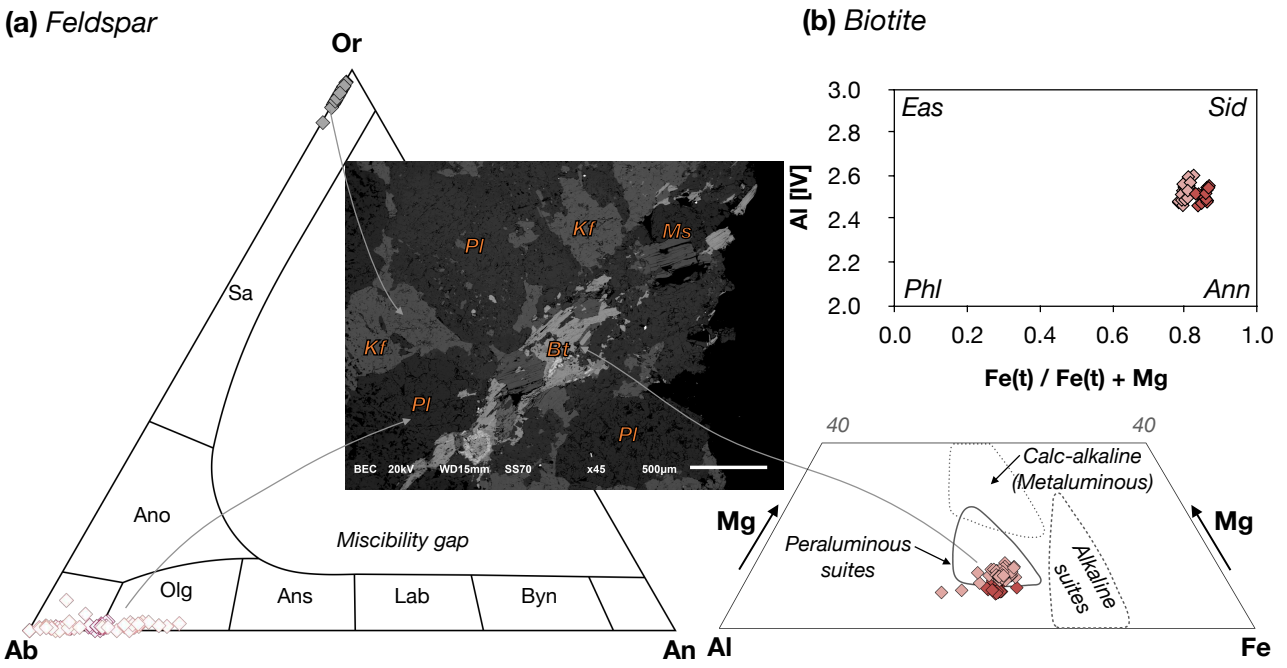


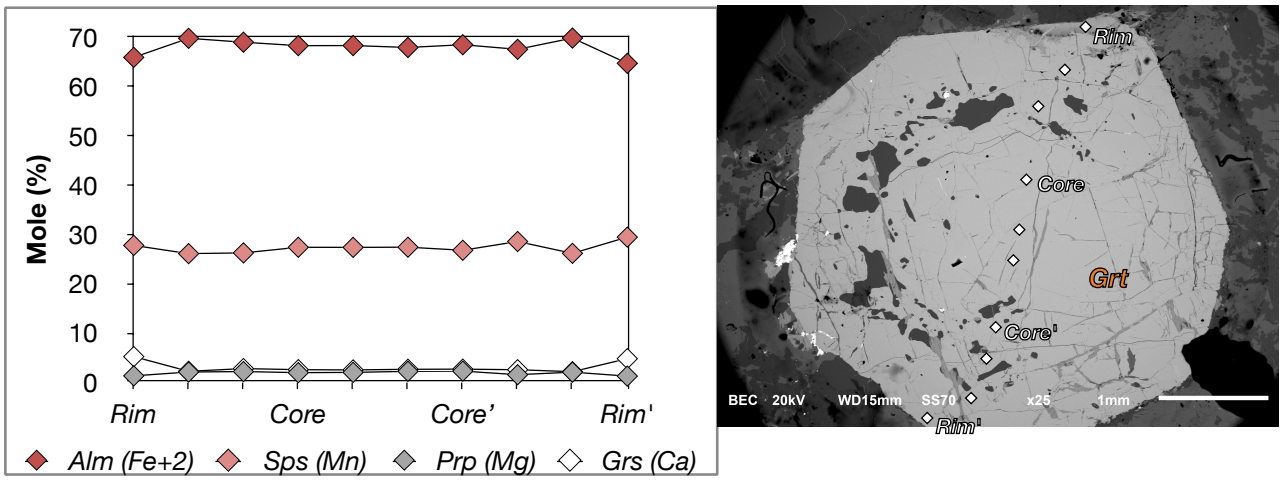
Figure 2.2: Main petrographic, mineral, and structural features of the sampled rocks. The left column is from Group 1 leucogranites, and the right column is from Group 2 leucogranites. (a) Two-mica leucogranite from GC1 sample highlighted the magmatic foliation marked by biotite and muscovite flakes. (b) Massive garnet-bearing leucogranite from GC7 sample highlighted a garnet grain. (c) Double-polarized microscope image from GC1 sample showing the intergranular textures between quartz, feldspars, and micas. Please note the presence of monazite grain at the center of the image. Single-polarized microscope image from GC6 sample showing the main texture of garnet grain (see the text for details). (e) SEM image showing a common mantle-core texture displayed by monazite, apatite, and allanite from the GC5A sample. (f) SEM image details of a garnet grain from GC7 sample. Anhedral quartz inclusions and chlorite filling fractures are common. Note the sharp contact with locally Ca-rich rims.

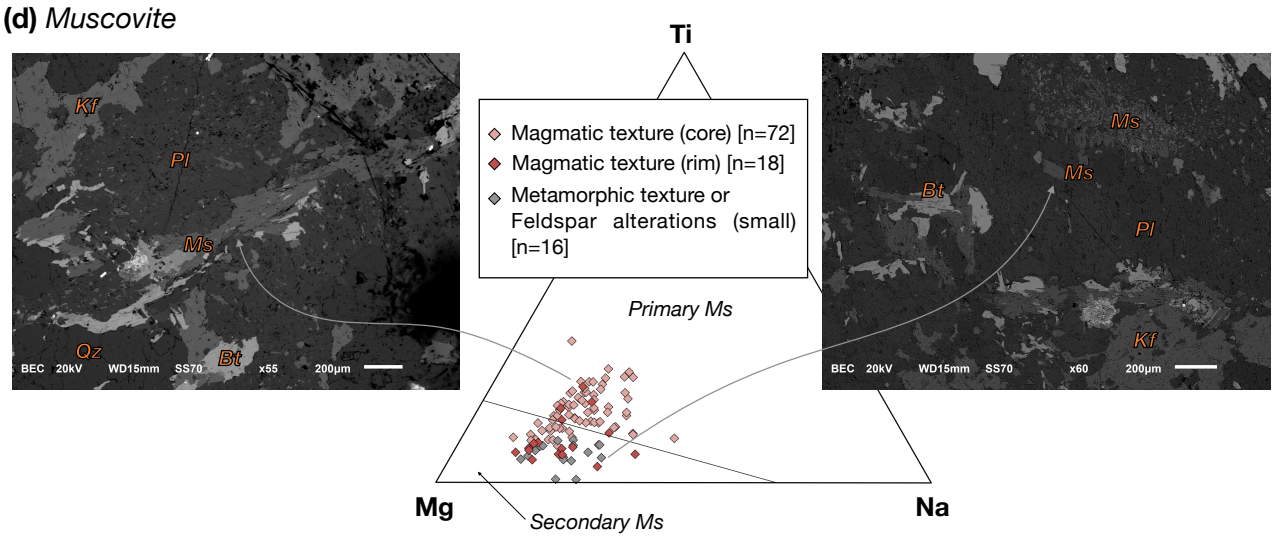
2.2.4.2.Mineral Chemistry

All mineral chemical compositions are provided in **Supplementary Material B** and they correspond to analyses done in all studied samples (i.e., GC1, GC2, GC5A, GC5B, GC6, and GC7). A summary of the observed compositional patterns is shown in **Figure 2.3**. Plagioclase crystals have similar compositions between cores and rims. In Group 1 leucogranites, a compositional variation between oligoclase to albite ($An_{1.3\text{-}22.4}$) is observed, whereas in Group 2 leucogranites, the plagioclase crystals commonly show a homogeneous albite composition ($An_{3.0\text{-}11.5}$) (**Fig. 2.3a**). The orthoclase content shows slight variation in both leucogranite groups, varying from $Or_{94.9}$ to $Or_{95.1}$ (**Fig. 2.3a**). Many K-feldspar crystals contain perthite lamellas of albitic composition. Biotite is ferroan in composition ($Fe^{2+}/[Mg+Fe^{2+}]> 0.8$) and plots in the field of peraluminous granites [**Fig. 2.3b** Abdel-Rahman (1994)]. Group 1 biotite MgO and TiO2 concentrations are slightly higher than those of Group 2 (**Fig. 2.3b**). However, no systematic difference can be observed for Al_2O_3, FeO^T, and K_2O contents. Garnet crystals show similar compositions and textural features between all Group 2 leucogranites. Coarse garnet crystals are Mn-rich almandine ($Alm_{67.1}$ $Sps_{27.8}$ $Pyr_{1.7}$ $Grs_{3.4}$) (**Fig. 2.3c**) and, in places, they have a Ca-rich rim ($Alm_{51.7}$ $Sps_{17.1}$ $Pyr_{0.6}$ $Grs_{30.6}$). The contact between cores and rims is sharp (**Fig. 2.2f**). Muscovite compositions were determined in large euhedral crystals that show sharp boundaries with other crystals, as well as in fine anhedral sericite (secondary muscovite) grains. When spatially possible, cores and rims were analyzed to assess whether or not the crystals were zoned. Most of the large crystals (>75%) fall in the primary (magmatic) muscovite field, as defined by Miller et al., (1981), whereas all fine crystals and feldspar alterations are Ti-poor and plot in the secondary muscovite field (**Fig. 2.3d**). The composition of muscovite rims shows some scatter in Ti-Mg-Na diagram but they remain dominantly Ti-poor (**Fig. 2.3d**).

Figure 2.3: Mineral chemistry of major phases from the leucogranite samples. (a) Feldspar composition plotted in ternary diagram of feldspar. (b) Biotite compositions of Al [IV] versus Fe#, and Mg-Al-Fe triangular diagram proposed by Abdel-Rahman (1994). (c) Garnet composition along a rim-rim profile. (d) Chemical ternary diagram of muscovite. A grey line separates the fields of primary plutonic muscovite composition from the field of secondary muscovite (after Miller et al., 1981). "Magmatic texture (core)", "Magmatic texture (rim)" and "metamorphic or alteration products" refer to textural criteria such as size distribution, association with minerals (feldspars), or association with shear zones. Mineral abbreviations from Warr (2021).


(a) Feldspar
Or
Ab
An
Sa
Ano
Olg
Ans
Lab
Byn
Miscibility gap
Pl
Kf
Ms
Kf
Bt
Pl
Pl
BEC 20kV WD15mm SS70 x45 500µm
(b) Biotite
Al [IV]
3.0
2.8
2.6
2.4
2.2
2.0
Eas
Sid
Phl
Ann
0.0
0.2
0.4
0.6
0.8
1.0
Fe(t) / Fe(t) + Mg
40
40
Calc-alkaline
(Metaluminous)
Mg
Mg
Peraluminous
suites
Alkaline
suites
Al
Fe


(c) Garnet
Mole (%)
70
60
50
40
30
20
10
0
Rim
Core
Core'
Rim'
Alm (Fe+2)
Sps (Mn)
Prp (Mg)
Grs (Ca)
Rim
Core
Grt
Core'
Rim'
BEC 20kV WD15mm SS70 x25 1mm


(d) Muscovite
Ti
Kf
Pl
Ms
Qz
Bt
BEC 20kV WD15mm SS70 x55 200µm
Magmatic texture (core) [n=72]
Magmatic texture (rim) [n=18]
Metamorphic texture or
Feldspar alterations (small)
[n=16]
Primary Ms
Ms
Ms
Bt
Pl
Kf
BEC 20kV WD15mm SS70 x60 200µm
Mg
Na
Secondary Ms

2.2.4.3.Geochemistry

Chemical analyses of the Cupim Pluton are given in **Supplementary Material B**. Both groups of leucogranites are silica-rich (SiO_2 = 71.96 to 75.33 wt.%) and have a granitic (*s.s.*) composition (**Fig. 2.4a**). They show high aluminum saturation index (ASI > 1.1) which corresponds to Al/(Ca–1.67P+Na+K) in molar proportions (reduction of Ca necessary to account for apatite crystallization). These granites also have low Fe_2O3 + MgO + TiO_2 contents (<2 wt.%) and low #Mg values (10-19). In the classical Shand (1943) diagram (**Fig. 2.4b**), they plot in the peraluminous field showing a positive correlation between molar A/CNK and A/NK ratios, like crustal-derived granitic melts (see Moyen et al., 2017). Cupim leucogranites are high-K (K_2O/Na_2O>1) and have high Al_2O_3/TiO_2 and low CaO/Na_2O ratios (>100 and <0.3, respectively). Silica content is negatively correlated with K_2O/Na_2O ratios, Al_2O_3/TiO_2 and CaO/Na_2O ratios, and Ti-poor samples are Na-rich. The increase of SiO_2 roughly correlates with a decrease in MgO, Fe_2O_3, and TiO_2 contents. Sample GC2 plots out of these correlations, probably due to chemical alteration. MnO contents are lower in Group 1 (<0.1 wt%) than in Group 2 (>0.1 wt%) leucogranites. In the classification diagram of Debon and Le Fort (1983), all samples plot in the felsic peraluminous field (f-P). In addition, according to Frost et al. (2001) classification diagram (**Fig. 2.4d**), all samples are alkali-calcic in composition, reflecting the Ca-poor composition of feldspars.

The leucogranites are rich in incompatible trace elements (LILE, HFSE, LREE, and HREE), they have low Sr + Ba contents (<700 ppm) and Sr/Ba ratios <0.4. Rb/Sr ratios are high and vary from 2.3-3.8 in Group 1 leucogranites to 5.7-8.0 in Group 2 leucogranites. A negative correlation can be seen between Rb/Ba and CaO/Na_2O, which indicates that Na-rich leucogranites have lower Ba contents. Since Rb/Ba and Rb/Sr are positively correlated, Ba-rich compositions are also richer in Sr (**Fig. 2.5a**). Zr contents are low in Group 1 (~100 ppm) and very low in Group 2 (<70 ppm) leucogranites, and they show a negative correlation with SiO_2, and positive correlation with MgO, Sr, and Zr/Hf ratios (**Fig. 2.5b**). Yttrium contents are high (>20 ppm), especially in Grt-bearing (Group 2) leucogranites, whereas Sr/Y is low (<5) in all samples.

In a chondrite-normalized diagram (Taylor and McLennan, 1985), REE show two different patterns. Group 1 monazite-bearing two-mica leucogranites exhibit a strongly fractionated pattern characterized by strong LREE-enrichment and moderate HREE-enrichment [$(La/Yb)_N$ from 7.2 to 19.8)]. On the contrary, Group 1 xenotime-two-mica and Group 2 garnet-bearing leucogranites exhibit poorly fractionated patterns characterized by moderate LREE- and HREE-enrichment [$(La/Yb)_N$ <5] (**Fig. 2.5c**). Strong negative Eu anomalies (Eu/Eu* = 0.22-0.11) are present in all samples but Group 2 have the strongest. In the incompatible-element diagram normalized to Archean shales (Taylor and McLennan, 2009) presented in **Figure 2.5d**, all samples show negative anomalies in Ba, Sr, and Ti, (**Fig. 2.5d**) but these anomalies are stronger in Group 2 leucogranites.

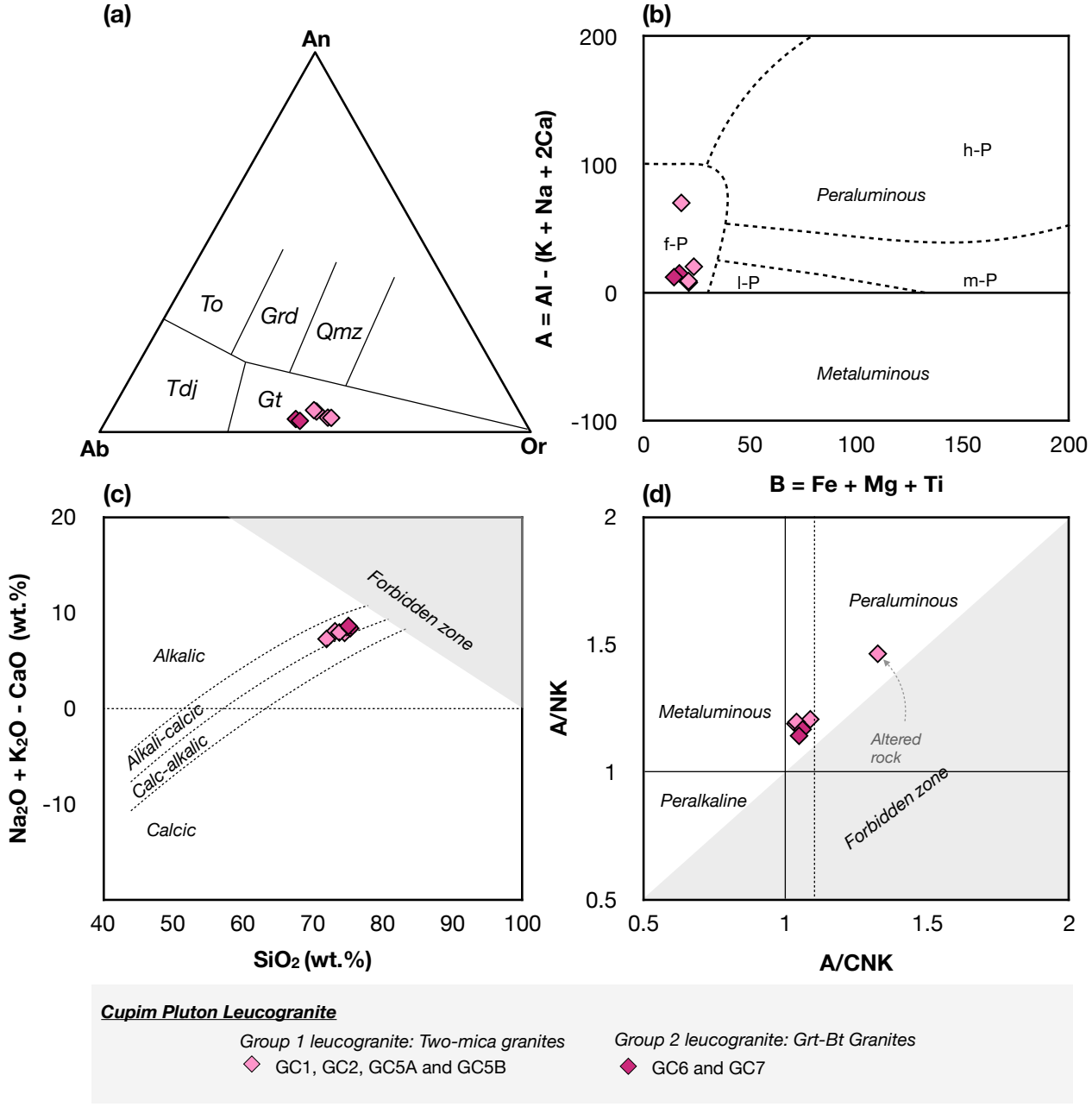
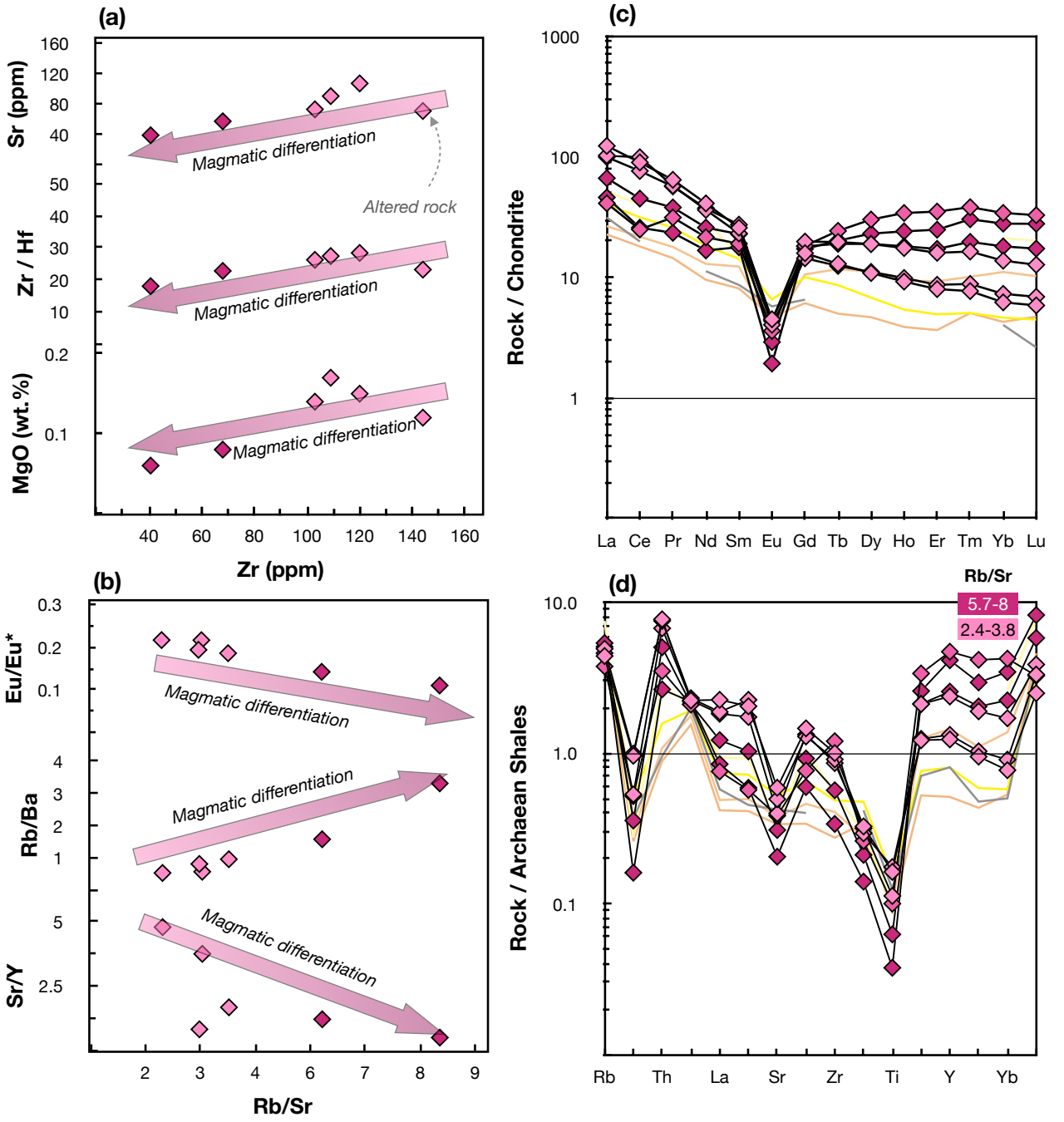


Figure 2.4: Major element geochemistry classification of the studied rocks. (a) CIPW-normative Ab-An-Or diagram of O'Connor (1965), with the fields defined by Barker (1979). To: tonalite, Gd: granodiorite, Tdj: trondhjemite, Gt: granite, qMz: quartz monzonite. (b) A-B milicationic diagram (Debon and Le Fort, 1983) with subdivisions according to Villaseca et al., (1998): l-P, m-P, and h-P are low-, medium-, and high-pressure peraluminous composition, and f-P is felsic-peraluminous. f-P field is partly defined by Tertiary High Himalaya granites (Villaseca et al., 1998), as well as Paleozoic collisional leucogranites (see Nabelek, 2020), Muscovite Peraluminous Granite (i.e. MPG Barbarin et al., 1999; Bonin et al., 2020; Moyen et al., 2017) and Archean-Paleoproterozoic Strong Peraluminous Granites (i.e., SPG, see Bucholz and Spencer, 2019; Poujol et al., 2021). (c) MALI diagram with classification limits defined by Frost et al., (2001). (d) A/CNK vs. A/NK proposed by Shand (1943) to define the alumina-alkalis composition. 'Altered rock' refers to the GC2 sample.



Cupim Pluton Leucogranite

Group 1 leucogranite

- Mnz bearing Ms-Bt-granite: GC1, GC5A and GC5B
- Xtm bearing Ms-Bt-granite: GC2

Group 2 leucogranite

- Grt-Bt-granite: GC6 and GC7

Himalayan Leucogranites

France-Lanord and Le Fort, 1988

- Average Himalayan Leucogranites

Cao et al., 2022

- Average Pliocene Himalayan Leucogranites
- Average Miocene Himalayan Leucogranites
- Average Oligocene Himalayan Leucogranites
- Average Eocene Himalayan Leucogranites

Figure 2.5: Trace element composition of the studied rocks from Cupim Pluton. (a) Rb/Sr vs. Eu/Eu* anomalies, Rb/Ba, and Sr/Y compositions of the leucogranites. (b) Zr (ppm) vs. Sr (ppm), Zr/Hf, and MgO (wt.%). Arrows in (b) and (d) suggest magmatic differentiation. 'Altered rock' refers to the GC2 sample. (c) Chondrite-normalized REE diagram (chondrite values from Taylor and McLennan, 1985). (d) Archean shale-normalized (Taylor and McLennan, 2009) multielement patterns from the leucogranites. Please note the non-normalized Rb/Sr ratio.

2.2.4.4.U-Th-Pb Geochronology

Zircon internal textures and external morphologies were characterized by both optical microscopy (transmitted light) and scanning electron microscopy (BSE and CL, see **Supplementary Material C**). **Figure 2.6** presents representative zircon textures with positions of laser-spot analyses. Analyzed crystals have pink/brown, brown/yellow, and grey colors, are prismatic, elongated to stubby, and have lengths of 120 to 600 μm with aspect ratios (length/width) varying from 1:1 to 4:1. The main textures observed in these zircon grains are: (i) prismatic, uniform to finely zoned grains and (ii) rounded cores surrounded by magmatic rims. (**Supplementary Material D**).

Thirty-one analyses were performed on seventeen zircon grains from sample GC1 (foliated Ms-Bt leucogranite; **Fig. 2.7a**). Seventeen analyses were done on nine cores, most of them with Archean $^{207}Pb/^{206}Pb$ ages. In three concordant analyses (Disc. < 1%) done on three different grains, the cores yielded a Concordia age of 2738 ± 17 Ma (2SD), whereas three sub-concordant analyses (Disc. < 5%) have Paleoarchean ages (ca. 3200 Ma, n = 2) and Paleoproterozoic (ca. 2150 Ma, n= 1) ages. Other analyses on cores have discordant to reverse discordant $^{207}Pb/^{235}U$ and $^{206}Pb/^{238}U$ ages, forming two different Discordia regression lines that produce upper-intercept ages around 2700 Ma (Fig. 2.7a). Fourteen analyses on twelve uniform grains and rims define a Discordia line with upper- and lower-intercept ages of 1991 ± 15 Ma and 572 ± 42 Ma (MSWD = 2.3), respectively. The Th/U ratios of these analyses vary from 0.10 to 0.48.

Eleven analyses were carried out on eight zircon grains from sample GC2 (equigranular Ms-Bt-leucogranite; **Fig. 2.7b**). Three of these grains have Archean cores, which exhibit $^{207}Pb/^{206}Pb$ ages at ca. 2850, 2700 and 2660 Ma. One core has two concordant U-Pb analyses (Disc.<2%) with ages around 2700 Ma. Six analyses were collected on five uniform zircon grains. One of these analyses yielded a concordant $^{207}Pb/^{235}U$ and $^{206}Pb/^{238}U$ age of 1994 ± 30 Ma. The remaining analyses gave discordant ages, which nevertheless form a Discordia line with an upper-intercept age of 2003 ± 38 Ma and a lower-intercept age of 714 ± 64 Ma. The Th/U ratios of these analyses are low (< 0.1).

Eighteen U-Pb analyses were performed on ten zircon grains from sample GC5A (Bt-Ms-leucogranite; **Fig. 2.7c**). All analyses produced discordant Paleoproterozoic $^{207}Pb/^{235}U$ and $^{206}Pb/^{238}U$ ages. In the Wetherill diagram, these analyses plot on a Discordia line with an upper-intercept age of 2013 ± 23 Ma and a lower-intercept age of 745 ± 40 Ma. The Th/U ratios of these analyses vary from 0.06 to 0.16.

Eighteen analyses were done in twelve zircon grains from sample GC5B (Bt-Ms-leucogranite; **Fig. 2.7d**). One zircon grain shows core/rim texture. Data for four analyzed cores plot on a Discordia with an upper-intercept age of 2709 ± 42 Ma (MSWD = 0.53; n = 4). Fourteen analyses done on eleven zircon grains with fine-oscillatory zoning plot on a well-defined Discordia line with intercepts at 1977 ± 25 Ma and 499 ± 38 Ma (MSWD = 1.7). The Th/U ratios in these analyses vary from 0.03 to 0.40.

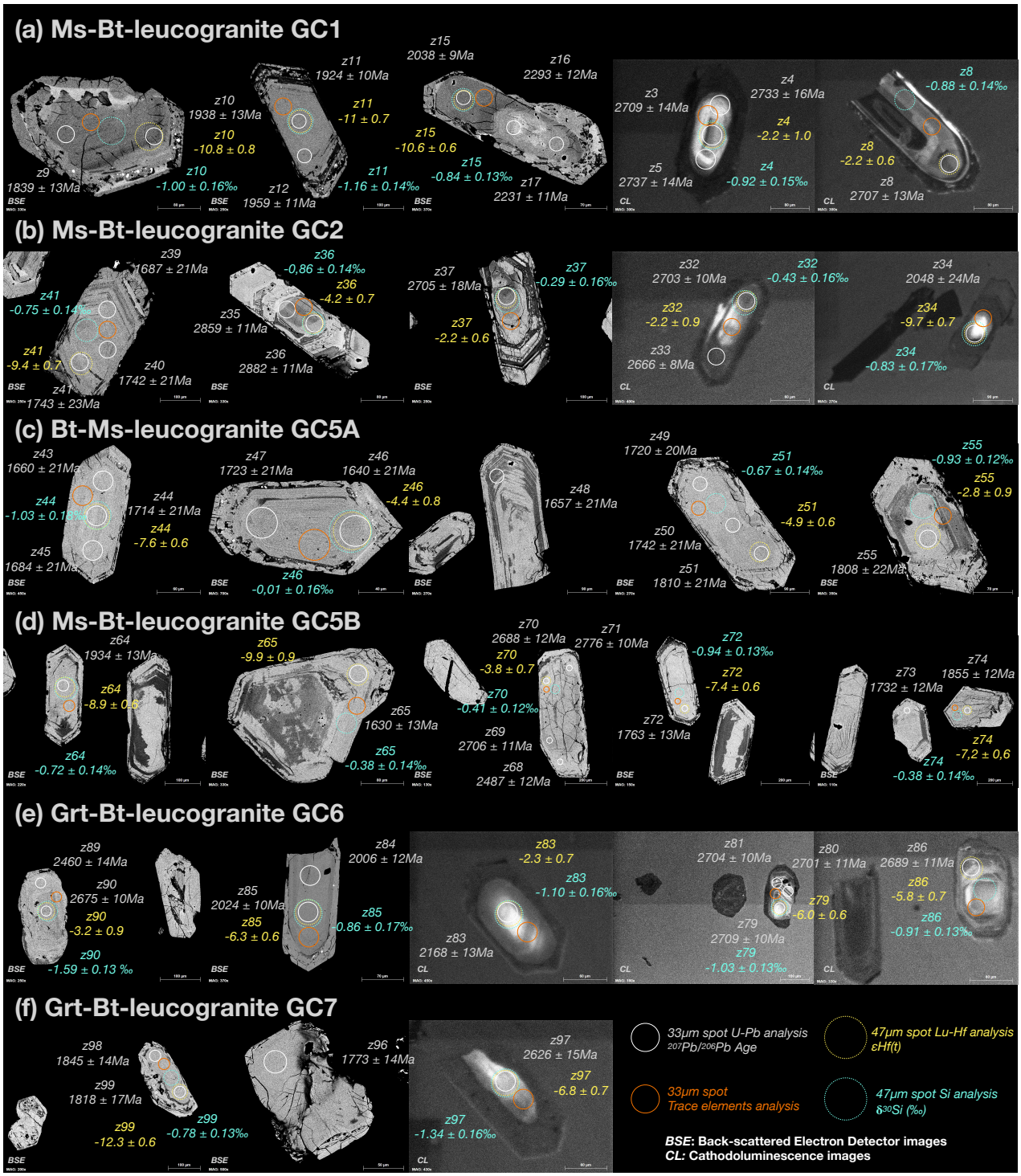
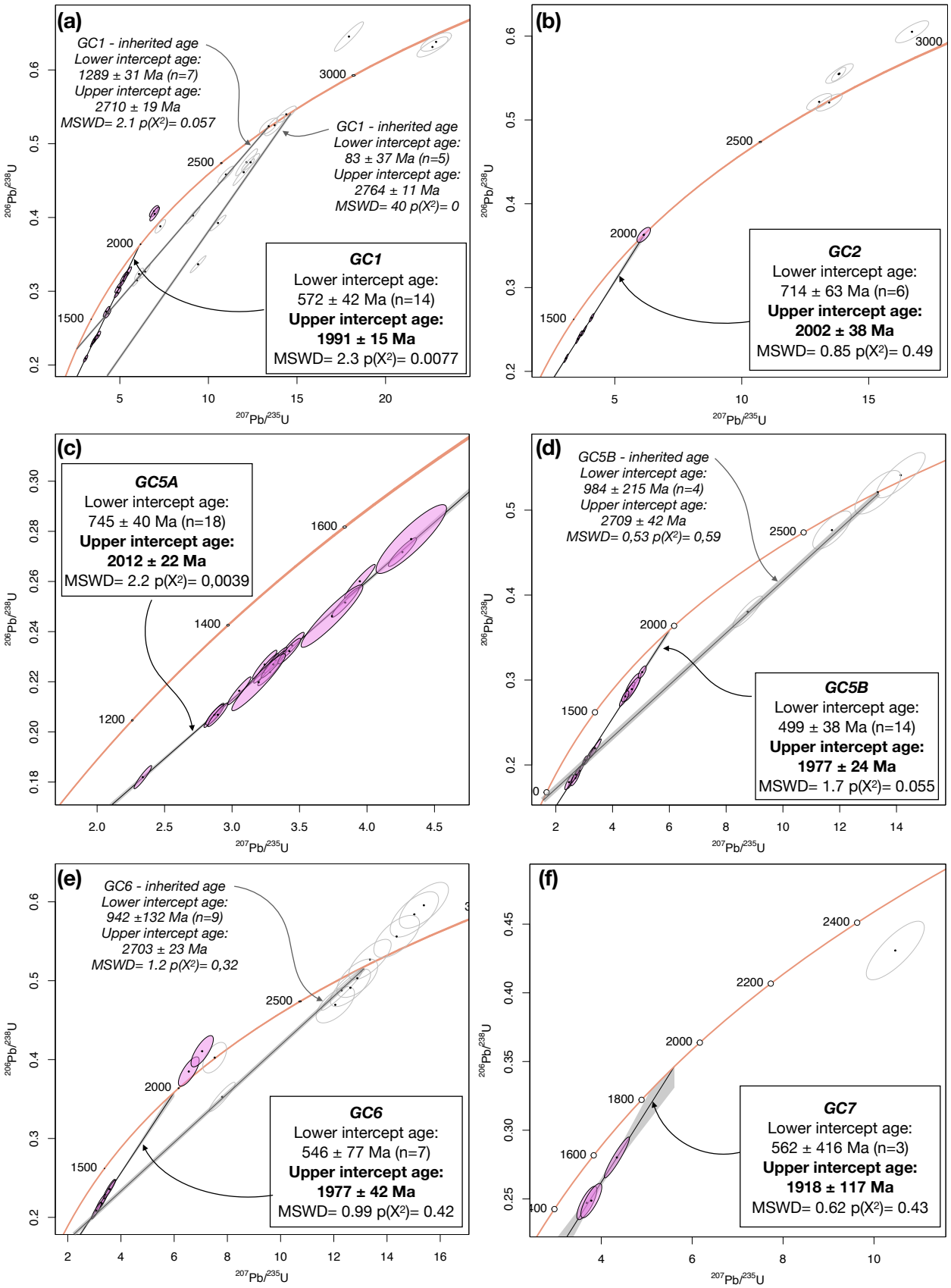


Figure 2.6: Representative SEM (BSE and CL) zircon images from the sampled rocks. The locations of laser spot analyses are indicated along with the spot name (e.g., z10). The corresponding $^{207}Pb/^{206}Pb$ dates are quoted with ±2SE uncertainty, in Ma. The calculated $\varepsilon_{Hf(t)}$ values are quoted with ±2SE uncertainty, while $\delta^{30}Si$ values are with ±2SD uncertainty.

Figure 2.7: Concordia diagrams ($^{206}Pb/^{238}U$ vs. $^{207}Pb/_{235}U$) for zircon grains from the Cupim Pluton leucogranite samples. Error ellipses and dates are displayed at 2σ level of uncertainty. Analyses were not corrected from common Pb. Hollow ellipses are from inherited zircon domains. Small inserts illustrate the calculated ages of inherited zircon grains. The *Mean Square Weighted Deviation (MSWD)* is a measure of goodness of fit that considers the relative importance of both internal and external reproducibility.


(a)
GC1 - inherited age
Lower intercept age:
1289 ± 31 Ma (n=7)
Upper intercept age:
2710 ± 19 Ma
MSWD= 2.1 p(X²)= 0.057
GC1 - inherited age
Lower intercept age:
83 ± 37 Ma (n=5)
Upper intercept age:
2764 ± 11 Ma
MSWD= 40 p(X²)= 0
GC1
Lower intercept age:
572 ± 42 Ma (n=14)
Upper intercept age:
1991 ± 15 Ma
MSWD= 2.3 p(X²)= 0.0077
(b)
GC2
Lower intercept age:
714 ± 63 Ma (n=6)
Upper intercept age:
2002 ± 38 Ma
MSWD= 0.85 p(X²)= 0.49
(c)
GC5A
Lower intercept age:
745 ± 40 Ma (n=18)
Upper intercept age:
2012 ± 22 Ma
MSWD= 2.2 p(X²)= 0,0039
(d)
GC5B - inherited age
Lower intercept age:
984 ± 215 Ma (n=4)
Upper intercept age:
2709 ± 42 Ma
MSWD= 0,53 p(X²)= 0,59
GC5B
Lower intercept age:
499 ± 38 Ma (n=14)
Upper intercept age:
1977 ± 24 Ma
MSWD= 1.7 p(X²)= 0.055
(e)
GC6 - inherited age
Lower intercept age:
942 ±132 Ma (n=9)
Upper intercept age:
2703 ± 23 Ma
MSWD= 1.2 p(X²)= 0,32
GC6
Lower intercept age:
546 ± 77 Ma (n=7)
Upper intercept age:
1977 ± 42 Ma
MSWD= 0.99 p(X²)= 0.42
(f)
GC7
Lower intercept age:
562 ± 416 Ma (n=3)
Upper intercept age:
1918 ± 117 Ma
MSWD= 0.62 p(X²)= 0.43
206Pb/238U
207Pb/235U

Seventeen U-Pb analyses were done on nine zircon grains from sample GC6 (equigranular Grt-Ms-Bt-leucogranite; **Fig. 2.7e**). Six of these grains show core/rim texture, and their cores mostly have Archean and subordinately Paleoproterozoic $^{207}Pb/^{206}Pb$ ages. These later have calculated $^{207}Pb/^{235}U$ and $^{206}Pb/^{238}U$ concordant ages around 2170 Ma. On the other hand, nine analyses performed in five cores produced a Discordia line with an upper-intercept age of 2703 ± 23 Ma (MSWD = 1.2). The remaining seven analyses were done in three uniform zircon grains. These analyses returned discordant $^{207}Pb/^{235}U$ and $^{206}Pb/^{238}U$ data with upper- and lower-intercept ages of 1977 ± 42 Ma and 546 ± 77 Ma (MSWD = 0.99), respectively. The Th/U ratios vary from 0.02 to 0.38.

Four analyses were done on three zircon grains from sample GC7 (equigranular Grt-Bt-leucogranite; **Fig. 2.7f**). One of these grains has a well-defined core/rim texture that gave a $^{207}Pb/^{206}Pb$ age of 2626 ± 15 Ma, though discordant (Disc. = 12%). Three analyses performed on uniform grains provided discordant data that form a Discordia line with a Paleoproterozoic upper-intercept age (1918 ± 117 Ma). The Th/U ratios vary from 0.04 to 0.55. Although only a few analyses were performed in this sample, the zircon grains show the same trend as the other samples, i.e., discordant Paleoproterozoic upper-intercept ages and inherited Archean cores.

2.2.4.5.Zircon Lu-Hf isotopes

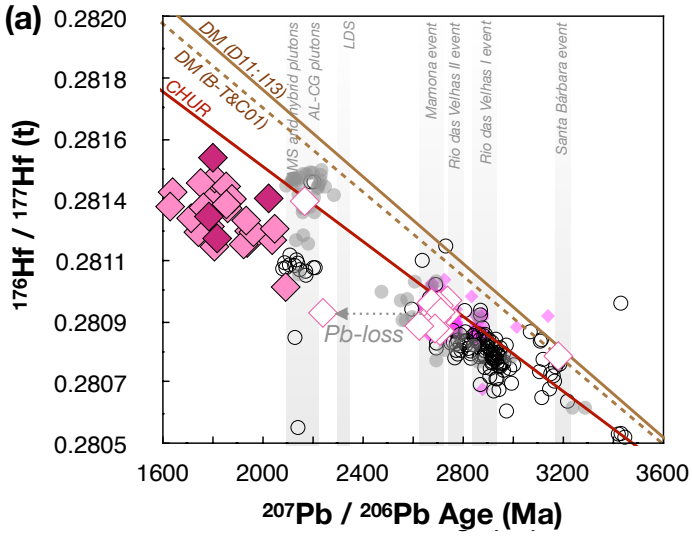
Forty-two Lu-Hf isotope analyses were conducted on forty-one selected zircon grains. **Table 2.2** provides a summary of the main results obtained. Twenty-six were located within grains and rims with uniform textures, and fifteen in cores. Paleoarchean and Neoarchean cores exhibit the lowest initial $^{176}Hf/^{177}Hf$ which ranges from 0.280881 ± 0.000021 to 0.281062 ± 0.000027 (2SD, n=14), whereas the ca. 2.16 Ga Paleoproterozoic cores display a more radiogenic Hf isotope composition of 0.281353 ± 0.000019 (2SD) (**Fig. 2.8a**). The depleted $^{176}Hf/^{177}Hf$ composition of the ca. 2.2 Ga Paleoproterozoic core (0.280960 ± 0.000027, 2SD) could potentially be attributed to the process of Pb-loss. The Paleoarchean core shows a positive ε_{Hf} of +3.0 ± 0.8 (2SD) at 3182 Ma, whereas the Neoarchean cores reveal a more negative $\varepsilon_{Hf(t)}$ value of around -3.0 ± 0.8 (2SD, n= 13) at 2700 Ma. The Paleoproterozoic zircon core displays relatively more enriched ε_{Hf} values of approximately -1.6 ± 0.7 (2SD) at 2168 Ma. In contrast, uniform zircon crystals and rims show more diverse initial $^{176}Hf/^{177}Hf$ compositions ranging from 0.281078 ± 0.000028 to 0.281529 ± 0.000020 (2SD, n = 26) and resulting in a wide negative range of $\varepsilon_{Hf(t)}$ values between -0.6 ± 0.7 and -16.4 ± 1.0, and average -8.1 ± 0.7 (2SD, n=26; **Fig. 2.8b**). The $^{176}Hf/^{177}Hf$ and $\varepsilon_{Hf(t)}$ variations for each sample is given in **Table 2.2**.

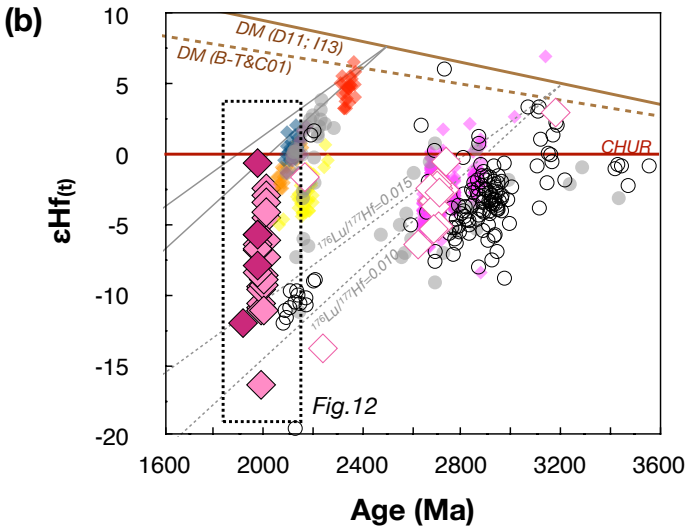
All measured zircon domains (cores and rims) show similar, overlapping $^{176}Lu/^{177}Hf$ ratios ranging from 0.000138 ± 0.000013 to 0.002168 ± 0.000058 (**Table 2.2**). On average $^{176}Lu/^{177}Hf$ ratios in both cores and uniform zircon grains and rims are quite consistent within uncertainty. Furthermore, no discernible correlation between the $^{176}Lu/^{177}Hf$ ratios and the $^{207}Pb/^{206}Pb$ ages for cores and uniform zircon grains and rims is visible.

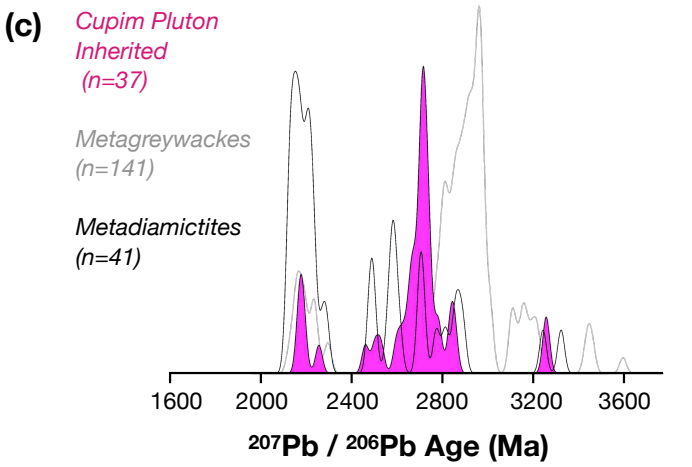
Table 2.2: Measured zircon Lu-Hf isotope compositions and calculated εHf(t) for Cupim leucogranite zircon crystals. Uncertainties correspond to 2σ confidential interval. 'm' and 'i' notations in Sample column refer to the number of analyses performed on magmatic and inherited domains, respectively.

Sample	$^{176}Hf/^{177}Hf$		$^{176}Lu/^{177}Hf$		$\varepsilon_{Hf(t)}$	
	Magmatic	***Inherited***	**Magmatic**	***Inherited***	**Magmatic**	***Inherited***
GC1 *(m=6, i=5)*	0.281078 ± 0.000028 to 0.281285 ± 0.000017	*0.280881 ± 0.000021 to 0.281062 ± 0.000027*	0.000234 ± 0.000004 to 0.000991 ± 0.000048	*0.000662 ± 0.000005 to 0.001650 ± 0.000097*	-16.4 ± 1.0 to -9.4 ± 0.6	*-2.5 ± 1.0 to +3.0 ± 0.8*
GC2 *(m=4, i=3)*	0.281261 ± 0.00020 to 0.281310 ± 0.000029	*0.281021 ± 0.000019 to 0.281040 ± 0.000017*	0.000138 ± 0.000013 to 0.002168 ± 0.000058	*0.001004 ± 0.000020 to 0.001117 ± 0.000096*	-11.1 ± 0.7 to -8.6 ± 1.0	*-3.3 ± 0.6 to -2.0 ± 0.9*
GC5A *(m=7, i=0)*	0.281323 ± 0.000018 to 0.281484 ± 0.000025		0.000800 ± 0.000017 to 0.001492 ± 0.000078		-7.3 ± 0.6 to -2.4 ± 0.9	
GC5B *(m=5, i=1)*	0.281320 ± 0.000016 to 0.281385 ± 0.000019	*0.281022 ± 0.000019*	0.000590 ± 0.000001 to 0.000953 ± 0.000027	*0.001161 ± 0.000025*	-8.4 ± 0.6 to -5.7 ± 0.7	*-3.3 ± 0.7*
GC6 *(m=3, i=6)*	0.281342 ± 0.000014 to 0.281529 ± 0.000020	*0.280938 ± 0.000019 to 0.281392 ± 0.000019*	0.000668 ± 0.000030 to 0.001246 ± 0.000007	*0.000650 ± 0.000015 to 0.001173 ± 0.000021*	-7.9 ± 0.5 to -0.6 ± 0.7	*-5.1* ± 0.6 to -1.6 ± 0.7
GC7 *(m=1, i=1)*	0.281240 ± 0.000017	*0.280947 ± 0.000020*	0.000548 ± 0.000037	*0.000666 ± 0.000015*	-12.0 ± 0.6	*-6.4 ± 0.7*

Figure 2.8: Hf isotope composition of leucogranites of the Cupim Pluton. (a) Initial $^{176}Hf/^{177}Hf$(t) vs. $^{207}Pb/^{206}Pb$ age. Grey vertical bars indicate the main magmatic stages in the southern São Francisco Craton. Dashed-arrow suggests a Pb-loss process. (b) ε_{Hf} vs. age space for magmatic and inherited zircon domains showing possible Lu/Hf evolution lines. These evolution lines require $^{176}Lu/^{177}Hf$ values of 0.01 and 0.015 (typical of crustal reservoirs), anchored to the mainly Hf model ages (TDM) in the Mineiro Belt (2.50 Ga; Moreira et al., 2020) and Quadrilátero Ferrífero (3.20 Ga; Albert at al. 2016) regions; with respectively $^{176}Hf/^{177}Hf$= 0.280850 and $^{176}Hf/^{177}Hf$= 0.281385 compositions. (c) KDE distribution of the inherited cores and detrital zircon ages (Moreira et al., 2020). See details for Depleted Mantle (DM) and Chondritic Uniform Reservoir (CHUR) reservoirs in Supplementary Material A.







Cupim Pluton leucogranites

- *Group 1 - Magmatic*
- *Group 2 - Magmatic*
- *Group 1 and 2 - Inherited*

Sedimentary country rocks (Moreira et al., 2020)

- *Metagreywackes (Rio das Mortes unit)*
- *Metadiamictites (Sabará Group)*

Basement rocks (Moreira et al., 2020; Albert et al., 2016)

- *Serra do Camapuã hybrid pluton*
- *Alto Maranhão Sanukitoid Suite*
- *Lagoa Dourada TTG Suite*
- *São Brás-Bombaça High-Ba-Sr Plutons*
- *Água-Limpa-Casa Grande TTG Plutons*
- *Bonfim Complex*

2.2.4.6.Zircon Trace elements

Trace element compositions of zircon grains from the same selected samples are given in **Supplementary Material D**. Fifty trace element analyses were done in forty-seven zircon crystals, focusing on zircon domains also analyzed for Si isotopes.

Hafnium contents in pristine uniform domains (cores and rims) range from 0.97 to 1.29 wt.%, with an average of 1.12 wt.% in zircon from Group 1 leucogranites and from 1.00 to 1.41 wt.% (average of 1.21 wt.%) in zircon from Group 2 leucogranites (**Fig. 2.9a**). Zircon cores exhibit Hf contents ranging from 1.08 to 1.43 wt.% (average of 1.23 wt.%). The Y contents vary from 0.07 to 0.34 wt.% (average of 0.16 wt.%) in Group 1 leucogranites, whereas Group 2 leucogranites have zircon crystals with lower and more homogeneous Y contents of 0.08 wt.% (**Fig. 2.9b**). Zircon cores have Y contents that vary from 0.08 to 0.24 wt.% (average of 0.15 wt.%). Thorium contents are always lower than U concentrations (see **Supplementary material D**), resulting in Th/U average ratios of 0.17, 0.21, and 0.43 for Group 1 and Group 2 leucogranite zircon uniform grains, rims, and cores, respectively. The REE compositions of pristine zircon grains are characteristic of terrestrial ones (Hoskin and Schaltegger, 2003), with a higher content of HREE than LREE, and positive Ce/Ce* and negative Eu/Eu* anomalies (**Fig. 9.2c**). Zircon grains in monazite-bearing two-mica leucogranites (Group 1) overall have lower LREE and higher HREE compared to Group 2 leucogranite zircon. The Ti contents range from 6 to 16 ppm in zircon from Group 1 leucogranites, whereas those of Group 2 leucogranites exhibit Ti contents that vary from 9 to 15 ppm (**Fig. 2.9a**). Ti-in-zircon temperatures (see in **Supplementary Material A**) range from 764 to 874 °C for Group 1 and from 811 to 868 °C for Group 2 leucogranite zircon crystals (**Fig. 2.9d**). Cores display a wider range of calculated Ti-in-zircon temperatures that varies between 737 and 925 °C.

2.2.4.7.Zircon Si isotopes

Silicon isotope compositions of zircon crystals from the same selected samples are presented in **Supplementary Material D**. Forty-nine Si isotope analyses were done on forty-six selected zircon crystals from the six leucogranite samples. Among these, eighteen analyses were located within zircon cores, whereas thirty-one were done in uniform crystals and rims. However, some of these analyses were done within altered domains as revealed by their trace element contents (see above). Thirteen analyses done in pristine uniform zircon grains and rims have δ^{30}Si that vary from -1.16 to -0.26‰ (average = -0.82 ± 0.17‰, 2SD, n=13), while five analyses from zircon cores with pristine composition have a similar, but a more uniform, δ^{30}Si values (-1.33 to -0.41‰; average -0.75 ± 0.16‰, 2SD). $\delta^{30}Si_{calc.}$ [= ^{29}Si / 0.5178] values calculated from theoretical predictions for mass-dependent equilibrium fractionation (0.5178, Guitreau et al., 2020 and references therein) between ^{29}Si and ^{30}Si isotopes are very similar to those of measured ^{30}Si isotope composition. $\delta^{30}Si_{calc.}$ from uniform zircon grains and rims vary from -1.13 to -0.46‰ (average = -0.77 ± 0.17‰; 2SD), and for

zircon cores from -1.02 to -0.69‰ (average = -0.87 ± 0.13%; 2SD; **Fig. 2.9b**). These values translate into apparent fractionation factors ($\Delta^{30}Si_{WR\text{-}Zrc}$ = $^{30}Si_{WR}$ - $^{30}Si_{zircon}$) from 0.15 to 0.86‰ for uniform zircon grains and rims, and from 0.11 to 1.04‰ for zircon cores (**Fig. 2.9d**) when S-type bulk-rock δ30Si value of -0.3‰ is applied (e.g., Savage et al., 2012).

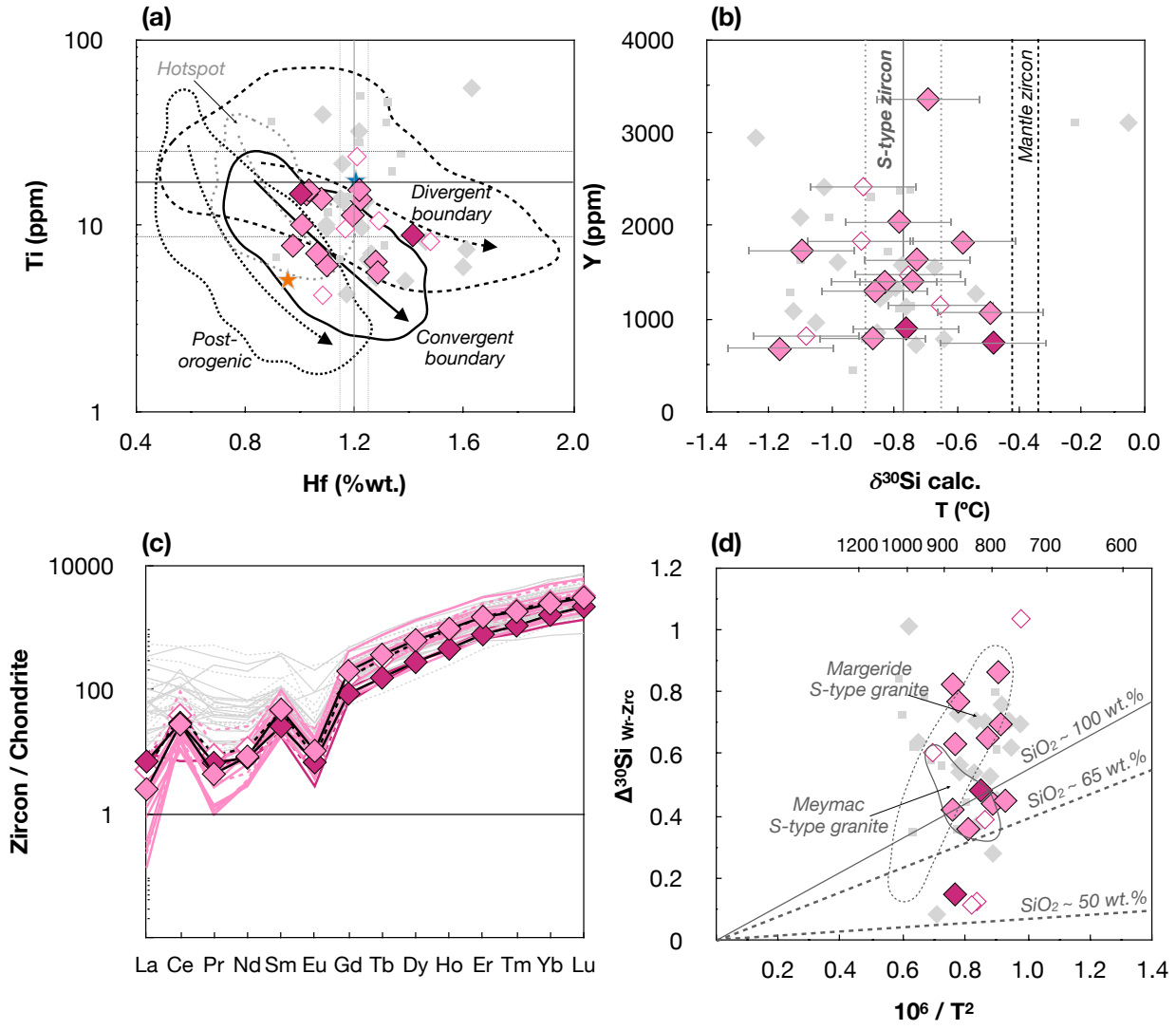


Figure 2.9: Zircon trace elements and silicon isotope composition from the Cupim Pluton leucogranites. Pink diamonds are pristine magmatic zircon grains, white diamonds are pristine inherited zircon grains. Altered magmatic and inherited zircon grains are tagged with square and diamond symbols in grey color. (a) Ti (ppm) vs. Hf (wt.%) zircon composition showing tectonic fields and trends according to Laurent et al. (2021). The orange star is the average composition of 3.46 Ga Barberton igneous zircon grains hosted in several granitic rocks (Laurent et al., 2021). The blue star represents the average zircon composition from S-type granites (Guitreau et al., 2022). (b) δ30Sicalc. vs. Y(ppm) composition. Vertical bars represent δ30Sicalc. values for zircon from the mantle (Trail et a., 2018) and S-type granites (Guitreau et al., 2022). (c) Chondrite normalized (Taylor and McLennan, 1985) patterns (full and colored lines) for zircon grains from the leucogranites. Patterns with diamond symbols refer to the respective average composition. (d) Calculated Ti-in-zircon temperatures vs. Δ30SiWR-Zrc for the analyzed zircon domains. Full and dashed lines indicate the related theoretic composition variation of rocks with 50%, 65%, and 100% of SiO2 (wt.%). Zircon composition from S-type granites is from Guitreau et al. (2022).

2.2.5.Discussion

2.2.5.1. Age of granite emplacement

Zircon grains and rims from all samples mostly yielded discordant data that form Pb-loss Discordia lines with Paleoproterozoic upper-intercept ages and Neoproterozoic lower-intercept ages. The upper-intercept ages vary from 1977 ± 42 to 2013 ± 38 Ma (excluding GC7 sample, which is 1918 Ma but has high calculated error 117 Ma; **Fig. 2.7**). The most concordant calculated U-Pb age for these zircon domains is 1994 ± 30 Ma (2SD; z34 from GC2). Zircon cores show mainly Neoarchean (around 2700 Ma) and subordinate Paleoproterozoic (~2170 Ma) $^{207}Pb/^{206}Pb$ ages (**Fig. 2.7**). The well-defined core/rim relationships, the rounded shape of the cores, the fine oscillatory zoning textures, and the elevated Th/U (mostly >0.1) of zircon rims and homogeneous crystals suggest that these latter are magmatic and represent the crystallization age of the Cupim Pluton. In contrast, their cores are inherited (**Table 2.3**).

Upper-intercept ages interpreted as reflecting magmatic crystallization of Cupim samples exhibit several millions of years of variation, but they overlap with each other uncertainty-considered, although large in some cases (**Fig. 2.7**). The average for upper-intercept ages is 1992 ± 32 Ma (2SD; n = 5), similar to the most concordant single age among all studied samples (see above). This average age could represent that of emplacement of the Cupim Pluton but the range displayed by upper-intercept ages could alternatively suggest protracted magmatism for at least 40 Myr. Given that most of crystallization ages discussed here correspond to U-Pb upper-intercept ages and that they all overlap within analytical uncertainty, we cannot objectively discriminate between a short and a large emplacement duration for Cupim magmas. In addition, we have not been able to identify clear field relationships (lithotype intrusions or cross-cuts) between Cupim lithologies due to outcropping conditions that could help favor one or the other hypothesis. As a consequence, we prefer to use caution and consider that the average age represents that of the emplacement of the Cupim Pluton and that the actual duration of magmatism is unknown.

Although the calculated lower-intercept ages coincide with the Brasiliano-Pan African orogenic event (Brito-Neves et al., 1999), no Neoproterozoic U-Th-Pb age was found in any sample that could suggest a complete resetting of the isotopic system or neoformation. Instead, the observed Pb-loss was probably caused by diffusion and leaching of zircon crystals with advanced radiation-damage accumulation during a thermal event (<600° C) (e.g., Mezger and Krogstad, 1997).

The Neoarchean inherited ages match well with the final high-K magmatic episode (2750-2600 Ma), also known as Mamona event, in the QF region (e.g., Bonfim Complex, Albert et al., 2016; Farina et al., 2015). The Paleoproterozoic (~2170 Ma) inherited age agrees with the second episode of crust formation proposed by Moreira et al. (2020). Together, the Kernel Density Estimation (KDE) of the inherited ages (n=37) mimics the detrital zircon spectrum age (n=141) of the metagreywackes from greenstone belts within the Mineiro Belt (Moreira et al., 2020) attesting the Archean contribution in the sedimentary basin.

The magmatic crystallization age of 1992 ± 32 Ma (2SD; n=5) for the Cupim leucogranites documents a regional younger hitherto unknown Paleoproterozoic episode within the southern São Francisco Craton. A younger local granodioritic dyke (1860 ± 8 Ma; 2SD, n=6) intruding metasedimentary rocks has been reported (Cabral et al., 2019), but its tectonic origin is unclear. In addition, the Mesoproterozoic São João del Rei basin contains detrital zircons with a significant population age of around 2000 Ma (Ribeiro et al., 2013).

Table 2.3: Summary of the main geochemical characteristics of Cupim leucogranite zircons. Si isotopes, calculated temperatures, Th/U ratios, and REE are from zircon crystals with pristine compositions. Uncertainties correspond to 2σ confidential interval.

Sample	Zircon U-Pb age (Ma)		Zircon $\varepsilon_{Hf(t)}$ values		Zircon $\delta^{30}Si$ values (‰)		Ti in zircon temperatures (°C)		Zircon Th/U		Zircon REE	
	Magmatic	*Inherited*	Magmatic	*Inherited*	Magmatic	*Inherited*	Magmatic	*Inherited*	Magmatic	*Inherited*	Magmatic	*Inherited*
GC1	1991 ± 15	*Arch. and Paleo.*	-16.4 ± 1.0 to -9.4 ± 0.6	*-2.5 ± 1.0 to 3.0 ± 0.8*	-1.06 ± 0.14 to -0.65 ± 0.16	*-0.99 ± 0.15 to -0.71 ± 0.15*	773 to 861	*803 to 982*	0.10 to 0.21	*0.10 to 0.45*	HREE-rich	*HREE-rich*
GC2	2003 ± 38	*Arch.*	-11.1 ± 0.7 to -8.6 ± 1.0	*-3.3 ± 0.7 to -2.0 ± 0.6*	-0.77 ± 0.14	*-0.54 ± 0.16*	1038	*1092*	0.09	*0.42*	HREE-rich	*HREE-rich*
GC5A	2013 ± 23		-7.3 ± 0.6 to -2.4 ± 0.9		-1.09 ± 0.16 to 0.88 ± 0.12		868 to 873		0.15 to 0.18		HREE-rich	
GC5B	1977 ± 25	*Arch.*	-8.4 ± 0.6 to -5.7 ± 0.7	*-3.3 ± 0.7*	-1.11 ± 0.27 to -0.81 ± 0.17	*-0.41 ± 0.12*	860 to 874	*830*	0.07 to 0.15	*1.17*	HREE-rich	*HREE-rich*
GC6	1977 ± 42	*Arch and Paleo.*	-7.9 ± 0.5 to -0.6 ± 0.7	*-5.3 ± 0.7 to -1.6 ± 0.7*	-0.43 ± 0.12		868		0.37		HREE-poor	
GC7	1918 ± 117	*Arch.*	*-12.0 ± 0.6*	-6.4 ± 0.7	-0.76 ± 0.13	*-1.25 ± 0.16*	811.5	*737*	0.05	*0.32*	HREE-poor	*HREE-rich*

2.2.5.2.Sources

Considering the paradigm of granite formation (details in Moyen et al., 2021), the low content of ferromagnesian and the presence of alumina-excess minerals, as well as the peraluminous nature of minerals and the peraluminous to strongly peraluminous, high-K, and low-MgO whole-rock composition of the Cupim leucogranites, preclude the possibility that these magmas were formed through the fractional crystallization of a basaltic liquid extracted from the (sub-lithospheric) mantle (Annen et al., 2006). Instead, the chemical composition of these rocks is consistent with that of experimental liquids produced through the melting of sedimentary materials (**Fig. 2.10a**) (see in Moyen, 2011). These liquids are experimentally produced by partial melting of pelites and greywackes, or chemically equivalent to synthetic materials. Pelite/greywacke source contribution can be estimated from the CaO/Na_2O values (Silvester, 1998), and temperature variations are mainly reflected by Al_2O_3/TiO_2 compositions of the melt (Patiño-Douce and Johnston, 1991). The Cupim leucogranites have a range of CaO/Na_2O and Al_2O_3/TiO_2 which suggests that the two-mica granites have lower clay sources and higher temperatures than the garnet-bearing granites (**Fig. 2.10b**). The composition of the two-mica granites is nearly similar to melts produced by melting of a muscovite-biotite-schist under pressures between 6 and 10 kbar and temperatures

from 750 to 825 °C (Patiño-Douce and Harris, 1998). The composition of the Cupim Leucogranites is also consistent with that of Neoarchean sediment-derived granites (**Fig. 2.10c**) (Laurent et al., 2014).

Fluid-absent and fluid-present melting processes are invoked to explain the production of these magmas (see Weinberg and Hasalová, 2015). In the fluid-absent melting, the melt is produced through the dehydration reaction of muscovite and/or biotite, which can take place between ~700 and 800°C depending on the source mineralogy. Otherwise, the addition of fluids (mainly water-fluxed) promotes the production of melts from a haplo-granitic quartz-feldspar ± aluminosilicate/ phyllosilicate system at relatively lower temperatures (>600 °C). Additionally, pelite-derived melts that were formed through muscovite dehydration in fluid-present conditions are much more voluminous, Rb/Sr-depleted, and Sr/Ba-enriched compared to pelite-derived melts formed in fluid-absent conditions because of the amount of feldspar left in the melting residue (Harris and Inger, 1992). The Rb/Sr and Sr/Ba ratios of the Cupim leucogranites suggest melting through muscovite/biotite dehydration under fluid-absent conditions like what is proposed for Himalayan leucogranites (Cao et al., 2022; Guo and Wilson, 2012; Harris and Inger, 1992). The Rb/Sr and Rb/ Ba ratios of these granites also suggest source heterogeneity (Sylvester, 1998) (**Fig. 2.10d**).

Cupim zircon crystals dated at 2000 Ma have negative initial ε_{Hf} values which is consistent with crustal reworking for the origin of Cupim magmas (**Fig. 2.8b**). Similarly, pristine 2000 Ma zircon crystals from Cupim leucogranites have average $\delta^{30}Si$ values that are similar to those of S-type granite zircons measured by Guitreau et al., (2022). No discernible difference was observed between zircon crystals from Group 1 (two-mica) and Group 2 (garnet-bearing) leucogranites (**Fig. 2.9a**). Apparent melt-zircon Si isotope fractionation factors ($\Delta^{30}Si_{WR\text{-}Zrc}$) calculated for Cupim leucogranites plot beyond the theoretical line that corresponds to a melt with 100 wt.% SiO_2 which should be considered as a limit (**Fig. 2.9d**). This is probably because the $\delta^{30}Si$ value used for S-type granites ($\delta^{30}Si_{WR}$ = -0.3‰; Savage et al., 2012) does not represent that of the actual melt from which zircon crystallized as also suggested in Guitreau et al. (2022). If we consider the lowest $\delta^{30}Si$ in our dataset (-1.2 to -1.0‰) together with a $\Delta^{30}Si_{WR\text{-}Zrc}$ of 0.4-0.5‰ to back-calculate the zircon parental melt $\delta^{30}Si$, we obtain values from -0.8 to -0.5‰, which fall in the range exhibited by continental shales and, most importantly, consistent with clay minerals (Opfergelt et al., 2010; Savage et al., 2013). Consequently, leucogranite $\delta^{30}Si$ signatures may be partly buffered by restitic minerals entrained in the melt and a $\delta^{30}Si_{WR}$ of -0.3‰ likely does not reflect that of the melt zircons crystallized in equilibrium with. This hypothesis may also account for the variable Si isotope signatures exhibited by Cupim zircon grains.

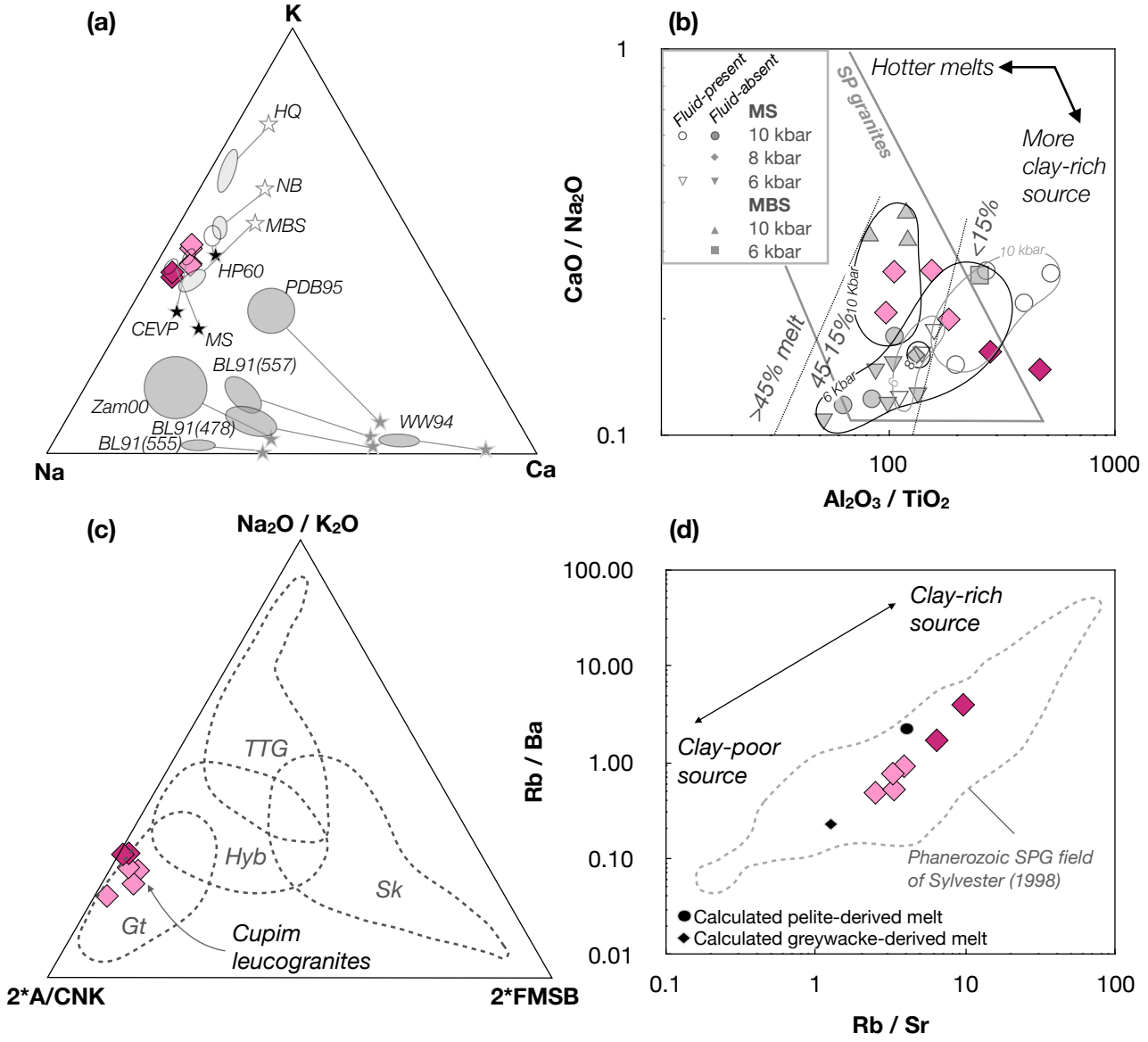


Figure 2.10: Source discrimination diagrams for the sampled leucogranites. (a) Na-K-Ca triangular diagram showing the relative composition of the leucogranites and the composition of experimental melts. Stars represent the source material composition, while ellipses represent the final products of melting. Dark grey symbols are TTG materials, and light grey and white symbols are meta-sedimentary materials. The abbreviations are the same as those used by Moyen (2011). (b) Al2O3 vs. CaO/Na2O composition for the studied samples and melts using different materials, and pressure and fluid activity. MS [Muscovite schist] and MBS [Muscovite–biotite schist] from Patiño Douce and Harris, 1998. Field of Strong Peraluminous Granites (SPG) defined by Sylvester et al., 1998. (c) Source diagram and classification proposed for Neoarchean granitoids (Laurent et al., 2014). The 2A/CNK pole suggests a sedimentary source. (d) Rb/Sr vs. Rb/Ba composition showing clay-rich and clay-poor heterogeneity of the produced melts (from Sylvester 1998).

2.2.5.3.Parental magma and magmatic processes

Continuing with the interpretation that these granites were dominantly crystallized from a single liquid formed by melting of a metagreywacke rock with an increasing contribution of clay,

we assume that the composition of Group 1 leucogranites could be similar to the most primitive magma that built the Cupim Pluton and that fractional crystallization is minimal. As a consequence, we modeled the partial melting of hypothetic sedimentary sources (i.e., Archean shales, Post-Archean Australian Shale (PAAS), the upper continental crust, and local sedimentary rock; Cabral et al., 2019; McLennan, 1989; Taylor and McLennan, 2009) with the goal to reproduce the REE composition of GC1 sample which has the highest mafic index (M') among Group 1 leucogranite. We also used the equations of batch melting and mineral-melt partition coefficients in rhyolitic melts listed in Rollinson and Pease (2021). The REE composition of the assumed parental magma can be best reproduced using an Archean shale source composition at moderate to high degrees of partial melting (~30% to 60%) and a restite with 94% Kfs + 6% Bt (**Fig. 2.11a**). K-Feldspar content may be overestimated because it could be replaced by sillimanite (Sil). However, we have not used this latter mineral in our model because of poorly constrained partition coefficients. This model can finally replicate the muscovite dehydration reaction (Ms+Qtz+ Pl → Kfs+Sil+Bt + melt Patiño-Douce and Harris, 1998). In these conditions, the metagreywacke protolith was rich in muscovite and aluminosilicate so that the solidus was reached before garnet and pyroxene could be stabilized in the residue.

The near-minimum melts leading to the formation of strongly peraluminous granites exhibit a highly evolved and uniform composition, yet subtle chemical variations may signify underlying magmatic differentiation processes (Tartèse and Boulvais, 2010). Analysis of Cupim leucogranites reveals a narrow SiO_2 variation, which does not exhibit a significant correlation with most major and trace elements (refer to **Supplementary Material B**). Notably, only Na_2O correlates with SiO_2, meaning that quartz-rich samples exhibit higher albite content. Discernible correlations between Al_2O_3 and K_2O variations, as well as inter-correlations among MgO, FeO^t, and TiO_2, suggest potential biotite/muscovite fractionation. The positive correlation observed between MgO and Zr contents (**Fig. 2.5b**), coupled with the prevalent presence of zircon inclusions in biotite, further supports the biotite fractionation hypothesis. Conversely, variations in Sr and Ba content exhibit a correlated pattern, along with correlations with some trace elements (e.g., La, Zr) and Mg#. The observed Sr and Ba variations may mirror the increasing fractionation of biotite, alkali feldspar, and plagioclase from a less evolved melt (Tartèse and Boulvais, 2010). The Sr+Ba composition of the two-mica Cupim leucogranites is higher than the garnet-bearing leucogranites (**Fig. 2.11b**). The Rb/Sr vs. Ba diagram (**Fig. 2.11c**) better indicates vapor-absent muscovite-dehydration melting (see Weinberg and Hasalová, 2015). The substantial variation in Ba concentrations (~300-90 ppm) relative to Sr (100-40 ppm) suggests that alkali feldspar and biotite fractionation play a more significant role than plagioclase, according to their partition coefficients (see Nabelek, 2020). This may explain the lower biotite and alkali feldspar content of garnet-bearing Cupim leucogranites. The elevated Sr and Ba contents observed in samples GC5A and GC5B may be attributed to the presence of porphyritic K-feldspar crystals. Variations of Rb/Sr ratios can be used to identify

magmatic differentiation processes alike what was done on Himalayan leucogranites (Cao et al., 2022). However, Rb/Sr variations and correlations with specific trace elements (e.g., La, Eu, Hf, Zr, see **Fig. 2.5a** and **Supplementary Material B**) in the Cupim leucogranites more likely reflect source heterogeneity rather than differentiation mechanisms upon cooling. Enrichment in Y and HREE likely results from garnet crystallization in samples with the highest Rb/Sr ratio.

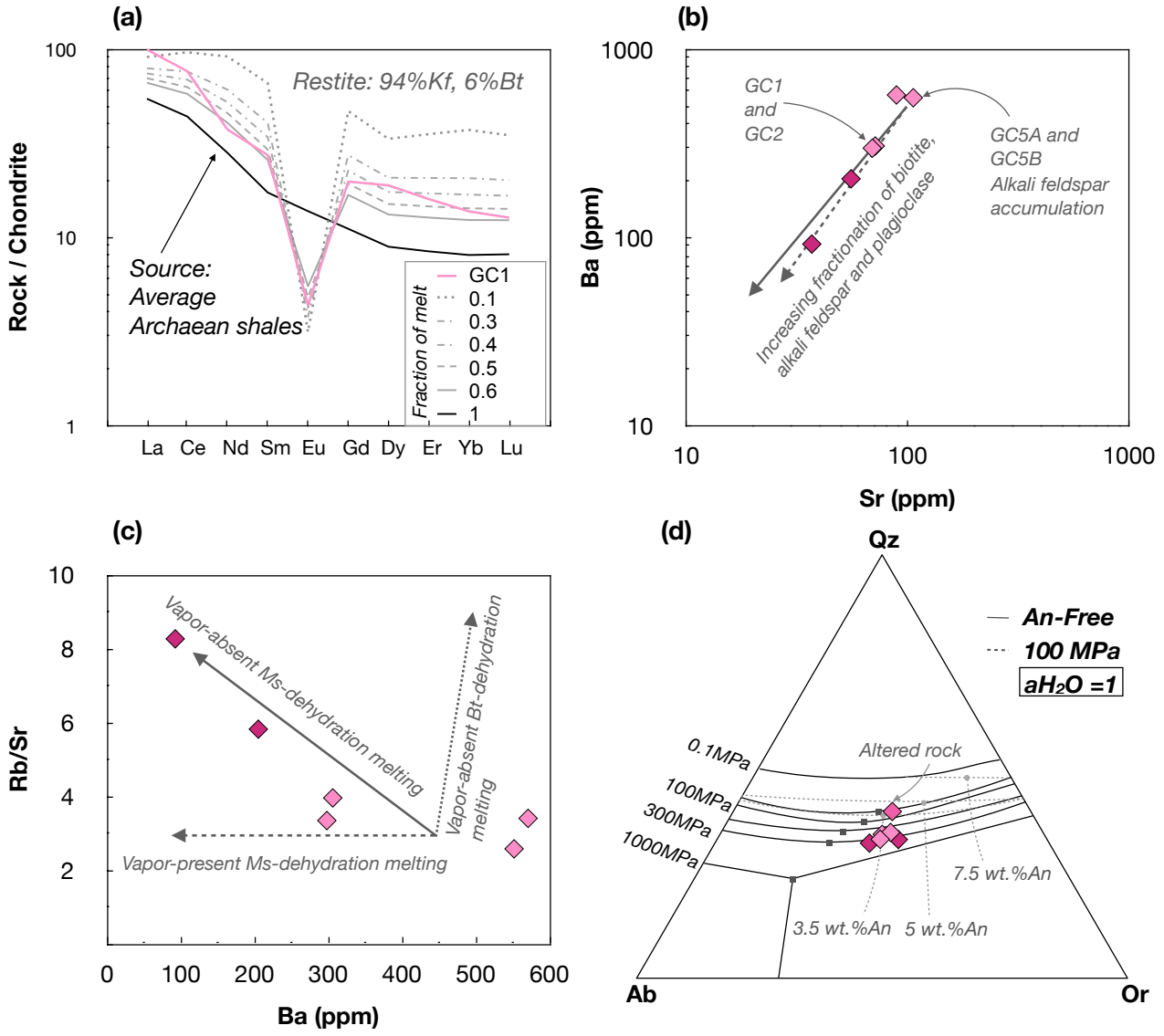


Figure 2.11: Petrogenetic parameters of the magmatic process for the Cupim leucogranites. (a) Chondrite-normalized REE patterns of melts derived from the partial melting Archean shales (Taylor and McLennan, 2009) source and left behind K-feldspar cumulate residue. The modeled melts are compared with the proposed parental magma of the leucogranites (GC1). Details of the models are given in the text. (b) Sr vs. Ba variation for the leucogranites. The solid and the dashed lines are theoretical evolutions of a liquid throughout the fractionation of biotite, alkali feldspar, and plagioclase fractionation (Tartèse and Bouvais, 2010). (c) Distinct behavior of Rb/Sr and Ba for different melting reactions (see Weinberg and Hasalová, 2015). Cupim leucogranites (from two-mica to garnet-bearing) mimic the muscovite dehydration reaction in the absence of aqueous fluids leading to an increase of Rb/Sr and a decrease in Ba. (d) Ternary projection of cotectic curves and minimum points (black squares) at various pressures and normative melt An contents, according to Tuttle and Bowen (1958). Shift from these minimum points to the right can indicate a decrease in water activity.

Muscovite/biotite dehydration melting usually produces peritectic minerals (e.g., Kfs, Sil, Bt, Grt, Crd, Opx) that can either remain in the melting residue as restitic minerals or be captured in newly formed liquids (Stevens et al., 2007; Villaros et al., 2009). Garnet entrainment occurs in the more Mg-Fe-rich, least-evolved peraluminous magmas (Stevens et al., 2007). The mineral chemistry of biotite and garnet of the Cupim leucogranites suggests that these minerals were crystallized from a peraluminous melt instead of having been entrained into it. Additionally, spessartine-rich (mol>10%) garnets are stable in silicic liquids at low pressures (5 kbar or less; Green, 1977). The normalized Ab-Qz-Or compositions of the Cupim leucogranites (**Fig. 2.11d**) actually suggest an emplacement at 3 kbar (300 MPa) (Tuttle and Bowen, 1958). **Table 2.4** summarizes the main petrogenetic parameters of Cupim Pluton leucogranites.

Table 2.4: Petrogenetic parameters for the Cupim Pluton leucogranites.

Zircon U-Pb age	~2000 Ma
Inherited age	Mostly Archean
Zircon Hf isotopes	Reworked, mixed sedimentary sources, $\varepsilon_{Hf(t)}$ = -8.1 ± 0.7 (*av., 2SD*)
Zircon Si isotopes	Light, δ^{30}Si = -0.82 ± 0.17‰ (*av., 2SD*)
Rock types	Two-mica to garnet bearing leucogranites
Ab-An-Or classif.[a]	Granite normative
Acc. Minerals	Zrn, Mnz, Ap, Aln, Xtm-Y
Major elements	
Silica content	Acid (72 to 75 wt.%)
ASI [b]	Strong peraluminous (ASI≥ 1.1)
A-B classif. [c]	Felsic-peraluminous
MALI [d]	Alkali-calcic
Mg#	Low (19-10)
K_2O/Na_2O	Potassic (>1.2)
CaO/Na_2O [e]	Low (<0.3)
Al_2O_3/TiO_2 [f]	High (97-466)
Trace elements	
Rb/Sr	Moderate to high (2.5-8.27)
Rb/Ba	Low to moderate (0.48-3.3)
Sr/Y	Low to moderate (0.5-4.77)
$(La/Yb)_N$	Low to moderate (1.2-19.83)
$(La/Sm)_N$	Low (2.16-4.77)
$(Gd/Yb)_N$	Low (0.53-2.56)
Eu/Eu* [g]	Negative (0.08-0.15)
HFSE (ppm)	High Th (16.7-48.8), High Nb (11.6-18.6), Low Zr (40.6-144), High Y (22.2-84.9)

[a] *Classification after Barker (1979)*
[b] *Molar Al/(Ca–1.67P+Na+K)] > 1.1*
[c] *Parameters according to Debon and Le Fort (1983) and classification after Villaseca et al. (1998)*
[d] *Classification according to Frost et al. (2001)*
[e] *According Sylvester et al. 1998*
[f] *According to Bucholz and Spencer 2019*
[g] *Eu/Eu* = $\{(Eu)_N / \sqrt{[(Sm)_N^2 + (Gd)_N^2]}\}$*

2.2.5.4. Hf isotope variations in zircon

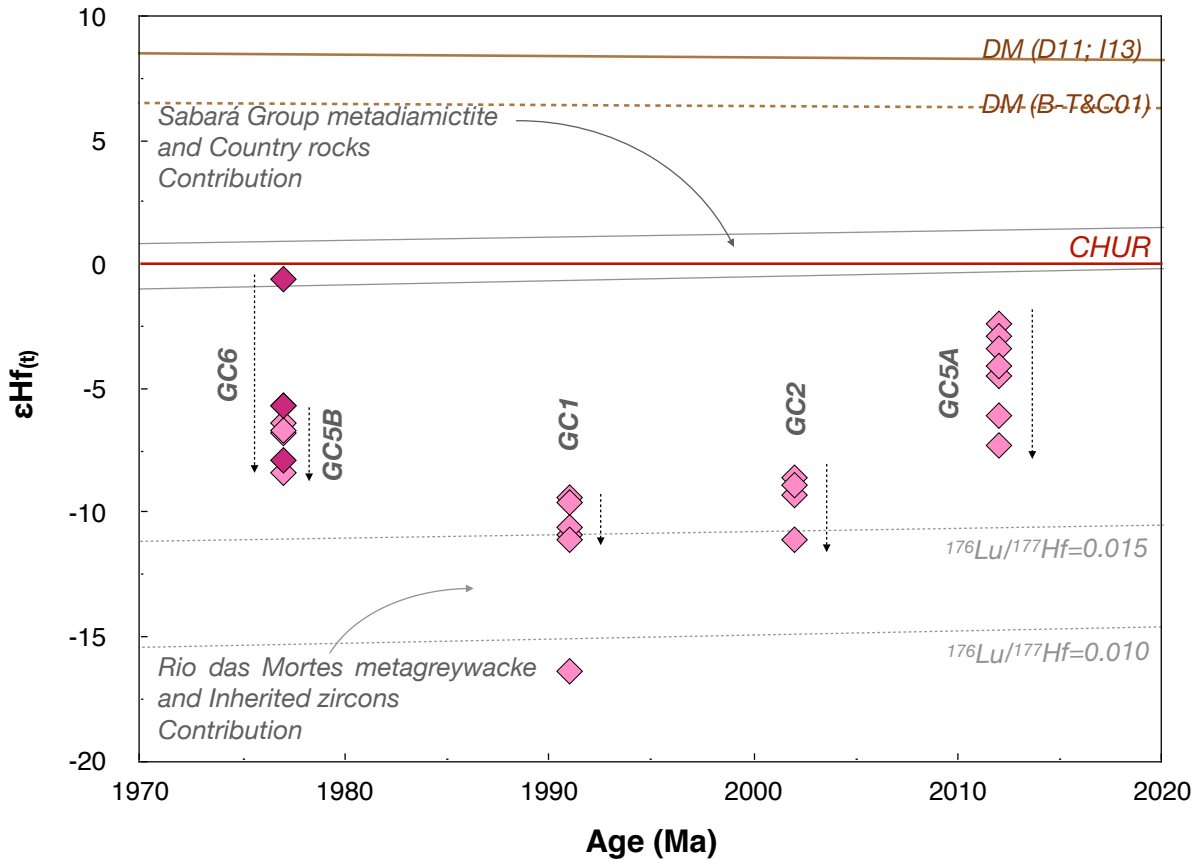
Magmatic zircon grains exhibit two types of ε_{Hf} variations. They vary between and within samples (**Fig. 2.12**). Importantly, the lack of apparent correlation between $\varepsilon_{Hf(t)}$ and $^{176}Yb/^{177}Hf$ for all samples demonstrates that the ε_{Hf} heterogeneity is a true feature of the zircon populations rather than an analytical artifact (Fisher et al., 2011).

The inter-sample variation can be attributed to different contributions from two main sources: (i) less radiogenic (more negative ε_{Hf} values) and (ii) more radiogenic (less negative ε_{Hf} values). Metagreywackes within the Mineiro Belt ($\varepsilon_{Hf(2000)}$~ -14, Moreira et al., 2020) and the Archean inherited zircons ($\varepsilon_{Hf(2000)}$~ -16) are good candidates for the source component (i), whereas metadiamictites of the Sabará Group ($\varepsilon_{Hf(2000)}$~ -1, Moreira et al., 2020) and the Paleoproterozoic juvenile country rocks ($\varepsilon_{Hf(2000)}$~ 0) (e.g., Lagoa Dourada and Alto Maranhão suites, Moreira et al., 2020) are plausible options for the source component (ii). Therefore, each sample from the Cupim Pluton could reflect the relative contribution of each source end-member. Magmatic zircon domains from GC6 (Group 2 leucogranites) have the least negative $\varepsilon_{Hf(t)}$ values of all samples, reflecting a more significant contribution from source (ii). Indeed, the geochemistry of Group 2 leucogranites suggests that they are derived from a more clay-rich (metadiamictite) source.

A third alternative is the contamination of the magma (originally with negative $\varepsilon_{Hf(t)}$ with the surrounding juvenile country rocks. However, no field relationship such as xenoliths was observed to support this assumption. Furthermore, possible magma contamination by assimilation of surrounding rocks (low-K and low-Rb/Sr), even in small fractions, would drastically change the composition of Cupim leucogranites.

On the other hand, the observed variations in ε_{Hf} values in the same sample should be considered individually. The lowest ε_{Hf} value (-16.4 ± 1.0, 2SD; z31) from GC1 may reflect the complex texture of the zircon grain and possible mixture between the composition of the core and rim domains. The lowest ε_{Hf} value (-11.1 ± 1.0, 2SD; z42) from GC2 may be indicative of mixing between pristine and altered domains. Zircon crystals from GC5A show a large variation in ε_{Hf} values (-7.3 ± 0.6 to -2.4 ± 0.9, 2SD). Interestingly, zircon grains from this sample do not have inherited domains and analyses were performed in relatively simple domains. The single analysis performed in the blurred texture zircon grain from GC6 shows the least negative ε_{Hf} value (-0.6 ± 0.7, 2SD) and may reflect the complete dissolution of a juvenile inherited grain.

Figure 2.12: Detailed area in ε_{Hf} vs. age space of magmatic zircon domains (excluding GC7 due to age uncertainty) showing variation between samples and on the same sample. Magmatic zircon grains are color-coded following Fig.8. Age (in Ma) refers to the upper intercept age calculated for each sample. The Lu/Hf evolution (grey lines) defines the two Hf radiogenic source end members, as shown in Fig.8b. Vertical dashed black arrows indicate variations in ε_{Hf} values from the same sample (see text for details).



2.2.5.5.Tectonic implications

Pure-crustal melting typically takes place during the syn-collisional stages of an orogen (e.g., Himalayan leucogranites, Hopkinson et al., 2017). In this case, there is no input of heat from basalts. Instead, fertile, and radioactive materials (e.g., sedimentary rocks) become able to produce granitic melts, depending on the subcrustal heat flow and heat production, when brought down into a double-thick imbricated crust (Bea et al., 2012). These melts are commonly associated with migmatitic gneissic complexes that could represent the lower crust partially melted. Alternatively, crustal-derived melts could be produced during post-collisional stages and in compressional/ extensional continental arcs (Jacob et al., 2021). Orogen collapse, exhumation, and asthenosphere upwelling drive decompression melting of the crust during post-collisional stages. Usually, these crustal melts are coeval with crustal-contaminated mantle-derived granitic magmas (e.g., Variscan French Massif Central, Couzinié et al., 2016; Moyen et al., 2017). On the other hand, large volumes of sediments are available to melt when pulled down into the continental arc trench or when heated by basaltic inputs into the back-arc of an active continental margin (slab retreating). Moreover, these melts are often contemporaneous with mantle-derived granitic magmas (e.g., Lachlan Fold Belt, Kemp et al., 2009). Archean crustal-derived melts are tentatively interpreted as the result of the melting of sediments buried during 'sagduction' when compressing hot lithospheres (Poujol et al., 2021).

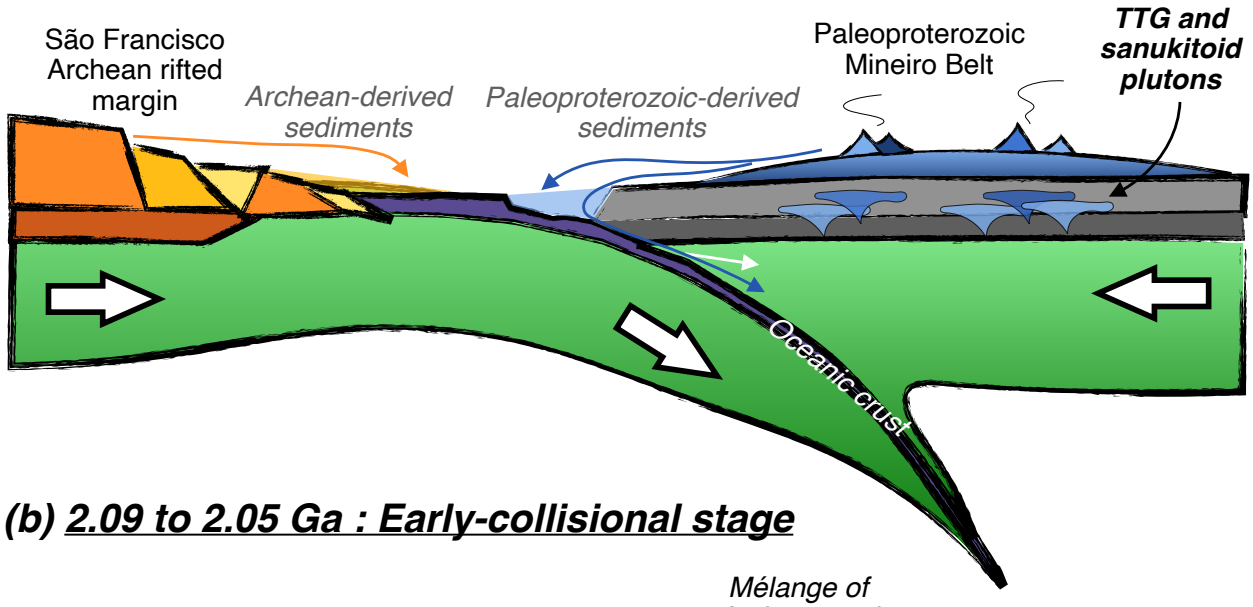
Anatexis at 2050 Ma is recorded by migmatite occurrence in the southern QF region (Carvalho et al., 2017). Additionally, this age is also recorded by metamorphic titanite and monazite grains from gneiss and granitic rocks within the QF and Mineiro belt region (Aguilar et al., 2017; Moreira et al., 2018). Therefore, we attributed this age to the regional metamorphic peak which is probably due to the accretion of the Paleoproterozoic belts to the Archean nuclei (previously called Transamazonian orogeny, Alkmim and Marshak, 1998). The P-T conditions at this stage, and perhaps progressive decompression, allowed crustal melting, magma ascent, and granitic emplacement that generated the Cupim Pluton 50 million years later, thereby, suggesting a prolongated collisional event. This geodynamic scenario is akin to the genesis of Himalayan leucogranites (Cao et al., 2022; Guo and Wilson, 2012).

Concerning the tectonic scenario proposed by Moreira et al. (2020), the Cupim leucogranites could add a final stage of magma production through crustal reworking at 2000 Ma. At this point, the Paleoproterozoic crust was amalgamated and compressed against the Archean nuclei of QF region. **Figure 2.13** sets out the proposed sequence of stages in the tectonic evolution of the Mineiro Belt. During the initial phase (pre-collisional, **Fig. 2.13a**), the subduction process results in a transition from TTG (2.35 Ga) to sanukitoid and hybrid magmas (2.12 Ga). The subsequent stage (2.09-2.05 Ga, **Fig. 2.13b**) marks the onset of a soft collision, whereby the oceanic plate is completely consumed and sediments from multiple origins are mixed into sedimentary basins. The gradual thickening of the continental crust also produces molten crustal rocks (migmatites). During the final stage (2.01-1.98 Ga, **Fig. 2.13c**), the orogen reaches its maximum thickness due to compression of Archean blocks and/or Palaeoproterozoic belts (e.g., Piedade Block, Mantiqueira complex; Bruno et al., 2021). Paleoproterozoic sedimentary rocks (with Archean and Paleoproterozoic provenance) were buried between the amalgamated crust and heated sufficiently to partially melt and produce the Cupim leucogranites (**Fig. 2.13c**).

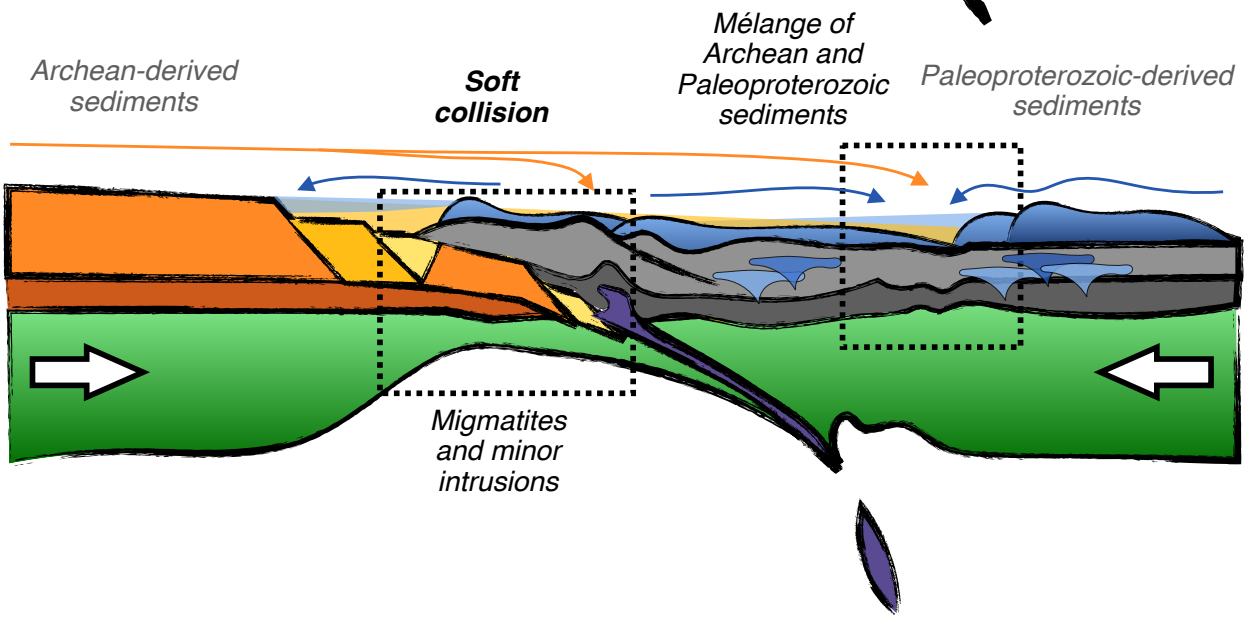
In the northern part of the São Francisco Craton, 2000 Ma peraluminous granites are also interpreted as products of partial melting of supracrustal material during the collision of the Jequié and Gavião Archean nuclei (Cuney et al., 1990). Likewise, 2000 Ma S-type granites in Gabon also mark the continental collision between São Francisco and Congo cratons during the Eburnean orogeny (Weber et al., 2016). The occurrence of sediment-derived magmatism in both localities indicates the assemblage of several Archean nuclei from the São Francisco-Congo cratons. This scenario could be globally correlated to the formation of the Columbia supercontinent.

Finally, the Cupim leucogranites mark the end of a shorter subduction-collision cycle (~130 Ma), preceded by a long period (~220 Ma) of TTG emplacement in the Mineiro Belt. This succession of periods is typical of the emplacement of Late-Archean granitoids, which represent the global initiation of "modern-style" plate tectonics (Laurent et al., 2014). As such, the Cupim leucogranites support the idea of a tectonic regime transition during the Paleoproterozoic (Moreira et al., 2020).

(a) 2.35 to 2.12 Ga : Pre-collisional stage



(b) 2.09 to 2.05 Ga : Early-collisional stage



(c) 2.01 to 1.98 Ga : Late-collisional stage

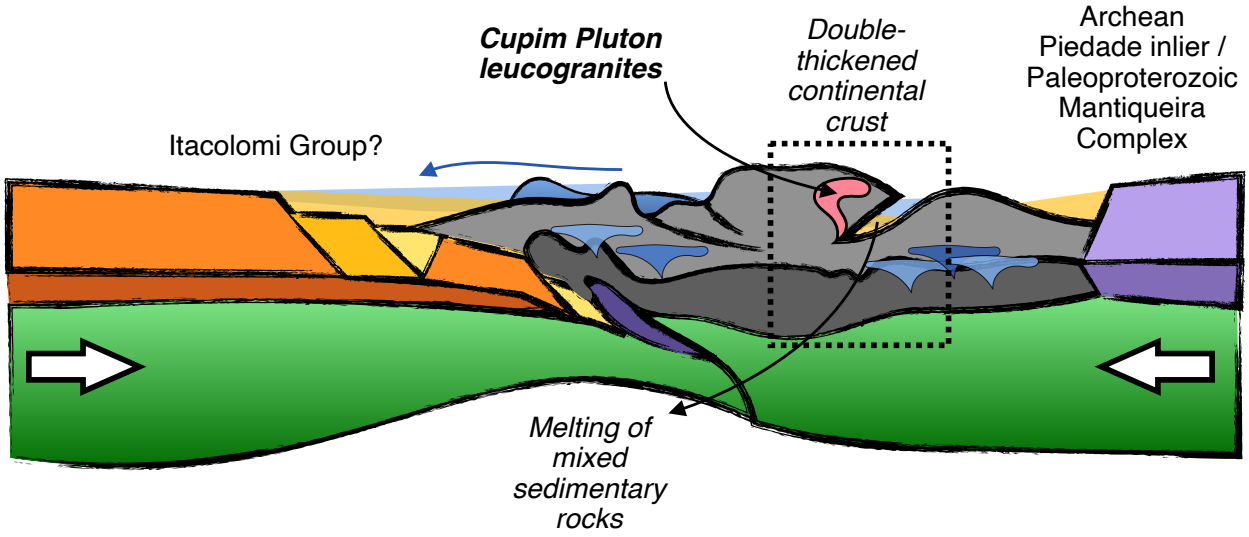


Figure 2.13: A proposed collisional tectonic scenario for the genesis of the Cupim Pluton leucogranites (not to scale). (a) Steepening of subducted oceanic slab generates TTG-sanukitoid magmas in the Mineiro Belt, which gradually approaches the rifted margin of the São Francisco Archean crust. From these two tectonic terrenes, forearc (Paleoproterozoic) and passive margin (Archean) sediments are deposited. (b) Consumption of oceanic crust promotes the onset of collision between the Mineiro Belt and the São Francisco rift margin. The soft collision heats the lower crust and generates migmatites and metamorphic fingerprints in both terranes. Sediments of Archean and Palaeoproterozoic provenance are mixed and deposited within the orogen. (c) Compression of the orogen by Archean inliers and/or Paleoproterozoic belts promotes horizontal shortening and vertical thickening of the orogen. This results in the melting of crustal lithologies (mainly sedimentary rocks) and generates peraluminous magmas that form the Cupim Pluton leucogranites.

2.2.6.Conclusions

Whole-rock and mineral chemical composition, linked with the geochronology and Hf-Si isotope data of magmatic and inherited zircon grains from Cupim Pluton, reveal a hitherto unknown episode of crustal reworking and production of sediment-derived magmas in the southern portion of the São Francisco Craton (Brazil). During a late collisional tectonic scenario, at ca. 2000 Ma, magma production was controlled by crustal reworking via melting of sedimentary rocks.

The chemical composition of the Cupim leucogranites suggests muscovite/biotite-dehydration melting as a key genetic process and its diversity can be linked to source heterogeneity and minor mineral fractionation. These claims are the same as those invoked to explain the genesis of modern S-type granites (e.g., Himalayan leucogranites). Inherited zircon cores, as well as subchondritic $\varepsilon_{Hf(t)}$ and light Si isotope compositions of magmatic zircon grains from Cupim leucogranites suggest parental magma formation by crust reworking, and Hf isotope variations suggest source mixing.

The inherited zircon grains from the Cupim leucogranites show that the sedimentary basins of the Mineiro Belt were fed mainly by detritus from the Archean core of the SFC. This elucidates their depositional environment and sheds light on the associated tectonics.

2.3. Supplementary material A

2.3.1. Methods

2.3.1.1. Sampling

Representative samples, i.e., rocks that represent the main lithotype of investigated outcrops, were collected by observing field relationships, whenever visible, discriminating different facies, and referencing geospatial position [Lat / Long]. The type-locality of the Cupim Pluton, labeled as GC2 [20°48'40.64"S / 43°48'25.98"W] (**Fig. 2.1c**), was defined by Santos and Baltazar (2013) in a poorly exposed outcrop composed of partially weathered rocks. This outcrop is located on the margins of the BR-040 highway (km 648) near a homonymous gas station. The best exposures are in two active quarries, to the north of the type-locality, in which sample GC1 [20°48'10.64"S / 43°47'45.72"W] was collected (**Fig. 2.1c**). Sampling sites for GC6 [20°51'49.27"S / 43°49'51.52"W] and GC7 [20°50'57.25"S / 43°49'22.02"W] sampling sites are located to the south of GC2, closer to the town of Pedra do Sino, and can be accessed via local roads. The GC5 exposure, where GC5A [20°54'45.34"S / 43°52'42.78"W] and GC5B [20°54'46.11"S / 43°52'40.85"W] samples were collected, is located at the southern end of the pluton, close to the Lenheiro shear zone (**Fig. 2.1c**). All representative collected samples have similar mineralogical content and are distinguished from their surrounding granitic rocks by the low content of mafic minerals and the presence of aluminous phases, e.g., muscovite and/or garnet. Collectively, these petrographic characteristics form the basis for the definition of the Cupim Pluton in this study.

2.3.1.2. Mineral chemistry

Selected thin sections and rock fragment epoxy mounts were carbon-coated for SEM/EDS analyses at the Laboratório de Microscopia e Microanálises (LMic) at the Universidade Federal de Ouro Preto, Brazil. Mineral chemical analyses were performed using JEOL scanning electron microscope (JSM-6510) in backscattered electron (BSE) mode and phase compositions quantified by energy dispersive X-ray spectroscopy (EDS) analysis using a Pentafex-INCA EDS Detector (Oxford Instruments). The primary electron beam was generated by a tungsten filament-type apparatus under high vacuum conditions. Analyses were done by applying an accelerating voltage of 20 kV, a work distance of 15 mm, and a spot size of 70 [in a reference scale of 0-100]. Standardless quantitative EDS analyses used a ratio of peak intensities to determine the relative abundance of major elements, mainly, that were converted and reported as percentage proportions in their oxide forms (SiO_2, TiO_2, Al_2O_3, CaO, MgO, FeO^t, MnO, Na_2O, K_2O, P_2O_5), using the Aztec software package (Oxford). X-ray counts with the set-up used were typically 7000 cps. The counting time was 50 s live time. Zr, REE, and Y were semi-quantified in their oxide forms when element-rich (e.g., monazite, xenotime, zircon) minerals were analyzed. Mineral identification was based on oxide compositions within the ranges listed in Deer et al. (2013).

2.3.1.3. Whole-rock geochemistry

Representative fresh to weakly altered samples were crushed at the *Laboratório de Preparação de Amostras* (LOPAG) in the *Departamento de Geologia at Universidade Federal de Ouro Preto*, Brazil. The crushing process involved classical comminution procedures using a jaw WC crusher and pan mill until the samples were pulverized and homogenized. Whole-rock major element analyses were conducted at the *Laboratoire Magmas et Volcans* (LMV, *Université Clermont Auvergne*, Clermont-Ferrand, France) using an Agilent 5800 ICP-OES. Whole-rock trace element analyses were done at Service d'Analyse des Roches et des Minéraux (SARM) which is hosted at *Centre de Recherches Pétrographiques et Géochimiques* (CRPG, Nancy, France) using an iCapQ ICP-MS and iCap6500 ICP-OES. All chemical analyses were carried out using certified reference materials such as DR-N and BHVO-1 for quality control. All measured major element concentrations for reference materials showed external reproducibility between <1 and 5% (2SD), except for P_2O_5 (8%). These measurements complied with certified values within an interval corresponding to less than 7%, most oxides agreeing within 4% of published values. The majority of determined trace element concentrations have 2SD analytical precisions better than 10% and so is accuracy on most elements. Uncertainties and detection limits for each element are provided in **Supplementary Material B**.

2.3.1.4. Heavy mineral concentration and separation

The concentration and separation of heavy minerals were conducted at the *Laboratório de Análises Minerais LAMIN* of the Geological Survey of Brazil (CPRM) hosted in the town of Caeté, Minas Gerais State, Brazil. For each of the six collected samples, three to five kilograms of fresh to weakly altered rock were crushed using a jaw crusher and carefully milled in a pan mill. Subsequently, heavy minerals were concentrated through panning and micro-panning techniques. The concentrated minerals were then separated into five size fractions (>250 μm, 250-177 μm, 177-125 μm, 125-74 μm, and <74 μm) using wet-sieving methods.

To further refine the separation, all size fractions were subjected to heavy-density liquids, specifically pure bromoform with a density of 2.89 g/cm^3. This process was followed by hand-imam and Franz magnetic separation. In the Frantz magnetic separation, the ruler was inclined at a twenty-degree angle counterclockwise in the long axes and a fifteen-degree angle counterclockwise in the perpendicular axes. The electric flow varied from 0.3, 0.5, 0.75 to 1A. The non-magnetic fractions, which were not attracted by any of the produced magnetic fields, were preferentially chosen for further selection under a binocular microscope.

2.3.1.5.Zircon imaging

Before analysis, zircon crystals from six Cupim Pluton samples (GC1, GC2, GC5A, GC5B, GC6, and GC7) were carefully handpicked and mounted in epoxy. The mounts were subsequently polished to zircon crystal half-thicknesses. They were then imaged using cathodoluminescence (CL) and back-scattered electron (BSE) techniques. All images can be found in the **Supplementary**

Material C. The imaging was performed using a Jeol JSM-5910LV scanning electron microscope at LMV. The acceleration voltage for both CL and BSE image acquisition was set to 15 kV. The CL and BSE images provided information about the internal textures and external morphology of the zircons, which guided the selection of crystals for analysis using LA-(MC)-ICP-MS and determined the spot locations for elemental and isotopic analysis.

A total of 39, 31, 38, 33, 30, and 18 zircon crystals were mounted and imaged from samples GC1, GC2, GC5A, GC5B, GC6, and GC7, respectively. From these, 30, 30, 34, 32, 24, and 11 zircon crystals, respectively, were selected for further LA-(MC)-ICP-MS analysis. The number of crystals mounted in epoxy was determined based on the quantity and quality of zircon grains available from each sample. The selection of zircons for LA-ICP-MS analysis was based on the preservation of magmatic textures and the absence of advanced metamictization and alteration features, as described in Corfu et al. (2003). Overall, zircon crystals analyzed had lengths that ranged from approximately 80 to 600 µm.

The observations of reflected light microscopy, BSE, and CL images were also used to classify the main zircon textures, according to Corfu et al. (2003). Therefore, the following features were described (see **Supplementary Material D**): (i) geometry (prismatic or rounded, elongated or stubby); (ii) average length (μm), (iii) color, in reflected light microscopy images; (iv) length-to-width ratio; (v) BSE and (vi) CL intensities; (vii) type of zoning; the presence, abundance and main features of (viii) fractures, (ix) alterations and (x) recrystallization domains. Based on these comprehensive observations and descriptions, we were able to determine the dominant texture exhibited by each zircon grain, such as uniform texture with altered borders; bright core, and dark rims. This information played a crucial role in selecting appropriate sampling locations for subsequent LA-(MC)-ICP-MS analyses as well as in further data interpretation. No U-Th-Pb analyses were performed in altered borders, as they do not evolve in a closed system (Geisler et al., 2007).

2.3.1.6. Zircon U-Th-Pb geochronology

U-Th-Pb isotope measurements were conducted at LMV using LA-ICP-MS for three sessions, utilizing a 193nm Resonetics Resolution M-50E laser ablation system coupled to a Thermo Scientific Element XR ICP-MS. The instrumental settings can be found in the **Supplementary material D**. The diameter of the spot size used was 33 μm and spots were placed in single textural zones of the zircons based on CL and BSE images. In feasible instances, both the core and rim of zircons were analyzed. Additionally, multiple spots within similar domains/crystals were analyzed to enhance the accuracy of the calculated ages. Measurements were aborted if non-radiogenic Pb concentrations were identified above the background ^{204}Pb signal at the onset of the analyses.

Measurements were done by standard bracketing using 91500 zircon reference material (1065.4 ± 0.3 Ma; Wiedenbeck et al., 1995) as primary standard for normalization, whereas AS3 (1099.1 ± 0.5 Ma; Paces and Miller, 1993) and Plešovice (337.13 ± 0.37 Ma; Sláma et al., 2008) zircons were used as secondary standards for quality control. In subsequent sessions, Plešovice zircon was used as a primary standard, and 91500 and AS3 zircons as secondary standards. The data were collected in batches that comprised six unknowns bracketed by four measurements of 91500 or Plešovice primary standards.

The *Iolite4* software (Petrus and Kamber, 2012; Paton et al., 2011) was used to process zircon U-Th-Pb data. Age calculations were done using a present-day $^{238}U/^{235}U$ ratio value of 137.818 (Hiess et al., 2012) and decay constants of 1.55125×10-10, 9.8485×10-10, and 4.9475×10-11 yr-1 for ^{238}U, ^{235}U, and ^{232}Th, respectively (Jaffey et al., 1971). Within the *Iolite4* software, it was possible to discern complex signals, which could indicate analysis of different crystal domains. Furthermore, the software facilitated the identification of non-radiogenic Pb through the detection of ^{204}Pb signal exceeding the background level, which is mostly related to the presence of ^{204}Hg in the LA-ICP-MS carrier gas. Any analysis exhibiting unreasonable signals or indicating the presence of non-radiogenic Pb was not considered further and therefore, not presented in this study.

Concordia plots were generated using the *IsoplotR* software (Vermeesch, 2018). To further interpret U-Pb ages and investigate potential correlations between ages and U concentrations resulting from radiation-damage-induced alteration, semi-quantitative concentrations of U, Th, and Pb were determined by external normalization to 91500 or Plešovice.

Table S.1 summarizes all calculated ages for the used zircon reference materials during each analytical session. All calculated ages agree well with consensus ages (**Table S.1**, see also **Supplementary Material D**) (Wiedenbeck et al., 1995; Paces and Miller, 1993; Sláma et al., 2008).

Table S.1: Summary of calculated ages for zircon reference materials used in this study. Concordia ages using the algorithm of Ludwig (1998). 2σ notation refers to 2 × standard deviation (STD). MSWD is the Mean Square of the Weighted Deviations for age homogeneity. n refers to the number of analyses used for each calculated age.

	Zircon Reference Material	Concordia Age (Ma)				Intercept Age (Ma)				Weighted Mean Average Age (Ma)											
		Age	2σ	MSWD	n	Upper Lower	2σ	MSWD	n	$^{206}Pb/^{238}U$	2σ	MSWD	n	$^{207}Pb/^{235}U$	2σ	MSWD	n	$^{207}Pb/^{206}Pb$	2σ	MSWD	n
Session 1																					
First sequence																					
	91500	1062.6	3.1	0.11	24					1062.4	3.1	0.031	24	1063.1	4.3	0.19	24	1065	12	0.24	24
	AS3	1170.2	7.7	25	5					1176.8	8.1	2.2	5	1153.9	9.9	0.97	5	1115.8	22.4	2.2	5
	Plešovice	348.8	2.2	0.00035	6					348.9	2.2	12	6	346.1	4.1	0.29	5	349	25	1.2	6
Second sequence																					
	91500	1062.0	2.9	0.14	12					1062.5	3.5	0.072	12	1063.4	3.7	0.39	12	1064.9	11	0.4	12
	AS3					1082 38	18 166	3.3	3	1172.5	7.6	52	3	1143.8	6.9	17	3	1085.2	14.8	1.5	3
	Plešovice	352.3	2.7	0.14	2					352.4	2.8	8.5	2	352	3.6	5.3	2	349	23	0.15	2
Session 2																					
	91500	1073	13	0.74	5					1068	17	1.1	5	1076	14	1.3	5	1092	46	0.18	5
	AS3					1078 167	62 1087	0.19	6	1138	17	5.8	6	1121	13	4.1	6	1085	31	0.17	6
	Plešovice	337.2	2.3	0.015	24					337.1	2.6	0.00058	24	337.3	2.9	0.0015	24	339	22	0.00088	24
Session 3																					
	91500	1044.8	6.1	0.3	5					1043.4	8.2	0.42	5	1046	7	1.4	5	1051	23	0.81	5
	AS3	1112.9	6.8	12	5					1122.6	8.7	3	5	1110	7	1.9	5	1087	16	0.73	5
	Plešovice	337.2	1.2	0.068	20					337.1	1.4	0.0054	20	337.3	1.5	0.012	20	339	12	0.012	20

2.3.1.7. Zircon Lu-Hf isotopes

Lu-Hf isotope measurements were done at LMV using the same laser-ablation system as for U-Th-Pb analyses but coupled with a *Thermo Scientific Neptune Plus MC-ICP-MS*. Operating conditions and instrument calibration can be found in the Supplementary material D. Lu-Hf analyses were done using 47 μm spots preferentially located on top of 30 μm pits of prior U-Th-Pb analyses in order to accurately associate U-Pb ages to corresponding Hf isotope signatures.

Zircons were analyzed as batches of eleven unknowns which included three standards and eight studied samples. Analyses were bracketed by the REE-absent MUN zircon standard (MUN-0; Fisher et al., 2011). The zircon reference material analyzed as unknowns, included 91500, MudTank, and three MUN zircons (MUN-1, MUN-3, and MUN-4) with low, medium, and high Yb/Hf ratios, respectively. These standards were used to monitor the quality of our data processing procedure as in Guitreau et al. (2019).

To determine the instrumental mass biases for Yb and Hf, the $^{173}Yb/^{171}Yb$ ratio was normalized to a value of 1.130172 (Segal et al., 2003), and the $^{179}Hf/^{177}Hf$ ratio was normalized to 0.7325 (Stevenson and Patchett, 1990). It was assumed that Lu fractionation followed that of Yb (Fisher et al., 2014). Isobaric interferences of ^{176}Yb and ^{176}Lu at mass 176 were corrected using values of 0.793813 for 176Yb/173Yb (Segal et al., 2003) and 0.02655 for $^{176}Lu/^{175}Lu$ (Fisher et al., 2014). Finally, in the first session, we observed a slight data offset (up to 0.001) on $^{178}Hf/^{177}Hf$ ratios relative to natural abundances and subsequently corrected $^{176}Hf/^{177}Hf$ ratios according to the offset observed in the $^{178}Hf/^{177}Hf$ ratios.

Lu-Hf analyses were conducted in a single analytical session. 91500 and MudTank zircons yielded average $^{176}Hf/^{177}Hf$ values of 0.282300 ± 0.000010 (2SD; n=6) and 0.282522 ± 0.000009 (2SD; n=6), respectively. These values closely match the consensus values of 0.282308 ± 0.000008 (Blichert-Toft, 2008) and 0.282507 ± 0.000006 (Woodhead and Hergt, 2005) within analytical uncertainty (**Table S.2**, see also **Supplementary Material D**). The average $^{176}Hf/^{177}Hf$ measured in MUN-1, MUN-3, and MUN-4 was 0.282134 ± 0.00007 (2SD; n = 12), 0.282127 ± 0.00007 (2SD; n = 6), and 0.282127 ± 0.000020 (2SD; n = 6), respectively. Our results for MUN zircons are, hence, in full agreement with the value of 0.282135 ± 0.000007 reported by Fisher et al. (2011) (**Table S.2**, see also **Supplementary Material D**), indicating that our Lu-Hf data have been accurately corrected for isobaric interferences caused by ^{176}Yb and ^{176}Lu.

We used the ^{176}Lu decay constant of 1.867 × 10-11 yr-1 from Scherer et al. (2001) and Söderlund et al. (2004) to calculate the initial Hf isotopic compositions. Uncertainties associated with the radiogenic-ingrowth correction were propagated using the algorithms of Ickert (2013), and ε_{Hf} values were calculated using the CHUR values provided by Iizuka et al. (2015).

Table S.2: Summary of Hf and Si isotope data for the analyzed zircon reference materials compared with equivalent data from the literature.

Literature values	Average $^{176}Hf/^{177}Hf$ (this study)	Average $\delta^{30}Si$ (this study)
91500 **$^{176}Hf/^{177}Hf$ = 0.282308 ± 0.000008** **Blichert-Toft (2008)**	*As secondary* 0.282300 ± 0.000010 (2SD; n=6)	
Plešovice **$\delta^{30}Si$ = -0.38 ± 0.18‰ (2SD)** **Guitreau et al., (2020, 2022),** **Trail et al., (2018)**		*As primary* -0.35 ± 0.23‰ (2SD)
MudTank **$^{176}Hf/^{177}Hf$ = 0.282507 ± 0.000006** **Woodhead and Hergt (2005)**	*As secondary* 0.282522 ± 0.000009 (2SD; n=6)	*As secondary* -0.38 ± 0.24‰ (2SD)
$\delta^{30}Si$ = -0.34 ± 0.03‰ **Trail et al., (2018)** **$\delta^{30}Si$ = -0.47 ± 0.17‰** **Guitreau et al., (2020, 2022)**		
MUN-0 **$^{176}Hf/^{177}Hf$ = 0.282135 ± 0.000007** **Fisher et al., (2011)**	*As primary* 0.282135 ± 0.000006 (2SD; n=12)	
MUN-1 **$^{176}Hf/^{177}Hf$ = 0.282135 ± 0.000007** **Fisher et al., (2011)** **$\delta^{30}Si$ ~ -2‰** **Guitreau et al., (2020, 2022)**	*As secondary* 0.282134 ± 0.00007 (2SD; n = 12)	*As secondary* -1.95 ± 0.23‰ (2SD)
MUN-3 **$^{176}Hf/^{177}Hf$ = 0.282135 ± 0.000007** **Fisher et al., (2011)**	*As secondary* 0.282127 ± 0.00007 (2SD; n = 6)	
MUN-4 **$^{176}Hf/^{177}Hf$ = 0.282135 ± 0.000007** **Fisher et al., (2011)**	*As secondary* 0.282127 ± 0.000020 (2SD; n = 6)	

2.3.1.8. Zircon trace elements

Trace element measurements were done at LMV during two sessions using the same LA-ICP-MS system as used for U-Th-Pb measurements. The analytical conditions followed the methodology described in Guitreau et al. (2022). Analytical spots (33 μm) were located next to pits that correspond to Si isotope analyses. Information regarding analytical conditions is given in **Supplementary material D**. Concentrations were determined using ^{28}Si as an internal standard and the synthetic glass standard SRM NIST 610 (Jochum et al., 2011) as the primary bracketing standard. The synthetic glass SRM NIST 612 (Jochum et al., 2011), together with zircon reference materials 91500 (Wiedenbeck et al., 2004), MudTank (Gain et al., 2019), and AS3 (Takehara et al., 2018) were analyzed for quality check. Batches of six unknowns and three quality-control

standards were bracketed by two analyses of NIST 610. Zircon trace element data were processed using *Iolite4* software (Petrus and Kamber, 2012; Paton et al. 2011). For all unknown zircon analyses, we used SiO_2 = 35.6 wt.% as the internal standard. In cases where such information was not available, we used stoichiometric values to convert ICP-MS counts/second into concentrations. The elemental concentrations acquired for SRM NIST 610 and NIST 612 consistently aligned with published values, deviating by no more than 4% (Jochum et al., 2011) (see **Supplementary Material D**). The zircon standards analyzed in this study largely matched the available published values for most elements, being that certain elemental concentrations either fell within the range of published values or were close (see **Supplementary Material D**). This can be attributed to compositional variations between batches of natural zircon reference materials (e.g., 91500, MudTank, and AS3) and/or alteration effects (e.g., Ca, Al, K, La contents) (Guitreau et al., 2022).

We assessed the impact of alteration on isotopic information according to: (i) the Light Rare Earth Element Index (LREE-I) of Bell et al. (2016), denoted as (Dy/Nd) + (Dy/Sm) ratios, which should exhibit LREE-I >30. This threshold was relaxed to a minimum value of 20, considering the uncertainties in analyses, as also performed in Laurent et al. (2021); (ii) whenever chondrite-normalized La concentrations were below 1, zircon data were considered pristine as proposed by Zeh et al. (2014), but we also considered as pristine concentrations <10 in order to account LA-ICP-MS analytical uncertainties since measured La concentrations remained very low.

Ti-in-zircon temperatures were determined using the method of Ferry and Watson (2007) with activity values of 0.95 for $aSiO_2$ and 0.45 for $aTiO_2$, as suggested by Guitreau et al. (2022).

2.3.1.9. Zircon Si isotopes

Si isotope measurements were performed at LMV during three separate sessions. The laser-ablation coupled with a MC-ICP-MS system was the same used for Lu-Hf measurements. All conditions and equipment are detailed in the **Supplementary material D**. Spot analyses of 47 μm were located preferentially on top of previously Lu-Hf spot analyses. Some Si spot analyses were located in the same domain as the previous analyses but not necessarily overlapping prior laser pits. Silicon isotope measurements followed closely the protocol conditions of Guitreau et al. (2020; 2022).

Si isotope analyses were done via standard bracketing using Plešovice zircon standard (Sláma et al., 2008) and MudTank (Black and Gulson, 1978) as well as MUN synthetic zircon standards MUN (MUN-1) (Fisher et al., 2011) as the secondary reference. Silicon isotope data, expressed in delta notation ($\delta^{29}Si$ and $\delta^{30}Si$), are reported in the **Supplementary material D**. These values represent per mil deviations from a reference (quartz NBS 28) and were calculated using the following equations: $\delta^{29}Si = [(({}^{29}Si/{}^{28}Si)_{sample} / ({}^{29}Si/{}^{28}Si)_{standard}) - 1] \times 1000$ and $\delta^{30}Si = [(({}^{30}Si/{}^{28}Si)_{sample} / ({}^{30}Si/{}^{28}Si)_{standard}) - 1] \times 1000$. Within-run precision is reported as 2 standard errors (2SE) whereas external reproducibility, obtained through multiple analyses of the same zircon, is reported as 2

standard deviations (2SD). Finally, we applied a background correction before calculating corrected values according to a mass-dependent equilibrium fractionation of 0.5178 between ^{29}Si and ^{30}Si measured values (Savage et al., 2014).

Plešovice zircon yielded $\delta^{30}Si$ value of -0.35 ± 0.23‰ (2SD), which is consistent with the value of -0.38 ± 0.18‰ (2SD; LA-MC-ICP-MS; Guitreau et al., 2020; 2022), as well as Si isotopic measurements using SIMS and S-MC-ICPMS (Trail et al., 2018; Guitreau et al., 2020) (**Table S.2**, see also **Supplementary Material D**). MudTank zircon gave a $\delta^{30}Si$ value of 0.38 ± 0.24‰, which is within error of the S-MC-ICP-MS value of 0.34 ± 0.03‰ reported by Trail et al. (2018) and the $\delta^{30}Si$ value of 0.47 ± 0.17‰ obtained by Guitreau et al. (2020; 2022) using LA-MC-ICP-MS (**Table S.2**, see also **Supplementary Material D**). The artificial zircon MUN-1 displayed a light isotope-enriched composition with a $\delta^{30}Si$ value of -1.95 ± 0.23‰ (2SD), similar to values close to 2‰ obtained by LA-MC-ICP-MS and S-MC-ICP-MS analytical methods (Guitreau et al., 2020; 2022) (**Table S.2**, see also **Supplementary Material D**).

3. Surrounding rocks: the widespread TTG magma production in the studied area

3.1. Preface

This Chapter, submitted to *Geochimica et Cosmochimica Acta*, provides a detailed petrological study of Rhyacian TTG rocks in the Mineiro Belt surrounding the S-type Cupim pluton (described in **Chapter 2**). These rocks vary from tonalite to trondhjemite (some of them are gneisses and migmatites) and have key-geochemical compositions of the TTG series (Na-rich, K and Fe-Mg-poor, and high-La/Yb, -Sr/Y and -LILE/HFSE). Zircon U-Th-Pb ages reveal three distinct episodes of TTG emplacement (2.15 Ga, 2.13 Ga, and 2.11 Ga) and a single partial melting event (2.04 Ga). Zircon Hf-Si isotopic compositions distinguish three sources with different radiogenic compositions, suggesting a long-, mid-, and short-evolution of Archean and Paleoproterozoic unsilicified oceanic crusts. In contrast to Archean TTGs, which typically exhibit heavier silicon isotopic signatures due to the silicification of basaltic oceanic crust, these Paleoproterozoic TTGs display lighter signatures. This suggests that silicification played a less significant role during their formation. This observation is consistent with the global depletion of dissolved silicon (DSi) in the oceans, attributed to the widespread deposition of banded iron formations (BIFs). The Cauê Formation of the Minas Supergroup, for example, is a local example of this phenomenon. Instead of silicification, we suggest that the recycling of hydrous, altered oceanic crust was the primary mechanism responsible for the fertilization of the basaltic protoliths. This process likely involved the formation of secondary minerals capable of retaining water, which ultimately contributed to the low silicon isotopic signatures observed in Paleoproterozoic TTGs.

3.2. Hafnium and Silicon isotope evidence for multiple unsilicified basaltic sources at the origin of Rhyacian TTG magmas in the Mineiro Belt (Brazil)

The following activities were developed by the first author under the supervision of Martin Guitreau and Leonardo Gonçalves: (i) sampling and sample preparation to geochemistry; (ii) picking and mount preparation of zircon grains; (iii) performance and reduction data of zircon U-Th-Pb, Lu-Hf and Si isotopes and trace element analyses. (iv) Wrote and drew figures for the manuscript. Heavy mineral separation was carried out with Cassiano Costa. All authors contributed to the conceptualization of the main idea of the paper.

Hafnium and Silicon isotope evidence for multiple unsilicified basaltic sources at the origin of Rhyacian TTG magmas in the Mineiro Belt (Brazil)

Syro Lacerda [a,b], Martin Guitreau [a], Leonardo Gonçalves [b], Hugo Moreira [c], Cristiane C. Castro [b], Stéphany Lopes [b], Sandro Mauri [d], Marco Aurélio Pinheiro [e], Cassiano Costa [f], Régis Doucelance [a]

[a] Laboratoire Magmas et Volcans, CNRS-UMR6524, IRD-UMR163, OPGC, Université Clermont Auvergne, F-63178 Aubière, France

[b] Universidade Federal de Ouro Preto, Departamento de Geologia, Ouro Preto, Brazil

[c] School of Earth and Environmental Sciences, University of Portsmouth, Burnaby Building, Burnaby Road, Portsmouth, PO1 3QL, UK

[d] Faculdade de Geologia, Universidade do Estado do Rio de Janeiro, Rio de Janeiro (RJ), Brazil

[e] Center of apllied geosciences, Geological Survey of Brazil - CPRM, Av. Pasteur 404, Rio de Janeiro, Brazil

[f] Geological Survey of Brazil – CPRM, Av Brazil 1731, Belo Horizonte 30140-002, Brazil

Abstract

Although typically Archean in age, tonalite-trondhjemite-granodiorite (TTG) rocks in the Mineiro Belt form a series of plutonic bodies and gneissic complexes crystallized during the Siderian and Rhyacian times. Their petrogenesis provides insight into sources, magmatic processes, and geodynamics during the early stages of plate tectonics. In this study, we report on the petrology of three TTG units described as (i) the Caranaíba gneiss, (ii) the Caatinga-Lamim Complex, and (iii) the Ressaquinha trondhjemite. The Caranaíba gneiss exhibits millimetric to centimetric banding composed mainly of oligoclase, quartz, and sagenitic (titanite needles) biotite with zircon and apatite inclusions. The Caatinga-Lamim complex is formed by biotite-hornblende-tonalite and migmatitic biotite-gneiss, often showing plagioclase accumulation textures. The Ressaquinha trondhjemite is weakly deformed and composed of oligoclase, quartz, and sagenitic biotite. The rocks are silicic (SiO_2= 67-71 wt.%), aluminum and sodium-rich (Al_2O_3>15 and Na_2O> 4 wt.%, respectively), weakly peraluminous (A/CNK= 1.01-1.05), and low K_2O contents (< 3 wt.%). They are magnesian (Fe# < 0.7), while Fe_2O_3 and MgO contents are moderate to low (15 to 2 wt.%). REE patterns show light-REE enrichment compared to heavy-REE composition (La_N/Yb_N= 22-56) and positive to absent Eu/Eu* anomalies (0.96-2.65). These compositions indicate high-temperature (>900° C) and medium-pressure melting conditions (7 kbar), leaving garnet-hornblende eclogite residues. The mineral and chemistry variation of the Caatinga-Lamim rocks suggests hornblende (minor apatite, zircon, and allanite) fractionation and plagioclase accumulation. Zircon U-Th-Pb dating indicates three episodes of crystallization at 2.15 Ga (Caranaíba gneiss), 2.13 Ga (Caatinga-Lamim complex), and 2.11 Ga (Ressaquinha trondhjemite), and a single anatexis event at 2.04 Ga

(Caatinga-Lamim neosome). Zircon Hf isotope signatures suggest the reworking of both Archean and Paleoproterozoic basaltic sources, and Si isotopes reveal that these latter were mostly unsilicified, contrary to Archean TTGs. This observation aligns with estimates of the global secular evolution of dissolved Si in oceans, which decreased over time, preventing silicification of seafloor basalts that further produced TTG magmas in an oceanic-arc scenario during Rhyacian times.

Keywords

Tonalite-trondhjemite-granodiorite, Zircon U-Th-Pb geochronology, Zircon Hf-Si isotopes, Mineiro Belt, São Francisco Craton, Rhyacian geodynamics.

3.2.1.Introduction

Tonalite-trondhjemite-granodiorite suites (TTG rocks, Moyen and Martin, 2012) are Na-rich felsic magmatic rocks (Janh et al., 1981) that make up most of the granitic-gneissic basement of Archean (and less abundant in Proterozoic) terranes (Laurent et al., 2014; Väisänen et al., 2012; Li et al., 2020a; Gibson et al., 2024; Penaye et al., 2004; Gao et al., 2022). Their chemistry, which is distinct from that of modern granitoids, can be accounted for by partial melting of Na-(LREE)-rich mafic (basaltic) rocks under P-T conditions of garnet-amphibole (± plagioclase) residue stability (Martin et al., 1987, 2014; Rapp et al., 1991). Field relationships and phase-equilibrium models also support this idea (Pourteau et al., 2020). Chemical variations are attributed to several melting-pressure conditions (Moyen, 2011) and mineral accumulation or fractionation processes (Laurent et al., 2020a; Kendrick et al., 2022). Their occurrence is episodic or continuous and compatible with many tectonic scenarios, not necessarily within the context of global plate tectonics (Laurent et al., 2024).

Whole-rock Nd and zircon Hf isotopic compositions are typically chondritic to above chondritic in Archean TTG rocks, reflecting their juvenile signature (Guitreau et al., 2012; Laurent et al., 2015). Furthermore, oxygen and silicon stable isotopes in Archean TTG rocks and their zircon crystals suggest that their hydrous basaltic source was somewhat altered and silicified before melting (**Fig.3.1**, Deng et al., 2019; André et al., 2019; Lei et al., 2023). However, the dissolved Si (DSi) composition of oceans, and consequently the silicification of seafloor basalts, is drastically affected by biosilicification processes (Conley et al., 2017). Lake Superior-type banded iron formations (BIFs) are oxidized Fe and Si associations that were deposited, mostly during the Paleoproterozoic, by biological processes (e.g., cyanobacteria) in an oceanic environment (Simonson et al., 2003; Klein, 2005; Bekker et al., 2010; Rasmussen et al., 2015). Biologically oxidized Fe could scavenge the DSi of seawater (Yee et al., 2003), precluding the silicification of seafloor basalts. Nevertheless, unsilicified basalts, or those with low modal quartz contents, rarely produce significant TTG melts at lithospheric P-T conditions (Roman and Arndt, 2020; Palin et al., 2016). Consequently,

alternative geodynamic processes must be considered for fertilizing the basaltic source, possibly through hydrous alteration (André et al., 2022).

In this paper, we present evidence for a prolonged episode of TTG generation (2.15 to 2.11 Ga) in the Mineiro Belt, southern São Francisco Craton, Brazil. We report mineral and whole-rock chemical data and zircon U-Pb, Lu-Hf, and silicon isotopic compositions to constrain potential sources, magmatic processes, and geodynamic implications. Hafnium and silicon isotopic composition of zircon grains from Rhyacian TTG rocks in the Mineiro Belt indicates multiple basaltic sources with less significant silicification than that required for Archean TTG sources. This finding is consistent with a secular decrease of dissolved Si in the oceans associated with the early emergence of life and the deposition of BIFs. It also suggests altered oceanic crust recycling, rather than silicification, as a pivotal key process for the genesis of Paleoproterozoic TTGs.

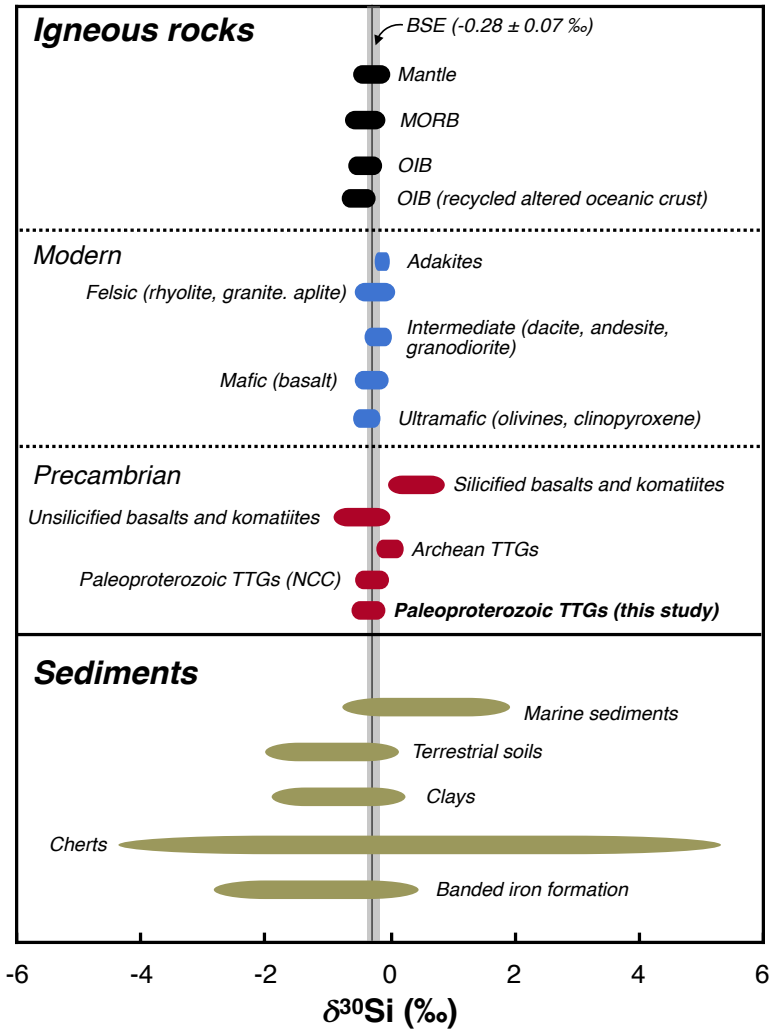


Figure 3.1: $\delta^{30}Si$ values for different rock types, modified from Kleine et al. (2018). BSE = Bulk Silica Earth. OIB (recycled altered oceanic crust) from Pringle et al. (2016). Adakite data (n=4) from Deng et al. (2019). Silicified and unsilicified basalts and komatiites from Abraham et al. (2011) and André et al. (2022). Archean TTGs of the Barberton Greenstone Belt, Kaapvaal Craton, from André et al. (2019). Paleoproterozoic TTGs of the North China Craton (NCC) from Zhou et al. (2024). Paleoproterozoic TTGs (this study) are calculated from zircon values (see the text for details).

3.2.2. Geological background

The Mineiro Belt (**Fig.3.2**) represents a portion of an orogen developed during the Paleoproterozoic (2.47-2.00 Ga) in eastern Brazil (Alkmim and Teixeira, 2017 and references therein). The orogen was formed in response to the amalgamation of the São Francisco-Congo proto-Craton and accreted by soft-collision (Lacerda et al., 2024). This promoted oceanic crust consumption, shortening Paleoproterozoic rift to foreland basins (Minas Supergroup, Alkmim and Martins-Neto, 2012), and metamorphic overprint (Cutts et al., 2019). The Minas Supergroup forms a ca. 6000 m thick first-order sequence from continental and marine to turbiditic syn-orogenic sediments (Alkmim and Martins-Neto, 2012). Marine sediments include Lake Superior-type BIFs and carbonates deposited along the Archean continental passive margin of the São Francisco Craton (Babinski et al., 1995; Spier et al., 2007; Teixeira et al., 2017; Sampaio et al., 2018).

The Mineiro Belt crust is mainly composed of granitic (l.s.) rocks, tectonic or intrusive, in contact with NE-SW orientated metavolcanic and sedimentary (greenstone) rocks (**Fig.3.2)**. Deformation is unambiguously distinguished in the greenstone rocks, locally apparent in granitic rocks, and concentrated in three regional shear zones (**Fig.3.2**, Lenheiro, Jeceaba-Bom Sucesso, and Congonhas-Itaverava, Nahas et al., 2023; Campos and Carneiro, 2008). Paragenesis of greenstone and granitic rocks (refers to orthogneiss in Teixeira et al., 2015) suggests greenschist to low-amphibolite facies during Paleoproterozoic metamorphic events (Ávila et al., 2010). On the other hand, Neoproterozoic metamorphic imprints are only recognized to the south of the Lenheiro shear zone (Campos-Neto et al., 2011; Söllner and Trouw, 1997).

Granitic rocks are diverse (tonalite, trondhjemite, granodiorite, granite) and form plutons, batholiths, suites; minor dikes, and pegmatite intrusions (**Fig.3.2**). In the northern part of the Mineiro Belt, their chemical composition allow four major groups to be distinguished: (i) TTG rocks (2.35 Ga Lagoa Dourada Suite, 2.18 Água Limpa-Casa Grande plutons, and 2.14 Ga Resende Costa Suite; Seixas et al., 2012; Lopes et al., 2024; Moreira et al., 2018); (ii) sanukitoid rocks (2.13 Ga Alto Maranhão Suite; Seixas et al., 2013; Moreira et al., 2020); (iii) Hybrid (High-Ba-Sr) granitoids (2.12 Ga São Brás-Bombaça Plutons, Serra do Camapuã Pluton; Moreira et al., 2018); (iv) sediment-derived (S-type) granites (2.00 Ga Cupim Pluton, 2.04 Ga Congonhas Pluton; Lacerda et al., 2024; Seixas, 2000). The zircon Hf-O isotopic composition of these granites suggests a short crustal (initial $^{176}Hf/^{177}Hf$ ~0.28140) evolution that produced TTG-sanukitoid-hybrid magmas with a temporal increase of mantle/sediment contributions (Moreira et al., 2020). On the other hand, the zircon grains from 2.18 Ga Água Limpa-Casa Grande plutons show significantly lower initial $^{176}Hf/^{177}Hf$ composition (~0.28130), suggesting an ancient Archean source component. Besides, zircon grains from S-type granites show scattered initial $^{176}Hf/^{177}Hf$ compositions that reflect the mixed (Archean and Paleoproterozoic) crustal source contributions (Lacerda et al., 2024).

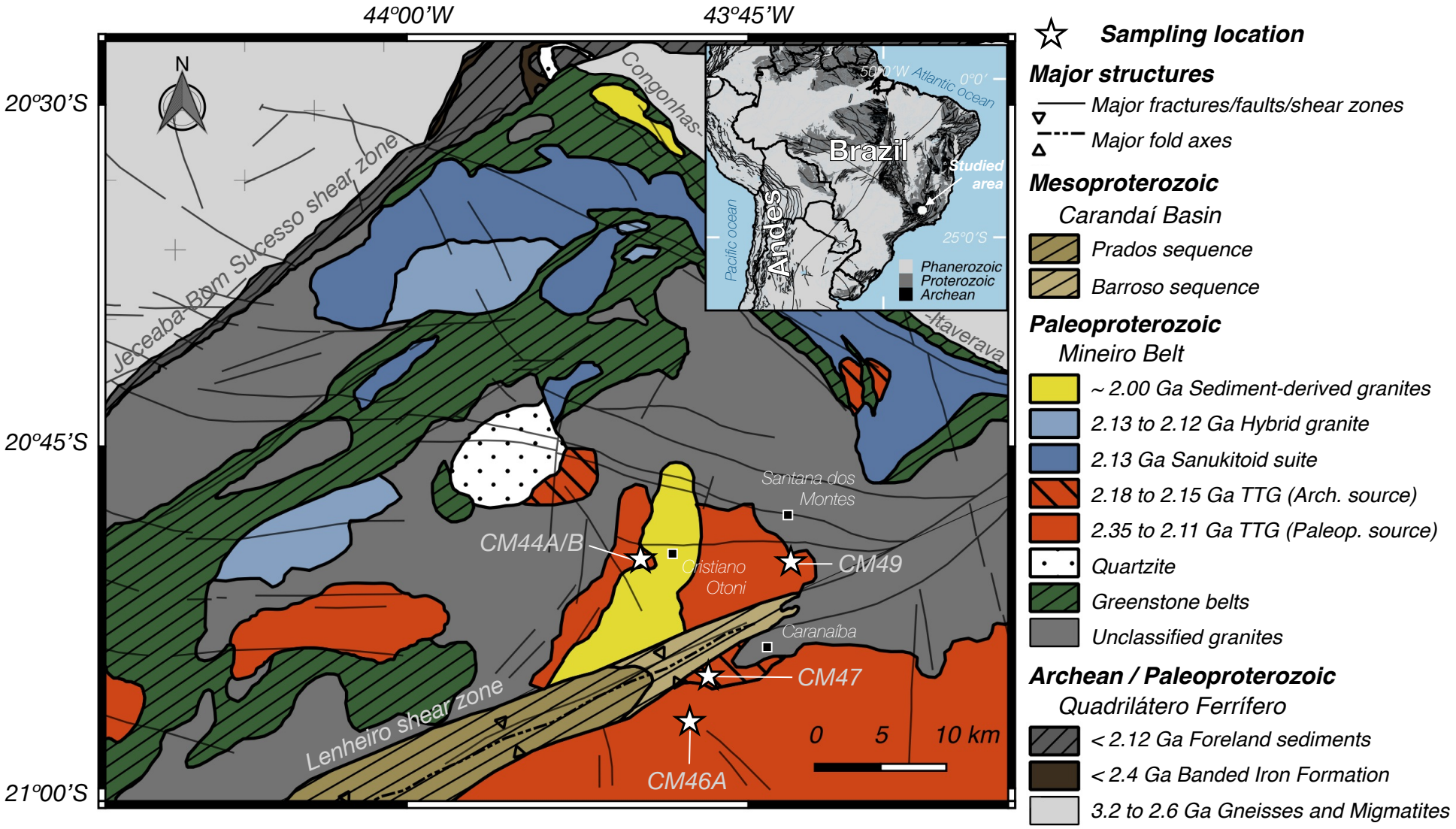


Figure 3.2: Simplified geological map of the northern part of the Mineiro Belt in the southern São Francisco Craton. Modified from published maps from Seixas (2000), Seixas et al. (2012, 2013), Moreira et al. (2018, 2020), Lacerda et al. (2024), and the Geological Survey of Brazil [Santos and Baltazar (2013)] based on this study. The inset shows the location of Archean, Proterozoic, and Phanerozoic crusts [from Tapias et al., (2019)] and the study area (indicated by the white arrow) on a map of Brazil in the South America geological context.

Zircon oxygen and apatite sulfur speciation from 2.35-2.12 Ga granitic suites in the Mineiro Belt provide insights into the surface conditions during orogen evolution (Moreira et al., 2020; 2023). The lower $\delta^{18}O$ and ΔFMQ (fayalite–magnetite–quartz buffer calculated via $S^{6+}/\Sigma S^{TOTAL}$ oxybarometer) values of 2.35 Ga TTG suite suggest high-temperature seawater alteration of the source and reduced redox conditions. On the other hand, the higher $\delta^{18}O$ and ΔFMQ values from the younger 2.13 sanukitoid suite highlight the interaction of oxidized sediments (from the arc itself) and the mantle. The change in the redox state of these magmas records the increase of oxygen levels in the atmosphere across the Great Oxidation Event (GOE) (Moreira et al., 2023). However, the deposition of BIFs (mostly before the initial rise of atmospheric oxygen) certainly has influenced the surface (seawater and atmosphere) conditions and related source alteration processes (e.g., hydration, oxidation, and silicification). Lake Superior-type BIFs form a ca. 350 m-thick package (Cauê Formation) in the southern São Francisco Craton, being the most important ore deposit in the Quadrilátero Ferrífero region (Spier et al., 2007). Its deposition age is poorly constrained but prudentially bracketed between 2620 Ma (bottom unity) and 2420 Ma (top unity), see Martínez-Dopico et al. (2017).

There is limited knowledge about the nature of the rocks formed spatially between the TTG and sanukitoid suites, which are intruded by the Cupim Pluton, also known as the Caatinga-Lamim Complex (Santos and Baltazar, 2013), as well as to the south of the Lenheiro shear zone [Ressaquinha Complex; 2010 ± 52 Ma (Rb/Sr method), Noce et al., 2000]. A combined petrological and isotopic characterization of these granitic units could provide additional information about sources and surface conditions regarding the interconnected interactions of the continent, ocean, and atmosphere realms.

3.2.3. Materials and Methods

Six samples (CM44A, CM44B-felsic, CM44B-mafic, CM46A, CM47, and CM49) were collected from four sites. Samples CM44A and CM44B [(Lat / Long) 20º50'10" S / 43º49'15" W] are, respectively, the neosome and paleosome of a migmatite rock collected from the slopes of a quarry in the Cristiano Otoni town. Two samples from the paleosome were prepared for geochemistry concerning more felsic or mafic portions; for simplicity, both will be referred to as CM44B. Sample CM46A [20º57'08" S / 43º47'35" W] is a granitic rock (l.s.), which is the dominant rock type in the outcrop and is locally cut by dykes of mafic rock. This sample is mapped as the Ressaquinha Complex, following Noce et al. (2000) and Santos and Baltazar (2013). Sample CM47 [20º55'20" S / 43º46'59" W] is a representative sample of a dominant gneiss rock from an outcrop near the town of Caranaíba, hereafter named Caranaíba gneiss. Sample CM49 [20º50'21" S / 43º43'08" W] is the main lithotype exposed at the Caatinga waterfall, close to the Santana dos Montes town. This rock is locally crosscut by light-colored aplitic and pegmatite rocks. This sample (and the migmatite rock) is called the Caatinga-Lamim Complex, following Santos and Baltazar (2013) map. Thin

sections from all six samples were prepared to show detailed mineral textures and microstructures. Mineral chemical analyses were conducted at the Laboratório de Microscopia e Microanálises (LMic) facilities at the Universidade Federal de Ouro Preto in Brazil, following the methodology outlined in Lacerda et al. (2024).

All samples were crushed (jaw crusher) and pulverized (Tema mill) to obtain sufficient material for whole-rock geochemical analysis and heavy mineral (e.g., zircon) separation. Major elements were measured using ICP-OES at Laboratoire Magmas et Volcans (LMV), Université Clermont-Auvergne, France, and at Laboratório de Geoquímica (LGqA), Universidade Federal de Ouro Preto. Most oxides are within 4% (RSD) of published values of certified materials (DR-N, BHVO-1, and GPS). On the other hand, trace elements were determined by ICP-MS technique at Service d'Analyse des Roches et des Minéraux (SARM), Centre de Recherches Pétrographiques et Géochimiques (CRPG, Nancy, France), and at LGqA. In most measurements, trace element concentrations have analytical precisions better than 10% (2SD; see **Supplementary Material A**).

Zircon crystals were concentrated using panning techniques, followed by heavy-density liquid (bromoform - 2.89 g/cm^3) and magnetic (hand-imam and Franz) separation procedures at the Laboratório de Análises Minerais - CPRM, Brazil. Non-magnetic zircon crystals (13, 2, 17, 23, and 35, from CM44A, CM44B, CM46A, CM47, and CM49, respectively) were hand-picked, embedded in epoxy resin, polished until their center were exposed, and further imaged using cathodoluminescence techniques at LMV to reveal internal textures. Scanning electron microscope (SEM) technical conditions were similar to those of Lacerda et al. (2024). LA-ICP-MS was used to analyze their U-Th-Pb and trace element contents, while Lu-Hf and silicon isotopic compositions were analyzed via LA-MC-ICP-MS, both hosted at LMV. Machine conditions are detailed in Supplementary Material B. Natural (Plešovice, 91500, AS3, MudTank) and synthetic (MUN) zircons were used as bracketing reference materials for calibration and quality control during the analytical sessions. U-Th-Pb and trace element data were reduced using Iolite 4 software (Petrus and Kamber, 2012; Paton et al., 2011), while in-house spreadsheets were used to process Lu-Hf and Si isotopes, considering instrumental biases, isobaric interferences, natural abundances, fractionation laws, and radiogenic decay ratios. This follows the same procedures as those of Lacerda et al. (2024). Wetherill diagrams were built using IsoplotR software (Vermeesch, 2018). ε_{Hf} and δ^{30}Si notations refer respectively to absolute and per mil deviations from CHUR (Iizuka et al., 2015) and quartz NBS 28 values.

All calculated ages, isotopes, and elemental compositions for the used reference materials agree within uncertainty with published data (see **Supplementary Material B**). **Table 1** provides the main isotopic results obtained from the zircon reference materials compared to the published acceptable values.

Table 3.1: Summary of analytical results obtained for zircon reference materials used in this study. Reported values for ^{176}Hf/^{177}Hf and δ^{30}Si isotopic compositions correspond to averages.

The value within brackets refers to the number of measurements considered to calculate averages. Errors are quoted as 2SE for ages and Hf isotopes, and 2SD for Si isotopes.

	91500	Plešovice	AS3	MudTank	Mun zircons
U-Pb Age (Ma)	1065.4 ± 0.3 [1]	337.1 ± 0.4 [3]	1099.1 ± 0.5 [5]		
$^{176}Hf/^{177}Hf$	0.282308 ± 0.000006 [2]			0.282507 ± 0.000006 [6]	0.282135 ± 0.000007 [7]
$\delta^{30}Si$ (‰)		-0.44 ± 0.21 ‰ [4]		-0.38 ± 0.23 [4]	-2.02 ± 0.27 [4]
U-Pb Age (Ma)					
Fist session	1064 ± 8 (16) [a,*]	349 ± 8 (3) [a]	1106 ± 17 (4) [a]		
Second session	1073 ± 13 (5) [a]	337 ± 2 (24) [a,*]	1085 ± 31 (6) [b]		
Third session	1067 ± 28 (9) [b]	337 ± 2 (40) [a,*]	1105 ± 21 (10) [c]		
Fourth session	1059 ± 12 (4) [a]	337 ± 3 (16) [a,*]	1104 ± 37 (4) [b]		
Fifth session	1051 ± 22 (5) [b]	337 ± 1 (20) [a,*]	1087 ± 15 (5) [a]		
$^{177}Hf/^{176}Hf$					
Average	0.282310 ± 0.000015 (8)			0.282516 ± 0.000011 (8)	0.282135 ± 0.000005 (16) *
$\delta^{30}Si$ (‰)					
Average		-0.35 ± 0.23 (93) *		-0.38 ± 0.24 (10)	-1.95 ± 0.23 (9)

*[a] Concordia age; [b] Weighted Mean Average $^{207}Pb/^{206}Pb$ age; [c] Upper intercept age; * Used as primary standard.*

Accepted reference values: [1]Wiedenbeck et al. (1995); [2]Blichert-Toft (2008); [3]Sláma et al. (2008); [4]Guitreau et al. (2022); [5]Paces and Miller (1993); [6]Woodhead and Hergt (2005); [7]Fisher et al. (2011).

3.2.4. Results

3.2.4.1. Petrography and mineralogy

Caatinga-Lamim rocks vary from tonalite (CM49, **Fig.3.3a**) to migmatitic trondhjemitic gneiss (CM44B, **Fig.3.3b**). The tonalite is coarse-grained, weakly foliated, and composed of plagioclase (45%), quartz (25%), amphibole (20%), and biotite (10%). Amphibole and plagioclase crystals are long shape-orientated, marking the rock foliation. Plagioclase crystals locally form whitish monomineralic aggregates (**Fig.3.3a**). In detail, coarse (~1 mm) plagioclase crystals are subhedral and locally surrounded by finer (< 0.5 mm) plagioclase anhedral crystals resembling cumulus and inter-cumulus texture (**Fig.3.4**). Amphibole forms coarse to fine greenish crystals with regular to interdigitated contact with plagioclase and biotite crystals. Zircon, titanite, and apatite are accessory phases commonly included or associated with amphiboles (**Fig.3.4**). Titanite grains are locally associated with epidote. In contrast, opaque minerals are often associated with ferromagnesian minerals (amphibole, biotite, titanite).

Meanwhile, the migmatitic gneiss is a metatexite composed of neosome (CM44A) and paleosome (CM44B) parts, showing irregular to diffusional contacts (**Fig.3.3b**). The neosome part is coarse-grained, mainly composed of quartz and plagioclase (leucosome), and is locally limited by dark selvages (melanosome). Dark minerals are scarce, with no apparent orientation. Quartz (25%) and plagioclase (55%) are subhedral and show irregular and lobate contacts (**Fig.3.4**). Minor muscovite (< 5%) and K-feldspar (< 5%) are anhedral crystals and interstitial with plagioclase and quartz. Biotite (< 10%) is partially transformed into chlorite. Thin (~1 mm) reddish garnet grains are locally present. Apatite and zircon grains are often included in plagioclase and biotite.

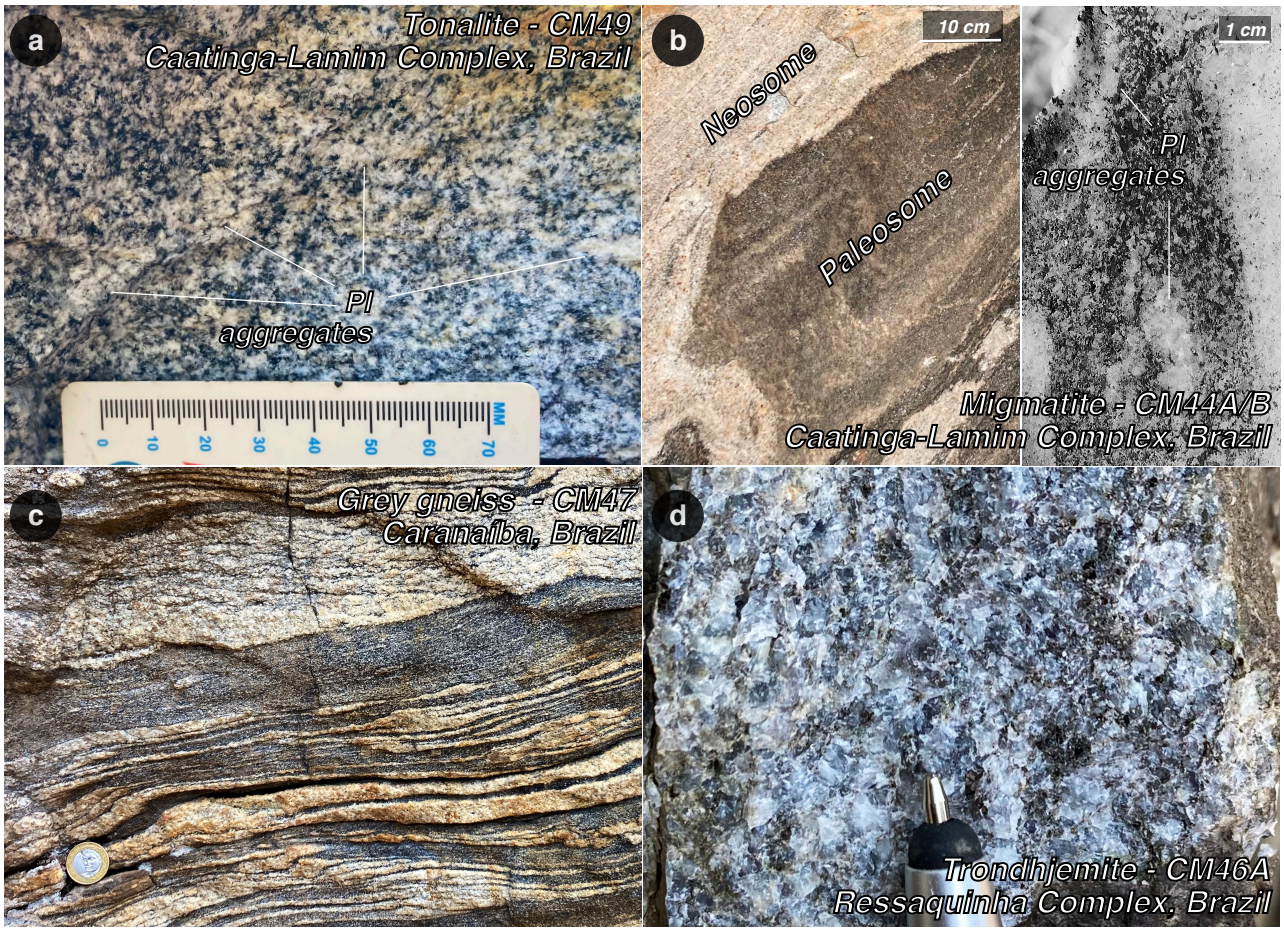


Figure 3.3: Petrographic features of the samples studied in this contribution. (a) Weakly-foliated Bt-Hbl-tonalite (CM49) from Caatinga-Lamim Complex. Plagioclase phenocrysts form shape-oriented cumulates surrounded by hornblende (and minor biotite) crystals. (b) Migmatitic Bt-gneiss from Caatinga-Lamim Complex. Its leucosome (CM44A) and melanosome parts exhibit lobate contacts, suggesting in-situ melt extraction. On the right is a detailed view of the partially melted gneiss, showing plagioclase cumulates embedded in biotite crystals. (c) Weakly-deformed tonalitic Bt-gneiss (CM47) from Caranaíba showing millimetric to centimetric dark bands mainly composed of biotite. Light bands are also milli- to centimetric but formed by plagioclase and quartz grains. Note a 17mm diameter coin to scale. (d) Weakly-deformed Bt-trondhjemite (CM46A) from Ressaquinha Complex with dark biotite presents as oriented flakes between unoriented plagioclase (whitish) and quartz (grayish to blueish) crystals.

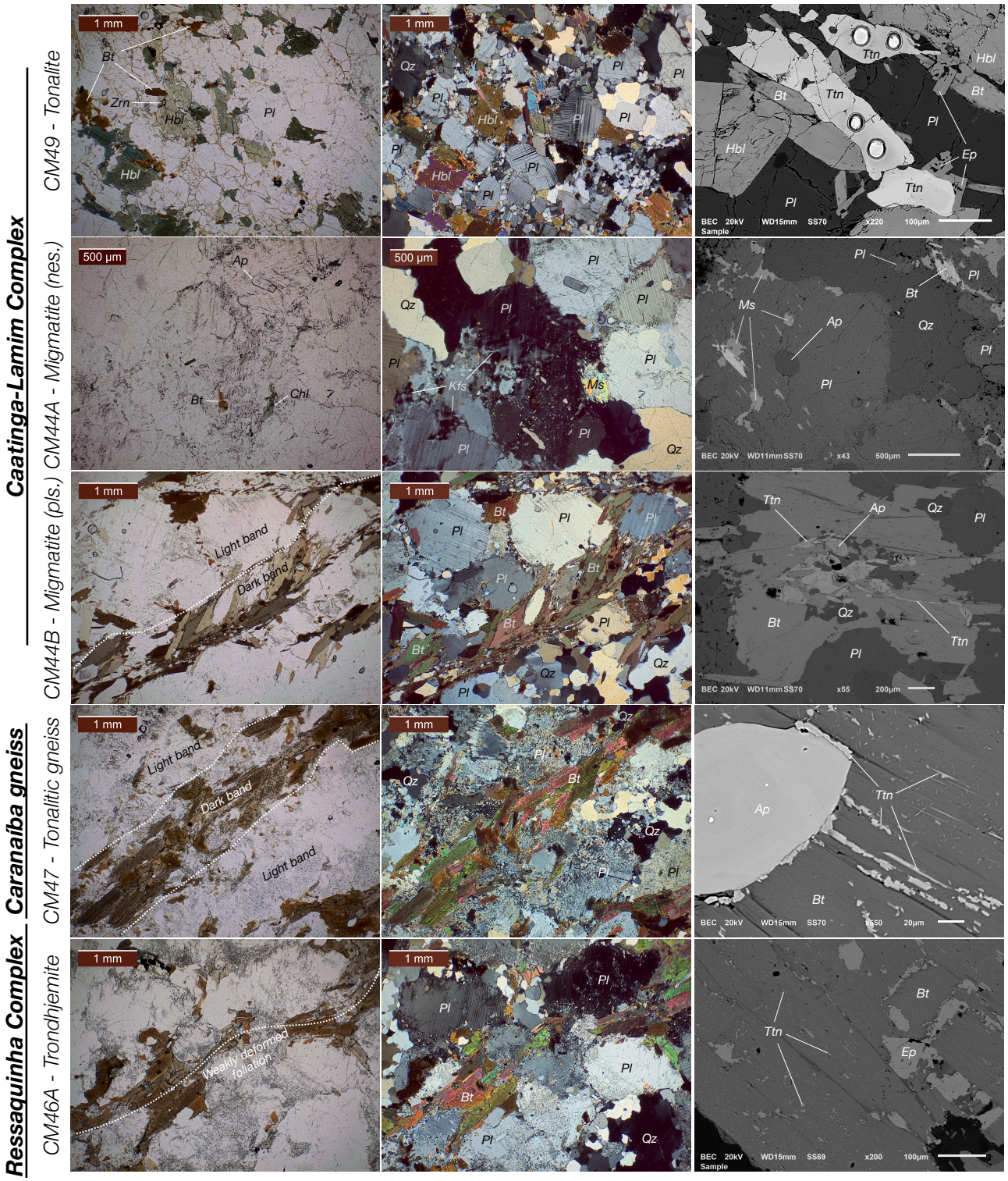


Figure 3.4: Micro-petrography and micro-textures observed on the TTG rocks. The left column shows polarized-light microscope images, the middle column shows cross-polarized microscope images, and the right column shows detailed SEM images. The geologic unit and sample number/lithology are given on the left of each set of images. See the text for detailed descriptions. Dashed lines outline large (>1 mm) plagioclase phenocrysts. The mineral abbreviation used is after Warr (2021). Pls.: paleosome; Nes.: neosome.

On the other hand, the paleosome part is a gneiss exhibiting centimetric (1-10 cm) light (quartz + plagioclase) and dark (biotite + plagioclase ± quartz) bands. Coarse plagioclase crystals also form small monomineralic aggregates within the dark bands of the gneiss (**Fig.3.3b**). Biotite flakes are banding-oriented and have local inclusions of apatite and colorless titanite grains (**Fig.3.4**). Plagioclase (45%) forms subhedral crystals that show sutured contacts between them. Quartz (25%) is often anhedral and shows lobular to cuspidal contacts (**Fig.3.4**), indicating partial melting. Isolated brownish titanite grains are locally associated with opaque minerals.

The Caranaíba gneiss (CM47, **Fig.3.3c**) has a heterogeneous appearance (thicker dark bands than light ones and sometimes the opposite) and shows local deformation features (e.g., asymmetric folds, boudin structures). The dark bands are composed mainly of biotite and plagioclase, while the light bands are rich in quartz and plagioclase. Plagioclase (40%) crystals are coarse to fine-grained and show advanced saussuritization. Quartz is finer and occurs as anhedral interstitial grains. Biotite forms brownish banding-oriented flakes commonly containing inclusions of zircon, apatite, and titanite needles (**Fig.3.4**).

The Ressaquinha trondhjemite (CM46A, **Fig.3.3d**) is a coarse-grained and weakly foliated rock with dark biotite flakes that locally form schlieren textures and define an apparent foliation. Quartz forms locally rounded blueish-grayish crystals (**Fig.3.3d**). Plagioclase (45%) crystals show saussuritization and irregular borders, forming lobate contacts between them and with quartz (**Fig.3.4**). Quartz (35%) forms anhedral crystals and locally shows internal micro-deformation (chessboard) structures. The foliation is also locally deformed, forming small folds and flanking biotite flakes. Apatite, zircon, and titanite needles (and epidote) are inclusions with (sagenitic) biotite (**Fig.3.4**).

3.2.4.2. Mineral chemistry

Plagioclase crystals in all samples are predominantly oligoclase (**Fig.3.5a**), with variations: they are sometimes richer in Ca in the tonalite (CM49) or richer in Na in the migmatite neosome. Biotite crystals have narrow Fe-Al-Mg compositions (**Fig.3.5b**), and calc-alkaline affinity (Abdel-Rahman, 1994). Biotite crystals from the migmatite neosome (CM44A) have a slightly more ferric composition (Fe#~0.6) than those from the other samples. Amphibole crystals from the tonalite (CM49) are classified as Mg-Fe-hornblende to Mg-hornblende according to Li et al. (2020b), or as Tschermakite to Magnesio-hornblende (Leake et al., 1997) (**Fig.3.5c**). The plagioclase-hornblende thermobarometer (temperature by Holland and Blundy, 1994; Blundy and Holland, 1990; and pressure by Schmidt, 1992 and Anderson and Smith, 1995) provides crystallization temperature conditions varying from 660-800º C (av. 743 ± 37º C, n=18, 1SD) and pressure from 3.6-5.9 kbar (av. 4.7 ± 0.7 kbar, n=18, 1SD) (**Fig.3.5d**). All analyzed opaque minerals from the Caatinga-Lamim rocks are Fe-sulphides (pyrrhotite).

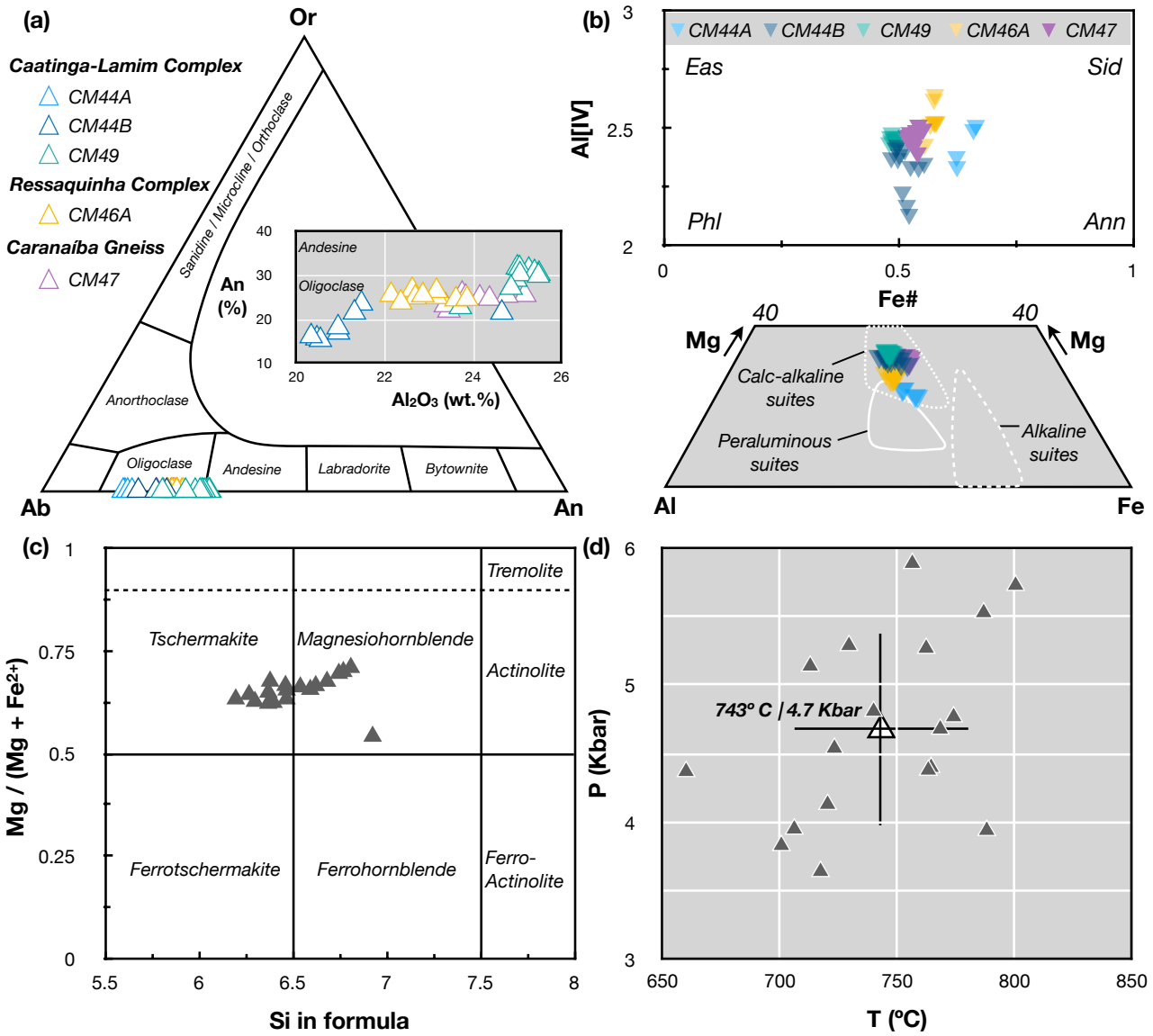


Figure 3.5: Notable geochemical features of major minerals from TTG samples studied herein. Color-code symbols: CM49 (green), CM44A/B (dark/light blue), CM46A (yellow), and CM47 (purple). (a) Trigonal feldspar diagram showing the molar Or-An-Ab contents of analyzed crystals. The small inset shows their Al2O3 (wt.%) vs. An (%) composition. (b) Amphibole classification in terms of tetrahedral Si vs. Mg# after Leake et al. (1997). (c) Al[iv] vs. Fe# (top) and trigonal Mg-Al-Fe (bellow) composition of biotite grains. Fields of nature compositions are after Abdel-Rahman (1994) and mineral abbreviations after Warr (2021). (d) P-T crystallization conditions calculated from amphibole-plagioclase thermobarometers (Blundy and Holland, 1990; Schmidt, 1992). Arithmetic average and related square deviation (1SD) values are highlighted.

3.2.4.3. Whole-rock Geochemistry

Granitoid and gneisses show SiO_2 contents ranging from 67 to 71 wt.%, and MgO + $Fe_2O_{3(t)}$ from 0.55 to 6.32 wt.%, reflecting the varying mode of ferromagnesian minerals (e.g., amphibole, biotite). They are alumina-rich (>15 wt.%) and belong to the high-Al_2O_3 trondhjemite group (Barker and Arth, 1976). Alkali contents (Na_2O+K_2O) vary from 6.08 to 8.46 wt.%, and Na_2O/K_2O

ratios range from 1.6 to 6.1, indicating Na-rich compositions. The higher K_2O contents reflect biotite modal-rich rocks (CM44B, CM47). The tonalite (CM49) has higher CaO contents (4.32 wt.%) than trondhjemite rocks, reflecting primary amphibole and subordinately Ca-rich plagioclase. The neosome part of the migmatite (CM44A) is silica (SiO_2 = 74.1 wt.%) and potassium richer (K_2O = 4.57 wt.%) compared with the paleosome counterpart (CM44B), reflecting the higher amounts of modal quartz and the presence of K-feldspar. Its Al_2O_3 and Na_2O contents are similar to the paleosome, but Na_2O/K_2O ratio value is lower than 1. Fe_2O_3, MnO, MgO, and CaO are minor concentrations (<1 wt.%) due to the very low modal of ferromagnesian minerals.

In normative-feldspar classification (**Fig.3.6a**, O'Connor, 1965), all granitic rocks (except CM44A) plot near the albite vertex, similar to TTG rocks, and are classified as trondhjemite (CM44B and CM46A), tonalite (CM49), and granodiorite (CM47). The increase of normative orthoclase in sample CM47 is likely an artifact, probably due to a large amount of biotite (not used in the CIPW-normalization), as K-feldspar grains are absent. The neosome rock (CM44A) is classified as granite s.s. outwards the TTG field and show normative corundum (> 1%), unlike the other samples. They fall within the metaluminous field (except CM44A, which is felsic-peraluminous) in the milli-cationic diagram of Debon and Le Fort, 1983 (**Fig.3.6b**), meaning Al concentration in plagioclase (and amphibole) rather than aluminous-rich minerals (biotite, muscovite). Mg# values exceed 30, except for the neosome rock sample (Mg#= 18), yet remain below those observed in adakitic volcanic (and sanukitoid) rocks (**Fig.3.6c**). In Shand's diagram (A/CNK vs. A/NK, **Fig.6d**), granitoid rocks are slightly peraluminous and plot in the TTG field (Moyen and Martin, 2012). The neosome shows higher A/CNK values (> 1.1) compared to other samples.

Except for the neosome rock, the concentration of LILE, such as Sr (395-956 ppm) and Ba (551-2008 ppm), is high, and that of Rb (35-196 ppm) is low. Sr/Ba ratios vary from 1.65 (CM49) to 0.35 (CM44B), which reflect biotite-poor and biotite-rich mineralogy. Y contents are low (<10 ppm), as well as mantle-compatible elements (Ni, V, and Cr) (<30, <50, and <60 ppm, respectively). Sr/Y ratios are high, varying from 50.5 (CM47) to 425 (CM49), similar to Archean TTG rocks. The Bayesian combination of probabilities, using SiO_2, K_2O, Sr, Ce, Nb, Ta, and Y contents for TTG classification proposed by Moyen (2011), classifies the granitoid rocks into two major groups: High-pressure TTG (CM49, CM44B) and Medium-pressure TTG (CM46A, CM47). However, we chose not to refer to this classification in the present study due to the ongoing debates surrounding the interpretation of TTG chemistry as a proxy for melting pressure (e.g., Laurent et al., 2024). The neosome rock shows lower Ba and Sr contents than the TTG rocks but has an elevated concentration in Y, producing a low Sr/Y ratio.

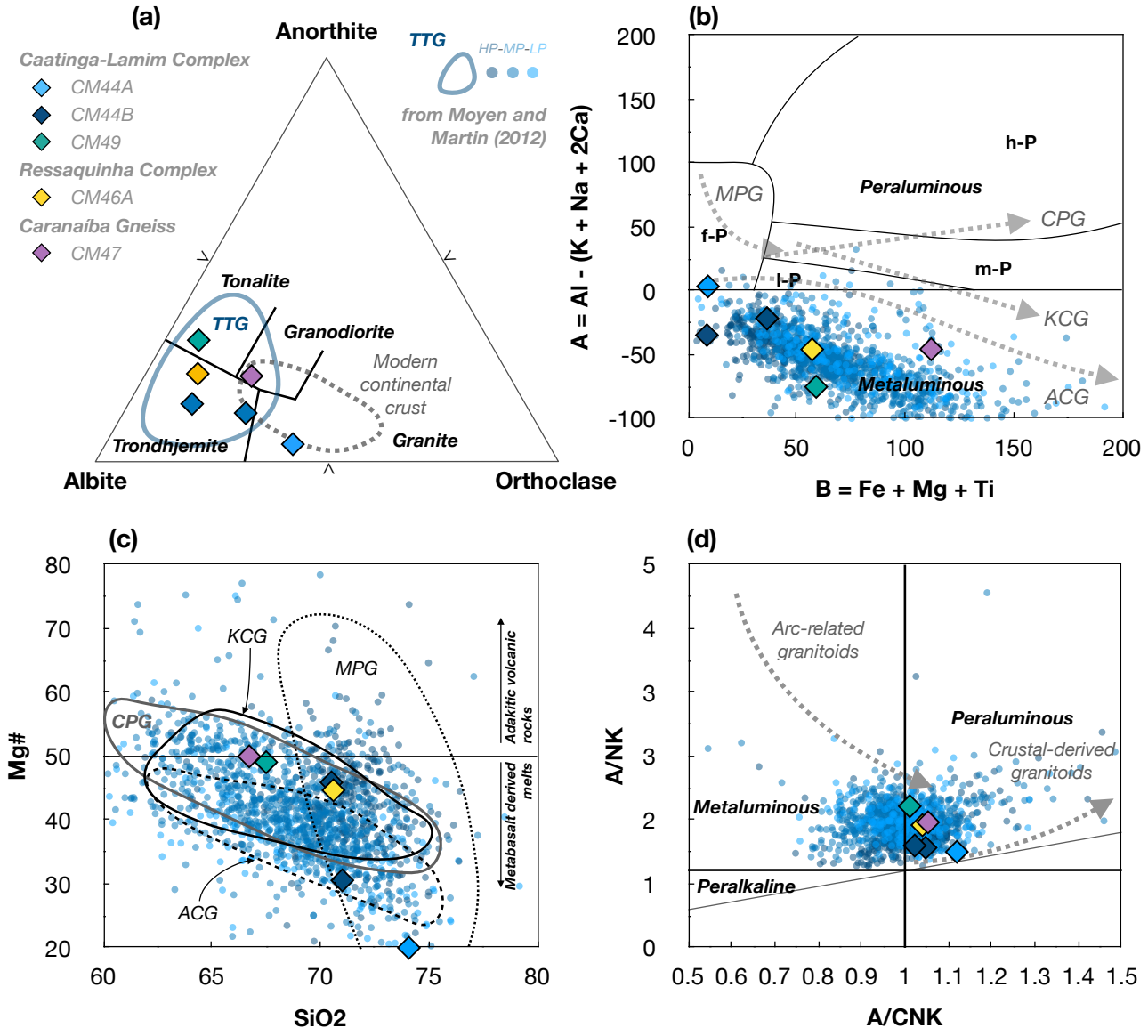


Figure 3.6: Major element geochemistry of the studied TTG rocks. (a) Normative Anorthite-Orthoclase-Albite triangular diagram (Barker, 1979; O'Connor, 1965) showing the different compositions of Archean TTG and modern continental crust (from Moyen and Martin, 2012). (b) A-B diagram (Debon and Le Fort, 1983; Villaseca et al., 1998). Arrows/fields represent the composition of TTG and modern granitoids based on the classification after Barbarin (1999): ACG - amphibole-rich calc-alkaline granitoids; KCG - K-rich and K-feldspar-porphyritic calc-alkaline granitoids; CPG - cordierite-bearing, biotite-rich peraluminous granitoids; MPG - muscovite-bearing peraluminous granitoids (from Moyen et al., 2017). (c) SiO2 vs. Mg# [= 100 × molar Mg/(Mg + Fe)]. The reference line Mg#= 50 roughly divides the compositions of experimental melts derived from metabasalt, and adakites from Condie (2005). (d) A/CNK vs. A/NK diagram (Shand, 1943), molar [Al/(Ca + Na + K)] vs. molar [Al/(Na + K)], respectively. Arrows/fields indicate the composition of arc-related granitoids (e.g., Kohistan batholith), crustal-derived granitoids, and TTG (Moyen and Martin, 2012).

In chondrite-normalized diagrams (**Fig.3.7a-b**), both TTG rocks exhibit strong LREE enrichment and only limited HREE enrichment [$(La/Yb)_N$> 20] similar to Archean TTG rocks (Moyen and Martin, 2012). However, the Caatinga-Lamim rocks (CM49, CM44B) have lower REE concentrations (Yb_N< 1) and higher positive Eu anomalies (Eu/Eu*> 1.5) than the Ressaquinha trondhjemite (CM46A) and Caranaíba gneiss (CM47). Conversely, the neosome rock (CM44A) shows strong enrichment of HREE [$(La/Yb)_N$ ~1] and negative Eu anomaly (Eu/Eu* = 0.3). In primitive mantle normalized multi-element diagrams, the rocks show TTG-like patterns (**Fig.3.7c-d**). CM44B sample shows relatively Rb-Ba enrichment, probably due to the high concentration of biotite in the dark gneissic bands. Caatinga-Lamim TTG rocks show negative Nb and P anomalies but positive Sr and Eu anomalies. In contrast, Ressaquinha trondhjemite (CM46A) and Caranaíba gneiss (CM47) have no Sr, nor Eu anomalies. The neosome rock, unlike the other samples, displays negative Ba, Sr, and Ti and no Nb anomalies.

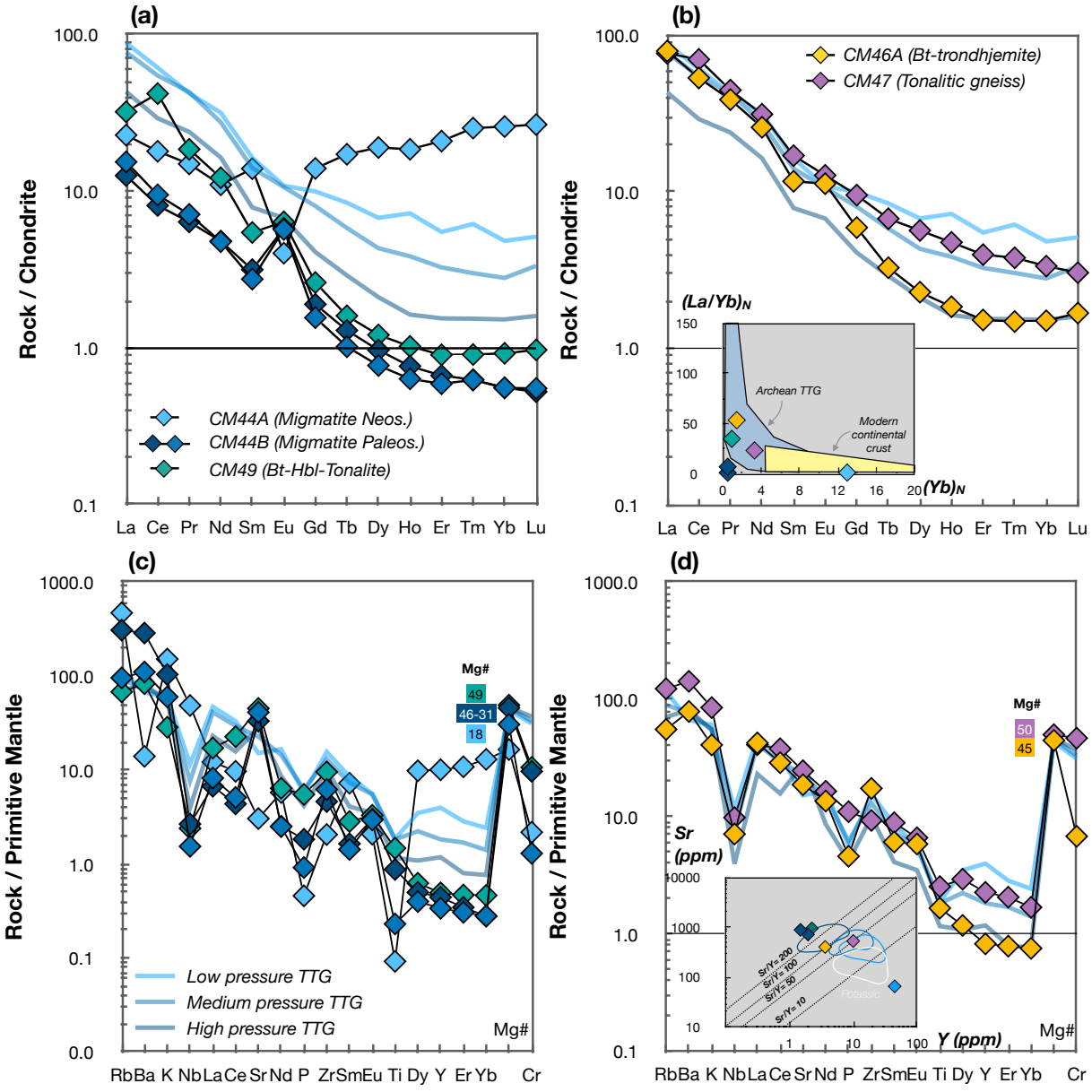


Figure 3.7: Incompatible element diagrams for the studied rocks [left column: Caatinga-Lamim complex (CM44A, CM44B, and CM49); right column: CM46A, and CM47]. The blueish line patterns represent average values for high-pressure 'Sodic-HP', medium-pressure 'Sodic-MP', and low-pressure 'Sodic-LP' TTG rocks from Moyen (2011). Small insets in (b) and (d) are (La/Yb)N vs. (Yb)N and Sr (ppm) vs. Y (ppm), respectively, with fields proposed in Moyen and Martin (2012) and Moyen (2011). In (a) and (b), REE concentrations are normalized to the chondrite values determined by Taylor and McLennan (1985). In (c) and (d), spider diagrams showing incompatible element concentrations (from Rb to Yb) are normalized to the primitive mantle values proposed by Sun and McDonough (1989). Note that Mg# [= 100 × molar (MgO / (MgO + 0.9 × Fe2O3(t)))] and Cr (ppm) are not normalized.

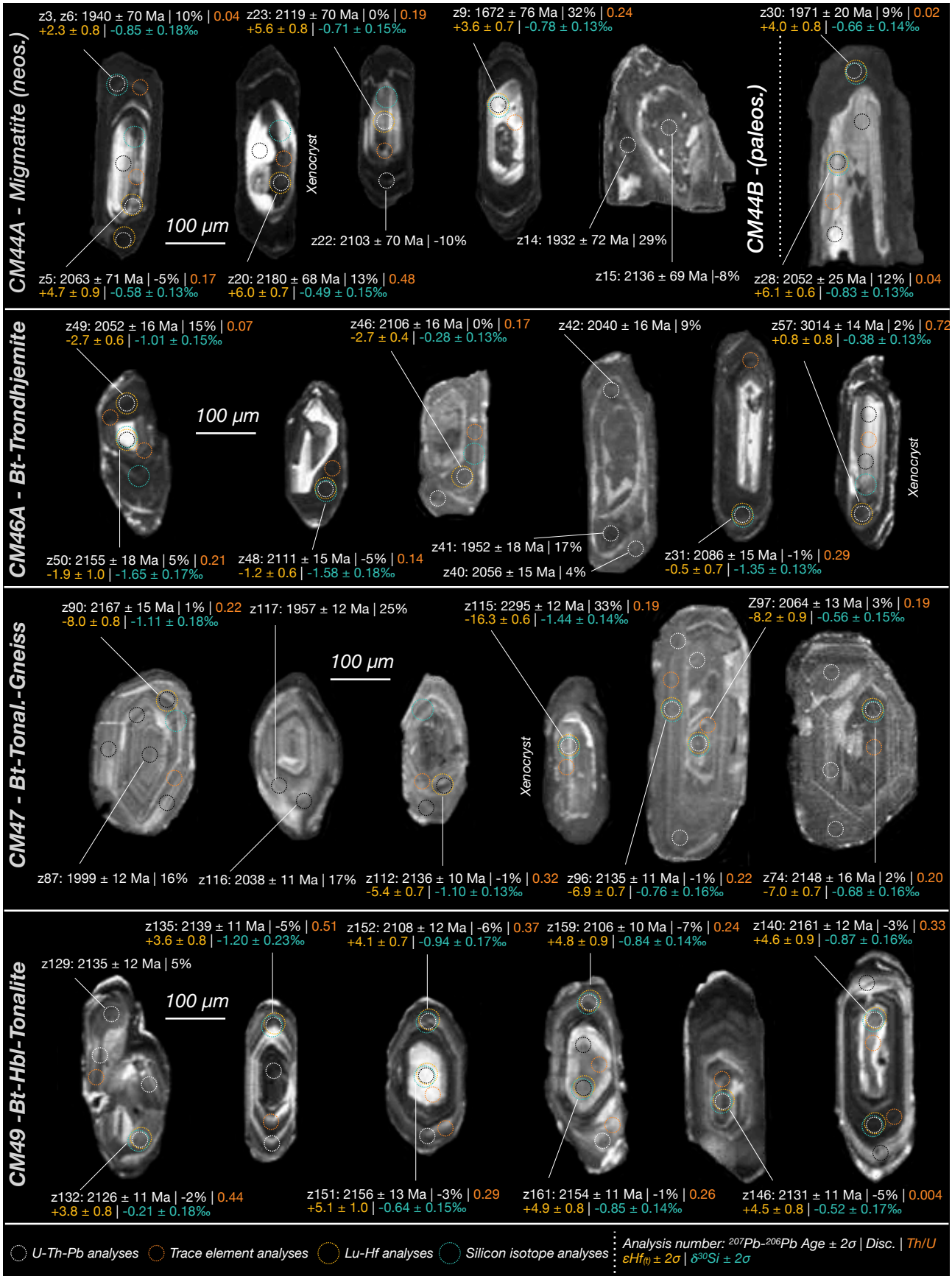
3.2.4.4. Zircon U-Pb dating

Zircon crystals from the neosome part of the migmatite (CM44A) are yellow/grey, prismatic elongated to rounded stubby, varying long-size from 150 to 400 µm. Most crystals show clear core/rim textures (**Fig.3.8**). Fifteen analyses performed on nine zircon rims, and uniform (blurred zoning) crystals, returned discordant analyses that form a Discordia line with an upper-intercept age of 2040 ± 22 Ma and lower-intercept age of 539 ± 62 Ma (MSWD= 2.1) (**Fig.3.9a**). Core analyses returned older ages that align with a recent Pb-loss Discordia line with an upper-intercept age of 2155 ± 19 Ma (MSWD= 1.5) (**Fig.3.9b**). The three most concordant analyses gave a similar Concordia age (2152 ± 22 Ma, MSWD= 0.1). Zircon cores exhibit Th/U ratios ranging from 0.07 to 0.97 whereas rims and crystals without cores show lower values between 0.03 and 0.41.

Two zircon crystals from the paleosome part of the migmatite rock (CM44B) are brow/yellowish, rounded, elongated, and have lengths of 150-250 µm (**Fig.3.8**). These grains show blurred zoning in high CL-intensity zones, sometimes with low CL-intensity rims. Seven analyses define a Discordia line with an upper-intercept age of 2134 ± 37 Ma and a lower-intercept age of 710 ± 65 Ma (**Fig.3.9c**). Th/U ratios have values that vary from 0.02 to 2.03.

Zircon grains from the tonalite (CM49) are greyish to pink/brownish, prismatic, mainly elongated (200-400 µm for long-size), exhibiting well-developed oscillatory zoning (**Fig.3.8**). Eighty-three analyses were done on thirty-four grains which define a recent Pb-loss Discordia line with an upper intercept age of 2122 ± 6 Ma (MSWD= 1.1) (**Fig.3.9d**). The twenty most concordant analyses (Disc.<5%) gave a Concordia age of 2132 ± 6 Ma (MSWD= 1.8). Th/U ratio values range from 0.02 to 0.93.

Figure 3.8: Cathodoluminescence images of representative zircon grains from the studied TTG rocks, showing the location of each analysis. The age labels refer to $^{207}Pb/^{206}Pb$ ages, with their discordance percentage indicated within brackets. Values corresponding to Lu-Hf data refer to ε_{Hf} units calculated according to interpreted sample ages, with quoted 2SE uncertainties. Silicon isotope data are reported as $\delta^{30}Si$ normalized to quartz NBS 28 values with 2SD uncertainties. Th/U ratios correspond to semi-quantitative concentrations determined by external normalization to the reference material used or calculated directly from the trace element analyses, which are consistent with each other for all analyses.


CM44A - Migmatite (neos.)
z3, z6: 1940 ± 70 Ma | 10% | 0.04
+2.3 ± 0.8 | -0.85 ± 0.18‰
z23: 2119 ± 70 Ma | 0% | 0.19
+5.6 ± 0.8 | -0.71 ± 0.15‰
z9: 1672 ± 76 Ma | 32% | 0.24
+3.6 ± 0.7 | -0.78 ± 0.13‰
z30: 1971 ± 20 Ma | 9% | 0.02
+4.0 ± 0.8 | -0.66 ± 0.14‰
CM44B -(paleos.)
Xenocryst
100 µm
z22: 2103 ± 70 Ma | -10%
z14: 1932 ± 72 Ma | 29%
z15: 2136 ± 69 Ma |-8%
z5: 2063 ± 71 Ma | -5% | 0.17
+4.7 ± 0.9 | -0.58 ± 0.13‰
z20: 2180 ± 68 Ma | 13% | 0.48
+6.0 ± 0.7 | -0.49 ± 0.15‰
z28: 2052 ± 25 Ma | 12% | 0.04
+6.1 ± 0.6 | -0.83 ± 0.13‰
CM46A - Bt-Trondhjemite
z49: 2052 ± 16 Ma | 15% | 0.07
-2.7 ± 0.6 | -1.01 ± 0.15‰
z46: 2106 ± 16 Ma | 0% | 0.17
-2.7 ± 0.4 | -0.28 ± 0.13‰
z42: 2040 ± 16 Ma | 9%
z57: 3014 ± 14 Ma | 2% | 0.72
+0.8 ± 0.8 | -0.38 ± 0.13‰
100 µm
Xenocryst
z50: 2155 ± 18 Ma | 5% | 0.21
-1.9 ± 1.0 | -1.65 ± 0.17‰
z48: 2111 ± 15 Ma | -5% | 0.14
-1.2 ± 0.6 | -1.58 ± 0.18‰
z41: 1952 ± 18 Ma | 17%
z40: 2056 ± 15 Ma | 4%
z31: 2086 ± 15 Ma | -1% | 0.29
-0.5 ± 0.7 | -1.35 ± 0.13‰
CM47 - Bt-Tonal.-Gneiss
z90: 2167 ± 15 Ma | 1% | 0.22
-8.0 ± 0.8 | -1.11 ± 0.18‰
z117: 1957 ± 12 Ma | 25%
z115: 2295 ± 12 Ma | 33% | 0.19
-16.3 ± 0.6 | -1.44 ± 0.14‰
Z97: 2064 ± 13 Ma | 3% | 0.19
-8.2 ± 0.9 | -0.56 ± 0.15‰
100 µm
Xenocryst
z87: 1999 ± 12 Ma | 16%
z116: 2038 ± 11 Ma | 17%
z112: 2136 ± 10 Ma | -1% | 0.32
-5.4 ± 0.7 | -1.10 ± 0.13‰
z96: 2135 ± 11 Ma | -1% | 0.22
-6.9 ± 0.7 | -0.76 ± 0.16‰
z74: 2148 ± 16 Ma | 2% | 0.20
-7.0 ± 0.7 | -0.68 ± 0.16‰
CM49 -Bt-Hbl-Tonalite
z135: 2139 ± 11 Ma | -5% | 0.51
+3.6 ± 0.8 | -1.20 ± 0.23‰
z152: 2108 ± 12 Ma | -6% | 0.37
+4.1 ± 0.7 | -0.94 ± 0.17‰
z159: 2106 ± 10 Ma | -7% | 0.24
+4.8 ± 0.9 | -0.84 ± 0.14‰
z140: 2161 ± 12 Ma | -3% | 0.33
+4.6 ± 0.9 | -0.87 ± 0.16‰
z129: 2135 ± 12 Ma | 5%
100 µm
z132: 2126 ± 11 Ma | -2% | 0.44
+3.8 ± 0.8 | -0.21 ± 0.18‰
z151: 2156 ± 13 Ma | -3% | 0.29
+5.1 ± 1.0 | -0.64 ± 0.15‰
z161: 2154 ± 11 Ma | -1% | 0.26
+4.9 ± 0.8 | -0.85 ± 0.14‰
z146: 2131 ± 11 Ma | -5% | 0.004
+4.5 ± 0.8 | -0.52 ± 0.17‰
U-Th-Pb analyses
Trace element analyses
Lu-Hf analyses
Silicon isotope analyses
Analysis number: 207Pb-206Pb Age ± 2σ | Disc. | Th/U
εHf(t) ± 2σ | δ30Si ± 2σ

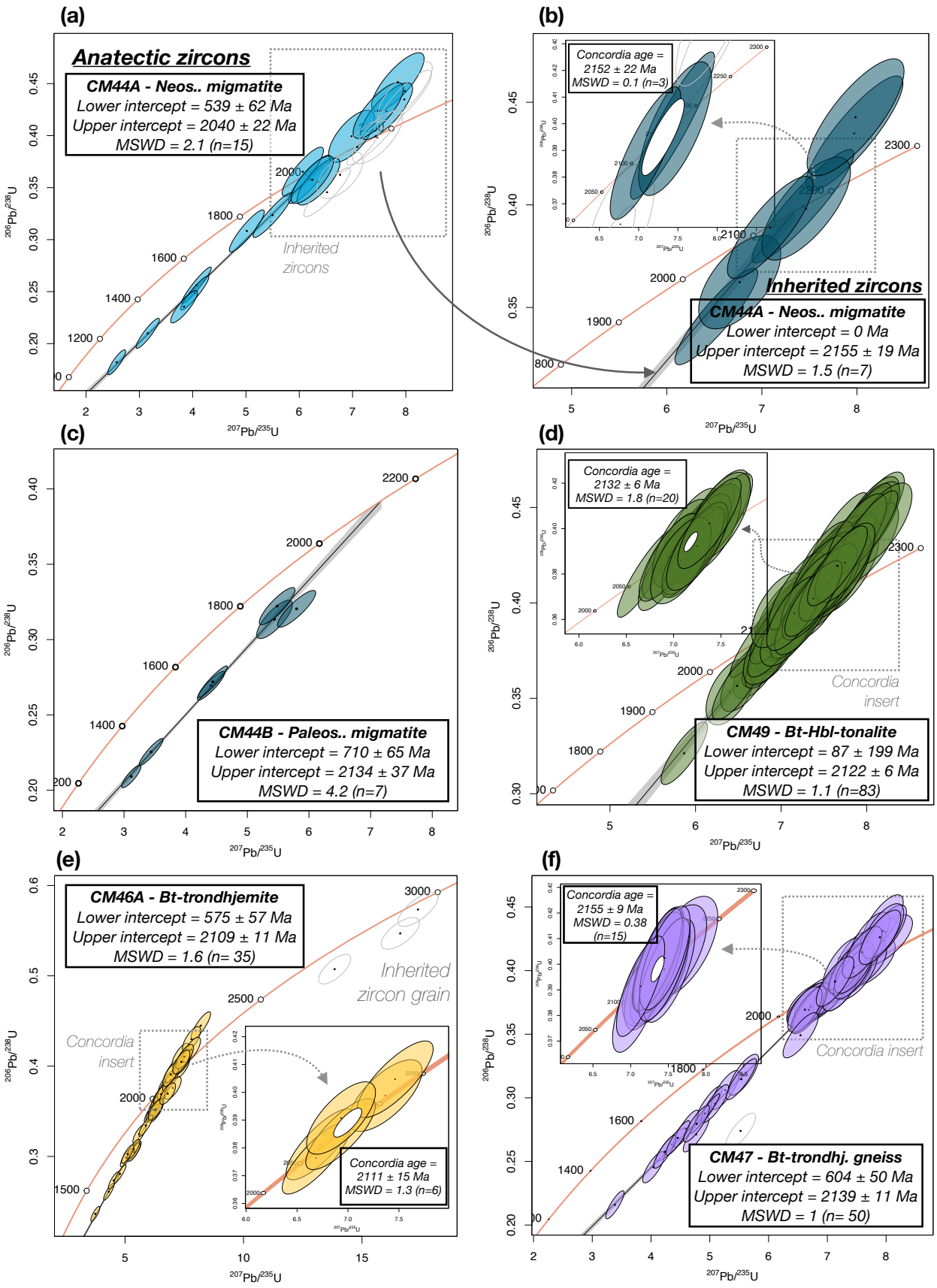


Figure 3.9: Geochronological results of the studied TTG rocks from the Caatinga-Lamim complex [(a) and (b) from sample CM44A; (c) from CM44B; (d) from sample CM49]. In (a), the colored ellipses represent anatectic (phenocryst) zircons, while the colorless ellipses indicate inherited (xenocryst) zircons. In (b), the analysis of the inherited zircon reveals a Discordia line. In contrast, the more concordant analyses produce a concordant age, as shown in the small inset

at the top left. In (c), the colored ellipses represent the analyses with negligible incorporation of common Pb, that define a Discordia line. In (d), all U-Th-Pb analyses form a well-defined Discordia line, while in the small inset, the age is calculated based on the most concordant analyses. Both approaches, using the discordant intercept and the Concordia method, yield similar ages for the sample. (e) CM46A, Ressaquinha trondhjemite. The colored ellipses represent all magmatic (phenocryst) zircons, while the colorless ellipses come from a single inherited zircon core (see zircon images in Figure 7). The more concordant analyses calculate a concordant age (small inset) consistent, within error, with the age calculated using the Discordia method. (f) CM47, Caranaíba gneiss. The colored ellipses represent all magmatic zircon grains, and the colorless ellipse likely indicates an inherited core. The small inset highlights the most concordant analysis, which calculates virtually the same age using all analyses with the Discordia method.

Seventeen zircon grains from the trondhjemite (CM46A) are pinkish to brownish, mostly prismatic, elongated to stubby, and exhibit patchy to blurred zoning in CL (**Fig.3.8**). A single crystal shows a rounded, high CL-intensity, well-zoned core and (altered) dark overgrows (**Fig.3.8**). Three analyses were performed on this single core that gave an apparent ($^{207}Pb/^{206}Pb$) Archean age (e.g., *z71*, 3014 ± 14 Ma, Disc.= 2%). Th/U ratio values for these analyses closely vary from 0.81 to 0.93. On the other hand, thirty-five analyses of the remaining crystals define a Discordia line with an upper-intercept age of 2109 ± 11 Ma and a lower-intercept age of 575 ± 57 Ma (**Fig.3.9e**). The six most concordant analyses (Disc.<5%) returned a virtually equivalent Concordia age of 2111 ± 15 Ma. Th/U ratio values range from 0.05 to 0.42.

Twenty-six zircon crystals from the tonalitic gneiss (CM47) are pinkish to brownish, rounded to prismatic, mostly stubby, and show well-preserved oscillatory zoning (**Fig.3.8**). A single crystal exhibits a texture that suggests a core/rim organization. A single analysis of this core has yielded a highly discordant Paleoproterozoic age ($^{207}Pb/^{206}Pb$= 2295 ± 12 Ma, Disc.= 33%). Conversely, fifty analyses performed on the remaining zircon grains align in a Discordia line with an upper-intercept age of 2139 ± 11 Ma and a lower-intercept age of 604 ± 50 Ma (MSWD= 1.0) (**Fig.3.9f**). The fifteen most concordant ages (Disc.< 5%) gave a similar within-error Concordia age of 2155 ± 9 Ma (MSWD= 0.38). Th/U ratio values of these analyses range from 0.13 to 0.41.

3.2.4.5. Zircon hafnium isotopes

Eighty-four Lu-Hf spot analyses were done on selected zircon grains, considering the spatial resolution and the concordance of U-Pb ages. TTG rocks from the Caatinga-Lamim Complex (CM44A/B, CM49 samples) have an initial $^{176}Hf/^{177}Hf_{(t)}$ composition ranging from 0.282490 to 0.281665 (average 0.281577 ± 0.000074; 2SD, n= 50) (**Fig.3.10a**). No discernible variations exist between anatectic, inherited, and magmatic zircon grains and domains. Calculated $\varepsilon_{Hf(t)}$ values are essentially positive (above CHUR) varying from +1.4 to +6.5 (average +4.2 ± 0.8, 2SD, n= 50) (**Fig.3.10b**). Sample CM46A (Ressaquinha trondhjemite) shows $^{176}Hf/^{177}Hf_{(t)}$ from 0.281360 to 281542 (average 0.281417 ± 0.000112; 2SD, n= 15) (**Fig.3.10a**). Calculated $\varepsilon_{Hf(t)}$ values are chondritic to negative and vary from -3.4 to +1.5 (average -1.6 ± 0.7, 2σ, n= 15) (**Fig.3.10b**). The xenocrystic zircon core has an initial $^{176}Hf/^{177}Hf_{(t)}$ composition of 0.280898 ± 0.000023, and a slightly positive

$\varepsilon_{Hf(t)}$ value (+0.8 ± 0.8) (not shown). Sample CM47 (Caranaíba gneiss) shows an initial $^{176}Hf/^{177}Hf_{(t)}$ composition of 0.280963 to 0.281272 (average 0.281206 ± 0.000145; 2SD, n= 15) (**Fig.3.10a**). Calculated $\varepsilon_{Hf(t)}$ values are negative and vary from -16.3 to -5.4 (average -7.8 ± 0.7; 2SD, n= 17) (**Fig.3.10b**). The zircon xenocryst has an initial $^{176}Hf/^{177}Hf_{(t)}$ of 0.280882 ± 0.000016, and strongly negative $\varepsilon_{Hf(t)}$ of -16.3 ± 0.3 (not shown).

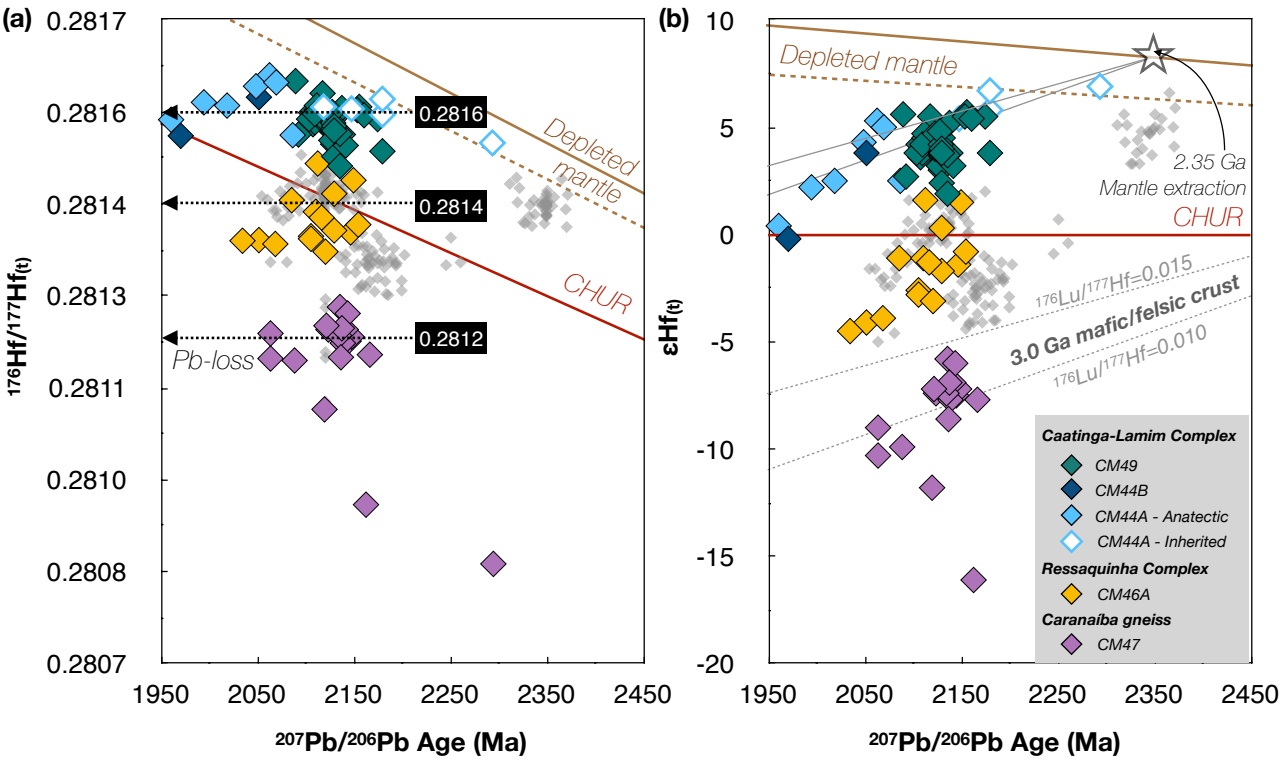


Figure 3.10: Zircon Lu-Hf isotopes of TTG rocks. The color code symbols for each sample are the sample used in Fig.5. Hollow symbols represent analyses performed on inherited zircon cores. Small gray diamonds refer to local TTG, sanukitoid, high Ba-Sr, and hybrid granitoids of Moreira et al. (2020). Depleted mantle curves were defined according to Dhuime (2011) and Ickert (2013) (full line), and Chauvel and Blichert-Toft (2001) (dashed line). CHUR values provided by Iizuka et al. (2015). (a) Initial $^{176}Hf/^{177}Hf$ composition vs. Pb-Pb apparent ages (Ma). Horizontal arrays define the average composition for each sample and suggest Pb-loss. (b) ε_{Hf} vs. Pb-Pb apparent age (Ma) space showing plausible Lu/Hf evolution arrays ($^{176}Lu/^{177}Hf$= 0.01-0.015) anchored at apparent TDM (e.g., 2.35 Ga, 3.00 Ga) ages.

3.2.4.6. Zircon trace elements

The trace element composition of zircon grains was used as a proxy to evaluate their pristine/ altered state. Seventy analyses were performed on 10, 1, 15, 16, and 17 zircon crystals from CM44A, CM44B, CM46A, CM47, and CM49, respectively. Chondrite-normalized REE patterns (**Fig.3.11a-b**) are similar to crustal terrestrial zircon grains (Hoskin and Schaltegger, 2003), showing HREE/ LREE enrichment and positive Ce and negative Eu anomalies when the altered compositions are excluded [LREE-I= (Dy/Nd) + (Dy/Sm) < 20, and La_N> 10; e.g., Laurent et al., 2020b]. Some zircon grains from CM46A sample show positive Eu/Eu* and their Hf contents and U/Yb ratios plot

within the continental domain (including from TTG rocks) zircon grains (Grimes et al., 2015; Guitreau et al., 2022) (**Fig.3.11d**). Th/U ratios from all zircon grains are higher than 0.1, except for the zircon grain from the paleosome part of the migmatite (*z30*, Th/U~0.02) (**Fig.3.11c**). Ti-in-zircon temperatures (Ferry and Watson, 2007) of all samples vary from 723 to 1015ºC, mostly between 750 and 850ºC (**Supplementary Material B**). There is no systematic discrepancy between the calculated temperatures and the samples.

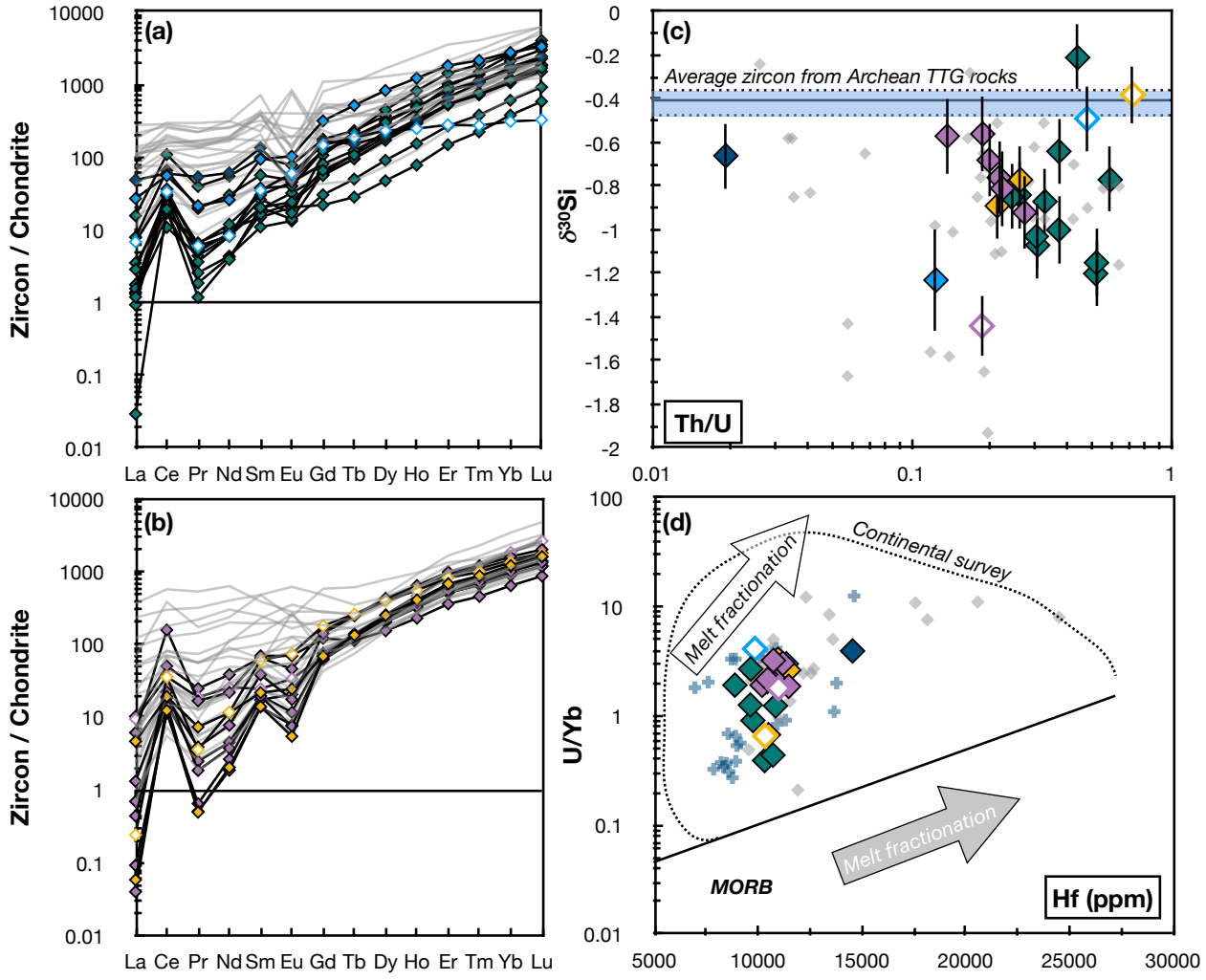


Figure 3.11: Trace elements and Si isotopes of zircon grains from TTG rocks. The color code symbols for each sample are the sample used in Fig.9. Gray pattern lines [in (a) and (b)] and small gray diamonds [in (c) and (d)] refer to altered zircon compositions. Chondrite-normalized REE diagrams of (a) Caatinga-Lamim complex and (b) Rassaquinha trondhjemite and Caranaíba gneiss. (c) δ30Si vs. Th/U composition. The shaded field shows the typical δ30Si composition of zircon grains from Archean TTG rocks (Guitreau et al., 2022), whereas the horizontal line indicates the signature of mantle-derived zircons (Trail et al., 2018). Error bars indicate 2SD uncertainties. (d) U/Yb vs. Hf (ppm) composition. Fields of continental survey and MORB zircon grains, as well as arrows indicating melt fractionation, are from Grimes et al. (2015). Small blue crosses refer to zircon grains from Archean TTG rocks (Guitreau et al., 2022).

3.2.4.7. Zircon silicon isotopes

Sixty-nine silicon isotope measurements were done on the same zircon grains/domains previously analyzed for trace elements. When altered zircon data are excluded, Caatinga-Lamim TTG rocks (CM44A/B and CM49) show a range of δ30Si from -1.23 to -0.21‰ (**Fig.3.11c**). Considering the migmatite rock (CM44A/B), lighter isotopic compositions are found in neosome zircons (*z11*, -1.23‰), whereas cores (*z20*, -0.49 ± 0.15‰) and zircons from the paleosome (*z30*, -0.66 ± 0.14‰) consistently have heavier compositions. Zircon grains from the tonalite (CM49) have a spread in δ^{30}Si composition that varies from -1.20 to -0.21‰ (average -0.88 ± 0.17‰, n= 12). Zircon grains from the Caranaíba gneiss (CM47) have δ^{30}Si compositions ranging from -0.92 to -0.56‰ (average -0.72 ± 0.15‰, n= 8) (**Fig.3.11c**). The zircon xenocryst has a lighter composition (*z129*, -1.44 ± 0.14‰). Zircon δ^{30}Si compositions for the trondhjemite rock (CM46A) vary from -0.89 to -0.77‰ (average -0.83 ± 0.12‰, n= 5) (**Fig.3.11c**) and the inherited core has a heavier composition (*z71*, -0.38 ± 0.13‰). Considering the relationship between $\Delta^{30}Si_{WR\text{-}Zrc}$ and temperature as a function of SiO_2 proposed by Guitreau et al. (2022), the calculated whole-rock δ^{30}Si average values of the TTG samples vary from -0.57 to -0.37‰ (**Supplementary Material B**). The neosome rock shows lighter calculated δ^{30}Si values (*z11*= -0.90‰). **Table 3.2** shows the main analytical results of zircon crystals from the studied rocks.

Table 3.2: Summary of analytical results obtained on zircon crystals from the studied rock.

Sample	U-Pb age (Ma)	$\varepsilon_{Hf(t)}$	Ti-in-zircon temperature (°C)	Zircon δ^{30}Si (‰)	Calculated whole-rock δ^{30}Si (‰)
	Intercept or Concordia	*Average*	*Range*	*Average*	*Average*
CM44A	2040 ± 22	+3.3	828	-1.23	-0.90
	2155 ± 19 (core)	*+5.2 (core)*	*836 (core)*	*-0.49 (core)*	*-0.17 (core)*
CM44B	2134 ± 37	+5.0	864	-0.66	-0.37
CM46A	2111 ± 15	-1.6	723 to 1015	-0.83	-0.52
	~ 3000 (core)	*+0.8 (core)*	*732 (core)*	*-0.38 (core)*	*-0.01 (core)*
CM47	2155 ± 9	-7.8	728 to 841	-0.72	-0.39
CM49	2132 ± 6	+4.2	740 to 942	-0.88	-0.57

3.2.5. Discussions

3.2.5.1. Ages of TTG emplacement and melting

Despite the absence of a clear relationship between the studied rocks, the U-Pb geochronological data allow us to distinguish and interpret at least three successive stages of TTG magma emplacement (~2150, 2130, and 2110 Ma) and a single episode of partial melting (2040 ± 22 Ma).

The older episode generated the tonalite protolith of Caranaíba gneiss at 2155 ± 9 Ma (concordant age, n= 15). This episode followed the emplacement of tonalite plutons at ca. 2.18 Ga (Moreira et al., 2018) to the north. In contrast, the older zircon xenocryst suggests the assimilation of country rocks (e.g., 2.2 Ga Serrinha-Tiradentes Suite, Ávila et al., 2010, 2014) during magma emplacement.

Tonalite magmas (CM49) were emplaced at 2132 ± 6 Ma (concordant age, n=20), building part of the Caatinga-Lamim Complex. The inherited cores of the neosome part of the migmatite rock (CM44A) and zircon grains from its paleosome part (CM44B) suggest a crystallization age at 2155 ± 22 Ma (concordant age, n=3), and 2134 ± 37 Ma (Discordia age, n=7), respectively. Ages of both samples from the Caatinga-Lamim Complex agree with uncertainty, and then we assume a crystallization age of ca. 2.13 Ga. This episode took place concurrently with the emplacement of sanukitoid-hybrid and TTG-reworked magmas to the north (Moreira et al., 2018; Seixas et al., 2013).

Trondhjemite magmas (CM46A) have crystalized at 2111 ± 15 Ma (concordant age, n=6), forming part of the Ressaquinha Complex, and ending the successive episodes of TTG emplacement. The interpreted crystallization age agrees with that previously reported by Noce et al. (2000), using whole-rock Rb-Sr isochron. The zircon xenocryst shows an Archean age, similar to inherited zircon grains from hybrid granites, which suggests an older crustal contribution (Moreira et al., 2018). Archean sediments filled Paleoproterozoic basins and acted as sources for sediment-derived magmas within the Mineiro Belt (Moreira et al., 2020; Lacerda et al., 2024).

Zircon overgrowths and newly formed grains from the neosome part of the migmatite (CM44A) mark anatexis at 2040 ± 22 Ma (Discordia age, n= 15). This age is correlated with metamorphic titanite grains from 2.13 Ga sanukitoid-hybrid plutons to the north (Moreira et al., 2018). Anatexis was also recorded at ca. 2050 Ma, forming Kinawa migmatite in the Quadrilátero Ferrífero region, caused by the early stage of soft collision with the Mineiro Belt (Carvalho et al., 2017).

3.2.5.2. Sources and melting conditions

The Al-, Na/K-, Sr/Y-, LREE/HREE-rich, and the low mantle-compatible (Mg#, V, Ni, Cr, Co) and large ion lithophile elements (LILE) composition of the studied granitic rocks allow us to classify them as TTGs (**Fig.3.12a**) (review in Moyen and Martin, 2012). Although TTG geological setting of formation is highly debated (Laurent et al., 2024; Martin et al., 2005; Moyen, 2011; Bédard et al., 2006; Hoffman et al., 2011), there is a consensus on the fact that TTG melts formed from partial melting (F~20-30%) of hydrous mafic source rock. Fractional crystallization of a basaltic liquid may also be an alternative mechanism to produce certain TTG magmas (Smithies et al., 2021) but low-temperature sensitive isotopes (e.g., Si, O) indicate that sources experienced surface alteration before being melted (André et al. 2019; Deng et al. 2019; Lei et al., 2023). Temperature conditions should be sufficient to trigger amphibole and plagioclase melting reactions (750-950º C), while pressure conditions are more variable (0.5 to 4 GPa) and can be inferred from pressure-

sensitive residual minerals (e.g., garnet, plagioclase, Martin, 1987). It is important to note that pressure proxy compositions (e.g., La/Yb and Sr/Y) cannot be used without a detailed evaluation of mineral accumulation/fractionation processes (Smithies et al., 2019; Laurent et al., 2020a; Kendrick et al., 2022).

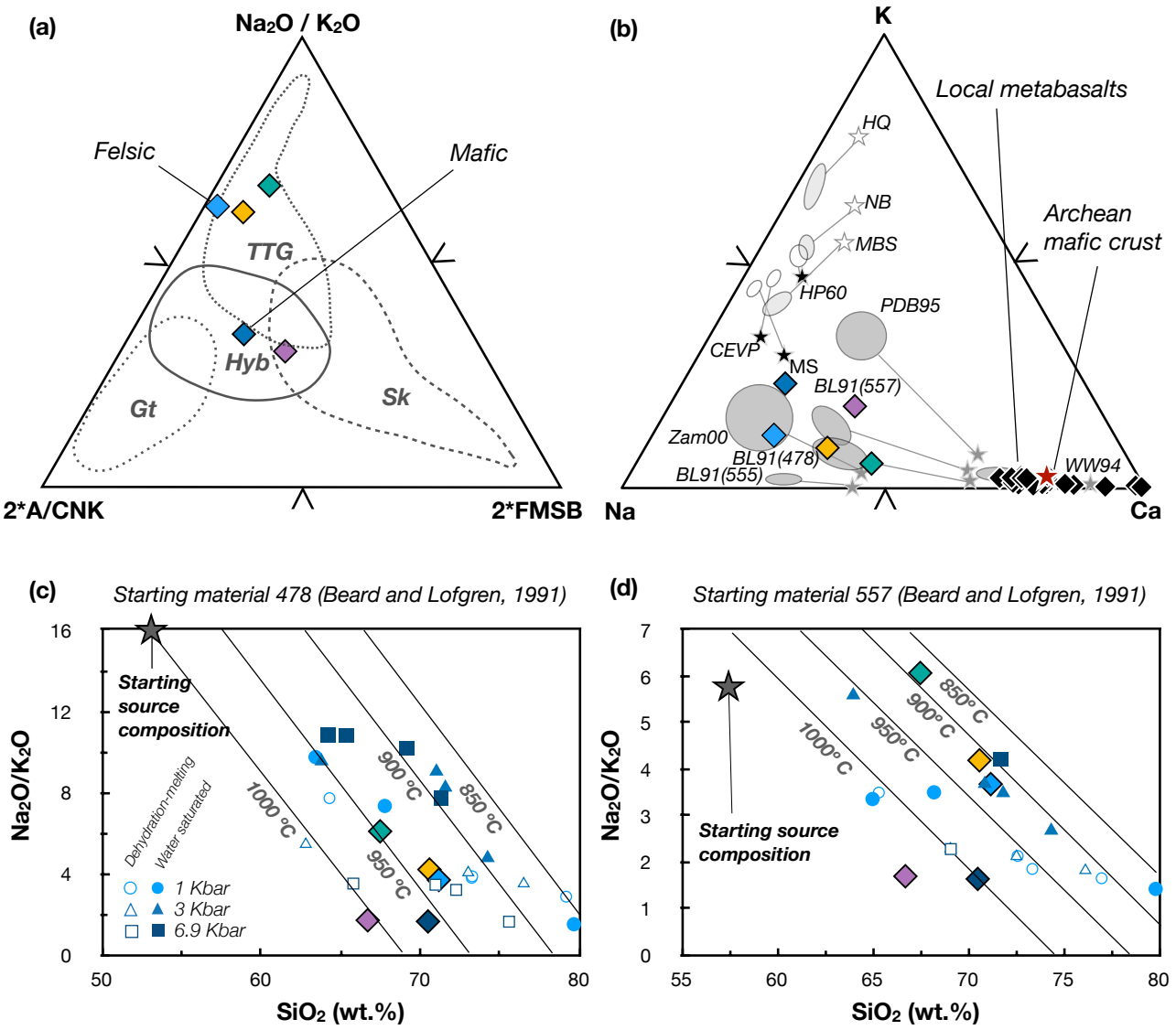


Figure 3.12: Plausible sources and melting conditions for TTG rocks. The color code and symbols for each sample are the same as those used in Fig. 9. (a) Trigonal source discrimination diagram for Neoarchean granitoids proposed by Laurent et al. (2014). Triangle vertices are: 2×A/CNK (molar [Al2O3/(CaO + K2O + Na2O)]; Na2O/K2O (wt.%) ratio; and 2×[FeOt + MgO + Sr + Ba] (wt.%) (FMSB). The TTG, Sk, Hyb and Gt fields designate TTG, sanukitoids, hybrid granitoids, and granitic (s.s.) suites respectively. (b) Na-K-Ca trigonal diagram shows several compositions of experimental melts (ellipses) and their starting material (stars), compiled by Moyen (2011). Dark grey: mafic sources; Light grey: sedimentary sources. Black diamonds represent local metabasalts (Teixeira et al., 2015), and the red star refers to the average composition of the mafic Archean crust (Taylor and McLennan, 2009). (c) Na2O/K2O vs. SiO2 composition of experimental melts from low-K andesite BL91(478), and (d) low-K calc-alkaline andesite BL91(557) performed by Beard and Lofgren (1991), compared with the studied samples.

Compared with the experimentally produced melts, the K-Ca-Na composition of all samples is similar to that of low-K andesite BL91(478), low-K calc-alkaline andesite BL91(557) [Beard and Lofgren (1991)], and ophiolites Zam00 [Zamora (2000)] (**Fig.3.12b**). Moreover, the composition of low-K andesites is quite similar to that of local metabasalts (Teixeira et al., 2015) and to that of the average composition of the mafic Archean crust (Taylor and McLennan, 2009).

To better estimate the P-T and hydrous activity melting conditions, we compared the Na_2O/ K_2O and SiO_2 composition of the studied rocks with the melts produced from the two andesitic materials [BL91(478) and BL91(557), Beard and Lofgren (1991)]. The composition of the studied rocks can be reproduced via dehydration melting of BL91(478) starting material at 6.9 Kbar and 900-950° C (for CM49, CM46A, and CM44A) and >950° C (for CM44B and CM47) P-T conditions (Fig.3.12c). The degree of melting ranges from 20 to 60%. Using the BL91(557) starting material, the composition of the studied rocks (CM49, CM46A, and CM44A) is most comparable to that of melts (F~23-63%) produced via water-saturated melting at lower pressure (1-3 Kbar) conditions (**Fig.3.12d**).

From the isotopic point of view, three distinctive zircon initial $^{176}Hf/^{177}Hf(t)$ compositions can be distinguished (**Fig.3.10a**). The Caranaíba tonalitic gneiss (CM47) shows the lowest initial $^{176}Hf/^{177}Hf_{(t)}$ values ~0.2812 (**Fig.3.10a**) that are comparable to the composition of zircon grains from 2.18 Ga tonalites of Casa Grande-Água Limpa plutons (Moreira et al., 2020). Its relatively light $\delta^{30}Si$ composition suggests no heavier $\delta^{30}Si$ (chert/silicification) contribution (**Fig.3.11c**). Similarly, the mantle-like $\delta^{18}O$ composition of zircon grains from the 2.18 Ga tonalites points to insignificant supracrustal contamination (Moreira et al., 2020). This finding supports the hypothesis of Archean source contribution to the Mineiro Belt's magmatism.

The Ressaquinha trondhjemite exhibits intermediate initial $^{176}Hf/^{177}Hf_{(t)}$ values ~0.2814 (**Fig. 3.10a**) similar to the composition of zircon grains from 2.35 Ga TTG rocks (Moreira et al., 2020; Lopes et al., 2024), 2.13-2.11 Ga sanukitoid, high Ba-Sr, and hybrid granitoids (Moreira et al., 2018, 2020). This isotope signature can be explained via partial melting and evolution of a mafic (oceanic) crust extracted from the mantle at ca. 2.5 Ga that melted during Siderian and Rhyacian times, with the latter involving mantle/sediment contribution. Similar to high Ba-Sr and hybrid granitoids (Moreira et al., 2020), a single inherited zircon grain from the Ressaquinha trondhjemite attests to minor Archean contribution. Interestingly, while $\delta^{30}Si$ compositions of magmatic zircon grains suggest a lighter $\delta^{30}Si$ contribution, the inherited core shows a heavier $\delta^{30}Si$ composition, comparable to that of the mantle (and Archean TTG) zircons (**Fig.3.11c**; Trail et al., 2018).

Zircon grains from the Caatinga-Lamim rocks show higher initial $^{176}Hf/^{177}Hf_{(t)}$ values ~0.2816 (**Fig.3.10a**), which suggests a reworking of a mafic crust with short crustal residence time as source material. Lu/Hf evolution lines point to mantle extraction (TDM) ages around 2.35 Ga (**Fig.3.10b**) when TTG magmas of the Lagoa Dourada Suite were also formed. Moreover, the higher initial

$^{176}Hf/^{177}Hf_{(t)}$ values and the absence of inherited zircon grains prevent an origin via reworking of pre-existing 2.35 Ga crust suggested for the genesis of the 2.14 Ga Resende Costa TTG Suite (Moreira et al., 2018). The spread in $\delta^{30}Si$ composition (-1.20 to -0.21‰, av. -0.88‰; **Fig.3.11c**) of the magmatic zircon grains from CM49 could be regarded as resulting from a less significant influence of superficial processes (silicification/alteration) in the source rock prior to melting.

3.2.5.3. Parental magma

It is reasonable to assert that granitic rocks rarely represent the crystallization of a magmatic liquid directly extracted from their source, given the variety of processes that can occur during magma ascent, emplacement, and storage in magma chambers (e.g., Barnes et al., 2019). In addition, new magma inputs can promote mixing and hybridization, and when added to partially crystallized (mushy) zones, can modify the original magma composition and the early crystallized mineral assemblages. Besides, post-magmatic processes (e.g., metamorphism and anatexis) can obliterate the primary textures, transform minerals, and change their primary composition.

Considering these premises, we evaluated the samples' field relationships, mineral assemblages, textures, and whole-rock geochemistry to identify which could represent the most pristine or less differentiated magmas. The Caatinga-Lamim rocks often show cumulative textures of plagioclase crystals that form aggregates of relatively large (>1 mm) grains (**Fig.3a-b**), sharing boundaries or surrounded by finer grains (**Fig.3.4**). In addition, the absence of hornblende in the most silica-rich rocks (CM44A/B), considering constant water-pressure conditions, may suggest that this mineral has been fractionated. Mineral and whole-rock chemistry also reflects this process, which will be discussed in the following subsection.

On the contrary, Ressaquinha trondhjemite and Caranaíba gneiss do not show mineral textures and chemical signatures that could directly reflect fractionation/accumulation processes. Therefore, we assumed these rocks could represent parental liquids to model their incompatible element composition using batch melting equations (Janoušek et al., 2016). We have used the partition coefficient of 21 elements (Rb, Ba, Th, U, Nb, Ta, K, La, Ce, Sr, Nd, Sm, Zr, Hf, Eu, Gd, Dy, Ti, Y, Er, and Yb) for ten plausible residual minerals (Hornblende, Clinopyroxene, Garnet, Ulvöspinel, Plagioclase, Rutile, Magnetite, Titanite, Zircon, and Apatite) listed in Martin et al. (2014).

Assuming a classical TTG source material for the studied granitoids (Archean basalt, Martin et al., 2014), the composition of the Caranaíba gneiss can be reproduced at moderate degrees of partial melting (F= 10-30%), leaving a hornblende-eclogitic residue with 54% Cpx, 27% Hbl, 11% Grt, 6% Usp, 2% Pl, and 0.12% Rt (**Fig.3.13**). The model-derived enrichment in Zr and Hf may suggest the presence of zircon as a trace component in the residue. Similarly, the composition of the Ressaquinha trondhjemite can be reached using higher degrees of partial melting (F= 20-50%), and residues richer in garnet instead of clinopyroxene, and in rutile and titanite instead of

ulvöspinel (45% Grt, 35% Cpx, 15% Hbl, 3% Pl, 1% Rt, 1% Ttn) (**Fig.3.13**). The degrees of partial melting in these models are comparable to the fractions of melts produced in experimental studies regarding major element composition (Moyen and Stevens, 2006). In addition, the garnet-rich residue composition can indicate that melting has occurred at higher pressures to form the Ressaquinha trondhjemite magmas.

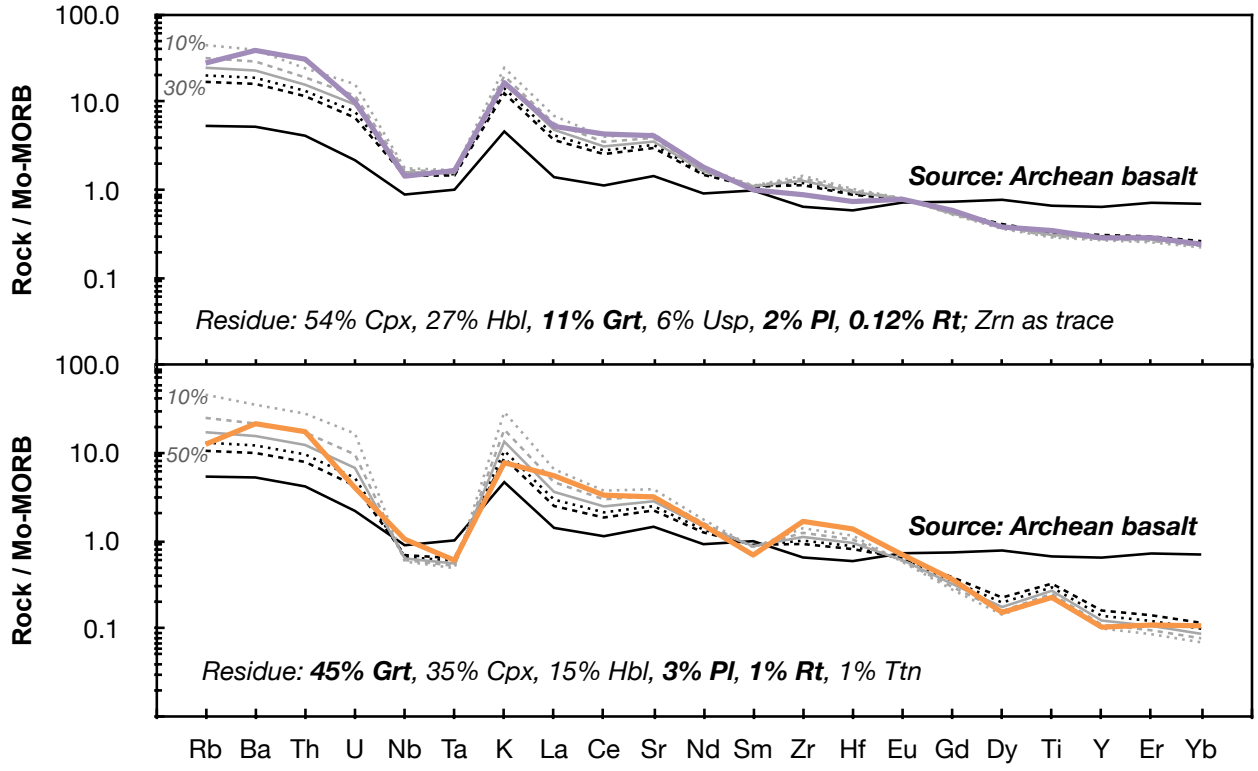


Figure 3.13: Average modern MORB (Mo-MORB) normalized multi-element diagram showing partial melting model results for possible parental magmas CM47 Caranaíba gneiss (top) and CM46A Ressaquinha trondhjemite (bottom). Fine gray dashed lines indicate the percentage of melting (e.g. F= 10-30%). 'Residue' refers to the residual mineral assemblage proportions used in the model. The mineral abbreviation used is after Warr, 2021.

3.2.5.4. Magmatic processes

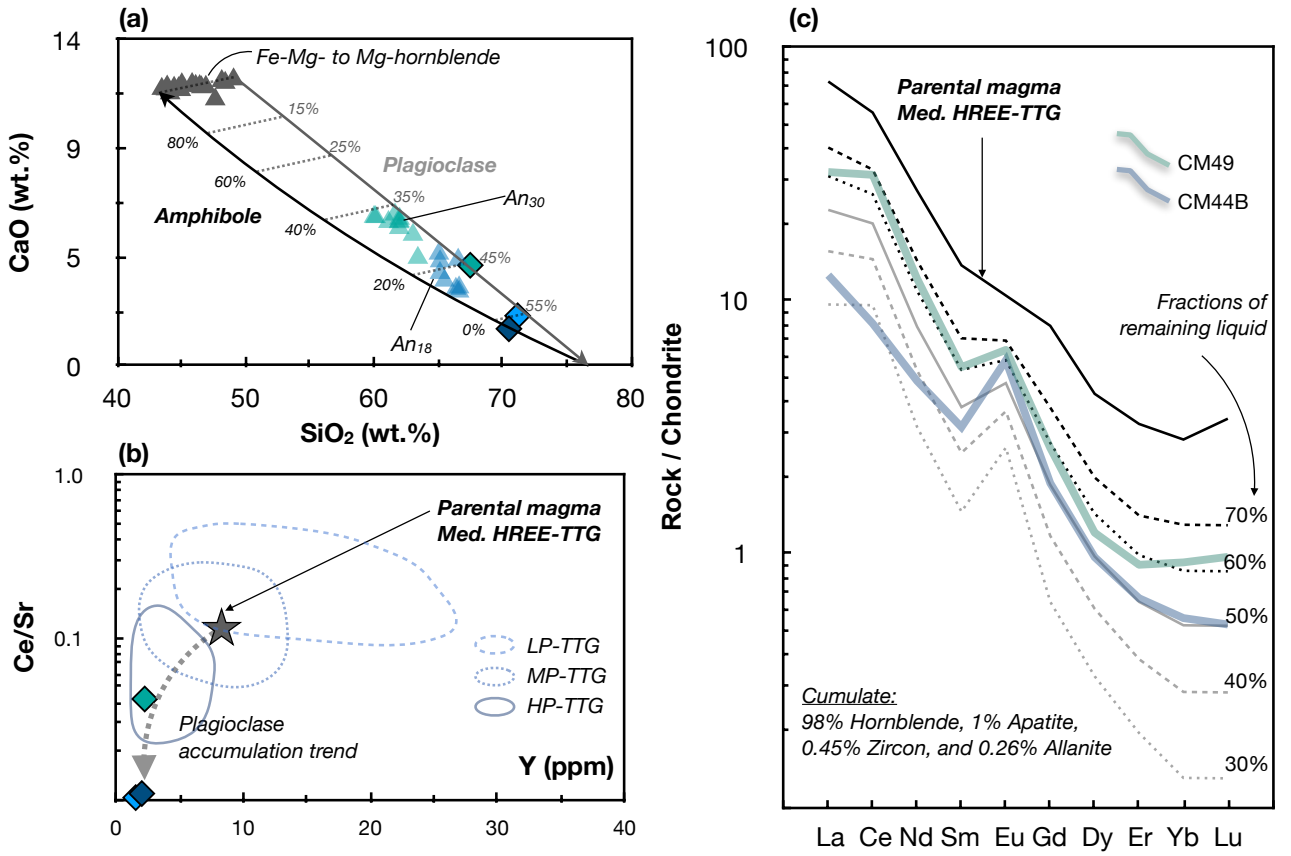
As briefly discussed above, it is not plausible to suggest that the Caatinga-Lamim rocks were formed from the direct crystallization of a single magmatic liquid: they show mineralogical textures and chemical variations that indicate fractional crystallization of hornblende and plagioclase accumulation, which certainly modified their parental magma composition. Moreover, the trondhjemitic gneiss underwent partial melting, which could alter its primary geochemistry. Instead, the combined CaO and SiO_2 composition of amphibole and plagioclase crystals, along with the whole-rock chemistry of these rocks (**Fig.3.14a**), indicate that amphibole fractionation occurred concurrently with plagioclase accumulation and sodium enrichment (An_{30} to An_{18}). The significant decline in the Ce/Sr ratio, along with the reduction of Y content in these rocks, also suggests the accumulation of plagioclase in the samples (**Fig.3.14b**) as was similarly observed in the Paleoarchean Barberton plagioclase-rich trondhjemites (Laurent et al., 2020a).

The low-REE composition and highly fractionated REE patterns with positive Eu/Eu* anomalies suggest amphibole fractionation and plagioclase accumulation. To access the former process, we have modeled the REE composition of the Caatinga-Lamim rocks using Rayleigh fractionation equations [$C_L/C_0 = F$ (D-1), where F is the fraction of the melt remaining and D is the bulk partition coefficient of the fractionating assemblage], and element-mineral partition coefficients listed in Martin et al. (2014), except for allanite that came from Rollinson and Pease (2021). The REE composition of the tonalite Caatinga-Lamim (CM49) is comparable to that of the liquid (C_L) produced by 30-40% fractional crystallization of hornblende, minor apatite, zircon, and allanite as trace phases (98% Hornblende, 1% Apatite, 0.45% Zircon, and 0.26% Allanite), from a medium-HREE TTG (Moyen and Martin, 2012) as parental magma (C_0) (**Fig.3.14c**). The fractionation values and assemblage are similar to those calculated by Liou et al. (2019) to explain the magmatic evolution of Neoarchean TTG rocks from North China Craton.

Increasing hornblende fractionation and plagioclase accumulation would lead to REE-poor compositions similar to those observed in the paleosome migmatite of Caatinga-Lamim (CM44B) (**Fig.3.14c**). However, partial melting certainly modified its primordial incompatible trace element composition (Sawyer, 1987), and access to magmatic processes could be meaningless. The contrasting normalized REE-patterns of the paleosome (CM44B: high $[La/Yb]_N$ and Eu/Eu*) and neosome (CM44A: low $[La/Yb]_N$ and Eu/Eu*) parts of the migmatite suggest low-pressure melting conditions, where plagioclase is stable and garnet unstable in the protolith (Roberts et al., 2024). Further detailed petrological studies based on the migmatites in the Mineiro Belt are necessary to constrain partial melting reactions and conditions.

Alternatively, the REE composition of the Caatinga-Lamim rocks could represent different proportions of crystals/melt caused by the variation in degrees of liquid–crystal separation in partially solidified parental magma (Kendrick et al., 2022).

Figure 3.14: Magmatic process models for Caatinga-Lamim rocks. (a) CaO (wt.%) vs. SiO2 (wt.%) composition, amphibole (dark triangles), and plagioclase (colored triangles). For color code and symbology used, refer to Fig.9. Arrows indicate amphibole fractionation (black line) and plagioclase accumulation (gray line) trends. The percentage labels are based on the modal mineral assemblage of each sample. 'Anx' refers to the normative composition of plagioclase crystals from the Caatinga-Lamim rocks. (b) Ce/Sr ratio vs. Y (ppm). The Caatinga-Lamim rocks show a positive correlation that suggests plagioclase accumulation (Laurent et al., 2020a) from a plausible parental magma [Med.HREE-TTG (Moyen and Martin, 2012)]. The bluish fields represent high-pressure 'HP', medium-pressure 'MP', and low-pressure 'LP' TTG rocks from Moyen (2011). (c) Chondrite-normalized REE diagram showing fractionation model results considering a Med.HREE-TTG parental magma composition. 'Cumulate' refers to the fractionated mineral proportion. Dashed gray lines indicate the composition of the fractionated remaining liquids. The fractions of the remaining liquid are also shown.



3.2.5.5. Surface implications

The heavy silicon signature of Archean TTG rocks (and hosted zircon grains) suggests that their hydrous-basaltic source material was silicified (or intercalated with chert) before melting (André et al., 2019; Deng et al., 2019; Guitreau et al., 2022; Murphy et al., 2024). In contrast, zircon grains from Paleoproterozoic TTG rocks in the Mineiro Belt have lower δ^{30}Si compositions, indicating a less significant silicification in the source or an insignificant contribution of silicified basalts (André et al., 2022). Regarding the evolution of the oceanic Si cycle through geologic time, the Precambrian DSi composition of seawater is higher (> 1000 µM) than the current levels (Siever, 1992; Conley et al., 2017). It drastically decreases during the Paleoproterozoic due to the deposition of BIFs, and gradually decreases during the Meso- and Neoproterozoic when the eukaryotic fauna becomes abundant (Conley et al., 2017).

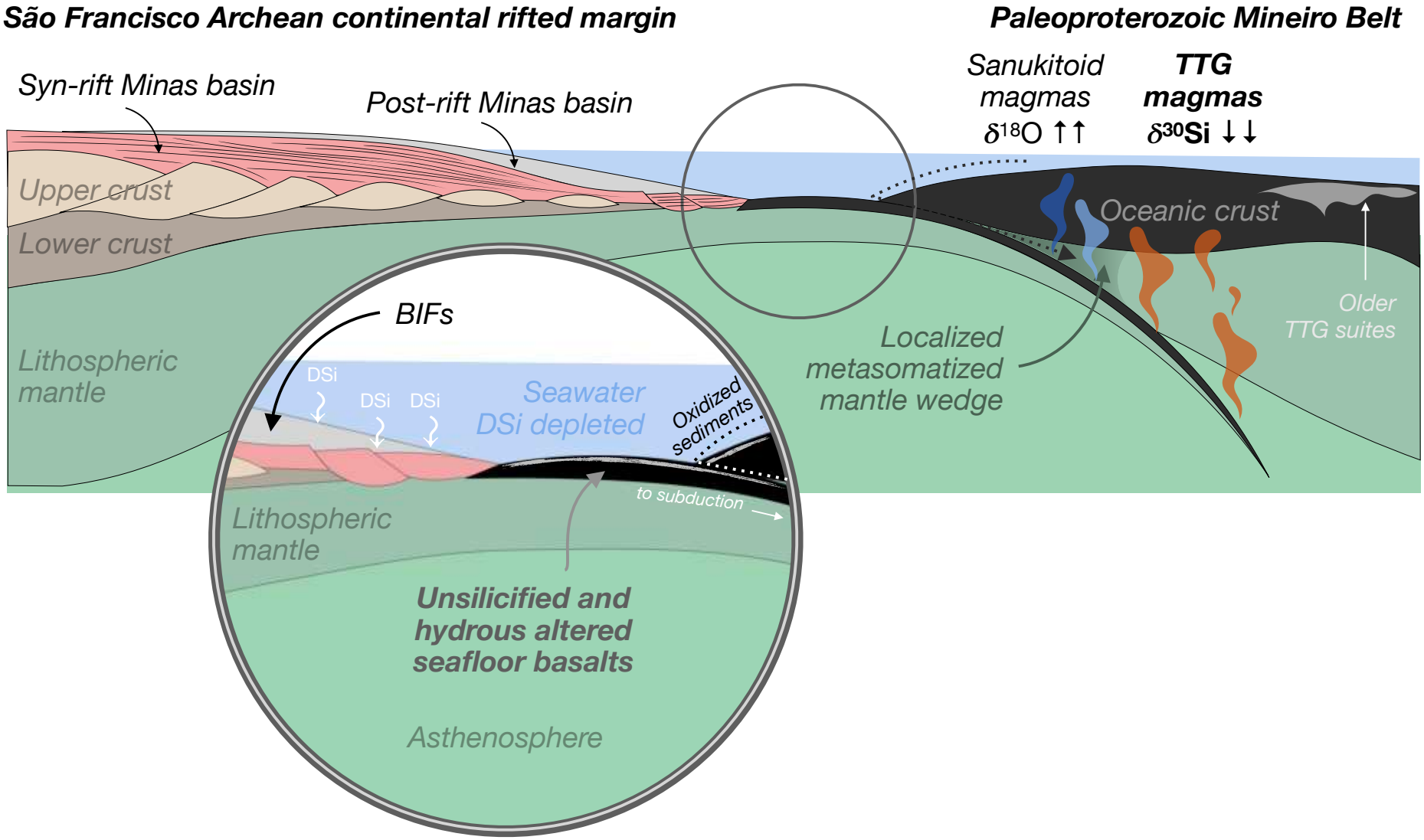
Considering a plausible reduced DSi composition of the oceans due to the global deposition of BIFs during the Paleoproterozoic, three main hypotheses could be accounted for to explain the lighter silicon isotopic composition of TTG rocks in the Mineiro Belt. First, depleted δ^{30}Si values and small δ^{18}O variations are related to the formation of hydrothermal high-T quartz (Kleine et al., 2018) in the lower parts of the oceanic crust (Deng et al., 2019). However, this assumes silicified rocks (gabbros and sheet dykes) and a Si-saturated composition of the oceans, which is not the case

in the Minero belt scenario. In addition, the mechanism of water introduction into the lower parts of oceanic crusts is poorly understood. Second, meteoric and glacial waters are proposed as lighter Si isotopic components of unsilicified basaltic sources for the genesis of 2.3 Ga TTG rocks in the North China Carton (Zhou et al., 2024). This hints at an intraplate tectonic scenario, supported by the subsequent emplacement of A and I-type granitic suites. There is no evidence for an intraplate tectonic scenario to produce granitic suites, nor defined A-type granites, in the Mineiro Belt. Then this hypothesis can be ruled out. Third, lower δ^{30}Si values of some Ocean Island Basalts (OIBs) reveal recycled altered oceanic crust and lithospheric mantle in their mantle sources (Pringle et al., 2016). Sub-mantle δ^{18}O values of 2.35 Ga TTG in the Mineiro Belt suggest high-temperature alteration of basaltic sources (Moreira et al., 2020). Alteration of basaltic rocks leads to the formation of secondary (clay) minerals that retain water and have lighter silicon isotope signatures (Ziegler et al., 2005). Water retention in neoformed clay minerals facilitates the melting conditions for basaltic sources to produce TTG magmas.

Figure 15 presents a proposed geodynamic scenario for the genesis of Paleoproterozoic TTG rocks, considering a simplified continental rift margin-seafloor-island arc system. Post-rift marine sediments (e.g., BIFs of the Cauê Formation) are deposited at the margins of the continental rifted margin of the São Francisco proto-craton (e.g., Quadrilátero Ferrífero region) during the early Paleoproterozoic, drastically reducing the local DSi oceanic composition. Offshore of the continent, potentially mafic parent sources (e.g., seafloor basalts) were extracted from the depleted mantle (Ávila et al., 2014; Seixas et al., 2012, 2013; Moreira et al., 2018, 2020; this study) and interacted with the depleted DSi seawater column. Instead of silicification, the seawater-rock interaction promotes source alteration and formation of hydrous secondary minerals with lighter silicon isotope compositions (e.g., smectite, kaolinite). Subsequently, during the Rhyacian, these unsilicified and hydrous-altered basalts underwent partial melting and produced low δ^{30}Si TTG magmas in the island-arc environment of the Mineiro Belt. Coeval sanukitoid magmas were formed by the interaction of TTG magmas and locally metasomatized mantle through oxidized arc sediments (Moreira et al., 2023).

Figure 3.15: Proposed geodynamic model for Paleoproterozoic TTG generation in the Mineiro Belt. Deposition of BIFs in the rifted passive margin of the Archean São Francisco continent scavenges the 30Si composition of the ocean. Coeval oceanic seafloor basalts interact with the Si-reduced seawater column and become unsilicified until recycled into the mantle during subduction in an island-arc scenario. Unsilicified basaltic subducted slabs underwent partial melting, producing low-Si TTG magmas. These melts locally interact with the metasomatized mantle wedge via oxidized sediments, which generate oxidized sanukitoid magmas (Moreira et al., 2023).

2.15-2.11 Ga: Island arc stage



3.2.6. Conclusions

This study establishes a new episode of TTG emplacement during Rhyacian times in the Mineiro Belt, southern São Francisco Craton, Brazil. The TTG magmas were formed by melting mafic rocks, similar in composition to the Archean mafic crust and local metabasalts. The major and trace element composition of these TTGs suggests temperature and pressure conditions ranging from 850 to 1000ºC, and from 4 to 7 kbar, respectively. The zircon initial $^{176}Hf/^{177}Hf$ for these rocks suggests mainly juvenile (Paleoproterozoic sources) and minor reworked (Archean source) magmatism. Furthermore, the silicon isotope composition of these zircon grains indicates an apparent absence of silicification processes, conversely to those proposed for Archean TTG source materials.

We suggest a geodynamic scenario for the formation of TTG in the Mineiro Belt, considering surface interactions such as the ocean, atmosphere, and sedimentation. The low Si isotopic signature of these Paleoproterozoic TTGs is consistent with the reduced dissolved Si composition of the oceans and suggests that recycling of hydrous altered basaltic crust is a key process in the genesis of TTG magmas.

4. Tracking igneous and metamorphic processes using other accessory minerals

4.1. Preface

This Chapter, in preparation to be submitted to *Contributions to Mineralogy and Petrology*, explores the potential of integrating U-Th-Pb geochronology and trace element composition of apatite and titanite grains from two end-member granitic rocks: TTG (Caatinga-Lamim Complex, **Chapter 3**) and Type-S (Cupim Pluton, **Chapter 2**). The internal texture observed in BSE and CL images, along with its trace element composition (mainly Y, Sr, LREE, Zr, and Pb), provides an effective tool for differentiating growths during igneous or metamorphic processes. When applicable, the REE composition of apatite and titanite grains/domains can efficiently act as tracers of the parental magma composition of their host rock. The role of simultaneous crystallization of rock-forming minerals is also discussed regarding their chemical temperature saturation. Additionally, the dating of apatite grains is a pioneering technique in the study area, and reveals an important accessory mineral in the reconstruction of igneous and metamorphic events.

4.2. Accessory minerals unveil Paleoproterozoic igneous and metamorphic processes in Mineiro Belt, Brazil

The following activities were developed by the first author under the supervision of Martin Guitreau and Leonardo Gonçalves: (i) apatite grains were picked and mounted; (ii) titanite grains were identified in thin sections; (iii) the performance and reduction data of apatite and titanite, along with U-Th-Pb and trace element analyses, were determined with Julie Mallens; (iv) imaging (CL and BSE) of apatite and titanite grains was conducted with Cristiane C. Gonçalves; (v) the manuscript was written and figures were drawn. Heavy mineral separation was carried out with Cassiano Costa. (vi) EMPA analyses were supervised by professors Marco Paulo Castro and Gláucia Queiroga (DEGEO/UFOP). All authors contributed to the conceptualization of the paper's main idea.

Accessory minerals unveil Paleoproterozoic igneous and metamorphic processes in the Mineiro Belt, Brazil

Syro Lacerda [a,b], Martin Guitreau [a], Leonardo Gonçalves [b], Julie Mallens [a], Hugo Moreira [c], Cristiane C. Castro [b], Marco Aurélio Pinheiro [d], Cassiano Costa [e], Régis Doucelance [a]

[a] Laboratoire Magmas et Volcans, CNRS-UMR6524, IRD-UMR163, OPGC, Université Clermont Auvergne, F-63178 Aubière, France

[b] Universidade Federal de Ouro Preto, Departamento de Geologia, Ouro Preto, Brazil

[c] School of Earth and Environmental Sciences, University of Portsmouth, Burnaby Building, Burnaby Road, Portsmouth, PO1 3QL, UK

[d] Center of apllied geosciences, Geological Survey of Brazil - CPRM, Av. Pasteur 404, Rio de Janeiro, Brazil

[f] Geological Survey of Brazil – CPRM, Av Brazil 1731, Belo Horizonte 30140-002, Brazil

Abstract

U-rich accessory minerals such as zircon, apatite, titanite, and rutile are widely used as geochronometers to date magmatic and metamorphic events and to constrain the depositional history of sedimentary basins. These minerals crystallize early during magma or lava cooling and preferentially incorporate incompatible elements, allowing the composition of the parental melt to be inferred from their partition coefficients. This study explores the U-Th-Pb and trace element compositions of apatite and titanite grains from (meta)igneous rocks of the Paleoproterozoic Mineiro Belt in the southern São Francisco Craton, Brazil, using LA-ICP-MS and EMPA techniques. Apatite and titanite from Caatinga-Lamim TTG rocks show complex textures and mineral associations, suggesting chemical remobilization and multiple crystallization events. Titanite grains associated with sulphate phases and characterized by dark BSE signals and high Y/Sr, REE, Nb, and U contents preserve a pristine igneous signature dated at ~2130 Ma. In contrast, chemically depleted titanite domains with light BSE intensities indicates isotopic resetting, likely due to metamorphism and anatexis during late orogenic stages. Apatite grains exhibit irregular core–rim zoning; less-altered REE- and Y/Sr-rich cores yield ages consistent with anatectic zircons (~2040 Ma), indicating a migmatitic origin. In contrast, apatite grains from the Cupim S-type granites are homogeneous, with higher Y/Sr ratios and lower Eu anomalies compared to those from TTG rocks, and yields ages of ~2000 Ma coeval with magmatic zircons. Whole-rock REE modeled patterns from igneous titanite compositions indicates a medium-pressure TTG parental magma, while igneous apatite compositions reflect S-type granite affinities and distinguish between clay-rich and clay-poor protoliths.

Keywords

Apatite and titanite U-Th-Pb geochronology, Apatite and titanite trace elements, Paleoproterozoic, Mineiro Belt, São Francisco Craton.

4.2.1.Introduction

Trace element composition of accessory minerals, particularly apatite, and titanite, has been shown to be a potential tool for identifying and distinguishing parental magma compositions, as well as magmatic and metamorphic processes, and detrital provenance (Bruand et al., 2014; 2017; 2020; Belousova et al., 2001; O'Suillivan et al., 2020). In addition, apatite and titanite are minerals widely used in thermochronological and geochronological studies [Lu-Hf (in apatite), U-Pb, Fission track, and (U-Th)/He] (e.g., Spencer et al., 2013; Chew et al., 2015). Unlike zircon, apatite and titanite can incorporate varying amounts of Pb during their crystallization (Frost et al., 2001; Kohn, 2017). Besides, they are more susceptible to conditions that induce open system behavior of Pb due to their lower closure temperatures (500-750º C), if compared with zircon (>900º C) (Cherniak, 2010). Both conditions lead to highly discordant analyses on the $^{206}Pb/^{206}Pb$ vs. $^{238}U/^{206}Pb$ (Tera-Wasserburg) space, challenging the interpretation of U-Pb ages and their correlation with magmatic, metamorphic, and tectonic events (Storey, 2006). Several approaches have been employed to address these challenges (see Chew et al., 2011), such as linear regression, assuming initial Pb concentrations according to global Pb evolution models (e.g., Stacey and Kramers, 1975), or measuring low-U minerals (e.g., feldspar) within the same rock (Bonamici and Blum, 2020). The use of a third isotope ratio (e.g., $^{204}Pb/^{206}Pb$, $^{208}Pb/^{232}Th$) provides an alternative method for correcting the effect of Pb incorporation during crystallization. However, these measurements require high precision, which somewhat limits the use of the LA-ICP-MS technique. More recently, efforts have been made to interpret the U-Pb data obtained from apatite and titanite by correlating them with their trace element compositions (Olierook et al. 2019; Appen et al., 2020; Droubi et al., 2023).

The São Francisco Craton is the most extensively studied Precambrian terrain on the South American continent (Heilbron et al., 2017). Most U-Pb geochronological studies in its southern part focus on zircon grains from felsic plutonic rocks (granitoid and gneiss) (see Moreira et al., 2020; Marimon et al., 2022). There is currently limited geochronological data on other accessory minerals, such as titanite, rutile, and monazite (Noce et al., 1998; Aguilar et al., 2017; Moreira et al., 2018; Pereira et al., 2019), and no apatite dating. Nevertheless, accessory mineral composition investigations are scarce (Moreira, 2019).

In this work, we report U-Th-Pb ages combined with trace element composition, determined via LA-ICP-MS, of titanite and apatite grains from two contrasting lithotypes (TTG and S-type granites) from the Paleoproterozoic Mineiro Belt, aiming to constrain the tectonomagmatic evolution of the southern São Francisco Craton. In addition, we intend to contribute to the potential use of trace elements of apatite and titanite in recognizing parental magma compositions, as well as magmatic and metamorphic processes, perhaps not observed in petrography, whole-rock, or zircon chemical composition.

4.2.2. Geological background

The São Francisco Craton (SFC, **Fig.4.1a**), situated in eastern Brazil, has been designed as a miniature continent, given the clear evidence it provides for some of the relevant phases of the early Earth's history on a relatively small, exposed surface (Romano et al., 2013; Moreira et al., 2024; Leitzke et al., 2024). It was shaped by Brasiliano orogenic systems involved in assembling western Gondwana between 640 and 500 Ma (Almeida et al., 2000). Rocks within SFC are as old as 3.6 Ga to 1.8 Ga (Oliveira et al., 2020) and have served as basements to foreland Ediacaran-Ordovician basins (Uhlein et al., 2017). In its southern lobe (**Fig.4.1b**), basement rocks are exposed and can be distinguished into two geochronological terrains: the Archean-Paleoproterozoic Quadrilátero Ferrífero and the Paleoproterozoic Mineiro Belt (Alkmim and Teixeira, 2017). Roughly sutured by large-scale shear zones (Jeceaba-Bom Sucesso and Congonhas-Itaverava; Nahas et al., 2023), these terrains have collided during Rhyacian-Orosirian times witnessed by Himalayan-type magmatism (Lacerda et al., 2024), partial melting (Carvalho et al., 2017; Lacerda et al., submitted), tectonic inversion of the Minas basin (Alkmim and Marshak, 1998), and regional metamorphism (Cutts et al., 2019).

Despite the well-documented crustal evolution of the Quadrilátero Ferrífero and the Mineiro Belt, heavily based on zircon systematics (U-Pb ages, Hf-O-isotopes (Albert et al. 2016; Moreira et al. 2020), some questions remain ambiguous or unclear regarding the nature of some plutonic bodies (e.g., Resende Costa suite, Teixeira et al., 2015; Moreira et al., 2018), as well as the growth of other accessory minerals during magmatic or metamorphic events. For the latter, titanite and monazite growth record different Archean and Paleoproterozoic magmatic and metamorphic events (**Fig4.1.b**, Machado et al., 1992; Noce et al., 1998; Aguilar et al., 2017; Moreira et al., 2018; Neves et al., 2023). Magmatic grains were partially or completely recrystallized and underwent isotopic resetting during thermal events at ca. 2080 and 1940 Ma (Aguilar et al., 2017). However, no study has yet shown how to systematically differentiate the nature of these phases beyond their tectonic events or zircon-related ages. U-Pb ages calculated on minerals that could incorporate common Pb (e.g., apatite, titanite, monazite) may be meaningless if Pb-corrections were not properly determined (Storey et al., 2006). Furthermore, even when it is often present on mafic and felsic rocks in the southern SFC, no apatite geochronology studies have been reported in the literature.

Plutonic bodies within the Mineiro Belt represent ideal candidates for investigating the nature of magmatic and metamorphic crystal growth, combining geochronological and trace element studies. The Caatinga-Lamim Complex comprises TTG rocks that contain an expressive amount of titanite and apatite crystals. Fractional crystallization of hornblende and plagioclase accumulation are suggested to explain magma differentiation of this complex regarding mineral textures and whole-rock chemistry (Lacerda et al., submitted). Zircon grains from these rocks define crystallization age at 2130 Ma and partial meting around 2040 Ma (Lacerda et al., submitted).

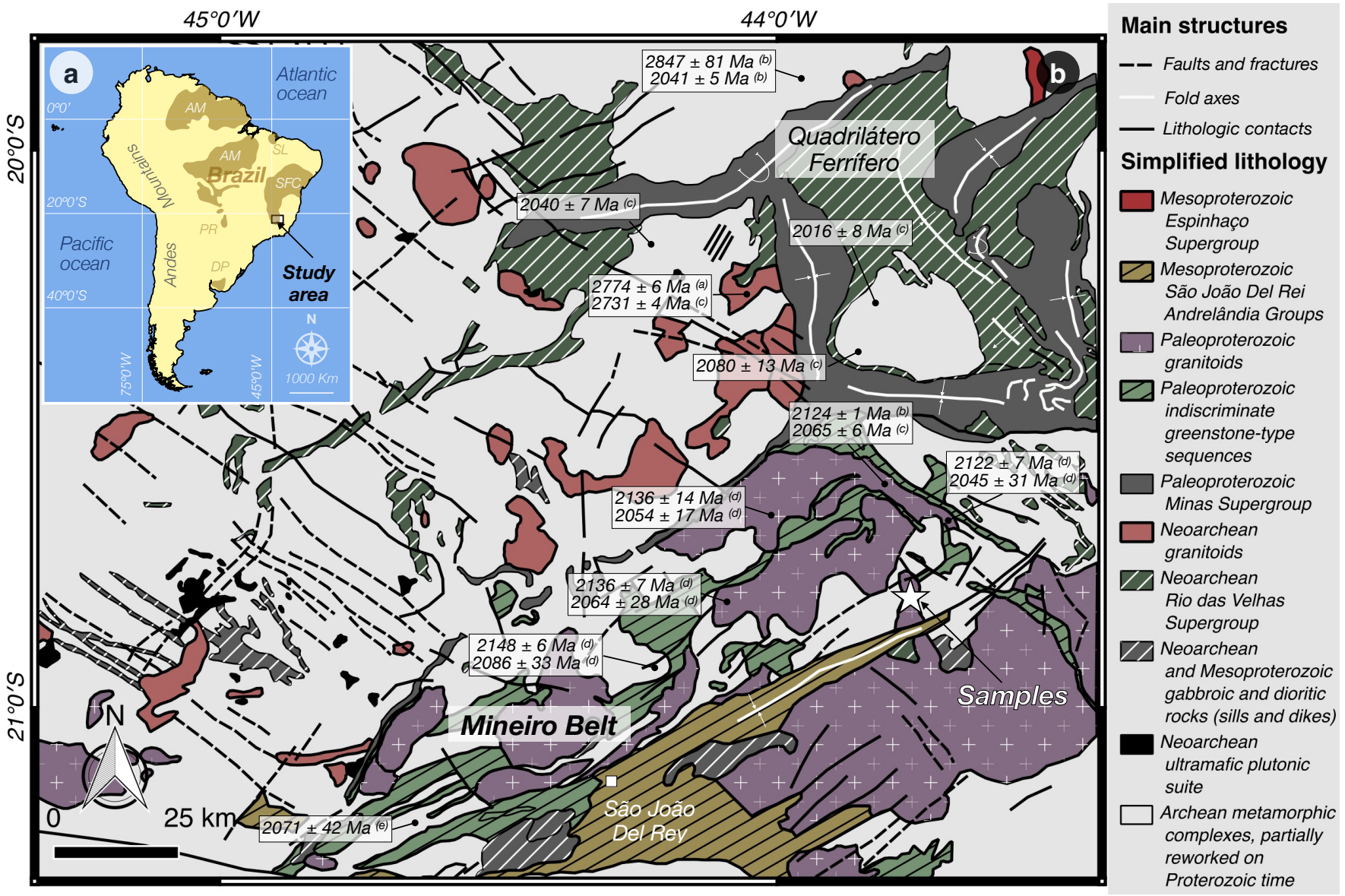


Figure 4.1: (a) Study area location in the South American continent context. Shadow areas represent Precambrian Cratons in the Brazilian shield: SFC – São Francisco; AM – Amazonas; PR – Paranapanema; SL – São Luís; DL – Rio de La Plata. (b) Geological map of the southern São Francisco Craton, modified from Campos et al. (2003), pointing to the Quadrilátero Ferrífero and Mineiro Belt regions (study area), available titanite ages, and sampling location (white star). Titanite ages were interpreted either as magmatic or metamorphic from [a] Machado and Carneiro (1992); [b] Noce et al. (1998); [c] Aguilar et al. (2017); [d] Moreira et al. (2018); [e] Neves et al. (2022).

However, no systematic chemical differences are observed in magmatic and anatexis zircon grains. The complex was intruded at 2.0 Ga by S-type Cupim leucogranites that are apatite-bearing and titanite-absent. Their mineral and whole-rock chemical compositions and Hf-Si zircon isotopes track the melting of mixed sedimentary sources and minimal magma differentiation (Lacerda et al., 2024).

4.2.3. Materials and Methods

Titanite grains were identified and selected on thin sections of two representative samples (CM44B and CM49) from the Caatinga-Lamim Complex. CM44B is a migmatitic biotite-orthogneiss, and CM49 is a weakly foliated Bt-Hbl-tonalite rock. Petrological details (e.g., petrography, mineralogy, geochemical, and zircon isotopic information) of these rocks are available in Lacerda et al. (submitted). On the other hand, apatite grains from CM44B gneiss and Cupim leucogranites (GC1, GC5A/B, and GC6) were hand-picked after heavy mineral separation and mounted in resin epoxy and polished to reveal their interiors. Cupim leucogranites are two-mica (GC1, GC5A/B) to garnet-bearing (GC6) S-type granites (Lacerda et al., 2024). Heavy mineral separation procedure was performed at the Laboratório de Análises Minerais (LAMIN) of the Geological Survey of Brazil (CPRM), Caeté, Brazil. Detailed information is provided in Lacerda et al. (2024).

Back-scattered electron (BSE) and cathodoluminescence (CL) images were acquired using a JEOL scanning electron microscope (SEM/JSM-6510) hosted at the Laboratório de Microscopia e Microanálises (LMic) at the Universidade Federal de Ouro Preto, Brazil. To produce high-resolution images, an acceleration voltage of 20 kV and a work distance of 15-23mm were calibrated on the SEM.

Major and minor element compositions were measured for selected apatite grains (15 from CM44B and 10 from Cupim leucogranites) using a JEOL JXA-8230 electron probe microanalysis (EMPA) system coupled to five wavelength dispersive spectrometers (WDS), also housed at LMic facilities. Analyses were performed using 15 kV acceleration voltage, 20 nA current, and 5 nm electron beam conditions. Twenty-three internal standard materials (minerals and glass) were used to calibrate the quantitative measurements (e.g., fluorapatite for CaO and P_2O_5, fluorite for F, pyrite for SO_3, anorthoclase for NaO, and phosphates for LREE). The concentration of each element measured for each standard varies by no more than 2% (1SD), except for V, which varies by 8% (1SD). Background concentrations have been continuously monitored and are generally less than 100 cps. All analytical results are provided in the **Supplementary Material**.

Trace elements and U-Th-Pb isotope analyses were conducted at the Laboratoire Magmas et Volcans (LMV), Aubière, France, using a 193nm Resonetics Resolution M-50E laser ablation system coupled to a Thermo Scientific Element XR ICP-MS. Trace element analyses have consisted of 25s of background followed by 60s of acquisition during laser ablation, with a fluence of 2.5 J.cm-2, a laser frequency of 2 Hz and a spot size of 27 µm (titanite) and 33 µm (apatite). Mass-related

concentrations (^{27}Al, ^{28}Si, ^{29}Si, ^{31}P, ^{39}K, ^{43}Ca, ^{44}Ca, ^{49}Ti, ^{51}V, ^{57}Fe, ^{66}Zn, ^{71}Ga, ^{85}Rb, ^{88}Sr, ^{89}Y, ^{90}Zr, ^{91}Zr, ^{96}Zr, ^{93}Nb, ^{137}Ba, ^{139}La, ^{140}Ce, ^{141}Pr, ^{146}Nd, ^{147}Sm, ^{153}Eu, ^{157}Gd, ^{159}Tb, ^{163}Dy, ^{165}Ho, ^{166}Er, ^{169}Tm, ^{172}Yb, ^{175}Lu, ^{178}Hf, ^{181}Ta, ^{206}Pb, ^{232}Th, ^{238}U) were determined using ^{43}Ca as an internal standard and the synthetic glass standard SRM NIST 610 (Jochum et al., 2011) as the primary for bracketing standard. The synthetic glass SRM NIST 612 (Jochum et al., 2011), together with titanite [CKHB (Cris Fisher's in-house standard), MKED1 and BLR1 (Ma et al., 2019), and Kola] and apatite [Durango (Chew et al. 2016), Sumé-1 (Lana et al., 2022), and Kovdor (Arzamastsev et al., 2009)] reference materials were analyzed for quality check. In cases where ^{43}Ca concentration data were not available, stoichiometric values of 20.3% pds. (for titanite) 39.7% pds. (for apatite) were employed to convert ICP-MS counts/second into concentrations, considering the structural formulas [fluorapatite, $Ca_5(PO_4)_3F$, and titanite, $CaTiSiO_5$]. The elemental concentrations acquired for SRM NIST 610 and NIST 612 consistently correlated with published values, displaying deviations of no more than 4% (Jochum et al., 2011). Apatite and titanite standards show concentrations generally conform to the available published values for most elements. Some element deviations may be attributed to compositional differences among batches of reference materials or the influence of alteration effects. Nonetheless, the chondrite-normalized Rare Earth Element (REE) patterns of mineral standards closely resembled those reported in the literature (see **Supplementary Material**).

Titanite and apatite U-Th-Pb analyses have taken in 25s of background followed by 60s of acquisition during laser ablation. Data acquisition was done using a fluence of 2.5 J.cm-2, a laser frequency of 2 Hz and a spot size of 33 µm (titanite) and 40 µm (apatite). Detailed analytical conditions are provided in Supplementary Material. Data were first reduced using Iolite4 software (Petrus and Kamber, 2012; Paton et al., 2011) for background subtraction, integration-time window definition and down-hole fractionation correction. Then, data were processed using in-house spreadsheets for external normalization using MKED1 (1521.02 ± 0.55 Ma, Spandler et al., 2016) and MAD 2 (474.25 ± 0.41, Thomson et al., 2012) for titanite and apatite, respectively. Common lead corrections were done using the two-stage terrestrial Pb evolution model of Stacey and Kramers (1975). We performed ^{207}Pb and ^{208}Pb corrections which determine the ratio between common lead and radiogenic lead, in a way of Chew et al. (2011). All apatite data presented in this paper are corrected for common lead using ^{208}Pb method, which leads to better concordance between $^{206}Pb/^{238}U$ ages and $^{208}Pb/^{232}Th$ ages, compared to the ^{207}Pb method. To calculate U-Th-Pb age, we used the following decay constants and ratio: $^{238}\lambda = 1.5512510^{-10}$ yr^{-1}, $^{235}\lambda = 9.848510^{-10}$ yr^{-1} (Jaffey et al. 1971); $^{232}\lambda = 4.947410^{-11}$ yr^{-1} (Le Roux and Glendenin, 1963); and $^{238}U/^{235}U = 137.818$ (Hiess et al., 2012). The calculated ages of primary and secondary standards, with a reasonable margin of error, are consistent with those reported in the literature (**Table 4.1**).

Table 4.1: Summary of calculated ages obtained for the apatite and titanite reference materials used. Into parenthesis are the number of analyses. Errors are quoted in 2SE for Discordia and $^{206}Pb/^{238}U$ Weighted Mean ages.

Reference Material	Accepted age (Ma)	Calculated age (Ma)	Weighted mean age (Ma)
Apatite			
MAD 2 (primary)	*474.25 ± 0.41* [1]	472 ± 2 (48) *	474 ± 12 (48)
Kovdor	*377.5 ± 3.5* [2]	376 ± 7 (11) *	385 ± 17 (11)
Sumé 1	*568.0 ± 3.1* [3]	579 ± 5 (11) *	567 ± 11 (11)
BRZ 1	*2078 ± 12* [4]	2044 ± 47 (12) *	2092 ± 62 (12)
Slyudyanka	*450 ± 15* [5]	482 ± 90 (5) *	421 ± 19 (11)
Titanite			
MKED1 (primary)	*1521.02 ± 0.55* [6]	1525 ± 2 (36) **	1519 ± 2 (36)
Khan	*518 ± 2* [7]	519 ± 2 (15/16) *	523 ± 10 (15/16)
BLR1	*1047.1 ± 0.4* [8]	1065 ± 17 (7/8) *	1061 ± 14 (7/8)
THBL	*1039 ± 23* [9]	1103 ± 75 (4/7) *	1097 ± 5 (4/7)

[1] *Thomson et al. (2012)*; [2] *Amelin et al. (2002)*; [3] *Lana et al. (2022)*; [4] *Apen et al. (2022)*; [5] *Chew et al. (2011)*; [6] *Spandler et al. (2016)*; [7] *Ma et al. (2019)*; [8] *Aleinikoff et al. (2007)*; [9] *Fisher et al. (2020)*.

** Discordia, Lower intercept age; ** Concordia age.*

4.2.4. Results

4.2.4.1. Texture and mineral phase equilibrium

Apatite grains from Cupim leucogranites are commonly observed as rounded to hexagonal inclusions in feldspars (**Fig.4.2a**) and locally form vermiform coronas with allanite surrounding monazite grains (Lacerda et al., 2024). Analyzed grains, ranging in size from 100 to 400 µm, are often homogenous in CL images and lack inclusions and internal fractures (except for *ap#14* and *ap#2*, which are highly fractured) (**Fig.4.3**). On the other hand, apatite crystals from Caatinga-Lamim gneiss form rounded colorless inclusions within biotite, commonly associated with colorless titanite grains (**Fig.4.2b**). Selected grains are rounded, stubby to elongated, varying long-size from 100 to 400 µm, and show simple to complex core and rim textures in CL images (**Fig.4.3**). Cores are dark crystal domains homogeneous (e.g., *ap#26*) or patchy (e.g., *ap#20*), and rims are finer light domains.

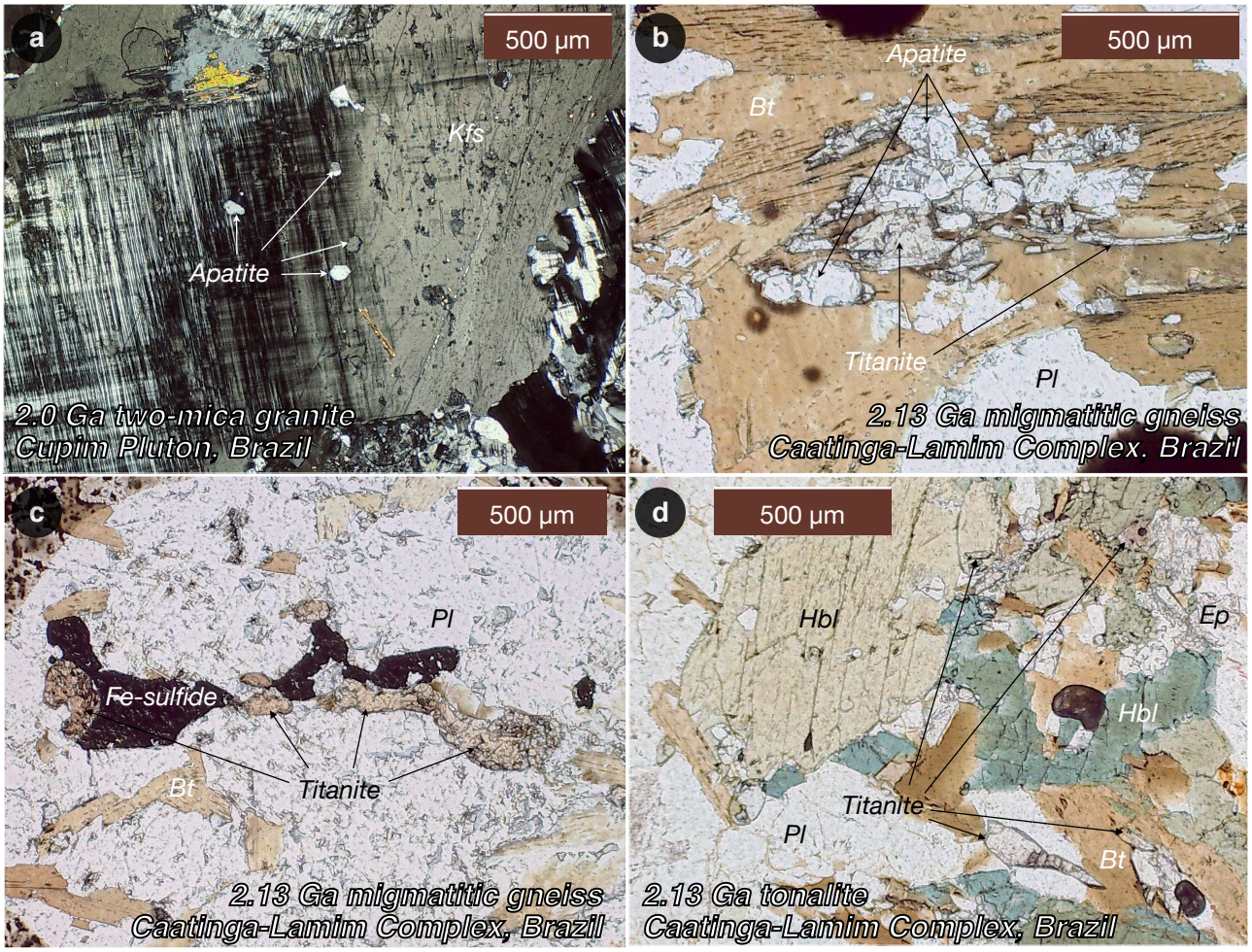


Figure 4.2: Optical microscope images [(a) double-cross polarized, (b-d) single-cross polarized] of apatite and titanite crystals from the studied rocks. (a) Apatite grains inclusions in a coarse K-feldspar crystal from two-mica Cupim leucogranites (Lacerda et al., 2024). (b) Prismatic to vermiform, colorless titanite and rounded apatite grains within biotite flakes from Caatinga-Lamim migmatitic gneiss (CM44B). (c) Rounded, brownish titanite grains associated with Fe-sulphide from Caatinga-Lamim migmatitic gneiss. (d) Prismatic, light brownish titanite grains between biotite, hornblende, and plagioclase crystals from Caatinga-Lamim tonalite (CM49).

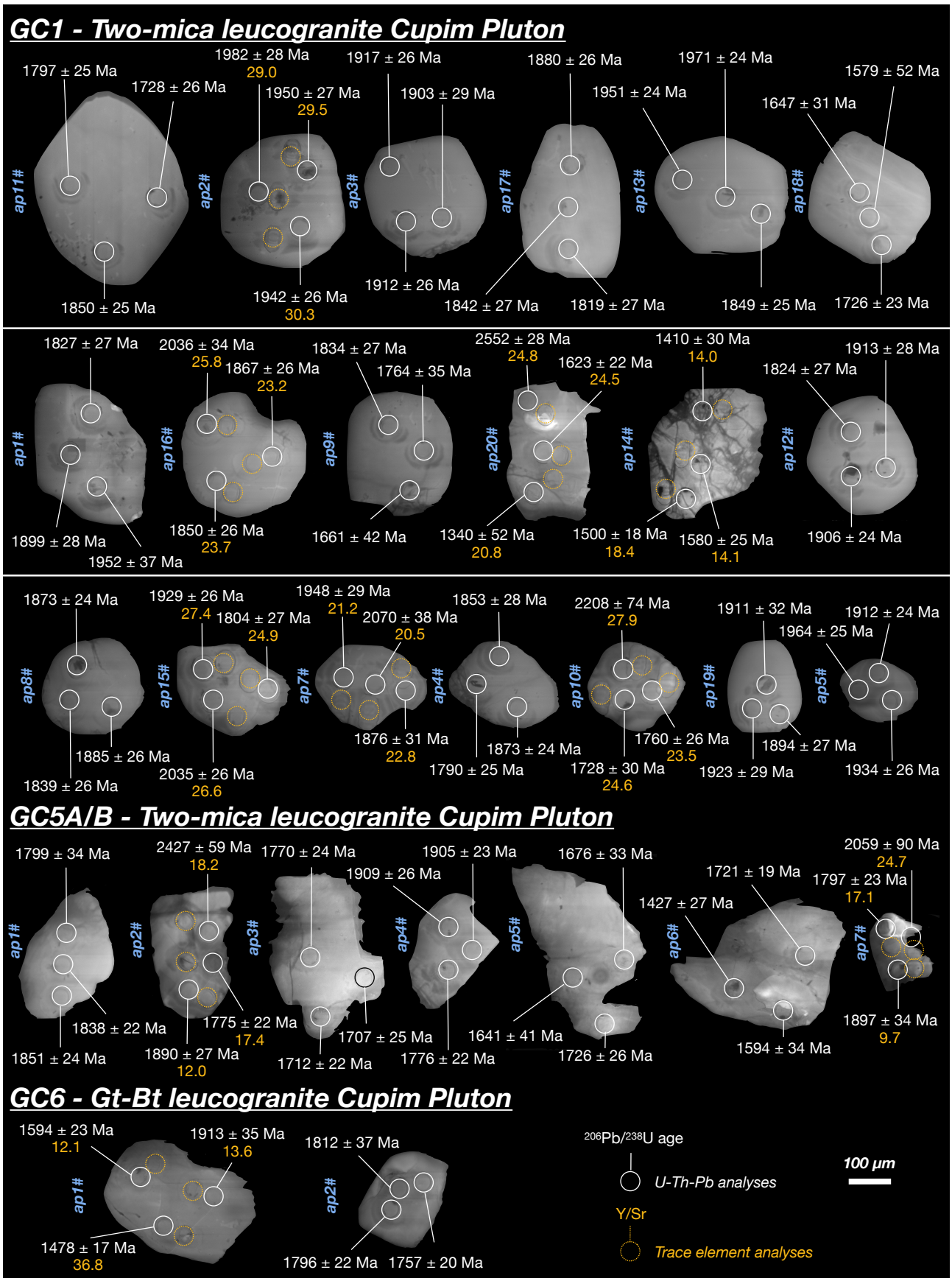
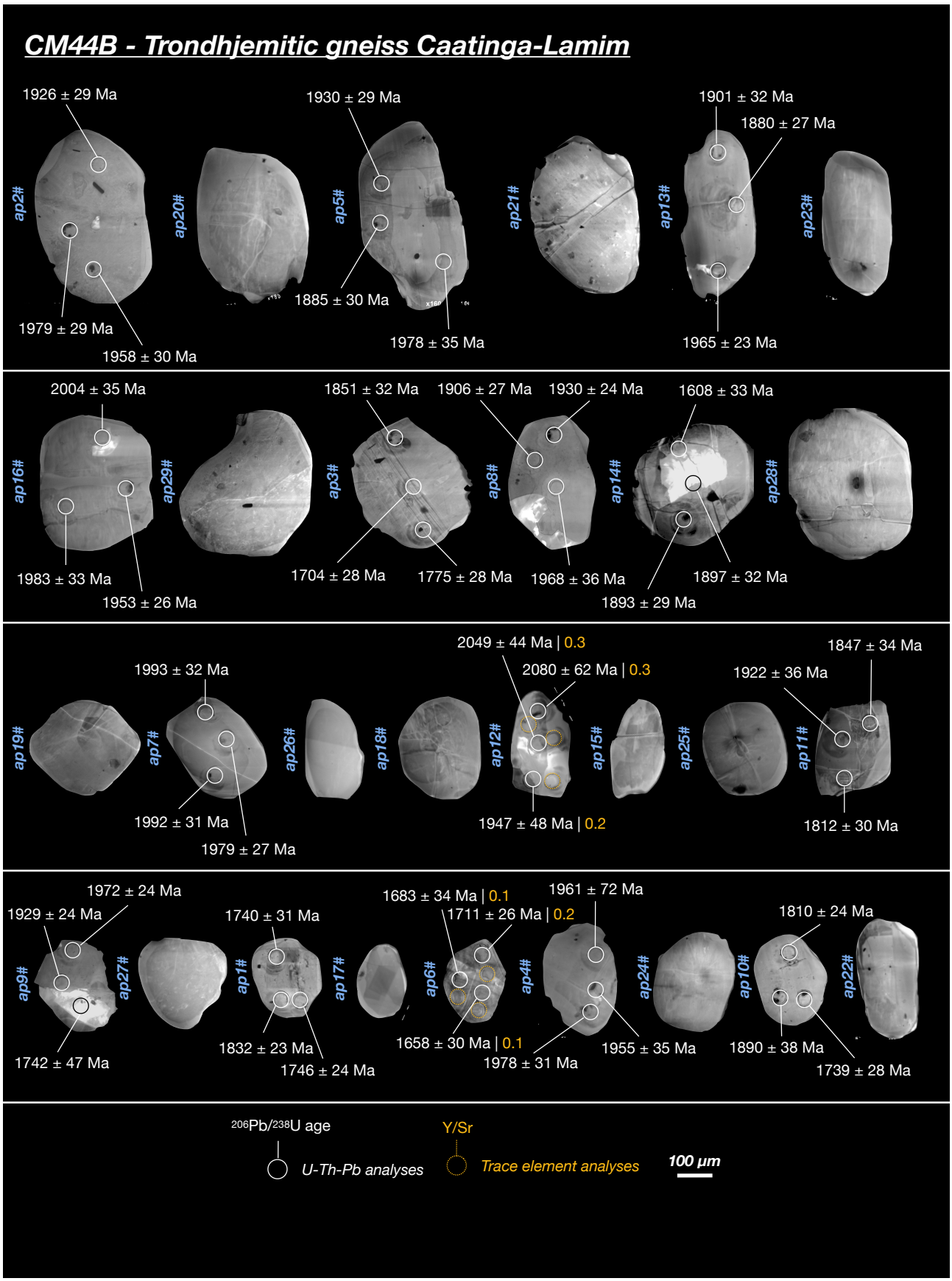


Figure 4.3: Cathodoluminescence (CL) images of apatite grains from Caatinga-Lamim migmatitic gneiss (CM44B; *mosaic 1*), and Cupim leucogranites (GC1, GC5a/B, and GC6; mosaic 2). Laser spot locations, the analysis number (e.g., ap#1), their respective U-Pb ages, and Y/Sr ratio values are also indicated.



(Continued - Mosaic 2)

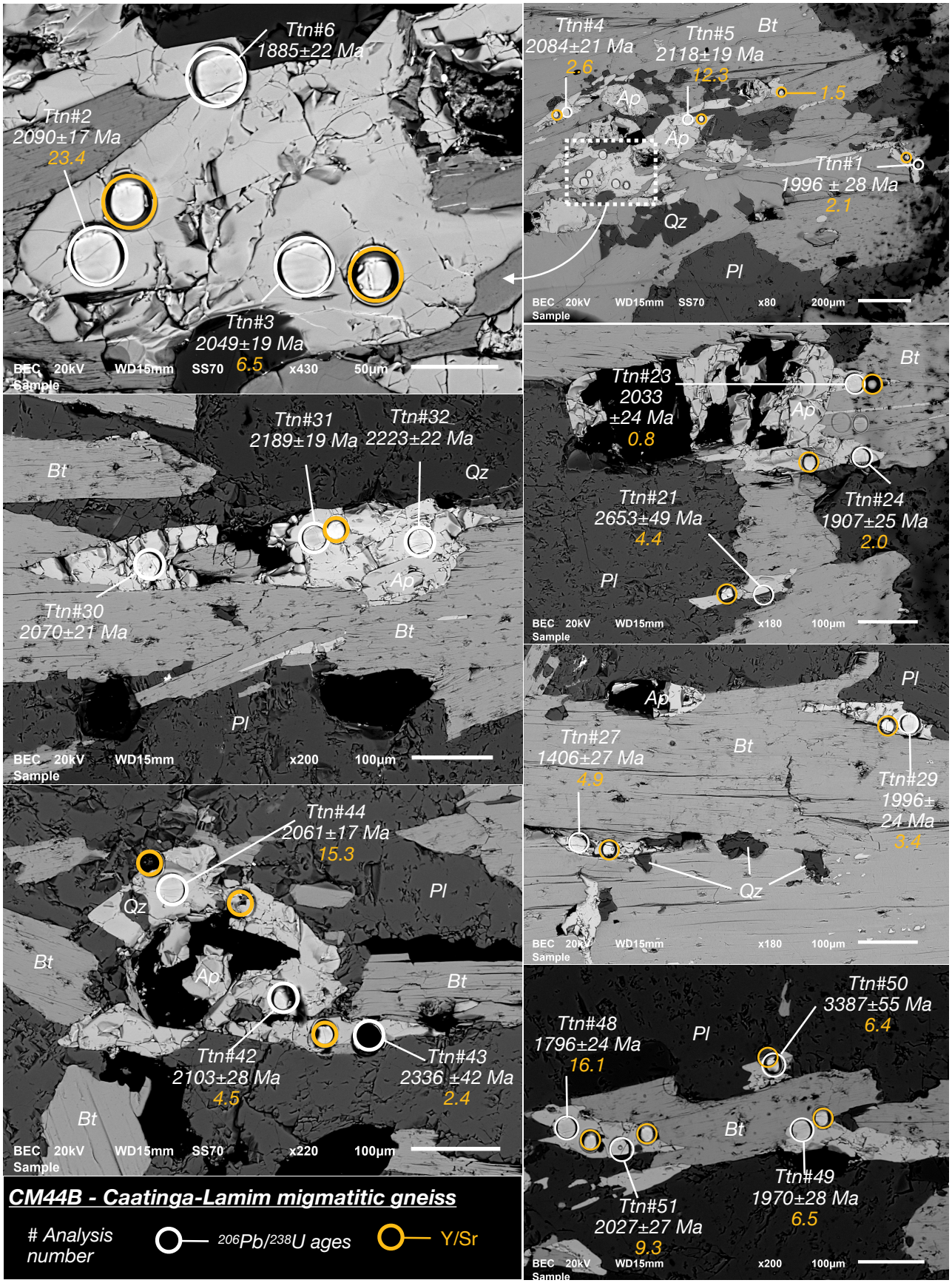
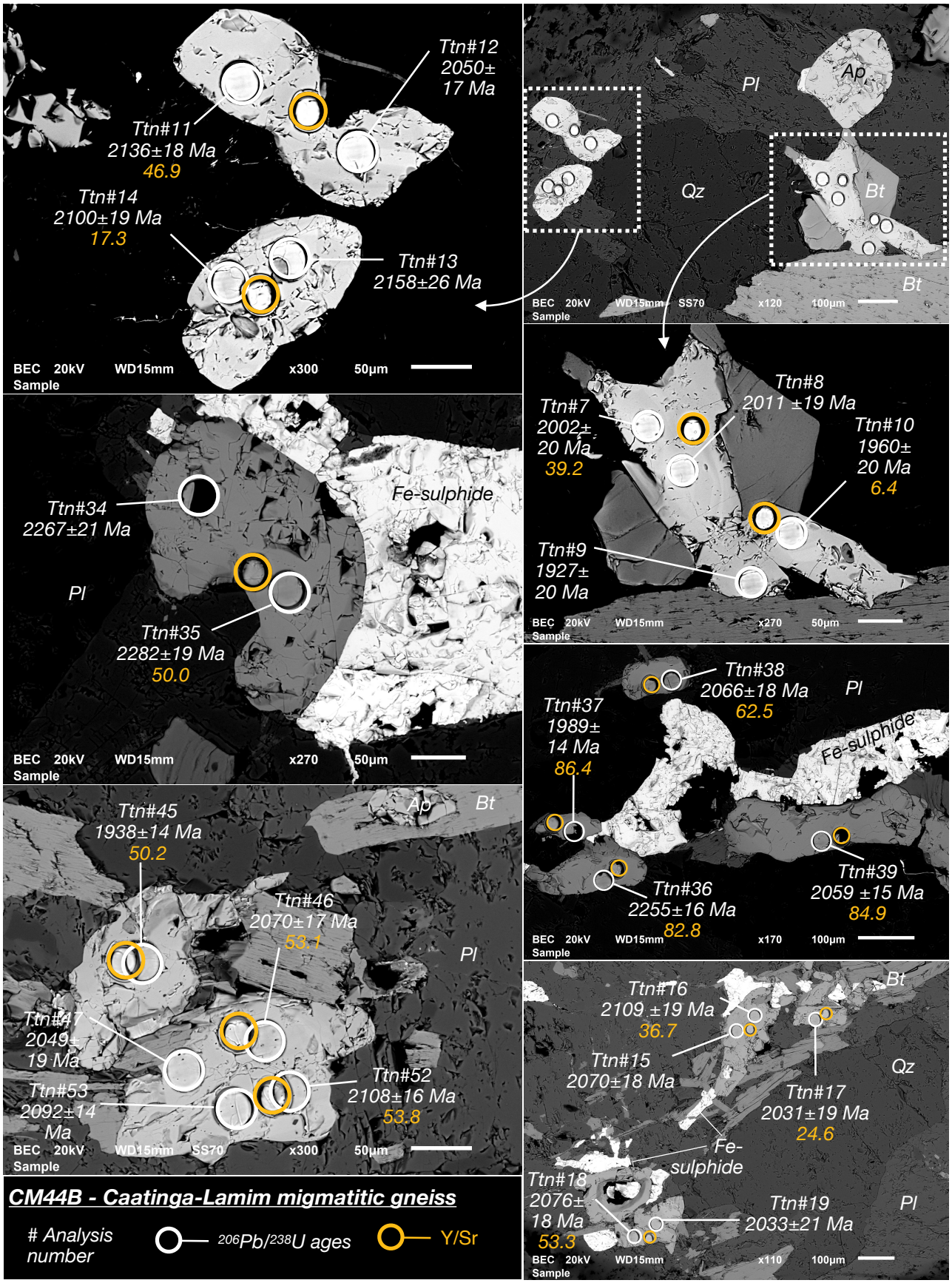
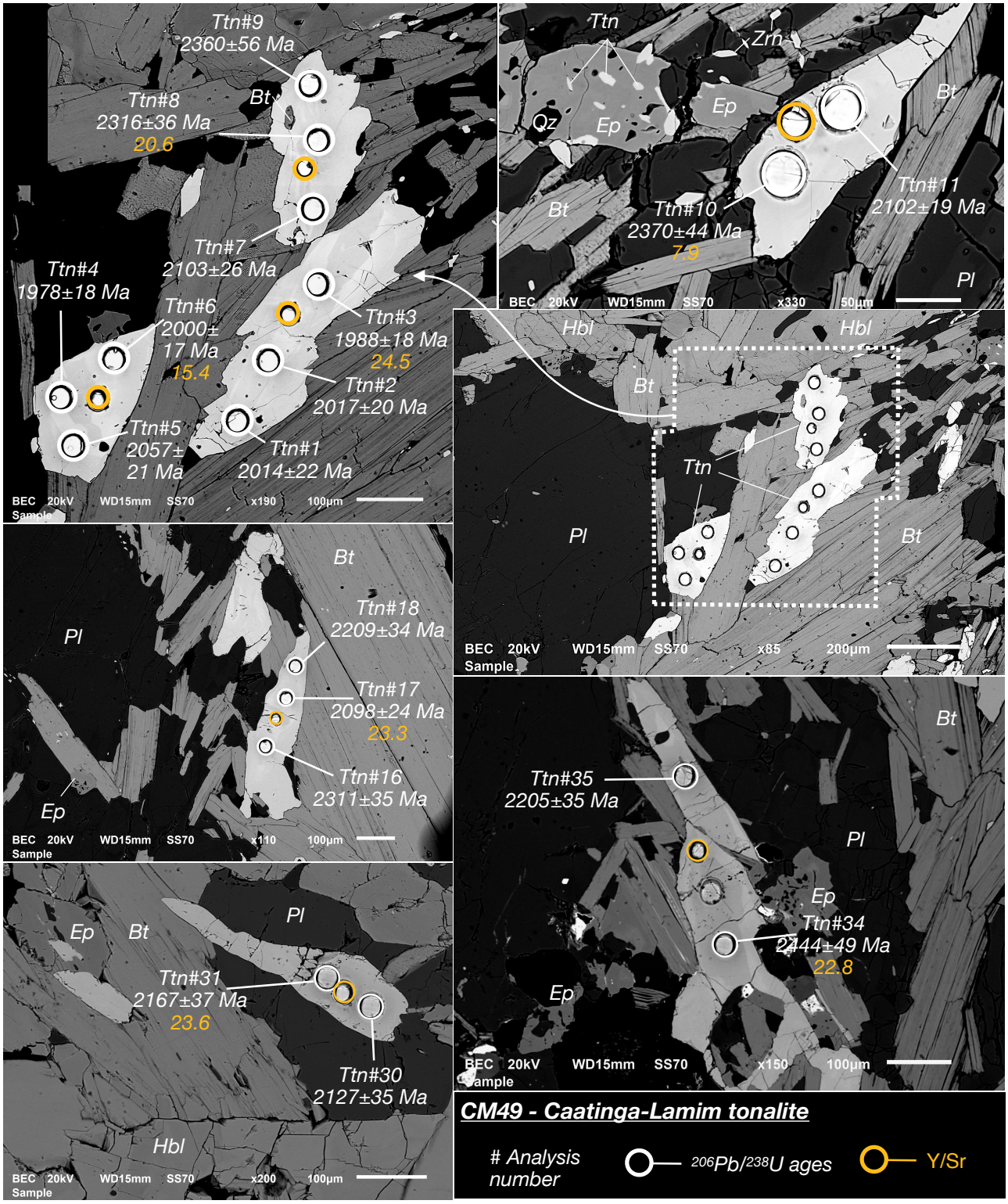


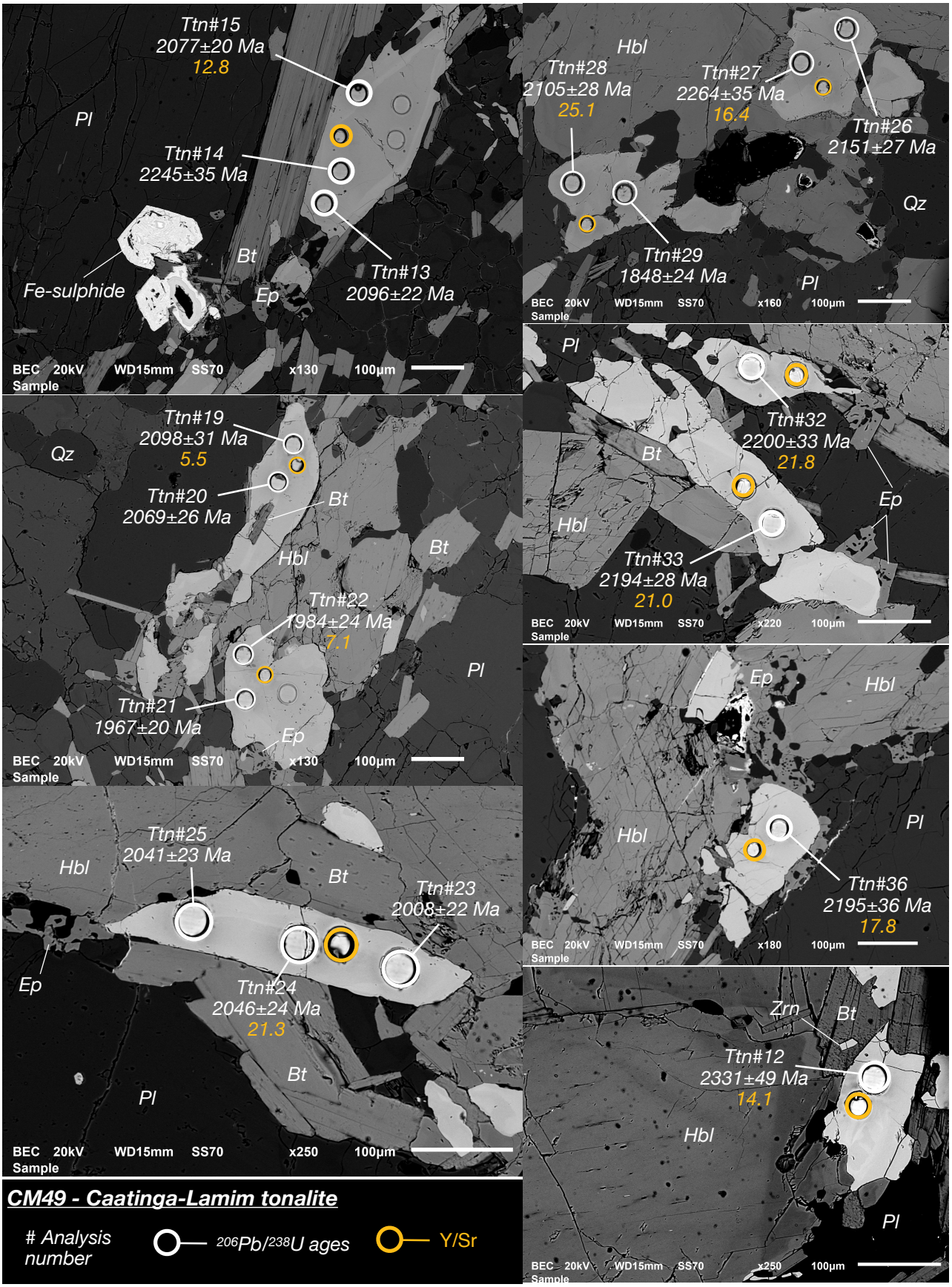
Figure 4.4: Backscattering electron (BSE) images focused on titanite grains from Caatinga-Lamim migmatitc gneiss (CM44B; type i – *mosaic 1*, and type ii – mosaic 2) and tonalite (CM49, mosaic 3 and 4). Laser spot locations, the analysis number (e.g., Ttn#1), their respective U-Pb ages, and Y/Sr ratio values are highlighted.



(Continued - Mosaic 2)



(Continued - Mosaic 3)



(Continued - Mosaic 4)

Titanite grains from the Caatinga-Lamim gneiss range in size from 100 to 200 µm and show different features (color, shape, inclusions) and phase associations that allow us to distinguish them into two types: (i) colorless, prismatic elongated, with biotite inclusions, and commonly associated with biotite and apatite (**Fig.4.2b**) and (ii) brownish, rounded, without inclusions, and locally associated with Fe-sulphide (pyrrhotite) (**Fig.4.2c**). BSE images reveal a homogeneous texture and light-gray color of type (i) and oscillatory to sector zoning (dark and light domains) of type (ii) (**Fig.4.4**). Conversely, titanite crystals from the tonalite sample (CM49) are colorless to light-brown, prismatic elongated to lobate, varying its long size from 100 to 300 µm, situated between plagioclase, hornblende, and biotite crystals (**Fig.4.4**). Simplectitic epidote crystals are also locally associated with titanites. BSE images commonly show dark/light domains forming patchy zoning (e.g., *Ttn#4-5*) or sometimes defining clear core/rim textures (e.g., *Ttn#13-15, Ttn#34*) (**Fig. 4.4**). Some crystals show minor biotite inclusions.

4.2.4.2. Apatite major elements and volatiles

Supplementary Material A provides the major element compositions of selected apatite grains from the Caatinga-Lamim TTG complex (CM44B) and S-type Cupim Pluton (GC1, GC5A/B, and GC6). All apatite grains are fluorapatite (F = 4.07-6.06 wt.%), and other volatile concentrations are low (e.g., Cl, SO_3 < 0.1 wt.%). On average, their CaO and P_2O_5 contents are 55 and 41 wt.%, respectively. No significant difference in rock-forming elements is observed, except for MnO, which is more concentrated in apatite grains from the S-type granites (av. 0.14 wt.%). Core and rim domains of apatite grains from the Caatinga-Lamim rock have no systematic differences in composition, but the rims (either CL-dark or -light) tend to be LREE-richer than cores (e.g., *ap#5*).

4.2.4.3. U-Pb dating

Eighty-four U-Th-Pb analyses were performed on twenty-eight separated apatite grains from Cupim S-type granites. Systematically, three spot analyses were performed on each apatite grain. Fifty-seven analyses performed on nineteen grains from the two-mica granite (GC1 sample) show discordant ages in Tera-Wasserburg diagram (**Fig.4.5a**), probably due to common Pb and/or Pb-loss effects. A Discordia line anchored to the magmatic zircon age of 2000 Ma (Lacerda et al., 2024) highlights some analyses that seem to preserve their magmatic isotopic system. These analyses perform a Discordia line with a lower intercept age at 2008 ± 30 Ma (n=32, MSWD=6.1) that is identical, considering the uncertainty, with the magmatic zircon age. Corrected ^{208}Pb analyses also show discordant ages that cluster around 2000 Ma (**Fig.4.5c**). However, no reliable age could be determined. On the other hand, the weighted mean $^{207}Pb/^{206}Pb$ ages after Pb correction are 2019 ± 29 Ma (n=49/57), identical with magmatic zircon ages (**Fig.4.5e**). Pb concentration and Th/U ratios of those analyses vary from 7 to 12 ppm and 0.1 to 1.2, respectively.

Analyses of the other two samples (GC5/B and GC6) from the Cupim pluton show similar behavior in Tera-Wasserburg diagrams, i.e. some of them preserved their isotopic composition,

producing discordant intercept ages equivalent to those of magmatic zircons (Lacerda et al., 2024). Weighted mean $^{207}Pb/^{206}Pb$ ages, after Pb correction, are also in agreement with magmatic zircon ages. These plots are provided in **Supplementary Material C**.

Forty-two analyses were conducted on fourteen selected apatite crystals from CM44B Caatinga-Lamim migmatitic gneiss. Again, three spot analyses were performed on each apatite grain, focusing on both dark cores and light rims when available. All analyses reproduce discordant ages (**Fig.4.5b**), suggesting common Pb incorporation and/or Pb-loss effects. From the texture, exsolution features of dark cores can be considered as small channels of the Pb-loss effect. Analyses performed on these affected domains certainly will produce younger $^{206}Pb/^{238}U$ ages. Therefore, considering only those performed in dark and homogeneous domains (e.g., *ap#7*), they define a Discordia line with lower-intercept age at 2040 ± 23 Ma (n=12, MSWD=11). The age is identical, with uncertainty, to the anatectic zircon age (Lacerda et al., submitted). Pb-corrected analyses (**Fig. 4.5d**) are less discordant and align with a Discordia line with an upper intercept age at 2036 ± 18 Ma (n=43, MSWD=2.9). The weighted mean $^{207}Pb/^{206}Pb$ age of these corrected analyses is younger, at 1977 ± 15 Ma (n=40/45) (**Fig.4.5f**). Pb concentrations vary from 4 to 14 ppm, while Th/U ratios are sharp from 0.1 to 0.4.

Eighty-nine in-situ U-Th-Pb analyses were performed on fifty-two titanite grains from Caatinga-Lamim rocks (53 analyses on 34 grains from CM44B and 36 on 18 crystals from CM49). Isotopic ratios and calculated ages related to observed textures are available in the **Supplementary Material**. Calculated $^{206}Pb/^{238}U$ and $^{207}Pb/^{235}U$ ages are slightly to moderate discordant or reverse discordant (Disc.= -11 to 42%) in Wetherill diagrams (**Fig.4.6**). Separately, 30 of 33 analyses performed on the type (ii) titanite grains delineate a recent Pb-loss Discordia line with an upper intercept age of 2132 ± 4 Ma (MSWD= 27) (**Fig.4.6a**). Three analyses (*Ttn#39-41*) performed in two grains return younger slightly reverse discordant ages around 2050 Ma. On the other hand, type (i) titanites display discordant ages that roughly align to a Discordia line, indicating common Pb incorporation [$(^{207}Pb/^{206}Pb)_c$= 0.61 ± 0.03], with lower intercept age of 1806 ± 17 Ma (MSWD= 13, n= 13/20). Th/U ratios range from 0.05 to 0.74. No discernible correlations are observed between Th/U and calculated ages, but type (ii) titanites commonly show lower values.

Analyses performed on dark (core) domains of titanite grains from CM49 tonalite show discordant ages (Disc.= 4 to 28%) in the Tera-Wasserburg diagram (**Fig.3.6b**). Fourteen of sixteen of those ages align to a common Pb [$(^{207}Pb/^{206}Pb)_c$= 1.10 ± 0.16] Discordia line with a lower intercept age of 2121 ± 26 Ma (MSWD= 4). A single analysis (*Ttn#10*) calculates an older age of 2370 ± 44 Ma. Similarly, ages from the light domains of those crystals are discordant to slightly concordant that align suggesting common Pb [$(^{207}Pb/^{206}Pb)_c$= 0.77 ± 0.11] and lower intercept age of 1991 ± 13 Ma (MSWD= 11, n=20). Th/U ratios vary from 0.02 to 1.13. Generally, dark domains show higher Th/U values and light domains have high-U contents.

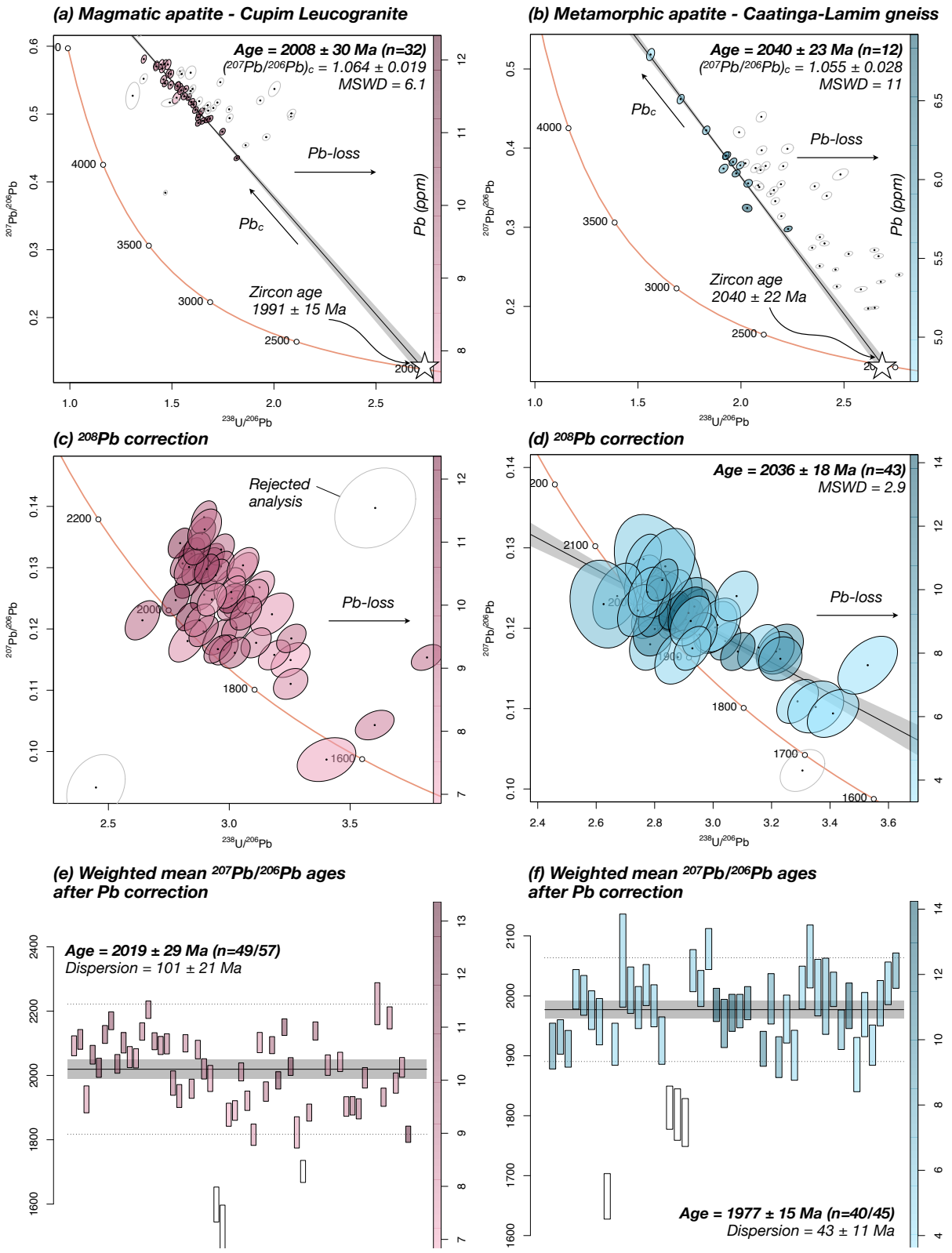


Figure 4.5: Different methods to calculate apatite ages from Cupim leucogranite (GC1, left column) and Caatinga-Lamim migmatitic gneiss (CM44B, right column). (a-b) Tera-Wasserburg diagrams show the analyses before 208Pb correction; colored ellipses represent those used in the Discordia line discrimination, and hollow ones are the rejected analyses (see the text for details). The scale bar denotes the Pb (ppm) concentration. The stars represent the zircon age for each sample from Lacerda et al. (2024, submitted). (c-d) Analyses after 208Pb correction in the Tera-Wasserburg space. (e-f) Weighted mean 207Pb/206Pb ages. Hollow bars are rejected analyses.

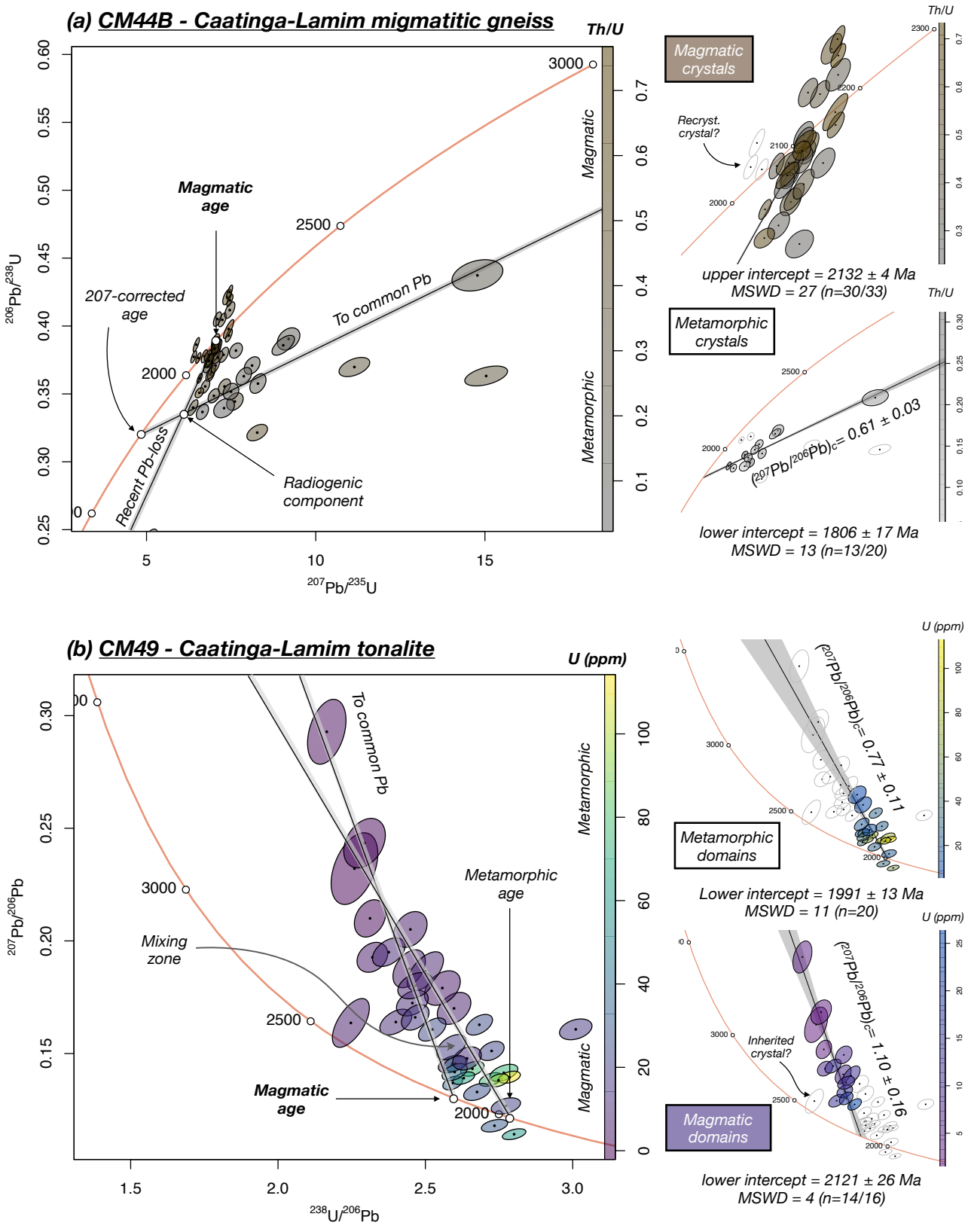


Figure 4.6: Titanite ages. (a) Wetherill diagram shows all analyses of titanite grains from Caatinga-Lamim migmatitic gneiss (CM44B); greyish ellipses are type (i), and brownish type (ii) titanite (see the text for details). The color scale bar refers to Th/U ratio values of the analyses. On the right, the analyses are shown separately by type and nature (magmatic and metamorphic). (b) Tera-Wasserburg diagram shows analyses performed on titanite grains from Caatinga-Lamim tonalite (CM49). On the right, the analyses are separated following the nature of the domains (magmatic or metamorphic). The color scale bar defines U (ppm) concentration of the analyses.

4.2.4.4.Mineral trace elements

Table 2 shows the average element concentration (ppm) and ratios for each analyzed crystal sample or crystal domain compared with those from TTG, sanukitoid, and S-type granite rocks from different Archean cratons and Mt Isa Inlier, Northwestern Queensland. Two apatite grains from Caatinga-Lamim gneiss (CM44B) were analyzed, focusing on their homogeneous (*ap#12*) and heterogeneous (*ap#6*) dark cores. Three spots per grain were performed to access intragrain chemical variations. Both have high Ca and P concentrations (>400,00 and >250,000 ppm, respectively) and elevated REE (540-2118 ppm) contents. Homogeneous, undisturbed, domains have higher REE concentrations than the heterogeneous ones but show similar chondrite-normalized REE patterns – LREE/HREE fractionation [$(La/Sm)_N$>1 and $(Gd/Yb)_N$>1] and slightly negative Eu anomalies (Eu/Eu* = 0.3-0.6) (**Fig.4.7a**). Sr is high (548-610 ppm), and Y is low (62-168 ppm), then Sr/Y ratios are high. V contents vary from 5 to 7 ppm, and Pb from 11 to 42 ppm. U concentrations are often higher than Th, and Th/U ratios are lower than 0.6.

Ten representative apatite grains from the Cupim leucogranites were selected for trace element analysis. Three spots per grain were performed next to the previously done U-Th-Pb spot analyses. They have high (>100,000 ppm) Ca and P, and elevated REE (550-3713 ppm) and Y (727-2691 ppm) concentrations. Sr contents are low, varying from 60 to 122 ppm, and V is often lower than unity (i.e., <1 ppm). Sr/Y ratios are therefore very low (<0.1). Pb, U, and Th contents vary between units and tens of ppm, with the former always more enriched than the latter, so Th/U ratios are often < 1. Chondrite-normalized REE patterns show a seagull-wing shape [$(La/Sm)_N$< 1, $(Gd/Yb)_N$> 1) and strongly negative Eu anomalies (Eu/Eu*<0.1) (**Fig.4.7b**). Two analyses performed on a single grain from the garnet-bearing leucogranite (GC6) show lower REE composition than those from two-mica granites (GC1, GC5A/B).

Thirty-eight in situ trace element analyses were conducted on 36 titanite grains from the Caatinga-Lamim gneiss (CM44B). Of these, 23 were performed on type (i) titanite, while the remaining were conducted on type (ii). When available, the spot analyses were located in the same domain (dark/light) previously analyzed for U-Th-Pb systematics. Both types have high concentrations (>10,000 ppm) of Ti, Ca, and Al. Fe contents are variable (from 2,710 to 89,407 ppm) in both titanite groups. Conversely, type (i) titanite grains have lower Sr, Y, Zr, Hf, Nb, and Ta concentrations compared with type (ii) ones. Y contents are always higher than Sr (except for *Ttn#10*), but type (ii) titanites show higher Y/Sr ratio values, indicating Y enrichment. Conversely, Nb/Ta ratio values are higher in type (i) titanites compared with type (ii). Pb, Th, U, and REE concentrations are also lower in type (i) than in type (ii) titanites. In chondrite-normalized diagrams, the titanite grains show concave shape patterns of LREE, and slightly fractionated HREE patterns [$(Gd/Yb)_N$ >1]. However, Sm_N values are always higher than Nd_N in type (ii) titanites, while Sm_N is often lower than Nd_N in type (ii) (**Fig.4.7c**). Markedly, Eu anomalies are highly positive (Eu/Eu*> 2) in type (i) titanites and frequently negative (Eu/Eu*< 1) in type (ii). Two

analyses (*Ttn#46* and *Ttn#52*) performed on the same crystal [type (ii) titanite] show flat-REE with less negative Eu anomaly patterns (**Fig.4.7c**).

Table 4.2: Average composition of apatite and titanite grains from the studied rocks compared with TTG, sanukitoid (Bruand et al., 2020), and S-type granites (Belousova et al., 2001). Element concentrations are in ppm. 'n' is the number of analyses. 'Bdl' refers to 'below the detection limit'.

Unity	**Caatinga-Lamim Complex**				**Cupim Pluton**				
Lithology	Migmatitic Bt-gneiss		Bt-Hbl-tonalite		Two-mica granite	Grt-Bt-granite	**TTG**	**Snk**	**S-type**
Sample	CM44B		CM49		GC1,5A/B	GC6			
Apatite	*Core i n= 3*	*Core ii n= 3*			*n= 27*	*n= 3*	*n= 201*	*n= 95*	*n=27*
V	5	6			< 1	< 1	5	7	bdl
Sr	553	600			81	64	492	656	124
Y	71	152			1729	1366	749	351	2443
Pb	11	35			20	21	7	8	bdl
Th	3	14			6	5	28	40	7
U	7	25			11	13	18	22	8
LREE	519	1755			1358	704	5397	7801	470
$(La/Sm)_N$	2.2	2.9			0.4	0.2	3.5	5.2	0.4
$(Gd/Yb)_N$	4.3	5.7			2.7	4.0	2.7	3.6	0.5
Eu/Eu*	0.5	0.3			0.07	0.02	0.4	0.4	0.2
Titanite	*Type i n=21*	*Type ii n=17*	*Dark n=10*	*Light n=7*			*n= 23*	*n= 146*	
V	488	571	558	620			195	651	
Sr	45	74	60	58			19	52	
Y	232	3427	1239	791			6113	1552	
Zr	44	217	149	187			62	361	
Nb	705	1802	615	376			1966	892	
Pb	41	408	43	25			50	50	
Th	10	176	10	8			29	175	
U	37	290	32	17			53	61	
LREE	541	6910	3359	1601			1741	10690	
$(La/Sm)_N$	0.4	0,4	0.2	0.2			0.3	2.1	
$(Gd/Yb)_N$	3.0	2.7	2.6	1.8			1.0	2.3	
Eu/Eu*	3.6	0.5	0.8	1.0			7	1.2	

Eu/Eu*= $Eu_N / \sqrt{[(Sm_N)^2+(Gd_N)^2]}$; Chondrite-normalization (N) after Boyton, 1974.

Seventeen analyses were performed on seventeen representative titanite grains from Caatinga-Lamim tonalite (CM49). Nine analyses were located in the dark (core) domains, six were performed on light (rim) domains, and the remaining two were between dark and light domains. Major and minor element concentrations (Ti, Ca, Al, Fe) are relatively similar in both domains. Generally, dark domains have higher Y and lower Sr concentrations, thus higher Y/Sr values, than light domains. Both domains show similar REE-normalized patterns, concave LREE shape, positive to slightly negative Eu anomalies (Eu/Eu*= 0.6-1.5), and flat to somewhat fractionated HREE patterns [$(Gd/Yb)_N$= 1.1-3.5] (Fig. 7d). There were no significant differences in REE, U, Th, and Pb concentrations between the dark and light domains.

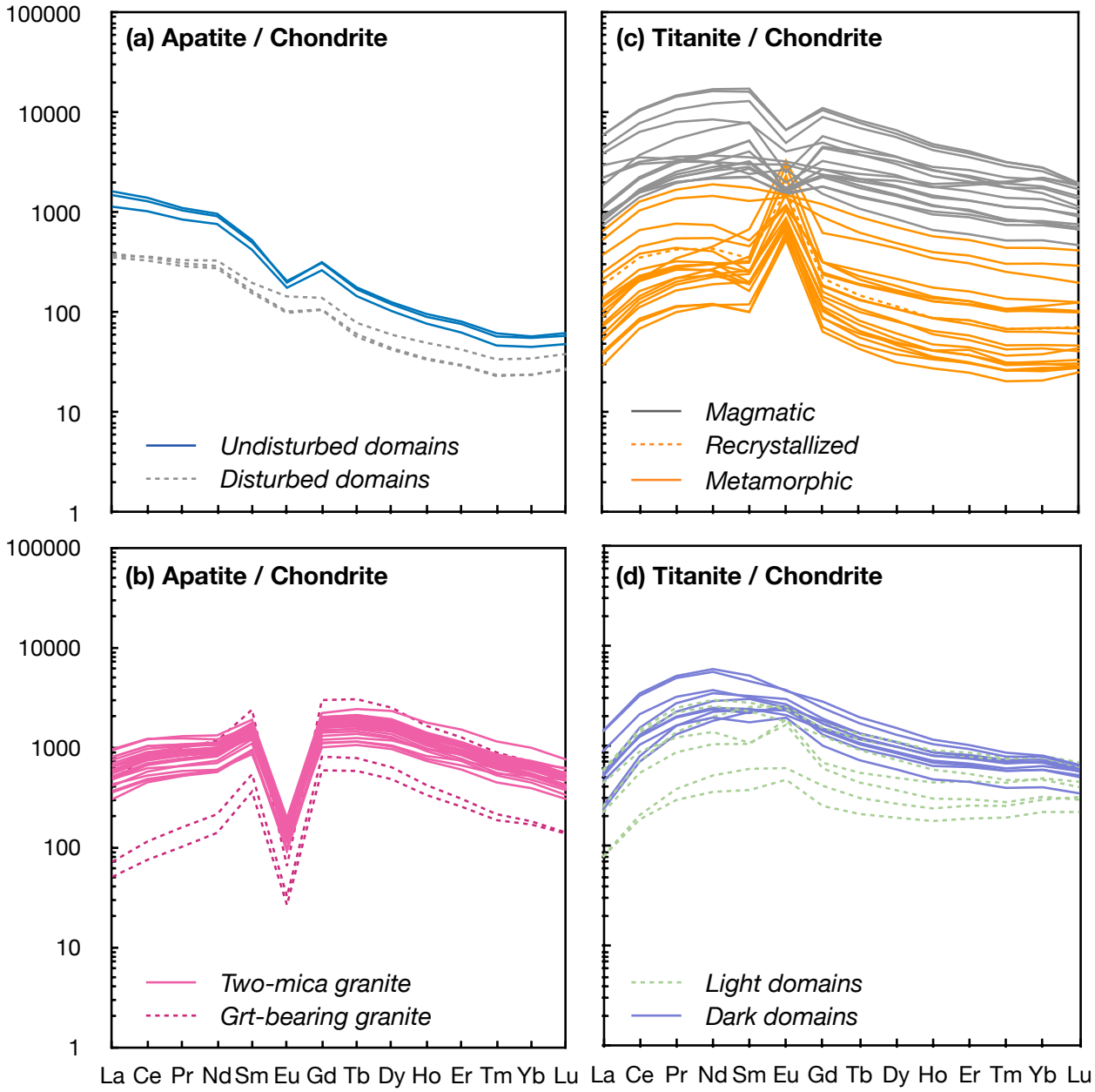


Figure 4.7: Chondrite-normalized (after Boyton, 1974) REE patterns of selected apatite (left column) and titanite (right column) grains. (a and c) Caatinga-Lamim migmatitic gneiss (CM44B). (b) Cupim leucogranites (GC1, GC5A/B, GC6). (d) Caatinga-Lamim tonalite (CM49).

4.2.5.Discussions

4.2.5.1. Apatite and titanite U-Th-Pb Ages

The contrasting ages, coupled with the trace element composition of apatite and titanite grains from Caatinga-Lamim Complex and Cupim Pluton, reveal at least two distinct growth episodes and a probable isotopic resetting event. Regarding the Caatinga-Lamim Complex, REE-rich type (ii) titanite from the migmatitic gneiss and dark domains of those from the tonalite show older ages around 2130 Ma, while REE-poor type (i) and light titanite domains have younger ages from 1991 to 1806 Ma. The older ages of titanites agree, error considered, with the calculated zircon ages from the same samples (Lacerda et al. submitted), indicating that both phases crystallized at around the same time.

Conversely, the younger ages probably record a post-magmatic event, e.g., metamorphism, fluid interaction, and/or partial melting. Partial melting is a plausible candidate as the gneiss sample has undergone partial melting at 2040 ± 22 Ma (n= 15, MSDW= 2.1) attested by newly formed anatectic zircon grains/rims from the leucosome (Lacerda et al., submitted). A single anhedral grain shows nearly concordant younger ages around 2.05 Ga. Although its texture resembles type (ii) titanite grains, i.e., rounded, brownish, and associated with pyrrhotite, its REE composition is like type (i) titanite, i.e., low-REE and positive Eu anomalies. We suggest that this crystal was recrystallized around 2.05 Ga, modified its trace element composition, and reset its U-Th-Pb isotopic composition at this time. The younger discordant ages of type (i) titanite could record an unknown younger (~1800 Ma) post-magmatic event. However, this age lacks geological meaning in the local geotectonic context. Alternatively, the calculated age is possibly an artifact of combined common-Pb incorporation (during anatexis at 2.05 Ga) and recent Pb-loss processes (as magmatic titanite crystals also record). The later process probably shifted the common-Pb Discordia line to younger and spurious ages.

Meanwhile, homogeneous apatite grains from the Cupim leucogranites and light rims of those from the Caatinga-Lamim migmatitic gneiss show ages around 2000 Ma. The apatite ages resemble magmatic zircon ages (2.01-1.98 Ga) from Cupim leucogranites, representing their crystallization (Lacerda et al., 2024). On the other hand, the apatite ages of Caatinga-Lamim gneiss are younger than those of unmolten zircon crystals (ca. 2130 Ma). These apatite ages resemble the younger titanite ages (see above), which also agree with anatectic zircon grains/rims from the leucosome portion of the migmatite (Lacerda et al., submitted). We propose that these apatite grains have crystallized from a melt produced during anatexis, remaining in the photolith, or have undergone recrystallization, resetting the U-Th-Pb isotopic system at this time.

4.2.5.2. Tracking parental magma or liquid composition

The LREE-Sr-Y compositions of titanite and apatite have been used to distinguish the nature of their host magmas, either Precambrian TTG and sanukitoids, or modern adakites and I- and S-type

granites (Bruand et al., 2020). The Caatinga-Lamim magmatic titanites are Y-rich like those from TTG rocks, but some crystals show slight Sr and LREE richer compositions, plotting outside the limits proposed in the diagram (**Fig.4.8a**). However, few analyses (n= 23) were used to delineate the 'TTG field' in this diagram. While their LREE concentrations are high, they are not as elevated as those observed in titanites from sanukitoids (typically >10,000 ppm). Sr and V contents are comparable to titanites from sanukitoids, but again, the range composition of those from TTG rocks could be biased to the small number of analyses. On the other hand, post-magmatic titanites have lower Y compositions than magmatic ones, showing a trend towards the Sr pole in the discrimination diagram (**Fig.4.8a**).

Apatites from the gneiss sample have low-Y and high-Sr composition, like those from the basalt-andesite-dacite-rhyolite (BADR) series and sanukitoids (**Fig.4.8b**). However, Y contents in these crystals are lower than the average composition of apatites from sanukitoid and TTG rocks but comparable with post-magmatic titanites (~100 ppm) (**Fig.4.8c**). Conversely, apatite crystals from Cupim leucogranites are Y-rich and Sr-poor, like those from S-type granites (**Fig.4.8b**). Sr in apatite and Sr whole-rock correlation from the studied rocks, fits well with the proposed by Bruand et al. (2014), which indicates no feldspar alteration (**Fig.4.8d**). Furthermore, the Sr composition in apatite crystals (~600 ppm) is approximately ten times higher than that of titanites (~60 ppm) from the Caatinga-Lamim gneiss, as also observed by Bruand et al. (2014, 2017).

Titanite has low partition coefficient values for Sr but high for Eu ($^{Sr\text{-titanite}}$ D <0.1 and Eu-titanite D ~10, Tiepolo et al., 2002). Therefore, considering that titanite and apatite crystallized together, we can assume that the Sr composition of the parental liquid/fluid was mainly incorporated into apatite than titanites, and in contrast, its Eu composition was readily captured by titanites.

Considering the early crystallization of accessory minerals (e.g., apatite, titanite) and their high compatibility with most trace elements, we modeled the parental magma/liquid's REE composition from the composition of the studied titanites/apatites. We used the Rayleigh fractional crystallization equation [$C_0 = C_R / D \times F^{(D-1)}$, where C_0 and C_R are the compositions of the parent magma and crystal (the instantaneous solid), respectively, F is the fraction of melt remaining, and D is the mineral partition coefficient], and partition coefficient values of apatite and titanite from Luhr et al. (1984).

The parental magma composition obtained from the average composition of primary titanites (type ii) from the Caatinga Lamim gneiss (Fig.4.9a) shows moderate fractionated REE patterns [$(La/Yb)_N$ ~3] and negative Eu anomalies (Eu/Eu* = 0.6). This parental magma composition resembles those of medium-pressure (or moderate HREE, Y) TTG rocks (Moyen and Martin, 2012; Laurent et al., 2024), suggested as magma precursor before hornblende fractionation (Lacerda et al. submitted), but with a significative HREE enrichment. The parental magma composition could be shifted due to the early and small amount of zircon crystallization, enriching the HREE composition of the remaining magma that has crystallized titanite grains subsequently. The

calculated parental magma composition, derived from the apatite composition (**Fig.4.9b**), aligns well with the MP-TTG composition, except for Eu anomalies that could be attributed to the simultaneous crystallization of post-magmatic titanite (see above). Similarly, the average composition of magmatic titanite domains from the Caatinga-Lamim tonalite (**Fig.4.9c**) back-calculate parental magma compositions that resemble MP-TTG magmas with a slightly LREE depletion. The depleted LREE composition of the calculated parental magma may be attributed to early or simultaneous crystallization of epidotes.

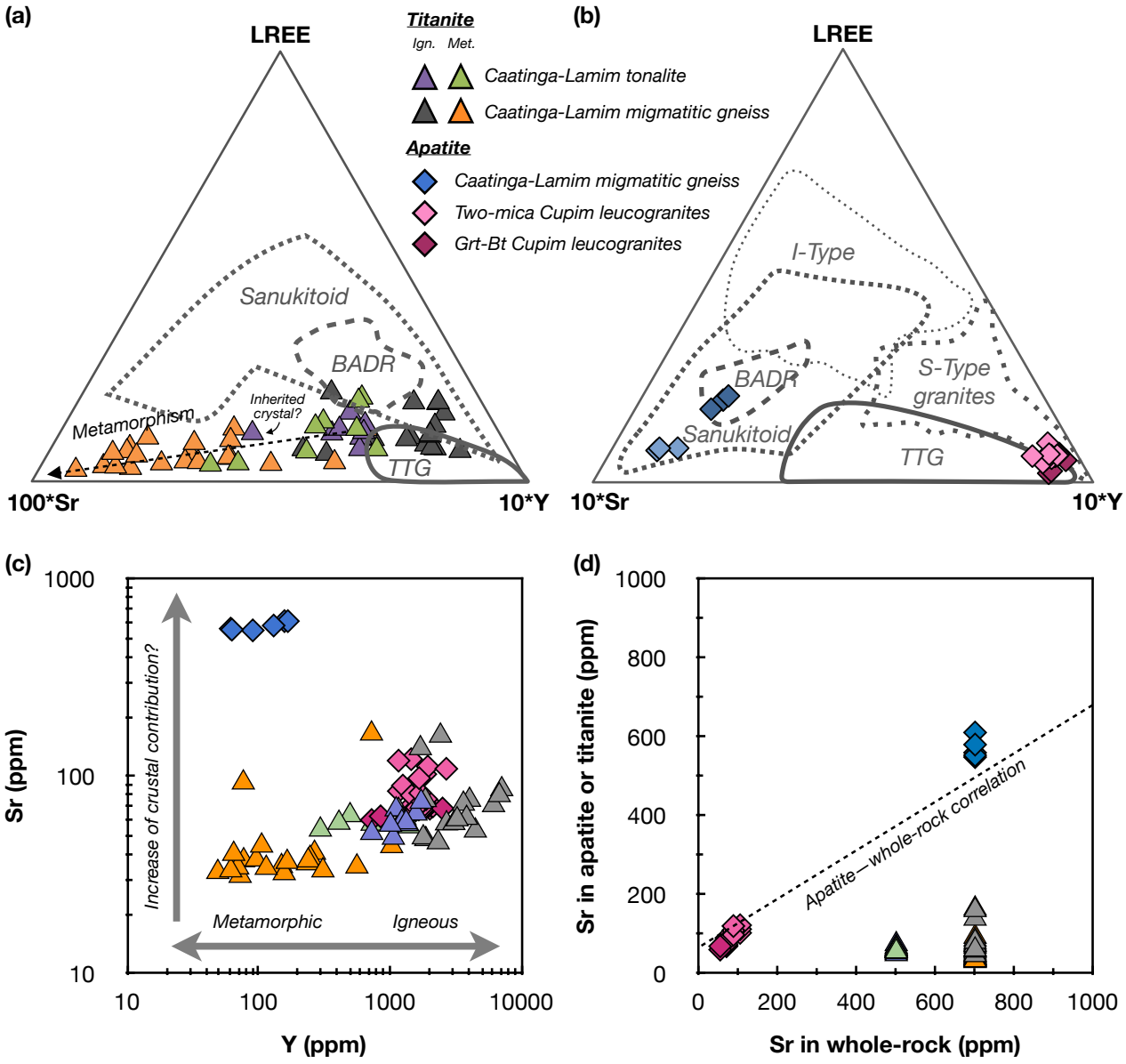


Figure 4.8: Host magma discrimination. (a) LREE-10*Y-100*Sr titanite discrimination diagram. Fields (TTG, sanukitoid, BARD) proposed by Bruand et al. 2020. The dashed arrow suggests the metamorphic trend. (b) LREE-10*Y-10*Sr apatite discrimination diagram. Fields (TTG, sanukitoid, BARD, I- and S-type) from Bruand et al. 2020. (c) Sr (ppm) vs. Y (ppm) concentration of titanite and apatite. The high Y concentration indicates igneous grains/domains, while low are mainly metamorphic. Sr enrichment could indicate the increase of crustal material into the host magma. (d) Sr (ppm) in apatite or titanite vs. Sr (ppm) whole-rock. The dashed line indicates the correlation trend suggested by Bruand et al. 2014.

Finally, the calculated parental magma composition from the average composition of apatites from the Cupim S-type granites (**Fig.4.9d**) seems to resemble the average whole-rock composition of these granites (Lacerda et al., 2024). The LREE and HREE composition differences between the calculated parental magma and the average whole-rock composition may be regarded as the early or simultaneous crystallization of monazite and garnet, respectively.

4.2.5.3. Magmatic and metamorphic processes

Considering *a* TiO_2 and *a* SiO_2 activities of 0.7 and 1, respectively, and pressure (P) of 0.5 Ga, from hornblende-plagioclase thermobarometers (see Lacerda et al. submitted), Zr-in-titanite temperatures (Hayden et al., 2008) of type (ii) titanite are higher (from 677 to 744° C) than those of type (i) (from 601 to 676° C) from the migmatitc gneiss (**Fig.4.10a**). Contrarily, dark and light domains of titanite grains from the tonalite calculate similar Zr-in-titanite temperatures (from 661 to 761° C). Both calculated temperatures are lower than those using Ti-in-zircon thermometers (see Lacerda et al. submitted), ranging from 740 to 940° C, suggesting that zircon crystallized earlier than titanite. The earlier zircon crystallization could explain the HREE-depleted composition of type (ii) titanite grains and dark domains.

The REE-depleted composition and highly positive Eu/Eu* values of type (i) titanites suggest that these crystals have a different nature, probably a metamorphic product of a reaction involving Ti-Ca-bearing minerals (e.g., Hornblende + Plagioclase + Water → Biotite + Titanite + Quartz). Alternatively, titanite (and apatite) crystals were crystallized from partial melting drops trapped in the mesosome.

Igneous titanite and, to a lesser extent, apatite crystals generally have richer Pb composition and higher Th/U ratios than metamorphic ones (**Fig.4.10b**). This compositional difference could be considered genetic, as Pb is more easily incorporated into the titanite lattice during higher-temperature crystallization processes (Tiepolo et al., 2002).

The trace element composition of apatite crystals from Cupim leucogranites, especially REE (**Fig.4.10d**), resembles those from migmatitic paragneiss (pelite and greywacke protoliths) within the Eocene Chugach Metamorphic Complex, Alaska (Biget et al., 2024). The Sr-Rb-Ba composition of these granites suggests that two-mica types have clay-poor metasedimentary sources, while garnet-bearing types have clay-rich ones (Lacerda et al., 2024). While the REE whole-rock composition of these granites only indicates the presence or absence of garnet/monazite, the apatite composition provides insight into the nature of the source. Those from garnet-bearing types show a relatively low REE composition, like those from clay-rich (pelitic) rocks (Biget et al., 2024).

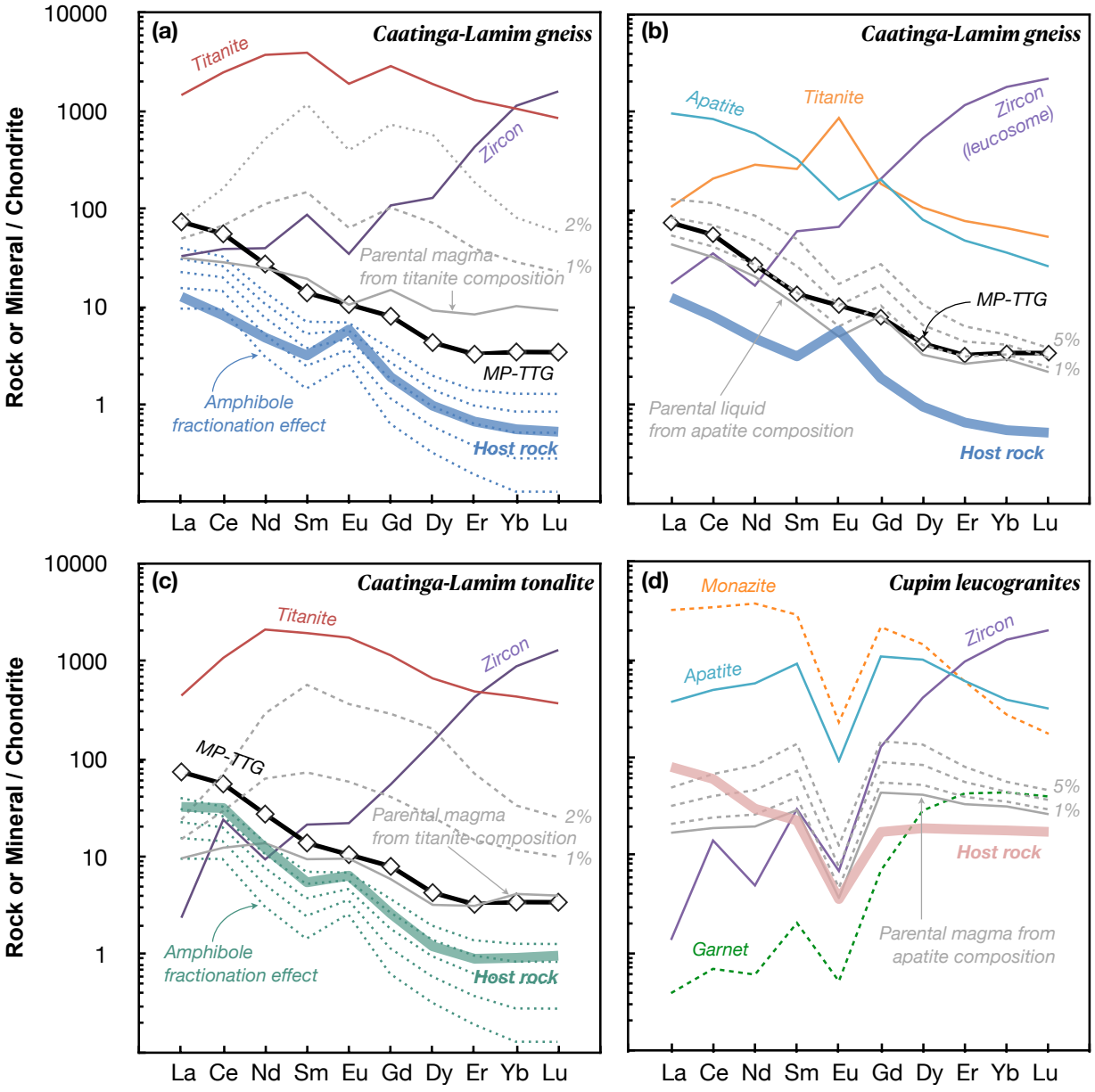


Figure 4.9: REE composition of the parental magma back-calculated from the apatite and titanite composition. (a) Parental magma composition modeled from the average composition of magmatic titanite grains from Caatinga-Lamim gneiss (CM44B) compared with medium-pressure TTG composition and whole-rock composition. Note the effect of hornblende fractionation and plagioclase accumulation (dashed patterns). Average zircon composition from Lacerda et al. submitted (b) using the average composition of apatite grains. (c) Parental magma composition obtained from the average composition of igneous titanite grains from Caatinga-Lamim tonalite (CM49). Note the effect of hornblende fractionation and plagioclase accumulation (dashed patterns). Average zircon composition from Lacerda et al. submitted (d) Parental magma calculated from the average composition of apatite grains from Cupim leucogranites compared to the whole-rock composition. Dashed patterns represent non-normalized partition coefficients of monazite and garnet.

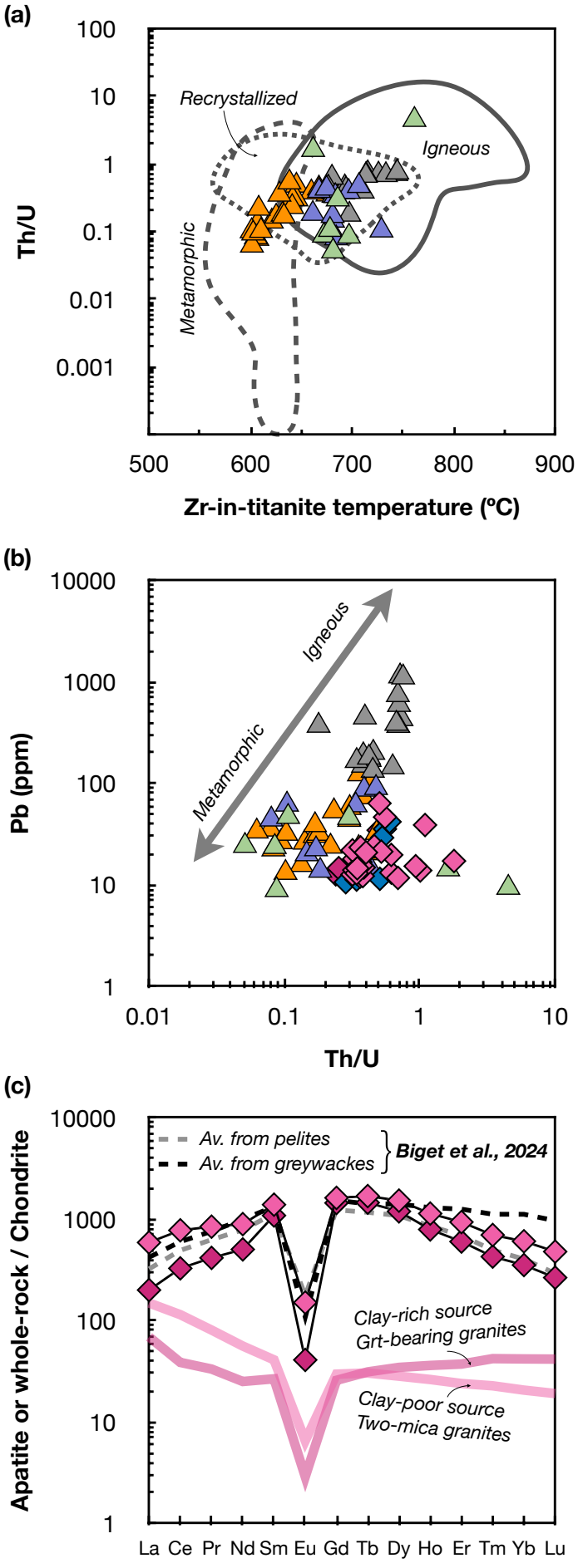

(a)
Recrystallized
Igneous
Metamorphic
Th/U
Zr-in-titanite temperature (°C)
(b)
Igneous
Metamorphic
Pb (ppm)
Th/U
(c)
Av. from pelites
Av. from greywackes
Biget et al., 2024
Clay-rich source
Grt-bearing granites
Clay-poor source
Two-mica granites
Apatite or whole-rock / Chondrite
La Ce Pr Nd Sm Eu Gd Tb Dy Ho Er Tm Yb Lu

Figure 4.10: Accessing igneous and metamorphic processes. Symbols used are the same as Fig.9. (a) Th/U vs. Zr-in-titanite temperature (°C) composition of titanite grains from Caatinga-Lamim rocks. Fields of igneous, recrystallized, and metamorphic titanite are proposed by Olierook et al., 2019. (b) Pb (ppm) vs. Th/U composition of titanite and apatite grains of the studied rocks. The arrow indicates the igneous-metamorphic trend. (d) Chondrite-normalized REE patterns of apatite grains from Cupim leucogranites compared with those from metagreywackes and pelite rocks (Biget et al., 2024). The whole-rock composition of two-mica and garnet-bearing leucogranites come from Lacerda et al. 2024.

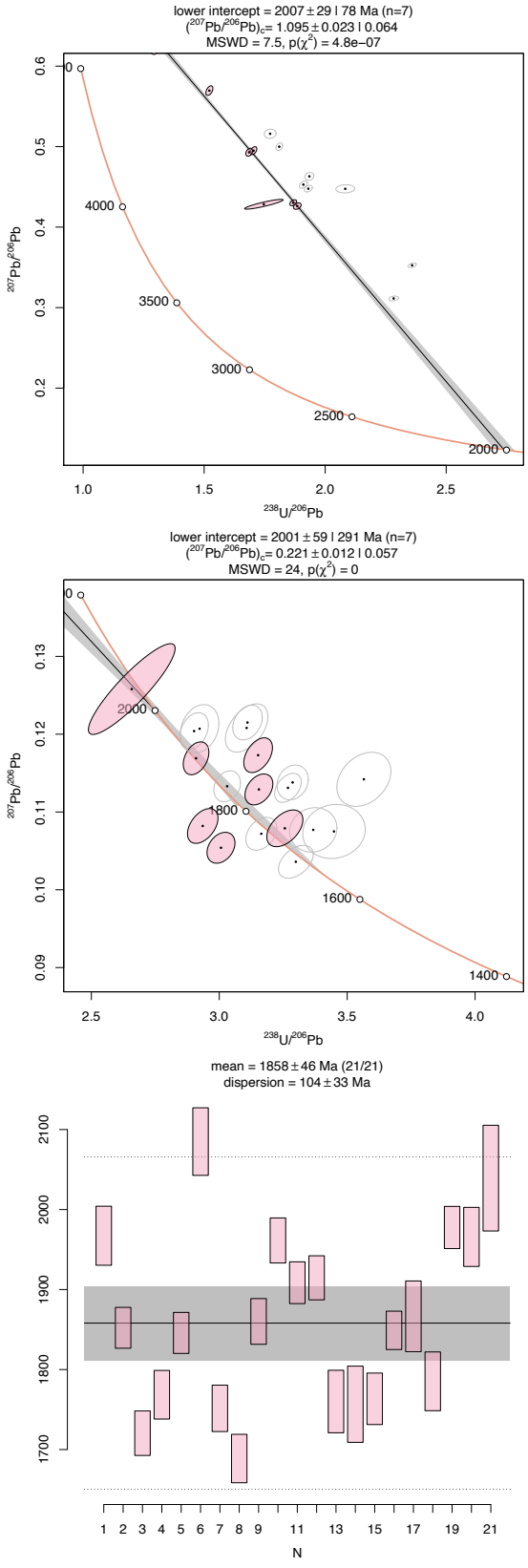
4.2.6. Conclusions

Combining U-Th-Pb ages and trace element composition of apatite and titanite grains from Paleoproterozoic granitic rocks within the Mineiro Belt provides clear information about igneous and metamorphic processes within the Southern São Francisco Craton, Brazil. This approach allows us to recognize two igneous and a single metamorphic event. High-Y-REE-Pb-Th/U titanite grains from Caatinga-Lamim TTG Complex show crystallization ages of 2130 Ma, while those with low composition show younger ages, around 2040 Ma. The latter is likely due to partial melting during a high metamorphic peak, which has also reset the U-Th-Pb isotopic system of low-Y apatite crystals from these rocks. In contrast, high-Y apatite crystals from the S-type Cupim Pluton show similar zircon ages, around 2000 Ma, but scattered ages probably due to younger low-temperature (<600^{o} C) processes.

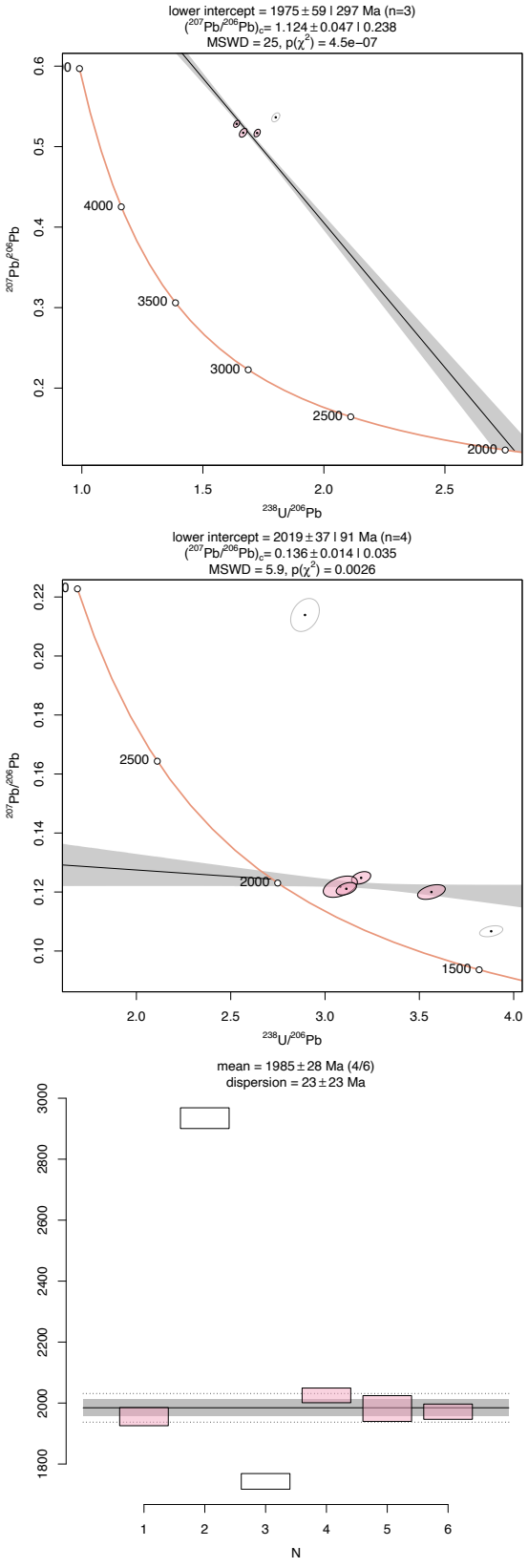
Titanite and apatite compositions are good tracers of the parental magma composition and give insights into rock crystallization history regarding mineral assemblage.

4.3. *Supplementary material C*

(a) GC5A/B apatite - Cupim Leucogranite



(b) GC6 apatite - Cupim Leucogranite



5. Building an ancient orogen

How the Precambrian orogens developed is a problem that has not yet been clarified, given that there is no well-defined paradigm for global geodynamics and tectonics. In this Thesis, I present a a geochemical approach to tackling this problem and argue that modern-day collisional orogenesis's geodynamics operated at 2.0 Ga in the Mineiro Belt.

Phanerozoic orogens are placed in convergent environments, as illustrated in the Wilson Cycle as pre- and sin-collisional stages. During the pre-collisional stage, the recycling of an oceanic lithosphere promotes the production of mantle-derived magmas that form magmatic arcs (e.g., the Andes Cordillera, the Western Pacific Volcanic System). When this oceanic plate is fully consumed, continental plates collide, uplifting mountain ranges (e.g., the Alpine-Himalayan orogen) and ultimately producing crustal-derived magmas. How long have these geodynamics and related magmatic processes been operating on Earth? Uniformitarianism predicts that the geologic processes of the early Earth were similar to those operating today. However, there are several lines of evidence that preclude this simple correlation. First, the presumably higher mantle temperatures and lithospheric geothermal gradients keep Precambrian orogens mechanically weaker and relatively hotter. This precludes the development of long-lived, large-scale, interconnected, and deeper subduction zones, and limits the thickening of continental crust during collision, drastically altering the source and mechanism of magma production and, consequently, crustal growth and reworking processes. Second, the structural fabric of some Precambrian orogens suggests that vertical tectonics was important in configuring the dome and keel architecture (e.g., Quadrilátero Ferrífero, eastern Brazil; Pilbara Craton, western Australia), probably due to high-intensity plume activity. Third, Precambrian orogens record monotonous high-temperature, low-pressure metamorphic conditions, in contrast to the conjugated metamorphic pairs, exhumed ultrahigh-pressure rocks, and well-defined suture zones of modern orogens. Fourth, the surface conditions of the Precambrian Earth (redox state and isotopic composition of the atmosphere and seawater) and the limited sub-aerial exposure of the continents influenced alteration and erosion processes and the sedimentological development of basins. Considering these temporal discrepancies, several efforts, including geochemical, isotopic, petrological, and numerical modeling studies, have been made to account for how geodynamics has worked in Precambrian terranes.

5.1. 'Hot' or 'cold' orogen ?

In order to understand the temporal and spatial evolution of orogens, the *Commission de la Carte Géologique du Monde* (CCGM - Paris, France) heads the "IGCP Project 667: The World Orogen Map" sponsored by UNESCO and the International Union of Geological Science (IUGS). They integrate a global compilation of geologic maps, identify orogenic regions, and subdivide them in time to recognize the internal structure of orogens and classify them according to their spatial zoning and

key orogenic attributes, which include magmatism, metamorphism, deformation, and sediment deposition (François et al., 2022). However, this global comparison is very simplistic when it comes to Precambrian geodynamics. They postulate a first division between "early Earth geodynamic processes (before 2.5 Ga)" and "modern orogens (after 2.5 Ga)" defined by the onset of plate tectonics, but a detailed discussion of how this tectonic transition occurred and the major implications to the orogenic systems is lacking. In addition, several studies propose that this transition was diachronic in different parts of the globe and may have occurred from the Eo-Archean to the Neoproterozoic (see Palin et al., 2020).

Instead, based on first-order structural and metamorphic features of Precambrian terranes, that reflect the mechanical behavior of the lithospheric mantle at different Moho temperatures, Chardon et al. (2009) define two orogen end members: 'ultra-hot orogens' (UHO) and 'cold orogens' (CO). CO refers to modern (Phanerozoic) tectonics, whereas UHO is characterized by long-lived homogeneous shortening, juvenile crustal growth, and three-dimensional flow over large continental domains without a stiff lithospheric mantle (Chardon et al., 2009; Cagnard et al., 2011). In between these two orogen end members, 'hot orogens' (HO) and 'mixed-hot orogens' (MHO) develop lithospheric shortening that supports a stiff upper mantle with high Moho temperatures (>900 ^{o}C). HO (representative of Cordilleran and mature collisional belts) define UHO flow patterns, limited magmatism, and uplift collapse-driven topography. In contrast, MHO (representative of magmatic arcs and Proterozoic collisional belts), like UHO, have high rates of juvenile crust production, but exhibit CO-like structural framework and kinematics. Considering the high proportion of juvenile granitoid bodies compared to reworked ones (Moreira et al., 2018; Lacerda et al., 2024; submitted), as well as the well-developed fabric of volcanic and sedimentary units, the Mineiro Belt could be classified as MHO, even if it shows lower metamorphic grades compared to typical granulite belts (e.g., Finnish Lapland Granulite Belt, Cagnard et al., 2011).

Recently developed thermo-mechanical numerical models try to reproduce the deformation state and melting vulnerability of the lithosphere during Precambrian orogenesis applying higher temperatures (Sizova et al., 2010; 2014; Gerya and Meilick, 2011; O'Niell et al., 2018; Maierová et al., 2025). Regarding the accretion of a 'hot' magmatic arc to continent by closing of continent-arc-back-arc system, Maierová et al. (2025) define two orogen's evolutionary styles: (i) subduction transference and (ii) polarity reversal. In the former, a significant part of the arc subduct and drag into the mantle, producing 'reclyced arc' magmas within the back-arc environment; whereas in the last, the arc is accreted, followed by the development of a new subduction zone underneath the arc. The new reversal subduction promotes maximum crustal thickening that can trigger melting of fertile materials (particularly sedimentary rocks). In the context of the Mineiro Belt, there is no evidence for accreted arc subduction or for recycled arc magmas in the back-arc environment. Rather, accretion by collision is proposed to occur in two stages (Lacerda et al., 2024). In the first

stage, the arc is accreted by soft collision, causing partial melting of the arc and fore-arc and isotopic resetting of low-temperature accessory phases (Aguilar et al., 2017; Carvalho et al., 2018; Lacerda et al., submitted; in prep.). In the next stage, the accretionary arc reaches its maximum thickness due to compression of Archean inliers (e.g., Piedade block; Bruno et al., 2020) and/or Paleoproterozoic arcs (Mantiqueira complex; Noce et al., 2007; Heilbron et al.,. 2010), triggering conditions for melting of meta-sedimentary rocks and production of S-type granites (Lacerda et al., 2024). Alternatively, the Mantiqueira arc may represent the reverse subduction phase that developed on the newly accreted continental margin.

5.2. Linking ages, crustal growth and reworking, tectonics, and geodynamics

In order to provide a comprehensive geotectonic and geodynamic orogenic evolution of the Mineiro Belt, **Table 5.1** summarizes the petrogenetic parameters of the main granitic bodies in its northern part.

Juvenile TTG magmas are produced and crystallized during the early and subsequent stages of the orogen's development. While some of these TTG magmas can track the repeated partial melting of short-lived Paleoproterozoic basaltic sources (e.g., 2.35 Ga Lagoa Dourada Suite, 2.14 Ga Resende Costa Suite, 2.13 Ga Caatinga-Lamim, and 2.11 Ga Ressaquinha Complexes), others suggest Archean source components (e.g., Água Limpa-Casa Grande plutons and Caranaíba gneiss). Sanukitoid, associated high Ba-Sr, and hybrid magmas are products of the interaction of different proportions of TTG magmas, mantle wedge, and sediments, and subsequent fractionation process. They are also juvenile magmas and can track the evolution of a Paleoproterozoic source (e.g., 2.13 Ga Alto Maranhão Suite), but some of those revel minor older contributions through inherited zircon crystals (e.g., 2.13 São Brás do Suaçuí and Bombaça plutons, 2.12 Ga Serra do Camapuã pluton). Peraluminous magmas are formed by the melting of sedimentary rocks during the final orogenic stages. They are primary products of crustal reworking and also suggest older source components (e.g., 2.00 Ga Cupim Pluton).

Therefore, in terms of sources, there were a shift from basaltic material, evolving to mantle (+sediments), and further to sediments. This source transition can be related to geotectonic and geodynamic changes probably due to the onset of modern plate tectonics, as well as proposed by Laurent et al., 2014. If the genesis of sanukitoid magmas is evidence for crustal recycling into the upper mantle via subduction, it is equally important to consider that the production of peraluminous magmas predicts sub-aerial weathering and erosion process, and continental crust stiffness and thickness enough to transfer sedimentary rocks into lower crustal levels to melt. These conditions are reached during the Orosirian (2050-2000 Ma) collisional accretion of the Mineiro belt to the Archean to Paleoproterozoic continental crust of the Quadrilátero Ferrífero region.

Table 5.1: Summary of petrogenetic parameters and implications for tectonics and geodynamics from several granitic unity in the northern part of the Mineiro Belt. $\varepsilon_{Hf(t)}$ are average values from zircon grains. $\varepsilon_{Nd(t)}$ are range values from whole-rock geochemistry. $\delta^{18}O$ and $\delta^{30}Si$ are average values from zircon grains. ΔFMQ refers to fayalite–magnetite–quartz buffer calculated via $S^{6+}/\Sigma S_{TOTAL}$ oxybarometer on apatite grains.

Granitic unity	Age	Petrology	Radiogenic isotopes	Stable isotopes and oxygen fugacity	Tectonics and geodynamics
Lagoa Dourada Suite [1] [2] [3] [4] [5]	Crystallization 2350 Ma	TTG (Paleop. source)	$\varepsilon_{Hf(t)}$ = +4.65 $\varepsilon_{Nd(t)}$ = +1 to +2.1	$\delta^{18}O$ = 4.36 ‰ ΔFMQ = -0.75 to -0.28	Intra-oceanic arc or oceanic plateaux. High-temperature source alteration. Reduced oxygen atmosphere.
Água Limpa-Casa Grande plutons [2][3] **and Caranaíba gneiss** [9]	Crystallization 2180-2160 Ma	TTG (Archean Source)	$\varepsilon_{Hf(t)}$ = -2.58 $\varepsilon_{Hf(t)}$ = -7.8 $\varepsilon_{Nd(t)}$ = -2.9	$\delta^{18}O$ = 5.42 ‰ $\delta^{30}Si$ = -0.72 ‰	Back-arc environment. Unaltered mafic source. Reduced DSi composition of the oceans.
Resende Costa Suite [2]	Crystallization 2140 Ma *Inherited 2350* Ma	TTG (Paleop. reworked)	$\varepsilon_{Hf(t)}$ = +4.9 (core) $\varepsilon_{Nd(t)}$ = +1.1 to +3.2	$\delta^{18}O$ = 4.96 ‰ (core) $\delta^{18}O$ = 4.27 ‰ (rim)	Intra-oceanic arc. Unaltered mafic source.
Alto Maranhão Suite [6] [7]	Crystallization 2130 Ma	Sanukitoid (TTG + Mantle +sediments)	$\varepsilon_{Hf(t)}$ = +0.51 $\varepsilon_{Nd(t)}$ = -1 to +0.9	$\delta^{18}O$ = 6.25 ‰ ΔFMQ = +0.80 to +1.24	Intra-oceanic arc. Mantle metasomatised via sediment input. Oxidized atmosphere.
São Brás do Suaçuí and Bombaça Plutons [2]	Crystallization 2130 Ma *Inherited Arch. to Paleop.*	High Ba-Sr (TTG + Mantle +sediments) *Fractionation*	$\varepsilon_{Hf(t)}$ = +0.21 $\varepsilon_{Nd(t)}$ = +0.3	$\delta^{18}O$ = 6.82‰	Intra-oceanic arc. Mantle metasomatised via sediment input.
Caatinga-Lamim Complex [9] [10]	Crystallization 2130 Ma *Anatexis 2040 Ma*	TTG (Paleop. source) *Partial melting*	$\varepsilon_{Hf(t)}$ = +4.2	$\delta^{30}Si$ = -0.88 ‰	Intra-oceanic arc. Reduced DSi composition of the oceans.
Serra do Camapuã Pluton [2]	Crystallization 2130-2120 Ma *Inherited Archean*	Hybrid (TTG + Mantle +sediments)	$\varepsilon_{Hf(t)}$ = -0.87 $\varepsilon_{Nd(t)}$ = -1.2 to -0.8	$\delta^{18}O$ = 5.57 ‰	Intra-oceanic arc. Mantle metasomatised via sediment input. Oxidized atmosphere.
Ressaquinha Complex [9]	Crystallization 2110 Ma *Inherited Archean*	TTG (Paleop. source)	$\varepsilon_{Hf(t)}$ = -1.6	$\delta^{30}Si$ = -0.83 ‰	Intra-oceanic arc. Reduced DSi composition of the oceans.
Congonhas Pluton [11]	Inferred crystallization 2.1 to 2.2 Ga	S-type (Arch. and Paleop. sources ?)	$\varepsilon_{Nd(t)}$ = -8 to -6		Continetal collision?
Cupim Pluton [8] [10]	Crystallization 2000 Ma *Inherited Arch. to Paleop.*	S-type (Arch. and Paleop. sources)	$\varepsilon_{Hf(t)}$ = -8.1	$\delta^{30}Si$ = -0.82 ‰	Continental collision. Mixing altered sedimentary sources.

[1] *Seixas et al., 2012*; [2] *Moreira et al., 2018*; [3] *Moreira et al., 2020*; [4] *Moreira et al., 2023*; [5] *Lopes et al., 2024*; [6] *Noce et al., 2000*; [7] *Seixas et al., 2013*; [8] *Lacerda et al., 2024*; [9] *Lacerda et al., submitted*; [10] *Lacerda et al., in prep.*; [11] *Seixas et al., 2017*.

It is also important to note that older Archean crust contributes to the genesis of some granitic magmas, either as potential sources (e.g., Água-Limpa-Casa Grande Plutons, Caranaíba gneiss, Cupim Pluton) or inherited xenocrystals (e.g., São-Brás do Suaçuí and Bombaça Plutons, Serra do

Camapuã Pluton, Ressaquinha Complex, and Cupim Pluton). This suggests a link between the Mineiro Belt and the Archean to Paleoproterozoic Quadrilátero Ferrífero region.

Silicon and oxygen isotopes in zircon and sulfur speciations in apatite from the granitic rocks unveil superficial processes and redox conditions during the orogen evolution. High-temperature (~400º C) alteration of the basaltic source is suggested for the genesis of some TTG magmas (e.g. Lagoa Dourada Suite), but the younger ones predict less significant alteration and silicification processes (e.g., Água-Limpa and Casa Grande Plutons, Caranaíba Gneiss, Caatinga-Lamim and Ressaquinha Complex). In addition, the sediment contribution for the genesis of sanukitoid, high Ba-Sr and hybrid magmas is imprinted in the higher oxygen isotope values (Moreira et al., 2020), as well as in the lower silicon isotope values from peraluminous granites (Lacerda et al., 2024). 2.35 Ga TTG and 2.13 Ga sanukitoid magmas record the rise of the oxygen atmospheric levels during the Great Oxidation Event (GOE). This event is related to early biological processes which also influenced continental and marine sedimentation mechanisms, and drastically changed the composition of the oceans. The lower silicon isotope composition of younger TTG magmas could reflect these shifts, since the deposition of banded iron formations (BIFs) globally reduce the dissolved silicon (DSi) from the oceans, inhibiting silicification of the source during pre-melting hydrous alteration. Also, this reinforced the idea of a connexion between the orogen and rifted passive margin of São Francisco continent.

Anatexis and metamorphism at 2050-2000 Ma are recognized in both terranes in migmatite rocks and peraluminous granites (e.g., Caatinga-Lamim Complex, Kinawa migmatite, Cupim Pluton) and imprinted in low-temperature accessory minerals (e.g. apatite, titanite, monazite), respectively. This stage is related to the orogen collisional accretion, when the continental crust reached its maximum thickness and reworking processes dominate.

There are several lines of evidence indicative of operation of an early plate tectonic episode during the Orosirian, including subduction related rocks (blueschists, eclogites, and ophioites), the formation of new passive margins and super-mountains, paleomagnetic and seismic interpretations, and syn-orogenic S-type magmatism and ore deposits (see Stern, 2023). However, it differs from the modern (Neoproterozoic) plate tectonic episode, since it was relatively shorter, lacked blueschists, preserved few ophiolites, and seems to have injected less water into the mantle by subduction (Stern, 2023). In the Mineiro Belt and Quadrilátero Ferrífero regions, no blueschist or eclogitic rocks have yet been identified, nor have ophiolite sequences been systematically described. Subduction related rocks are rather represented by 2.13 Ga sanukitoid and high Ba-Sr rocks. Paleomagnetic data are scarce in the region and applied in local scale for suite emplacement (see Nahas et al., 2023). On the other hand, the development of a passive margin in the Quadrilátero Ferrífero region records the break up of the continental crust to form new oceanic crust as part of the Wilson/Supercontinent cycle (Alkmim and Martin-Neto, 2012). Probability density distributions of the detrital zircon ages from metagreywackes in the Mineiro Belt region

also suggest extensional/passive margin depositional environment (Moreira et al., 2020). In addition, the identification of S-type granitic plutons (e.g., Cupim Pluton, Lacerda et al., 2024, Congonhas Pluton, Seixas et al., 2017) marks the final orogenic stage by continental collision that cause super-mountain. Furthermore, orogenic gold deposits hosted in Congonhas-Itaverava Lineament are products of hydrothermal alteration caused by fluids from subduction zones (Corrêa-Neto et al., 2012). All these records within the southern São Francisco Craton, i.e., Mineiro Belt and Quadrilátero Ferrífero region, attest to the operation of plate tectonics and modern-like orogenic style during the Orosirian, as suggested from orogens of a similar age around the world (see in Stern, 2023).

Considering the Archean-Paleoproterozoic Transition (APT) as a period of major geodynamic changes due to the thermo-mechanic evolution of the lithosphere (Laurent et a, 2014), and that local parameters (e.g., geometry and rheology of the crust, kinetic and sedimentation mechanisms) certainly have influenced of when it took place in different portions around the globe, I argue that the Mineiro Belt represents a younger exemple of the first subduction-collision cycles on Earth. There are voluminous sanukitoid and associated high Ba-Sr suites, which implies mantle hybridization; a major tectono-metamorphic event at ca. 2.05 Ga recorded by low-temperature accessory minerals; as well as a sequential production TTG-sanukitoid-peraluminous granitic magmas, via mechanisms that mimics modern plate tectonics, i.e. the subduction-collision cycle. During the early stages of the orogeny, the converging oceanic crust may have been stacked or unstably subducted into the mantle. In the first scenario, the base of the thick mafic pile formed could melt to produce TTG magmas, and eclogitic residues sank into the mantle. Now, if the converging oceanic crust is thick and dense enough, slabs could subduct into the 'hot' mantle, melting and also producing TTG magmas. The fact is that both scenarios predict oceanic crust consumption to produce juvenile TTG melts. In the subsequent stage, the mantle is hybridized by crustal components (e.g., TTG and sediment melts) during the end of subduction, and melted, producing sanukitoid magmas, which rase through the crust and fractionated to high Ba-Sr magmas. At this point, the oceanic slabs could also be melted to produce coeval TTG magmas, but they are certainly less volumetrically significant than sanukitoid and associated magmas. Crustal reworking starts to replace juvenile magma production. The cycle ends by the collision of this newly formed and partially juvenile continental crust against older adjacent crustal terranes. Anatectic magmas are mostly produced at this time, and S-type granites and migmatites record this final orogenic episode, when crust reworking processes dominates. The accretion by collision probably have implied to build cratonic keels (Perchuk et al., 2020) which promoted lithospheric stabilization and shield to subsequent orogenic cycles.

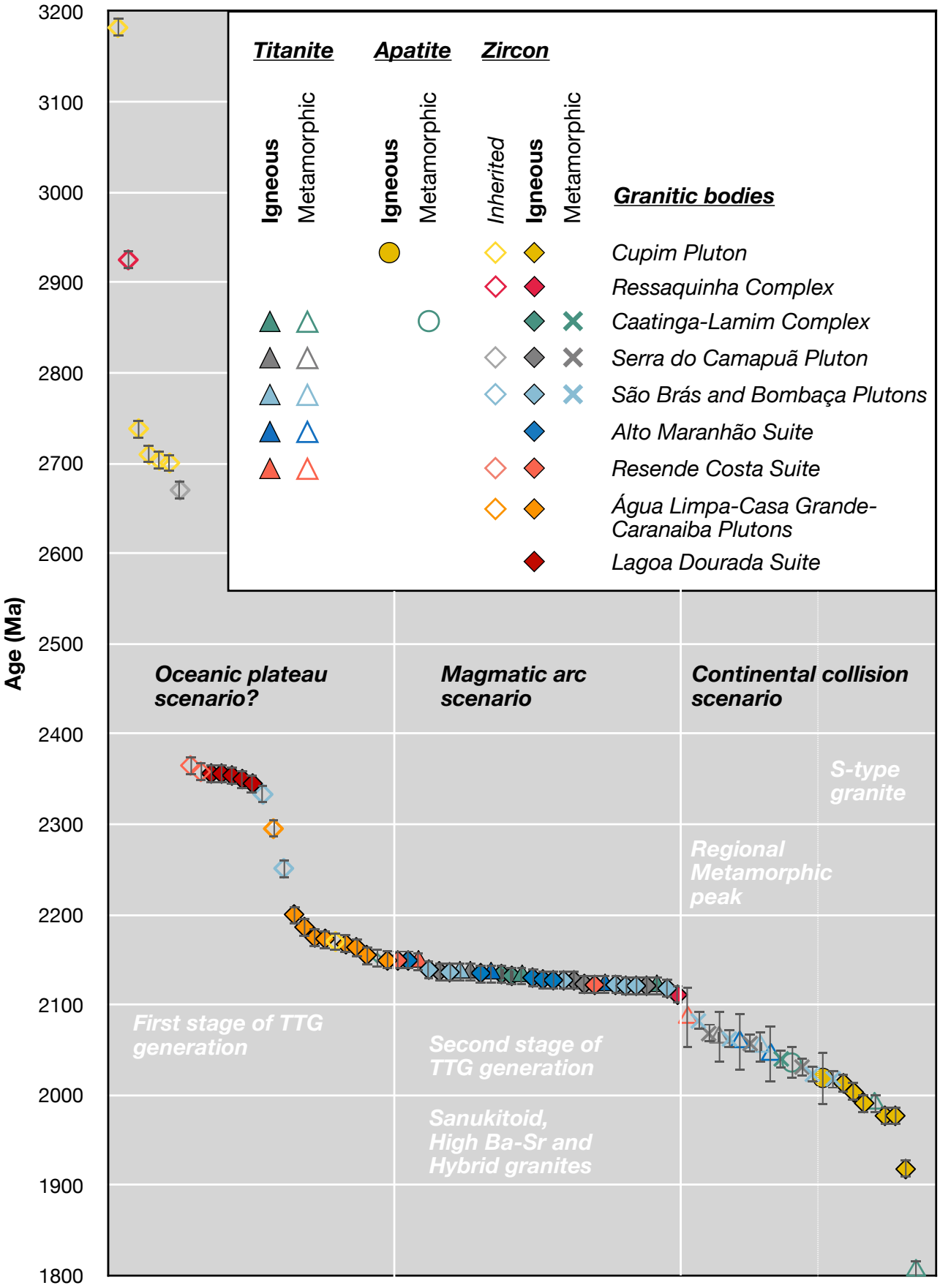


Figure 5.1: Compilation of zircon, titanite and apatite U-Pb ages of magmatic bodies in the northern part of the Mineiro Belt and corresponding magmatism during orogenic evolution. Data from Noce (1995), Seixas et al. (2012; 2013), Moreira et al. (2018; 2020), and this thesis. All U-Pb analyses were performed by LA-ICP-MS or ID-TIMS.

6. Perspectives and future direction

6.1. Introduction

This thesis demonstrates that combining petrological and geochemical studies with isotopic analyses in igneous rocks, considering secular evolution and cycling mechanisms, is essential for understanding continental crustal evolution and Earth's geodynamics. Paleoproterozoic TTG rocks and S-type granites are indicative of crustal alteration, erosion, and recycling and reworking processes, such as modern subduction-collision cycles. S-type granites imply an evolved mechanism of mixing of sedimentary sources and their transfer into a thick and rigid continental crust during collision, as suggested for the genesis of Himalayan leucogranites. Furthermore, TTG rocks suggest seafloor hydrous alteration and crustal reworking during subduction rather than silicification to fertilize basaltic sources. The transition from silicification to fluid alteration as the dominant mechanism of source fertilization is associated with the secular evolution of the dissolved silicon (DSi) composition of the oceans, which shift towards lower modern values. However, the respective roles of fluid phases and modal quartz in TTG formation remain poorly constrained. To advance our understanding, it is crucial to conduct more 'sophisticated' geochemical and isotopic analyses of these TTG rocks and local basalts. These analyses will help us determine the dominant control on alteration processes and expand our knowledge beyond the 'classical' whole-rock compositions and zircon isotopic data.

One obvious alternative would be to study potential fluid compositions by evaluating SiO_2 and mobile element (e.g., K, Rb, Ba, U, Th, Pb) contents of TTG rocks and basalts. However, magma fractionation, country rock assimilation, or post-magmatic (metamorphic) processes may limit this approach. Instead, analysis of germanium [Ge] compositions and germanium-silicon [Ge/Si] molar ratios provide evidence for fundamental changes in the alteration and geodynamic processes of crustal formation. This is because the Ge/Si ratio is only slightly fractionated during melting and magmatic differentiation. This chapter presents an alternative approach based on this latter method that may offer insights into this remaining question.

6.2. Rationale

A multi-proxy approach that combines Ge/Si with $\delta^{30}Si$ has proven to be an effective tracer for studying fluid-rock-soil interactions and defining rock alteration processes in modern and primitive Earth systems (e.g., Delvigne et al., 2016; Fernandez et al., 2021; André et al., 2022; Ackerman et al., 2023). The Paleoproterozoic TTG magmatism in the Mineiro Belt can provide insights to constrain geochemical weathering of continental and oceanic crusts during the earlier subduction-collision cycles on Earth. Significant tectonic, atmospheric, and oceanic changes occurred during this time (Dewey, 2021; Stern, 2023; Holland, 2006; Conley et al., 2011). The production of felsic and mafic magmas also underwent significant changes during this era (Keller

and Shoene, 2012; Moreira et al., 2018). Consequently, the rates of growth, reworking, and recycling of the continental crust also changed (Dhuime et al., 2011; Condie et al., 2018; Hawkesworth et al., 2020). These changes certainly have had a significant impact on rock-surface interactions and the mechanisms of crust alteration. If the transition from early-middle Archean Ge-depleted to Ge-enriched post-Archean felsic crust highlights the significance of late intra-crustal reworking and/or crust-mantle recycling (André et al., 2022), it is advisable to test this hypothesis in the Paleoproterozoic. To this end, I propose a comprehensive study of the tectonic and geodynamic evolved Paleoproterozoic seafloor using silicon isotopes and germanium systematics. This approach will allow us to reconstruct a plausible scenario of crust formation and recycling, potentially representing a transitional stage between those proposed for the Archean and the present.

6.3. Scientific issue

Macro- and micro-scale field evidence, petrological experimental studies, and heavy stable isotope signatures converge to assign TTG rocks as a result of intracrustal crystallization of Na-rich magmas produced by melting of surface-interacting hydrous basaltic rocks (Laurent et al., 2024 and references therein). In addition, trace element partial melt modeling suggests LILE-enriched (K, Rb, Ba, Th, U) basaltic rocks with compositions similar to Archean basalts (48 < SiO_2 < 54 wt%) as potential sources of TTG parental magmas (Martin et al., 2014). This source enrichment has been tentatively explained by modern analogous tectonic processes (see Palin et al., 2016): (i) or thickening of mafic crusts and melting of their lower parts, like a modern oceanic plateau scenario, (ii) or slab melting of mafic crust at convergent zones, like a modern subduction scenario. Besides local arguments in favor of the former or the latter scenario that make this debate endless (see Moyen and Laurent, 2018), the rheological conditions of a hotter Precambrian lithosphere limit direct correlations with modern tectonic systems (Gerya, 2014). Away from this debate, a third new explanation for source enrichment highlights the key role of seafloor (basalt) alteration processes in the genesis of Archean TTGs (André et al., 2019). These rocks show heavy silicon isotope signatures and low-Ge/Si ratios linked to their source composition, i.e., not derived of phase segregation, fractional crystallization, or metamorphic reactions (André et al., 2022). This implies a low-T, Si-saturated seawater circulation within a seafloor chert-tamponed paleo-aquifer (~10m of depth) which leads to silicification of basalts via precipitation of low-Ge/Si phases (e.g., quartz, feldspars, He et al., 2019). However, post-Archean granitoids and adakites (TTG-like lavas) show higher Ge/Si ratio values and suggest changes in the Earth geodynamics.

The unusually lighter silicon isotopic composition of Paleoproterozoic TTGs (-0.57‰ < $\delta^{30}Si$ < -0.37‰, Lacerda et al., submitted) compared to Archean TTGs (-0.14‰ < $\delta^{30}Si$ < +0.15‰, André et al., 2019; Deng et al., 2019) suggests a less significant contribution of seawater Si component to their protoliths. Applying the Ge/Si approach to these rocks, as well as determining the Ge/Si and silicon isotopic composition of potential protoliths, e.g., local mafic rocks (amphibolites and

metagabbros, cf. Teixeira et al., 2021), could trace how alteration processes operated during a transitional geodynamic scenario in which the early appearance of life forms, the maturation of sedimentary basins, and the efficiency of fluid circulation changed the Si composition of the oceans and, consequently, the silicon cycle.

6.4. Proposed analyses

Whole-rock Ge and Si isotopes compositions can be measured using ICP-MS techniques after sample preparation (crushing and milling) and dissolution. For Ge determinations, the solution should be dissolved by fusion with lithium metaborate flux (1000 °C for 1 h in platinum crucibles with a 1:8 flux to sample ratio) and diluted in 5% HNO_3 in order to reduce the dissolved salt matrix (Delvigne et al., 2016). For silicon, the sample powders should be digested with a NaOH solution, sufficiently dissolved by HNO_3 to avoid silicic acid polymerization (recommended solution pH ~2), eluded and purified using columns of cation exchange resins, conditioned with different HCl and HNO_3 pre-cleaning and Milli-Q water rinse steps. Detailed solution preparation procedures for Si analyses can be found in André et al. (2019), Hughes et al. (2011), and Deng et al., (2019). Ge concentrations can be analyzed via High Resolution-ICP-MS (e.g., Thermo Scientific Element 2, Element XR High Resolution ICP-MS) using ^{74}Ge isotope in medium-resolution mode with ^{115}In or ^{99}Ru as internal standard. Very precise measurements (in order of p.p.b. and p.p.t.) are reported in Delvigne et al. (2016) and André et al., (2022), at the Royal Museum for Central Africa and Vrije Universiteit Brussel, both in Belgium. Si isotopes can be determined using MC-ICP-MS (e.g., Nu Plasma II, Neptune), considering mass bias and drift corrections, like introducing external dopings, applying exponential mass bias laws, and by the standard-sample bracketing method (as used in this thesis). Good analytical accuracy were performed at the Institut de Physique de Globe de Paris and at Pôle Spectrométrie Ocean (Brest), in France, at the Université Libre de Bruxelles, in Belgium, and at ETH Zürich in Switzerland (Georg et a., 2006; Fitoussi and Bourdon, 2012; Deng et al., 2019; André et al., 2019, 2022).

References

Abdel-Rahman, A.F.M., 1994. Nature of Biotites from Alkaline, Calc-alkaline, and Peraluminous Magmas. J. Petrol. 35, 525–541. https://doi.org/10.1093/petrology/35.2.525

Abraham, K., Hofmann, A., Foley, S.F., Cardinal, D., Harris, C., Barth, M.G., Andre, L., 2011. Coupled silicon-oxygen isotope fractionation traces Archaean silicification. Earth Planet. Sci. Lett. 301, 222–230. https://doi.org/10.1016/j.epsl.2010.11.002

Ackerman, L., Poitrasson, F., Magna, T., Polák, L., Ďurišová, J., 2023. Seawater silica cycling and chert formation at the Neoproterozoic–Cambrian transition: Insights from δ30Si and Ge/Si systematics of hydrothermal cherts from the Bohemian Massif. Chem. Geol. 634. https://doi.org/10.1016/j.chemgeo.2023.121598

Aguilar, C., Alkmim, F.F., Lana, C., Farina, F., 2017. Palaeoproterozoic assembly of the São Francisco craton, SE Brazil: New insights from U–Pb titanite and monazite dating. Precambrian Res. 289, 95–115. https://doi.org/https://doi.org/10.1016/j.precamres.2016.12.001

Albert, C., Farina, F., Lana, C., Stevens, G., Storey, C., Gerdes, A., Dopico, C.M., 2016. Archean crustal evolution in the Southern São Francisco craton, Brazil: Constraints from U-Pb, Lu-Hf and O isotope analyses. Lithos 266–267, 64–86. https://doi.org/10.1016/j.lithos.2016.09.029

Aleinikoff, J.N., Wintsch, R.P., Tollo, R.P., Unruh, D.M., Fanning, C.M., Schmitz, M.D., 2007. Ages and origins of rocks of the Killingworth dome, south-central Connecticut: Implications for the tectonic evolution of southern New England. Am. J. Sci. 307, 63–118. https://doi.org/10.2475/01.2007.04

Alkmim, F.F., Kuchenbecker, M., Reis, H.L.S., Pedrosa-Soares, A.C., 2017. The Araçuaí Belt BT - São Francisco Craton, Eastern Brazil: Tectonic Genealogy of a Miniature Continent, in: Heilbron, M., Cordani, U.G., Alkmim, F.F. (Eds.), . Springer International Publishing, Cham, pp. 255–276. https://doi.org/10.1007/978-3-319-01715-0_14

Alkmim, F.F., Marshak, S., 1998. Transamazonian Orogeny in the Southern São Francisco Craton Region, Minas Gerais, Brazil: Evidence for Paleoproterozoic collision and collapse in the Quadrilátero Ferrífero. Precambrian Res. 90, 29–58. https://doi.org/10.1016/s0301-9268(98)00032-1

Alkmim, F.F., Martins-Neto, M.A., 2012. Proterozoic first-order sedimentary sequences of the São Francisco craton, eastern Brazil. Mar. Pet. Geol. 33, 127–139. https://doi.org/10.1016/j.marpetgeo.2011.08.011

Alkmim, F.F., Teixeira, W., 2017. The Paleoproterozoic mineiro belt and the Quadrilátero Ferrífero, in: São Francisco Craton, Eastern Brazil: Tectonic Genealogy of a Miniature Continent PP - New York, NY. Springer Berlin Heidelberg.

Allègre, C., Manhès, G., Lewin, É., 2001. Chemical composition of the Earth and the volatility control on planetary genetics. Earth Planet. Sci. Lett. 185, 49–69. https://doi.org/https://doi.org/10.1016/S0012-821X(00)00359-9

Almeida, F.F.M. De, Brito Neves, B.B. De, Dal Ré Carneiro, C., 2000. The origin and evolution of the South American platform. Earth Sci. Rev. 50, 77–111. https://doi.org/10.1016/S0012-8252(99)00072-0

Amelin, Y., Zaitsev, A.N., 2002. Precise geochronology of phoscorites and carbonatites: The critical role of U-series disequilibrium in age interpretations. Geochim. Cosmochim. Acta 66, 2399–2419. https://doi.org/10.1016/S0016-7037(02)00831-1

Anderson, J.L., Smith, D.R., 1995. The effects of temperature and fO2 on the Al-in-hornblende barometer. Am. Mineral. 80, 549–559. https://doi.org/10.2138/am-1995-5-614

André, L., Abraham, K., Hofmann, A., Monin, L., Kleinhanns, I.C., Foley, S., 2019. Early continental crust generated by reworking of basalts variably silicified by seawater. Nat. Geosci. 12, 769–773. https://doi.org/10.1038/s41561-019-0408-5

André, L., Monin, L., Hofmann, A., 2022. The origin of early continental crust: New clues from coupling Ge/Si ratios with silicon isotopes. Earth Planet. Sci. Lett. 582, 117415. https://doi.org/10.1016/j.epsl.2022.117415

Annen, C., Blundy, J.D., Sparks, R.S.J., 2006. The genesis of intermediate and silicic magmas in deep crustal hot zones. J. Petrol. 47, 505–539. https://doi.org/10.1093/petrology/egi084

Antoine, C., Bruand, E., Guitreau, M., Devidal, J.-L., 2020. Understanding Preservation of Primary Signatures in Apatite by Comparing Matrix and Zircon-Hosted Crystals From the Eoarchean Acasta Gneiss Complex (Canada). Geochemistry, Geophys. Geosystems 21, e2020GC008923. https://doi.org/https://doi.org/10.1029/2020GC008923

Apen, F.E., Wall, C.J., Cottle, J.M., Schmitz, M.D., Kylander-Clark, A.R.C., Seward, G.G.E., 2022. Apatites for destruction: Reference apatites from Morocco and Brazil for U-Pb petrochronology and Nd and Sr isotope geochemistry. Chem. Geol. 590, 120689. https://doi.org/10.1016/j.chemgeo.2021.120689

Arzamastsev, A.A., Arzamastseva, L. V., Bea, F., Montero, P., 2009. Trace elements in minerals as indicators of the evolution of alkaline ultrabasic dike series: LA-ICP-MS data for the magmatic provinces of northeastern Fennoscandia and Germany. Petrology 17, 46–72. https://doi.org/10.1134/S0869591109010032

Ávila, C.A., Teixeira, W., Bongiolo, E.M., Dussin, I.A., Vieira, T.A.T., 2014. Rhyacian evolution of subvolcanic and metasedimentary rocks of the southern segment of the Mineiro belt, São Francisco Craton, Brazil. Precambrian Res. 243, 221–251. https://doi.org/10.1016/j.precamres.2013.12.028

Ávila, C.A., Teixeira, W., Cordani, U.G., Moura, C.A.V., Pereira, R.M., 2010. Rhyacian (2.23-2.20 Ga) juvenile accretion in the southern São Francisco craton, Brazil: Geochemical and isotopic

evidence from the Serrinha magmatic suite, Mineiro belt. J. South Am. Earth Sci. 29, 464–482. https://doi.org/10.1016/j.jsames.2009.07.009

Babinski, M., Chemale, F., Van Schmus, W.R., 1995. The Pb Pb age of the Minas Supergroup carbonate rocks, Quadrilátero Ferrífero, Brazil. Precambrian Res. 72, 235–245. https://doi.org/10.1016/0301-9268(94)00091-5

Barbarin, B., 1999. A review of the relationships between granitoid types, their origins and their geodynamic environments. Lithos 46, 605–626. https://doi.org/10.1016/S0024-4937(98)00085-1

Barbosa, N., Teixeira, W., Ávila, C.A., Montecinos, P.M., Bongiolo, E.M., Vasconcelos, F.F., 2019. U-Pb geochronology and coupled Hf-Nd-Sr isotopic-chemical constraints of the Cassiterita Orthogneiss (2.47–2.41-Ga) in the Mineiro belt, São Francisco craton: Geodynamic fingerprints beyond the Archean-Paleoproterozoic Transition. Precambrian Res. 326, 399–416. https://doi.org/10.1016/j.precamres.2018.01.017

Barbosa, N.S., Teixeira, W., Ávila, C.A., Montecinos, P.M., Bongiolo, E.M., 2015. 2.17-2.10Ga plutonic episodes in the Mineiro belt, São Francisco Craton, Brazil: U-Pb ages, geochemical constraints and tectonics. Precambrian Res. 270, 204–225. https://doi.org/10.1016/j.precamres.2015.09.010

Barker, F., 1979. Chapter 1 - Trondhjemite: Definition, Environment and Hypotheses of Origin, in: BARKER, F.B.T.-D. in P. (Ed.), Trondhjemites, Dacites, and Related Rocks. Elsevier, pp. 1–12. https://doi.org/https://doi.org/10.1016/B978-0-444-41765-7.50006-X

Barker, F., Arth, J.G., 1976. Generation of trondhjemitic-tonalitic liquids and Archean bimodal trondhjemite-basalt suites. Geology 4, 596–600. https://doi.org/10.1130/0091-7613(1976)4<596:GOTLAA>2.0.CO;2

Barnes, C.G., Werts, K., Memeti, V., Ardill, K. (2019). Most granitoid rocks are cumulates: deductions from hornblende compositions and zircon saturation. Journal of petrology 80, 2227-2240, https://doi.org/10.1093/petrology/egaa008

Beard, J.S., Lofgren, G.E., 1991. Dehydration melting and water-saturated melting of basaltic and andesitic greenstones and amphibolites at 1, 3, and 6. 9 kb. J. Petrol. 32, 365–401. https://doi.org/10.1093/petrology/32.2.365

Bédard, J.H., 2006. A catalytic delamination-driven model for coupled genesis of Archaean crust and sub-continental lithospheric mantle. Geochim. Cosmochim. Acta 70, 1188–1214. https://doi.org/10.1016/j.gca.2005.11.008

Bekker, A., Krapež, B., Slack, J.F., Planavsky, N., Hofmann, A., Konhauser, K.O., Rouxel, O.J., 2012. Iron formation: The sedimentary product of a complex interplay among mantle, tectonic, oceanic, and biospheric processes-a reply. Econ. Geol. 107, 379–380. https://doi.org/10.2113/econgeo.107.2.379

Bell, E.A., Boehnke, P., Harrison, T.M., 2016. Recovering the primary geochemistry of Jack Hills zircons through quantitative estimates of chemical alteration. Geochim. Cosmochim. Acta 191, 187–202. https://doi.org/https://doi.org/10.1016/j.gca.2016.07.016

Belousova, E.A., Walters, S., Griffin, W.L., O'Reilly, S.Y., 2001. Trace-element signatures of apatites in granitoids from the Mt Isa Inlier, Northwestern Queensland. Aust. J. Earth Sci. 48, 603–619. https://doi.org/10.1046/j.1440-0952.2001.00879.x

Biget, T., Bruand, E., Pereira, I., Boyet, M., Gasser, D., Stüwe, K., Langone, A., 2024. The chemical and Sm–Nd isotopic behaviour of accessory minerals in metasediments along the LP-HT Chugach Metamorphic Complex (Alaska). Contrib. to Mineral. Petrol. 179. https://doi.org/10.1007/s00410-024-02185-2

Black, L.P., Gulson, B.L., 1978. The age of the Mud Tank carbonatite, Strangways Range, Northern Territory. BMR J. Aust. Geol. Geophys. 3, 227–232.

Blichert-Toft, J., 2008. The Hf isotopic composition of zircon reference material 91500. Chem. Geol. 253, 252–257. https://doi.org/https://doi.org/10.1016/j.chemgeo.2008.05.014

Blichert-Toft, J., Albarède, F., 2008. Hafnium isotopes in Jack Hills zircons and the formation of the Hadean crust. Earth Planet. Sci. Lett. 265, 686–702. https://doi.org/https://doi.org/10.1016/j.epsl.2007.10.054

Blundy, J.D., Holland, T.J.B., 1990. Calcic amphibole equilibria and a new amphibole-plagioclase geothermometer. Contrib. to Mineral. Petrol. 104, 208–224. https://doi.org/10.1007/BF00306444

Bonin, B., Janoušek, V., Moyen, J.-F., 2020. Chemical variation, modal composition and classification of granitoids. Geol. Soc. Spec. Publ. https://doi.org/10.1144/SP491-2019-138

Bonin, B., Moyen, J.-F., 2011. Magmatisme et roches magmatiques. Dunod, Paris.

Bouvier, A., Vervoort, J.D., Patchett, P.J., 2008. The Lu–Hf and Sm–Nd isotopic composition of CHUR: Constraints from unequilibrated chondrites and implications for the bulk composition of terrestrial planets. Earth Planet. Sci. Lett. 273, 48–57. https://doi.org/https://doi.org/10.1016/j.epsl.2008.06.010

Boynton, W. V, 1984. Chapter 3 - Cosmochemistry of the Rare Earth Elements: Meteorite Studies, in: Henderson, P.B.T.-D. in G. (Ed.), Rare Earth Element Geochemistry. Elsevier, pp. 63–114. https://doi.org/https://doi.org/10.1016/B978-0-444-42148-7.50008-3

Brito Neves, B.B., Campos Neto, M.D.C., Fuck, R.A., 1999. From Rodinia to Western Gondwana: An approach to the Brasiliano-Pan African cycle and orogenic collage. Episodes 22, 155–166. https://doi.org/10.18814/epiiugs/1999/v22i3/002

Bruand, E., Fowler, M., Laurent, C.S.O., Antoine, C., Guitreau, M., Heilimo, E., Nebel, O., 2020. Accessory mineral constraints on crustal evolution: elemental fingerprints for magma discrimination. Geochemical Perspect. Lett. 13, 7–12. https://doi.org/https://doi.org/10.7185/geochemlet.2006

Bruand, E., Fowler, M., Storey, C., Darling, J., 2017. Apatite trace element and isotope applications to petrogenesis and provenance. American Mineralogist 102, 75–84. https://doi.org/doi:10.2138/am-2017-5744

Bruand, E., Storey, C., Fowler, M., 2014. Accessory Mineral Chemistry of High Ba–Sr Granites from Northern Scotland: Constraints on Petrogenesis and Records of Whole-rock Signature. J. Petrol. 55, 1619–1651. https://doi.org/10.1093/petrology/egu037

Bruno, H., Elizeu, V., Heilbron, M., de Morisson Valeriano, C., Strachan, R., Fowler, M., Bersan, S., Moreira, H., Dussin, I., Guilherme do Eirado Silva, L., Tupinambá, M., Almeida, J., Neto, C., Storey, C., 2020. Neoarchean and Rhyacian TTG-Sanukitoid suites in the southern São Francisco Paleocontinent, Brazil: Evidence for diachronous change towards modern tectonics. Geosci. Front. 11, 1763–1787. https://doi.org/10.1016/j.gsf.2020.01.015

Bucholz, C.E., Spencer, C.J., 2019. Strongly Peraluminous Granites across the Archean-Proterozoic Transition. J. Petrol. 60, 1299–1348. https://doi.org/10.1093/petrology/egz033

Cabral, A.R., Zeh, A., Vianna, N.C., Ackerman, L., Pašava, J., Lehmann, B., Chrastný, V., 2019. Molybdenum-isotope signals and cerium anomalies in Palaeoproterozoic manganese ore survive high-grade metamorphism. Sci. Rep. 9. https://doi.org/10.1038/s41598-019-40998-5

Cagnard, F., Barbey, P., Gapais, D., 2011. Transition between "Archaean-type" and "modern-type" tectonics: Insights from the Finnish Lapland Granulite Belt. Precambrian Res. 187, 127–142. https://doi.org/10.1016/j.precamres.2011.02.007

Campos Neto, M. da C., Basei, M.A.S., Assis Janasi, V. de, Moraes, R., 2011. Orogen migration and tectonic setting of the Andrelândia Nappe system: An Ediacaran western Gondwana collage, south of São Francisco craton. J. South Am. Earth Sci. 32, 393–406. https://doi.org/https://doi.org/10.1016/j.jsames.2011.02.006

Campos, J.C.S., Carneiro, M.A., 2008. Neoarchean and Paleoproterozoic granitoids marginal to the Jeceaba-Bom Sucesso lineament (SE border of the southern São Francisco craton): Genesis and tectonic evolution. J. South Am. Earth Sci. 26, 463–484. https://doi.org/10.1016/j.jsames.2008.09.002

Campos, J.C.S., Carneiro, M.A., Basei, M.A.S., 2003. U-Pb evidence for late Neoarchean crustal reworking in the southern São Francisco Craton (Minas Gerais, Brazil). An. Acad. Bras. Cienc. 75, 497–511. https://doi.org/10.1590/s0001-37652003000400008

Cao, H.-W., Pei, Q.-M., Santosh, M., Li, G.-M., Zhang, L.-K., Zhang, X.-F., Zhang, Y.-H., Zou, H., Dai, Z.-W., Lin, B., Tang, L., Yu, X., 2022. Himalayan leucogranites: A review of geochemical and isotopic characteristics, timing of formation, genesis, and rare metal mineralization. Earth-Science Rev. 234. https://doi.org/10.1016/j.earscirev.2022.104229

Cardoso, C.D., Ávila, C.A., Neumann, R., Oliveira, E.P., Valeriano, C. de M., Dussin, I.A., 2019. A Rhyacian continental arc during the evolution of the Mineiro belt, Brazil: Constraints from

the Rio Grande and Brumado metadiorites. Lithos 326–327, 246–264. https://doi.org/10.1016/j.lithos.2018.12.025

Carvalho, B.B., Janasi, V.A., Sawyer, E.W., 2017. Evidence for Paleoproterozoic anatexis and crustal reworking of Archean crust in the São Francisco Craton, Brazil: A dating and isotopic study of the Kinawa migmatite. Precambrian Res. 291, 98–118. https://doi.org/https://doi.org/10.1016/j.precamres.2017.01.019

Carvalho, B.B., Sawyer, E.W., Janasi, V.A., 2016. Crustal reworking in a shear zone: Transformation of metagranite to migmatite. J. Metamorph. Geol. 34, 237–264. https://doi.org/10.1111/jmg.12180

Cashman, K. V, Sparks, R.S.J., Blundy, J.D., 2017. Vertically extensive and unstable magmatic systems: A unified view of igneous processes. Science (80-.). 355. https://doi.org/10.1126/science.aag3055

Cawood, P.A., Hawkesworth, C.J., Dhuime, B., 2012. Detrital zircon record and tectonic setting. Geology 40, 875–878. https://doi.org/10.1130/G32945.1

Caxito, F. de A., Alkmim, F.F., 2023. The role of V-shaped oceans and ribbon continents in the Brasiliano/PanAfrican assembly of western Gondwana. Sci. Rep. 13, 1–17. https://doi.org/10.1038/s41598-023-28717-7

Chappell, B.W., White, A.J.R., 1974. Two Contrasting Granite Types. Pacific Geol. 8, 173–174.

Chardon, D., Gapais, D., Cagnard, F., 2009. Flow of ultra-hot orogens: A view from the Precambrian, clues for the Phanerozoic. Tectonophysics 477, 105–118. https://doi.org/10.1016/j.tecto.2009.03.008

Chauvel, C., Blichert-Toft, J., 2001. A hafnium isotope and trace element perspective on melting of the depleted mantle. Earth Planet. Sci. Lett. 190, 137–151. https://doi.org/https://doi.org/10.1016/S0012-821X(01)00379-X

Chew, D.M., Babechuk, M.G., Cogné, N., Mark, C., O'Sullivan, G.J., Henrichs, I.A., Doepke, D., McKenna, C.A., 2016. (LA,Q)-ICPMS trace-element analyses of Durango and McClure Mountain apatite and implications for making natural LA-ICPMS mineral standards. Chem. Geol. 435, 35–48. https://doi.org/10.1016/j.chemgeo.2016.03.028

Chew, D.M., Sylvester, P.J., Tubrett, M.N., 2011. U-Pb and Th-Pb dating of apatite by LA-ICPMS. Chem. Geol. 280, 200–216. https://doi.org/10.1016/j.chemgeo.2010.11.010

Chu, N.-C., Taylor, R.N., Chavagnac, V., Nesbitt, R.W., Boella, R.M., Milton, J.A., German, C.R., Bayon, G., Burton, K., 2002. Hf isotope ratio analysis using multi-collector inductively coupled plasma mass spectrometry: an evaluation of isobaric interference corrections. J. Anal. At. Spectrom. 17, 1567–1574. https://doi.org/10.1039/B206707B

Condie, K.C., 2005. TTGs and adakites: Are they both slab melts? Lithos 80, 33–44. https://doi.org/10.1016/j.lithos.2003.11.001

Condie, K.C., 2018. A planet in transition: The onset of plate tectonics on Earth between 3 and 2 Ga? Geosci. Front. 9, 51–60. https://doi.org/10.1016/j.gsf.2016.09.001

Conley, D.J., Frings, P.J., Fontorbe, G., Clymans, W., Stadmark, J., Hendry, K.R., Marron, A.O., De La Rocha, C.L., 2017. Biosilicification drives a decline of dissolved si in the oceans through geologic time. Front. Mar. Sci. 4. https://doi.org/10.3389/fmars.2017.00397

Corfu, F., Hanchar, J.M., Hoskin, P.W.O., Kinny, P., 2003. Atlas of Zircon Textures. Rev. Mineral. Geochemistry 53, 469–500. https://doi.org/10.2113/0530469

Corrêa-Neto, A.V., Almeida, A.M., Neto, V.C., Guerrero, J.C., 2012. Alteração Hidrotermal em Zona de Cisalhamento Associada ao Lineamento Congonhas, Sul do Quadrilátero Ferrífero, Minas Geraisl. Anuário do Inst. Geociências - UFRJ 35_2, 55–64. https://doi.org/10.11137/2012_2_55_64

Couzinié, S., Laurent, O., Moyen, J.-F., Zeh, A., Bouilhol, P., Villaros, A., 2016. Post-collisional magmatism: Crustal growth not identified by zircon Hf–O isotopes. Earth Planet. Sci. Lett. 456, 182–195. https://doi.org/10.1016/j.epsl.2016.09.033

Cuney, M., Sabaté, P., Vidal, P., Marinho, M.M., Conceiçao, H., 1990. The 2 Ga peraluminous magmatism of the Jacobina - Contendas Mirante Belt (Bahia) Brazil): Major and trace-element geochemistry and metallogenic potential. J. Volcanol. Geotherm. Res. 44, 123–141. https://doi.org/10.1016/0377-0273(90)90015-8

Cutts, K., Lana, C., Alkmim, F., Farina, F., Moreira, H., Coelho, V., 2019. Metamorphism and exhumation of basement gneiss domes in the Quadrilátero Ferrífero: Two stage dome-and-keel evolution? Geosci. Front. 10, 1765–1787. https://doi.org/10.1016/j.gsf.2019.02.009

De Biévre, P., Taylor, P.D.P., 1993. Table of the isotopic compositions of the elements. Int. J. Mass Spectrom. Ion Process. 123, 149–166. https://doi.org/https://doi.org/10.1016/0168-1176(93)87009-H

Debon, F., Le Fort, P., 1983. A chemical–mineralogical classification of common plutonic rocks and associations. Trans. R. Soc. Edinb. Earth Sci. 73, 135–149. https://doi.org/DOI: 10.1017/S0263593300010117

Deer, W.A., Howie, R.A., Zussman, J., 2013. An Introduction to the Rock-Forming Minerals, An Introduction to the Rock-Forming Minerals. https://doi.org/10.1180/dhz

Degler, R., Pedrosa-Soares, A., Novo, T., Tedeschi, M., Silva, L.C., Dussin, I., Lana, C., 2018. Rhyacian-Orosirian isotopic records from the basement of the Araçuaí-Ribeira orogenic system (SE Brazil): Links in the Congo-São Francisco palaeocontinent. Precambrian Res. 317, 179–195. https://doi.org/10.1016/j.precamres.2018.08.018

Delvigne, C., Opfergelt, S., Cardinal, D., Hofmann, A., André, L., 2016. Desilication in Archean weathering processes traced by silicon isotopes and Ge/Si ratios. Chem. Geol. 420, 139–147. https://doi.org/10.1016/j.chemgeo.2015.11.007

Deng, Z., Chaussidon, M., Guitreau, M., Puchtel, I.S., Dauphas, N., Moynier, F., 2019. An oceanic subduction origin for Archaean granitoids revealed by silicon isotopes. Nat. Geosci. 12, 774–778. https://doi.org/10.1038/s41561-019-0407-6

Dewey, J.F., Kiseeva, E.S., Pearce, J.A., Robb, L.J., 2021. Precambrian tectonic evolution of Earth: an outline. South African J. Geol. 124, 141–162. https://doi.org/10.25131/sajg.124.0019

Dhuime, B., Hawkesworth, C., Cawood, P., 2011. When continents formed. Science (80-.). https://doi.org/10.1126/science.1201245

Dickin, A.P., n.d. Radiogenic Isotope Geology, Second Edition.

Farina, F., Albert, C., Lana, C., 2015. The Neoarchean transition between medium- and high-K granitoids: Clues from the Southern São Francisco Craton (Brazil). Precambrian Res. 266, 375–394. https://doi.org/10.1016/j.precamres.2015.05.038

Faure, G., Mensing, T.M., 2005. Isotopes: principles and applications, 3rd ed. ed. Hoboken (N.J.): Wiley.

Fernandez, N.M., Perez-Fodich, A., Derry, L.A., Druhan, J.L., 2021. A first look at Ge/Si partitioning during amorphous silica precipitation: Implications for Ge/Si as a tracer of fluid-silicate interactions. Geochim. Cosmochim. Acta 297, 158–178. https://doi.org/10.1016/j.gca.2021.01.007

Ferry, J.M., Watson, E.B., 2007. New thermodynamic models and revised calibrations for the Ti-in-zircon and Zr-in-rutile thermometers. Contrib. to Mineral. Petrol. 154, 429–437. https://doi.org/10.1007/s00410-007-0201-0

Fisher, C.M., Bauer, A.M., Luo, Y., Sarkar, C., Hanchar, J.M., Vervoort, J.D., Tapster, S.R., Horstwood, M., Pearson, D.G., 2020. Laser ablation split-stream analysis of the Sm-Nd and U-Pb isotope compositions of monazite, titanite, and apatite – Improvements, potential reference materials, and application to the Archean Saglek Block gneisses. Chem. Geol. 539, 119493. https://doi.org/https://doi.org/10.1016/j.chemgeo.2020.119493

Fisher, C.M., Hanchar, J.M., Samson, S.D., Dhuime, B., Blichert-Toft, J., Vervoort, J.D., Lam, R., 2011. Synthetic zircon doped with hafnium and rare earth elements: A reference material for in situ hafnium isotope analysis. Chem. Geol. 286, 32–47. https://doi.org/10.1016/j.chemgeo.2011.04.013

Fisher, C.M., Vervoort, J.D., Hanchar, J.M., 2014. Guidelines for reporting zircon Hf isotopic data by LA-MC-ICPMS and potential pitfalls in the interpretation of these data. Chem. Geol. 363, 125–133. https://doi.org/10.1016/j.chemgeo.2013.10.019

Fitoussi, C., Bourdon, B., 2012. Silicon isotope evidence against an enstatite chondrite earth. Science (80-.). 335, 1477–1480. https://doi.org/10.1126/science.1219509

Flanagan, F.J., 1986. Reference Samples in Geology and Geochemistry. Geostand. Newsl. 10, 195–264. https://doi.org/https://doi.org/10.1111/j.1751-908X.1986.tb00828.x

François, C., Pubellier, M., Robert, C., Bulois, C., Jamaludin, S.N.F., Oberhänsli, R., Faure, M., St-Onge, M.R., 2022. Temporal and spatial evolution of orogens: a guide for geological mapping. Episodes. https://doi.org/10.18814/epiiugs/2021/021025

Frost, B.R., Barnes, C.G., Collins, W.J., Arculus, R.J., Ellis, D.J., Frost, C.D., 2001. A geochemical classification for granitic rocks. J. Petrol. 42, 2033–2048. https://doi.org/10.1093/petrology/42.11.2033

Frost, C.D., Mueller, P.A., Mogk, D.W., Frost, B.R., Henry, D.J., 2023. Creating Continents: Archean Cratons Tell the Story. GSA Today 33, 4–10. https://doi.org/10.1130/GSATG541A.1

Gain, S.E.M., Gréau, Y., Henry, H., Belousova, E., Dainis, I., Griffin, W.L., O'Reilly, S.Y., 2019. Mud Tank Zircon: Long-Term Evaluation of a Reference Material for U-Pb Dating, Hf-Isotope Analysis and Trace Element Analysis. Geostand. Geoanalytical Res. 43, 339–354. https://doi.org/10.1111/ggr.12265

Gao, M., Zhang, Z.-J., Cheng, Q.-M., Grujic, D., Santosh, M., 2022. Paleoproterozoic TTG gneisses and granites of the Huai'an Complex: Geochemical and zircon U-Pb-Hf data provide insights into subduction history and crustal growth. Precambrian Res. 380, 106823. https://doi.org/https://doi.org/10.1016/j.precamres.2022.106823

Geisler, T., Schaltegger, U., Tomaschek, F., 2007. Re-equilibration of zircon in aqueous fluids and melts. Elements 3, 43–50. https://doi.org/10.2113/gselements.3.1.43

Georg, R.B., Reynolds, B.C., Frank, M., Halliday, A.N., 2006. New sample preparation techniques for the determination of Si isotopic compositions using MC-ICPMS. Chem. Geol. 235, 95–104. https://doi.org/10.1016/j.chemgeo.2006.06.006

Georg, R.B., West, A.J., Basu, A.R., Halliday, A.N., 2009. Silicon fluxes and isotope composition of direct groundwater discharge into the Bay of Bengal and the effect on the global ocean silicon isotope budget. Earth Planet. Sci. Lett. 283, 67–74. https://doi.org/https://doi.org/10.1016/j.epsl.2009.03.041

Gerdes, A., Zeh, A., 2009. Zircon formation versus zircon alteration - New insights from combined U-Pb and Lu-Hf in-situ LA-ICP-MS analyses, and consequences for the interpretation of Archean zircon from the Central Zone of the Limpopo Belt. Chem. Geol. 261, 230–243. https://doi.org/10.1016/j.chemgeo.2008.03.005

Gerya, T. V., Meilick, F.I., 2011. Geodynamic regimes of subduction under an active margin: effects of rheological weakening by fluids and melts. J. Metamorph. Geol. 29, 7–31. https://doi.org/https://doi.org/10.1111/j.1525-1314.2010.00904.x

Gerya, T., 2014. Precambrian geodynamics: Concepts and models. Gondwana Res. 25, 442–463. https://doi.org/10.1016/j.gr.2012.11.008

Gibson, G.M., Champion, D.C., Doublier, M.P., 2024. The Paleoproterozoic Trans-Australian Orogen: Its magmatic and tectonothermal record, links to northern Laurentia, and

implications for supercontinent assembly. Geol. Soc. Am. Bull. 1–27. https://doi.org/10.1130/B36255.1

Green, T.H., 1977. Garnet in silicic liquids and its possible use as a P-T indicator. Contrib. to Mineral. Petrol. 65, 59–67. https://doi.org/10.1007/BF00373571

Grimes, C.B., Wooden, J.L., Cheadle, M.J., John, B.E., 2015. "Fingerprinting" tectono-magmatic provenance using trace elements in igneous zircon. Contrib. to Mineral. Petrol. 170, 1–26. https://doi.org/10.1007/s00410-015-1199-3

Guitreau, M., Blichert-Toft, J., 2014. Implications of discordant U-Pb ages on Hf isotope studies of detrital zircons. Chem. Geol. 385, 17–25. https://doi.org/10.1016/j.chemgeo.2014.07.014

Guitreau, M., Blichert-Toft, J., Martin, H., Mojzsis, S.J., Albarède, F., 2012. Hafnium isotope evidence from Archean granitic rocks for deep-mantle origin of continental crust. Earth Planet. Sci. Lett. 337–338, 211–223. https://doi.org/10.1016/j.epsl.2012.05.029

Guitreau, M., Blichert-Toft, J., Mojzsis, S.J., Roth, A.S.G., Bourdon, B., Cates, N.L., Bleeker, W., 2014. Lu-Hf isotope systematics of the Hadean-Eoarchean Acasta Gneiss Complex (Northwest Territories, Canada). Geochim. Cosmochim. Acta 135, 251–269. https://doi.org/10.1016/j.gca.2014.03.039

Guitreau, M., Boyet, M., Paquette, J.L., Gannoun, A., Konc, Z., Benbakkar, M., Suchorski, K., Hénot, J.M., 2019. Hadean protocrust reworking at the origin of the Archean Napier Complex (Antarctica). Geochemical Perspect. Lett. 12, 7–11. https://doi.org/10.7185/GEOCHEMLET.1927

Guitreau, M., Gannoun, A., Deng, Z., Chaussidon, M., Moynier, F., Barbarin, B., Marin-Carbonne, J., 2022. Stable isotope geochemistry of silicon in granitoid zircon. Geochim. Cosmochim. Acta 316, 273–294. https://doi.org/10.1016/j.gca.2021.09.029

Guitreau, M., Gannoun, A., Deng, Z., Marin-Carbonne, J., Chaussidon, M., Moynier, F., 2020. Silicon isotope measurement in zircon by laser ablation multiple collector inductively coupled plasma mass spectrometry. J. Anal. At. Spectrom. 35, 1597–1606. https://doi.org/10.1039/d0ja00214c

Guitreau, M., Mukasa, S.B., Loudin, L., Krishnan, S., 2017. New constraints on the early formation of the Western Dharwar Craton (India) from igneous zircon U-Pb and Lu-Hf isotopes. Precambrian Res. 302, 33–49. https://doi.org/https://doi.org/10.1016/j.precamres.2017.09.016

Guo, Z., Wilson, M., 2012. The Himalayan leucogranites: Constraints on the nature of their crustal source region and geodynamic setting. Gondwana Res. 22, 360–376. https://doi.org/10.1016/j.gr.2011.07.027

Harris, N.B.W., Inger, S., 1992. Trace element modelling of pelite-derived granites. Contrib. to Mineral. Petrol. 110, 46–56. https://doi.org/10.1007/BF00310881

Hawkesworth, C.J., Cawood, P.A., Dhuime, B., 2020. The Evolution of the Continental Crust and the Onset of Plate Tectonics. Front. Earth Sci. 8. https://doi.org/10.3389/feart.2020.00326

Hawkesworth, C.J., Kemp, A.I.S., 2006. Using hafnium and oxygen isotopes in zircons to unravel the record of crustal evolution. Chem. Geol. 226, 144–162. https://doi.org/https://doi.org/10.1016/j.chemgeo.2005.09.018

Hayden, L.A., Watson, E.B., Wark, D.A., 2008. A thermobarometer for sphene (titanite). Contrib. to Mineral. Petrol. 155, 529–540. https://doi.org/10.1007/s00410-007-0256-y

He, D., Lee, C.-T.A., Yu, X., Farner, M., 2019. Ge/Si Partitioning in Igneous Systems: Constraints From Laser Ablation ICP-MS Measurements on Natural Samples. Geochemistry, Geophys. Geosystems 20, 4472–4486. https://doi.org/https://doi.org/10.1029/2019GC008514

Heilbron, M., Cordani, U.G., Alkmim, F.F., 2017. São Francisco Craton, Eastern Brazil. Reg. Geol. Rev. 326. https://doi.org/10.1007/978-3-319-01715-0

Heilbron, M., Duarte, B.P., Valeriano, C. de M., Simonetti, A., Machado, N., Nogueira, J.R., 2010. Evolution of reworked Paleoproterozoic basement rocks within the Ribeira belt (Neoproterozoic), SE-Brazil, based on U-Pb geochronology: Implications for paleogeographic reconstructions of the São Francisco-Congo paleocontinent. Precambrian Res. 178, 136–148. https://doi.org/10.1016/j.precamres.2010.02.002

Heilbron, M., Ribeiro, A., Valeriano, C.M., Paciullo, F. V, Almeida, J.C.H., Trouw, R.J.A., Tupinambá, M., Eirado Silva, L.G., 2017. The Ribeira Belt BT - São Francisco Craton, Eastern Brazil: Tectonic Genealogy of a Miniature Continent, in: Heilbron, M., Cordani, U.G., Alkmim, F.F. (Eds.), . Springer International Publishing, Cham, pp. 277–302. https://doi.org/10.1007/978-3-319-01715-0_15

Hiess, J., Condon, D.J., McLean, N., Noble, S.R., 2012. 238U/235U Systematics in Terrestrial Uranium-Bearing Minerals. Science (80-.). 335, 1610–1614. https://doi.org/10.1126/science.1215507

Hoffmann, J.E., Münker, C., Næraa, T., Rosing, M.T., Herwartz, D., Garbe-Schönberg, D., Svahnberg, H., 2011. Mechanisms of Archean crust formation inferred from high-precision HFSE systematics in TTGs. Geochim. Cosmochim. Acta 75, 4157–4178. https://doi.org/10.1016/j.gca.2011.04.027

Holland, H.D., 2006. The oxygenation of the atmosphere and oceans. Philos. Trans. R. Soc. B Biol. Sci. 361, 903–915. https://doi.org/10.1098/rstb.2006.1838

Holland, T., Blundy, J., 1994. Non-ideal interactions in calcic amphiboles and their bearing on amphibole-plagioclase thermometry. Contrib. to Mineral. Petrol. 116, 433–447. https://doi.org/10.1007/BF00310910

Hopkinson, T.N., Harris, N.B.W., Warren, C.J., Spencer, C.J., Roberts, N.M.W., Horstwood, M.S.A., Parrish, R.R., EIMF, 2017. The identification and significance of pure sediment-derived granites. Earth Planet. Sci. Lett. 467, 57–63. https://doi.org/10.1016/j.epsl.2017.03.018

Hoskin, P.W.O., Schaltegger, U., 2003. The Composition of Zircon and Igneous and Metamorphic Petrogenesis. Rev. Mineral. Geochemistry 53, 27–62. https://doi.org/10.2113/0530027

Hughes, H.J., Sondag, F., Cocquyt, C., Laraque, A., Pandi, A., André, L., Cardinala, D., 2011. Effect of seasonal biogenic silica variations on dissolved silicon fluxes and isotopic signatures in the Congo River. Limnol. Oceanogr. 56, 551–561. https://doi.org/10.4319/lo.2011.56.2.0551

Ickert, R.B., 2013. Algorithms for estimating uncertainties in initial radiogenic isotope ratios and model ages. Chem. Geol. 340, 131–138. https://doi.org/https://doi.org/10.1016/j.chemgeo.2013.01.001

Iizuka, T., Yamaguchi, T., Hibiya, Y., Amelin, Y., 2015. Meteorite zircon constraints on the bulk Lu−Hf isotope composition and early differentiation of the Earth. Proc. Natl. Acad. Sci. 112, 5331–5336. https://doi.org/10.1073/pnas.1501658112

Jacob, J.-B., Moyen, J.-F., Fiannacca, P., Laurent, O., Bachmann, O., Janoušek, V., Farina, F., Villaros, A., 2021. Crustal melting vs. fractionation of basaltic magmas: Part 2, Attempting to quantify mantle and crustal contributions in granitoids. Lithos 402–403. https://doi.org/10.1016/j.lithos.2021.106292

Jaffey, A.H., Flynn, K.F., Glendenin, L.E., Bentley, W.C., Essling, A.M., 1971. Precision Measurement of Half-Lives and Specific Activities of 235U and 238U. Phys. Rev. C 4, 1889–1906. https://doi.org/10.1103/PhysRevC.4.1889

Jahn, B.-M., Glikson, A.Y., Peucat, J.J., Hickman, A.H., 1981. REE geochemistry and isotopic data of Archean silicic volcanics and granitoids from the Pilbara Block, Western Australia: implications for the early crustal evolution. Geochim. Cosmochim. Acta 45, 1633–1652. https://doi.org/https://doi.org/10.1016/S0016-7037(81)80002-6

Janoušek, V., Moyen, J.-F., Martin, H., Erban, V., Farrow, C., 2016. Geochemical Modelling of Igneous Processes – Principles And Recipes in R Language, Geochemical Modelling of Igneous Processes – Principles And Recipes in R Language. https://doi.org/10.1007/978-3-662-46792-3

Jayananda, M., Guitreau, M., Aadhiseshan, K.R., Miyazaki, T., Chung, S.L., 2023. Origin of the oldest (3600–3200 Ma) cratonic core in the Western Dharwar Craton, Southern India: Implications for evolving tectonics of the Archean Earth. Earth-Science Rev. 236, 104278. https://doi.org/https://doi.org/10.1016/j.earscirev.2022.104278

Jochum, K.P., Weis, U., Stoll, B., Kuzmin, D., Yang, Q., Raczek, I., Jacob, D.E., Stracke, A., Birbaum, K., Frick, D.A., Günther, D., Enzweiler, J., 2011. Determination of Reference Values for NIST SRM 610–617 Glasses Following ISO Guidelines. Geostand. Geoanalytical Res. 35, 397–429. https://doi.org/https://doi.org/10.1111/j.1751-908X.2011.00120.x

Keller, C.B., Schoene, B., 2012. Statistical geochemistry reveals disruption in secular lithospheric evolution about 2.5 Gyr ago. Nature 485, 490–493. https://doi.org/10.1038/nature11024

Kemp, A.I.S., Hawkesworth, C.J., 2014. Growth and Differentiation of the Continental Crust from Isotope Studies of Accessory Minerals, in: Holland, H.D., Turekian, K.K.B.T.-T. on G. (Second E. (Eds.), . Elsevier, Oxford, pp. 379–421. https://doi.org/https://doi.org/10.1016/B978-0-08-095975-7.00312-0

Kemp, A.I.S., Hawkesworth, C.J., Foster, G.L., Paterson, B.A., Woodhead, J.D., Hergt, J.M., Gray, C.M., Whitehouse, M.J., 2007. Magmatic and Crustal Differentiation History of Granitic Rocks from Hf-O Isotopes in Zircon. Science (80-.). 315, 980–983. https://doi.org/10.1126/science.1136154

Kendrick, J., Duguet, M., Yakymchuk, C., 2022. Diversification of Archean tonalite-trondhjemite-granodiorite suites in a mushy middle crust. Geology 50, 76–80. https://doi.org/10.1130/G49287.1

Kinny, P.D., Compston, W., Williams, I.S., 1991. A reconnaissance ion-probe study of hafnium isotopes in zircons. Geochim. Cosmochim. Acta 55, 849–859. https://doi.org/https://doi.org/10.1016/0016-7037(91)90346-7

Klein, C., 2005. Some Precambrian Banded Iron-Formations (BiIFs) From Around The World: Their Age, Geologic Setting, Mineralogy, Metamorphism, Geochemistry, And Origin. American Mineralogist 90, 1473–1499. https://doi.org/doi:10.2138/am.2005.1871

Kleine, B.I., Stefánsson, A., Halldórsson, S.A., Whitehouse, M.J., Jónasson, K., 2018. Silicon and oxygen isotopes unravel quartz formation processes in the Icelandic crust. Geochemical Perspect. Lett. 7, 5–11. https://doi.org/10.7185/geochemlet.1811

Košler, J., Sylvester, P.J., 2003. Present Trends and the Future of Zircon in Geochronology: Laser Ablation ICPMS. Rev. Mineral. Geochemistry 53, 243–275. https://doi.org/10.2113/0530243

Kranendonk, M.J. van, Bennett, V., Hoffmann, E. (Eds.), 2019. Earth's Oldest Rocks, 2nd ed. Elsevier.

Lacerda, S., Guitreau, M., Gonçalves, L., Moreira, H., Gonçalves, C.C., Pinheiro, M.A., Castro, C.C. e., Doucelance, R., 2024. Paleoproterozoic sediment-derived magmas reveal a late orogenic stage in the southern São Francisco Craton, Brazil: Evidence from petrogenesis of the 2.0 Ga Cupim Pluton leucogranites. Lithos 490–491. https://doi.org/10.1016/j.lithos.2024.107852

Lacerda, S.G., Soares, W., Gonçalves, L., Gonçalves, C., Marco, Pinheiro, A., 2021. Petrografia e geoquímica do granitoide Cupim: implicações de leucogranitos peraluminosos na porção setentrional do Cinturão Mineiro, sul do Cráton São Francisco, Minas Gerais, Brasil., in: Geologia, S.B. de (Ed.), Contribuições à Ciência e Técnica Dos(as) Jovens Geólogos(as) Brasileiros(As). Brasilia, pp. 104–118.

Lana, C., Alkmim, F.F., Armstrong, R., Scholz, R., Romano, R., Nalini, H.A., 2013. The ancestry and magmatic evolution of Archaean TTG rocks of the Quadrilátero Ferrífero province, southeast Brazil. Precambrian Res. 231, 157–173. https://doi.org/10.1016/j.precamres.2013.03.008

Lana, C., Gonçalves, G.O., Mazoz, A., Buick, I., Kamo, S., Scholz, R., Wang, H., Moreira, H., Babinski, M., Queiroga, G., 2022. Assessing the U-Pb, Sm-Nd and Sr-Sr Isotopic Compositions of the Sumé Apatite as a Reference Material for LA-ICP-MS Analysis. Geostand. Geoanalytical Res. 46, 71–95. https://doi.org/10.1111/ggr.12413

Laurent, O., Björnsen, J., Wotzlaw, J.F., Bretscher, S., Pimenta Silva, M., Moyen, J.F., Ulmer, P., Bachmann, O., 2020a. Earth's earliest granitoids are crystal-rich magma reservoirs tapped by silicic eruptions. Nat. Geosci. 13, 163–169. https://doi.org/10.1038/s41561-019-0520-6

Laurent, O., Guitreau, M., Bruand, E., Moyen, J.F., 2024. At the Dawn of Continents: Archean Tonalite-Trondhjemite-Granodiorite Suites. Elements 20, 174–179. https://doi.org/10.2138/gselements.20.3.174

Laurent, O., Martin, H., Moyen, J.F., Doucelance, R., 2014. The diversity and evolution of late-Archean granitoids: Evidence for the onset of "modern-style" plate tectonics between 3.0 and 2.5 Ga. Lithos 205, 208–235. https://doi.org/10.1016/j.lithos.2014.06.012

Laurent, O., Moyen, J.-F., Wotzlaw, J.-F., Björnsen, J., Bachmann, O., 2021. Early Earth zircons formed in residual granitic melts produced by tonalite differentiation. Geology. https://doi.org/10.1130/g49232.1

Laurent, O., Moyen, J.-F., Wotzlaw, J.-F., Björnsen, J., Bachmann, O., 2020b. Early Earth zircons formed in residual granitic melts produced by tonalite differentiation. Geology 50, 437–441. https://doi.org/10.1130/G49232.1

Laurent, O., Zeh, A., 2015. A linear Hf isotope-age array despite different granitoid sources and complex Archean geodynamics: Example from the Pietersburg block (South Africa). Earth Planet. Sci. Lett. 430, 326–338. https://doi.org/10.1016/j.epsl.2015.08.028

Le Maitre, R.W., Bateman, P., Bonin, B., Le Bas, M.J., Streckeisen, A., Zanettin, B. (Eds.), 2002. Classification and nomenclature, in: Igneous Rocks: A Classification and Glossary of Terms: Recommendations of the International Union of Geological Sciences Subcommission on the Systematics of Igneous Rocks. Cambridge University Press, Cambridge, pp. 3–42. https://doi.org/DOI: 10.1017/CBO9780511535581.006

Leake, B.E., Woolley, A.R., Arps, C.E.S., Birch, W.D., Gilbert, M.C., Grice, J.D., Hawthorne, F.C., Kato, A., Kisch, H.J., Krivovichev, V.G., Linthout, K., Laird, J., Mandarino, J., Maresch, W. V, Nickel, E.H., Rock, N.M.S., Schumacher, J.C., Smith, D.C., Stephenson, N.C.N., Ungaretti, L., Whittaker, E.J.W., Youzhi, G., 1997. Nomenclature of Amphiboles; Report of the Subcommittee on Amphiboles of the International Mineralogical Association Commission on New Minerals and Mineral Names. Mineral. Mag. 61, 295–310. https://doi.org/DOI: 10.1180/minmag.1997.061.405.13

Lei, K., Zhang, Q., Liu, Y., Lu, K., Wu, L.G., He, S., Li, X.H., 2023. Heavy silicon and oxygen isotope signatures of TTGs formed in distinct tectonic settings. Precambrian Res. 397, 107202. https://doi.org/10.1016/j.precamres.2023.107202

Leitzke, F.P., Pakulla, J.J., Tusch, J., Ravindran, A., Gordilho-Barbosa, R., Zincone, S.A., Hellers, M., Martins, A.A., Spreafico, R.R., Yang, R., Wombacher, F., Barbosa, J.S.F., Münker, C., 2024. Evidence for a missing late veneer from 182W and 142Nd systematics in the Archean São Francisco Craton. Earth Planet. Sci. Lett. 647, 119022. https://doi.org/https://doi.org/10.1016/j.epsl.2024.119022

Li, J., Liu, H., Wang, K., Cai, W., 2020a. Paleoproterozoic adakitic rocks in qingchengzi district, northeastern jiao-liao-ji belt: Implications for petrogenesis and tectonism. Minerals 10, 1–17. https://doi.org/10.3390/min10080684

Li, X., Zhang, C., Behrens, H., Holtz, F., 2020b. Calculating amphibole formula from electron microprobe analysis data using a machine learning method based on principal components regression. Lithos 362–363, 105469. https://doi.org/https://doi.org/10.1016/j.lithos.2020.105469

Liou, P., Guo, J., 2019. Generation of Archaean TTG Gneisses Through Amphibole-Dominated Fractionation. J. Geophys. Res. Solid Earth 124, 3605–3619. https://doi.org/10.1029/2018JB017024

Lopes, S.R., Gonçalves, L., Gonçalves, C.C., Moreira, H., Lacerda, S., Armond, P.V., 2024. Diversity of Siderian magmatic pulses revealed by intracrustal melting of oceanic crust in the Mineiro Belt, southern São Francisco Craton. Lithos 488–489, 107806. https://doi.org/https://doi.org/10.1016/j.lithos.2024.107806

Luhr, J.F., Carmichael, I.S.E., Varekamp, J.C., 1984. The 1982 eruptions of El Chichón Volcano, Chiapas, Mexico: Mineralogy and petrology of the anhydritebearing pumices. J. Volcanol. Geotherm. Res. 23, 69–108. https://doi.org/https://doi.org/10.1016/0377-0273(84)90057-X

Ma, Q., Evans, N.J., Ling, X.X., Yang, J.H., Wu, F.Y., Zhao, Z.D., Yang, Y.H., 2019. Natural Titanite Reference Materials for In Situ U-Pb and Sm-Nd Isotopic Measurements by LA-(MC)-ICP-MS. Geostand. Geoanalytical Res. 43, 355–384. https://doi.org/10.1111/ggr.12264

Machado, N., Carneiro, M., 1992. U–Pb evidence of late Archean tectono-thermal activity in the southern São Francisco shield, Brazil. Can. J. Earth Sci. 29, 2341–2346. https://doi.org/10.1139/e92-182

Maierová, P., Schulmann, K., Gerya, T., 2025. Numerical simulations of subduction, relamination and accretion of magmatic arcs – implications for continent-ocean convergent margins. Earth Planet. Sci. Lett. 652. https://doi.org/10.1016/j.epsl.2024.119192

Marimon, R.S., Trouw, R.A.J., Dantas, E.L., 2020. Significance of age periodicity in the continental crust record: The São Francisco Craton and adjacent Neoproterozoic orogens as a case study. Gondwana Res. https://doi.org/10.1016/j.gr.2020.05.010

Martin, H., 1987. Petrogenesis of archaean trondhjemites, tonalites, and granodiorites from Eastern Finland: Major and trace element geochemistry. J. Petrol. 28, 921–953. https://doi.org/10.1093/petrology/28.5.921

Martin, H., Moyen, J.F., Guitreau, M., Blichert-Toft, J., Le Pennec, J.L., 2014. Why Archaean TTG cannot be generated by MORB melting in subduction zones. Lithos 198–199, 1–13. https://doi.org/10.1016/j.lithos.2014.02.017

Martin, H., Moyen, J.F., Rapp, R., 2009. The sanukitoid series: Magmatism at the Archaean-Proterozoic transition, in: Earth and Environmental Science Transactions of the Royal Society of Edinburgh. pp. 15–33. https://doi.org/10.1017/S1755691009016120

Martin, H., Smithies, R.H., Rapp, R., Moyen, J.F., Champion, D., 2005. An overview of adakite, tonalite-trondhjemiten-granodiorite (TTG), and sanukitoid: Relationships and some implications for crustal evolution. Lithos 79, 1–24. https://doi.org/10.1016/j.lithos.2004.04.048

Martínez Dopico, C.I., Lana, C., Moreira, H.S., Cassino, L.F., Alkmim, F.F., 2017. U–Pb ages and Hf-isotope data of detrital zircons from the late Neoarchean-Paleoproterozoic Minas Basin, SE Brazil. Precambrian Res. 291, 143–161. https://doi.org/10.1016/j.precamres.2017.01.026

McLennan, S.M., 2019. Rare earth elements in sedimentary rocks: Influence of provenance and sedimentary processes, in: Geochemistry and Mineralogy of Rare Earth Elements. pp. 169–200.

Moreira, H., Cassino, L., Lana, C., Storey, C., Albert, C., 2019. Insights into orogenic processes from drab schists and minor intrusions: Southern São Francisco Craton, Brazil. Lithos 346–347. https://doi.org/10.1016/j.lithos.2019.07.013

Moreira, H., Seixas, L., Storey, C., Fowler, M., Lasalle, S., Stevenson, R., Lana, C., 2018. Evolution of Siderian juvenile crust to Rhyacian high Ba-Sr magmatism in the Mineiro Belt, southern São Francisco Craton. Geosci. Front. 9, 977–995. https://doi.org/10.1016/j.gsf.2018.01.009

Moreira, H., Storey, C., Bruand, E., Darling, J., Fowler, M., Cotte, M., Villalobos-Portillo, E.E., Parat, F., Seixas, L., Philippot, P., Dhuime, B., 2023. Sub-arc mantle fugacity shifted by sediment recycling across the Great Oxidation Event. Nat. Geosci. 16, 922–927. https://doi.org/10.1038/s41561-023-01258-4

Moreira, H., Storey, C., Fowler, M., Seixas, L., Dunlop, J., 2020. Petrogenetic processes at the tipping point of plate tectonics: Hf-O isotope ternary modelling of Earth's last TTG to sanukitoid transition. Earth Planet. Sci. Lett. 551. https://doi.org/10.1016/j.epsl.2020.116558

Moreira, H.S., 2019. Evolution of the continental crust of central southern Brazil: implications for the onset of subduction-driven plate tectonics. University of Portsmouth.

Moyen, J.-F., 2011. The composite Archaean grey gneisses: Petrological significance, and evidence for a non-unique tectonic setting for Archaean crustal growth. Lithos 123, 21–36. https://doi.org/10.1016/j.lithos.2010.09.015

Moyen, J.-F., Janoušek, V., Laurent, O., Bachmann, O., Jacob, J.-B., Farina, F., Fiannacca, P., Villaros, A., 2021. Crustal melting vs. fractionation of basaltic magmas: Part 1, granites and paradigms. Lithos 402–403. https://doi.org/10.1016/j.lithos.2021.106291

Moyen, J.-F., Laurent, O., Chelle-Michou, C., Couzinié, S., Vanderhaeghe, O., Zeh, A., Villaros, A., Gardien, V., 2017. Collision vs. subduction-related magmatism: Two contrasting ways of granite formation and implications for crustal growth. Lithos 277, 154–177. https://doi.org/10.1016/j.lithos.2016.09.018

Moyen, J.-F., Martin, H., 2012. Forty years of TTG research. Lithos 148. https://doi.org/10.1016/j.lithos.2012.06.010

Moyen, J.-F., Stevens, G., Kisters, A.F.M., Belcher, R.W., Lemirre, B., 2019. TTG Plutons of the Barberton Granitoid-Greenstone Terrain, South Africa, in: Earth's Oldest Rocks. Elsevier, pp. 615–653. https://doi.org/10.1016/B978-0-444-63901-1.00025-3

Moyen, J-F., Laurent, O., 2018. Archaean tectonic systems: A view from igneous rocks. Lithos. https://doi.org/10.1016/j.lithos.2017.11.038

Moyen, J-F., Stevens, G., 2006. Experimental constraints on TTG petrogenesis: Implications for archean geodynamics. Geophys. Monogr. Ser. 164, 149–175. https://doi.org/10.1029/164GM11

Murphy, M.E., Macdonald, J.E., Fischer, S., Gardiner, N.J., White, R.W., Savage, P.S., 2024. Silicon isotopes in an Archaean migmatite confirm seawater silicification of TTG sources. Geochim. Cosmochim. Acta 368, 34–49. https://doi.org/10.1016/j.gca.2024.01.018

Nabelek, P.I., 2020. Petrogenesis of leucogranites in collisional orogens. Geol. Soc. Spec. Publ. 491, 179–207. https://doi.org/10.1144/SP491-2018-181

Nahas, I., Gonçalves, L., Gonçalves, C.C., Raposo, M.I.B., 2023. Unraveling the relationship between a tonalitic pluton and shear zones: Insights from magnetic fabrics and microstructures of the Alto Maranhão batholith, Mineiro belt, southern São Francisco craton. J. Struct. Geol. 172, 104887. https://doi.org/https://doi.org/10.1016/j.jsg.2023.104887

Noce, C.M., 1995. Geocronologia dos eventos magmáticos, sedimentares e metamórficos na região do Quadrilátero Ferrífero, Minas Gerais. Universidade de Sao Paulo. https://doi.org/https://doi.org/10.11606/T.44.2016.tde-05012016-154125

Noce, C.M., Machado, N., Teixeira, W., 1998. U-Pb geochronology of gneisses and granitoids in the Quadrilátero Ferrífero (southern São Francisco craton): age constraints for archean and paleoproterozoic magmatism and metamorphism. Rev. Bras. Geociências 28, 95–102. https://doi.org/10.25249/0375-7536.199895102

Noce, C.M., Pedrosa-Soares, A.C., da Silva, L.C., Armstrong, R., Piuzana, D., 2007. Evolution of polycyclic basement complexes in the Araçuaí Orogen, based on U-Pb SHRIMP data: Implications for Brazil-Africa links in Paleoproterozoic time. Precambrian Res. 159, 60–78. https://doi.org/10.1016/j.precamres.2007.06.001

Noce, C.M., Teixeira, W., Quéméneur, J.J.G., Martins, V.T.S., Bolzachini, É., 2000. Isotopic signatures of Paleoproterozoic granitoids from the southern São Francisco Craton and implications for

the evolution of the Transamazonian Orogeny. J. South Am. Earth Sci. 13, 225–239. https://doi.org/https://doi.org/10.1016/S0895-9811(00)00019-5

O'Connor, J.T., 1965. A classification of quartz-rich igneous rocks based on feldspar ratios.

O'Neill, C., Turner, S., Rushmer, T., 2018. The inception of plate tectonics: a record of failure. Philos. Trans. R. Soc. A Math. Phys. Eng. Sci. 376, 20170414. https://doi.org/10.1098/rsta.2017.0414

O'Sullivan, G., Chew, D., Kenny, G., Henrichs, I., Mulligan, D., 2020. The trace element composition of apatite and its application to detrital provenance studies. Earth-Science Rev. 201, 103044. https://doi.org/10.1016/j.earscirev.2019.103044

Olierook, H.K.H., Taylor, R.J.M., Erickson, T.M., Clark, C., Reddy, S.M., Kirkland, C.L., Jahn, I., Barham, M., 2019. Unravelling complex geologic histories using U–Pb and trace element systematics of titanite. Chem. Geol. 504, 105–122. https://doi.org/10.1016/j.chemgeo.2018.11.004

Oliveira, E.P., McNaughton, N.J., Zincone, S.A., Talavera, C., 2020. Birthplace of the São Francisco Craton, Brazil: Evidence from 3.60 to 3.64 Ga Gneisses of the Mairi Gneiss Complex. Terra Nov. 32, 281–289. https://doi.org/10.1111/ter.12460

Opfergelt, S., Cardinal, D., André, L., Delvigne, C., Bremond, L., Delvaux, B., 2010. Variations of δ30Si and Ge/Si with weathering and biogenic input in tropical basaltic ash soils under monoculture. Geochim. Cosmochim. Acta 74, 225–240. https://doi.org/10.1016/j.gca.2009.09.025

Paces, J.B., Miller Jr., J.D., 1993. Precise U-Pb ages of Duluth Complex and related mafic intrusions, northeastern Minnesota: Geochronological insights to physical, petrogenetic, paleomagnetic, and tectonomagmatic processes associated with the 1.1 Ga Midcontinent Rift System. J. Geophys. Res. Solid Earth 98, 13997–14013. https://doi.org/https://doi.org/10.1029/93JB01159

Palin, R.M., Santosh, M., Cao, W., Li, S.-S., Hernández-Uribe, D., Parsons, A., 2020. Secular change and the onset of plate tectonics on Earth. Earth-Science Rev. 207, 103172. https://doi.org/https://doi.org/10.1016/j.earscirev.2020.103172

Palin, R.M., White, R.W., Green, E.C.R., 2016. Partial melting of metabasic rocks and the generation of tonalitic–trondhjemitic–granodioritic (TTG) crust in the Archaean: Constraints from phase equilibrium modelling. Precambrian Res. 287, 73–90. https://doi.org/10.1016/j.precamres.2016.11.001

Patchett, P.J., 1983. Importance of the Lu-Hf isotopic system in studies of planetary chronology and chemical evolution. Geochim. Cosmochim. Acta 47, 81–91. https://doi.org/https://doi.org/10.1016/0016-7037(83)90092-3

Patiño Douce, A.E., Harris, N., 1998. Experimental constraints on Himalayan anatexis. J. Petrol. 39, 689–710. https://doi.org/10.1093/petroj/39.4.689

Patiño Douce, A.E., Johnston, A.D., 1991. Phase equilibria and melt productivity in the pelitic system: implications for the origin of peraluminous granitoids and aluminous granulites. Contrib. to Mineral. Petrol. 107, 202–218. https://doi.org/10.1007/BF00310707

Paton, C., Hellstrom, J., Paul, B., Woodhead, J., Hergt, J., 2011. Iolite: Freeware for the visualisation and processing of mass spectrometric data. J. Anal. At. Spectrom. 26, 2508–2518. https://doi.org/10.1039/C1JA10172B

Pearce, J.A., Harris, N.B.W., Tindle, A.G., 1984. Trace Element Discrimination Diagrams for the Tectonic Interpretation of Granitic Rocks. J. Petrol. 25, 956–983. https://doi.org/10.1093/petrology/25.4.956

Penaye, J., Toteu, S.F., Tchameni, R., Van Schmus, W.R., Tchakounté, J., Ganwa, A., Minyem, D., Nsifa, E.N., 2004. The 2.1 Ga West Central African Belt in Cameroon: Extension and evolution. J. African Earth Sci. 39, 159–164. https://doi.org/10.1016/j.jafrearsci.2004.07.053

Perchuk, A.L., Gerya, T. V., Zakharov, V.S., Griffin, W.L., 2020. Building cratonic keels in Precambrian plate tectonics. Nature 586, 395–401. https://doi.org/10.1038/s41586-020-2806-7

Pereira, I., Storey, C., Darling, J., Lana, C., Alkmim, A.R., 2019. Two billion years of evolution enclosed in hydrothermal rutile: Recycling of the São Francisco Craton Crust and constraints on gold remobilisation processes. Gondwana Res. 68, 69–92. https://doi.org/10.1016/j.gr.2018.11.008

Petrus, J.A., Kamber, B.S., 2012. VizualAge: A Novel Approach to Laser Ablation ICP-MS U-Pb Geochronology Data Reduction. Geostand. Geoanalytical Res. 36, 247–270. https://doi.org/https://doi.org/10.1111/j.1751-908X.2012.00158.x

Pinheiro, M.A.P., Ávila, C.A., Bongiolo, E.M., Magalhães, J.R., Vilela, F.T., Tedeschi, M.F., 2021. Reavaliação do potencial mineral das sequências metavulcanossedimentares a sudoeste do Quadrilátero Ferrífero – área de Nazareno- MG: texto e mapa geológico integrado, escala 1: 100.000. Belo Horizonte. https://doi.org/978-65-5664-028-0.

Pitcher, W.S., 1997. The Nature and Origin of Granite, 2nd ed. Springer Dordrecht. https://doi.org/https://doi.org/10.1007/978-94-011-5832-9

Poitrasson, F., Zambardi, T., 2015. An Earth-Moon silicon isotope model to track silicic magma origins. Geochim. Cosmochim. Acta 167, 301–312.

Poitrasson, F., 2017. Silicon Isotope Geochemistry. Rev. Mineral. Geochemistry 82, 289–344. https://doi.org/10.2138/rmg.2017.82.8

Poujol, M., Jaguin, J., Moyen, J.-F., Boulvais, P., Paquette, J.-L., 2021. Archaean S-Type granites: petrology, geochemistry and geochronology of the Lekkersmaak and Willie plutons, Kaapvaal Craton, South Africa. South African J. Geol. 124, 87–110. https://doi.org/10.25131/sajg.124.0004

Pourteau, A., Doucet, L.S., Blereau, E.R., Volante, S., Johnson, T.E., Collins, W.J., Li, Z.X., Champion, D.C., 2020. TTG generation by fluid-fluxed crustal melting: Direct evidence from the Proterozoic Georgetown Inlier, NE Australia. Earth Planet. Sci. Lett. 550. https://doi.org/10.1016/j.epsl.2020.116548

Pringle, E.A., Moynier, F., Savage, P.S., Jackson, M.G., Moreira, M., Day, J.M.D., 2016. Silicon isotopes reveal recycled altered oceanic crust in the mantle sources of Ocean Island Basalts. Geochim. Cosmochim. Acta 189, 282–295. https://doi.org/10.1016/j.gca.2016.06.008

Rapp, R.P., Watson, E.B., Miller, C.F., 1991. Partial melting of amphibolite/eclogite and the origin of Archean trondhjemites and tonalites. Precambrian Res. 51, 1–25. https://doi.org/https://doi.org/10.1016/0301-9268(91)90092-O

Rasmussen, B., Krapež, B., Muhling, J.R., Suvorova, A., 2015. Precipitation of iron silicate nanoparticles in early Precambrian oceans marks Earth's first iron age. Geology 43, 303–306. https://doi.org/10.1130/G36309.1

Roberts, N.M.W., Hernández-Montenegro, J.D., Palin, R.M., 2024. Garnet stability during crustal melting: Implications for chemical mohometry and secular change in arc magmatism and continent formation. Chem. Geol. 659. https://doi.org/10.1016/j.chemgeo.2024.122142

Roberts, N.M.W., Spencer, C.J., 2015. The zircon archive of continent formation through time. Geol. Soc. London, Spec. Publ. 389, 197–225. https://doi.org/10.1144/SP389.14

Rollinson, H., Pease, V., 2021. Using Geochemical Data, in: Using Geochemical Data: To Understand Geological Processes. Cambridge University Press, Cambridge.

Rollinson, H., Pease, V., 2021. Using Geochemical Data: To Understand Geological Processes. Using Geochemical Data To Understand Geol. Process.

Roman, A., Arndt, N., 2020. Differentiated Archean oceanic crust: Its thermal structure, mechanical stability and a test of the sagduction hypothesis. Geochim. Cosmochim. Acta 278, 65–77. https://doi.org/10.1016/j.gca.2019.07.009

Romano, R., Lana, C., Alkmim, F.F., Stevens, G., Armstrong, R., 2013. Stabilization of the southern portion of the São Francisco craton, SE Brazil, through a long-lived period of potassic magmatism. Precambrian Res. 224, 143–159. https://doi.org/10.1016/j.precamres.2012.09.002

Sampaio, G.M.S., Pufahl, P.K., Raye, U., Kyser, K.T., Abreu, A.T., Alkmim, A.R., Nalini, H.A., 2018. Influence of weathering and hydrothermal alteration on the REE and δ56Fe composition of iron formation, Cauê Formation, Iron Quadrangle, Brazil. Chem. Geol. 497, 27–40. https://doi.org/10.1016/j.chemgeo.2018.08.014

Sant'Anna Neves, C.V. de, Ávila, C.A., Bongiolo, E.M., Neumann, R., Teixeira, W., Faulstich, F.R.L., Heilbron, M., Geraldes, M.C., Valeriano, C. de M., 2023. Preserved interactions between acid and intermediate magmas in a 2.15–2.10 Ga Rhyacian continental arc: Insights from

petrographic, geochemical and isotopic data of the Macuco de Minas metagranitoid, Mineiro belt, Brazil. Lithos 440–441. https://doi.org/10.1016/j.lithos.2023.107048

Santos, L.D., Baltazar, O.F., 2013. Carta geológica: folha Conselheiro Lafaiete, SF. 23-XA-VI.

Savage, P. S., Wimpenny, J., Harvey, J., Yin, Q., Moynier, F., 2013. Investigating the effects of abyssal peridotite alteration on Si, Mg and Zn isotopes, in: AGU Fall Meeting Abstracts. AA(Washington University in Saint Louis, Department of Earth and Planetary Science), AB(University of California, Davis, Department of Physics), AC(University of Leeds, School of Earth and Environment), AD(University of California, Davis, Department of Ph, pp. V54A-06.

Savage, P.S., Armytage, R.M.G., Georg, R.B., Halliday, A.N., 2014. High temperature silicon isotope geochemistry. Lithos 190–191, 500–519. https://doi.org/10.1016/j.lithos.2014.01.003

Savage, P.S., Georg, R.B., Armytage, R.M.G., Williams, H.M., Halliday, A.N., 2010. Silicon isotope homogeneity in the mantle. Earth Planet. Sci. Lett. 295, 139–146. https://doi.org/10.1016/j.epsl.2010.03.035

Savage, P.S., Georg, R.B., Williams, H.M., Burton, K.W., Halliday, A.N., 2011. Silicon isotope fractionation during magmatic differentiation. Geochim. Cosmochim. Acta 75, 6124–6139. https://doi.org/10.1016/j.gca.2011.07.043

Savage, P.S., Georg, R.B., Williams, H.M., Halliday, A.N., 2013. The silicon isotope composition of the upper continental crust. Geochim. Cosmochim. Acta 109, 384–399. https://doi.org/10.1016/j.gca.2013.02.004

Savage, P.S., Georg, R.B., Williams, H.M., Turner, S., Halliday, A.N., Chappell, B.W., 2012. The silicon isotope composition of granites. Geochim. Cosmochim. Acta 92, 184–202. https://doi.org/10.1016/j.gca.2012.06.017

Savage, Paul S., Georg, R.B., Williams, H.M., Halliday, A.N., 2013. Silicon isotopes in granulite xenoliths: Insights into isotopic fractionation during igneous processes and the composition of the deep continental crust. Earth Planet. Sci. Lett. 365, 221–231. https://doi.org/10.1016/j.epsl.2013.01.019

Sawyer, E.W., 1987. The role of partial melting and fractional crystallization in determining discordant migmatite leucosome compositions. J. Petrol. 28, 445–473. https://doi.org/10.1093/petrology/28.3.445

Scherer, E., Munker, C., Mezger, K., 2001. Calibration of the lutetium-hafnium clock. Science 293, 683–687. https://doi.org/10.1126/science.1061372

Schmidt, M.W., 1992. Amphibole composition in tonalite as a function of pressure: an experimental calibration of the Al-in-hornblende barometer. Contrib. to Mineral. Petrol. 110, 304–310. https://doi.org/10.1007/BF00310745

Schmitz, M.D., Bowring, S.A., Ireland, T.R., 2003. Evaluation of Duluth Complex anorthositic series (AS3) zircon as a U-Pb geochronological standard: New high-precision isotope dilution

thermal ionization mass spectrometry results. Geochim. Cosmochim. Acta 67, 3665–3672. https://doi.org/10.1016/S0016-7037(03)00200-X

Schoene, B., 2014. U–Th–Pb Geochronology, in: Holland, H.D., Turekian, K.K.B.T.-T. on G. (Second E. (Eds.), . Elsevier, Oxford, pp. 341–378. https://doi.org/https://doi.org/10.1016/B978-0-08-095975-7.00310-7

Segal, I., Halicz, L., Platzner, I.T., 2003. Accurate isotope ratio measurements of ytterbium by multiple collection inductively coupled plasma mass spectrometry applying erbium and hafnium in an improved double external normalization procedure. J. Anal. At. Spectrom. 18, 1217–1223. https://doi.org/10.1039/B307016F

Seixas, L.A.R., Bardintzeff, J.M., Stevenson, R., Bonin, B., 2013. Petrology of the high-Mg tonalites and dioritic enclaves of the ca. 2130Ma Alto Maranhão suite: Evidence for a major juvenile crustal addition event during the Rhyacian orogenesis, Mineiro Belt, southeast Brazil. Precambrian Res. 238, 18–41. https://doi.org/10.1016/j.precamres.2013.09.015

Seixas, L.A.R., 2000. Pétrologie de la suite TTG de la bordure nord du batholite d'Alto Maranhão et du Pluton Congonhas, Minas Gerais, Brésil. Université de Paris-Sud XI.

Seixas, L.A.R., Bonin, B., Stevenson, R., Bardintzeff, J.-M., 2017. The Congonhas Pluton: a new occurrence of orbicular granodiorite, in: Goldschmidt2017. European Association of Geochemistry, Paris.

Seixas, L.A.R., David, J., Stevenson, R., 2012. Geochemistry, Nd isotopes and U–Pb geochronology of a 2350Ma TTG suite, Minas Gerais, Brazil: Implications for the crustal evolution of the southern São Francisco craton. Precambrian Res. 196–197, 61–80. https://doi.org/10.1016/j.precamres.2011.11.002

Shand, S.J., 1943. Eruptive Rocks. Their Genesis Composition. Classification, and Their Relation to Ore-Deposits with a Chapter on Meteorite. John Wiley & Sons, Ltd, New York.

Siever, R., 1992. The silica cycle in the Precambrian. Geochim. Cosmochim. Acta 56, 3265–3272. https://doi.org/https://doi.org/10.1016/0016-7037(92)90303-Z

Silva, M.M., Ávila, C.A., Tavares, F.M., Barbosa, N.S., Teixeira, W., 2021. Genesis of the Gentio Metagranitoid: Post-Collisional High-K Plutonism within the Mineiro Belt, São Francisco Craton, Brazil. J. Earth Sci. 32, 1374–1396. https://doi.org/10.1007/s12583-021-1469-0

Simonson, B.M., 2003. Origin and evolution of large Precambrian iron formations, in: Chan, M.A., Archer, A.W. (Eds.), Extreme Depositional Environments: Mega End Members in Geologic Time. Geological Society of America, p. 0. https://doi.org/10.1130/0-8137-2370-1.231

Sizova, E., Gerya, T., Brown, M., 2014. Contrasting styles of Phanerozoic and Precambrian continental collision. Gondwana Res. 25, 522–545. https://doi.org/10.1016/j.gr.2012.12.011

Sizova, E., Gerya, T., Brown, M., Perchuk, L.L., 2010. Subduction styles in the Precambrian: Insight from numerical experiments. Lithos 116, 209–229. https://doi.org/10.1016/j.lithos.2009.05.028

Sláma, J., Košler, J., Condon, D.J., Crowley, J.L., Gerdes, A., Hanchar, J.M., Horstwood, M.S.A., Morris, G.A., Nasdala, L., Norberg, N., Schaltegger, U., Schoene, B., Tubrett, M.N., Whitehouse, M.J., 2008. Plešovice zircon — A new natural reference material for U–Pb and Hf isotopic microanalysis. Chem. Geol. 249, 1–35. https://doi.org/https://doi.org/10.1016/j.chemgeo.2007.11.005

Smithies, R.H., Champion, D.C., Van Kranendonk, M.J., 2009. Formation of Paleoarchean continental crust through infracrustal melting of enriched basalt. Earth Planet. Sci. Lett. 281, 298–306. https://doi.org/10.1016/j.epsl.2009.03.003

Smithies, R.H., Lu, Y., Johnson, T.E., Kirkland, C.L., Cassidy, K.F., Champion, D.C., Mole, D.R., Zibra, I., Gessner, K., Sapkota, J., De Paoli, M.C., Poujol, M., 2019. No evidence for high-pressure melting of Earth's crust in the Archean. Nat. Commun. 10, 1–12. https://doi.org/10.1038/s41467-019-13547-x

Smithies, R.H., Lu, Y., Kirkland, C.L., Johnson, T.E., Mole, D.R., Champion, D.C., Martin, L., Jeon, H., Wingate, M.T.D., Johnson, S.P., 2021. Oxygen isotopes trace the origins of Earth's earliest continental crust. Nature 592, 70–75. https://doi.org/10.1038/s41586-021-03337-1

Söderlund, U., Patchett, P.J., Vervoort, J.D., Isachsen, C.E., 2004. The 176Lu decay constant determined by Lu–Hf and U–Pb isotope systematics of Precambrian mafic intrusions. Earth Planet. Sci. Lett. 219, 311–324. https://doi.org/https://doi.org/10.1016/S0012-821X(04)00012-3

Söllner, F., Trouw, R.A.J., 1997. The Andrelândia depositional cycle (Minas Gerais/Brazil), a post-transamazonic sequence south of the São Francisco Craton: Evidence from U-Pb dating on zircons of a metasediment. J. South Am. Earth Sci. 10, 21–28. https://doi.org/https://doi.org/10.1016/S0895-9811(97)00002-3

Sousa, S.S. da C.G., Ávila, C.A., Neumann, R., Faulstich, F.R.L., Scholz, R., 2023. Monazite age and composition from a granite-pegmatite system: A link between pegmatites of the São João del Rei Pegmatitic Province and the newly defined high-K Restinga Metagranite, Minas Gerais, Brazil. J. South Am. Earth Sci. 123, 104232. https://doi.org/https://doi.org/10.1016/j.jsames.2023.104232

Souza, G.F., Slater, R.D., Dunne, J.P., Sarmiento, J.L., 2014. Deconvolving the controls on the deep ocean's silicon stable isotope distribution. Earth Planet. Sci. Lett. 398, 66–76. https://doi.org/https://doi.org/10.1016/j.epsl.2014.04.040

Spandler, C., Hammerli, J., Sha, P., Hilbert-Wolf, H., Hu, Y., Roberts, E., Schmitz, M., 2016. MKED1: A new titanite standard for in situ analysis of Sm-Nd isotopes and U-Pb geochronology. Chem. Geol. 425, 110–126. https://doi.org/10.1016/j.chemgeo.2016.01.002

Spencer, C.J., Kirkland, C.L., Roberts, N.M.W., Evans, N.J., Liebmann, J., 2020. Strategies towards robust interpretations of in situ zircon Lu–Hf isotope analyses. Geosci. Front. 11, 843–853. https://doi.org/10.1016/j.gsf.2019.09.004

Spencer, C.J., Kirkland, C.L., Taylor, R.J.M., 2016. Strategies towards statistically robust interpretations of in situ U-Pb zircon geochronology. Geosci. Front. 7, 581–589. https://doi.org/10.1016/j.gsf.2015.11.006

Spier, C.A., de Oliveira, S.M.B., Sial, A.N., Rios, F.J., 2007. Geochemistry and genesis of the banded iron formations of the Cauê Formation, Quadrilátero Ferrífero, Minas Gerais, Brazil. Precambrian Res. 152, 170–206. https://doi.org/10.1016/j.precamres.2006.10.003

Stacey, J.S., Kramers, J.D., 1975. Approximation of terrestrial lead isotope evolution by a two-stage model. Earth Planet. Sci. Lett. 26, 207–221. https://doi.org/10.1016/0012-821X(75)90088-6

Stern, R.A., Bleeker, W., 1998. Age of the World's Oldest Rocks Refined Using Canada's SHRIMP: The Acasta Gneiss Complex, Northwest Territories, Canada 25.

Stern, R.J., 2023. The Orosirian (1800–2050 Ma) plate tectonic episode: Key for reconstructing the Proterozoic tectonic record. Geosci. Front. 14, 101553. https://doi.org/10.1016/j.gsf.2023.101553

Stevens, G., Villaros, A., Moyen, J.-F., 2007. Selective peritectic garnet entertainment as the origin of geochemical diversity in S-type granites. Geology 35, 9–12. https://doi.org/10.1130/G22959A.1

Stevenson, R.K., Patchett, P.J., 1990. Implications for the evolution of continental crust from Hf isotope systematics of Archean detrital zircons. Geochim. Cosmochim. Acta 54, 1683–1697. https://doi.org/10.1016/0016-7037(90)90400-F

Storey, C.D., Jeffries, T.E., Smith, M., 2006. Common lead-corrected laser ablation ICP–MS U–Pb systematics and geochronology of titanite. Chem. Geol. 227, 37–52. https://doi.org/https://doi.org/10.1016/j.chemgeo.2005.09.003

Streckeisen, A., 1976. To each plutonic rock its proper name, Earth-Science Reviews.

Sun, S. -s., McDonough, W.F., 1989. Chemical and isotopic systematics of oceanic basalts: implications for mantle composition and processes. Geol. Soc. London, Spec. Publ. 42, 313–345. https://doi.org/10.1144/GSL.SP.1989.042.01.19

Sylvester, P.J., 1998. Post-collisional strongly peraluminous granites. Lithos 45, 29–44. https://doi.org/10.1016/S0024-4937(98)00024-3

Takehara, M., Horie, K., Hokada, T., Kiyokawa, S., 2018. New insight into disturbance of U-Pb and trace-element systems in hydrothermally altered zircon via SHRIMP analyses of zircon from the Duluth Gabbro. Chem. Geol. 484, 168–178. https://doi.org/10.1016/j.chemgeo.2018.01.028

Tapias, J.G., Ramírez, N.E.M., Carlos, S., 2019. Geological Map of South America Scale 1:5 000 000. Paris. https://doi.org/https://doi.org/10.32685/10.143.2019.929

Tartèse, R., Boulvais, P., 2010. Differentiation of peraluminous leucogranites "en route" to the surface. Lithos 114, 353–368. https://doi.org/10.1016/j.lithos.2009.09.011

Taylor, S.R., McLennan, S.M., 1985. The Continental Crust: its Composition and Evolution. An Examination of the Geochemical Record Preserved in Sedimentary Rocks., The Continental Crust: its Composition and Evolution. An Examination of the Geochemical Record Preserved in Sedimentary Rocks.

Taylor, S.R., McLennan, S.M., 2009. Planetary Crusts: Their composition, origin and evolution, Cambridge. ed. Cambridge University Press, Cambridge, New York, Melbourne, Madrid, Cape Town, Singapore, São Paulo.

Teixeira, N.L., Caxito, F.A., Rosière, C.A., Pecoits, E., Vieira, L., Frei, R., Sial, A.N., Poitrasson, F., 2017. Trace elements and isotope geochemistry (C, O, Fe, Cr) of the Cauê iron formation, Quadrilátero Ferrífero, Brazil: Evidence for widespread microbial dissimilatory iron reduction at the Archean/Paleoproterozoic transition. Precambrian Res. 298, 39–55. https://doi.org/10.1016/j.precamres.2017.05.009

Teixeira, W., Ávila, C.A., Dussin, I.A., Bongiolo, E., 2021. U-Pb provenance fingerprints of metavolcanic-sedimentary successions of the Mineiro belt: Proxies for the continuity of plate tectonics through the Paleoproterozoic. Geosci. Front. https://doi.org/10.1016/j.gsf.2021.101293

Teixeira, W., Ávila, C.A., Dussin, I.A., Corrêa Neto, A. V, Bongiolo, E.M., Santos, J.O., Barbosa, N.S., 2015. A juvenile accretion episode (2.35-2.32Ga) in the Mineiro belt and its role to the Minas accretionary orogeny: Zircon U-Pb-Hf and geochemical evidences. Precambrian Res. 256, 148–169. https://doi.org/10.1016/j.precamres.2014.11.009

Teixeira, W., Ávila, C.A., Nunes, L.C., 2008. Nd-Sr isotopic geochemistry and U-Pb geochronology of the Fé granitic gneiss and Lajedo granodiorite: implications for paleoproterozoic evolution of the mineiro belt, southern São Francisco Craton, Brazil . Geol. USP. Série Científica 8, 53–74. https://doi.org/10.5327/Z1519-874x2008000100005

Teixeira, W., Figueiredo, M.C.H., 1991. An outline of Early Proterozoic crustal evolution in the São Francisco craton, Brazil: a review. Precambrian Res. 53, 1–22. https://doi.org/10.1016/0301-9268(91)90003-S

Thomson, S.N., Gehrels, G.E., Ruiz, J., Buchwaldt, R., 2012. Routine low-damage apatite U-Pb dating using laser ablation-multicollector- ICPMS. Geochemistry, Geophys. Geosystems 13. https://doi.org/10.1029/2011GC003928

Tiepolo, M., Oberti, R., Vannucci, R., 2002. Trace-element incorporation in titanite: Constraints from experimentally determined solid/liquid partition coefficients. Chem. Geol. 191, 105–119. https://doi.org/10.1016/S0009-2541(02)00151-1

Trail, D., Boehnke, P., Savage, P.S., Liu, M.-C., Miller, M.L., Bindeman, I., 2018. Origin and significance of Si and O isotope heterogeneities in Phanerozoic, Archean, and Hadean zircon. Proc. Natl. Acad. Sci. 115, 10287–10292. https://doi.org/10.1073/pnas.1808335115

Uhlein, G.J., Uhlein, A., Stevenson, R., Halverson, G.P., Caxito, F.A., Cox, G.M., 2017. Early to late Ediacaran conglomeratic wedges from a complete foreland basin cycle in the southwest São Francisco Craton, Bambuí Group, Brazil. Precambrian Res. 299, 101–116. https://doi.org/https://doi.org/10.1016/j.precamres.2017.07.020

Väisänen, M., Johansson, Å., Andersson, U.B., Eklund, O., Hölttä, P., 2012. Palaeoproterozoic adakite-and TTG-like magmatism in the Svecofennian orogen, SW Finland. Geol. Acta 10, 351–371. https://doi.org/10.1344/105.000001761

Valeriano, C.M., 2017. The northern Brasília belt. São Fr. Craton, East. Brazil 205–220.

Vermeesch, P., 2018. IsoplotR: A free and open toolbox for geochronology. Geosci. Front. 9, 1479–1493. https://doi.org/https://doi.org/10.1016/j.gsf.2018.04.001

Vervoort, J.D., Blichert-Toft, J., 1999. Evolution of the depleted mantle: Hf isotope evidence from juvenile rocks through time. Geochim. Cosmochim. Acta 63, 533–556. https://doi.org/https://doi.org/10.1016/S0016-7037(98)00274-9

Vervoort, J.D., Jonathan Patchett, P., 1996. Behavior of hafnium and neodymium isotopes in the crust: Constraints from Precambrian crustally derived granites. Geochim. Cosmochim. Acta 60, 3717–3733. https://doi.org/https://doi.org/10.1016/0016-7037(96)00201-3

Vervoort, J.D., Kemp, A.I.S., 2016. Clarifying the zircon Hf isotope record of crust-mantle evolution. Chem. Geol. 425, 65–75. https://doi.org/10.1016/j.chemgeo.2016.01.023

Vervoort, J.D., Patchett, P.J., Albarède, F., Blichert-Toft, J., Rudnick, R., Downes, H., 2000. Hf–Nd isotopic evolution of the lower crust. Earth Planet. Sci. Lett. 181, 115–129. https://doi.org/https://doi.org/10.1016/S0012-821X(00)00170-9

Vigneresse, J.L., 2004. A new paradigm for granite generation, in: The Fifth Hutton Symposium on the Origin of Granites and Related Rocks. Geological Society of America. https://doi.org/10.1130/0-8137-2389-2.11

Villaseca, C., Barbero, L., Herreros, V., 1998. A re-examination of the typology of peraluminous granite types in intracontinental orogenic belts. Trans. R. Soc. Edinb. Earth Sci. 89, 113–119. https://doi.org/DOI: 10.1017/S0263593300007045

Volante, S., Blereau, E., Guitreau, M., Tedeschi, M., van Schijndel, V., Cutts, K., 2024. Current applications using key mineral phases in igneous and metamorphic geology: perspectives for the future. Geol. Soc. London, Spec. Publ. 537. https://doi.org/10.1144/sp537-2022-254

Wang, W., Wei, H.-Z., Jiang, S.-Y., Liu, X., Lei, F., Lin, Y.-B., Zhao, Y., 2019. Silicon Isotope Geochemistry: Fractionation Linked to Silicon Complexations and Its Geological Applications. Molecules. https://doi.org/10.3390/molecules24071415

Warr, L.N., 2021. IMA–CNMNC approved mineral symbols. Mineral. Mag. 85, 291–320. https://doi.org/10.1180/mgm.2021.43

Watkins, J.M., Clemens, J.D., Treloar, P.J., 2007. Archaean TTGs as sources of younger granitic magmas: Melting of sodic metatonalites at 0.6-1.2 GPa. Contrib. to Mineral. Petrol. 154, 91–110. https://doi.org/10.1007/s00410-007-0181-0

Wiedenbeck, M., Allé, P., Corfu, F., Griffin, W.L., Meier, M., Oberli, F., Quadt, A. von, Roddick, J.C., Spiegle, W., 1995. Three Natural Zircon Standards for U-Th-Pb, Lu-Hf, Trace Element and REE Analyses. Geostand. Newsl. 19, 1–23. https://doi.org/https://doi.org/10.1111/j.1751-908X.1995.tb00147.x

Wiedenbeck, M., Hanchar, J.M., Peck, W.H., Sylvester, P., Valley, J., Whitehouse, M., Kronz, A., Morishita, Y., Nasdala, L., Fiebig, J., Franchi, I., Girard, J.-P., Greenwood, R.C., Hinton, R., Kita, N., Mason, P.R.D., Norman, M., Ogasawara, M., Piccoli, P.M., Rhede, D., Satoh, H., Schulz-Dobrick, B., Skår, O., Spicuzza, M.J., Terada, K., Tindle, A., Togashi, S., Vennemann, T., Xie, Q., Zheng, Y.-F., 2004. Further Characterisation of the 91500 Zircon Crystal. Geostand. Geoanalytical Res. 28, 9–39. https://doi.org/https://doi.org/10.1111/j.1751-908X.2004.tb01041.x

Woodhead, J.D., Hergt, J.M., 2005. A Preliminary Appraisal of Seven Natural Zircon Reference Materials for In Situ Hf Isotope Determination. Geostand. Geoanalytical Res. 29, 183–195. https://doi.org/https://doi.org/10.1111/j.1751-908X.2005.tb00891.x

Yee, N., Phoenix, V.R., Konhauser, K.O., Benning, L.G., Ferris, F.G., 2003. The effect of cyanobacteria on silica precipitation at neutral pH: implications for bacterial silicification in geothermal hot springs. Chem. Geol. 199, 83–90. https://doi.org/https://doi.org/10.1016/S0009-2541(03)00120-7

Zamora, D., 2000. Fusion de la croute oceanique subductee: approche experimentale et geochimique. Universite Blaise-Pascal, Clermont-Ferrand.

Zeh, A., Stern, R.A., Gerdes, A., 2014. The oldest zircons of Africa—Their U–Pb–Hf–O isotope and trace element systematics, and implications for Hadean to Archean crust–mantle evolution. Precambrian Res. 241, 203–230. https://doi.org/https://doi.org/10.1016/j.precamres.2013.11.006

Zhou, Y., Zhai, M., Mitchell, R.N., Cawood, P.A., Huang, G., Spencer, C.J., Chen, M., Li, Y., Zhao, T., Wu, T., 2024. Low δ18O and δ30Si TTG at ca. 2.3 Ga Hints at an Intraplate Rifting Onset of the Paleoproterozoic Supercontinent Cycle. J. Geophys. Res. Solid Earth 129, 1–22. https://doi.org/10.1029/2023JB027306

Ziegler, K., Chadwick, O.A., Brzezinski, M.A., Kelly, E.F., 2005. Natural variations of δ30Si ratios during progressive basalt weathering, Hawaiian Islands. Geochim. Cosmochim. Acta 69, 4597–4610. https://doi.org/10.1016/j.gca.2005.05.008

Appendix

1. *Rock-forming mineral chemistry*
2. *Whole-rock geochemistry*
3. *Zircon CL and BSE images*
4. *Apatite CL images*
5. *Titanite BSE images*
6. *LA-(MC)-ICP-MS conditions*
7. *U-Pb zircon geochronology (LA-ICP-MS)*
8. *U-Pb apatite geochronology (LA-ICP-MS)*
9. *U-Pb titanite geochronology (LA-ICP-MS)*
10. *Zircon Lu-Hf isotope analyses (LA-MC-ICP-MS)*
11. *Zircon Silicon isotope analyses (LA-MC-ICP-MS)*
12. *Zircon trace element analyses (LA-ICP-MS)*
13. *Apatite major and minor element analyses (EMPA)*
14. *Apatite trace element analyses (LA-ICP-MS)*
15. *Titanite trace element analyses (LA-ICP-MS)*

Feldspar analyses.

Date	***2022 August 24-26***										
Pluton	**Cupim Leucogranite**										
Sample	**GC1**										
Field	**1**				**2**		**3**				**6**
Spectrum	***9***	***10***	***11 (b)***	***12 (k)***	***15 (k) (b)***	***16 (k)***	***23 (k)***	***24 (k)***	***25***	***26***	***42***
SiO2	64.8	65.03	64.84	64.81	64.71	64.83	64.79	64.9	67.58	63.51	65.38
TiO2	0	0	0	0	0	0	0	0	0	0	0
Al2O3	22.39	22.27	22.41	18.54	18.5	18.63	18.56	18.58	20.59	23.19	22.07
FeOt	0	0	0	0	0	0	0	0	0	0	0
MgO	0	0	0	0	0	0	0	0	0	0	0
CaO	3.33	3.05	3.33	0	0	0	0	0	1.13	4.26	2.98
Na2O	9.33	9.54	9.29	0.63	0.4	1.11	0.69	0.79	10.62	8.91	9.33
K2O	0.14	0.11	0.13	16.01	16.39	15.44	15.96	15.73	0.08	0.13	0.24
Total	**99.99**	**100**	**100**	**99.99**	**100**	**100.01**	**100**	**100**	**100**	**100**	**100**
Numbers of ions on the basis of 32 O											
Si	11.4	11.44	11.4	11.96	11.96	11.96	11.96	11.96	11.8	11.2	11.48
Al	4.64	4.6	4.64	4.04	4.04	4.04	4.04	4.04	4.24	4.84	4.56
Fe	0	0	0	0	0	0	0	0	0	0	0
Mg	0	0	0	0	0	0	0	0	0	0	0
Na	3.2	3.24	3.16	0.24	0.16	0.4	0.24	0.28	3.6	3.04	3.16
Ca	0.64	0.56	0.64	0	0	0	0	0	0.2	0.8	0.56
K	0.04	0.04	0.04	3.76	3.88	3.64	3.76	3.72	0	0.04	0.04
Z	16.04	16.04	16.04	16	16	16	16	16	16.04	16.04	16.04
X	3.84	3.84	3.84	4	4	4.04	4	4	3.84	3.88	3.8
An	16.34	14.92	16.41	0	0	0	0	0	5.53	20.74	14.79
Ab	82.84	84.44	82.83	5.64	3.58	9.85	6.17	7.09	94.01	78.5	83.79
Or	0.82	0.64	0.76	94.36	96.42	90.15	93.83	92.91	0.47	0.75	1.42
Type	**Oligoclase**	**Oligoclase**	**Oligoclase**	**K-Felds**	**K-Felds**	**K-Felds**	**K-Felds**	**K-Felds**	**Albite**	**Oligoclase**	**Oligoclase**

	7			8		9		10		11	12	14	
43 (k)	*49 (b)*	*50*	*56 (k)*	*57 (k)*	*63 (b)*	*64*	*73*	*74*	*82*	*87 (k)*	*98*	*99*	
64.76	68.07	65.15	64.99	64.35	68.56	65.08	67.65	64.57	66.39	64.64	65.2	64.53	
0	0	0	0	0	0	0	0	0	0	0	0	0	
18.62	20.38	22.41	18.63	18.48	20.03	22.22	20.69	22.55	21.6	18.58	22.07	22.55	
0	0	0	0	0	0	0	0	0	0	0	0	0	
0	0	0	0	0	0	0	0	0	0	0	0	0	
0	0.81	3.14	0	0	0.42	3.1	1.19	3.39	2.17	0	2.93	3.37	
0.67	10.74	9.22	0.61	0.59	10.85	9.52	10.41	9.23	9.75	0.37	9.65	9.35	
15.96		0.09	15.77	16.57	0.14	0.08	0.06	0.26	0.1	16.41	0.15	0.2	
100.01	**100**	**100.01**	**100**	**99.99**	**100**	**100**	**100**	**100**	**100.01**	**100**	**100**	**100**	
11.96	11.88	11.44	12	11.92	11.96	11.44	11.8	11.36	11.64	11.96	11.48	11.36	
4.04	4.2	4.64	4.04	4.04	4.12	4.6	4.24	4.68	4.44	4.04	4.56	4.68	
0	0	0	0	0	0	0	0	0	0	0	0	0	
0	0	0	0	0	0	0	0	0	0	0	0	0	
0.24	3.64	3.12	0.2	0.2	3.68	3.24	3.52	3.16	3.32	0.12	3.28	3.2	
0	0.16	0.6	0	0	0.08	0.6	0.24	0.64	0.4	0	0.56	0.64	
3.76	0	0.04	3.72	3.92	0.04	0	0	0.04	0.04	3.88	0.04	0.04	
16	16.08	16.08	16.04	15.96	16.08	16.04	16.08	16.04	16.08	16	16.04	16.04	
4	3.8	3.76	3.92	4.12	3.76	3.84	3.76	3.84	3.72	4	3.88	3.88	
0	4	15.75	0	0	2.08	15.18	5.92	16.62	10.89	0	14.24	16.42	
6	96	83.71	5.55	5.13	97.1	84.35	93.72	81.87	88.52	3.31	84.89	82.42	
94	0	0.54	94.45	94.87	0.82	0.47	0.36	1.52	0.6	96.69	0.87	1.16	
K-Felds	**Albite**	**Oligoclase**	**K-Felds**	**K-Felds**	**Albite**	**Oligoclase**	**Albite**	**Oligoclase**	**Oligoclase**	**K-Felds**	**Oligoclase**	**Oligoclase**	

		GC2									GC5A		
			2		2 (Tab2)		4	7	8		10	1	
101 (k)	*102*	*11 (k)*	*12*	*14 (k)*	*15 (k)*	*28*	*39*	*45*	*46 (k)*	*55 (k)*	*9*	*11 (k)*
64.73	65.6	64.93	67.72	64.85	64.88	64.79	64.65	63.95	64.54	64.79	65.54	64.69
0	0	0	0	0	0	0	0	0	0	0	0	0
18.51	21.93	18.55	20.32	18.65	18.57	22.36	22.54	22.97	18.55	18.59	21.96	18.43
0	0	0	0	0	0	0	0	0	0	0	0	0
0	0	0	0	0	0	0	0	0	0	0	0	0
0	2.73	0	0.87	0	0	3.16	3.25	3.96	0	0	2.88	0
0.39	9.74	0.52	11.02	0.74	0.44	9.51	9.44	8.97	0.69	0.65	9.5	0.4
16.37		16	0.08	15.76	16.11	0.18	0.12	0.15	15.53	15.97	0.12	16.49
100	**100**	**100**	**100.01**	**100**	**100**	**100**	**100**	**100**	**99.31**	**100**	**100**	**100.01**
11.96	11.52	12	11.84	11.96	12	11.4	11.36	11.28	11.96	11.96	11.52	11.96
4.04	4.52	4.04	4.2	4.04	4.04	4.64	4.68	4.76	4.04	4.04	4.56	4.04
0	0	0	0	0	0	0	0	0	0	0	0	0
0	0	0	0	0	0	0	0	0	0	0	0	0
0.12	3.32	0.2	3.72	0.28	0.16	3.24	3.24	3.08	0.24	0.24	3.24	0.16
0	0.52	0	0.16	0	0	0.6	0.6	0.76	0	0	0.56	0
3.88	0	3.76	0	3.72	3.8	0.04	0.04	0.04	3.68	3.76	0.04	3.88
16	16.04	16.04	16.04	16.04	16.04	16.04	16.04	16.04	16.04	16	16.04	16
4	3.84	3.96	3.92	3.96	3.96	3.88	3.84	3.84	3.92	4	3.8	4.04
0	13.41	0	4.16	0	0	15.35	15.87	19.44	0	0	14.25	0
3.49	86.59	4.71	95.38	6.66	3.99	83.61	83.43	79.68	6.33	5.83	85.05	3.56
96.51	0	95.29	0.46	93.34	96.01	1.04	0.7	0.88	93.67	94.17	0.71	96.44
K-Felds	**Oligoclase**	**K-Felds**	**Albite**	**K-Felds**	**K-Felds**	**Oligoclase**	**Oligoclase**	**Oligoclase**	**K-Felds**	**K-Felds**	**Oligoclase**	**K-Felds**

2		2 (Tab2)	3	4	5	5 (Tab2)			7				8
13 (k)	*14*	*19 (k)*	*24 (k)*	*38*	*41*	*45*	*46*		*58*	*59 (k)*	*60 (inc Kf)*	*62 (k)*	*63 (k)*
64.89	66.31	64.92	64.73	64.81	62.91	65.12	67.58		64.63	64.53	68.98	64.96	64.84
0	0	0	0	0	0	0	0		0	0	0	0	0
18.56	21.57	18.71	18.57	22.43	23.44	22.18	20.51		22.36	18.75	19.84	18.66	18.6
0	0	0	0	0	0	0	0		0	0	0	0	0
0	0	0	0	0	0	0	0		0	0	0	0	0
0	1.46	0	0	3.22	4.66	3.51	1.01		3.07	0	0.25	0	0
0.29	10.15	0.36	0.47	9.41	8.78	8.94	10.79		9.84	0.69	10.84	0.73	0.71
16.27	0.5	16.01	16.23	0.12	0.22	0.25	0.1		0.1	16.03	0.09	15.65	15.85
100.01	**99.99**	**100**	**100**	**99.99**	**100.01**	**100**	**99.99**		**100**	**100**	**100**	**100**	**100**
12	11.64	11.96	11.96	11.4	11.12	11.44	11.8		11.4	11.92	12	11.96	11.96
4.04	4.44	4.08	4.04	4.64	4.88	4.6	4.24		4.64	4.08	4.08	4.04	4.04
0	0	0	0	0	0	0	0		0	0	0	0	0
0	0	0	0	0	0	0	0		0	0	0	0	0
0.12	3.44	0.12	0.16	3.2	3	3.04	3.64		3.36	0.24	3.64	0.28	0.24
0	0.28	0	0	0.6	0.88	0.68	0.2		0.56	0	0.04	0	0
3.84	0.12	3.76	3.84	0.04	0.04	0.04	0.04		0.04	3.8	0	3.68	3.72
16.04	16.08	16.04	16	16.04	16	16.04	16.04		16.04	16	16.08	16.04	16
3.92	3.84	3.88	4	3.84	3.96	3.76	3.88		3.96	4.04	3.72	3.96	4
0	7.15	0	0	15.79	22.39	17.56	4.89		14.62	0	1.25	0	0
2.64	89.94	3.3	4.22	83.51	76.35	80.95	94.53		84.81	6.14	98.21	6.62	6.37
97.36	2.92	96.7	95.78	0.7	1.26	1.49	0.58		0.57	93.86	0.54	93.38	93.63
K-Felds	**Albite**	**K-Felds**	**K-Felds**	**Oligoclase**	**Oligoclase**	**Oligoclase**	**Albite**	**Oligoclase**	**K-Felds**	**Albite**		**K-Felds**	**K-Felds**

GC5B														
9	**10**					**2**				**4**		**6**		
69 (k)	***70 (k)***	***71 (k)***	***72 (k)***	***73***	***74***	***15 (k) (b)***	***16 (k)***	***17***	***18 (b)?***	***32***	***33 (b)?***	***38***	***39 (b)***	
64.59	65.07	64.81	65.04	68.85	66.57	64.6	64.82	67.95	67.44	65.55	65.36	68.35	68.06	
0	0	0	0	0	0	0	0	0	0	0	0	0	0	
18.96	18.74	18.73	19.08	20	21.05	18.6	18.67	20.56	20.73	22.17	22.05	20.15	20.3	
0	0	0	0	0	0	0	0	0	0	0	0	0	0	
0	0	0	0	0	0	0	0	0	0	0	0	0	0	
0	0	0	0	0.29	0.63	0	0	0.93	1.35	2.38	3.11	0.61	0.6	
0.7	0.39	0.74	0.41	10.8	10.67	0.55	0.69	10.55	10.42	9.8	9.48	10.81	10.92	
15.75	15.79	15.72	15.47	0.06	0.95	16.26	15.82		0.07	0.1		0.08	0.12	
100	**99.99**	**100**	**100**	**100**	**99.87**	**100.01**	**100**	**99.99**	**100.01**	**100**	**100**	**100**	**100**	
11.92	12	11.96	11.96	12	11.72	11.96	11.96	11.84	11.8	11.48	11.48	11.92	11.88	
4.12	4.08	4.08	4.12	4.12	4.36	4.04	4.08	4.24	4.28	4.6	4.56	4.16	4.16	
0	0	0	0	0	0	0	0	0	0	0	0	0	0	
0	0	0	0	0	0	0	0	0	0	0	0	0	0	
0.24	0.12	0.28	0.16	3.64	3.64	0.2	0.24	3.56	3.52	3.32	3.24	3.64	3.68	
0	0	0	0	0.04	0.12	0	0	0.16	0.24	0.44	0.6	0.12	0.12	
3.72	3.72	3.68	3.64	0	0.2	3.84	3.72	0	0	0.04	0	0	0.04	
16.04	16.04	16.04	16.08	16.08	16.08	16	16.04	16.08	16.04	16.08	16.04	16.08	16.04	
3.96	3.84	3.96	3.76	3.72	3.96	4.04	3.96	3.76	3.8	3.8	3.8	3.8	3.84	
0	0	0	0	1.46	2.99	0	0	4.65	6.65	11.76	15.35	3.01	2.93	
6.33	3.62	6.68	3.87	98.18	91.64	4.89	6.22	95.35	92.94	87.65	84.65	96.52	96.38	
93.67	96.38	93.32	96.13	0.36	5.37	95.11	93.78	0	0.41	0.59	0	0.47	0.7	
K-Felds	**K-Felds**	**K-Felds**	**K-Felds**	**Albite**	**Albite**	**K-Felds**	**K-Felds**	**Albite**	**Albite**	**Oligoclase**	**Oligoclase**	**Albite**	**Albite**	

7	11					13		15	16		17	
41 (k)	*57*	*58*	*59*	*60*	*61 (k)*	*72*	*73*	*88 (k) (inc gt)*	*94*	*95 (b)*	*96 (k)*	*97 (b) (k)*
64.34	67.25	67.88	64.87	64.76	64.84	68.25	68.44	64.74	66.98	65.14	64.74	65.03
0	0	0	0	0	0	0	0	0	0	0	0	0
18.35	20.72	20.13	22.24	22.44	18.54	20.19	20.11	18.53	21.03	21.99	18.65	18.59
0	0	0	0	0	0	0	0	0	0	0	0	0
0	0	0	0	0	0	0	0	0	0	0	0	0
0	1.18	0.47	3.17	3.28	0	0.65	0.47	0	1.51	2.92	0	0
0.31	10.76	11.38	9.55	9.31	0.5	10.85	10.89	0.31	10.38	9.77	0.71	0.72
16.99	0.08	0.14	0.18	0.2	16.12	0.07	0.09	16.42	0.1	0.18	15.9	15.67
99.99	**99.99**	**100**	**100.01**	**99.99**	**100**	**100.01**	**100**	**100**	**100**	**100**	**100**	**100.01**
11.96	11.76	11.88	11.4	11.4	11.96	11.92	11.92	11.96	11.72	11.48	11.96	12
4	4.28	4.16	4.6	4.64	4.04	4.16	4.12	4.04	4.32	4.56	4.04	4.04
0	0	0	0	0	0	0	0	0	0	0	0	0
0	0	0	0	0	0	0	0	0	0	0	0	0
0.12	3.64	3.84	3.24	3.16	0.16	3.68	3.68	0.12	3.52	3.32	0.24	0.24
0	0.24	0.08	0.6	0.6	0	0.12	0.08	0	0.28	0.56	0	0
4.04	0	0.04	0.04	0.04	3.8	0	0.04	3.88	0.04	0.04	3.76	3.68
15.96	16.04	16.04	16.04	16.04	16	16.04	16.08	16	16.04	16.04	16	16.04
4.12	3.88	3.96	3.88	3.84	3.96	3.8	3.8	4	3.84	3.92	4	3.96
0	5.69	2.21	15.34	16.11	0	3.19	2.32	0	7.4	14.03	0	0
2.7	93.85	97	83.62	82.73	4.5	96.4	97.15	2.79	92.02	84.94	6.36	6.53
97.3	0.46	0.79	1.04	1.17	95.5	0.41	0.53	97.21	0.58	1.03	93.64	93.47
K-Felds	**Albite**	**Albite**	**Oligoclase**	**Oligoclase**	**K-Felds**	**Albite**	**Albite**	**K-Felds**		**Albite**	**Oligoclase**	**K-Felds**	**K-Felds**

					GC6A							
					1			2	3	7		10
99 (k) (inc)	*100 (inc)*	*101 (k) (inc)*	*102 (k)*	*103 (k)*	*1*	*2 (b)*	*3 (k)*	*14*	*16 (k)*	*35*	*36 (k)*	*45*
64.87	68.2	64.74	64.63	64.68	68.06	68.12	64.94	67.45	64.95	68.07	64.99	65.95
0	0	0	0	0	0	0	0	0	0	0	0	0
18.62	20.57	18.68	18.48	18.44	20.25	20.3	18.5	20.63	18.61	20.44	18.7	21.65
0	0	0	0	0	0	0	0	0	0	0	0	0
0	0	0	0	0	0	0	0	0	0	0	0	0
0	1.02	0	0	0	0.61	0.75	0	1.26	0	0.9	0	2.3
0.57	9.83	0.66	0.52	0.38	10.98	10.71	0.59	10.59	0.57	10.5	0.79	10.03
15.93	0.25	15.92	16.38	16.51	0.1	0.12	15.98	0.07	15.88	0.09	15.53	0.07
99.99	**99.87**	**100**	**100.01**	**100.01**	**100**	**100**	**100.01**	**100**	**100.01**	**100**	**100.01**	**100**
11.96	11.88	11.96	11.96	11.96	11.88	11.88	12	11.8	12	11.88	11.96	11.56
4.04	4.24	4.08	4.04	4.04	4.16	4.16	4.04	4.24	4.04	4.2	4.04	4.48
0	0	0	0	0	0	0	0	0	0	0	0	0
0	0	0	0	0	0	0	0	0	0	0	0	0
0.2	3.32	0.24	0.2	0.12	3.72	3.64	0.2	3.6	0.2	3.56	0.28	3.4
0	0.2	0	0	0	0.12	0.16	0	0.24	0	0.16	0	0.44
3.76	0.04	3.76	3.88	3.88	0.04	0.04	3.76	0	3.72	0.04	3.64	0
16.04	16.12	16	16	16	16.04	16.08	16	16.04	16.04	16.08	16.04	16.04
3.96	3.56	4	4.04	4.04	3.84	3.8	3.96	3.84	3.96	3.72	3.92	3.84
0	5.34	0	0	0	2.96	3.7	0	6.14	0	4.5	0	11.2
5.16	93.1	5.93	4.6	3.38	96.46	95.6	5.31	93.45	5.17	94.97	7.18	88.39
94.84	1.56	94.07	95.4	96.62	0.58	0.7	94.69	0.41	94.83	0.54	92.82	0.41
K-Felds	**Albite**	**K-Felds**	**K-Felds**	**K-Felds**	**Albite**	**Albite**	**K-Felds**	**Albite**	**K-Felds**	**Albite**	**K-Felds**	**Oligoclase**

GC7A

1						**2**				**3**	
103	***104***	***108 (k)***	***109 (k) (b)***	***110***	***111 (b)***	***1 (k)***	***2 (k)***	***3 (b)***	***4***	***7***	***8 (b)***
66.28	66.2	64.34	64.83	66.31	66.18	64.82	64.75	67.31	66.8	66.2	66.61
0	0	0	0	0	0	0	0	0	0	0	0
21.52	21.57	18.72	18.61	21.4	21.44	18.54	18.61	20.67	21.27	21.47	21.25
0	0	0	0	0	0	0	0	0	0	0	0
0	0	0	0	0	0	0	0	0	0	0	0
2.2	2.15	0	0	2.08	2.29	0	0	1.26	2.01	2.13	1.79
9.99	9.99	0.52	0.55	10.14	9.8	0.56	0.57	10.64	9.92	10	10.25
	0.09	16.43	16	0.08	0.28	16.08	16.07	0.11		0.21	0.11
99.99	**100**	**100.01**	**99.99**	**100.01**	**99.99**	**100**	**100**	**99.99**	**100**	**100.01**	**100.01**
11.6	11.6	11.92	11.96	11.64	11.6	11.96	11.96	11.76	11.68	11.6	11.68
4.44	4.44	4.08	4.04	4.44	4.44	4.04	4.04	4.28	4.4	4.44	4.4
0	0	0	0	0	0	0	0	0	0	0	0
0	0	0	0	0	0	0	0	0	0	0	0
3.4	3.4	0.2	0.2	3.44	3.32	0.2	0.2	3.6	3.36	3.4	3.48
0.4	0.4	0	0	0.4	0.44	0	0	0.24	0.36	0.4	0.32
0	0.04	3.88	3.76	0	0.08	3.8	3.8	0.04	0	0.04	0.04
16.04	16.04	16	16.04	16.04	16.04	16	16	16.04	16.08	16.04	16.04
3.8	3.8	4.08	3.96	3.84	3.84	4	4	3.88	3.76	3.84	3.84
10.85	10.57	0	0	10.13	11.25	0	0	6.1	10.07	10.4	8.74
89.15	88.9	4.59	4.97	89.4	87.11	5.03	5.12	93.26	89.93	88.38	90.62
0	0.53	95.41	95.03	0.46	1.64	94.97	94.88	0.63	0	1.22	0.64
Oligoclase	**Oligoclase**	**K-Felds**	**K-Felds**	**Oligoclase**	**Oligoclase**	**K-Felds**	**K-Felds**	**Albite**	**Oligoclase**	**Oligoclase**	**Albite**

	5	6 (Tab3)				7		8			9	
35 (k) (inc gt)		*47*	*48*	*49*	*50 (k)*	*54 (b)*	*55*	*62 (b)*	*63*	*77 (inc gt)*	*78 (inc gt)*	
	64.99	66.61	66.36	66.54	64.7	66.73	66.39	66.22	66.21	64.82	64.75	
	0	0	0	0	0	0	0	0	0	0	0	
	18.64	21.18	21.44	21.52	18.62	21.15	21.45	21.43	21.46	18.54	18.49	
	0	0	0	0	0	0	0	0	0	0	0	
	0	0	0	0	0	0	0	0	0	0	0	
	0	1.86	2.13	2.12	0	1.79	2.12	2.19	2.23	0	0	
	0.48	10.23	9.98	9.74	0.61	10.16	9.9	10.01	9.83	0.44	0.68	
	15.88	0.11	0.09	0.08	16.07	0.16	0.15	0.15	0.26	16.19	16.08	
	99.99	**99.99**	**100**	**100**	**100**	**99.99**	**100.01**	**100**	**99.99**	**99.99**	**100**	
	12	11.68	11.64	11.64	11.96	11.68	11.64	11.6	11.6	11.96	11.96	
	4.04	4.36	4.44	4.44	4.04	4.36	4.44	4.44	4.44	4.04	4.04	
	0	0	0	0	0	0	0	0	0	0	0	
	0	0	0	0	0	0	0	0	0	0	0	
	0.16	3.48	3.4	3.32	0.2	3.44	3.36	3.4	3.36	0.16	0.24	
	0	0.36	0.4	0.4	0	0.32	0.4	0.4	0.4	0	0	
	3.72	0.04	0.04	0	3.8	0.04	0.04	0.04	0.04	3.8	3.8	
	16.04	16.04	16.04	16.08	16	16.04	16.04	16.04	16.04	16	16	
	3.92	3.84	3.8	3.72	4	3.84	3.8	3.84	3.8	3.96	4.04	
	0	9.07	10.49	10.68	0	8.79	10.49	10.69	10.97	0	0	
	4.39	90.29	88.98	88.83	5.45	90.28	88.63	88.44	87.51	3.97	6.04	
	95.61	0.64	0.53	0.48	94.55	0.94	0.88	0.87	1.52	96.03	93.96	
K-Felds		**Albite**	**Oligoclase**	**Oligoclase**	**K-Felds**	**Albite**	**Oligoclase**	**Oligoclase**	**Oligoclase**	**K-Felds**	**K-Felds**	

				GC7B							
		10		3		4 (Tab2)	5			6	8
79 (inc gt)	*81*	*87*	*88*	*15*	*18 (k)*	*22 (inc Kf)*	*34*	*35*	*36*	*39 (k)*	*64*
64.82	64.94	66.19	66.18	66.72	64.84	66.37	66.4	66.51	66.17	64.66	66.48
0	0	0	0	0	0	0	0	0	0	0	0
18.56	18.61	21.42	21.53	21.28	18.49	21.62	21.62	21.38	21.51	18.5	21.49
0	0	0	0	0	0	0	0	0	0	0	0
0	0	0	0	0	0	0	0	0	0	0	0
0	0	2.17	2.15	1.99	0	2.28	2.13	2.21	2.05	0	2.26
0.57	0.38	10.09	10.04	9.89	0.62	9.63	9.75	9.81	10.14	0.43	9.63
16.05	16.07	0.13	0.1	0.12	16.05	0.1	0.1	0.1	0.13	16.4	0.14
100	**100**	**100**	**100**	**100**	**100**	**100**	**100**	**100.01**	**100**	**99.99**	**100**
11.96	12	11.6	11.6	11.68	11.96	11.6	11.64	11.64	11.6	11.96	11.64
4.04	4.04	4.44	4.44	4.4	4.04	4.48	4.44	4.4	4.44	4.04	4.44
0	0	0	0	0	0	0	0	0	0	0	0
0	0	0	0	0	0	0	0	0	0	0	0
0.2	0.12	3.44	3.4	3.36	0.24	3.28	3.32	3.32	3.44	0.16	3.28
0	0	0.4	0.4	0.36	0	0.44	0.4	0.4	0.4	0	0.44
3.8	3.8	0.04	0.04	0.04	3.8	0.04	0.04	0.04	0.04	3.88	0.04
16	16.04	16.04	16.04	16.08	16	16.08	16.08	16.04	16.04	16	16.08
4	3.92	3.88	3.84	3.76	4	3.72	3.72	3.76	3.88	4.04	3.72
0	0	10.54	10.52	9.94	0	11.5	10.71	11.01	9.97	0	11.38
5.12	3.47	88.71	88.9	89.35	5.55	87.9	88.69	88.4	89.27	3.83	87.78
94.88	96.53	0.75	0.58	0.71	94.45	0.6	0.6	0.59	0.75	96.17	0.84
K-Felds	**K-Felds**	**Oligoclase**	**Oligoclase**	**Albite**	**K-Felds**	**Oligoclase**	**Oligoclase**	**Oligoclase**	**Albite**	**K-Felds**	**Oligoclase**

8 (Tab2)			**9**
71 (inc Kf)	***72 (inc)***	***73 (k)***	***81 (k) (inc Gt)***
66.4	66.29	64.54	64.86
0	0	0	0
21.44	21.59	18.53	18.57
0	0	0	0
0	0	0	0
2.14	2.13	0	0
9.83	9.87	0.38	0.51
0.18	0.12	16.55	16.05
99.99	**100**	**100**	**99.99**
11.64	11.6	11.96	11.96
4.44	4.44	4.04	4.04
0	0	0	0
0	0	0	0
3.32	3.36	0.12	0.2
0.4	0.4	0	0
0.04	0.04	3.92	3.8
16.08	16.08	16	16
3.8	3.76	4.04	3.96
10.62	10.58	0	0
88.31	88.71	3.37	4.61
1.06	0.71	96.63	95.39
Oligoclase	**Oligoclase**	**K-Felds**	**K-Felds**

Feldspar analyses.

Date	***22-Aug***							**24-Sep**	
Unit	**Caatinga-Lamim Complex**								**Ressaquinh**
Sample	**CM44A**				**CM44B**				**CM46A**
Field	**1**	**2**			**2**	**3**	**4**	**5**	**1**
Spectrum	***5***	***4***	***5***	***7***	***2***	***1***	***2***	***79***	***1***
SiO2	66.39	66.64	66.64	65.51	65.07	65.15	65.16	66.57	59.7
TiO2	0	0	0	0	0	0	0	0	0
Al2O3	20.46	20.54	20.33	20.95	21.47	20.94	21.31	24.65	23.17
FeOt	0	0	0	0	0	0	0	0	0
MgO	0	0	0	0	0	0	0	0	0
CaO	3.32	3.2	3.38	3.67	4.83	4	4.5	4.57	4.98
Na2O	9.83	9.73	9.65	9.87	8.63	9.91	9.03	9.19	8.22
K2O	0	0	0	0	0	0	0	0	0
Total	**100**	**100.11**	**100**	**100**	**100**	**100**	**100**	**104.98**	**96.07**
Numbers of ions on the basis of 8 O									
Si	2.92	2.92	2.93	2.89	2.87	2.88	2.87	2.80	2.75
Al	1.06	1.06	1.05	1.09	1.11	1.09	1.11	1.22	1.26
Fe	0.00	0.00	0.00	0.00	0.00	0.00	0.00	0.00	0.00
Mg	0.00	0.00	0.00	0.00	0.00	0.00	0.00	0.00	0.00
Ca	0.16	0.15	0.16	0.17	0.23	0.19	0.21	0.21	0.25
Na	0.84	0.83	0.82	0.84	0.74	0.85	0.77	0.75	0.73
K	0.00	0.00	0.00	0.00	0.00	0.00	0.00	0.00	0.00
Z	3.98	3.98	3.98	3.97	3.98	3.97	3.98	4.02	4.01
X	0.99	0.98	0.98	1.02	0.96	1.04	0.98	0.95	0.98
An	**16**	**15**	**16**	**17**	**24**	**18**	**22**	**22**	**25**
Ab	84	85	84	83	76	82	78	78	75
Or	0	0	0	0	0	0	0	0	0
Class.	**Oligoclase**	**Oligoclase**	**Oligoclase**	**Oligoclase**	**Oligoclase**	**Oligoclase**	**Oligoclase**	**Oligoclase**	**Oligoclase**

a Complex								Caatinga Lamim Comple CM49	
	3		4					1	2
2	*9*	*12*	*5*	*1*	*4*	*48*	*49*	*13*	*7*
60.32	61.15	57.5	59.24	62.07	57.56	58.18	58.61	61.65	61.97
0	0	0	0	0	0	0	0	0	0
23.17	23.61	22.62	22.69	23.86	22.14	22.36	22.86	25.26	25.49
0	0	0	0	0	0	0	0	0	0
0	0	0	0	0	0	0	0	0	0
5.28	4.92	5.02	4.85	5.05	4.87	4.49	4.89	6.51	6.18
8.1	8.35	7.61	8.03	8.53	7.83	7.92	7.89	7.9	7.83
0	0	0	0	0	0	0	0	0	0
96.87	**98.03**	**92.75**	**94.81**	**99.51**	**92.4**	**92.95**	**94.25**	**101.32**	**101.47**
2.76	2.76	2.74	2.76	2.76	2.76	2.76	2.75	2.70	2.71
1.25	1.25	1.27	1.25	1.25	1.25	1.25	1.26	1.30	1.31
0.00	0.00	0.00	0.00	0.00	0.00	0.00	0.00	0.00	0.00
0.00	0.00	0.00	0.00	0.00	0.00	0.00	0.00	0.00	0.00
0.26	0.24	0.26	0.24	0.24	0.25	0.23	0.25	0.31	0.29
0.72	0.73	0.70	0.73	0.73	0.73	0.73	0.72	0.67	0.66
0.00	0.00	0.00	0.00	0.00	0.00	0.00	0.00	0.00	0.00
4.00	4.01	4.01	4.01	4.01	4.01	4.02	4.01	4.01	4.02
0.98	0.97	0.96	0.97	0.98	0.98	0.96	0.96	0.98	0.95
26	**25**	**27**	**25**	**25**	**26**	**24**	**26**	**31**	**30**
74	75	73	75	75	74	76	74	69	70
0	0	0	0	0	0	0	0	0	0
Oligoclase	**Oligoclase**	**Oligoclase**	**Oligoclase**	**Oligoclase**	**Oligoclase**	**Oligoclase**	**Oligoclase**	**Andesine**	**Andesine**

ex								14-Oct Caranaíba gneiss CM47		
	4	**6**	**7**		**8**	**9**	**11**	**12**	**1**	**2**
	11	***14***	***11***	***12***	***4***	***19***	***12***	***16***	**11**	**28**
	60.14	61.98	63.43	60.02	62.01	61.14	62	63.05	62.26	64.07
	0	0	0	0	0	0	0	0	0	0
	25	24.97	23.71	25.05	25.39	25.06	25.48	24.86	23.45	25.17
	0	0	0	0	0	0	0	0	0	0
	0	0	0	0	0	0	0	0	0	0
	6.4	5.93	4.65	6.41	6.33	6.19	6.22	5.64	4.54	5.47
	7.59	8.02	8.7	7.65	7.88	7.88	8.05	8.35	8.88	8.8
	0	0	0	0	0	0	0	0	0	0
	99.13	**100.9**	**100.49**	**99.13**	**101.61**	**100.27**	**101.75**	**101.9**	**99.13**	**103.51**
	2.69	2.72	2.79	2.69	2.71	2.70	2.70	2.74	2.78	2.74
	1.32	1.29	1.23	1.32	1.31	1.31	1.31	1.27	1.23	1.27
	0.00	0.00	0.00	0.00	0.00	0.00	0.00	0.00	0.00	0.00
	0.00	0.00	0.00	0.00	0.00	0.00	0.00	0.00	0.00	0.00
	0.31	0.28	0.22	0.31	0.30	0.29	0.29	0.26	0.22	0.25
	0.66	0.68	0.74	0.66	0.67	0.68	0.68	0.70	0.77	0.73
	0.00	0.00	0.00	0.00	0.00	0.00	0.00	0.00	0.00	0.00
	4.01	4.01	4.01	4.01	4.01	4.01	4.01	4.01	4.01	4.01
	0.97	0.96	0.96	0.97	0.96	0.97	0.97	0.97	0.98	0.98
	32	**29**	**23**	**32**	**31**	**30**	**30**	**27**	**22**	**26**
	68	71	77	68	69	70	70	73	78	74
	0	0	0	0	0	0	0	0	0	0
	Andesine	**Oligoclase**	**Oligoclase**	**Andesine**	**Andesine**	**Andesine**	**Oligoclase**	**Oligoclase**	**Oligoclase**	**Oligoclase**

		3			
29	**30**	**42**	**44**	**45**	**50**
63.23	60.75	61.72	61.16	62.44	62.64
0	0	0	0	0	0
24.76	23.75	23.37	23.83	24.15	24.37
0	0	0	0	0	0
0	0	0	0	0	0
5.34	5.18	4.61	5.08	5.16	5.1
8.67	8.21	8.41	8.36	8.57	8.59
0	0	0	0	0	0
102	**97.89**	**98.11**	**98.43**	**100.32**	**100.7**
2.74	2.75	2.78	2.75	2.75	2.75
1.27	1.27	1.24	1.26	1.26	1.26
0.00	0.00	0.00	0.00	0.00	0.00
0.00	0.00	0.00	0.00	0.00	0.00
0.25	0.25	0.22	0.24	0.24	0.24
0.73	0.72	0.73	0.73	0.73	0.73
0.00	0.00	0.00	0.00	0.00	0.00
4.01	4.01	4.02	4.01	4.01	4.01
0.98	0.97	0.96	0.97	0.98	0.97
25	**26**	**23**	**25**	**25**	**25**
75	74	77	75	75	75
0	0	0	0	0	0
Oligoclase	**Oligoclase**	**Oligoclase**	**Oligoclase**	**Oligoclase**	**Oligoclase**

Biotite analyses.

Date	***2022 August 24-26***								
Pluton	**Leucogranito Cupim**								
Sample	**GC1**								
Field	*Field 1*		*Field 3*		*Field 4*	*Field 5*	*Field 7*		*Field 13*
Spectrum	*Spectrum 2*	*Spectrum 7*	*Spectrum 21*	*Spectrum 22*	*Spectrum 28*	*Spectrum 36*	*Spectrum 47*	*Spectrum 48*	*Spectrum 92*
SiO2	34.49	34.82	34.09	34.56	35.33	34.59	35.5	34.63	34.72
TiO2	2.3	2.29	2.96	3.06	2.43	2.54	2.67	2.75	2.65
Al2O3	17.46	17.23	16.79	16.82	17.97	17.34	17.48	17.04	16.91
FeOt	28.7	28.58	29.53	28.59	27.5	28.79	27.34	28.38	28.3
MnO	0.41	0.44	0.46	0.45	0.46	0.47	0.46	0.46	0.5
MgO	3.75	3.8	3.65	3.73	3.98	3.92	4.25	4.03	4.12
K2O	9.45	9.59	9.17	9.47	9.16	9.07	9.14	9.48	9.51
Total	**96.56**	**96.75**	**96.65**	**96.68**	**96.83**	**96.72**	**96.84**	**96.77**	**96.71**
Number of ions on the basis of 24 (O, OH, F) or 22 oxygen equivalents									
Si	5.45	5.49	5.41	5.46	5.5	5.45	5.53	5.45	5.47
Al[IV]	2.55	2.51	2.59	2.54	2.5	2.55	2.47	2.55	2.53
Al[VI]	0.7	0.69	0.55	0.59	0.8	0.66	0.73	0.62	0.61
Ti	0.27	0.27	0.35	0.36	0.28	0.3	0.31	0.33	0.31
Fet	3.79	3.77	3.92	3.77	3.58	3.79	3.56	3.74	3.73
Mn	0.05	0.06	0.06	0.06	0.06	0.06	0.06	0.06	0.07
Mg	0.88	0.89	0.86	0.88	0.92	0.92	0.99	0.95	0.97
K	1.9	1.93	1.86	1.91	1.82	1.82	1.81	1.9	1.91

		GC2							GC5A
	Field 14	*Field 1*	*Field 4*		*Field 5*	*Field 7*	*Field 9*	*Field 10*	*Field 1*
Spectrum 93	*Spectrum 96*	*Spectrum 1*	*Spectrum 24*	*Spectrum 26*	*Spectrum 33*	*Spectrum 37*	*Spectrum 48*	*Spectrum 52*	*Spectrum 5*
34.44	35.29	34.92	35.07	35.08	35.17	34.2	34.97	34.48	35.56
2.39	2.06	2.98	2.1	2.53	2	2.54	2.36	1.69	2.37
16.91	17.49	18.22	18.37	18.34	18.7	17.8	18.18	18.73	17.76
28.88	27.73	27.42	27.73	27.22	27.35	28.75	27.89	28.62	27.34
0.37	0.46	0.35	0.39	0.42	0.32	0.39	0.37	0.34	0.32
4.06	4.32	3.63	3.66	3.77	3.84	3.44	3.58	3.78	3.97
9.61	9.45	9.29	9.43	9.55	9.5	9.62	9.39	9.12	9.58
96.66	**96.8**	**96.81**	**96.75**	**96.91**	**96.88**	**96.74**	**96.74**	**96.76**	**96.9**
5.45	5.52	5.44	5.48	5.47	5.47	5.4	5.47	5.41	5.54
2.55	2.48	2.56	2.52	2.53	2.53	2.6	2.53	2.59	2.46
0.6	0.74	0.79	0.86	0.83	0.91	0.71	0.82	0.87	0.8
0.28	0.24	0.35	0.25	0.3	0.23	0.3	0.28	0.2	0.28
3.82	3.63	3.58	3.62	3.55	3.56	3.8	3.65	3.75	3.56
0.05	0.06	0.05	0.05	0.06	0.04	0.05	0.05	0.05	0.04
0.96	1.01	0.84	0.85	0.88	0.89	0.81	0.84	0.88	0.92
1.94	1.89	1.85	1.88	1.9	1.89	1.94	1.87	1.82	1.9

			GC5B					GC6	
	Field 2	*Field 8*	*Field 2*		*Field 4*	*Field 10*		*Field 2*	*Field 5*
Spectrum 6	*Spectrum 15*	*Spectrum 68*	*Spectrum 13*	*Spectrum 14*	*Spectrum 30*	*Spectrum 53*	*Spectrum 55*	*Spectrum 11*	*Spectrum 27*
35.47	35.23	34.71	35.5	34.93	34.6	35.29	34.96	34.95	35.57
2.03	2.13	2.43	2.4	2.4	2.4	2.35	2.38	2.22	1.89
18.28	18.23	17.77	18.29	17.95	18.04	18.12	18.15	18.36	18.73
27.52	27.4	28.12	27.34	27.93	28.35	27.57	27.81	28.2	27.99
0.34	0.38	0.4	0.28	0.26	0.37	0.36	0.36	0.35	0.32
4.07	4.07	4.07	3.83	3.64	3.61	3.69	3.71	3.07	3.08
9.15	9.44	9.33	9.25	9.52	9.41	9.48	9.28	9.41	9.23
96.86	**96.88**	**96.83**	**96.89**	**96.63**	**96.78**	**96.86**	**96.65**	**96.56**	**96.81**
5.51	5.49	5.44	5.51	5.48	5.43	5.5	5.47	5.49	5.54
2.49	2.51	2.56	2.49	2.52	2.57	2.5	2.53	2.51	2.46
0.86	0.84	0.72	0.86	0.8	0.77	0.83	0.82	0.88	0.98
0.24	0.25	0.29	0.28	0.28	0.28	0.28	0.28	0.26	0.22
3.58	3.57	3.69	3.55	3.66	3.72	3.6	3.64	3.7	3.65
0.04	0.05	0.05	0.04	0.03	0.05	0.05	0.05	0.05	0.04
0.94	0.95	0.95	0.89	0.85	0.85	0.86	0.87	0.72	0.72
1.81	1.88	1.87	1.83	1.9	1.88	1.89	1.85	1.88	1.83

	GC7A							
	Field 1		*Field 6*			*Field 7*		*Field 8*
Spectrum 28	*Spectrum 106*	*Spectrum 107*	*Spectrum 40*	*Spectrum 41*	*Spectrum 42*	*Spectrum 51*	*Spectrum 52*	*Spectrum 56*
35.07	35.46	35.11	35.19	35.17	35.21	35.12	34.64	34.64
1.81	1.65	1.59	1.46	1.51	1.54	1.56	1.54	1.46
18.88	19.11	18.9	19.24	19	19.33	18.71	18.79	18.98
28.05	28.09	28.68	28.41	28.81	28.3	28.83	29.27	29.34
0.27	0.35	0.37	0.33	0.34	0.32	0.37	0.37	0.33
3.23	2.87	2.75	2.56	2.57	2.7	2.61	2.65	2.66
9.28	9.18	9.28	9.26	9.24	9.3	9.29	9.14	9.2
96.59	**96.71**	**96.68**	**96.45**	**96.64**	**96.7**	**96.49**	**96.4**	**96.61**
5.49	5.53	5.5	5.52	5.51	5.5	5.52	5.47	5.46
2.51	2.47	2.5	2.48	2.49	2.5	2.48	2.53	2.54
0.97	1.04	1	1.07	1.03	1.06	0.99	0.96	0.98
0.21	0.19	0.19	0.17	0.18	0.18	0.18	0.18	0.17
3.67	3.66	3.76	3.72	3.78	3.7	3.79	3.86	3.86
0.04	0.05	0.05	0.04	0.05	0.04	0.05	0.05	0.04
0.75	0.67	0.64	0.6	0.6	0.63	0.61	0.62	0.62
1.85	1.83	1.86	1.85	1.85	1.85	1.86	1.84	1.85

		Field10	
Spectrum 57	*Spectrum 58*	*Spectrum 84*	*Spectrum 85*
35.17	34.93	34.7	34.75
1.51	1.59	1.62	1.6
19.18	19.04	19.39	19.27
28.44	28.61	28.75	28.82
0.33	0.31	0.33	0.3
2.62	2.67	2.48	2.52
9.27	9.51	9.39	9.41
96.52	**96.66**	**96.66**	**96.67**
5.51	5.48	5.45	5.46
2.49	2.52	2.55	2.54
1.05	1.01	1.04	1.02
0.18	0.19	0.19	0.19
3.73	3.76	3.77	3.78
0.04	0.04	0.04	0.04
0.61	0.62	0.58	0.59
1.85	1.9	1.88	1.89

Biotite analyses.

Date	***Aug-22***								
Pluton	**Caatinga-Lamim Complex**								
Sample	**CM44A**				**CM44B**				
Field	***1***		***2***		***1***		***2***	***3***	***4***
Spectrum	***1***	***2***	***1***	***6***	***3***	***4***	***1***	***3***	***4***
SiO2	38.24	37.97	36.63	36.46	40.02	39.96	38.62	39.81	38.08
TiO2	2.76	2.83	2.62	2.54	0	0	1.89	2.2	2.34
Al2O3	16.35	16.65	16.18	16.18	15.47	16.4	15.92	15.8	15.03
FeOt	23.89	23.94	26.82	27.4	22.24	21.58	21.98	20.88	23.09
MnO	0	0	0	0	0	0	0	0	0
MgO	8.02	8.07	7.71	7.7	11.34	11.23	11.06	11.27	10.35
Na2O	0	0	0	0	0	0	0	0	0
K2O	10.74	10.53	10.05	9.72	10.92	10.83	10.53	10.03	11.11
Cr2O3	0	0	0	0	0	0	0	0	0
Total	**100**	**99.99**	**100.01**	**100**	**99.99**	**100**	**100**	**99.99**	**100**
Number of ions on the basis of 24 (O, OH, F) or 22 oxygen equivalents									
Si	5.67	5.63	5.51	5.50	5.88	5.84	5.67	5.78	5.66
Al[IV]	2.33	2.37	2.49	2.50	2.12	2.16	2.33	2.22	2.34
Al[VI]	0.53	0.54	0.39	0.37	0.55	0.66	0.43	0.48	0.29
Ti	0.31	0.32	0.30	0.29	0.00	0.00	0.21	0.24	0.26
Cr	0.00	0.00	0.00	0.00	0.00	0.00	0.00	0.00	0.00
Fet	2.96	2.97	3.38	3.45	2.73	2.64	2.70	2.54	2.87
Mn	0.00	0.00	0.00	0.00	0.00	0.00	0.00	0.00	0.00
Mg	1.77	1.78	1.73	1.73	2.48	2.45	2.42	2.44	2.29
K	2.03	1.99	1.93	1.87	2.04	2.02	1.97	1.86	2.11

	24-Sep							**24-Sep**	
	Caatinga-Lamim Complex							**Ressaquinha Complex**	
	CM44B							**CM46A**	
5	**5**		**7**	**9**		**1**			
3	***77***	***78***	***105***	***138***	***139***	***12***	***13***	***7***	***15***
38.53	38.03	39.03	36.51	38.14	41.77	38.84	37.48	33.4	33.59
2.35	1.82	1.84	1.49	1.63	1.64	1.7	1.53	1.52	1.7
15.66	16.8	17.88	16.72	17.3	19.43	17.61	17.13	16.91	16.97
22.29	20.04	20.43	20.97	20.91	20.97	20.56	20.18	22.17	22.6
0	0.38	0.39	0.5	0.4	0.42	0.41	0.42	0	0.25
10.49	11.24	11.66	10.92	11.03	12.44	11.42	11.37	9.1	9.21
0	0	0	0	0	0	0	0	0	0
10.67	9.52	9.86	9.34	9.75	9.88	9.52	9.44	8.4	8.09
0	0	0	0	0	0	0	0	0	0
99.99	**97.83**	**101.09**	**96.45**	**99.16**	**106.55**	**100.06**	**97.55**	**91.5**	**92.41**
5.68	5.64	5.59	5.54	5.60	5.63	5.62	5.58	5.39	5.37
2.32	2.36	2.41	2.46	2.40	2.37	2.38	2.42	2.61	2.63
0.39	0.57	0.61	0.53	0.60	0.72	0.63	0.59	0.60	0.56
0.26	0.20	0.20	0.17	0.18	0.17	0.19	0.17	0.18	0.20
0.00	0.00	0.00	0.00	0.00	0.00	0.00	0.00	0.00	0.00
2.75	2.48	2.45	2.66	2.57	2.37	2.49	2.51	2.99	3.02
0.00	0.05	0.05	0.06	0.05	0.05	0.05	0.05	0.00	0.03
2.30	2.48	2.49	2.47	2.41	2.50	2.46	2.52	2.19	2.19
2.00	1.80	1.80	1.81	1.83	1.70	1.76	1.79	1.73	1.65

							Caatinga Lamim Complex CM49		
2	**3**			**5**			**1**		
7	***12***	***13***	***14***	***38***	***43***	***46***	***12***	***11***	***16***
34.72	34.15	35.21	35.64	34.32	34.54	34.57	37.93	37.86	37.16
1.62	1.65	1.13	1.39	1.31	1.62	1.58	2	1.75	1.75
16.78	16.38	16.38	17.57	17.03	16.83	16.85	16.7	17.05	16.92
21.86	21.27	21.27	20.88	21.42	21.73	21.87	21.2	20.83	20.25
0.23	0	0	0	0.22	0.15	0.18	0	0	0.21
8.94	9.05	9.48	9.59	8.8	8.79	8.82	11.92	12.06	11.96
0	0	0	0	0	0	0	0	0	0
9.3	9.05	9.26	9.29	9.14	9.23	9.27	9.37	9.46	9.51
0	0	0	0	0	0	0	0	0	0
93.45	**91.55**	**92.73**	**94.36**	**92.24**	**92.89**	**93.14**	**99.12**	**99.01**	**97.76**
5.48	5.49	5.58	5.52	5.48	5.48	5.48	5.57	5.56	5.53
2.52	2.51	2.42	2.48	2.52	2.52	2.52	2.43	2.44	2.47
0.61	0.60	0.63	0.72	0.69	0.63	0.63	0.46	0.50	0.50
0.19	0.20	0.13	0.16	0.16	0.19	0.19	0.22	0.19	0.20
0.00	0.00	0.00	0.00	0.00	0.00	0.00	0.00	0.00	0.00
2.89	2.86	2.82	2.70	2.86	2.89	2.90	2.60	2.56	2.52
0.03	0.00	0.00	0.00	0.03	0.02	0.02	0.00	0.00	0.03
2.11	2.17	2.24	2.21	2.10	2.08	2.08	2.61	2.64	2.65
1.87	1.86	1.87	1.83	1.86	1.87	1.87	1.75	1.77	1.80

								14-Oct Caraníba gneiss CM47	
		2	**6**		**8**	**9**	**11**	**1**	
18	***19***	***27***	***11***	***12***	***5***	***17***	***11***	**1**	**8**
37.69	37.42	37.48	37.02	37.86	37.67	37.78	37.02	36.74	35.44
1.85	1.64	1.62	1.5	2.12	1.84	1.61	1.49	1.58	1.91
16.99	16.66	16.82	16.82	16.86	16.92	17.34	16.78	17.29	16.75
20.82	20.8	20.54	19.96	20.67	20.04	20.36	20.3	21.39	20.94
0.23	0	0.23	0	0	0	0	0.18	0.31	0.35
11.82	11.91	11.58	11.85	11.92	12.1	12.16	11.9	10.25	9.86
0	0	0	0	0	0	0	0	0	0
9.57	9.32	9.12	9.46	9.69	9.35	9.59	9.56	9.78	9.45
0	0	0	0	0	0	0	0	0	0
98.97	**97.75**	**97.39**	**96.61**	**99.12**	**97.92**	**98.84**	**97.23**	**97.34**	**94.7**
5.55	5.57	5.59	5.56	5.55	5.57	5.54	5.54	5.53	5.49
2.45	2.43	2.41	2.44	2.45	2.43	2.46	2.46	2.47	2.51
0.49	0.49	0.54	0.54	0.47	0.52	0.54	0.51	0.60	0.56
0.20	0.18	0.18	0.17	0.23	0.20	0.18	0.17	0.18	0.22
0.00	0.00	0.00	0.00	0.00	0.00	0.00	0.00	0.00	0.00
2.56	2.59	2.56	2.51	2.54	2.48	2.50	2.54	2.69	2.72
0.03	0.00	0.03	0.00	0.00	0.00	0.00	0.02	0.04	0.05
2.59	2.64	2.57	2.65	2.61	2.67	2.66	2.66	2.30	2.28
1.80	1.77	1.73	1.81	1.81	1.76	1.80	1.83	1.88	1.87

						2			3
18	**19**	**20**	**21**	**22**	**23**	**31**	**33**	**36**	**40**
36.4	35.9	34.35	35.83	38.21	36.87	36.85	37.43	36.32	37.2
1.32	1.41	1.81	1.47	1.81	1.55	1.76	1.62	1.56	1.46
17.44	16.45	16.04	16.94	17.55	17.37	17.66	17.52	17.29	17.63
20.95	20.57	20.68	20.93	21.69	21.41	20.68	21.56	21.22	21.05
0.3		0.34	0.35	0.27	0.35	0.29	0.3	0.29	0.39
10.15	9.77	9.34	10	10.6	10.32	10.2	10.4	10.18	10.63
0	0	0	0	0	0	0	0	0	0
9.39	9.32	9.12	9.53	9.68	9.66	9.65	9.56	9.55	9.84
0	0	0	0	0	0	0	0	0	0.2
95.95	**93.42**	**91.68**	**95.05**	**99.81**	**97.53**	**97.09**	**98.39**	**96.41**	**98.4**
5.54	5.61	5.51	5.53	5.58	5.54	5.53	5.56	5.52	5.53
2.46	2.39	2.49	2.47	2.42	2.46	2.47	2.44	2.48	2.47
0.67	0.64	0.55	0.61	0.61	0.61	0.66	0.62	0.61	0.62
0.15	0.17	0.22	0.17	0.20	0.18	0.20	0.18	0.18	0.16
0.00	0.00	0.00	0.00	0.00	0.00	0.00	0.00	0.00	0.02
2.67	2.69	2.78	2.70	2.65	2.69	2.60	2.68	2.70	2.62
0.04	0.00	0.05	0.05	0.03	0.04	0.04	0.04	0.04	0.05
2.30	2.28	2.23	2.30	2.31	2.31	2.28	2.30	2.31	2.35
1.82	1.86	1.87	1.88	1.80	1.85	1.85	1.81	1.85	1.86

41	47	49	54
37.2	37.43	37.86	36.66
1.65	1.6	1.42	1.55
17.36	17.62	17.93	17.22
20.58	21.06	21.27	20.64
0.25	0.35	0.31	0.37
10.56	10.67	10.87	10.32
0	0	0	0
9.71	9.82	10.01	9.66
0.33	0.18	0	0.28
97.64	**98.73**	**99.67**	**96.7**
5.56	5.54	5.55	5.54
2.44	2.46	2.45	2.46
0.61	0.61	0.64	0.61
0.19	0.18	0.16	0.18
0.04	0.02	0.00	0.03
2.57	2.61	2.61	2.61
0.03	0.04	0.04	0.05
2.35	2.35	2.37	2.33
1.85	1.85	1.87	1.86

Amphibole analyses. Classifitcation according to Li et al., 2020.

Date	***24-Sep***					
Pluton	**Caatinga Lamim Camplex**					
Sample	**CM49**					
Field	***1***					
Spectrum	***17***	***23***	***24***	***25***	***26***	***28***
SiO2	45.85	44.14	49.08	45.05	43.82	48.16
TiO2	0.79	0.44	0.46	1.02	1.12	0.72
Al2O3	11.19	12.72	9.04	11.64	12.12	9.01
FeOt	20.09	20.2	18.18	20.61	20.58	18.74
MnO	0.36	0.3	0.32	0.29	0.36	0.36
MgO	10.4	9.04	12.17	9.74	9.38	11.75
CaO	12.12	11.72	12.32	12.11	11.89	12.25
Na2O	0	0	0	0	0	0
K2O	0.65	0.64	0.35	0.79	0.9	0.4
Total	**101.45**	**99.2**	**101.92**	**101.25**	**100.17**	**101.39**
Number of ions on the basis of 23 O, OH, F)						
Si	6.46	6.37	6.81	6.40	6.30	6.75
Al	1.54	1.63	1.19	1.60	1.70	1.25
Al	0.32	0.53	0.29	0.35	0.35	0.23
Ti	0.08	0.05	0.05	0.11	0.12	0.08
Fe3+	1.27	1.26	1.08	1.21	1.28	1.12
Mg	2.19	1.95	2.52	2.06	2.01	2.45
Fe2+	1.09	1.18	1.03	1.24	1.19	1.07
Mn	0.04	0.04	0.04	0.04	0.04	0.04
Ca	1.83	1.81	1.83	1.84	1.83	1.84
K	0.12	0.12	0.06	0.14	0.17	0.07
Class.	**Mg-Fe-Hornblende**	**Mg-Hornblende**	**Mg-Hornblende**	**Mg-Hornblende**	**Mg-Fe-Hornblende**	**Mg-Fe-Hornblende**

Li, X., Zhang, C., Behrens, H., Holtz, F., 2020. Calculating amphibole formula from electron microprobe analysis data using a machine learning meth

			4	**6**	**7**
29	***30***	***31***	***7***	***10***	***9***
43.91	44.45	44.4	46.92	44.97	47.65
0.45	0.35	1.03	0.87	0.87	0.35
13.49	11.84	11.18	10.85	10.9	8.76
20.09	19.99	20.56	19.43	19.88	16.94
0.34	0.34	0.26	0	0.28	0.29
9.28	10	9.95	10.66	10.1	11.26
12.01	11.96	12	12	11.86	11.46
0	0	0	0	0	0
0.64	0.59	0.74	0.56	0.67	0.28
100.21	**99.52**	**100.12**	**101.29**	**99.53**	**96.99**
6.27	6.38	6.37	6.59	6.47	6.93
1.73	1.62	1.63	1.41	1.53	1.07
0.54	0.38	0.26	0.39	0.32	0.43
0.05	0.04	0.11	0.09	0.09	0.04
1.31	1.38	1.32	1.12	1.25	0.00
1.98	2.14	2.13	2.23	2.17	2.44
1.09	1.02	1.15	1.17	1.14	2.06
0.04	0.04	0.03	0.00	0.03	0.04
1.84	1.84	1.85	1.81	1.83	1.79
0.12	0.11	0.14	0.10	0.12	0.05
Mg-Hornblende	**Mg-Fe-Hornblende**	**Mg-Fe-Hornblende**	**Mg-Hornblende**	**Mg-Fe-Hornblende**	**Mg-Hornblende**

od based on principal components regression. Lithos 362–363, 105469. https://doi.org/https://doi.org/10.1016/j.lithos.2020.105469

8	**9**		**12**		
8	***16***	***18***	***12***	***13***	***14***
43.49	46.44	44.8	48.43	46.13	46.57
0.44	0.88	0.98	0.43	0.74	0.72
14.37	10.15	11.16	9.22	10.98	9.49
20.5	18.78	19.61	18.64	19.32	18.65
0.3	0.37	0.29	0.3	0.26	0.3
8.77	10.78	9.88	11.76	10.52	11.03
11.91	12.03	11.94	12.17	12.04	11.98
0	0	0	0	0	0
0.53	0.51	0.68	0.42	0.6	0.44
100.31	**99.94**	**99.34**	**101.37**	**100.59**	**99.18**
6.20	6.62	6.47	6.77	6.54	6.68
1.80	1.38	1.53	1.23	1.46	1.32
0.61	0.33	0.37	0.29	0.38	0.29
0.05	0.09	0.11	0.05	0.08	0.08
1.37	1.09	1.14	1.13	1.16	1.11
1.86	2.29	2.13	2.45	2.22	2.36
1.08	1.15	1.23	1.05	1.13	1.13
0.04	0.05	0.04	0.04	0.03	0.04
1.82	1.84	1.85	1.82	1.83	1.84
0.10	0.09	0.13	0.08	0.11	0.08
Mg-Hornblende	**Mg-Fe-Hornblende**	**Mg-Fe-Hornblende**	**Mg-Fe-Hornblende**	**Mg-Hornblende**	**Mg-Fe-Hornblende**

Garnet anayses.

Date	***2022 August 24-26***						
Pluton	**Cupim Leucogranite**						
Sample	**GC5B**						
Field	***Field 1***					***Field 15***	
Spectrum	***Spectrum 1***	***Spectrum 2***	***Spectrum 3***	***Spectrum 4***	***Spectrum 5***	***Spectrum 79***	***Spectrum 80***
SiO2	37.91	36.91	37.07	37.02	37.02	34.09	36.44
TiO2	0	0	0	0	0	0	0
Al2O3	20.89	20.51	20.6	20.56	20.55	19.18	20.58
FeOt	18.54	18.59	18.12	17.51	16.78	21.13	17.38
Cr2O3	0	0	0	0	0	0	0
MnO	7.87	8.46	8.74	9.36	9.93	9.56	10.44
MgO	0.16	0.14	0.17	0.14	0.09	0.14	0.12
CaO	12.52	13.28	13.25	13.42	13.72	13.5	13.06
Total	**97.89**	**97.89**	**97.95**	**98.01**	**98.09**	**97.6**	**98.02**
Numbers of ions on the basis of 24 O							
Si	6.12	6.02	6.03	6.02	6.02	5.74	5.96
AlIV	-0.12	-0.02	-0.03	-0.02	-0.02	0.26	0.04
AlVI	4.1	3.96	3.98	3.96	3.95	3.55	3.92
Cr	0	0	0	0	0	0	0
Fe3+	0	0	0	0	0.04	1.05	0.18
Ti	0	0	0	0	0	0	0
Mg	0.04	0.03	0.04	0.03	0.02	0.04	0.03
Fe2+	2.52	2.53	2.47	2.38	2.24	1.87	2.19
Mn	1.08	1.17	1.2	1.29	1.37	1.36	1.45
Ca	2.17	2.32	2.31	2.34	2.39	2.44	2.29
Mol per cent end-members							
Almandine	43.29	41.85	40.95	39.41	37.22	33.21	36.85
Andradite	0	0	0	0	1.05	23.84	4.35
Grossular	37.44	38.3	38.36	38.69	39.7	42.43	38.4
Pyrope	0.67	0.56	0.68	0.56	0.36	0.61	0.49
Spessartine	18.61	19.29	20	21.33	22.72	23.75	24.26

			GC7A					
			Field 4					
Spectrum 81	***Spectrum 82***	***Spectrum 83***	***Spectrum 14***	***Spectrum 15***	***Spectrum 16***	***Spectrum 17***	***Spectrum 18***	***Spectrum 19***
36.66	36.69	36.6	35.11	34.95	34.88	34.74	34.82	34.61
0	0	0	0	0	0	0	0	0
20.48	20.26	20.33	20.13	19.98	20.25	19.94	19.98	19.72
15.77	15.13	15.66	27.93	29.07	29.41	29.79	29.63	29.82
0	0	0	0	0	0	0	0	0
11.85	12.23	11.78	11.7	11.11	11.05	11.12	11.11	11.32
0.08	0.1	0.04	0.3	0.35	0.38	0.39	0.36	0.34
13.37	13.88	13.82	1.66	1.25	0.71	0.65	0.73	0.8
98.21	**98.29**	**98.23**	**96.83**	**96.71**	**96.68**	**96.63**	**96.63**	**96.61**
5.98	5.98	5.97	5.96	5.96	5.94	5.94	5.95	5.93
0.02	0.02	0.03	0.04	0.04	0.06	0.06	0.05	0.07
3.91	3.87	3.88	3.99	3.97	4.01	3.96	3.97	3.92
0	0	0	0	0	0	0	0	0
0.16	0.22	0.22	0.06	0.11	0.07	0.15	0.12	0.22
0	0	0	0	0	0	0	0	0
0.02	0.02	0.01	0.08	0.09	0.1	0.1	0.09	0.09
1.98	1.84	1.91	3.9	4.03	4.12	4.1	4.11	4.04
1.64	1.69	1.63	1.68	1.6	1.59	1.61	1.61	1.64
2.34	2.42	2.42	0.3	0.23	0.13	0.12	0.13	0.15
33.23	30.83	32.13	65.44	67.75	69.36	69.21	69.19	68.36
4	5.31	5.29	1.57	2.59	1.64	3.54	2.81	5.21
39.07	40.53	40.45	5.07	3.83	2.18	2	2.25	2.48
0.33	0.41	0.16	1.27	1.49	1.62	1.67	1.54	1.46
27.38	28.23	27.26	28.22	26.92	26.83	27.11	27.02	27.7

			Field 5					
Spectrum 20	***Spectrum 21***	***Spectrum 22***	***Spectrum 24***	***Spectrum 25***	***Spectrum 26***	***Spectrum 27***	***Spectrum 28***	***Spectrum 29***
34.98	33.93	34.83	34.79	36.42	34.74	34.75	34.98	34.67
0	0	0	0	0	0	0	0	0
19.85	19.34	19.95	19.96	20.9	19.85	20.02	20.11	19.87
29.45	29.76	29.58	28.43	27.24	28.49	28.85	29.47	29.36
0	0	0	0	0	0	0	0	0
11.28	11.6	10.96	11.68	10.62	11.94	11.3	10.69	11.74
0.35	0.31	0.39	0.28	0.34	0.24	0.33	0.33	0.28
0.75	1.69	0.94	1.64	1.38	1.51	1.46	1.07	0.74
96.66	**96.63**	**96.65**	**96.78**	**96.9**	**96.77**	**96.71**	**96.65**	**96.66**
5.97	5.86	5.95	5.93	6.09	5.93	5.93	5.96	5.94
0.03	0.14	0.05	0.07	-0.09	0.07	0.07	0.04	0.06
3.97	3.79	3.96	3.95	4.21	3.93	3.96	4	3.95
0	0	0	0	0	0	0	0	0
0.09	0.52	0.13	0.18	-0.45	0.2	0.17	0.06	0.18
0	0	0	0	0	0	0	0	0
0.09	0.08	0.1	0.07	0.08	0.06	0.08	0.08	0.07
4.11	3.73	4.08	3.86	4.29	3.85	3.93	4.13	4.01
1.63	1.7	1.59	1.69	1.5	1.73	1.63	1.54	1.7
0.14	0.31	0.17	0.3	0.25	0.28	0.27	0.2	0.14
68.9	64.35	68.79	65.32	69.85	65.21	66.54	69.43	67.83
2.21	11.81	3.19	4.27	-12.14	4.78	4.08	1.48	4.24
2.3	5.34	2.89	5.05	4.06	4.66	4.5	3.28	2.29
1.49	1.36	1.67	1.2	1.39	1.03	1.42	1.41	1.2
27.31	28.95	26.65	28.43	24.7	29.11	27.54	25.88	28.68

							Field 9	
Spectrum 30	***Spectrum 31***	***Spectrum 32***	***Spectrum 36***	***Spectrum 37***	***Spectrum 38***	***Spectrum 39***	***Spectrum 67***	***Spectrum 68***
34.63	34.4	34.54	35.35	34.83	37.02	34.91	49.42	36.37
0	0	0	0	0	0	0	0	0
19.95	19.8	19.84	19.93	19.94	21.11	20.15	16.52	20.54
29.27	29.85	29.9	26.16	29.76	20.92	29.4	17.87	21.62
0	0	0	0	0	0	0	0	0
11.74	11.19	11.03	10.78	10.58	7.26	10.71	6.2	7.14
0.26	0.31	0.4	0.23	0.49	0.14	0.44	0.14	0.16
0.83	1.05	0.88	4.58	1.03	11.17	1.04	7.81	11.71
96.68	**96.6**	**96.59**	**97.03**	**96.63**	**97.62**	**96.65**	**97.96**	**97.54**
5.93	5.9	5.92	5.97	5.95	6.04	5.95	7.56	5.98
0.07	0.1	0.08	0.03	0.05	-0.04	0.05	-1.56	0.02
3.95	3.91	3.93	3.93	3.96	4.09	3.99	4.54	3.96
0	0	0	0	0	0	0	0	0
0.18	0.28	0.23	0.15	0.14	-0.2	0.09	-3.38	0.09
0	0	0	0	0	0	0	0	0
0.07	0.08	0.1	0.06	0.12	0.03	0.11	0.03	0.04
3.99	3.98	4.04	3.53	4.09	3.06	4.09	5.83	2.88
1.7	1.63	1.6	1.54	1.53	1	1.55	0.8	0.99
0.15	0.19	0.16	0.83	0.19	1.95	0.19	1.28	2.06
67.6	67.84	68.5	59.32	69.01	50.5	68.95	72.02	48.22
4.32	6.51	5.44	3.7	3.49	-5.07	2.12	1747.53	2.19
2.57	3.27	2.73	13.88	3.17	32.33	3.19	16.93	34.49
1.12	1.34	1.73	0.97	2.1	0.56	1.88	0.42	0.66
28.71	27.55	27.05	25.83	25.73	16.61	25.98	10.62	16.63

Spectrum 69	*Spectrum 70*	*Spectrum 71*	*Spectrum 72*	*Spectrum 73*	*Spectrum 74*	*Spectrum 75*	*Spectrum 83*	**GC7B** *Field 1* *Spectrum 1*
33.84	34.77	35.11	35.64	35.37	34.74	39.71	34.79	36.65
0	0	0	0	0	0	0	0	0
20.91	19.88	19.95	20.24	20.11	19.81	22.39	19.81	20.72
28.3	29.13	28.43	28.41	29.16	30.02	17.74	29.51	20.38
0	0	0	0	0	0	0	0	0
11.61	10.99	10.92	10.92	10.5	10.79	6.9	11.2	6.97
0.3	0.45	0.31	0.37	0.54	0.44	0.21	0.32	0.1
1.83	1.47	2.04	1.19	1.01	0.78	10.43	1.03	12.88
96.79	**96.69**	**96.76**	**96.77**	**96.69**	**96.58**	**97.38**	**96.66**	**97.7**
5.78	5.94	5.97	6.03	6	5.95	6.3	5.95	5.99
0.22	0.06	0.03	-0.03	0	0.05	-0.3	0.05	0.01
3.99	3.93	3.97	4.06	4.02	3.94	4.49	3.94	3.98
0	0	0	0	0	0	0	0	0
0.35	0.19	0.09	-0.14	-0.04	0.17	-1.23	0.16	0.04
0	0	0	0	0	0	0	0	0
0.08	0.11	0.08	0.09	0.14	0.11	0.05	0.08	0.02
3.66	3.95	3.94	4.17	4.18	4.11	3.64	4.04	2.74
1.68	1.59	1.57	1.56	1.51	1.56	0.93	1.62	0.96
0.33	0.27	0.37	0.22	0.18	0.14	1.77	0.19	2.26
63.83	66.77	66.12	68.93	69.52	69.4	56.36	68.19	45.84
7.72	4.65	2.32	-3.5	-0.89	4.08	-40.07	3.91	0.97
5.79	4.53	6.22	3.58	3.06	2.41	28.14	3.17	37.65
1.32	1.93	1.32	1.55	2.28	1.89	0.79	1.37	0.41
29.06	26.77	26.34	25.95	25.14	26.3	14.72	27.26	16.11

Spectrum 2	*Spectrum 3*	*Spectrum 4*	*Spectrum 5*	*Spectrum 6*	*Spectrum 7*	*Spectrum 8*	*Spectrum 9*	*Field 7 Spectrum 42*
35.94	33.48	34.9	34.31	34.93	33.65	34.48	37.2	34.94
0	0	0	0	0	0	0	0	0
20.72	19.2	19.98	19.73	20.07	19.19	19.55	21.78	19.99
27.44	30.95	29.62	30.04	29.41	30.86	30.3	24.28	23.84
0	0	0	0	0	0	0	0	0
10.97	11.6	10.98	11.33	11	11.52	10.98	9.86	7.03
0.39	0.43	0.43	0.44	0.45	0.37	0.47	0.46	0.17
1.43	0.82	0.73	0.73	0.79	0.91	0.78	0.66	11.32
96.89	**96.48**	**96.64**	**96.58**	**96.65**	**96.5**	**96.56**	**94.24**	**97.29**
6.04	5.82	5.96	5.9	5.96	5.84	5.92	6.25	5.84
-0.04	0.18	0.04	0.1	0.04	0.16	0.08	-0.25	0.16
4.14	3.75	3.98	3.89	3.99	3.76	3.88	4.55	3.78
0	0	0	0	0	0	0	0	0
-0.27	0.64	0.1	0.31	0.08	0.59	0.29	-1.23	0.55
0	0	0	0	0	0	0	0	0
0.1	0.11	0.11	0.11	0.11	0.1	0.12	0.12	0.04
4.15	3.79	4.12	3.97	4.1	3.83	4.04	4.73	2.75
1.56	1.71	1.59	1.65	1.59	1.69	1.6	1.4	1
0.26	0.15	0.13	0.13	0.14	0.17	0.14	0.12	2.03
68.27	66.12	69.28	67.84	68.99	66.47	68.57	73.81	47.53
-6.96	14.21	2.43	7.34	2.05	13.21	6.84	-38.63	12.39
4.26	2.62	2.24	2.28	2.42	2.9	2.42	1.9	34.71
1.62	1.91	1.84	1.91	1.92	1.64	2.03	1.84	0.73
25.85	29.34	26.64	27.97	26.67	28.99	26.97	22.45	17.04

Spectrum 43	*Spectrum 44*	*Spectrum 45*	*Spectrum 46*	*Spectrum 47*	*Spectrum 48*	*Spectrum 49*	*Spectrum 50*	*Spectrum 51*
25.32	29.81	34.51	35.15	33.25	35.97	35.54	34.85	21.96
0	0	0	0	0	0	0	0	0
14.57	17.02	20.16	20.16	19.24	20.7	20.51	19.88	12.98
38.17	34.22	29.87	29.52	31.39	27.79	28.03	28.04	42.99
0	0	0	0	0	0	0	0	0
15.68	13.35	10.95	10.7	11.44	11.4	11.37	11.4	15.46
0.25	0.28	0.46	0.47	0.41	0.34	0.36	0.26	0.25
1.68	1.43	0.65	0.65	0.7	0.65	1.01	2.37	1.48
95.67	**96.11**	**96.6**	**96.65**	**96.43**	**96.85**	**96.82**	**96.8**	**95.12**
4.91	5.44	5.9	5.98	5.79	6.05	6.01	5.94	4.47
1.09	0.56	0.1	0.02	0.21	-0.05	-0.01	0.06	1.53
2.24	3.1	3.97	4.02	3.74	4.16	4.09	3.93	1.59
0	0	0	0	0	0	0	0	0
3.93	2.1	0.19	0	0.7	-0.32	-0.15	0.2	5.26
0	0	0	0	0	0	0	0	0
0.07	0.08	0.12	0.12	0.11	0.09	0.09	0.07	0.08
1.76	2.89	4.06	4.2	3.81	4.25	4.12	3.78	1.25
2.58	2.06	1.59	1.54	1.69	1.62	1.63	1.64	2.67
0.35	0.28	0.12	0.12	0.13	0.12	0.18	0.43	0.32
38.97	55.53	69.12	70.24	66.77	69.81	68.35	63.9	31.46
56.21	37.55	4.5	-0.04	15.16	-8.31	-3.67	4.8	65.5
7.11	5.14	2.02	1.98	2.26	1.94	3.04	7.29	7.22
1.47	1.4	1.99	1.99	1.84	1.41	1.51	1.11	1.7
52.45	37.93	26.87	25.78	29.14	26.84	27.09	27.7	59.62

	Field 9						**Mount VII** ***Field 1***	
Spectrum 52	***Spectrum 74***	***Spectrum 75***	***Spectrum 76***	***Spectrum 77***	***Spectrum 78***	***Spectrum 79***	***Spectrum 80***	***Spectrum 6***
30.16	35.88	36	25.22	33.22	38.51	35.5	34.51	36.58
0	0	0	0	0	0	0	0	0
17.65	20.8	21.58	14.37	18.85	23	20.36	19.78	20.81
33.31	22.75	26.6	39.95	31.64	25.09	29.01	29.52	21.92
0	0	0	0	0	0	0	0	0
13.08	6.76	11.23	14.74	11.63	9.04	10.62	11.65	6.25
0.27	0.1	0.31	0.25	0.39	0.91	0.48	0.32	0.13
1.75	11.13	1.25	0.92	0.68	0.61	0.74	0.87	11.83
96.22	**97.42**	**96.97**	**95.45**	**96.41**	**97.16**	**96.71**	**96.65**	**97.52**
5.45	5.92	6.01	4.92	5.8	6.23	6.01	5.92	6
0.55	0.08	-0.01	1.08	0.2	-0.23	-0.01	0.08	0
3.21	3.97	4.26	2.22	3.68	4.62	4.07	3.92	4.01
0	0	0	0	0	0	0	0	0
1.92	0.15	-0.41	3.94	0.76	-1.31	-0.12	0.25	-0.01
0	0	0	0	0	0	0	0	0
0.07	0.02	0.08	0.07	0.1	0.22	0.12	0.08	0.03
2.92	2.98	4.16	2.04	3.79	4.79	4.24	3.96	3.02
2	0.95	1.59	2.43	1.72	1.24	1.52	1.69	0.87
0.34	1.97	0.22	0.19	0.13	0.11	0.13	0.16	2.08
55.72	50.4	68.58	45.12	66.41	74.9	70.42	67.33	50.35
34.68	3.69	-10.64	56.54	16.51	-40.87	-3.16	5.85	-0.37
6.22	33.23	3.72	3.91	2.19	1.7	2.23	2.7	34.65
1.33	0.42	1.28	1.48	1.75	3.52	2.02	1.38	0.53
36.73	15.96	26.42	49.5	29.65	19.88	25.34	28.59	14.47

Spectrum 7	*Spectrum 8*	*Spectrum 9*	*Spectrum 10*	*Spectrum 11*	*Spectrum 12*	*Spectrum 13*	*Spectrum 14*	*Spectrum 15*
35.16	35.06	35.01	35.13	34.95	35.03	34.87	34.91	34.96
0	0	0	0	0	0	0	0	0
20.2	20.08	20.14	20.12	20.19	19.98	19.94	19.88	19.97
27.27	28.82	29.61	29.58	29.64	29.75	29.29	29.79	29.6
0	0	0	0	0	0	0	0	0
12.83	11.46	10.76	10.57	10.6	10.67	11.33	10.86	10.83
0.22	0.37	0.5	0.52	0.54	0.47	0.37	0.47	0.51
1.22	0.94	0.62	0.71	0.72	0.73	0.88	0.71	0.78
96.9	**96.73**	**96.64**	**96.63**	**96.64**	**96.63**	**96.68**	**96.62**	**96.65**
5.97	5.97	5.96	5.98	5.95	5.97	5.95	5.96	5.96
0.03	0.03	0.04	0.02	0.05	0.03	0.05	0.04	0.04
4.01	4	4.01	4.01	4	3.99	3.97	3.96	3.97
0	0	0	0	0	0	0	0	0
0.02	0.05	0.05	0.02	0.07	0.06	0.12	0.11	0.09
0	0	0	0	0	0	0	0	0
0.06	0.09	0.13	0.13	0.14	0.12	0.09	0.12	0.13
3.85	4.05	4.17	4.19	4.15	4.17	4.05	4.13	4.12
1.85	1.65	1.55	1.52	1.53	1.54	1.64	1.57	1.56
0.22	0.17	0.11	0.13	0.13	0.13	0.16	0.13	0.14
64.45	67.87	69.94	70.15	69.8	69.97	68.2	69.47	69.2
0.61	1.25	1.12	0.39	1.62	1.53	2.95	2.72	2.31
3.72	2.87	1.9	2.17	2.21	2.23	2.7	2.18	2.39
0.93	1.57	2.13	2.21	2.3	2	1.58	2.01	2.17
30.9	27.68	26.03	25.48	25.69	25.8	27.52	26.35	26.24

Spectrum 16	*Spectrum 17*	*Spectrum 18*	*Spectrum 19*	*Spectrum 20*	*Spectrum 21*	*Spectrum 22*	*Spectrum 23*	*Spectrum 24*
34.83	34.89	34.81	34.7	34.66	34.69	34.63	34.64	34.59
0	0	0	0	0	0	0	0	0
19.93	20.05	20.01	19.98	19.96	19.92	19.91	19.85	19.74
29.75	29.73	29.86	29.98	29.98	30.04	29.97	29.01	30.28
0	0	0	0	0	0	0	0	0
10.83	10.78	10.78	10.74	10.79	10.8	11	12.02	10.85
0.55	0.49	0.48	0.52	0.51	0.48	0.46	0.32	0.44
0.73	0.69	0.67	0.69	0.7	0.66	0.64	0.86	0.66
96.62	**96.63**	**96.61**	**96.61**	**96.6**	**96.59**	**96.61**	**96.7**	**96.56**
5.95	5.95	5.95	5.93	5.93	5.93	5.93	5.93	5.93
0.05	0.05	0.05	0.07	0.07	0.07	0.07	0.07	0.07
3.96	3.98	3.97	3.96	3.95	3.95	3.94	3.93	3.92
0	0	0	0	0	0	0	0	0
0.14	0.1	0.12	0.17	0.18	0.17	0.19	0.2	0.22
0	0	0	0	0	0	0	0	0
0.14	0.12	0.12	0.13	0.13	0.12	0.12	0.08	0.11
4.1	4.14	4.13	4.1	4.09	4.11	4.08	3.93	4.1
1.57	1.56	1.56	1.55	1.56	1.56	1.59	1.74	1.58
0.13	0.13	0.12	0.13	0.13	0.12	0.12	0.16	0.12
69.07	69.62	69.65	69.42	69.28	69.53	69.14	66.58	69.49
3.38	2.36	2.96	3.98	4.32	4.07	4.54	4.85	5.22
2.25	2.12	2.06	2.13	2.16	2.04	1.98	2.66	2.04
2.35	2.09	2.06	2.23	2.19	2.06	1.98	1.38	1.9
26.33	26.17	26.23	26.21	26.37	26.37	26.9	29.39	26.57

			Mount IV *Field 1*					
Spectrum 25	***Spectrum 26***	***Spectrum 27***	***Spectrum 2***	***Spectrum 3***	***Spectrum 4***	***Spectrum 5***	***Spectrum 6***	***Spectrum 7***
34.44	34.4	34.33	36.35	34.9	35.01	34.78	34.96	34.81
0	0	0	0	0	0	0	0	0
19.76	19.84	19.65	20.49	20.02	19.89	19.98	20.05	20.04
30.12	29.75	29.1	21.38	29.44	29.36	29.05	29.28	29.81
0	0	0	0	0	0	0	0	0
11.01	11.24	11.79	7.93	11.11	11.14	11.55	11.32	10.78
0.51	0.47	0.39	0.09	0.45	0.31	0.33	0.35	0.48
0.73	0.92	1.43	11.33	0.74	0.94	1.02	0.71	0.69
96.57	**96.62**	**96.69**	**97.57**	**96.66**	**96.65**	**96.71**	**96.67**	**96.61**
5.91	5.9	5.89	5.98	5.95	5.97	5.94	5.96	5.94
0.09	0.1	0.11	0.02	0.05	0.03	0.06	0.04	0.06
3.91	3.91	3.87	3.96	3.98	3.97	3.96	3.99	3.98
0	0	0	0	0	0	0	0	0
0.28	0.29	0.36	0.08	0.1	0.08	0.15	0.07	0.12
0	0	0	0	0	0	0	0	0
0.13	0.12	0.1	0.02	0.11	0.08	0.08	0.09	0.12
4.02	3.95	3.79	2.85	4.09	4.11	3.99	4.1	4.13
1.6	1.63	1.71	1.11	1.61	1.61	1.67	1.64	1.56
0.13	0.17	0.26	2	0.14	0.17	0.19	0.13	0.13
68.45	67.43	64.76	47.76	68.85	68.86	67.32	68.91	69.59
6.47	6.71	8.31	2.1	2.43	1.88	3.59	1.65	2.9
2.27	2.87	4.46	33.39	2.27	2.88	3.14	2.18	2.12
2.21	2.04	1.69	0.37	1.92	1.32	1.41	1.49	2.06
27.07	27.67	29.09	18.48	26.96	26.95	28.12	27.42	26.23

	Field 2							
Spectrum 8	***Spectrum 14***	***Spectrum 15***	***Spectrum 16***	***Spectrum 17***	***Spectrum 18***	***Spectrum 19***	***Spectrum 20***	***Spectrum 21***
35	63.57	34.61	34.73	35.17	29.07	34.9	34.78	34.8
0	0	0	0	0	0	0	0	0
20.13	10.91	19.69	19.87	20.01	20.47	19.94	20	20.08
28.1	13.55	29.54	27.51	27.62	37.53	28.3	29.19	28.82
0	0	0	0	0	0	0	0	0
11.78	5.41	11.82	12.22	12.46	6.57	12.15	11.62	12.09
0.32	0.1	0.32	0.24	0.25	1.66	0.26	0.32	0.29
1.48	4.92	0.67	2.31	1.35	0.43	1.25	0.79	0.66
96.81	**98.46**	**96.65**	**96.88**	**96.86**	**95.73**	**96.8**	**96.7**	**96.74**
5.95	9.09	5.94	5.92	5.98	5.2	5.95	5.94	5.94
0.05	-3.09	0.06	0.08	0.02	0.8	0.05	0.06	0.06
3.99	4.93	3.92	3.91	3.99	3.51	3.96	3.97	3.98
0	0	0	0	0	0	0	0	0
0.09	-6.91	0.22	0.25	0.05	1.86	0.13	0.13	0.11
0	0	0	0	0	0	0	0	0
0.08	0.02	0.08	0.06	0.06	0.44	0.07	0.08	0.07
3.9	8.77	4	3.65	3.87	3.54	3.89	4.02	3.99
1.7	0.66	1.72	1.76	1.79	1	1.75	1.68	1.75
0.27	0.75	0.12	0.42	0.25	0.08	0.23	0.14	0.12
65.6	84.27	67.62	62.04	64.82	70.76	65.57	67.9	67.3
2.2	143.76	5.28	5.84	1.25	30.94	3.2	3.24	2.77
4.53	8.29	2.07	7.13	4.11	1.58	3.84	2.43	2.03
1.36	0.23	1.38	1.03	1.06	8.51	1.11	1.37	1.24
28.5	7.21	28.92	29.8	30	19.14	29.48	28.3	29.42

		Field 3					Field 5	
Spectrum 22	***Spectrum 23***	***Spectrum 28***	***Spectrum 29***	***Spectrum 30***	***Spectrum 31***	***Spectrum 32***	***Spectrum 43***	***Spectrum 45***
34.74	34.95	35.6	34.99	34.82	34.93	35.02	35.5	34.98
0	0	0	0	0	0	0	0	0
19.86	19.92	20.28	20.11	20.15	20.02	20.03	20.16	20.17
29.02	27.46	26.89	28.62	29.35	29	28.88	27.6	29.57
0	0	0	0	0	0	0	0	0
11.79	12.52	12.06	11.12	11.16	11.54	11.63	11.62	10.76
0.34	0.24	0.22	0.38	0.5	0.42	0.43	0.29	0.47
0.95	1.78	1.89	1.54	0.69	0.81	0.72	1.7	0.7
96.7	**96.87**	**96.94**	**96.76**	**96.67**	**96.72**	**96.71**	**96.87**	**96.65**
5.94	5.95	6.01	5.95	5.94	5.96	5.97	6.01	5.96
0.06	0.05	-0.01	0.05	0.06	0.04	0.03	-0.01	0.04
3.94	3.95	4.05	3.98	3.99	3.98	3.99	4.03	4.01
0	0	0	0	0	0	0	0	0
0.18	0.15	-0.09	0.1	0.11	0.1	0.07	-0.06	0.05
0	0	0	0	0	0	0	0	0
0.09	0.06	0.06	0.1	0.13	0.11	0.11	0.07	0.12
3.96	3.75	3.9	3.96	4.06	4.03	4.04	3.97	4.15
1.71	1.81	1.73	1.6	1.61	1.67	1.68	1.67	1.55
0.17	0.32	0.34	0.28	0.13	0.15	0.13	0.31	0.13
66.87	63.18	64.7	66.75	68.59	67.74	67.84	65.93	69.8
4.25	3.62	-2.36	2.37	2.69	2.41	1.63	-1.41	1.29
2.93	5.46	5.69	4.72	2.12	2.48	2.2	5.13	2.14
1.46	1.02	0.92	1.62	2.14	1.79	1.83	1.22	2
28.74	30.34	28.69	26.92	27.14	27.98	28.13	27.72	26.05

Spectrum 46	*Spectrum 47*	*Spectrum 48*	*Spectrum 49*	*Spectrum 50*	*Spectrum 51*	*Spectrum 52*	*Spectrum 53*	*Field 6 Spectrum 58*
34.94	35.06	34.9	34.82	34.84	34.78	34.74	34.56	36.37
0	0	0	0	0	0	0	0	0
20.23	19.98	19.95	19.96	19.84	19.89	19.78	19.84	20.57
29.32	29.1	29.32	29.31	29.61	29.17	30.22	28.57	20.31
0	0	0	0	0	0	0	0	0
10.81	11.32	11.26	11.25	11	11.71	10.71	12	8.63
0.49	0.44	0.45	0.5	0.51	0.34	0.46	0.27	0.11
0.88	0.81	0.79	0.83	0.84	0.8	0.67	1.52	11.71
96.67	**96.71**	**96.67**	**96.67**	**96.64**	**96.69**	**96.58**	**96.76**	**97.7**
5.95	5.97	5.96	5.94	5.95	5.95	5.95	5.91	5.97
0.05	0.03	0.04	0.06	0.05	0.05	0.05	0.09	0.03
4.01	3.98	3.97	3.96	3.95	3.95	3.94	3.91	3.96
0	0	0	0	0	0	0	0	0
0.07	0.06	0.11	0.14	0.15	0.15	0.17	0.26	0.1
0	0	0	0	0	0	0	0	0
0.12	0.11	0.11	0.13	0.13	0.09	0.12	0.07	0.03
4.1	4.07	4.06	4.03	4.06	4	4.14	3.81	2.68
1.56	1.63	1.63	1.63	1.59	1.7	1.55	1.74	1.2
0.16	0.15	0.14	0.15	0.15	0.15	0.12	0.28	2.06
69.01	68.31	68.33	67.94	68.5	67.56	69.85	64.72	44.96
1.67	1.59	2.77	3.49	3.68	3.66	4.12	6.1	2.55
2.7	2.48	2.43	2.55	2.58	2.46	2.07	4.71	34.49
2.09	1.87	1.92	2.14	2.18	1.46	1.97	1.16	0.45
26.2	27.34	27.32	27.36	26.74	28.51	26.11	29.41	20.1

Spectrum 59	*Spectrum 60*	*Spectrum 61*	*Spectrum 62*	*Spectrum 63*	*Spectrum 64*
34.84	34.83	34.82	34.84	34.73	34.71
0	0	0	0	0	0
19.9	20.1	19.95	20.09	19.95	19.84
29.63	30.02	29.89	30.07	29.98	29.24
0	0	0	0	0	0
10.93	10.51	10.38	10.31	10.55	11.07
0.45	0.43	0.5	0.5	0.48	0.51
0.89	0.7	1.06	0.77	0.92	1.31
96.64	**96.59**	**96.6**	**96.58**	**96.61**	**96.68**
5.95	5.95	5.94	5.95	5.94	5.93
0.05	0.05	0.06	0.05	0.06	0.07
3.96	3.99	3.96	3.99	3.95	3.92
0	0	0	0	0	0
0.14	0.1	0.14	0.1	0.17	0.22
0	0	0	0	0	0
0.11	0.11	0.13	0.13	0.12	0.13
4.08	4.18	4.11	4.18	4.1	3.94
1.58	1.52	1.5	1.49	1.53	1.6
0.16	0.13	0.19	0.14	0.17	0.24
68.77	70.45	69.35	70.43	69.37	66.76
3.35	2.33	3.49	2.48	3.97	5.18
2.74	2.15	3.26	2.37	2.84	4.04
1.93	1.84	2.14	2.14	2.06	2.19
26.57	25.56	25.25	25.06	25.73	27.01

Major (wt. %) and trace element (ppm) data of the investigated leucogranites from Cupim Pluton. <L.D refers to mesured analyses below the detection limit.

	Laboratory	*LMV / SARM*	*LMV / SARM*	*LMV / SARM*	*LMV / SARM*	*LMV / SARM*	*LMV / SARM*	Average	2SD	Average	2SD
	Sample #	GC1	GC2	GC5A	GC5B	GC6	GC7				
	Magmatic body	Cupim Pluton	Cupim Pluton	Cupim Pluton	Cupim Pluton	Cupim Pluton	Cupim Pluton				
	Lithology group	Group 1	Group 1	Group 1	Group 1	Group 2	Group 2				
	Lithology, mineralogy	*Mus-Bt-Leucogranite*	*Y-Xtm-Mus-Bt-Leucogranite*	*Mus-Bt-Leucogranite*	*Mus-Bt-Leucogranite*	*Grt-Bt-Leucogranite*	*Grt-Bt-Leucogranite*	*Group 1*		*Group 2*	
Whole Rock Major Elements (Unnormalized - wt.%)	SiO_2	73.79	71.96	74.54	73.17	75.33	75.07	**73.37**	**2.18**	**75.2**	**0.37**
	TiO_2	0.09	0.08	0.13	0.14	0.05	0.03	**0.11**	**0.06**	**0.04**	**0.03**
	Al_2O_3	13.95	14.74	13.76	13.62	14.08	13.98	**14.02**	**1**	**14.03**	**0.14**
	Fe_2O_3	1.31	1.09	1.26	1.4	1.14	1	**1.27**	**0.26**	**1.07**	**0.2**
	FeO^T	*1.18*	*0.98*	*1.13*	*1.26*	*1.03*	*0.9*	**1.14**	**0.23**	**0.96**	**0.18**
	MnO	0.02	0.02	0.02	0.03	0.1	0.15	**0.02**	**0.01**	**0.13**	**0.07**
	MgO	0.14	0.12	0.15	0.17	0.08	0.06	**0.15**	**0.04**	**0.07**	**0.03**
	CaO	0.99	0.59	0.97	0.7	0.68	0.61	**0.81**	**0.4**	**0.65**	**0.1**
	Na_2O	3.7	2.95	3.65	3.36	4.13	4.12	**3.42**	**0.69**	**4.13**	**0.01**
	K_2O	5.16	4.83	5.15	5.33	4.87	5.05	**5.12**	**0.42**	**4.96**	**0.25**
	P_2O_5	0.03	0.02	0.03	0.03	0.02	0.01	**0.03**	**0.01**	**0.02**	**0.01**
	H_2O^+	0.16	1.35	0.1	0.16	0.06	0.06	**0.44**	**1.21**	**0.06**	**0.00**
	H_2O^-	0.33	1.8	0.37	0.54	0.29	0.17	**0.76**	**1.40**	**0.23**	**0.17**
	Total	**99.05**	**96.29**	**99.53**	**97.81**	**100.37**	**99.98**	**98.17**	**2.9**	**100.17**	**0.55**
Whole Rock Major Elements (Normalized to 100%)	SiO_2	74.5	74.73	74.89	74.81	75.06	75.09	**74.73**	**0.34**	**75.07**	**0.04**
	TiO_2	0.09	0.08	0.13	0.14	0.05	0.03	**0.11**	**0.06**	**0.04**	**0.03**
	Al_2O_3	14.08	15.31	13.82	13.93	14.03	13.98	**14.29**	**1.38**	**14.01**	**0.06**
	FeO^T	1.19	1.02	1.14	1.29	1.02	0.9	**1.16**	**0.22**	**0.96**	**0.17**
	MnO	0.02	0.02	0.02	0.03	0.1	0.15	**0.02**	**0.01**	**0.12**	**0.07**
	MgO	0.14	0.12	0.15	0.17	0.08	0.06	**0.15**	**0.04**	**0.07**	**0.03**
	CaO	1	0.61	0.97	0.72	0.68	0.61	**0.83**	**0.38**	**0.64**	**0.1**
	Na_2O	3.74	3.06	3.67	3.44	4.11	4.12	**3.48**	**0.61**	**4.12**	**0.01**
	K_2O	5.21	5.02	5.17	5.45	4.85	5.05	**5.21**	**0.36**	**4.95**	**0.28**
	P_2O_5	0.03	0.02	0.03	0.03	0.02	0.01	**0.03**	**0.01**	**0.01**	**0.01**
	Total	100	100	100	100	100	100	**100**	**3.41**	**100**	**0**
Whole-rock major element ratios and indices	**FeO+MgO+TiO2**	1.42	1.23	1.42	1.6	1.15	0.99	**1.42**	**0.31**	**1.07**	**0.23**
	Mg#	17.47	17.91	19.08	19.39	12.21	10.62	**18.46**	**1.84**	**11.42**	**2.24**
	FeO/(FeO+MgO)	0.89	0.89	0.88	0.88	0.93	0.94	**0.89**	**0.01**	**0.93**	**0.01**
	MALI	7.95	7.47	7.87	8.17	8.29	8.56	**7.86**	**0.59**	**8.43**	**0.38**
	ASI	1.11	1.39	1.11	1.14	1.11	1.09	**1.19**	**0.27**	**1.1**	**0.03**
	Al_2O_3/TiO_2	155	184.25	105.85	97.29	281.6	466	**135.6**	**82.43**	**373.8**	**260.78**
	CaO/Na_2O	0.27	0.2	0.27	0.21	0.16	0.15	**0.24**	**0.07**	**0.16**	**0.02**
	K2O/Na2O	1.39	1.64	1.41	1.59	1.18	1.23	**1.51**	**0.25**	**1.2**	**0.07**
	Ba + Sr	377.4	367.2	658	660	260.5	129.2	**515.65**	**331.16**	**194.85**	**185.69**
	Rb/Sr	3.88	3.27	2.5	3.33	5.82	8.27	**3.24**	**1.13**	**7.04**	**3.46**
	Rb/Ba	0.91	0.76	0.48	0.52	1.58	3.3	**0.67**	**0.4**	**2.44**	**2.44**
	Sr/Y	1.67	0.82	4.77	3.74	1.2	0.5	**2.75**	**3.65**	**0.85**	**1**
	(La/Yb)N	7.23	1.2	19.83	14.04	3.68	1.65	**10.58**	**16.2**	**2.67**	**2.87**
	(La/Sm)N	3.64	2.16	4.77	4.42	2.91	2.59	**3.75**	**2.32**	**2.75**	**0.45**
	(Gd/Yb)N	1.44	0.53	2.56	1.97	1	0.62	**1.63**	**1.72**	**0.81**	**0.54**
	Eu/Eu*	0.13	0.14	0.15	0.15	0.1	0.08	**0.14**	**0.02**	**0.09**	**0.03**
Zircon Saturation Temperature Calculations	**Na**	0.12	0.1	0.12	0.11	0.13	0.13	**0.11**	**0.02**	**0.13**	**0**
	K	0.11	0.11	0.11	0.12	0.1	0.11	**0.11**	**0.01**	**0.11**	**0.01**
	Ca	0.02	0.01	0.02	0.01	0.01	0.01	**0.01**	**0.01**	**0.01**	**0**
	Al	0.28	0.3	0.27	0.27	0.28	0.27	**0.28**	**0.03**	**0.27**	**0**
	Si	1.24	1.24	1.25	1.24	1.25	1.25	**1.24**	**0.01**	**1.25**	**0**
	M	0.78	0.61	0.78	0.74	0.76	0.76	**0.73**	**0.16**	**0.76**	**0.01**
	$\ln(Dz_{rc\text{-}melt})$	8.48	8.14	8.33	8.42	8.89	9.41	**8.34**	**0.29**	**9.15**	**0.73**
	Zrc. Sat. T (Miller et al., 2003) - ºC	793.7	837.8	807.42	801.58	759.87	718.37	**810.12**	**38.58**	**739.12**	**58.68**
	Zrc. Sat. T (Boehnke et al., 2013) - ºC	768.57	829.1	785.35	779.45	728.42	678.89	**790.62**	**53.16**	**703.65**	**70.05**
Trace elements (ppm)	**Sn**	9.47	1.66	2.35	3.07	3.43	2.01	**4.14**	**7.20**	**2.72**	**2.01**
	Be	2.29	2.83	1.74	1.82	4.02	3.24	**2.17**	**1.00**	**3.63**	**1.10**
	Cs	5.33	3.55	5.98	6.04	7.85	6.64	**5.23**	**2.32**	**7.25**	**1.71**
	Rb	277	226	265	296	323	305	**266.00**	**59.13**	**314.00**	**25.46**
	Sr	71.4	69.2	106	89	55.5	36.9	**83.90**	**34.39**	**46.20**	**26.30**
	Ba	306	298	552	571	205	92.3	**431.75**	**300.12**	**148.65**	**159.38**
	Ta	1.19	1.21	1.06	1.37	3.34	1.51	**1.21**	**0.25**	**2.43**	**2.59**
	Th	42.5	22.1	48.8	47.6	31.8	16.7	**40.25**	**24.81**	**24.25**	**21.35**
	U	38.4	6.93	59.9	14.7	10.6	10.5	**29.98**	**48.04**	**10.55**	**0.14**
	Pb	69.2	108	73.1	72.2	84	75.5	**80.63**	**36.65**	**79.75**	**12.02**
	Zr	103	144	120	109	68	40.6	**119.00**	**36.18**	**54.30**	**38.75**
	Hf	3.93	6.22	4.23	3.98	2.99	2.26	**4.59**	**2.19**	**2.63**	**1.03**
	Nb	13.8	12.7	11.6	14.2	18.6	18.4	**13.08**	**2.34**	**18.50**	**0.28**
	Y	42.8	84.9	22.2	23.8	46.1	74.5	**43.43**	**58.38**	**60.30**	**40.16**
	V	2.1	1.5	3.1	3.1	1.4	< L.D.	**2.45**	**1.58**	**1.40**	
	Cr	1.4	1.3	1.4	1.2	1.6	1.2	**1.33**	**0.19**	**1.40**	**0.57**
	Co	72.3	56	80.1	71.4	81.5	71.4	**69.95**	**20.17**	**76.45**	**14.28**
	Ni	< L.D.	< L.D.	< L.D.	< L.D.	< L.D.	< L.D.	-	-	-	-
	Cu	< L.D.	< L.D.	< L.D.	< L.D.	< L.D.	< L.D.	-	-	-	-
	Zn	42.5	36.5	36.1	42.5	36.5	24.1	**39.40**	**7.17**	**30.30**	**17.54**
	Ga	20.8	22	19.9	21.3	24.5	25.8	**21.00**	**1.77**	**25.15**	**1.84**
	Mo	< L.D.	< L.D.	< L.D.	< L.D.	< L.D.	< L.D.	-	-	-	-
	La	36.5	15.1	45.2	37.6	24.4	16.9	**33.60**	**25.85**	**20.65**	**10.61**
	Ce	73	23.9	86	94.9	43.1	24.7	**69.45**	**63.34**	**33.90**	**26.02**
	Pr	7.78	4.3	8.83	7.89	5.21	3.21	**7.20**	**3.98**	**4.21**	**2.83**
	Nd	26.6	15.3	29.2	25.8	18.4	11.9	**24.23**	**12.25**	**15.15**	**9.19**
	Sm	6.32	4.4	5.96	5.35	5.28	4.11	**5.51**	**1.68**	**4.70**	**1.65**
	Eu	0.38	0.31	0.39	0.35	0.25	0.17	**0.36**	**0.07**	**0.21**	**0.12**
	Gd	6.06	5.58	4.86	4.41	5.54	5.27	**5.23**	**1.47**	**5.41**	**0.38**
	Tb	1.14	1.41	0.75	0.72	1.1	1.17	**1.01**	**0.66**	**1.14**	**0.10**
	Dy	7.2	11.5	4.14	4.23	7.22	8.79	**6.77**	**6.92**	**8.01**	**2.22**
	Ho	1.49	2.91	0.79	0.84	1.54	2.05	**1.51**	**1.98**	**1.80**	**0.72**
	Er	3.98	8.75	1.99	2.16	4.29	6.19	**4.22**	**6.30**	**5.24**	**2.69**
	Tm	0.58	1.36	0.27	0.31	0.7	1.08	**0.63**	**1.01**	**0.89**	**0.54**
	Yb	3.41	8.49	1.54	1.81	4.48	6.92	**3.81**	**6.45**	**5.70**	**3.45**
	Lu	0.49	1.25	0.22	0.26	0.66	1.06	**0.56**	**0.95**	**0.86**	**0.57**
Chondrite (Taylor and McLennan, 1985) normalized REE values	**La**	99.46	41.14	123.16	102.45	66.49	46.05	**91.55**	**70.44**	**56.27**	**28.90**
	Ce	76.28	24.97	89.86	99.16	45.04	25.81	**72.57**	**66.19**	**35.42**	**27.19**
	Pr	56.79	31.39	64.45	57.59	38.03	23.43	**52.55**	**29.05**	**30.73**	**20.65**
	Nd	37.41	21.52	41.07	36.29	25.88	16.74	**34.07**	**17.23**	**21.31**	**12.93**
	Sm	27.36	19.05	25.8	23.16	22.86	17.79	**23.84**	**7.27**	**20.32**	**7.16**
	Eu	4.37	3.6	4.49	4.05	2.91	1.93	**4.13**	**0.80**	**2.42**	**1.38**
	Gd	19.8	18.24	15.88	14.41	18.1	17.22	**17.08**	**4.80**	**17.66**	**1.25**
	Tb	19.66	24.31	12.95	12.45	18.97	20.17	**17.34**	**11.38**	**19.57**	**1.71**
	Dy	18.9	30.18	10.87	11.1	18.95	23.07	**17.76**	**18.17**	**21.01**	**5.83**
	Ho	17.51	34.2	9.22	9.88	18.1	24.09	**17.70**	**23.24**	**21.09**	**8.48**
	Er	15.98	35.14	7.99	8.67	17.23	24.86	**16.95**	**25.31**	**21.04**	**10.79**
	Tm	16.38	38.2	7.7	8.82	19.69	30.34	**17.77**	**28.31**	**25.01**	**15.06**
	Yb	13.75	34.23	6.21	7.3	18.06	27.9	**15.37**	**26.01**	**22.98**	**13.91**
	Lu	12.73	32.81	5.85	6.9	17.32	27.82	**14.57**	**25.05**	**22.57**	**14.85**

Miller, C. F., McDowell, S. M. & Mapes, R. W. (2003). Hot and cold granites? Implications of856zircon saturation temperatures and preservation of inheritance. Geology 31, 529-532.
Boehnke, P., Watson, E. B., Trail, D., Harrison, T. M. & Schmitt, A. K. (2013). Zircon saturation759re-revisited. Chemical Geology 351, 324-334.
Taylor, S.R., McLennan, S.M., 1985. The Continental Crust: Its Composition and Evolution, Blackwell. ed. Oxford.

Location, nature, mineralogy and whole-rock geochemical compositions of samples from the Mineiro belt TTG rocks.

Sample	CM44A	CM44B-felsic	CM44B-mafic	CM46A	CM47	CM49
Latitude S	20°50'10"	20°50'10"	20°50'10"	20°57'08"	20°55'20"	20°50'21"
Longitude W	43°49'15"	43°49'15"	43°49'15"	43°47'35"	43°46'59"	43°43'08"
Geological Unit [a]	Caatinga-Lamim complex	Caatinga-Lamim complex	Caatinga-Lamim complex	Ressaquinha complex	Caranaíba gneiss	Caatinga-Lamim complex
Rock type	Trondhjemite (neosome)	Trondhjemite (paleosome)	Trondhjemite (paleosome)	Trondhjemite	Tonalitic gneiss	Tonalite
Major minerals [b]	Pl, Qz, Bt/Chl	Pl, Qz, Bt	Bt, Pl, Qz	Pl, Qz, Bt	Pl, Qz, Bt	Pl, Amp, Qz, Bt
Minor / accessory minerals [b]	Kfs, Ms, Grt, Zrn	Ap, Zrn	Ap, Ttn, OP, Zrn	Ttn, Ep, Ap, Zrn	Ttn, Ep, Ap, Zrn	Ttn, Ep, Ap, OP, Zrn
Laboratory	*LGqA/UFOP*	*LMV/SARM*	*LMV/SARM*	*LMV/SARM*	*LMV/SARM*	*LMV/SARM*
Major elements (wt.%) [c]						
SiO_2	74.09	71.20	70.52	70.61	66.73	67.51
TiO_2	0.02	0.05	0.19	0.36	0.55	0.32
Al_2O_3	15.1	17.19	15.37	15.68	16.17	17.57
$Fe_2O_{3(t)}$	0.6	0.45	1.47	2.33	4.20	2.24
MnO	0.08	0.01	0.03	0.03	0.06	0.03
MgO	0.06	0.10	0.63	0.95	2.12	1.09
CaO	0.72	2.15	1.59	2.90	3.01	4.32
Na_2O	4.36	6.65	5.10	5.15	4.32	5.22
K_2O	4.57	1.81	3.13	1.23	2.56	0.86
P_2O_5	0.01	0.02	0.04	0.10	0.24	0.12
LOI	0.39	0.27	0.19	0.88	0.79	0.38
Total	100	99.90	98.26	100.22	100.75	99.66
Trace elements (p.p.m.) [d]						
V	< L.D.	3.2	12.7	27.5	56.2	29.9
Cr	2	1	10	7	47	11
Co	68	66	42	83	70	88
Ni	2	< L.D.	6	6	30	10
Cu	2	6	2	9	16	6
Zn	21	13	51	34	76	29
Ga	28	23	25	20	21	19
Rb	299	61	196	35	78	43
Sr	64	870	702	395	520	956
Y	46	2	2	4	10	2
Zr	23	70	52	195	104	107
Nb	34	1.1	1.9	5.1	7.0	1.7
Cs	8	3.2	16.5	0.8	2.7	6.3
Ba	98	773	2008	551	995	581
La	8.38	5.7	4.6	29.2	28.2	11.8
Ce	17.2	9.1	7.8	51.2	67.3	40.2
Pr	2.1	1.0	0.9	5.3	6.1	2.5
Nd	7.8	3.4	3.4	18.4	22.3	8.7
Sm	3.22	0.64	0.73	2.70	3.94	1.26
Eu	0.35	0.50	0.51	0.98	1.11	0.56
Gd	4.28	0.48	0.58	1.81	2.92	0.80
Tb	0.99	0.06	0.08	0.19	0.39	0.09
Dy	7.25	0.29	0.37	0.87	2.16	0.46
Ho	1.58	0.05	0.07	0.16	0.41	0.09
Er	5.2	0.15	0.17	0.38	0.99	0.23
Tm	0.9	0.02	0.02	0.05	0.14	0.03
Yb	6.42	0.14	0.14	0.37	0.83	0.23
Lu	1.02	0.02	0.02	0.06	0.12	0.04
Hf	1.8	2.0	1.9	4.8	2.6	2.3
Ta	3.3	0.3	0.5	0.2	0.6	0.2
Pb	53.8	23.0	23.9	10.9	16.1	8.2
Th	14	0.7	0.7	6.6	11.7	5.7
U	29	0.9	1.1	0.6	1.4	0.5

[a] *According to Noce et al. (2000), Silva and Baltazar (2013), and this work.*

[b] *Major phases are considered to be >1% modal, minor and accessory phases <1% modal, and are listed by order of decreasing abundance. Abbreviations from Warr, 2021.*

[c] *Typical uncertainties on major element contents (RSD) are 1 to 6% relative for concentrations >1 wt.% and 2 to 8% relative for concentrations <1 wt.%*

[d] *Typical uncertainties on trace element contents (2 S.D.) are 5 to 20% relative for concentrations >10 ppm; 5 to 20% relative for concentrations between >1 ppm; and 10 to 20% relative for concentrations >0.1 ppm. < L.D. denotes bellow detection limit concentration (e.g. L.D.Ni= 2p.p.m.).*

Chemical composition of the quality-control reference materials used during whole-rock chemical analyses at the LMV. Certified composition are from USGS and CRPG (Nancy, France).2SD= 2 × Standard deviation and RSD(%)= Average - Certified

Technique	**ICP-OES**	**ICP-OES**	**ICP-OES**	**Average**	**2SD**	**Certified compositio**	**RSD (%)**
Equipment	**Agilent 5800**	**Agilent 5800**	**Agilent 5800**				
Ref. Material	**DR-N**	**DR-N**	**DR-N**				
Date	**44833**	**44833**	**44833**				
Laboratory	***LMV***	***LMV***	***LMV***				
SiO_2	52.73	52.61	52.39	**52.58**	0.34	52.85	**0.52**
TiO_2	1.1	1.09	1.09	**1.09**	0.01	1.09	**0.31**
Al_2O_3	17.73	17.72	17.62	**17.69**	0.12	17.52	**0.97**
Fe_2O_3	9.66	9.61	9.57	**9.61**	0.09	9.7	**0.89**
FeO^T	*8.69*	*8.65*	*8.61*	***8.65***	*0.08*	*8.73*	***0.89***
MnO	0.23	0.23	0.23	**0.23**	0	0.22	**4.55**
MgO	4.37	4.36	4.34	**4.36**	0.03	4.4	**0.98**
CaO	7	6.98	6.95	**6.98**	0.05	7.05	**1.04**
Na_2O	2.98	2.95	2.93	**2.95**	0.05	2.99	**1.23**
K_2O	1.74	1.73	1.71	**1.73**	0.03	1.7	**1.57**
P_2O_5	0.23	0.23	0.24	**0.23**	0.01	0.25	**6.67**
Ba	0.0387	0.0387	0.0387	**0.0387**	0	0.0385	**0.52**
Sr	0.0391	0.039	0.0389	**0.039**	0	0.04	**2.5**
H_2O^+	2.22	2.22	2.22	**2.22**	0	2.22	**0**
H_2O^-	0.25	0.25	0.25	**0.25**	0	0.25	**0**
Total	**96.88**	**96.62**	**96.19**	**96.56**	0.7	**96.88**	**0.32**

Chemical composition of the quality-control reference materials used during whole-rock chemical analyses at the LMV. Certified composition are from USGS and CRPG (Nancy, France).2SD= 2 × Standard deviation and RSD(%)= Average - Certified content÷Certified content×100.

Technique	**ICP-OES**	**ICP-OES**	**ICP-OES**	**Average**	**2SD**	**Certified composition**	**RSD (%)**
Equipment	**Agilent 5800**	**Agilent 5800**	**Agilent 5800**				
Ref. Material	**BHVO-1**	**BHVO-1**	**BHVO-1**				
Date	**44833**	**44833**	**44833**				
Laboratory	***LMV***	***LMV***	***LMV***				
SiO_2	49.59	49.75	49.72	**49.69**	0.17	49.94	**0.51**
TiO_2	2.85	2.85	2.84	**2.85**	0.01	2.71	**5.04**
Al_2O_3	13.82	13.87	13.84	**13.84**	0.05	13.8	**0.31**
Fe_2O_3	12.26	12.39	12.35	**12.33**	0.13	12.23	**0.84**
FeO^T	*11.03*	*11.15*	*11.11*	***11.1***	0.12	*11*	***0.84***
MnO	0.18	0.18	0.18	**0.18**	0	0.17	**5.88**
MgO	7.35	7.37	7.37	**7.36**	0.02	7.23	**1.84**
CaO	11.43	11.48	11.47	**11.46**	0.05	11.4	**0.53**
Na_2O	2.3	2.31	2.29	**2.3**	0.02	2.26	**1.77**
K_2O	0.53	0.55	0.53	**0.54**	0.02	0.52	**3.21**
P_2O_5	0.27	0.26	0.29	**0.27**	0.03	0.27	**1.23**
Ba	0.0133	0.0135	0.0133	**0.01**	0	0.01	**3.84**
Sr	0.0389	0.039	0.039	**0.039**	0	0.0403	**3.31**
H_2O^+	0.16	0.16	0.16	**0.16**	0	0.16	**0**
H_2O^-	0.05	0.05	0.05	**0.05**	0	0.05	**0**
Total	**99.4**	**99.82**	**99.69**	**99.64**	0.43	**99.36**	**0.28**

Chemical composition of the quality-control reference materials used during whole-rock chemical analyses at the LMV. Certified composition are from USGS and CRPG (Nancy, France).2SD= 2 × Standard deviation and RSD(%)= Average - Certified content÷Certified content×100.

Technique	**ICP-OES**	**ICP-OES**	**Average**	**2SE**	**Certified composition**	**RSD (%)**	**ICP-OES**	**ICP-OES**	**Average**	**2SE**	**Certified composition**	**RSD (%)**
Equipment	**Agilent 5800**	**Agilent 5800**					**Agilent 5800**	**Agilent 5800**				
Ref. Material	**DR-N**	**DR-N**					**BHVO-1**	**BHVO-1**				
Date	**44883**	**44883**					**44883**	**44883**				
Laboratory	***LMV***	***LMV***					***LMV***	***LMV***				
SiO_2	52.95	53.42	**53.19**	0.7	52.85	**0.63**	50.08	50.11	**50.1**	0.04	49.94	**0.31**
TiO_2	1.09	1.11	**1.1**	0	1.09	**0.92**	2.88	2.88	**2.88**	0	2.71	**6.27**
Al_2O_3	17.57	17.71	**17.64**	0.2	17.52	**0.68**	13.76	13.76	**13.76**	0	13.8	**0.29**
Fe_2O_3	9.89	10	**9.95**	0.2	9.7	**2.53**	12.68	12.7	**12.69**	0.03	12.23	**3.76**
FeO^T	*8.9*	*9*	***8.95***	0.1	*8.73*	***2.53***	*11.41*	*11.43*	***11.42***	0.03	*11*	***3.76***
MnO	0.23	0.23	**0.23**	0	0.22	**4.55**	0.18	0.18	**0.18**	0	0.17	**5.88**
MgO	4.49	4.54	**4.52**	0.1	4.4	**2.61**	7.57	7.59	**7.58**	0.03	7.23	**4.84**
CaO	7.21	7.26	**7.24**	0.1	7.05	**2.62**	11.82	11.82	**11.82**	0	11.4	**3.68**
Na_2O	2.94	2.94	**2.94**	0	2.99	**1.67**	2.27	2.26	**2.27**	0.01	2.26	**0.22**
K_2O	1.7	1.71	**1.71**	0	1.7	**0.29**	0.51	0.53	**0.52**	0.03	0.52	**0**
P_2O_5	0.23	0.23	**0.23**	0	0.25	**8**	0.27	0.28	**0.28**	0.01	0.27	**1.85**
Ba	0.0388	0.0393	**0.0391**	0	0.0385	**1.43**	0.0134	0.0135	**0.01**	0	0.01	**3.24**
Sr	0.0386	0.0391	**0.0389**	0	0.04	**2.88**	0.0387	0.0389	**0.0388**	0	0.0403	**3.72**
H_2O^+	2.22	2.22	**2.22**	0	2.22	**0**	0.16	0.16	**0.16**	0	0.16	**0**
H_2O^-	0.25	0.25	**0.25**	0	0.25	**0**	0.05	0.05	**0.05**	0	0.05	**0**
Total	**97.39**	**98.23**	**97.81**	1.2	**96.88**	**0.96**	**100.8**	**100.89**	**100.85**	0.12	**99.36**	**1.5**

Reproducibility of the major element analyses comparing the composition of two duplicated 'unknown' samples. RSD(%)= | First analysis content - Second analysis content| ÷ First analysis content × 100

Technique	**ICP-OES**	**ICP-OES**	**RSD (%)**	**ICP-OES**	**ICP-OES**	**RSD (%)**
Equipment	**Agilent 5800**	**Agilent 5800**		**Agilent 5800**	**Agilent 5800**	
Ref. Material	**GC2**	**GC2**		**GC5B**	**GC5B**	
Date	**44833**	**44883**		**44833**	**44883**	
Laboratory	***LMV***	***LMV***		***LMV***	***LMV***	
SiO_2	70.69	71.96	**1.8**	72.47	73.17	**0.97**
TiO_2	0.08	0.08	**0**	0.13	0.14	**7.69**
Al_2O_3	14.75	14.74	**0.07**	13.89	13.62	**1.94**
Fe_2O_3	1.15	1.09	**5.22**	1.4	1.4	**0**
FeO^T	*1.03*	*0.98*	**5.22**	*1.26*	*1.26*	**0**
MnO	0.02	0.02	**0**	0.03	0.03	**0**
MgO	0.12	0.12	**0**	0.15	0.17	**13.33**
CaO	0.55	0.59	**7.27**	0.69	0.7	**1.45**
Na_2O	2.88	2.95	**2.43**	3.39	3.36	**0.88**
K_2O	4.75	4.83	**1.68**	5.49	5.33	**2.91**
P_2O_5	0.01	0.02	**100**	0.02	0.03	**50**
Ba	0.0322	0.0334	**3.73**	0.0639	0.0631	**1.25**
Sr	0.0071	0.0071	**0**	0.0092	0.0089	**3.26**
H_2O^+	1.59	1.35	**15.09**	0.14	0.16	**14.29**
H_2O^-	1.49	1.8	**20.81**	0.49	0.54	**10.2**
Total	**94.92**	**96.33**	**1.48**	**97.59**	**97.88**	**0.3**

	ICP-MS iCapQ et ICP-OES iCap6500 (Sc uniquement)	As	Ba	Be	Bi	Cd	Co	Cr
Incertitudes (%) en fonction de la teneur	>100µg/g							
	>50 µg/g	<5%	<5%	<5%		<10%	<5%	
	>10 µg/g	<15%	<15%	<15%	<5%	<15%	<10%	<5%
	>1 µg/g	<20%	**		<10%		<20%	<10%
	>0.5 µg/g							
	>0.1 µg/g	**		<20%	<20%	<20%	**	**
	>0.01 µg/g			**	**	**		
es de détermin	L.D. µg/g	0.5	5.5	0.05	0.045	0.02	0.08	0.5

*** L'incertitude sur la mesure est calculée pour 200mg d'échantillon préparé. Elle devient importante (>25%) sur une plage de concentration si*

Cs	Cu	Ga	Ge	Hf	In	Mo	Nb	Ni	Pb
	<8%		<5%		<5%	<5%	<5%		<10%
<5%	<20%	<5%		<5%		<15%		<5%	
<15%	**	<10%	<10%	<10%	<15%	<20%	<10%	**	<20%
<20%		<20%	<20%	<15%	<20%	**	<20%		**
**		**	**	**	**		**		
0.02	2	0.02	0.04	0.03	0.03	0.5	0.015	2	0.45

'tuée entre la limite de détermination et la plus faible concentration pour laquelle un pourcentage d'erreur est indiqué.

Rb	Sb	Sn	Sr	Ta	Th	U	V	W
<5%		<5%	<5%	<5%	<5%	<5%	<5%	<5%
<15%	<5%	<15%	<10%			<10%	<10%	<10%
<20%	<10%	<20%	<20%	<10%	<10%	<15%	<15%	<20%
**	<20%	**	**	<20%	<20%	<20%	**	**
	**			**	**	**		
0.15	0.06	0.3	0.7	0.004	0.02	0.01	0.85	0.8

Y	Zn	Zr	La	Ce	Pr	Nd	Sm	Eu	Gd
<5%	<10%	<5%		<5%	<5%	<5%			
	<20%	<15%	<5%	<10%	<10%	<15%	<5%		<5%
<15%	**	**	<15%	<15%			<15%	<5%	<10%
<20%			<20%	<20%	<20%	<20%	<20%	<10%	<20%
**			**	**	**	**	**	**	**
0.02	7	1.5	0.02	0.03	0.004	0.016	0.005	0.002	0.005

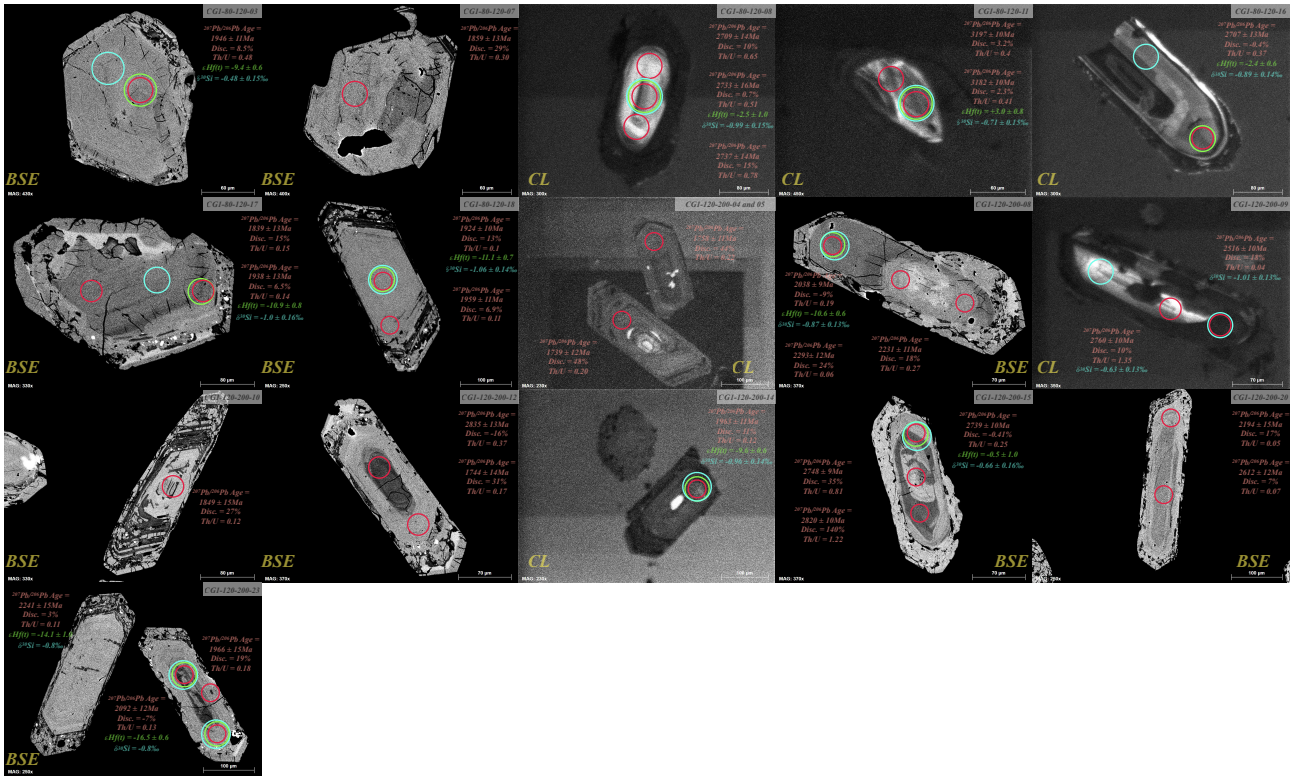
Tb	Dy	Ho	Er	Tm	Yb	Lu
<5%		<5%		<5%	<5%	
<10%	<5%				<10%	<5%
<15%	<10%	<10%	<5%	<10%	<15%	<10%
<20%	<15%	<20%	<10%	<20%	<20%	<20%
**	**	**	**	**	**	**
0.001	0.004	0.001	0.002	0.001	0.002	0.001

Chemical composition of the quality-control reference materials used during whole-rock chemical analyses at the LGqA/UFOP. Certified composition are from USGS. 1SD= Standard deviation and RSD(%)= | Measured - Certified content | ÷ Certified content × 100.

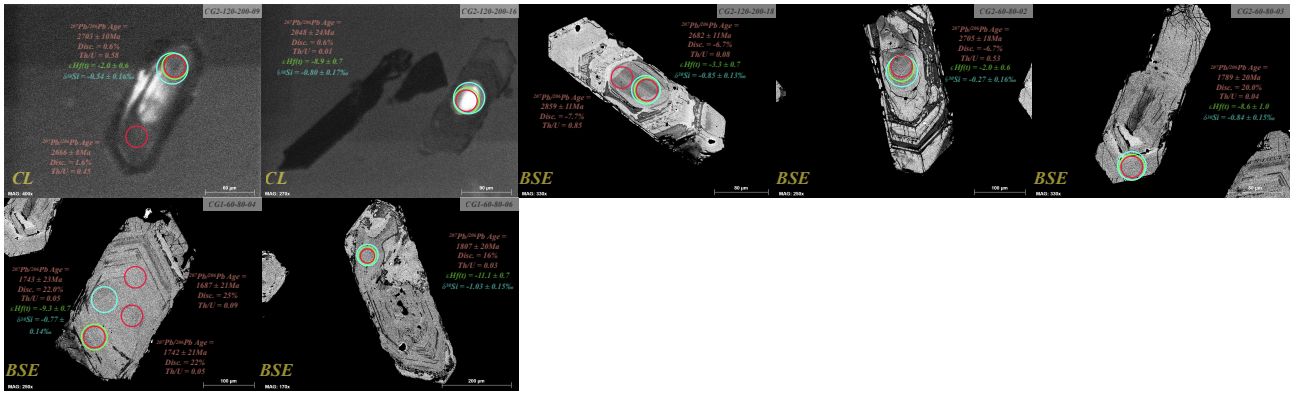
Laboratory	GPS-2 *LGqA/UFOP*	***Certified composition***	***1SD***	**RSD(%)**
Major elements (wt.%) *				
SiO_2	70.74	*66.6*	*0.8*	6
TiO_2	0.61	*0.66*	*0.02*	8
Al_2O_3	13.4	*14.9*	*0.2*	10
$Fe_2O_{3\,(T)}$	4.23	*4.9*	*0.16*	14
MnO	0.05	*0.04*	*0.01*	25
MgO	0.9	*0.96*	*0.03*	6
CaO	1.82	*2.1*	*0.06*	13
Na_2O	2.8	*2.78*	*0.09*	1
K_2O	5.21	*5.38*	*0.14*	3
P_2O_5	0.24	*0.29*	*0.02*	17
LOI				#DIV/0!
Trace elements (p.p.m.) **				
V	< L.D.	*52*	*2*	
Cr	21.5	*20*	*6*	8
Co	7.81	*7.3*	*0.8*	7
Ni	17.6	*17*	*2*	4
Cu	45.6	*43*	*4*	6
Zn	124	*120*	*10*	3
Ga	26.3	*22*	*2*	20
Rb	260	*245*	*7*	6
Sr	274	*240*	*10*	14
Y	26.7	*28*	*2*	5
Zr	107	*550*	*30*	81
Nb	27.9	*27*	*2*	3
Cs	1.28	*1.2*	*0.1*	7
Ba	1545	*1340*	*44*	15

La	207	*180*	*12*	15
Ce	495	*410*	*30*	21
Pr	60.9	*51*	*5*	19
Nd	226	*200*	*12*	13
Sm	28.7	*27*	*1*	6
Eu	5.73	*2.3*	*0.1*	149
Gd	19.4	*12*	*2*	62
Tb	1.73			
Dy	6.5	*6.1*		7
Ho	1.04	*1*	*0.1*	4
Er	2.81	*2.2*		28
Tm	0.29	*0.29*	*0.02*	0
Yb	1.54	*1.6*	*0.2*	4
Lu	0.21	*0.23*	*0.03*	9
Hf	2.95	*14*	*1*	79
Ta	0.93			
Pb	46	*42*	*3*	10
Th	98.6	*105*	*8*	6
U	2.15	*2.4*	*0.19*	10

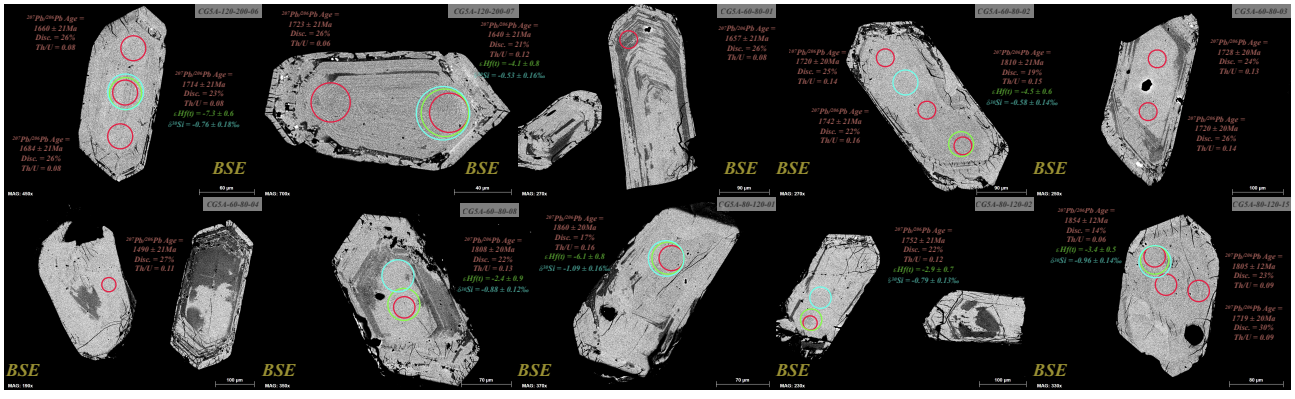
GC1 - Ms-Bt-leucogranite



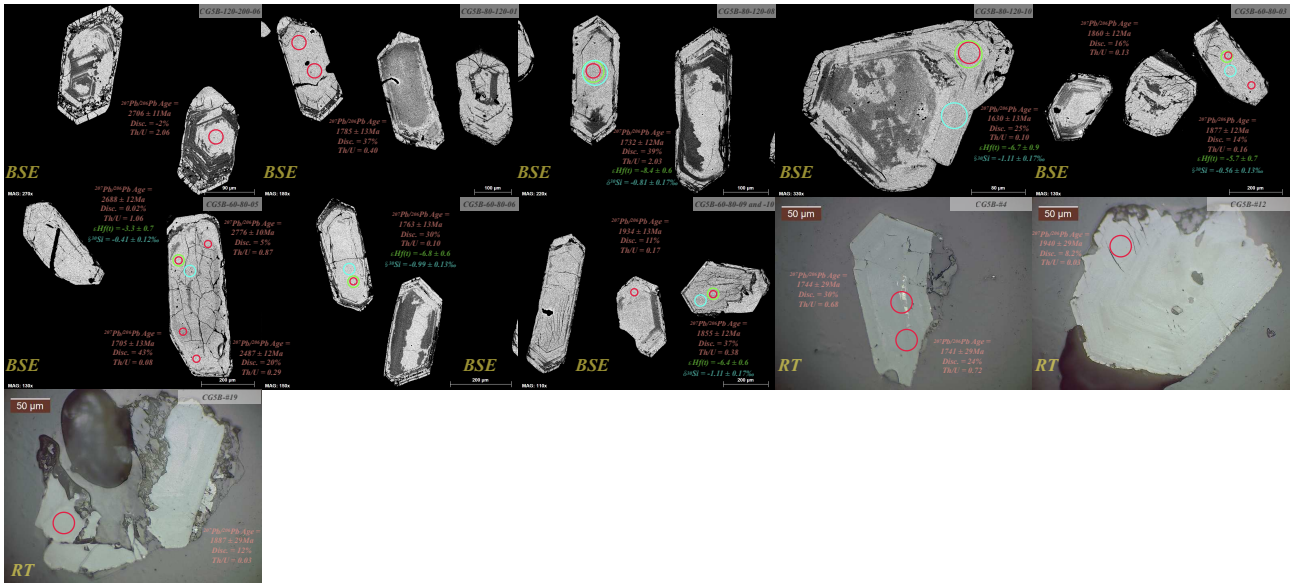
GC2 - Xtm-Ms-Bt-leucogranite



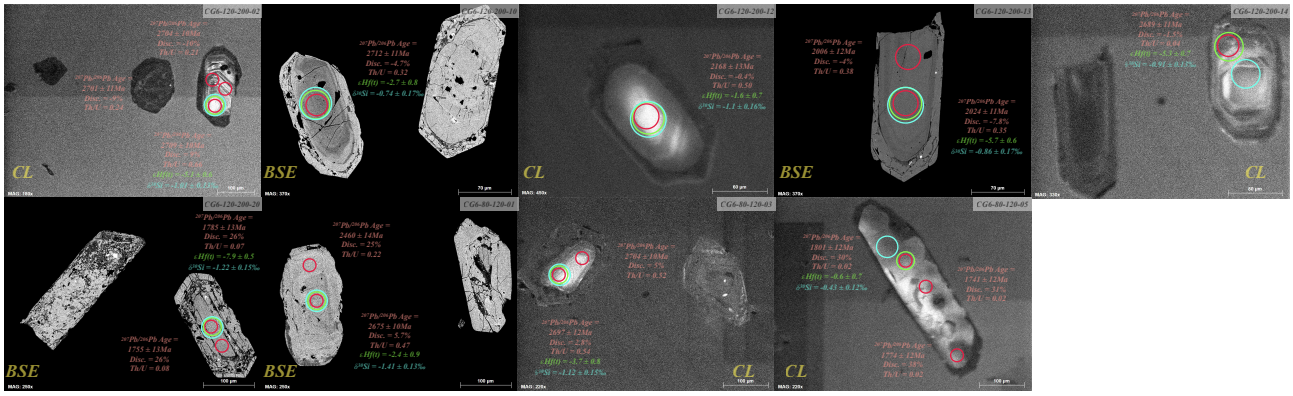
GC5A - Mus-Bt-leucogranite



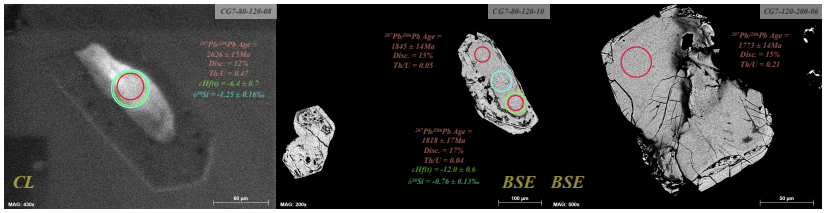
GCB - Ms-Bt-leucogranite



GC6 - Grt-(Ms)-Bt-leucogranite



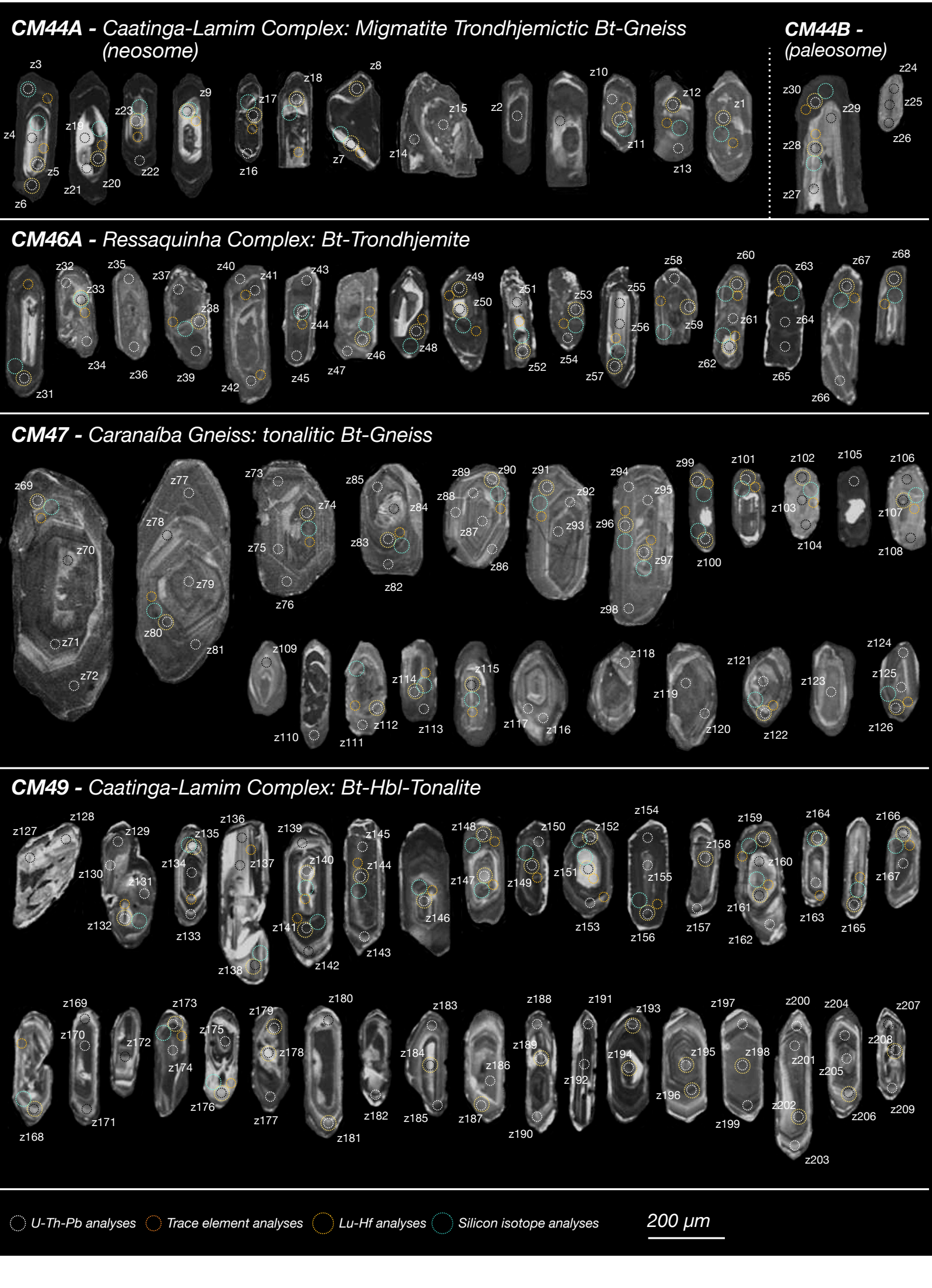
GC7 - Grt-Bt-leucogranite

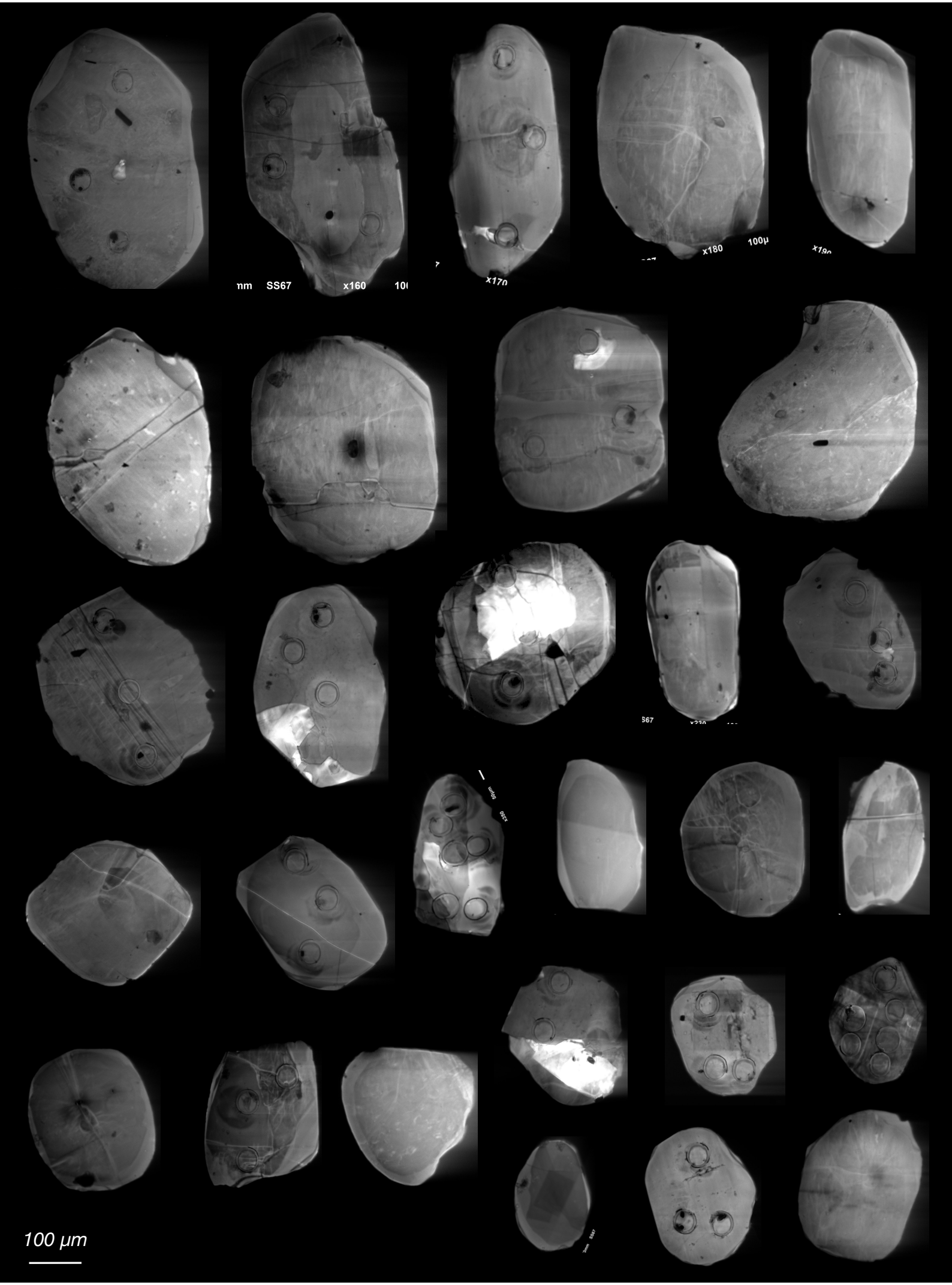


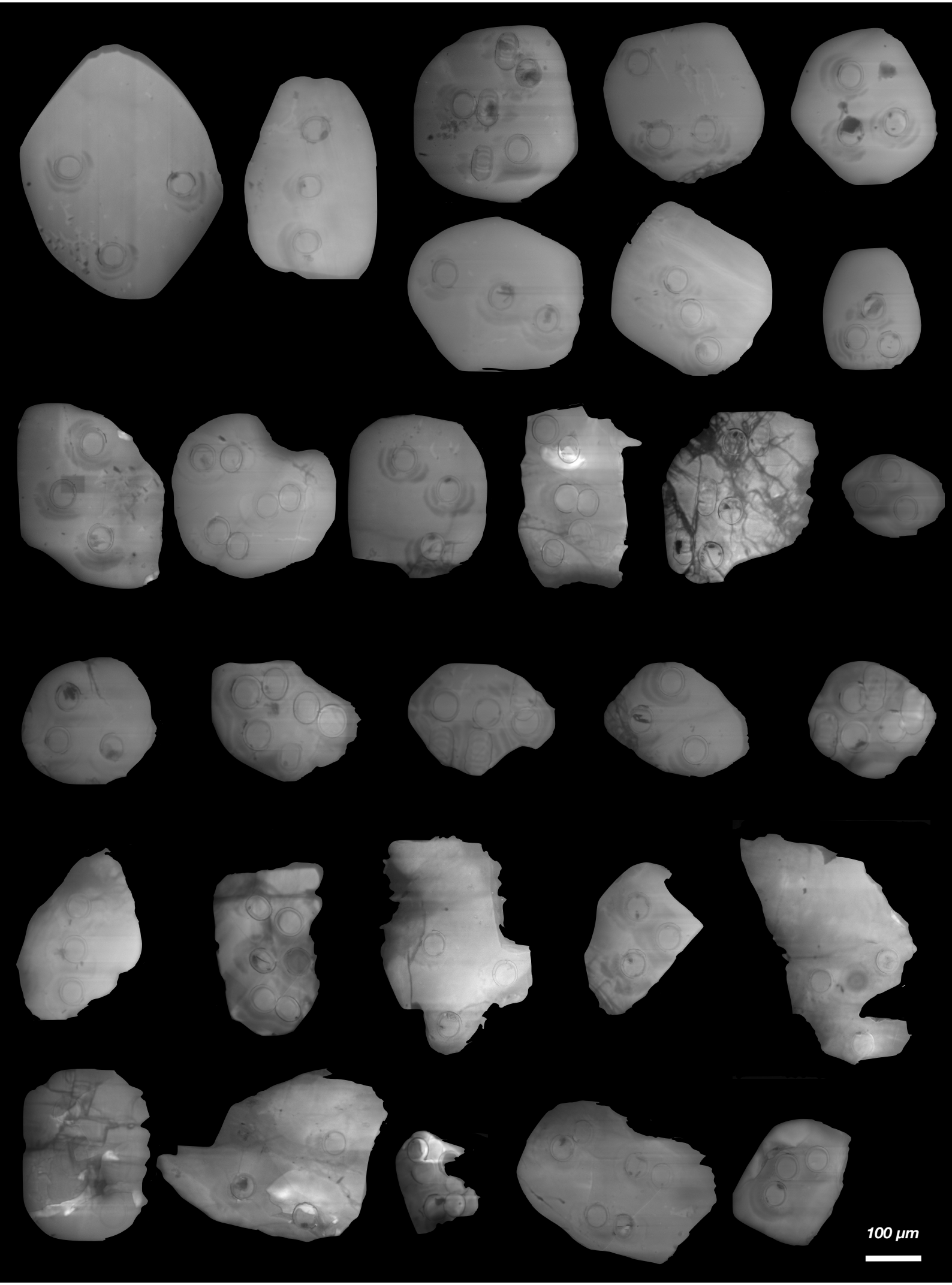
Grey labels in the right-top of each image relates the name of each crystal analyzed. BSE: Back-scattered Electron Detector images; CL: Cathodoluminescence images; RL: Reflected light microscopy image. Red circles represent the location of the spots (diameter of 33μm) for U-Pb analyses; Green circles represent the location of the spots (47μm) for Lu-Hf analyses and Blue circles represent the location of the spots (47μm) for Si isotopes analyses. The same color-scheme text shows the main results of $^{207}Pb/^{206}Pb$ ages and its discordance percentage (Disc.) associated. Th/U ratio. εHf(t) and $\delta^{30}Si$ calculated values for each analysis.

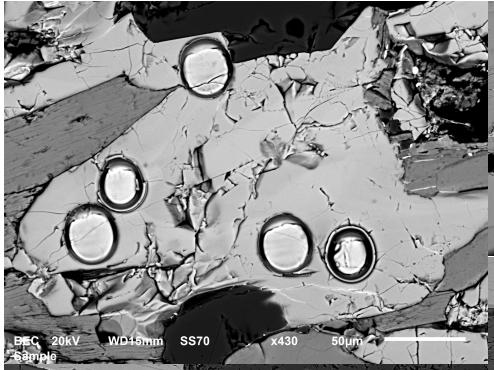
Sample		Zircon textures												LA-(MC)-ICP-MS analyses			
Spot number	*In this paper*	*Geometry*	*Colour*	*Size long (um)*	*Ratio*	*BSE intensity*	*CL intensity*	*Inclusions*	*Zoning*	*Alteration*	*Fractures*	*Recryst.*	*Main Texture*	*Spot locus*	*Hf isotopes*	*Si isotopes*	*Trace Elements*
GC1																	
GC1-80-120-3.1	z1	Prismatic stubby	Brown/Yellow	200	1:1	medium	medium	scarce	blurred	on borders	fine radials	on borders	Uniform, altered borders	Center	Y	Y	Y
GC1-80-120-7.2	z2	Prismatic stubby	Pink/Brown	200	1:1	medium	medium	scarce	blurred	none	fine radials	none	Uniform	Center top			
GC1-80-120-8.1	*z3*	*Prismatic elongated*	*Brown/Yellow*	*300*	*3:1*		*high*	*none*	*fine-scale*			*Core/Rim*	Core/Rim	*Core top*			
GC1-80-120-8.2	*z4*	*Prismatic elongated*	*Brown/Yellow*	*300*	*3:1*		*high*	*none*	*fine-scale*			*Core/Rim*	Core/Rim	*Core center*	*Y*	*Y*	*Y*
GC1-80-120-8.3	*z5*	*Prismatic elongated*	*Brown/Yellow*	*300*	*3:1*		*high*	*none*	*fine-scale*			*Core/Rim*	Core/Rim	*Core down*			
GC1-80-120-11.1	*z6*	*Prismatic stubby*	*Pink/Brown*	*200*	*2:1*		*high*	*scarce*	*blurred*				*Core/Rim*	*Core top*			
GC1-80-120-11.2	*z7*	*Prismatic stubby*	*Pink/Brown*	*200*	*2:1*		*high*	*scarce*	*blurred*				*Core/Rim*	*Core down*	*Y*	*Y*	*Y*
GC1-80-120-16.3	*z8*	*Prismatic elongated*	*Pink/Grey*	*250*	*2:1*		*medium*		*blurred*	*on borders*		*on borders*	*Core/Rim*	*Core*	*Y*	*Y*	*Y*
GC1-80-120-17.1	z9	Prismatic stubby	Pink/Brown	300	1:1	medium	medium	on borders	fine-scale	on borders	fine radials	on borders	Uniform, altered borders	Center left			
GC1-80-120-17.3	z10	Prismatic stubby	Pink/Brown	300	1:1	medium to low	medium to high	on borders	fine-scale	on borders	fine radials	on borders	Uniform, altered borders	Center right	Y	Y	Y
GC1-80-120-18.1	z11	Prismatic elongated	Brown/Yellow	400	3:1	medium	medium	on borders	blurred	on borders	on borders	on borders	Uniform, altered borders	Center	Y	Y	Y
GC1-80-120-18.3	z12	Prismatic elongated	Brown/Yellow	400	3:1	medium	medium	on borders	blurred	on borders	on borders	on borders	Uniform, altered borders	Center down			
GC1-120-200-4.1	z13	Prismatic elongated	Pink/Brown	250	3:1		medium		fine-scale	on borders		Core/Rim	Core/Rim	Rim			
GC1-120-200-5.1	z14	Prismatic elongated	Yellow	200	2:1		medium	on center	blurred	on borders		Uniform	Uniform				
GC1-120-200-8.3	z15	Prismatic elongated	Pink/Brown	300	3:1	medium	medium to low		blurred	on borders	fine radials	on borders	Core/Rim	Rim	Y	Y	Y
GC1-120-200-8.1	*z16*	*Prismatic elongated*	*Pink/Brown*	*300*	*3:1*	*medium to high*	*medium*		*blurred*	*on borders*	*fine radials*	*on borders*	*Core/Rim*	*Core*			
GC1-120-200-8.4	*z17*	*Prismatic elongated*	*Pink/Brown*	*300*	*3:1*	*medium to low*	*high*		*blurred*	*on borders*	*fine radials*	*on borders*	*Core/Rim*	*Core*			
GC1-120-200-9.1	*z18*	*Prismatic elongated*	*Pink/Brown*	*300*	*3:1*		*high*		*fine-scale*	*on borders*	*on borders*	*Core/Rim*	Core/Rim	*Core*	*Y*	*Y*	
GC1-120-200-9.3	*z19*	*Prismatic elongated*	*Pink/Brown*	*300*	*3:1*		*low*		*none*	*on borders*	*on borders*	*Core/Rim*	Core/Rim	*Rim*	*Y*	*Y*	
GC1-120-200-10.1	z20	Prismatic elongated	Brown	300	3:1	medium	medium	abundant	fine-scale	abundant	on borders		Uniform, altered borders	Center			
GC1-120-200-12.1	*z21*	*Prismatic elongated*	*Pink/Brown*	*250*	*3:1*	*low*	*high*	*on borders*	*blurred*	*on borders*	*on borders, randomly on center*	*on borders*	*Core/Rim*	*Core*			
GC1-120-200-12.3	z22	Prismatic elongated	Pink/Brown	250	3:1	medium	medium	on borders	fine-scale	on borders	on borders, randomly on center	on borders	Core/Rim	Rim			
GC1-120-200-14.3	z23	Prismatic elongated	Pink/Brown	250	2:1	medium to high		blurred	on borders		Uniform, altered borders		Uniform, altered borders	Center left	Y	Y	Y
GC1-120-200-15.3	*z24*	*Prismatic elongated*	*Grey*	*200*	*2:1*	*medium*	*low*	*on borders*	*fine-scale*	*on borders*	*fine radials*	*on borders*	*Core/Rim*	*Core top*	*Y*	*Y*	*Y*
GC1-120-200-15.1	*z25*	*Prismatic elongated*	*Grey*	*200*	*2:1*	*medium to low*	*low to high*	*on borders*	*blurred*	*on borders*	*fine radials*	*on borders*	*Core/Rim*	*Core center*			
GC1-120-200-15.2	*z26*	*Prismatic elongated*	*Grey*	*200*	*2:1*	*low*	*high*	*on borders*	*blurred*	*on borders*	*fine radials*	*on borders*	*Core/Rim*	*Core down*			
GC1-120-200-20.3	*z27*	*Prismatic elongated*	*Pink/Brown*	*350*	*3:1*	*high*		*on borders*	*blurred*	*on borders*	*scarce*		*Uniform, altered borders*	*Center top*			
GC1-120-200-20.1	*z28*	*Prismatic elongated*	*Pink/Brown*	*350*	*3:1*	*medium*		*on borders*	*blurred*	*on borders*	*scarce*		*Uniform, altered borders*	*Center*			
GC1-120-200-23.2	*z29*	*Prismatic elongated*	*Pink/Brown*	*300*	*3:1*	*medium*	*low*	*abundant*	*fine-scale*	*on borders*	*on borders*		*Core/Rim*	*Rim top*	*Y*	*Y*	*Y*
GC1-120-200-23.1	z30	Prismatic elongated	Pink/Brown	300	3:1	low	high	abundant	blurred	on borders	on borders		Core/Rim	Core			
GC1-120-200-23.3	z31	Prismatic elongated	Pink/Brown	300	3:1	medium	low	abundant	fine-scale	on borders	on borders		Core/Rim	Rim down	Y	Y	Y
GC2																	
GC2-120-200-9.3	*z32*	*Prismatic elongated*	*Pink/Brown*	*200*	*3:1*		*medium*		*blurred*			*on borders*	*Core/Rim*	*Center top*	*Y*	*Y*	*Y*
GC2-120-200-9.2	*z33*	*Prismatic elongated*	*Pink/Brown*	*200*	*3:1*		*medium*		*blurred*			*on borders*	*Core/Rim*	*Center down*			
GC2-120-200-16.1	z34	Prismatic elongated	Pink/Brown	200	3:1	low	high	scarce	large scale	abundant	fine radials, randomly on center		Core/Rim	Center	Y	Y	Y
GC2-120-200-18.2	*z35*	*Prismatic elongated*	*Pink/Brown*	*300*	*4:1*	*low*	*high*	*scarce*	*large scale*	*abundant*	*fine radials, randomly on center*		*Core/Rim*	*Center left*			
GC2-120-200-18.1	*z36*	*Prismatic elongated*	*Pink/Brown*	*300*	*4:1*	*low*	*high*	*scarce*	*large scale*	*abundant*	*fine radials, randomly on center*		*Core/Rim*	*Center right*	*Y*	*Y*	*Y*
GC2-60-80-2.1	*z37*	*Prismatic elongated*	*Pink/Brown*	*350*	*3:1*	*low*	*high*	*scarce*	*fine scale*	*abundant*	*abundant*	*on borders*	*Core/Rim*	*Center top*	*Y*	*Y*	*Y*
GC2-60-80-3.3	z38	Prismatic elongated	Pink/Brown	300	3:1	medium	medium	none	blurred	abundant	abundant	none	Uniform, altered, fractured	Down	Y	Y	Y
GC2-60-80-4.3	z39	Prismatic stubby	Pink/Brown	300	2:1	medium	medium	on borders	fine scale	on borders	fine radials on borders	none	Uniform, altered borders	Top			
GC2-60-80-4.1	z40	Prismatic stubby	Pink/Brown	300	2:1	medium	medium	on borders	fine scale	on borders	fine radials on borders	none	Uniform, altered borders	Center			
GC2-60-80-4.2	z41	Prismatic stubby	Pink/Brown	300	2:1	medium	medium	on borders	fine scale	on borders	fine radials on borders	none	Uniform, altered borders	Down	Y	Y	Y
GC2-60-80-6.5	z42	Prismatic elongated	Pink/Brown	600	3:1	high	medium	scarce	fine scale	on borders	fine on center		Uniform, altered borders	Top	Y	Y	Y
GC5A																	
GC5A-120-200-6.3	z43	Prismatic stubby	Yellow	200	2:1	medium	medium	scarce	fine scale	on borders	fine radials	none	Uniform, altered borders	Top			
GC5A-120-200-6.2	z44	Prismatic stubby	Yellow	200	2:1	medium	medium	scarce	fine scale	on borders	fine radials	none	Uniform, altered borders	Center	Y	Y	Y
GC5A-120-200-6.1	z45	Prismatic stubby	Yellow	200	2:1	medium	medium	scarce	fine scale	on borders	fine radials	none	Uniform, altered borders	Down			
GC5A-120-200-7.3	z46	Prismatic stubby	Brown	150	2:1	medium	medium	on borders	fine scale	on borders	on borders	none	Uniform, altered borders	Right	Y	Y	Y
GC5A-120-200-7.1	z47	Prismatic stubby	Brown	150	2:1	medium	medium	on borders	fine scale	on borders	on borders	none	Uniform, altered borders	Left			
GC5A-60-80-1.3	z48	Prismatic elongated	Pink/Brown	400	3:1	high	low	none	large scale	on borders	on borders		Uniform, altered borders	Center top			
GC5A-60-80-2.3	z49	Prismatic elongated	Pink/Brown	400	3:1	high	low	on borders	blurred	on borders	fine radials	none	Uniform, altered borders	Top			
GC5A-60-80-2.1	z50	Prismatic elongated	Pink/Brown	400	3:1	high	low	on borders	blurred	on borders	fine radials	none	Uniform, altered borders	Center			
GC5A-60-80-2.2	z51	Prismatic elongated	Pink/Brown	400	3:1	high	low	on borders	blurred	on borders	fine radials	none	Uniform, altered borders	Down	Y	Y	Y
GC5A-60-80-3.1	z52	Prismatic stubby	Pink/Brown	350	3:1	high	low	on borders	large scale	on borders	fine radials	none	Uniform, altered borders	Center top			
GC5A-60-80-3.3	z53	Prismatic stubby	Pink/Brown	350	3:1	high	low	on borders	large scale	on borders	fine radials	none	Uniform, altered borders	Center down			
GC5A-60-80-4.4	z54	Prismatic stubby	Pink/Brown	400	2:1	high	low	on borders	blurred	on borders	on borders		Uniform, altered borders	Center right			
GC5A-60-80-8.1	z55	Prismatic stubby	Pink/Brown	250	2:1	high	low	some	large scale	on borders	fine radials	on borders	Uniform, altered borders	Center	Y	Y	Y
GC5A-80-120-1.1	z56	Prismatic stubby	Pink/Brown	200	2:1	medium	medium	scarce	blurred	on borders	randomly	on borders	Uniform, altered borders	Center	Y	Y	Y
GC5A-80-120-2.3	z57	Prismatic stubby	Pink/Brown	250	2:1	high	medium	scarce	blurred	on borders	abundant	on borders	Uniform, altered borders	Down	Y	Y	Y
GC5A-80-120-15.3	z58	Prismatic stubby	Pink/Brown	200	1:1	medium	medium	some	fine scale	randomly	on borders	Uniform, altered borders	Uniform, altered borders	Center			
GC5A-80-120-15.1	z59	Prismatic stubby	Pink/Brown	200	1:1	medium	medium	some	fine scale	randomly	on borders	Uniform, altered borders	Uniform, altered borders	Top	Y	Y	Y
GC5A-80-120-15.2	z60	Prismatic stubby	Pink/Brown	200	1:1	medium	medium	some	fine scale	randomly	on borders	Uniform, altered borders	Uniform, altered borders	Right			
GC5B																	
GC5B-120-200-6.2	z61	Prismatic stubby	Pink/Brown	120	1:1	high	medium	none	fine scale	on borders	on borders		Uniform, altered borders	Center			
GC5B-80-120-1.2	z62	Prismatic elongated	Pink/Brown	300	3:1	high	medium	scarce	blurred	on borders	fine radials	on borders	Uniform, altered borders	Center top			
GC5B-80-120-1.3	z63	Prismatic elongated	Pink/Brown	300	3:1	high	medium	scarce	blurred	on borders	fine radials	on borders	Uniform, altered borders	Center down			
GC5B-80-120-8.2	z64	Prismatic elongated	Pink/Brown	350	3:1	medium	medium	scarce	blurred	on borders	on borders	on borders	Uniform, altered borders	Center	Y	Y	Y
GC5B-80-120-10.4	z65	Prismatic stubby	Pink/Brown	250	1:1	high	medium	scarce	fine scale	abundant	on borders		Uniform, altered borders	Right	Y	Y	Y
GC5B-60-80-3.4	z66	Prismatic elongated	Pink/Brown	400	3:1	high	medium	some	fine scale	scarce	randomly	on borders	Uniform, altered borders	Right			
GC5B-60-80-3.2	z67	Prismatic elongated	Pink/Brown	400	3:1	high	low	some	fine scale	scarce	randomly	on borders	Uniform, altered borders	Top	Y	Y	Y

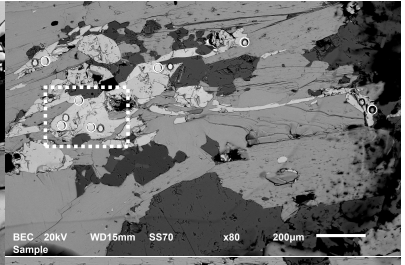
GC5B-60-80-5.1	*z68*	*Prismatic elongated*	*Pink/Brown*	*600*	*3:1*	*high*	*low*	*none*	*large scale*	*on borders*	*abundant*	*on borders*	*Core/Rim*	*Down*			
GC5B-60-80-5.2	*z69*	*Prismatic elongated*	*Pink/Brown*	*600*	*3:1*	*medium*	*medium*	*none*	*large scale*	*on borders*	*abundant*	*on borders*	*Core/Rim*	*Center down*			
GC5B-60-80-5.5	*z70*	*Prismatic elongated*	*Pink/Brown*	*600*	*3:1*	*medium*	*low*	*none*	*large scale*	*on borders*	*abundant*	*on borders*	*Core/Rim*	*Center top*	*Y*	*Y*	*Y*
GC5B-60-80-5.6	*z71*	*Prismatic elongated*	*Pink/Brown*	*600*	*3:1*	*high*	*low*	*none*	*large scale*	*on borders*	*abundant*	*on borders*	*Core/Rim*	*Top*			
GC5B-60-80-6.4	z72	Prismatic elongated	Pink/Brown	400	3:1	high	medium	on borders	none	on borders	randomly	none	Uniform, altered borders	Down	Y	Y	Y
GC5B-60-80-9.3	z73	Prismatic stubby	Pink/Brown	350	2:1	high	low	none	large scale	on borders	on borders	none	Uniform, altered borders	Top			
GC5B-60-80-10.1	z74	Prismatic stubby	Pink/Brown	350	2:1	medium	medium	none	large scale	abundant	abundant	on borders	Uniform, altered borders	Center	Y	Y	Y
GC5B-#4-2	z75	Prismatic stubby	Pink/Brown	200	2:1						fine radials		Uniform, altered borders	Center			
GC5B-#4-3	z76	Prismatic stubby	Pink/Brown	200	2:1						fine radials		Uniform, altered borders	Down			
GC5B-#12-2	z77	Prismatic stubby	Pink/Brown	250	1:1						fine radials		Uniform, altered borders	Right			
GC5B-#19-3	z78	Prismatic stubby	Pink/Brown	250	1:1						scarce			Down			
GC6																	
GC6-120-200-2.1	*z79*	*Prismatic stubby*	*Pink/Brown*	*200*	*2:1*		*high*	*scarce*	*fine scale*			*Core/Rim*	Core/Rim	*Down*	*Y*	*Y*	*Y*
GC6-120-200-2.2	*z80*	*Prismatic stubby*	*Pink/Brown*	*200*	*2:1*		*high*	*scarce*	*fine scale*			*Core/Rim*	Core/Rim	*Top right*			
GC6-120-200-2.3	*z81*	*Prismatic stubby*	*Pink/Brown*	*200*	*2:1*		*high*	*scarce*	*fine scale*			*Core/Rim*	Core/Rim	*Top left*			
GC6-120-200-10.1	*z82*	*Prismatic stubby*	*Grey/Brown*	*200*	*2:1*	*medium*	*high*	*none*	*fine scale*	*on borders*	*randomly*	*on borders*	*Core/Rim*	*Center*	*Y*	*Y*	*Y*
GC6-120-200-12.1	*z83*	*Prismatic stubby*	*Grey/Brown*	*200*	*2:1*		*high*		*blurred*			*on borders*	*Core/Rim*	*Center*	*Y*	*Y*	*Y*
GC6-120-200-13.1	z84	Prismatic elongated	Yellow/Brown	250	3:1	medium	low	scarce	fine scale	on borders	on borders	on borders	Uniform, altered borders	Top			
GC6-120-200-13.2	z85	Prismatic elongated	Yellow/Brown	250	3:1	medium	low	scarce	fine scale	on borders	on borders	on borders	Uniform, altered borders	Center	Y	Y	Y
GC6-120-200-14.3	*z86*	*Prismatic stubby*	*Grey/Brown*	*250*	*2:1*		*medium*		*fine scale*		*on borders*	*Core/Rim*	Core/Rim	*Top*	*Y*	*Y*	*Y*
GC6-120-200-20.1	z87	Prismatic elongated	Pink/Brown	200	3:1	medium	medium	some	blurred	abundant	on borders	on borders	Uniform, altered borders	Top	Y	Y	Y
GC6-120-200-20.2	z88	Prismatic elongated	Pink/Brown	200	3:1	medium	medium	some	blurred	abundant	on borders	on borders	Uniform, altered borders	Down			
GC6-80-120-1.1	*z89*	*Prismatic stubby*	*Grey/Brown*	*200*	*2:1*	*high*	*low*	*abundant*	*none*	*on borders*	*randomly*	*on borders*	*Dark uniform*	*Top*			
GC6-80-120-1.2	*z90*	*Prismatic stubby*	*Grey/Brown*	*200*	*2:1*	*medium*	*low*	*abundant*	*none*	*on borders*	*randomly*	*on borders*	*Dark uniform*	*Center*	*Y*	*Y*	*Y*
GC6-80-120-3.2	*z91*	*Prismatic stubby*	*Brown*	*200*	*1:1*	*low*	*high*	*some*	*fine scale*	*abundant*	*abundant*	*none*	*Core/Rim*	*Left*	*Y*	*Y*	*Y*
GC6-80-120-3.1	*z92*	*Prismatic stubby*	*Brown*	*200*	*1:1*	*low*	*high*	*some*	*fine scale*	*abundant*	*abundant*	*none*	*Core/Rim*	*Right*			
GC6-80-120-5.4	z93	Prismatic elongated	Grey/Brown	500	4:1	low	medium	some	blurred	on borders	randomly	none	Uniform, altered borders	Down			
GC6-80-120-5.3	z94	Prismatic elongated	Grey/Brown	500	4:1	low	high	some	blurred	on borders	randomly	none	Uniform, altered borders	Center down			
GC6-80-120-5.2	z95	Prismatic elongated	Grey/Brown	500	4:1	low	medium	some	blurred	on borders	randomly	none	Uniform, altered borders	Center top	Y	Y	Y
GC7																	
CG7-120-200-6.1	z96	Prismatic stubby	Brown	150	1:1	high	medium	some	blurred	on borders	abundant	on borders	Uniform blurred zoning	Top			
CG7-80-120-8.1	*z97*	*Prismatic stubby*	*Pink/Brown*	*200*	*2:1*	*low*	*high*	*abundant*	*blurred*	*on borders*	*randomly*	*on borders*	*Core/Rim*	*Center*	*Y*	*Y*	*Y*
CG7-80-120-10.3	z98	Prismatic stubby	Pink/Brown	200	2:1	medium	medium	some	blurred	on borders	scarce	on borders	Uniform blurred zoning	Top			
CG7-80-120-10.1	z99	Prismatic stubby	Pink/Brown	200	2:1	medium	medium	some	blurred	on borders	scarce	on borders	Uniform blurred zoning	Down	Y	Y	Y

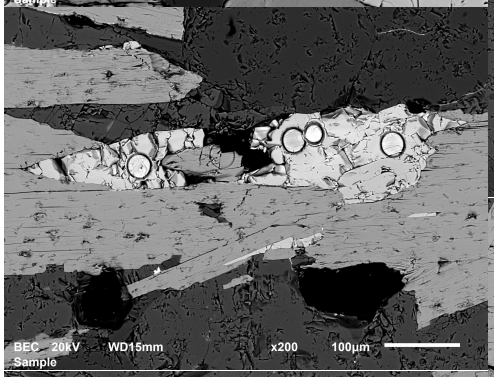

CM44A - Caatinga-Lamim Complex: Migmatite Trondhjemictic Bt-Gneiss (neosome)
CM44B - (paleosome)
CM46A - Ressaquinha Complex: Bt-Trondhjemite
CM47 - Caranaíba Gneiss: tonalitic Bt-Gneiss
CM49 - Caatinga-Lamim Complex: Bt-Hbl-Tonalite
U-Th-Pb analyses
Trace element analyses
Lu-Hf analyses
Silicon isotope analyses
200 µm

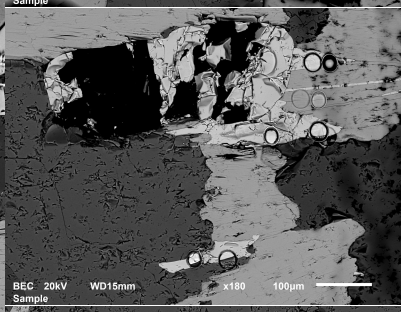

SS67
x160
x180
100µ
100 µm


100 µm

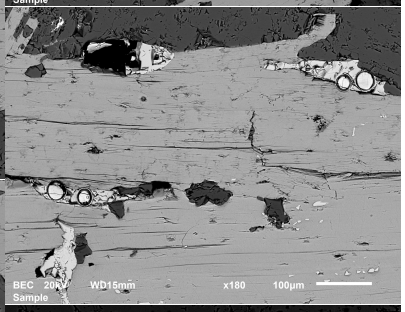


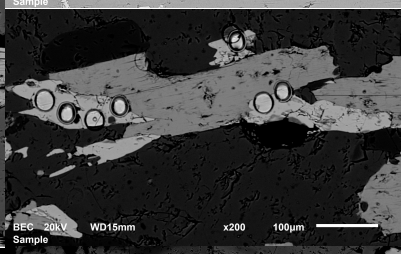


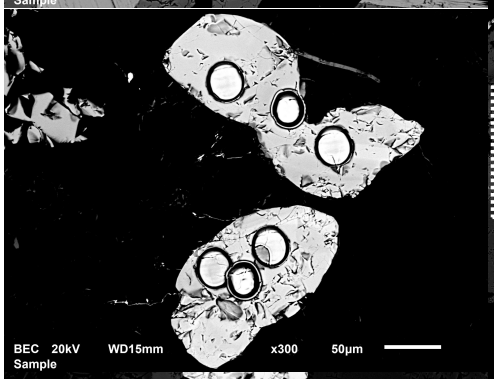


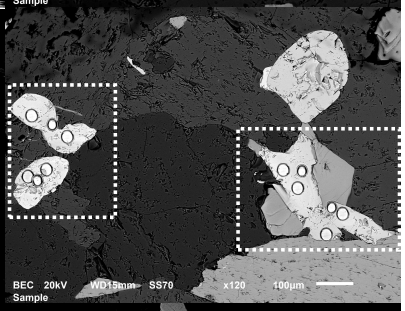


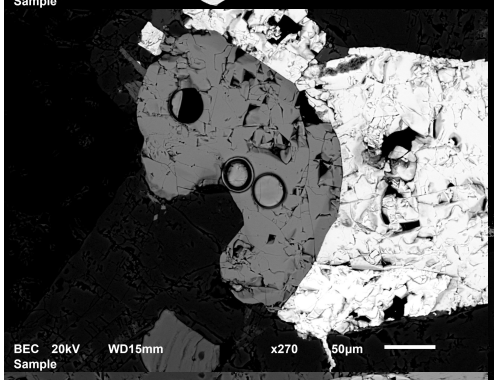


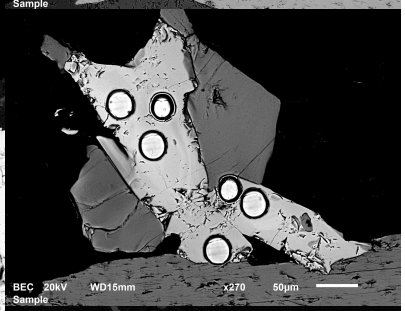


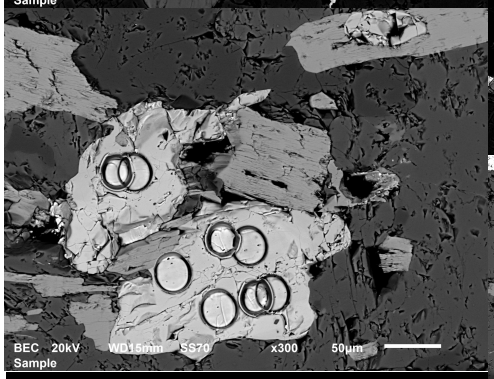


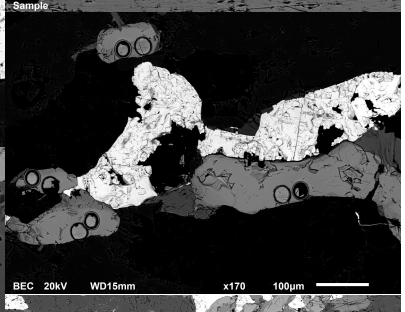


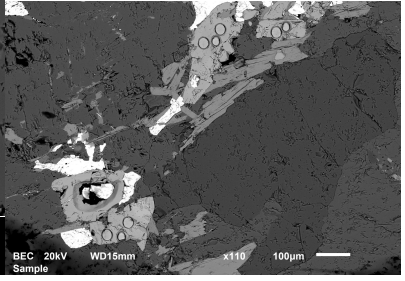




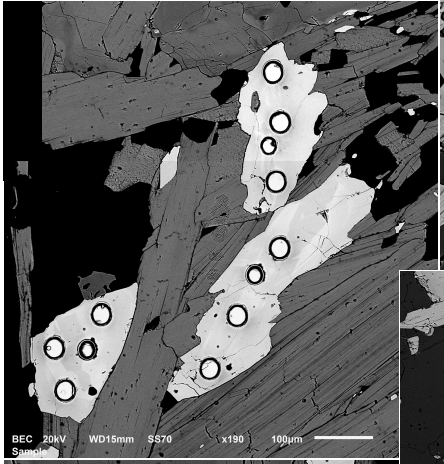


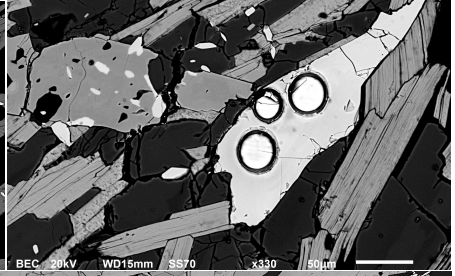


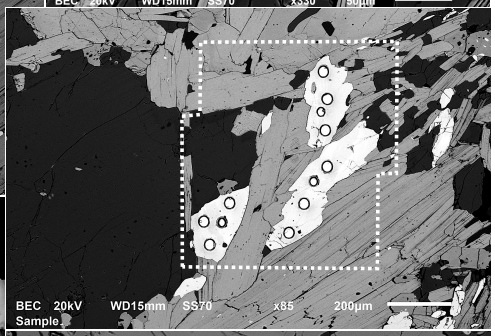


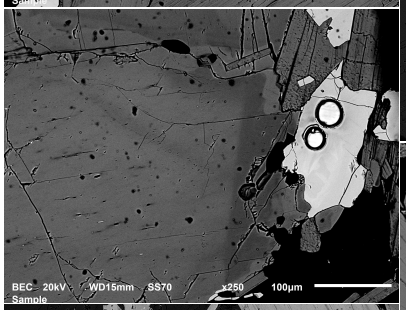


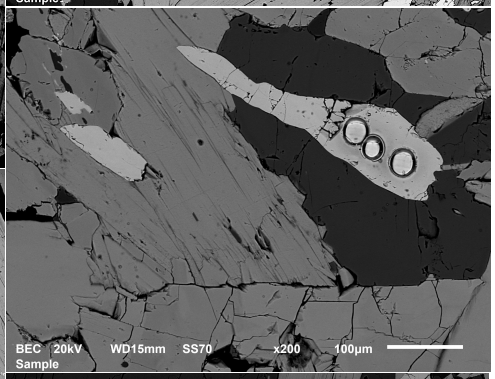
CM44B - Caatinga-Lamim migmatitic gneiss

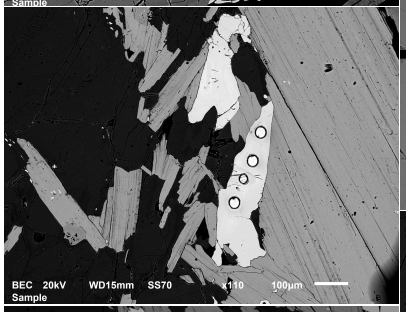


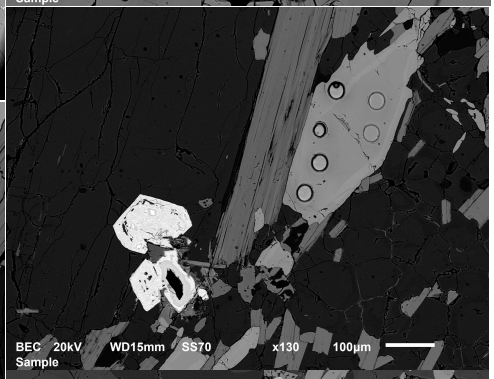


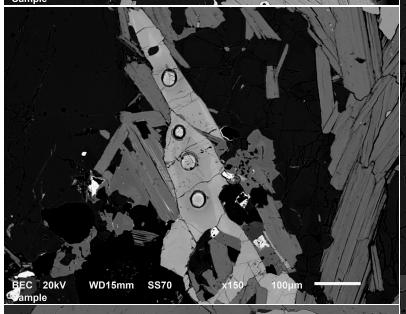


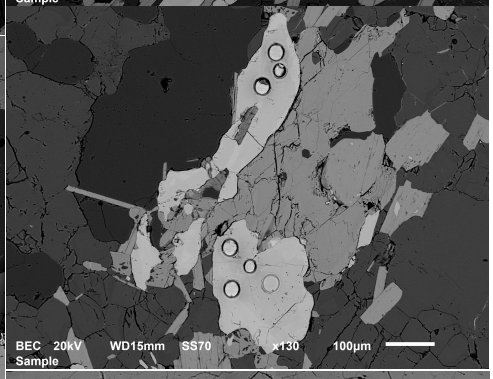


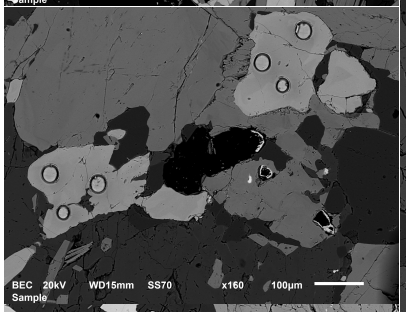


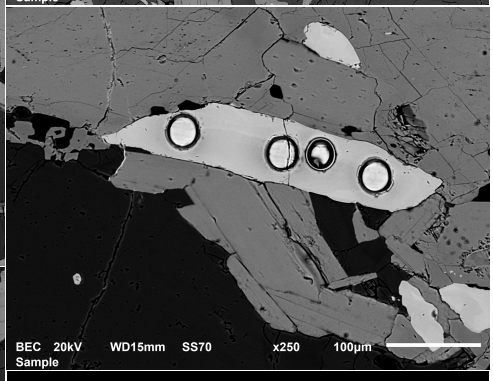


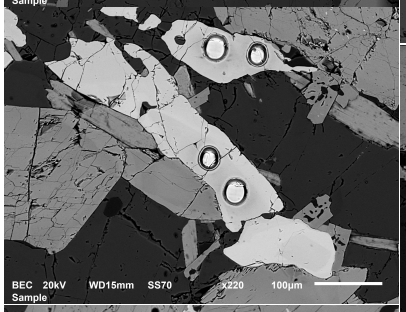


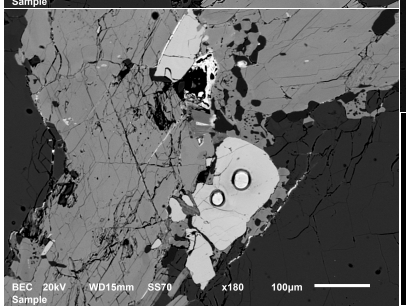












CM49 - Caatinga-Lamim tonalite

LA-(MC)-ICP-MS analytical conditions in the following sessions for zircon analyses

Analysis	**U-Pb geochronology**					
Laboratory	**Laboratoire Magmas et Volcans**					
Session Date	**November 24, 2022**	**November 28, 2022**	**December 8, 2022**	**December 12, 2022**	**December 15, 2022**	**February 16, 2023**
Cup configuration	N.A.	N.A.	N.A.	N.A.	N.A.	N.A.
Mass measured	204, 206, 207, 208, 232, 238	204, 206, 207, 208, 232, 238	204, 206, 207, 208, 232, 238	204, 206, 207, 208, 232, 238	204, 206, 207, 208, 232, 238	204, 206, 207, 208, 232, 238
ICP-MS model	Thermo Element XR	Thermo Element XR	Thermo Element XR	Thermo Element XR	Thermo Element XR	Thermo Element XR
Interface type	Jet (high sensitivity)	Jet (high sensitivity)	Jet (high sensitivity)	Jet (high sensitivity)	Jet (high sensitivity)	Jet (high sensitivity)
Cones	X-Cones	X-Cones	X-Cones	X-Cones	X-Cones	X-Cones
Resistors	Counting/Analog	Counting/Analog	Counting/Analog	Counting/Analog	Counting/Analog	Counting/Analog
Resolution	High (M/ΔM=7800)	High (M/ΔM=7800)	High (M/ΔM=7800)	High (M/ΔM=7800)	High (M/ΔM=7800)	High (M/ΔM=7800)
Forward Power	1300W	1300W	1300W	1300W	1300W	1300W
Auxiliary gas (Ar)	0,76 L/min	0,82 L/min	0,8 L/min	0,8 L/min	0,8 L/min	0,8 L/min
Ar sample	~1 L/min	~1 L/min	~1 L/min	~1 L/min	~1 L/min	~1 L/min
Additional gas (N2)	7,5mL/min	7,25mL/min	10mL/min	13mL/min	11ml/min	12ml/min
Oxide ThO/Th	~1%	~2 %	~1%	~1%	~1%	~1%
SQUID	On	On	On	On	On	On
Data aquisition	Time resolved analyses	Time resolved analyses	Time resolved analyses	Time resolved analyses	Time resolved analyses	Time resolved analyses
Scanning mode	Pick-jumping	Pick-jumping	Pick-jumping	Pick-jumping	Pick-jumping	Pick-jumping
Integration time per isotope	5ms	5ms	5ms	5ms	5ms	5ms
Background counting time	20-30s	20-30s	20-30s	20-30s	20-30s	20-30s
Sample measurement time	60s	60s	60s	60s	60s	60s
Measurement type	Standard bracketing	Standard bracketing	Standard bracketing	Standard bracketing	Standard bracketing	Standard bracketing
External standard	91500, AS3, Plešovice	91500, AS3, Plešovice	91500, AS3, Plešovice	91500, AS3, Plešovice	91500, AS3, Plešovice	91500, AS3, Plešovice
Laser model	**Resonetics Resolution M-50E**	**Resonetics Resolution M-50E**	**Resonetics Resolution M-50E**	**Resonetics Resolution M-50E**	**Resonetics Resolution M-50E**	**Resonetics Resolution M-50E**
Wavelength	193nm	193nm	193nm	193nm	193nm	193nm
Pulse duration	5ns	5ns	5ns	5ns	5ns	5ns
Energy	~6 mJ	~6 mJ	~6 mJ	~6 mJ	~6 mJ	~7 mJ
Fluence	~2,5J/cm^2	~2,5J/cm^2	~2,5J/cm^2	~2,5J/cm^2	~2,5J/cm^2	~2,5J/cm^2
Frequency	4Hz	4Hz	4Hz	4Hz	4Hz	4Hz
Spot size	33μm	33μm	33μm	33μm	33μm	33μm
Carrier gas	He	He	He	He	He	He
Carrier gas flow	0,75 L/min	0,75 L/min	0,75 L/min	0,75 L/min	0,75 L/min	0,8 L/min

Analysis	**Lu-Hf isotopes**		**Si isotopes**		
Laboratory	**Laboratoire Magmas et Volcans**		**Laboratoire Magmas et Volcans**		
Session Date	**February 24, 2023**	**February 27, 2023**	**February 27, 2023**	**February 28, 2023**	**March 1st, 2023**
Cup configuration	L4 L3 L2 L1 C H1 H2 H3	L4 L3 L2 L1 C H1 H2 H3	L4 L2 H1	L4 L2 H1	L4 L2 H1
Mass measured	171 173 174 175 176 177 178 179	171 173 174 175 176 177 178 179	28 29 30	28 29 30	28 29 30
ICP-MS model	Thermo Neptune Plus	Thermo Neptune Plus	Thermo Neptune Plus	Thermo Neptune Plus	Thermo Neptune Plus
Interface type	Jet (high sensitivity)	Jet (high sensitivity)	Jet (high sensitivity)	Jet (high sensitivity)	Jet (high sensitivity)
Cones	X-Cones	X-Cones	X-Cones	X-Cones	X-Cones
Resistors	10^{11} Ohms	10^{11} Ohms	10^{11} Ohms	10^{11} Ohms	10^{11} Ohms
Resolution	Low	Low	Low	Low	Low
Forward Power	1200W	1200W	1200W	1200W	1200W
Auxiliary gas (Ar)	0,72 L/min	0,83 L/min	0,83 L/min	0,83 L/min	0,84 L/min
Ar sample	~1 L/min	~1 L/min	~1 L/min	~1 L/min	~1 L/min
Additional gas (N2)	3,75mL/min	3,8mL/min	N.A.	N.A.	N.A.
Oxide ThO/Th	~1%	~1%	~1%	~1%	~1%
SQUID	On	On	On	On	On
Data aquisition	Time resolved analyses	Time resolved analyses	Time resolved analyses	Time resolved analyses	Time resolved analyses
Scanning mode	Static multi-collection	Static multi-collection	Static multi-collection	Static multi-collection	Static multi-collection
Integration time per isotope	1s	1s	1s	1s	1s
Background counting time	10s	10s	10s	10s	10s
Sample measurement time	60s	60s	60s	60s	60s
Measurement type	Internal and external normalization	Internal and external normalization	Standard bracketing	Standard bracketing	Standard bracketing
External standard	MUN zircons, 91500, MudTank	MUN zircons, 91500, MudTank	MUN zircons, Plešovice, MudTank	MUN zircons, Plešovice, MudTank	MUN zircons, Plešovice, MudTank
Laser model	**Resonetics Resolution M-50E**	**Resonetics Resolution M-50E**	**Resonetics Resolution M-50E**	**Resonetics Resolution M-50E**	**Resonetics Resolution M-50E**
Wavelength	193nm	193nm	193nm	193nm	193nm
Pulse duration	5ns	5ns	5ns	5ns	5ns
Energy	~8,5 mJ	~8,5 mJ	~8,4 mJ	~8,7 mJ	~8,5 mJ
Fluence	~3J/cm^2	~3J/cm^2	~3J/cm^2	~3J/cm^2	~3J/cm^2
Frequency	6Hz	6Hz	6Hz	6Hz	6Hz
Spot size	47μm	47μm	47μm	47μm	47μm
Carrier gas	He	He	He	He	He
Carrier gas flow	0,725 L/min	0,725 L/min	0,775 L/min	0,85 L/min	0,85 L/min

Analysis	**Trace element concentrations**	
Laboratory	**Laboratoire Magmas et Volcans**	
Session Date	**May 02, 2023**	**May 03, 2023**
Cup configuration	N.A.	N.A.
Mass measured	27-29, 39, 43, 44, 49, 51, 66, 71, 85, 88-91, 93, 96, 137, 139-141, 146, 147, 153, 157, 159, 163, 165, 166, 169, 172, 175, 178, 181, 206, 232, 238	27-29, 39, 43, 44, 49, 51, 66, 71, 85, 88-91, 93, 96, 137, 139-141, 146, 147, 153, 157, 159, 163, 165, 166, 169, 172, 175, 178, 181, 206, 232, 238
ICP-MS model	Thermo Element XR	Thermo Element XR
Interface type	Jet (high sensitivity)	Jet (high sensitivity)
Cones	X-Cones	X-Cones
Resistors	Counting/Analog	Counting/Analog
Resolution	Low	Low
Forward Power	1300W	1300W
Auxiliary gas (Ar)	0,8 L/min	0,8 L/min
Ar sample	0,867 L/min	0,878 L/min
Additional gas (N2)	13ml/min	13ml/min
Oxide ThO/Th	~1%	~1%
SQUID	On	On
Data aquisition	Time resolved analyses	Time resolved analyses
Scanning mode	Mass scan	Mass scan
Integration time per isotope	5ms	5ms
Background counting time	20-30s	20-30s
Sample measurement time	60s	60s
Measurement type	Standard bracketing	Standard bracketing
External standard	NIST 610, NIST 612, AS3, 91500, MudTank	NIST 610, NIST 612, AS3, 91500, MudTank
Laser model	**Resonetics Resolution M-50E**	**Resonetics Resolution M-50E**
Wavelength	193nm	193nm
Pulse duration	5ns	5ns
Energy	~7 mJ	~7 mJ
Fluence	~2,5J/cm^2	~2,5J/cm^2
Frequency	2Hz	2Hz
Spot size	33μm	33μm
Carrier gas	He	He
Carrier gas flow	0,7 L/min	0,725 L/min

LA-(MC)-ICP-MS analytical conditions in the following sessions for apatites analyses

Analysis	**U-Pb geochronology**	**Trace element concentrations**
Laboratory	**Laboratoire Magmas et Volcans**	**Laboratoire Magmas et Volcans**
Session Date	**February 17, 2023**	**May 03, 2023**
Cup configuration	N.A.	N.A.
Mass measured	204, 206, 207, 208, 232, 238	27-29, 39, 43, 44, 49, 51, 66, 71, 85, 88-91, 93, 96, 137, 139-141, 146, 147, 153, 157, 159, 163, 165, 166, 169, 172, 175, 178, 181, 206, 232, 238
ICP-MS model	Thermo Element XR	Thermo Element XR
Interface type	Jet (high sensitivity)	Jet (high sensitivity)
Cones	X-Cones	X-Cones
Resistors	Counting/Analog	Counting/Analog
Resolution	High (M/ΔM=7800)	Low
Forward Power	1300W	1300W
Auxiliary gas (Ar)	0,91 L/min	0,8 L/min
Ar sample	0,78 L/min	0,878 L/min
Additional gas (N2)	13ml/min	14ml/min
Oxide ThO/Th	~1%	~1%
SQUID	On	On
Data aquisition	Time resolved analyses	Time resolved analyses
Scanning mode	Pick-jumping	Mass scan
Integration time per isotope	5ms	5ms
Background counting time	20-30s	20-30s
Sample measurement time	60s	60s
Measurement type	Standard bracketing	Standard bracketing
External standard	MAD, Kovdor, Sumé 1, Bahia, Slyud.	NIST 610, NIST 612, Durango, Kovdor, Sumé 1
Laser model	**Resonetics Resolution M-50E**	**Resonetics Resolution M-50E**
Wavelength	193nm	193nm
Pulse duration	5ns	5ns
Energy	~7 mJ	~7 mJ
Fluence	~2,5J/cm^2	~2,5J/cm^2
Frequency	2Hz	2Hz
Spot size	40μm	33μm
Carrier gas	He	He
Carrier gas flow	0,8 L/min	0,7 L/min

LA-(MC)-ICP-MS analytical conditions in the following sessions for titanite analyses

Analysis	**U-Pb geochronology**	**Trace element concentrations**
Laboratory	**Laboratoire Magmas et Volcans**	**Laboratoire Magmas et Volcans**
Session Date	**June 5, 2023**	**September 28, 2023**
Cup configuration	N.A.	N.A.
Mass measured	204, 206, 207, 208, 232, 238	27-29, 39, 43, 44, 49, 51, 66, 71, 85, 88-91, 93, 96, 137, 139-141, 146, 147, 153, 157, 159, 163, 165, 166, 169, 172, 175, 178, 181, 206, 232, 238
ICP-MS model	Thermo Element XR	Thermo Element XR
Interface type	Jet (high sensitivity)	Jet (high sensitivity)
Cones	X-Cones	X-Cones
Resistors	Counting/Analog	Counting/Analog
Resolution	High (M/ΔM=7800)	Low
Forward Power	1300W	1300W
Auxiliary gas (Ar)	0,80 L/min	0,82 L/min
Ar sample	0,879 L/min	0,785 L/min
Additional gas (N2)	12ml/min	12ml/min
Oxide ThO/Th	~1%	~0,8%
SQUID	On	On
Data aquisition	Time resolved analyses	Time resolved analyses
Scanning mode	Pick-jumping	Mass scan
Integration time per isotope	5ms	5ms
Background counting time	20-30s	20-30s
Sample measurement time	60s	60s
Measurement type	Standard bracketing	Standard bracketing
External standard	MKED1, Khan, BLR1, TH-Bear Lake	NIST 610, NIST 612, CKHB, MKED1, BLR1, Kola
Laser model	Resonetics Resolution M-50E	Resonetics Resolution M-50E
Wavelength	193nm	193nm
Pulse duration	5ns	5ns
Energy	~7 mJ	~7 mJ
Fluence	~2,5J/cm^2	~2,5J/cm^2
Frequency	2Hz	2Hz
Spot size	33μm	27μm
Carrier gas	He	He
Carrier gas flow	0,75 L/min	0,8 L/min

LA-ICP-MS zircon U-Th-Pb analyses for Cupim Pluton samples. Italic symbols are inherited zircons. Disc.(%) and Disc. Dist.(%) are calculated directly from IsoplotR (Vermeesch, 2018) using the relative age difference (%) between the 206Pb/238U and 207Pb/206Pb ages; and as proposed by Guitreau et al., 2014, respectively. [Th/U]m. and [Th/U]calc. are provided directly from Iolite4 (Petrus and Kamber, 2012; Paton et al., 2011), and calculated using the equations proposed by Guitreau and Flahaut, 2019. Uncertainties correspond to 2σ confidential interval.

Sample	This work	Type from texture	Domain	Isotope ratios										Age (Ma)								Elemental data									
				$^{207}Pb/^{235}U$	±2σ	$^{206}Pb/^{238}U$	±2σ	Rho	$^{207}Pb/^{206}Pb$	±2σ	$^{208}Pb/^{232}Th$	±2σ	$^{207}Pb/^{235}U$	±2σ	$^{206}Pb/^{238}U$	±2σ	$^{207}Pb/^{206}Pb$	±2σ	Disc.(%)	Disc. Dist.(%)	$^{208}Pb/^{232}Th$	±2σ	Pb (ppm)	Th (ppm)	U (ppm)	Final U/Th	±2σ	Th/U	$[Th/U]_m$	$^{208}Pb/^{206}Pb$	$[Th/U]_{calc.}$
GC1																															
80-120-3.1	z1	Uniform. altered borders	Magmatic	4.9137	0.1574	0.3051	0.0058	0.8885	0.1195	0.0008	0.0313	0.0008	1804	28	1717	29	1946	11	9	15	623	15	136	475	984	2.10	0.04	0.48	0.48	0.05	0.17
80-120-7.2	z2	Uniform	Magmatic	3.5853	0.1165	0.2342	0.0043	0.8437	0.1140	0.0008	0.0287	0.0013	1544	26	1356	22	1860	13	29	31	571	26	79	308	954	3.27	0.11	0.31	0.31	0.04	0.13
80-120-8.1	*z3*	*Core/Rim*	*Inherited*	*12.1530*	*0.4973*	*0.4749*	*0.0148*	*0.9412*	*0.1865*	*0.0017*	*0.0811*	*0.0052*	*2608*	*40*	*2499*	*66*	*2709*	*15*	*10*	*9*	*1571*	*97*	*85*	*135*	*195*	*1.55*	*0.06*	*0.65*	*0.65*	*0.11*	*0.40*
80-120-8.2	*z4*	*Core/Rim*	*Inherited*	*13.7418*	*0.4597*	*0.5251*	*0.0114*	*0.8109*	*0.1893*	*0.0020*	*0.1109*	*0.0045*	*2732*	*31*	*2718*	*49*	*2733*	*17*	*1*	*0*	*2122*	*82*	*119*	*129*	*248*	*1.99*	*0.06*	*0.50*	*0.51*	*0.11*	*0.39*
80-120-8.3	*z5*	*Core/Rim*	*Inherited*	*11.9930*	*0.4871*	*0.4614*	*0.0147*	*0.9717*	*0.1896*	*0.0012*	*0.0641*	*0.0019*	*2588*	*39*	*2433*	*65*	*2737*	*11*	*15*	*13*	*1254*	*36*	*76*	*141*	*179*	*1.35*	*0.03*	*0.74*	*0.74*	*0.10*	*0.38*
80-120-11.1	*z6*	*Core/Rim*	*Inherited*	*22.6462*	*0.7070*	*0.6312*	*0.0110*	*0.8029*	*0.2523*	*0.0016*	*0.1754*	*0.0034*	*3210*	*30*	*3152*	*43*	*3197*	*10*	*3*	*-2*	*3266*	*58*	*161*	*97*	*242*	*2.46*	*0.04*	*0.41*	*0.41*	*0.11*	*0.43*
80-120-11.2	*z7*	*Core/Rim*	*Inherited*	*22.8516*	*0.6986*	*0.6381*	*0.0102*	*0.6930*	*0.2500*	*0.0016*	*0.1769*	*0.0034*	*3219*	*30*	*3180*	*40*	*3182*	*10*	*2*	*-4*	*3292*	*58*	*225*	*141*	*344*	*2.42*	*0.02*	*0.41*	*0.42*	*0.12*	*0.43*
80-120-16.3	*z8*	*Core/Rim*	*Inherited*	*13.4018*	*0.4155*	*0.5237*	*0.0089*	*0.6836*	*0.1862*	*0.0014*	*0.1434*	*0.0028*	*2707*	*29*	*2714*	*37*	*2707*	*13*	*0*	*0*	*2707*	*49*	*99*	*73*	*197*	*2.68*	*0.03*	*0.37*	*0.38*	*0.10*	*0.38*
80-120-17.1	z9	Uniform. altered borders	Magmatic	4.2377	0.1430	0.2724	0.0057	0.9022	0.1127	0.0008	0.0862	0.0023	1679	27	1551	28	1839	13	15	17	1673	43	113	137	931	6.70	0.07	0.15	0.15	0.05	0.16
80-120-17.3	z10	Uniform. altered borders	Magmatic	5.2409	0.1751	0.3192	0.0064	0.8966	0.1190	0.0008	0.0899	0.0025	1855	29	1784	31	1938	13	7	9	1737	47	88	104	758	7.39	0.11	0.14	0.14	0.04	0.13
80-120-18.1	z11	Uniform. altered borders	Magmatic	4.8804	0.1543	0.2980	0.0054	0.9000	0.1180	0.0007	0.0906	0.0021	1800	28	1680	27	1924	10	13	13	1755	40	73	87	876	10.30	0.10	0.10	0.10	0.03	0.10
80-120-18.3	z12	Uniform. altered borders	Magmatic	5.4472	0.1762	0.3251	0.0065	0.9052	0.1205	0.0008	0.0857	0.0028	1892	29	1812	31	1959	11	7	7	1659	51	87	106	952	8.98	0.17	0.11	0.11	0.03	0.10
120-200-4.1	z13	Core/Rim	Magmatic	3.4814	0.1225	0.2307	0.0052	0.9465	0.1066	0.0007	0.0668	0.0016	1518	27	1338	27	1739	12	48	23	1305	30	319	506	2526	4.97	0.04	0.20	0.20	0.06	0.20
120-200-5.1	z14	Uniform	Magmatic	3.5475	0.1219	0.2342	0.0050	0.9420	0.1077	0.0006	0.0721	0.0019	1531	26	1354	26	1759	11	44	24	1406	35	404	591	2701	4.57	0.04	0.22	0.22	0.07	0.23
120-200-8.3	z15	Core/Rim	Magmatic	6.9312	0.2100	0.4084	0.0063	0.7339	0.1259	0.0006	0.1157	0.0021	2101	27	2208	29	2038	9	-9	-8	2212	38	160	149	734	5.00	0.03	0.20	0.20	0.06	0.20
120-200-8.1	*z16*	*Core/Rim*	*Inherited*	*6.4220*	*0.2283*	*0.3267*	*0.0076*	*0.9380*	*0.1457*	*0.0010*	*0.0913*	*0.0027*	*2026*	*30*	*1818*	*36*	*2293*	*12*	*24*	*25*	*1763*	*50*	*70*	*78*	*1248*	*16.07*	*0.15*	*0.06*	*0.06*	*0.02*	*0.06*
120-200-8.4	*z17*	*Core/Rim*	*Inherited*	*5.9620*	*0.1944*	*0.3148*	*0.0065*	*0.9148*	*0.1405*	*0.0009*	*0.0275*	*0.0008*	*1967*	*28*	*1761*	*32*	*2231*	*11*	*18*	*25*	*547*	*15*	*86*	*330*	*1120*	*3.64*	*0.10*	*0.27*	*0.28*	*0.02*	*0.09*
120-200-9.1	*z18*	*Core/Rim*	*Inherited*	*12.3813*	*0.4128*	*0.4748*	*0.0095*	*0.9033*	*0.1924*	*0.0013*	*0.0313*	*0.0008*	*2628*	*30*	*2500*	*41*	*2760*	*11*	*10*	*12*	*623*	*16*	*70*	*257*	*166*	*0.74*	*0.03*	*1.36*	*1.37*	*0.09*	*0.33*
120-200-9.3	*z19*	*Core/Rim*	*Inherited*	*9.1295*	*0.3201*	*0.4027*	*0.0092*	*0.9517*	*0.1661*	*0.0010*	*0.1082*	*0.0042*	*2341*	*32*	*2175*	*42*	*2516*	*10*	*18*	*16*	*2069*	*77*	*41*	*42*	*899*	*22.94*	*0.67*	*0.04*	*0.04*	*0.01*	*0.04*
120-200-10.1	z20	Uniform. altered borders	Magmatic	3.7672	0.1220	0.2402	0.0045	0.7948	0.1133	0.0010	0.0994	0.0024	1583	26	1387	23	1849	15	27	27	1914	44	224	243	2038	8.19	0.18	0.12	0.12	0.05	0.18
120-200-12.1	*z21*	*Core/Rim*	*Inherited*	*17.9332*	*0.6613*	*0.6453*	*0.0161*	*0.9332*	*0.2015*	*0.0016*	*0.2021*	*0.0060*	*2976*	*35*	*3200*	*62*	*2835*	*13*	*-16*	*-17*	*3721*	*103*	*105*	*55*	*146*	*2.63*	*0.04*	*0.38*	*0.38*	*0.12*	*0.44*
120-200-12.3	z22	Core/Rim	Magmatic	3.0680	0.0987	0.2087	0.0038	0.8050	0.1070	0.0008	0.0664	0.0014	1422	24	1221	20	1744	14	31	33	1299	27	202	319	1882	5.69	0.07	0.18	0.18	0.06	0.19
120-200-14.3	z23	Uniform. altered borders	Magmatic	5.2029	0.1836	0.3142	0.0075	0.9475	0.1207	0.0008	0.0920	0.0025	1846	30	1758	36	1963	11	11	12	1777	47	112	128	1012	7.77	0.09	0.13	0.13	0.04	0.13
120-200-15.3	*z24*	*Core/Rim*	*Inherited*	*14.3961*	*0.4506*	*0.5399*	*0.0090*	*0.8247*	*0.1900*	*0.0011*	*0.0763*	*0.0033*	*2774*	*31*	*2781*	*38*	*2739*	*10*	*0*	*-4*	*1481*	*62*	*43*	*68*	*271*	*4.24*	*0.15*	*0.24*	*0.24*	*0.03*	*0.12*
120-200-15.1	*z25*	*Core/Rim*	*Inherited*	*10.5399*	*0.3613*	*0.3925*	*0.0086*	*0.9407*	*0.1910*	*0.0011*	*0.0450*	*0.0024*	*2474*	*32*	*2129*	*40*	*2748*	*9*	*35*	*24*	*891*	*47*	*147*	*380*	*467*	*1.31*	*0.06*	*0.76*	*0.77*	*0.09*	*0.32*
120-200-15.2	*z26*	*Core/Rim*	*Inherited*	*9.4171*	*0.3593*	*0.3366*	*0.0093*	*0.9696*	*0.1997*	*0.0012*	*0.0101*	*0.0007*	*2364*	*35*	*1862*	*45*	*2821*	*10*	*140*	*37*	*202*	*14*	*46*	*554*	*453*	*0.88*	*0.04*	*1.14*	*1.15*	*0.03*	*0.13*
120-200-20.3	*z27*	*Uniform. altered borders*	*Inherited*	*6.0832*	*0.2003*	*0.3234*	*0.0065*	*0.8294*	*0.1378*	*0.0012*	*0.1237*	*0.0029*	*1982*	*29*	*1803*	*32*	*2194*	*15*	*17*	*21*	*2355*	*51*	*40*	*34*	*683*	*20.01*	*0.19*	*0.05*	*0.05*	*0.02*	*0.07*
120-200-20.1	*z28*	*Uniform. altered borders*	*Inherited*	*10.9855*	*0.3641*	*0.4583*	*0.0092*	*0.8843*	*0.1761*	*0.0012*	*0.1966*	*0.0053*	*2516*	*32*	*2427*	*41*	*2613*	*12*	*7*	*9*	*3620*	*89*	*115*	*62*	*731*	*14.04*	*0.96*	*0.07*	*0.07*	*0.03*	*0.11*
120-200-23.2	*z29*	*Core/Rim*	*Inherited*	*7.2856*	*0.2405*	*0.3880*	*0.0074*	*0.8147*	*0.1415*	*0.0013*	*0.1125*	*0.0026*	*2142*	*30*	*2111*	*34*	*2241*	*15*	*3*	*10*	*2153*	*47*	*66*	*64*	*571*	*8.98*	*0.12*	*0.11*	*0.11*	*0.03*	*0.12*
120-200-23.1	z30	Core/Rim	Magmatic	4.3286	0.1409	0.2701	0.0051	0.8039	0.1211	0.0010	0.0804	0.0018	1694	27	1539	26	1966	15	19	27	1562	33	120	164	903	5.50	0.06	0.18	0.18	0.05	0.19
120-200-23.3	z31	Core/Rim	Magmatic	6.9649	0.2200	0.4048	0.0076	0.8481	0.1299	0.0009	0.1266	0.0027	2105	28	2188	35	2092	12	-7	-2	2408	49	84	74	581	7.93	0.07	0.13	0.13	0.04	0.14
GC2																															
120-200-9.3	*z32*	*Core/Rim*	*Inherited*	*13.4428*	*0.4123*	*0.5208*	*0.0082*	*0.7484*	*0.1858*	*0.0011*	*0.1437*	*0.0027*	*2710*	*29*	*2701*	*35*	*2703*	*10*	*1*	*-1*	*2714*	*48*	*284*	*211*	*367*	*1.72*	*0.01*	*0.58*	*0.59*	*0.16*	*0.59*
120-200-9.2	*z33*	*Core/Rim*	*Inherited*	*13.0501*	*0.3976*	*0.5216*	*0.0080*	*0.7038*	*0.1816*	*0.0010*	*0.1436*	*0.0026*	*2682*	*29*	*2705*	*34*	*2666*	*9*	*-2*	*-2*	*2712*	*46*	*296*	*230*	*498*	*2.19*	*0.01*	*0.46*	*0.46*	*0.13*	*0.46*
120-200-16.1	z34	Core/Rim	Magmatic	6.1407	0.2146	0.3628	0.0072	0.6683	0.1264	0.0017	0.2435	0.0349	1994	30	1994	34	2048	24	0	6	4173	514	2	1	51	68.48	1.56	0.01	0.01	0.01	0.03
120-200-18.2	*z35*	*Core/Rim*	*Inherited*	*16.7074*	*0.5281*	*0.6052*	*0.0106*	*0.7833*	*0.2044*	*0.0014*	*0.1687*	*0.0032*	*2916*	*30*	*3051*	*43*	*2859*	*11*	*-8*	*-7*	*3150*	*54*	*450*	*299*	*319*	*1.18*	*0.05*	*0.85*	*0.86*	*0.24*	*0.88*
120-200-18.1	*z36*	*Core/Rim*	*Inherited*	*13.8501*	*0.4389*	*0.5554*	*0.0094*	*0.8221*	*0.1836*	*0.0012*	*0.1648*	*0.0041*	*2739*	*29*	*2845*	*39*	*2682*	*11*	*-7*	*-7*	*3079*	*71*	*89*	*57*	*699*	*13.07*	*0.26*	*0.08*	*0.08*	*0.02*	*0.08*
60-80-2.1	*z37*	*Core/Rim*	*Inherited*	*13.8184*	*0.2240*	*0.5546*	*0.0068*	*0.7859*	*0.1860*	*0.0020*	*0.1552*	*0.0028*	*2736*	*15*	*2845*	*29*	*2705*	*18*	*-7*	*-4*	*2916*	*48*	*200*	*140*	*268*	*1.90*	*0.02*	*0.53*	*0.53*	*0.15*	*0.54*
60-80-3.3	z38	Uniform. altered. fractured	Magmatic	3.6295	0.0729	0.2431	0.0043	0.9171	0.1096	0.0012	0.0816	0.0021	1555	16	1401	22	1789	20	20	25	1584	39	45	60	1525	25.27	0.26	0.04	0.04	0.01	0.05
60-80-4.3	z39	Uniform. altered borders	Magmatic	3.0839	0.0645	0.2156	0.0041	0.9230	0.1037	0.0012	0.0627	0.0016	1426	16	1257	21	1688	21	25	28	1227	30	196	323	3351	10.58	0.08	0.09	0.10	0.03	0.10
60-80-4.1	z40	Uniform. altered borders	Magmatic	3.7844	0.0847	0.2483	0.0050	0.9569	0.1096	0.0012	0.0817	0.0022	1588	18	1427	25	1791	20	24	22	1585	40	76	99	2434	24.97	0.22	0.04	0.04	0.01	0.05
60-80-4.2	z41	Uniform. altered borders	Magmatic	3.5529	0.0758	0.2386	0.0045	0.9301	0.1068	0.0012	0.0689	0.0016	1533	17	1377	23	1743	21	22	22	1346	30	98	154	3086	20.67	0.33	0.05	0.05	0.01	0.05
60-80-6.5	z42	Uniform. altered borders	Magmatic	4.0866	0.0748	0.2639	0.0040	0.8746	0.1107	0.0013	0.1433	0.0032	1650	15	1508	20	1807	21	16	17	2705	56	92	71	2318	33.19	0.38	0.03	0.03	0.02	0.06
GC5A																															
120-200-6.3	z43	Uniform. altered borders	Magmatic	2.8659	0.0596	0.2066	0.0039	0.9411	0.1022	0.0011	0.0682	0.0017	1372	16	1210	21	1661	21	26	31	1332	32	95	149	1987	13.28	0.11	0.08	0.08	0.03	0.09
120-200-6.2	z44	Uniform. altered borders	Magmatic	3.2417	0.0727	0.2268	0.0046	0.9426	0.1051	0.0012	0.0806	0.0027	1461	17	1316	24	1714	21	23	26	1563	51	119	155	1946	13.24	0.31	0.08	0.08	0.03	0.09
120-200-6.1	z45	Uniform. altered borders	Magmatic	3.0537	0.0699	0.2164	0.0045	0.9526	0.1035	0.0012	0.0768	0.0019	1418	18	1260	23	1685	21	26	28	1494	36	129	171	2044	11.98	0.10	0.08	0.08	0.03	0.10
120-200-7.3	z46	Uniform. altered borders	Magmatic	2.8722	0.0535	0.2068	0.0033	0.8838	0.1011	0.0011	0.0677	0.0014	1372	14	1211	18	1640	21	21	29	1323	26	158	244	1883	7.97	0.09	0.13	0.13	0.04	0.14
120-200-7.1	z47	Uniform. altered borders	Magmatic	3.2812	0.0731	0.2238	0.0043	0.9388	0.1057	0.0012	0.0870	0.0021	1470	17	1300	23	1723	21	26	26	1685	38	100	120	1957	16.06	0.14	0.06	0.06	0.02	0.08
60-80-1.3	z48	Uniform. altered borders	Magmatic	2.8950	0.0603	0.2068	0.0038	0.9328	0.1020	0.0011	0.0695	0.0017	1377	15	1210	20	1657	21	26	29	1357	33	185	266	3192	11.93	0.10	0.08	0.08	0.03	0.10
60-80-2.3	z49	Uniform. altered borders	Magmatic	3.2521	0.0742	0.2254	0.0048	0.9530	0.1056	0.0012	0.0715	0.0020	1466	17	1307	25	1721	20	25	27	1394	37	166	234	1638	6.91	0.06	0.14	0.15	0.05	0.16
60-80-2.1	z50	Uniform. altered borders	Magmatic	3.4451	0.0716	0.2345	0.0042	0.9247	0.1069	0.0012	0.0766	0.0020	1511	16	1356	22	1742	21	22	24	1490	36	142	198	1277	6.43	0.07	0.16	0.16	0.05	0.18
60-80-2.2	z51	Uniform. altered borders	Magmatic	3.9471	0.0917	0.2601	0.0054	0.9553	0.1108	0.0012	0.0852	0.0023	1618	18	1487	27	1810	21	19	20	1650	42	144	174	1186	6.78	0.07	0.15	0.15	0.05	0.17
60-80-3.1	z52	Uniform. altered borders	Magmatic	3.3224	0.0691	0.2286	0.0041	0.9419	0.1059	0.0012	0.0729	0.0018	1482	16	1325	21	1728	20	24	26	1421	33	180	260	2018	7.67	0.07	0.13	0.13	0.04	0.14
60-80-3.3	z53	Uniform. altered borders	Magmatic	3.3059	0.0731	0.2269	0.0043	0.9497	0.1060	0.0012	0.0756	0.0019	1480	17	1316	23	1728	20	26	26	1473	35	200	276	2131	7.68	0.07	0.13	0.13	0.04	0.15
60-80-4.4	z54	Uniform. altered borders	Magmatic	2.3389	0.0527	0.1819	0.0037	0.9414	0.0933	0.0011	0.0740	0.0019	1221	16	1076	20	1490	21	27	30	1441	35	151	207	1893	9.02	0.08	0.11	0.11	0.05	0.15
60-80-8.1	z55	Uniform. altered borders	Magmatic	3.8389	0.0824	0.2516	0.0048	0.9456	0.1107	0.0012	0.0845	0.0020	1595	16	1444	24	1808	20	22	22	1638	37	237	298	2358	7.91	0.07	0.13	0.13	0.04	0.15
80-120-1.1	z56	Uniform. altered borders	Magmatic	4.2627	0.0841	0.2717	0.0046	0.9217	0.1139	0.0013	0.0847	0.0020	1684	16	1549	23	1860	20	17	19	1643	36	143	168	1101	6.42	0.06	0.16	0.16	0.05	0.17
80-120-2.3	z57	Uniform. altered borders	Magmatic	3.4247	0.0686	0.2322	0.0041	0.9158	0.1074	0.0012	0.0775	0.0018	1509	16	1344	21	1752	21	22	26	1510	35	164	228	1932	8.41	0.08	0.12	0.12	0.04	0.14
80-120-15.3	z58	Uniform. altered borders	Magmatic	3.7406	0.1843	0.2462	0.0100	0.9378	0.1105	0.0007	0.0849	0.0061	1576	38	1419	52	1805	12	23	24	1648	115	506	202	1798	10.53	0.09	0.09	0.10	0.03	0.11
80-120-15.1	z59	Uniform. altered borders	Magmatic	4.3280	0.2106	0.2769	0.0111	0.8881	0.1135	0.0008	0.1017	0.0072	1696	40	1576	56	1854	12	14	17	1957	131	463	155	2191	16.59	0.12	0.06	0.06	0.02	0.08
80-120-15.2	z60	Uniform. altered borders	Magmatic	3.1967	0.1602	0.2198	0.0091	0.9501	0.1054	0.0007	0.0699	0.0051	1455	39	1281	48	1719	12	30	28	1365	95	583	278	2753	11.09	0.08	0.09	0.09	0.03	0.10
GC5B																															
120-200-6.2	z61	Uniform. altered borders	Magmatic	2.8321	0.1441	0.1933	0.0082	0.9513	0.1046	0.0007	0.0606	0.0045	1363	38	1141	45	1705	13	43	35	1188	84	998	593	19688	12.47	0.10	0.08	0.08	0.03	0.09
80-120-1.2	z62	Uniform. altered borders	Magmatic	2.5780	0.1284	0.1816	0.0075	0.9467	0.1019	0.0007	0.0621	0.0044	1292	36	1076	41	1656	13	78	37	1217	83	1676	1007	4090	4.28	0.03	0.23	0.24	0.08	0.28
80-120-1.3	z63	Uniform. altered borders	Magmatic	3.1902	0.1546	0.2110	0.0087	0.9470	0.1093	0.0007	0.0420	0.0033	1454	39	1232	46	1785	12	37	33	830	63	1299	1078	2526	2.48	0.08	0.40	0.41	0.08	0.28
120-200-8.2	z64	Uniform. altered borders	Magmatic	4.7148	0.2296	0.2935	0.0117	0.8193	0.1186	0.0009	0.1005	0.0070	1767	41	1658	58	1934	13	11	17	1936	129	450	158	810	5.88	0.06	0.17	0.17	0.06	0.20
120-200-10.4	z65	Uniform. altered borders	Magmatic	2.4664	0.1198	0.1798	0.0072	0.8519	0.1005	0.0007	0.0569	0.0040	1261	36	1065	39	1630	13	25	38	1118	77	512	336	2485	9.91	0.07	0.10	0.10	0.03	0.11
60-80-3.4	z66	Uniform. altered borders	Magmatic	4.5163	0.2210	0.2834	0.0114	0.9269	0.1139	0.0008	0.1029	0.0073	1732	41	1608	58	1860	12	16	14	1981	134	400	133	1091	7.62	0.06	0.13	0.13	0.05	0.17
60-80-3.2	z67	Uniform. altered borders	Magmatic	4.6817	0.2273	0.2892	0.0116	0.8874	0.1150	0.0008	0.1024	0.0072	1762	39	1636	57	1877	12	14	12	1971	134	437	140	1007	6.32	0.05	0.16	0.16	0.06	0.20
60-80-5.1	*z68*	*Core/Rim*	*Inherited*	*8.7607*	*0.4195*	*0.3804*	*0.0149*	*0.8815*	*0.1631*	*0.0012*	*0.1295*	*0.0093*	*2313*	*46*	*2080*	*71*	*2487*	*12*	*20*	*17*	*2459*	*165*	*1292*	*299*	*1058*	*3.40*	*0.04*	*0.29*	*0.30*	*0.10*	*0.36*
60-80-5.2	*z69*	*Core/Rim*	*Inherited*	*14.1536*	*0.6910*	*0.5411*	*0.0215*	*0.8140*	*0.1861*	*0.0012*	*0.1697*	*0.0120*	*2758*	*47*	*2786*	*90*	*2706*	*11*	*-2*	*-6*	*3168*	*206*	*7609*	*1366*	*650*	*0.49*	*0.00*	*2.06*	*2.07*	*0.65*	*2.37*
60-80-5.5	*z70*	*Core/Rim*	*Inherited*	*13.3414*	*0.6503*	*0.5211*	*0.0206*	*0.7317*	*0.1840*	*0.0013*	*0.1632*	*0.0114*	*2703*	*46*	*2702*	*87*	*2688*	*12*	*0*	*-2*	*3054*	*198*	*3193*	*621*	*574*	*0.94*	*0.01*	*1.06*	*1.07*	*0.33*	*1.21*
60-80-5.6	*z71*	*Core/Rim*	*Inherited*	*11.7283*	*0.5450*	*0.4765*	*0.0181*	*0.7264*	*0.1828*	*0.0011*	*0.1143*	*0.0076*	*2582*	*43*	*2511*	*79*	*2676*	*10*	*5*	*9*	*2187*	*137*	*1873*	*525*	*576*	*1.13*	*0.03*	*0.89*	*0.89*	*0.21*	*0.78*
60-80-6.4	z72	Uniform. altered borders	Magmatic	2.6893	0.1311	0.1846	0.0073	0.8372	0.1081	0.0008	0.0483	0.0034	1324	36	1092	40	1763	13	30	42	953	66	189	129	1175	9.92	0.13	0.10	0.10	0.03	0.09
60-80-9.3	z73	Uniform. altered borders	Magmatic	2.7086	0.1347	0.1888	0.0078	0.9429	0.1062	0.0007	0.0565	0.0040	1327	35	1114	42	1733	12	39	40	1109	76	2117	11373	5613	6.08	0.05	0.16	0.17	0.05	0.17
60-80-10.1	z74	Uniform. altered borders	Magmatic	3.3939	0.1665	0.2194	0.0090	0.9480	0.1136	0.0007	0.0631	0.0044	1499	37	1277	47	1855	12	37	35	1236	84	8292	-1976	3212	2.65	0.02	0.38	0.38	0.11	0.38
#4-2	z75	Uniform. altered borders	Magmatic	3.0205	0.0714	0.2043	0.0040	0.9192	0.1068	0.0017	0.0540	0.0040	1411	18	1198	21	1744	29	30	34	1062	76	2091	1484	2160	2.11	0.14	0.47	0.48	0.13	0.43
#4-3	z76	Uniform. altered borders	Magmatic	3.0356	0.0699	0.2059	0.0039	0.7880	0.1066	0.0017	0.0530	0.0038	1416	18	1207	21	1741	29	24	33	1043	74	1846	1395	1924	2.10	0.15	0.48	0.48	0.12	0.42
#12-2	z77	Uniform. altered borders	Magmatic	5.0445	0.1128	0.3093	0.0058	0.7090	0.1190	0.0019	0.0806	0.0058	1827	19	1737	28	1940	29	8	12	1567	109	74	33	1002	34.25	2.14	0.03	0.03	0.01	0.03
#19-3	z78	Uniform. altered borders	Magmatic	4.4505	0.1004	0.2807	0.0053	0.6633	0.1155	0.0018	0.0849	0.0060	1722	18	1595	27	1887	29	12	18	1646	112	81	33	1180	35.61	1.99	0.03	0.03	0.01	0.03
GC6																															
120-200-2.1	*z79*	*Core/Rim*	*Inherited*	*12.0564*	*0.5818*	*0.4694*	*0.0185*	*0.6358*	*0.1865*	*0.0012*	*0.1258*	*0.0084*	*2608*	*45*	*2480*	*81*	*2709*	*10*	*9*	*10*	*2395*	*151*	*2651*	*1453*	*587*	*1.51*	*0.02*	*0.66*	*0.67*	*0.18*	*0.65*
120-200-2.2	*z80*	*Core/Rim*	*Inherited*	*15.0279*	*0.7321*	*0.5841*	*0.0232*	*0.6610*	*0.1856*	*0.0012*	*0.1615*	*0.0112*	*2816*	*46*	*2964*	*94*	*2701*	*11*	*-9*	*-13*	*3026*	*195*	*271*	*60*	*183*	*4.17*	*0.02*	*0.24*	*0.24*	*0.07*	*0.24*
120-200-2.3	*z81*	*Core/Rim*	*Inherited*	*15.3861*	*0.7443*	*0.5956*	*0.0234*	*0.6820*	*0.1

120-200-12.1	*z83*	*Core/Rim*	*Inherited*	*7.5236*	*0.3610*	*0.4025*	*0.0156*	*0.5474*	*0.1356*	*0.0010*	*0.1157*	*0.0080*	*2174*	*43*	*2180*	*72*	*2168*	*13*	*0*	*-1*	*2213*	*146*	*187*	*55*	*109*	*2.00*	*0.01*	*0.50*	*0.50*	*0.14*	*0.51*
120-200-13.1	z84	Uniform. altered borders	Magmatic	6.5507	0.3155	0.3849	0.0150	0.7577	0.1236	0.0008	0.1068	0.0074	2051	43	2100	69	2007	12	-4	-6	2050	136	1523	482	1266	2.62	0.01	0.38	0.39	0.11	0.37
120-200-13.2	z85	Uniform. altered borders	Magmatic	7.0533	0.3378	0.4106	0.0160	0.7635	0.1248	0.0008	0.1116	0.0078	2118	42	2218	72	2024	11	-8	-11	2138	141	1689	509	1457	2.85	0.02	0.35	0.35	0.10	0.34
120-200-14.3	*z86*	*Core/Rim*	*Inherited*	*13.3593*	*0.6423*	*0.5269*	*0.0206*	*0.7346*	*0.1842*	*0.0012*	*0.1297*	*0.0091*	*2704*	*45*	*2727*	*87*	*2689*	*11*	*-2*	*-2*	*2464*	*162*	*441*	*112*	*281*	*2.51*	*0.03*	*0.40*	*0.40*	*0.10*	*0.36*
120-200-20.1	z87	Uniform. altered borders	Magmatic	3.5513	0.1780	0.2360	0.0099	0.9405	0.1093	0.0008	0.0754	0.0055	1534	38	1364	51	1785	13	26	26	1470	104	279	122	1792	14.48	0.17	0.07	0.07	0.02	0.08
120-200-20.2	z88	Uniform. altered borders	Magmatic	3.2434	0.1596	0.2185	0.0088	0.9104	0.1076	0.0008	0.0697	0.0050	1465	38	1274	47	1756	13	26	30	1361	93	293	139	1785	12.68	0.11	0.08	0.08	0.03	0.09
80-120-1.1	*z89*	*Dark uniform*	*Inherited*	*7.8043*	*0.3921*	*0.3527*	*0.0149*	*0.9211*	*0.1607*	*0.0013*	*0.1117*	*0.0080*	*2205*	*45*	*1945*	*71*	*2461*	*14*	*25*	*24*	*2140*	*145*	*1222*	*380*	*1775*	*4.64*	*0.05*	*0.22*	*0.22*	*0.07*	*0.25*
80-120-1.2	*z90*	*Dark uniform*	*Inherited*	*12.2958*	*0.6154*	*0.4876*	*0.0203*	*0.9581*	*0.1827*	*0.0011*	*0.1316*	*0.0095*	*2620*	*47*	*2554*	*87*	*2675*	*10*	*6*	*5*	*2494*	*171*	*1157*	*294*	*648*	*2.13*	*0.05*	*0.47*	*0.47*	*0.13*	*0.46*
80-120-3.2	*z91*	*Core/Rim*	*Inherited*	*12.8826*	*0.6187*	*0.5032*	*0.0196*	*0.6048*	*0.1850*	*0.0013*	*0.1458*	*0.0102*	*2670*	*45*	*2627*	*84*	*2697*	*12*	*3*	*2*	*2750*	*179*	*388*	*91*	*167*	*1.87*	*0.01*	*0.54*	*0.54*	*0.16*	*0.57*
80-120-3.1	*z92*	*Core/Rim*	*Inherited*	*12.6254*	*0.6073*	*0.4910*	*0.0192*	*0.7130*	*0.1859*	*0.0011*	*0.1112*	*0.0080*	*2651*	*45*	*2574*	*83*	*2704*	*10*	*5*	*5*	*2128*	*146*	*367*	*110*	*208*	*1.91*	*0.03*	*0.52*	*0.53*	*0.12*	*0.44*
80-120-5.4	z93	Uniform. altered borders	Magmatic	3.2779	0.1661	0.2177	0.0091	0.9610	0.1087	0.0007	0.0826	0.0061	1469	38	1268	48	1774	12	38	31	1601	112	67	27	1127	43.77	0.32	0.02	0.02	0.01	0.03
80-120-5.3	z94	Uniform. altered borders	Magmatic	3.0779	0.1525	0.2085	0.0086	0.9259	0.1067	0.0007	0.0873	0.0063	1423	37	1221	46	1742	13	31	32	1690	116	67	26	1492	59.95	0.46	0.02	0.02	0.01	0.02
80-120-5.2	z95	Uniform. altered borders	Magmatic	3.5830	0.1801	0.2357	0.0098	0.9560	0.1103	0.0007	0.1040	0.0076	1542	39	1362	51	1801	12	30	27	1997	138	84	27	1381	51.77	0.41	0.02	0.02	0.01	0.03
GC7																															
120-200-6.1	z96	Uniform. blurred zoning	Magmatic	3.6830	0.1781	0.2471	0.0098	0.7795	0.1086	0.0009	0.0745	0.0052	1566	39	1423	50	1773	14	15	22	1453	98	1080	487	1933	4.77	0.62	0.21	0.21	0.06	0.22
80-120-8.1	*z97*	*Core/Rim*	*Inherited*	*10.4688*	*0.5141*	*0.4308*	*0.0172*	*0.7853*	*0.1774*	*0.0015*	*0.1589*	*0.0111*	*2475*	*46*	*2308*	*78*	*2626*	*15*	*12*	*15*	*2980*	*194*	*716*	*154*	*281*	*2.12*	*0.32*	*0.47*	*0.48*	*0.18*	*0.64*
80-120-10.3	z98	Uniform. blurred zoning	Magmatic	3.7819	0.1857	0.2487	0.0101	0.7892	0.1113	0.0010	0.1391	0.0115	1589	38	1431	52	1818	17	17	24	2623	204	218	51	1174	24.73	3.11	0.04	0.04	0.02	0.08
80-120-10.1	z99	Uniform. blurred zoning	Magmatic	4.3436	0.2230	0.2802	0.0120	0.9436	0.1130	0.0009	0.1035	0.0075	1696	42	1590	60	1845	14	15	16	1988	137	249	80	1540	20.31	3.18	0.05	0.05	0.02	0.06

Guitreau, M., Blichert-Toft, J., 2014. Implications of discordant U-Pb ages on Hf isotope studies of detrital zircons. Chem. Geol. 385, 17–25. https://doi.org/10.1016/j.chemgeo.2014.07.014

Guitreau, M., Flahaut, J., 2019. Record of low-temperature aqueous alteration of Martian zircon during the late Amazonian. Nat. Commun. 10, 1–9. https://doi.org/10.1038/s41467-019-10382-y

Paton, C., Hellstrom, J., Paul, B., Woodhead, J., Hergt, J., 2011. Iolite: Freeware for the visualisation and processing of mass spectrometric data. J. Anal. At. Spectrom. 26, 2508–2518. https://doi.org/10.1039/C1JA10172B

Petrus, J.A., Kamber, B.S., 2012. VizualAge: A Novel Approach to Laser Ablation ICP-MS U-Pb Geochronology Data Reduction. Geostand. Geoanalytical Res. 36, 247–270. https://doi.org/https://doi.org/10.1111/j.1751-908X.2012.00158.x

Vermeesch, P., 2018. IsoplotR: A free and open toolbox for geochronology. Geosci. Front. 9, 1479–1493. https://doi.org/https://doi.org/10.1016/j.gsf.2018.04.001

LA-ICP-MS zircon U-Th-Pb analyses for the studied samples. Italic symbols are inherited zircons. Grey labels refer to common-Pb analyses. Disc.(%) and Disc. Dist.(%) are calculated directly from IsoplotR (Vermeesch, 2018) using the relative age difference (%) between the 206Pb/238U and 207Pb/206Pb ages; and as proposed by Guitreau et al., 2014, respectively. [Th/U]m. and [Th/U]calc. are provided directly from Iolite4 (Petrus and Kamber, 2012; Paton et al., 2011), and calculated using the equations proposed by Guitreau and Flahaut, 2019.

Sample	This work	Type from texture	Domain	Isotope ratios										Age (Ma)										Elemental data									
				$^{207}Pb/^{235}U$	±2σ	$^{206}Pb/^{238}U$	±2σ	Rho	$^{207}Pb/^{206}Pb$	±2σ	$^{208}Pb/^{232}Th$	±2σ		$^{207}Pb/^{235}U$	±2σ	$^{206}Pb/^{238}U$	±2σ	$^{207}Pb/^{206}Pb$	±2σ	Disc.(%)	Disc. Dist.(%)	$^{208}Pb/^{232}Th$	±2σ	Pb (ppm)	Th (ppm)	U (ppm)	Final U/Th	±2σ	Th/U	$[Th/U]_{m.}$	$^{208}Pb/^{206}Pb$	$[Th/U]_{calc.}$
CM44A																																	
1.2	z1	Patchy zoning with bright borders	Magmatic	6.1971	0.3190	0.3581	0.0187	0.8865	0.1247	0.0049	0.1103	0.0069	1999	45	1972	89	2019	69	3	1	2113.04	125.08	111.38	102.76	552.89	5.30	0.05	0.19	0.19	0.06	0.20
2.1	z2	Uniform blurried zoning	Magmatic	4.0721	0.2231	0.2561	0.0141	0.9459	0.1147	0.0045	0.0775	0.0051	1637	46	1465	72	1870	71	24	23	1505.77	95.73	140.45	181.32	1202.83	6.73	0.11	0.15	0.15	0.05	0.16
4.1	z3	Ocilatory zoned core and blurred rims	Magmatic	5.0165	0.2643	0.3083	0.0163	0.9033	0.1193	0.0047	0.1648	0.0103	1814	45	1728	80	1940	70	10	13	3078.03	179.17	35.35	24.56	704.21	30.68	0.43	0.03	0.03	0.02	0.06
4.2	z4	Ocilatory zoned core and blurred rims	Magmatic	7.8496	0.3972	0.4514	0.0228	0.7976	0.1264	0.0050	0.1293	0.0078	2209	46	2401	103	2046	70	-14	-21	2456.55	139.92	41.99	36.38	223.77	5.91	0.14	0.17	0.17	0.05	0.17
4.3	z5	Ocilatory zoned core and blurred rims	Magmatic	6.9845	0.3493	0.3994	0.0202	0.6829	0.1277	0.0050	0.1237	0.0075	2107	45	2164	93	2063	71	-5	-6	2356.38	134.22	30.53	27.40	100.94	3.70	0.04	0.27	0.27	0.08	0.30
4.4	z6	Ocilatory zoned core and blurred rims	Magmatic	6.0672	0.3121	0.3653	0.0190	0.8638	0.1207	0.0048	0.1099	0.0070	1979	45	2006	91	1961	69	-2	-3	2104.96	127.32	24.72	23.70	648.13	27.41	0.31	0.04	0.04	0.01	0.04
9.1	z7	Patchy zoning	Magmatic	6.3595	0.3240	0.3558	0.0182	0.7775	0.1297	0.0051	0.0914	0.0057	2022	44	1962	88	2087	69	6	6	1769.32	106.63	29.14	33.24	547.16	16.51	0.25	0.06	0.06	0.02	0.06
9.3	z8	Patchy zoning	Magmatic	5.5026	0.2970	0.3235	0.0173	0.9242	0.1230	0.0049	0.0698	0.0044	1888	46	1801	84	1995	70	10	10	1361.93	82.30	13.37	19.50	707.15	38.11	0.74	0.03	0.03	0.01	0.02
12.2	z9	Core/Rim	Magmatic	2.5744	0.1351	0.1821	0.0097	0.8743	0.1028	0.0041	0.0511	0.0032	1288	38	1077	52	1672	76	32	38	1007.03	62.05	41.15	87.56	2436.20	27.95	0.46	0.04	0.04	0.01	0.03
17.2	z10	Blurred zoning core dark rim	Magmatic	7.6387	0.3928	0.4236	0.0219	0.7919	0.1311	0.0052	0.1140	0.0072	2185	46	2273	99	2107	70	-7	-10	2180.24	131.50	88.59	80.86	489.38	6.10	0.07	0.16	0.17	0.04	0.16
17.3	z11	Blurred zoning core dark rim	Magmatic	6.2454	0.3207	0.3576	0.0184	0.7857	0.1269	0.0050	0.1018	0.0063	2007	46	1968	87	2049	70	4	4	1958.24	115.76	210.40	221.87	874.14	3.93	0.05	0.25	0.26	0.07	0.26
18.1	z12	Patchy zoning and uniform dark rim	Magmatic	7.4823	0.3802	0.4241	0.0217	0.7848	0.1281	0.0051	0.1429	0.0087	2169	46	2277	98	2070	71	-9	-12	2698.16	153.35	49.11	38.07	704.59	18.81	0.32	0.05	0.05	0.02	0.06
18.3	z13	Patchy zoning and uniform dark rim	Magmatic	4.0385	0.2130	0.2487	0.0132	0.9274	0.1175	0.0046	0.0757	0.0048	1635	42	1433	69	1912	70	27	27	1472.85	89.55	408.43	557.69	1385.79	2.45	0.03	0.41	0.41	0.13	0.44
19.1	z14	Blurred zoning core dark rim	Magmatic	3.8391	0.2027	0.2355	0.0125	0.8645	0.1186	0.0047	0.1372	0.0089	1597	43	1361	65	1932	72	29	33	2593.68	158.44	156.36	118.52	1986.34	17.65	0.46	0.06	0.06	0.03	0.12
19.4	*z15*	*Blurred zoning core dark rim*	*Inherited*	*7.9719*	*0.4121*	*0.4348*	*0.0226*	*0.8717*	*0.1333*	*0.0053*	*0.1317*	*0.0083*	*2222*	*46*	*2322*	*101*	*2136*	*69*	*-8*	*-11*	*2496.10*	*147.76*	*1066.70*	*842.58*	*862.75*	*1.03*	*0.02*	*0.97*	*0.98*	*0.30*	*1.04*
22.3	z16	Patchy zoning with bright borders	Magmatic	3.1572	0.1759	0.2099	0.0116	0.9111	0.1093	0.0044	0.0748	0.0052	1435	42	1225	61	1785	74	32	34	1454.41	96.89	38.81	51.77	1182.55	22.67	0.31	0.04	0.04	0.02	0.05
22.2	*z17*	*Patchy zoning with bright borders*	*Inherited*	*7.4312*	*0.4314*	*0.3993*	*0.0223*	*0.9204*	*0.1342*	*0.0054*	*0.1467*	*0.0127*	*2147*	*51*	*2163*	*105*	*2148*	*72*	*0*	*-2*	*2724.07*	*213.77*	*53.86*	*40.57*	*358.66*	*8.48*	*0.13*	*0.12*	*0.12*	*0.04*	*0.15*
23.2	*z18*	*Patchy zoning and uniform dark rim*	*Inherited*	*6.5215*	*0.3512*	*0.3456*	*0.0189*	*0.8983*	*0.1369*	*0.0055*	*0.0638*	*0.0047*	*2038*	*48*	*1914*	*93*	*2180*	*69*	*13*	*14*	*1245.36*	*88.27*	*5.13*	*8.63*	*118.90*	*13.94*	*0.81*	*0.07*	*0.07*	*0.01*	*0.05*
24.2	*z19*	*Core/Rim*	*Inherited*	*6.7672*	*0.3476*	*0.3623*	*0.0183*	*0.5900*	*0.1349*	*0.0055*	*0.1146*	*0.0072*	*2076*	*46*	*1991*	*87*	*2151*	*72*	*7*	*7*	*2194.19*	*132.90*	*2.85*	*2.70*	*18.71*	*6.97*	*0.10*	*0.14*	*0.14*	*0.05*	*0.16*
24.3	*z20*	*Core/Rim*	*Inherited*	*7.4654*	*0.3754*	*0.3982*	*0.0202*	*0.7147*	*0.1365*	*0.0054*	*0.1173*	*0.0071*	*2165*	*45*	*2158*	*93*	*2180*	*68*	*1*	*1*	*2241.14*	*128.67*	*88.10*	*80.41*	*190.60*	*2.36*	*0.02*	*0.42*	*0.43*	*0.13*	*0.44*
24.5	*z21*	*Core/Rim*	*Inherited*	*7.4130*	*0.3935*	*0.4099*	*0.0221*	*0.8466*	*0.1310*	*0.0053*	*0.1276*	*0.0080*	*2155*	*47*	*2209*	*101*	*2106*	*73*	*-4*	*-7*	*2424.76*	*143.49*	*36.59*	*29.23*	*135.27*	*4.72*	*0.06*	*0.21*	*0.21*	*0.07*	*0.23*
25.2	*z22*	*Core/Rim*	*Inherited*	*7.9851*	*0.4105*	*0.4427*	*0.0230*	*0.7881*	*0.1310*	*0.0052*	*0.1434*	*0.0088*	*2222*	*47*	*2358*	*103*	*2103*	*70*	*-10*	*-15*	*2705.99*	*156.04*	*61.24*	*45.29*	*170.92*	*3.81*	*0.05*	*0.26*	*0.26*	*0.09*	*0.30*
25.3	*z23*	*Core/Rim*	*Inherited*	*7.0877*	*0.3630*	*0.3890*	*0.0200*	*0.8278*	*0.1319*	*0.0052*	*0.1210*	*0.0075*	*2117*	*46*	*2115*	*93*	*2119*	*70*	*0*	*-1*	*2305.99*	*135.50*	*58.35*	*50.03*	*149.65*	*3.08*	*0.06*	*0.32*	*0.33*	*0.10*	*0.36*
CM44B																																	
1.1	z24	Homogeneous blurred zoning	Magmatic	4.4109	0.1816	0.2694	0.0078	0.8971	0.1193	0.0010	0.0912	0.0034	1710	35	1535	39	1941	15	18	23	1764.91	63.76	46.11	51.26	605.75	11.75	0.11	0.09	0.09	0.03	0.10
1.2	z25	Homogeneous blurred zoning	Magmatic	3.1173	0.1281	0.2091	0.0061	0.8604	0.1088	0.0010	0.1191	0.0046	1433	32	1222	32	1771	18	31	34	2279.59	83.29	34.28	30.99	1362.02	46.26	1.75	0.02	0.02	0.01	0.04
1.3	z26	Homogeneous blurred zoning	Magmatic	4.4394	0.1949	0.2720	0.0086	0.9314	0.1189	0.0010	0.1267	0.0050	1707	36	1547	43	1935	15	21	22	2405.69	89.18	56.30	45.82	889.23	19.38	0.23	0.05	0.05	0.02	0.08
5.5	z27	Bright patchy zoning core and dark rim	Magmatic	3.4392	0.1579	0.2254	0.0073	0.9137	0.1106	0.0012	0.1210	0.0048	1504	36	1307	38	1803	20	38	30	2305.81	86.48	39.85	35.13	691.90	19.86	0.34	0.05	0.05	0.03	0.09
5.4	z28	Bright patchy zoning core and dark rim	Magmatic	5.4418	0.2365	0.3134	0.0104	0.7870	0.1268	0.0019	0.1765	0.0065	1888	37	1755	51	2052	25	12	17	3283.82	112.20	60.48	40.18	463.22	11.73	0.29	0.09	0.09	0.05	0.17
5.2	z29	Bright patchy zoning core and dark rim	Magmatic	5.7993	0.2538	0.3204	0.0100	0.8678	0.1286	0.0015	0.1107	0.0041	1940	38	1788	49	2073	20	14	13	2125.41	76.66	29.74	30.48	186.44	6.18	0.08	0.16	0.16	0.06	0.20
5.1	z30	Bright patchy zoning core and dark rim	Magmatic	5.4835	0.2367	0.3222	0.0101	0.8639	0.1215	0.0014	0.0987	0.0043	1890	37	1796	49	1971	20	9	8	1899.03	78.13	30.78	31.74	690.14	22.05	0.37	0.05	0.05	0.01	0.05
CM46A																																	
1.1	z31	Bright core blurred zoning rim	Magmatic	6.7254	0.2683	0.3813	0.0103	0.8075	0.1295	0.0011	0.1118	0.0038	2072	36	2080	48	2086	15	-1	1	2142.44	69.87	58.65	56.36	233.44	4.16	0.04	0.24	0.24	0.07	0.25
3.1	z32	Complex patchy zoning	Magmatic	5.0518	0.2016	0.2986	0.0081	0.8121	0.1232	0.0011	0.0935	0.0033	1826	35	1684	41	1999	15	13	18	1805.47	61.02	31.44	36.90	224.30	6.13	0.06	0.16	0.16	0.05	0.18
3.2	z33	Complex patchy zoning	Magmatic	6.2972	0.2541	0.3495	0.0096	0.7758	0.1311	0.0013	0.1264	0.0047	1816	36	1932	45	2106	18	7	9	2403.12	84.17	38.00	32.22	182.61	5.63	0.06	0.18	0.18	0.06	0.23
3.3	z34	Complex patchy zoning	Magmatic	5.4096	0.2197	0.3064	0.0085	0.8207	0.1281	0.0012	0.1118	0.0038	1882	35	1721	42	2067	16	15	19	2142.66	71.04	40.97	40.34	225.48	5.62	0.06	0.18	0.18	0.07	0.23
4.1	z35	Blurred zoning	Magmatic	3.7456	0.1528	0.2364	0.0067	0.8340	0.1154	0.0011	0.0746	0.0027	1578	33	1366	35	1881	17	25	30	1452.71	50.80	42.93	61.19	287.98	4.62	0.05	0.22	0.22	0.07	0.24
4.3	z36	Blurred zoning	Magmatic	4.3162	0.1793	0.2609	0.0076	0.8630	0.1197	0.0011	0.0821	0.0030	1689	34	1494	39	1947	18	21	25	1592.98	55.52	46.92	61.18	268.99	4.36	0.04	0.23	0.23	0.07	0.25
5.1	z37	Patchy zoning fine bright rim	Magmatic	6.1278	0.2549	0.3506	0.0104	0.8789	0.1273	0.0011	0.1115	0.0041	1988	37	1933	49	2059	16	5	7	2133.63	74.50	43.66	41.53	238.67	5.72	0.06	0.17	0.18	0.06	0.20
5.2	z38	Patchy zoning fine bright rim	Magmatic	7.3669	0.2902	0.3988	0.0104	0.6922	0.1342	0.0012	0.1375	0.0046	2153	35	2162	48	2147	16	-1	-1	2601.86	82.42	28.92	22.70	152.99	6.72	0.06	0.15	0.15	0.05	0.18
5.3	z39	Patchy zoning fine bright rim	Magmatic	6.4200	0.2529	0.3652	0.0097	0.7641	0.1281	0.0011	0.1099	0.0037	2032	35	2005	46	2067	15	2	3	2108.37	68.83	48.22	47.20	288.68	6.11	0.05	0.16	0.16	0.05	0.17
6.1	z40	Patchy zoning fine bright rim	Magmatic	6.2880	0.2558	0.3585	0.0099	0.8456	0.1272	0.0011	0.1076	0.0038	2011	36	1972	47	2056	15	4	4	2064.02	69.10	38.66	38.84	255.69	6.56	0.07	0.15	0.15	0.05	0.16
6.2	z41	Patchy zoning fine bright rim	Magmatic	4.5269	0.1867	0.2735	0.0078	0.8318	0.1201	0.0012	0.0876	0.0032	1731	34	1556	39	1952	18	17	22	1695.45	58.90	32.07	37.95	220.89	5.70	0.06	0.18	0.18	0.06	0.20
6.4	z42	Patchy zoning fine bright rim	Magmatic	5.6072	0.2226	0.3248	0.0087	0.7689	0.1261	0.0011	0.0998	0.0034	1915	35	1811	42	2040	16	9	13	1921.34	62.11	41.35	44.28	262.84	5.96	0.05	0.17	0.17	0.05	0.18
7.1	z43	Blurred zoning bright rim	Magmatic	6.2022	0.2491	0.3511	0.0096	0.8353	0.1285	0.0011	0.1048	0.0036	2000	35	1938	46	2074	14	6	7	2014.07	65.52	64.10	65.47	276.54	4.25	0.04	0.24	0.24	0.07	0.25
7.2	z44	Blurred zoning bright rim	Magmatic	6.6872	0.2686	0.3764	0.0104	0.8260	0.1296	0.0011	0.1139	0.0040	2066	35	2056	49	2090	15	1	2	2178.66	72.19	47.43	44.60	248.11	5.63	0.05	0.18	0.18	0.05	0.19
7.3	z45	Blurred zoning bright rim	Magmatic	6.5292	0.2604	0.3687	0.0099	0.7608	0.1289	0.0012	0.1113	0.0038	2048	35	2021	46	2078	17	2	3	2131.31	68.75	61.47	59.61	254.64	4.29	0.04	0.23	0.23	0.07	0.25
9.2	z46	Bright core patchy zoning	Magmatic	6.9267	0.2749	0.3850	0.0103	0.7936	0.1309	0.0011	0.1185	0.0040	2099	35	2099	48	2106	16	0	0	2263.30	71.89	92.65	83.72	403.31	4.79	0.04	0.21	0.21	0.06	0.23
9.3	z47	Bright core patchy zoning	Magmatic	7.0245	0.2776	0.3950	0.0104	0.7185	0.1301	0.0011	0.1239	0.0042	2111	35	2144	48	2094	15	-3	-2	2360.58	75.43	69.85	59.81	334.23	5.65	0.05	0.18	0.18	0.06	0.20
11.3	z48	Bright core blurred zoning rim	Magmatic	7.3363	0.2893	0.4118	0.0108	0.7470	0.1313	0.0011	0.1409	0.0050	2151	36	2221	49	2111	15	-5	-5	2660.82	88.25	15.64	12.37	203.40	16.68	0.18	0.06	0.06	0.02	0.07
18.1	z49	Brigh core zoning rim	Magmatic	5.3836	0.2145	0.3048	0.0083	0.8125	0.1270	0.0011	0.1004	0.0035	1878	34	1713	41	2052	16	15	18	1932.54	64.55	10.91	11.36	198.33	19.54	0.22	0.05	0.05	0.02	0.06
18.2	z50	Brigh core zoning rim	Magmatic	7.0206	0.2813	0.3758	0.0101	0.7021	0.1348	0.0014	0.1188	0.0041	2110	36	2054	47	2155	18	5	4	2268.24	74.44	11.92	10.94	30.56	3.03	0.03	0.33	0.33	0.11	0.37
19.1	z51	Bright core patchy zoning	Magmatic	8.1972	0.3315	0.4449	0.0123	0.8503	0.1333	0.0011	0.1383	0.0049	2247	36	2368	55	2138	15	-9	-14	2615.78	86.64	201.79	136.92	260.45	2.36	0.03	0.42	0.43	0.13	0.47
19.3	z52	Bright core patchy zoning	Magmatic	7.3864	0.2931	0.4053	0.0107	0.7714	0.1315	0.0013	0.1364	0.0047	2155	36	2195	51	2113	17	-3	-6	2582.68	83.12	163.18	119.03	270.85	2.51	0.08	0.40	0.40	0.14	0.48
20.2	z53	Patchy zoning fine bright rim	Magmatic	7.4618	0.3013	0.4047	0.0111	0.7936	0.1329	0.0013	0.1449	0.0052	2163	36	2188	51	2130	16	-2	-5	2731.40	91.56	190.96	138.58	537.76	4.08	0.04	0.24	0.25	0.09	0.31
20.3	z54	Patchy zoning fine bright rim	Magmatic	7.8088	0.3093	0.4297	0.0114	0.7151	0.1313	0.0013	0.1285	0.0043	2206	36	2304	52	2110	17	-7	-12	2444.67	78.42	92.58	78.49	419.00	5.36	0.05	0.19	0.19	0.06	0.20
21.1	*z55*	*Core/rim*	*Inherited*	*16.6155*	*0.6502*	*0.5470*	*0.0142*	*0.6694*	*0.2225*	*0.0019*	*0.1547*	*0.0052*	*2910*	*37*	*2810*	*59*	*2995*	*14*	*6*	*8*	*2906.25*	*91.19*	*181.93*	*125.77*	*152.24*	*1.20*	*0.01*	*0.84*	*0.84*	*0.24*	*0.88*
21.2	*z56*	*Core/rim*	*Inherited*	*13.8445*	*0.5450*	*0.5073*	*0.0132*	*0.6928*	*0.2020*	*0.0018*	*0.1362*	*0.0045*	*2736*	*38*	*2643*	*56*	*2838*	*14*	*6*	*10*	*2579.63*	*80.70*	*168.75*	*135.35*	*160.52*	*1.24*	*0.01*	*0.81*	*0.81*	*0.22*	*0.80*
21.3	*z57*	*Core/rim*	*Inherited*	*17.3635*	*0.6790*	*0.5735*	*0.0151*	*0.7146*	*0.2251*	*0.0020*	*0.1524*	*0.0050*	*2953*	*38*	*2921*	*61*	*3014*	*14*	*2*	*6*	*2865.75*	*88.49*	*520.04*	*389.01*	*357.32*	*1.07*	*0.01*	*0.93*	*0.94*	*0.25*	*0.93*
22.3	z58	Large zoning bright rim	Magmatic	6.3253	0.2562	0.3525	0.0098	0.8197	0.1333	0.0013	0.1273	0.0044	2017	36	1946	47	2136	17	6	12	2420.39	78.16	310.02	311.84	949.30	4.46	0.05	0.22	0.23	0.08	0.29
22.2	z59	Large zoning bright rim	Magmatic	6.9316	0.2723	0.3908	0.0105	0.7052	0.1317	0.0012	0.1209	0.0041	2100	35	2124	48	2117	16	-2	1	2305.09	74.46	245.72	246.26	785.14	3.90	0.04	0.26	0.26	0.08	0.28
23.1	z60	Bright core patchy/blurred rim	Magmatic	5.8600	0.2409	0.3341	0.0095	0.8674	0.1259	0.0011	0.1091	0.0039	1952	36	1855	46	2035	16	9	8	2091.03	70.42	35.37	35.44	184.10	5.49	0.05	0.18	0.18	0.06	0.21
23.2	z61	Bright core patchy/blurred rim	Magmatic	5.3560	0.2154	0.3081	0.0087	0.7922	0.1247	0.0012	0.1102	0.0038	1874	35	1729	43	2019	17	13	15	2110.96	69.28	19.29	19.17	172.99	9.66	0.13	0.10	0.10	0.04	0.13
23.3	z62	Bright core patchy/blurred rim	Magmatic	7.8078	0.3036	0.4182	0.0110	0.7210	0.1344	0.0012	0.1285	0.0043	2207	36	2250	50	2150	16	-3	-7	2443.07	76.77	45.16	38.71	114.04	3.02	0.04	0.33	0.33	0.10	0.36
24.1	z63	Patchy zoning fine bright rim	Magmatic	7.5151	0.2999	0.4105	0.0109	0.7401	0.1320	0.0012	0.1277	0.0044	2171	36	2215	50	2121	17	-3	-6	2427.97	78.34	43.39	36.83	195.93	5.40	0.05	0.19	0.19	0.06	0.20
24.2	z64	Patchy zoning fine bright rim	Magmatic	5.1135	0.2070	0.3026	0.0083	0.8204	0.1223	0.0011	0.0979	0.0034	1833	35	1702	41	1985	16	12	16	1886.04	62.37	48.14	54.21	225.50	4.16	0.04	0.24	0.24	0.08	0.27
24.3	z65	Patchy zoning fine bright rim	Magmatic	6.2845	0.2478	0.3516	0.0093	0.7030	0.1282	0.0012	0.1072	0.0036	2013	34	1940	44	2069	16	6	6	2057.24	66.22	40.69	41.52	253.71	6.00	0.08	0.17	0.17	0.05	0.18
25.1	z66	Patchy zoning fine bright rim	Magmatic	4.7876	0.2037	0.2806	0.0083	0.8998	0.1222	0.0011	0.0901	0.0034	1774	35	1591	42	1981	16	19	21	1742.35	62.66	43.81	52.38	315.63	5.91	0.07	0.17	0.17	0.05	0.19
25.3	z67	Patchy zoning fine bright rim	Magmatic	6.7989	0.2686	0.3696	0.0096	0.6976	0.1316	0.0012	0.1040	0.0035	2084	35	2026	45	2116	17	5	3	1999.20	64.11	53.15	56.50	366.48	6.39	0.06	0.16	0.16	0.04	0.16
29.1	z68	Bright core blurred rim	Magmatic	7.3747	0.2909	0.4046	0.0107	0.7131	0.1327	0.0012	0.1292	0.0044	2157	35	2188	49	2130	16	-3	-3	2455.90	77.94	102.33	85.93	310.10	3.61	0.03	0.28	0.28	0.09	0.31
CM47																																	
1.1	z69	Uniform fine zoned	Magmatic	7.6982	0.3686	0.4069	0.0158	0.5937	0.1337	0.0010	0.1145	0.0080	2195	43	2200	72	2145	13	0	-6	2190.88	144.99	155.58	46.81	269.79	7.88	0.05	0.13	0.13	0.04	0.13
1.2	z70	Uniform fine zoned	Magmatic	7.9774	0.3799	0.4236	0.0164	0.6761	0.1335	0.0009	0.1189	0.0083	2227	43	2276	74	2142	12	-4	-10	2270.06	150.26	145.54	41.44	242.91	7.35	0.10	0.14	0.14	0.04	0.14
1.4	z71	Uniform fine zoned	Magmatic	7.5545	0.3653	0.4039	0.0156	0.5985	0.1337	0.0008	0.1154	0.0080	2179	44	2187	71	2145	11	-1	-4	2207.24	145.64	265.86	77.92	384.45	5.35	0.04	0.19	0.19	0.05	0.19
1.5	z72	Uniform fine zoned	Magmatic	7.3248	0.3489	0.3948	0.0152	0.6063	0.1330	0.0008	0.1100	0.0077	2151	42	2144	70	2136	11	1	-2	2109.51	140.49	244.65	74.81	335.27	4.65	0.02	0.22	0.22	0.06	0.21
2.4	z73	Uniform fine zoned	Magmatic	6.8449	0.3234	0.3771	0.0145	0.6002	0.1332	0.0008	0.1052	0.0073	2091	41	2062	68	2139	11	2	5	2020.99	132.88	381.45	125.77	442.77	3.87	0.02	0.26	0.26	0.07	0.26
2.3	z74	Uniform fine zoned	Magmatic	6.9195	0.3349	0.3802	0.0151	0.7012	0.1339	0.0013	0.1122	0.0079	2100	43	2077	71	2148	16	2	5	2148.88	142.91	787.36	261.64	758.28	3.31	0.03	0.30	0.30	0.09	0.32
2.2	z75	Uniform fine zoned	Magmatic	6.7032	0.3179	0.3728	0.0141	0.5798	0.1332	0.0008	0.1014	0.0071	2072	42	2042	66	2138	11	2	7	1951.69	129.40	356.95	125.09	394.96	3.75	0.02	0.27	0.27	0.07	0.26
2.1	z76	Uniform fine zoned	Magmatic	6.7894	0.3240	0.3774	0.0146	0.7105	0.1330	0.0008	0.1041	0.0072	2083	42	2064	68	2137	11	2	6	2002.11	131.71	428.76	146.77	453.80	3.65	0.03	0.27	0.28	0.08	0.27
3.1	z77	Uniform fine zoned	Magmatic	6.6999	0.3214	0.3747	0.0146	0.6536	0.1328	0.0009	0.1013	0.0076	2073	43	2051	68	2134	11	2	6	1949.96	129.37	559.45	194.68	531.14	3.14	0.02	0.32	0.32	0.09	0.31
3.2	z78	Uniform fine zoned	Magmatic	6.7234	0.3

7.3	z93	Uniform fine zoned	Magmatic	4.5914	0.1741	0.2758	0.0117	0.8670	0.1227	0.0009	0.0819	0.0040	1745	32	1568	59	1994	14	19	25	1590.93	73.60	708.88	289.78	710.34	2.44	0.03	0.41	0.41	0.12	0.43
8.1	z94	Uniform fine zoned bright rim	Magmatic	7.3747	0.2660	0.4024	0.0161	0.7277	0.1335	0.0009	0.1151	0.0052	2157	32	2179	74	2141	11	-2	-2	2202.02	93.94	444.99	129.90	496.38	3.88	0.03	0.26	0.26	0.07	0.26
8.2	z95	Uniform fine zoned bright rim	Magmatic	7.3596	0.2647	0.4018	0.0160	0.7267	0.1329	0.0008	0.1093	0.0050	2154	32	2178	75	2133	11	-2	-3	2096.15	90.38	584.43	179.35	529.65	3.00	0.02	0.33	0.34	0.09	0.32
8.3	z96	Uniform fine zoned bright rim	Magmatic	7.3719	0.2652	0.4005	0.0160	0.6803	0.1329	0.0008	0.1092	0.0049	2156	32	2171	75	2135	11	-1	-3	2095.35	89.70	386.96	118.46	499.16	4.22	0.03	0.24	0.24	0.07	0.23
8.4	z97	Uniform fine zoned bright rim	Magmatic	6.2769	0.2288	0.3607	0.0145	0.7022	0.1278	0.0009	0.1112	0.0051	2013	32	1985	69	2064	13	3	5	2130.31	91.77	463.01	139.89	611.34	4.55	0.03	0.22	0.22	0.07	0.24
8.5	z98	Uniform fine zoned bright rim	Magmatic	7.4594	0.2690	0.4104	0.0165	0.6611	0.1339	0.0009	0.1138	0.0051	2167	32	2216	75	2146	11	-4	-3	2177.57	92.75	692.50	203.03	509.67	2.69	0.02	0.37	0.37	0.10	0.37
10.1	z99	Uniform blurred zoning bright core	Magmatic	6.5942	0.2433	0.3760	0.0154	0.8164	0.1296	0.0009	0.1118	0.0052	2056	32	2056	72	2089	12	0	3	2141.99	94.35	477.09	139.18	498.97	4.27	0.03	0.23	0.24	0.07	0.25
10.3	z100	Uniform blurred zoning bright core	Magmatic	7.6211	0.2767	0.4158	0.0168	0.7239	0.1351	0.0009	0.1150	0.0052	2185	32	2240	76	2163	12	-4	-3	2199.26	94.31	663.99	194.07	608.11	3.73	0.03	0.27	0.27	0.07	0.26
11.1	z101	Bright patchy zoned core blurred rim	Magmatic	7.2548	0.2620	0.4052	0.0163	0.7232	0.1318	0.0008	0.1130	0.0051	2142	32	2192	75	2120	11	-4	-3	2162.84	93.10	352.11	103.79	429.97	4.96	0.04	0.20	0.20	0.06	0.20
13.1	z102	Patchy zoned bright rim	Magmatic	7.3505	0.2654	0.4018	0.0162	0.7488	0.1332	0.0008	0.1153	0.0052	2153	32	2176	74	2137	11	-2	-2	2204.83	94.69	377.99	110.76	363.97	3.38	0.02	0.30	0.30	0.09	0.30
13.2	z103	Patchy zoned bright rim	Magmatic	5.2607	0.1932	0.3062	0.0124	0.7978	0.1245	0.0009	0.0921	0.0042	1859	31	1722	62	2018	13	13	16	1780.53	76.95	151.59	56.47	283.84	5.26	0.04	0.19	0.19	0.06	0.20
13.3	z104	Patchy zoned bright rim	Magmatic	6.6180	0.2354	0.3693	0.0146	0.6529	0.1304	0.0008	0.1145	0.0051	2060	31	2025	69	2100	11	3	4	2191.39	91.96	236.65	72.47	287.06	4.15	0.05	0.24	0.24	0.08	0.26
16.1	z105	Uniform blurred zoning bright core	Magmatic	7.9342	0.2876	0.4376	0.0177	0.7400	0.1335	0.0008	0.1279	0.0058	2223	33	2339	79	2141	10	-9	-10	2432.17	103.23	276.31	77.94	429.54	5.77	0.03	0.17	0.17	0.05	0.18
17.1	z106	Uniform blured zoning	Magmatic	7.7135	0.2781	0.4248	0.0171	0.7083	0.1338	0.0008	0.1222	0.0055	2197	33	2281	77	2146	10	-6	-6	2330.39	99.21	286.03	83.08	383.77	4.73	0.06	0.21	0.21	0.06	0.22
17.2	z107	Uniform blured zoning	Magmatic	6.4399	0.2519	0.3706	0.0157	0.9249	0.1278	0.0009	0.1098	0.0052	2030	35	2029	74	2064	12	1	3	2104.92	95.27	318.41	100.49	462.40	4.64	0.04	0.22	0.22	0.06	0.23
17.3	z108	Uniform blured zoning	Magmatic	7.9924	0.2851	0.4304	0.0171	0.7415	0.1359	0.0008	0.1309	0.0058	2228	32	2307	77	2174	10	-6	-7	2485.24	104.21	300.03	79.28	362.37	4.60	0.04	0.22	0.22	0.07	0.24
19.3	z109	Uniform large zoned	Magmatic	4.7669	0.1767	0.2713	0.0112	0.8510	0.1246	0.0008	0.0803	0.0037	1776	32	1546	57	2020	12	25	24	1560.18	68.91	383.86	151.37	591.29	3.45	0.02	0.29	0.29	0.09	0.30
20.3	z110	Uniform blurred zoning dark core	Magmatic	6.5453	0.2411	0.3492	0.0143	0.7978	0.1330	0.0008	0.0929	0.0042	2052	33	1930	68	2136	11	10	9	1796.22	77.96	363.30	124.38	432.03	2.98	0.03	0.34	0.34	0.09	0.32
22.4	z111	Fine/Blurred zoning dark core	Magmatic	7.4451	0.2719	0.3980	0.0163	0.7314	0.1337	0.0008	0.1133	0.0052	2165	33	2159	75	2145	10	1	-3	2168.28	94.14	170.73	49.62	266.74	4.89	0.04	0.20	0.21	0.06	0.21
22.3	z112	Fine/Blurred zoning dark core	Magmatic	7.4541	0.2702	0.4024	0.0163	0.6895	0.1331	0.0008	0.1226	0.0055	2166	32	2179	75	2136	10	-1	-4	2338.92	99.64	244.04	67.10	272.27	3.79	0.05	0.26	0.27	0.08	0.29
25.4	z113	Fine/Blurred zoning bright rim	Magmatic	7.9443	0.2865	0.4311	0.0173	0.6799	0.1343	0.0009	0.1287	0.0058	2224	32	2310	78	2152	11	-6	-9	2446.08	104.28	179.84	49.09	236.27	5.03	0.04	0.20	0.20	0.06	0.21
25.3	z114	Fine/Blurred zoning bright rim	Magmatic	7.5927	0.2706	0.4143	0.0164	0.7138	0.1336	0.0008	0.1146	0.0052	2183	32	2234	75	2144	10	-4	-5	2192.36	94.70	222.69	68.24	231.59	3.73	0.07	0.27	0.27	0.07	0.26
26.2	z115	*Core/Rim*	*Inherited?*	*5.5250*	*0.2038*	*0.2740*	*0.0112*	*0.7837*	*0.1457*	*0.0010*	*0.1043*	*0.0050*	*1902*	*32*	*1560*	*57*	*2295*	*12*	*33*	*35*	*2002.96*	*90.80*	*263.00*	*87.90*	*418.21*	*4.78*	*0.06*	*0.21*	*0.21*	*0.08*	*0.29*
28.3	z116	Fine zoning bright rim	Magmatic	5.0890	0.1865	0.2954	0.0120	0.8406	0.1259	0.0008	0.0855	0.0039	1831	31	1667	60	2038	11	17	21	1657.35	72.29	257.22	100.12	402.35	3.81	0.03	0.26	0.26	0.08	0.27
28.4	z117	Fine zoning bright rim	Magmatic	4.0435	0.1493	0.2454	0.0099	0.7954	0.1203	0.0008	0.0660	0.0030	1641	30	1415	52	1957	12	25	31	1290.95	56.31	188.99	91.07	388.31	3.96	0.03	0.25	0.25	0.07	0.24
29.3	z118	Large zoning dark blurred core	Magmatic	4.9190	0.2008	0.2877	0.0125	0.9561	0.1250	0.0008	0.1034	0.0046	1794	34	1626	62	2025	12	21	22	1987.48	84.56	231.31	74.58	371.54	4.99	0.07	0.20	0.20	0.07	0.25
30.2	z119	Fine/Blurred zoning bright rim	Magmatic	4.2365	0.1548	0.2576	0.0105	0.8572	0.1205	0.0008	0.0799	0.0037	1679	30	1476	53	1982	12	23	28	1555.11	69.52	199.26	80.72	358.37	4.34	0.03	0.23	0.23	0.07	0.25
30.3	z120	Fine/Blurred zoning bright rim	Magmatic	4.4562	0.1648	0.2684	0.0109	0.8834	0.1213	0.0008	0.0824	0.0039	1719	30	1533	56	1974	12	21	25	1599.27	71.60	184.28	73.82	338.43	4.53	0.03	0.22	0.22	0.07	0.24
31.2	z121	Uniform large zoned	Magmatic	4.7744	0.1773	0.2796	0.0116	0.8547	0.1230	0.0009	0.0845	0.0039	1778	31	1589	59	1998	12	20	22	1639.26	73.14	375.11	143.03	457.13	3.34	0.02	0.30	0.30	0.09	0.32
31.1	z122	Uniform large zoned	Magmatic	7.8950	0.2859	0.4262	0.0172	0.7368	0.1332	0.0008	0.1151	0.0052	2217	33	2287	78	2138	11	-5	-10	2200.82	94.65	322.55	91.16	316.92	3.83	0.03	0.26	0.26	0.07	0.25
32.2	z123	Uniorm blurred core dark rim	Magmatic	4.7878	0.1830	0.2841	0.0120	0.9077	0.1214	0.0008	0.0865	0.0041	1778	31	1612	60	1972	12	19	20	1676.19	76.50	583.94	208.09	579.57	3.51	0.03	0.29	0.29	0.09	0.31
36.1	z124	Uniform large zoned	Magmatic	5.5762	0.2045	0.3182	0.0130	0.7703	0.1270	0.0009	0.0992	0.0046	1911	32	1780	64	2052	12	12	15	1910.85	84.33	763.87	250.86	621.46	3.17	0.02	0.32	0.32	0.10	0.35
36.2	z125	Uniform large zoned	Magmatic	5.5365	0.2071	0.3146	0.0130	0.8672	0.1274	0.0009	0.0897	0.0042	1902	32	1763	65	2058	12	14	16	1734.87	78.26	500.15	180.05	520.59	3.32	0.03	0.30	0.30	0.09	0.30
36.3	z126	Uniform large zoned	Magmatic	7.1317	0.2579	0.3914	0.0158	0.7611	0.1320	0.0008	0.1129	0.0051	2126	32	2129	74	2122	10	0	-1	2162.36	92.31	422.14	124.81	453.22	3.85	0.02	0.26	0.26	0.08	0.27
CM49																																	
2.2	z127	Patchy zoned	Magmatic	5.8680	0.2215	0.3212	0.0134	0.8330	0.1323	0.0009	0.0363	0.0022	1953	33	1794	65	2127	12	15	17	722.68	42.62	67.81	62.27	121.27	2.01	0.07	0.50	0.50	0.06	0.20
2.3	z128	Patchy zoned	Magmatic	6.9303	0.2507	0.3799	0.0153	0.6509	0.1322	0.0009	0.1057	0.0048	2101	32	2075	71	2125	12	2	2	2030.31	87.70	96.22	30.03	118.97	4.11	0.03	0.24	0.24	0.07	0.24
3.1	z129	Geminated large zoned fine bright rim	Magmatic	6.7396	0.2447	0.3681	0.0149	0.6807	0.1331	0.0010	0.1030	0.0046	2076	32	2019	70	2135	12	5	6	1981.66	85.19	201.08	64.67	202.65	3.21	0.02	0.31	0.31	0.09	0.31
3.2	z130	Geminated large zoned fine bright rim	Magmatic	6.4046	0.2310	0.3534	0.0142	0.5300	0.1316	0.0009	0.0961	0.0043	2032	31	1950	68	2115	13	7	9	1855.44	81.37	117.03	40.55	109.09	2.78	0.02	0.36	0.36	0.10	0.35
3.3	z131	Geminated large zoned fine bright rim	Magmatic	6.5843	0.2380	0.3605	0.0142	0.6588	0.1325	0.0008	0.0983	0.0044	2056	32	1985	68	2130	11	6	8	1895.10	81.30	204.31	69.40	174.19	2.52	0.02	0.40	0.40	0.11	0.38
3.4	z132	Geminated large zoned fine bright rim	Magmatic	7.2894	0.2621	0.4012	0.0160	0.6892	0.1323	0.0009	0.1113	0.0050	2146	32	2174	74	2126	11	-2	-3	2132.85	90.46	219.17	66.42	179.99	2.66	0.02	0.38	0.38	0.11	0.37
4.1	z133	Fine zoned dark core	Magmatic	8.0802	0.2940	0.4464	0.0181	0.7800	0.1324	0.0008	0.1318	0.0060	2238	33	2378	81	2127	11	-10	-14	2501.48	107.35	467.82	122.06	223.45	1.80	0.01	0.56	0.56	0.17	0.58
4.2	z134	Fine zoned dark core	Magmatic	7.6673	0.2867	0.4358	0.0179	0.8518	0.1291	0.0009	0.1257	0.0058	2189	34	2332	80	2082	12	-11	-13	2392.53	104.52	1330.44	359.33	566.81	1.54	0.02	0.65	0.66	0.19	0.66
4.3	z135	Fine zoned dark core	Magmatic	7.5222	0.2730	0.4164	0.0168	0.7267	0.1331	0.0008	0.1166	0.0053	2175	33	2243	77	2139	11	-5	-4	2228.75	95.26	267.35	78.29	162.75	2.01	0.02	0.50	0.50	0.14	0.49
5.1	z136	Patchy zoned with fine bright rim	Magmatic	8.0206	0.2936	0.4439	0.0181	0.7581	0.1332	0.0009	0.1269	0.0059	2231	33	2367	81	2139	12	-10	-11	2413.60	105.23	273.76	72.15	135.62	1.81	0.02	0.55	0.56	0.16	0.56
5.2	z137	Patchy zoned with fine bright rim	Magmatic	7.9308	0.2914	0.4390	0.0180	0.7866	0.1330	0.0009	0.1308	0.0060	2220	33	2344	81	2135	12	-9	-11	2483.47	107.95	286.42	73.72	138.89	1.89	0.02	0.53	0.53	0.16	0.56
5.4	z138	Patchy zoned with fine bright rim	Magmatic	7.1958	0.2654	0.3891	0.0160	0.7655	0.1326	0.0009	0.1113	0.0052	2134	34	2117	74	2129	12	1	-1	2131.94	94.54	453.86	134.34	248.40	2.08	0.05	0.48	0.48	0.14	0.49
7.1	z139	Large scale zoned patchy zoned core	Magmatic	6.8470	0.2476	0.3743	0.0151	0.7693	0.1316	0.0008	0.1020	0.0046	2091	33	2049	71	2116	10	4	3	1962.41	84.63	243.41	80.91	445.11	5.52	0.22	0.18	0.18	0.05	0.17
7.2	z140	Large scale zoned patchy zoned core	Magmatic	7.7894	0.2859	0.4155	0.0169	0.7637	0.1351	0.0010	0.1236	0.0057	2205	33	2239	77	2161	12	-3	-5	2355.31	101.75	352.22	99.48	229.42	2.36	0.02	0.42	0.43	0.13	0.45
7.3	z141	Large scale zoned patchy zoned core	Magmatic	7.1934	0.2590	0.3948	0.0157	0.7877	0.1314	0.0008	0.1101	0.0050	2134	33	2145	74	2116	11	-1	-2	2110.68	90.21	1158.77	351.87	675.06	1.95	0.01	0.51	0.52	0.14	0.51
7.4	z142	Large scale zoned patchy zoned core	Magmatic	8.0326	0.2920	0.4417	0.0179	0.7359	0.1319	0.0009	0.1282	0.0058	2233	33	2357	80	2120	12	-9	-14	2436.54	104.58	566.53	150.55	456.41	3.05	0.03	0.33	0.33	0.10	0.34
8.1	z143	Large scale zoned , blurred core, fine bright rim	Magmatic	7.3690	0.2672	0.4068	0.0164	0.7485	0.1308	0.0008	0.1199	0.0054	2156	33	2199	75	2106	11	-3	-6	2287.68	97.51	491.18	138.86	396.54	2.89	0.02	0.35	0.35	0.10	0.36
8.3	z144	Large scale zoned , blurred core, fine bright rim	Magmatic	7.2402	0.2601	0.3955	0.0159	0.7111	0.1319	0.0008	0.1100	0.0050	2141	32	2147	73	2121	10	-1	-3	2108.55	90.56	393.19	121.27	385.96	3.35	0.05	0.30	0.30	0.08	0.29
8.4	z145	Large scale zoned , blurred core, fine bright rim	Magmatic	7.4744	0.2715	0.4058	0.0165	0.7102	0.1324	0.0009	0.1143	0.0053	2169	32	2196	77	2127	12	-2	-5	2187.27	95.25	356.95	104.45	333.90	3.26	0.03	0.31	0.31	0.09	0.31
9.3	z146	Large scale zoning, fine bright rim	Magmatic	7.7758	0.2811	0.4210	0.0169	0.8115	0.1326	0.0008	0.1257	0.0057	2203	33	2265	76	2131	11	-5	-9	2391.84	102.55	521.09	142.69	441.14	2.98	0.03	0.34	0.34	0.10	0.36
10.2	z147	Large scale zoning, fine bright rim	Magmatic	7.5009	0.2733	0.4043	0.0164	0.8063	0.1332	0.0008	0.1192	0.0054	2172	32	2187	75	2138	11	-1	-4	2275.15	98.22	963.94	271.84	490.14	1.85	0.03	0.54	0.54	0.16	0.56
10.3	z148	Large scale zoning, fine bright rim	Magmatic	6.9916	0.2531	0.3929	0.0158	0.7756	0.1298	0.0008	0.1193	0.0056	2108	32	2135	73	2093	11	-2	-2	2275.98	101.13	41.32	12.36	574.38	57.55	1.96	0.02	0.02	0.01	0.02
11.2	z149	Patchy zoning, fine bright rim	Magmatic	6.7109	0.2501	0.3802	0.0158	0.8988	0.1296	0.0008	0.1021	0.0048	2070	33	2075	73	2090	11	0	2	1962.67	88.50	730.47	236.52	393.05	1.86	0.02	0.54	0.54	0.15	0.51
11.3	z150	Patchy zoning, fine bright rim	Magmatic	7.3356	0.2694	0.4128	0.0168	0.8252	0.1301	0.0008	0.0688	0.0032	2150	33	2226	77	2095	11	-6	-7	1345.25	60.32	130.21	67.45	311.64	5.41	0.13	0.18	0.19	0.03	0.11
12.2	z151	Large zonong, bright core, fine bright rim	Magmatic	7.5702	0.2742	0.4107	0.0165	0.6036	0.1346	0.0010	0.1198	0.0054	2181	32	2217	75	2156	13	-3	-3	2286.40	98.19	80.45	22.91	79.58	3.57	0.02	0.28	0.28	0.08	0.29
12.1	z152	Large zonong, bright core, fine bright rim	Magmatic	7.7019	0.2830	0.4236	0.0173	0.7857	0.1310	0.0009	0.1168	0.0054	2194	33	2275	78	2108	12	-6	-11	2232.16	97.29	2101.49	610.52	737.05	1.45	0.02	0.69	0.70	0.19	0.68
12.3	z153	Large zonong, bright core, fine bright rim	Magmatic	7.7703	0.2875	0.4249	0.0174	0.8880	0.1318	0.0008	0.1260	0.0059	2201	33	2284	80	2119	10	-6	-10	2396.84	106.12	1851.47	498.63	765.68	2.02	0.02	0.50	0.50	0.15	0.52
13.1	z154	Blurred zoning, fine bright rim	Magmatic	7.6773	0.2785	0.4251	0.0172	0.7795	0.1304	0.0008	0.1254	0.0056	2192	33	2283	78	2100	11	-7	-11	2251.97	100.62	736.59	200.18	1748.80	11.07	0.03	0.09	0.09	0.03	0.09
13.2	z155	Blurred zoning, fine bright rim	Magmatic	7.4705	0.2719	0.4083	0.0165	0.7557	0.1322	0.0009	0.1252	0.0057	2168	33	2206	76	2124	12	-3	-5	2385.21	104.25	794.24	211.29	530.23	2.80	0.05	0.36	0.36	0.11	0.39
13.3	z156	Blurred zoning, fine bright rim	Magmatic	7.3142	0.2689	0.3993	0.0164	0.8127	0.1327	0.0009	0.1307	0.0059	2148	33	2164	75	2131	12	-1	-2	2482.07	106.15	615.74	154.11	601.05	3.97	0.18	0.25	0.25	0.08	0.29
15.1	z157	Large scale zoning, blurred core	Magmatic	7.5576	0.2822	0.4206	0.0175	0.8824	0.1305	0.0008	0.1250	0.0058	2176	34	2260	79	2102	12	-7	-9	2378.70	104.98	1517.19	402.41	764.14	1.89	0.02	0.53	0.53	0.16	0.56
15.3	z158	Large scale zoning, blurred core	Magmatic	7.1768	0.2614	0.3979	0.0162	0.7136	0.1311	0.0010	0.1047	0.0047	2132	32	2161	77	2110	13	-2	-3	2011.92	86.36	982.19	321.84	657.42	1.98	0.03	0.51	0.51	0.13	0.47
16.1	z159	Fine zoning, fine bright rim	Magmatic	7.6204	0.2752	0.4242	0.0171	0.7308	0.1307	0.0008	0.1215	0.0057	2186	32	2280	78	2106	10	-7	-10	2317.72	101.98	665.07	180.45	378.19	1.98	0.02	0.50	0.51	0.15	0.51
16.2	z160	Fine zoning, fine bright rim	Magmatic	8.0177	0.2909	0.4313	0.0174	0.6921	0.1355	0.0009	0.1211	0.0055	2232	32	2310	78	2169	12	-6	-8	2309.87	98.50	141.05	38.70	155.88	3.86	0.03	0.26	0.26	0.07	0.26
16.3	z161	Fine zoning, fine bright rim	Magmatic	7.3887	0.2659	0.4001	0.0160	0.6332	0.1345	0.0008	0.1106	0.0050	2159	31	2169	74	2154	11	-1	-1	2119.84	90.38	219.13	66.51	203.04	2.92	0.02	0.34	0.35	0.10	0.34
16.4	z162	Fine zoning, fine bright rim	Magmatic	7.5534	0.2716	0.4214	0.0169	0.7498	0.1311	0.0008	0.1254	0.0057	2180	34	2267	78	2110	10	-7	-8	2387.36	102.57	415.11	112.84	259.65	2.26	0.02	0.44	0.44	0.13	0.47
17.1	z163	Large zoning, fine bright rim	Magmatic	7.0027	0.2528	0.3942	0.0159	0.7005	0.1288	0.0008	0.1152	0.0052	2111	33	2141	73	2079	12	-2	-4	2293.82	95.10	528.00	153.41	400.32	2.66	0.04	0.38	0.38	0.11	0.39
17.3	z164	Large zoning, fine bright rim	Magmatic	7.7594	0.2831	0.4243	0.0172	0.7433	0.1322	0.0008	0.1301	0.0060	2201	32	2279	78	2124	11	-6	-10	2471.52	106.59	362.62	92.56	308.12	3.30	0.07	0.30	0.31	0.09	0.33
18.3	z165	Patchy zoning, fine bright rim	Magmatic	6.9327	0.2515	0.3828	0.0154	0.7991	0.1313	0.0008	0.1025	0.0047	2100	32	2088	72	2112	11	1	1	1972.30	85.81	530.60	173.24	302.14	1.71	0.02	0.59	0.59	0.16	0.56
19.1	z166	Fine zoning, fine bright rim	Magmatic	7.2719	0.2616	0.4009	0.0161	0.6635	0.1316	0.0008	0.1121	0.0050	2144	32	2172	74	2118	11	-2	-3	2147.12	91.22	329.23	99.73	209.59	2.06	0.02	0.49	0.49	0.14	0.48
19.2	z167	Fine zoning, fine bright rim	Magmatic	6.4856	0.2384	0.3565	0.0145	0.7929	0.1313	0.0009	0.0884	0.0041	2041	32	1964	69	2113	12	7	7	1710.89	75.55	339.95	132.73	372.24	2.84	0.04	0.35	0.35	0.09	0.31
20.3	z168	Patchy zoning core, large scale zoning rim	Magmatic	7.3633	0.2685	0.4048	0.0164	0.7786	0.1324	0.0009	0.1142	0.0052	2154	32	2191	76	2127	11	-3	-4	2185.96	95.61	201.23	60.10	242.53	4.08	0.03	0.24	0.25	0.07	0.25
21.1	z169	Fine scale zoning	Magmatic	7.5172	0.2709	0.4190	0.0169	0.7014	0.1311	0.0008	0.1176	0.0053	2175	32	2255	77	2109	11	-6	-8	2246.85	95.74	644.04	186.13	591.66	3.18	0.04	0.31	0.32	0.09	0.31
21.2	z170	Fine scale zoning	Magmatic	6.9372	0.2492	0.3761	0.0150	0.7286	0.1327	0.0008	0.1056	0.0047	2102	32	2057	70	2132	10	4	3	2029.15	85.91	642.17	207.22	436.46	2.22	0.03	0.45	0.45	0.13	0.45
21.4	z171	Fine scale zoning	Magmatic	7.0294	0.2537	0.3818	0.0153	0.7616	0.1322	0.0008	0.1056	0.0047	2114	32	2084	71	2125	11	3	1	2029.03	86.70	459.64	148.19	334.92	2.33	0.02	0.43	0.43	0.12	0.42
22.2	z172	Fine scale zoning, fine bright rim	Magmatic	6.8878	0.2509	0.3737	0.0151	0.7825	0.1318	0.0008	0.1075	0.0049	2095	32	2046	71	2120	11	4	2	2063.55	89.30	1127.08	352.77	605.00	1.86	0.04	0.54	0.54	0.16	0.55
23.1	z173	Fine scale/patchy zoning, fine bright rim	Magmatic	7.2841	0.2647	0.3957	0.0160	0.7155	0.1321	0.0008	0.1084	0.0049	2146	33	2148	74

34.2	z195	Fine scale zoning, fine bright rim	Magmatic	7.6656	0.2826	0.4123	0.0166	0.7127	0.1360	0.0015	0.1177	0.0056	2192	33	2225	76	2175	19	-3	-2	2248.33	100.31	681.02	201.66	578.27	2.53	0.09	0.40	0.40	0.11	0.40
34.3	z196	Fine scale zoning, fine bright rim	Magmatic	7.4934	0.2773	0.4166	0.0168	0.7952	0.1321	0.0015	0.1184	0.0056	2170	33	2244	77	2123	19	-6	-6	2261.79	100.91	1161.03	344.20	753.58	2.06	0.02	0.49	0.49	0.14	0.49
35.1	z197	Fine scale zoning, fine bright rim	Magmatic	7.4292	0.2758	0.4145	0.0168	0.7531	0.1320	0.0014	0.1162	0.0055	2163	34	2234	77	2122	19	-6	-5	2220.88	100.24	890.12	272.45	619.60	2.31	0.02	0.43	0.44	0.12	0.43
35.2	z198	Fine scale zoning, fine bright rim	Magmatic	7.3351	0.2743	0.4066	0.0165	0.8053	0.1325	0.0015	0.1192	0.0057	2151	34	2199	77	2129	20	-4	-3	2275.31	103.23	673.94	194.06	480.72	2.54	0.04	0.39	0.40	0.12	0.41
35.3	z199	Fine scale zoning, fine bright rim	Magmatic	7.7039	0.2829	0.4165	0.0167	0.6581	0.1319	0.0014	0.1196	0.0056	2196	33	2244	76	2121	19	-4	-9	2283.14	100.88	441.74	124.81	394.72	3.36	0.03	0.30	0.30	0.09	0.30
36.1	z200	Fine scale zoning, blurred core, fine bright rim	Magmatic	7.5948	0.2794	0.4118	0.0166	0.7252	0.1316	0.0014	0.1243	0.0058	2183	33	2222	76	2117	19	-3	-8	2369.50	106.37	572.72	154.34	393.84	2.67	0.03	0.37	0.38	0.11	0.40
36.2	z201	Fine scale zoning, blurred core, fine bright rim	Magmatic	7.2508	0.2668	0.3922	0.0158	0.7358	0.1325	0.0014	0.1147	0.0054	2142	32	2132	73	2129	19	1	-2	2194.62	98.12	403.15	120.35	332.69	2.95	0.02	0.34	0.34	0.10	0.35
36.3	z202	Fine scale zoning, blurred core, fine bright rim	Magmatic	7.3438	0.2707	0.4003	0.0162	0.7582	0.1325	0.0015	0.1164	0.0055	2153	33	2170	74	2129	19	-1	-3	2225.00	99.55	551.28	164.13	398.04	2.64	0.02	0.38	0.38	0.11	0.39
36.4	z203	Fine scale zoning, blurred core, fine bright rim	Magmatic	7.1542	0.2640	0.3946	0.0160	0.7346	0.1314	0.0014	0.1114	0.0052	2130	33	2144	75	2115	20	-1	-2	2134.38	95.07	818.52	248.18	392.98	1.73	0.02	0.58	0.58	0.16	0.58
37.1	z204	Fine scale zoning, fine bright rim	Magmatic	7.8783	0.2895	0.4357	0.0176	0.7491	0.1317	0.0014	0.1259	0.0059	2216	34	2332	78	2118	19	-9	-12	2396.90	105.76	1602.98	433.31	752.49	1.83	0.01	0.55	0.55	0.16	0.56
37.2	z205	Fine scale zoning, fine bright rim	Magmatic	7.9982	0.2994	0.4369	0.0179	0.8500	0.1318	0.0015	0.1318	0.0064	2228	33	2336	81	2119	19	-8	-14	2503.25	114.75	412.84	107.19	348.07	3.47	0.04	0.29	0.29	0.09	0.31
37.3	z206	Fine scale zoning, fine bright rim	Magmatic	7.5482	0.2798	0.4107	0.0166	0.7383	0.1325	0.0015	0.1184	0.0056	2177	33	2217	76	2128	20	-3	-6	2260.52	101.57	186.17	53.25	177.31	3.42	0.03	0.29	0.29	0.09	0.30
38.1	z207	Fine scale zoning, fine bright rim	Magmatic	7.7464	0.2856	0.4211	0.0170	0.7233	0.1329	0.0015	0.1257	0.0059	2200	33	2264	77	2135	19	-5	-8	2393.75	104.89	279.06	73.79	210.94	2.85	0.06	0.35	0.35	0.11	0.37
38.2	z208	Fine scale zoning, fine bright rim	Magmatic	7.3791	0.2743	0.4023	0.0163	0.8065	0.1326	0.0015	0.1097	0.0052	2156	33	2178	75	2130	19	-2	-3	2105.17	96.04	265.54	81.35	247.89	3.10	0.03	0.32	0.32	0.09	0.31
38.3	z209	Fine scale zoning, fine bright rim	Magmatic	7.6591	0.2866	0.4194	0.0171	0.8230	0.1323	0.0015	0.1185	0.0056	2189	33	2256	77	2128	19	-5	-8	2262.49	101.36	265.86	77.88	203.78	2.78	0.05	0.36	0.36	0.10	0.36

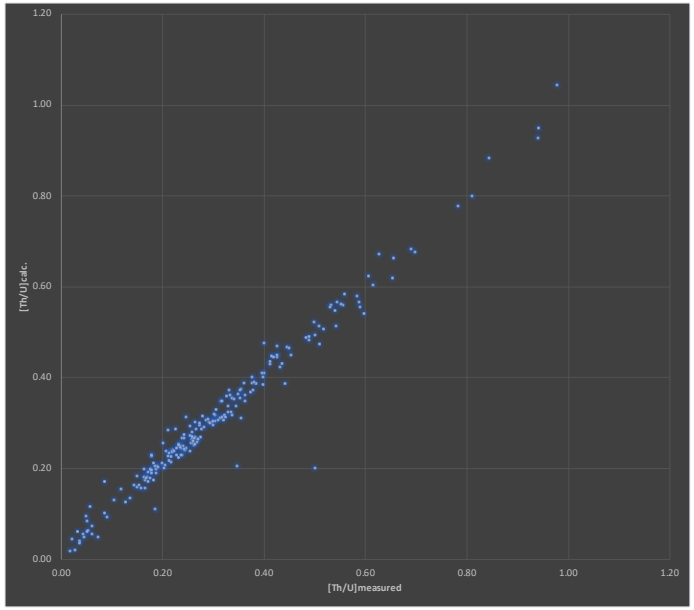
Guitreau, M., Blichert-Toft, J., 2014. Implications of discordant U-Pb ages on Hf isotope studies of detrital zircons. Chem. Geol. 385, 17–25. https://doi.org/10.1016/j.chemgeo.2014.07.014

Guitreau, M., Flahaut, J., 2019. Record of low-temperature aqueous alteration of Martian zircon during the late Amazonian. Nat. Commun. 10, 1–9. https://doi.org/10.1038/s41467-019-10382-y

Paton, C., Hellstrom, J., Paul, B., Woodhead, J., Hergt, J., 2011. Iolite: Freeware for the visualisation and processing of mass spectrometric data. J. Anal. At. Spectrom. 26, 2508–2518. https://doi.org/10.1039/C1JA10172B

Petrus, J.A., Kamber, B.S., 2012. VizualAge: A Novel Approach to Laser Ablation ICP-MS U-Pb Geochronology Data Reduction. Geostand. Geoanalytical Res. 36, 247–270. https://doi.org/https://doi.org/10.1111/j.1751-908X.2012.00158.x

Vermeesch, P., 2018. IsoplotR: A free and open toolbox for geochronology. Geosci. Front. 9, 1479–1493. https://doi.org/https://doi.org/10.1016/j.gsf.2018.04.001



U-Th-Pb isotopic composition, calculated ages, and elemental composition for the used zircon reference materials. Uncertainties correspond to 2σ confidential interval.

November 26, 2022

Standard	Isotope ratios 207Pb/235U	±2σ	206Pb/238U	±2σ	Rho	207Pb/206Pb	±2σ	Age (Ma) 207Pb/235U	±2σ	206Pb/238U	±2σ	207Pb/206Pb	±2σ	Disc.(%)	208Pb/232Th	±2σ	Elemental data Pb (ppm)	Th (ppm)	U (ppm)	Final U/Th	Th/U
Sequence 1																					
91500																					
1065.4 ± 0.3 Ma																					
Wiedenbeck et al., (1995)	1.8519	0.0585	0.1790	0.0038	0.2720	0.0742	0.0008	0.0537	0.0010	1064	21	1061	15	1037	23	0	1058	20	15	30	81	2.66	0.28	0.38
	1.8501	0.0584	0.1795	0.0038	0.4367	0.0749	0.0008	0.0538	0.0010	1062	21	1064	15	1058	21	0	1060	20	15	31	83	2.67	0.28	0.37
	1.8458	0.0589	0.1788	0.0037	0.4269	0.0754	0.0008	0.0536	0.0011	1060	21	1060	15	1068	22	0	1056	20	15	31	82	2.67	0.30	0.37
	1.8446	0.0583	0.1795	0.0038	0.3505	0.0748	0.0008	0.0536	0.0010	1064	21	1064	15	1054	22	0	1059	20	15	30	80	2.66	0.27	0.38
	1.8391	0.0581	0.1793	0.0038	0.3900	0.0747	0.0007	0.0539	0.0011	1058	21	1063	15	1059	21	-1	1061	20	16	32	84	2.67	0.28	0.37
	1.8638	0.0589	0.1793	0.0039	0.4289	0.0749	0.0008	0.0537	0.0011	1066	22	1063	16	1058	22	0	1059	21	16	31	83	2.65	0.30	0.38
	1.8599	0.0592	0.1793	0.0038	0.4204	0.0750	0.0008	0.0538	0.0011	1068	21	1063	16	1061	22	1	1059	20	15	30	80	2.68	0.28	0.37
	1.8496	0.0585	0.1790	0.0037	0.3836	0.0755	0.0008	0.0539	0.0010	1060	21	1061	15	1070	22	0	1057	20	15	30	80	2.66	0.27	0.38
	1.8412	0.0579	0.1792	0.0038	0.4334	0.0745	0.0007	0.0539	0.0011	1059	21	1062	15	1047	20	0	1062	20	15	31	82	2.67	0.25	0.38
	1.8473	0.0594	0.1791	0.0038	0.4317	0.0750	0.0008	0.0537	0.0011	1060	21	1062	15	1055	23	0	1057	20	15	30	80	2.67	0.28	0.37
	1.8758	0.0601	0.1792	0.0038	0.4063	0.0752	0.0008	0.0541	0.0011	1070	21	1062	15	1069	22	1	1064	21	15	31	82	2.68	0.33	0.37
	1.8370	0.0588	0.1791	0.0038	0.4485	0.0742	0.0008	0.0535	0.0011	1057	21	1062	15	1056	22	0	1055	21	15	31	82	2.67	0.31	0.37
	1.8342	0.0582	0.1788	0.0038	0.4058	0.0747	0.0008	0.0538	0.0011	1056	21	1060	15	1050	22	0	1059	21	15	31	82	2.69	0.31	0.37
	1.8486	0.0587	0.1793	0.0039	0.5109	0.0748	0.0008	0.0537	0.0011	1061	21	1063	16	1054	21	0	1059	20	15	30	80	2.65	0.30	0.38
	1.8464	0.0598	0.1787	0.0039	0.4615	0.0747	0.0009	0.0536	0.0011	1060	21	1060	16	1055	23	0	1055	21	15	30	80	2.65	0.28	0.38
	1.8555	0.0610	0.1794	0.0039	0.4051	0.0742	0.0010	0.0539	0.0011	1063	22	1063	16	1059	22	0	1061	21	16	36	97	2.68	0.29	0.37
	1.8335	0.0588	0.1793	0.0039	0.4234	0.0749	0.0009	0.0538	0.0011	1056	21	1063	16	1059	24	-1	1060	22	15	31	83	2.66	0.32	0.38
	1.8509	0.0585	0.1793	0.0039	0.4002	0.0754	0.0008	0.0536	0.0011	1062	21	1063	15	1069	22	0	1061	20	15	30	80	2.67	0.32	0.37
	1.8262	0.0591	0.1791	0.0039	0.4967	0.0749	0.0009	0.0540	0.0011	1054	22	1063	16	1053	23	-1	1062	21	16	32	86	2.67	0.31	0.37
	1.8696	0.0598	0.1795	0.0039	0.3409	0.0749	0.0009	0.0539	0.0011	1066	21	1061	16	1056	24	1	1060	21	15	30	79	2.67	0.32	0.38
	1.8615	0.0603	0.1788	0.0038	0.4767	0.0752	0.0009	0.0536	0.0011	1065	21	1060	16	1061	24	1	1054	21	15	30	81	2.67	0.30	0.38
	1.8411	0.0587	0.1791	0.0038	0.4652	0.0742	0.0008	0.0536	0.0011	1060	21	1062	15	1044	23	0	1061	20	15	31	83	2.68	0.32	0.37
	1.8333	0.0584	0.1794	0.0038	0.3365	0.0745	0.0009	0.0537	0.0011	1055	21	1064	15	1044	23	-1	1058	21	15	31	82	2.67	0.30	0.37
	1.8741	0.0611	0.1787	0.0039	0.4977	0.0756	0.0009	0.0537	0.0011	1071	22	1060	16	1074	26	2	1057	21	16	32	86	2.67	0.33	0.38
AS-3																					
1099.1 ± 0.5 Ma																					
Paces and Miller (1993)	2.1463	0.0654	0.2039	0.0031	0.5058	0.0763	0.0005	0.0636	0.0012	1163	21	1196	17	1099	14	-4	1245	22	74	128	262	2.05	0.22	0.49
	2.0923	0.0655	0.2008	0.0033	0.5222	0.0766	0.0007	0.0618	0.0012	1145	21	1179	18	1105	18	-4	1214	23	42	75	170	2.26	0.25	0.44
	2.0717	0.0644	0.1995	0.0032	0.6245	0.0761	0.0006	0.0618	0.0012	1139	22	1172	17	1092	16	-4	1212	23	73	128	265	2.08	0.25	0.48
	2.1353	0.0705	0.1975	0.0036	0.6428	0.0770	0.0009	0.0618	0.0013	1158	23	1161	20	1117	20	0	1210	25	57	105	218	2.08	0.23	0.48
	2.1357	0.0682	0.1986	0.0034	0.7173	0.0764	0.0007	0.0622	0.0012	1159	22	1167	18	1099	17	-1	1220	24	52	90	192	2.15	0.26	0.47
Plesovice																					
337.13 ± 0.37 Ma																					
Sláma et al., (2008)	0.4051	0.0126	0.0562	0.0009	0.4613	0.0528	0.0005	0.0172	0.0003	345	9	353	5	311	20	-3	346	7	13	80	662	8.39	0.83	0.12
	0.4022	0.0126	0.0536	0.0008	0.5149	0.0531	0.0005	0.0170	0.0004	343	9	336	5	326	21	2	341	7	10	66	616	9.29	1.04	0.11
	0.4083	0.0127	0.0561	0.0009	0.4754	0.0532	0.0005	0.0174	0.0004	348	9	352	5	326	21	-1	359	8	11	66	608	9.32	0.95	0.11
	0.4101	0.0128	0.0552	0.0009	0.5042	0.0538	0.0005	0.0174	0.0004	349	9	346	5	354	20	1	348	7	12	74	640	8.52	0.94	0.12
	0.4109	0.0126	0.0549	0.0008	0.4948	0.0537	0.0005	0.0172	0.0003	345	9	344	5	337	20	0	346	7	12	75	655	8.74	1.00	0.11
	0.4325	0.0136	0.0582	0.0009	0.5515	0.0537	0.0005	0.0190	0.0004	365	10	365	6	352	21	0	380	8	12	68	651	9.79	1.28	0.10
Sequence 2																					
91500																					
	1.8570	0.0324	0.1795	0.0031	0.4252	0.0745	0.0010	0.0538	0.0010	1066	12	1064	11	1049	28	0	1059	20	15	30	80	2.66	0.29	0.38
	1.8406	0.0329	0.1789	0.0030	0.3941	0.0749	0.0011	0.0537	0.0010	1058	12	1061	11	1061	28	0	1057	20	15	30	80	2.67	0.31	0.37
	1.8354	0.0329	0.1793	0.0031	0.4327	0.0748	0.0011	0.0536	0.0010	1056	12	1064	11	1063	29	0	1055	19	15	30	80	2.65	0.30	0.38
	1.8548	0.0335	0.1790	0.0031	0.4304	0.0745	0.0011	0.0539	0.0010	1065	12	1061	11	1073	29	0	1060	20	15	30	80	2.67	0.30	0.37
	1.8673	0.0341	0.1797	0.0032	0.3872	0.0751	0.0011	0.0539	0.0010	1068	12	1065	12	1061	29	0	1062	20	15	31	82	2.67	0.32	0.37
	1.8643	0.0337	0.1793	0.0031	0.3986	0.0747	0.0011	0.0538	0.0010	1066	12	1063	11	1060	29	0	1060	20	15	30	80	2.66	0.32	0.38
	1.8504	0.0338	0.1794	0.0031	0.3965	0.0745	0.0011	0.0536	0.0010	1062	12	1064	12	1044	29	0	1060	20	15	30	80	2.67	0.28	0.38
	1.8669	0.0339	0.1790	0.0031	0.4197	0.0751	0.0011	0.0540	0.0010	1067	11	1062	11	1064	29	0	1063	20	15	30	80	2.67	0.30	0.37
	1.8649	0.0332	0.1791	0.0031	0.3778	0.0756	0.0011	0.0537	0.0010	1067	12	1062	11	1078	27	-1	1057	20	15	30	80	2.67	0.30	0.38
	1.8361	0.0327	0.1793	0.0031	0.4981	0.0742	0.0011	0.0536	0.0010	1058	11	1063	11	1038	27	-1	1058	20	15	30	80	2.67	0.30	0.37
	1.8402	0.0327	0.1791	0.0031	0.3788	0.0748	0.0011	0.0537	0.0011	1058	12	1062	11	1055	29	0	1056	20	15	30	80	2.67	0.31	0.37
	1.8303	0.0335	0.1792	0.0031	0.3804	0.0751	0.0011	0.0538	0.0010	1065	12	1063	11	1054	29	0	1059	20	15	30	80	2.67	0.30	0.38
AS-3																					
	2.1475	0.0377	0.2073	0.0035	0.7164	0.0765	0.0009	0.0646	0.0012	1163	12	1214	14	1103	24	-6	1268	23	55	93	197	2.12	0.28	0.47
	2.1136	0.0364	0.2030	0.0034	0.6808	0.0762	0.0009	0.0631	0.0012	1154	13	1191	13	1094	24	-5	1236	22	47	80	164	2.05	0.26	0.49
	2.0079	0.0330	0.1908	0.0032	0.5808	0.0760	0.0009	0.0577	0.0010	1117	11	1125	12	1090	24	-1	1133	20	60	113	238	2.11	0.24	0.47
Plesovice																					
	0.4200	0.0070	0.0569	0.0006	0.5988	0.0537	0.0006	0.0174	0.0003	356	5	357	4	353	27	0	349	7	12	77	734	9.60	1.08	0.10
	0.4087	0.0069	0.0556	0.0006	0.5442	0.0535	0.0007	0.0177	0.0003	348	5	349	4	341	28	0	354	7	13	77	742	9.76	1.17	0.10

December 8, 2022

Standard	Isotope ratios 207Pb/235U	2 SE	206Pb/238U	2 SE	Rho	207Pb/206Pb	2 SE	Age (Ma) 207Pb/235U	2 SE	206Pb/238U	2 SE	207Pb/206Pb	2 SE	Disc.(%)	208Pb/232Th	2 SE	Elemental data Pb (ppm)	Th (ppm)	U (ppm)	Final U/Th	Th/U
91500																					
	1.86647	0.03107	0.17931	0.00703	0.30909	0.07582	0.00085	0.05515	0.00385	1068	32	1063	38	1061	22	1	1085	74	49	39	106	3.69		0.27
	1.87585	0.09132	0.18018	0.00705	0.36352	0.07559	0.00077	0.05635	0.00395	1072	32	1068	38	1076	21	1	1108	76	45	28	91	3.38		0.30
	1.86471	0.09460	0.18060	0.00723	0.33609	0.07592	0.00077	0.05607	0.00405	1067	33	1063	40	1054	20	0	1081	76	38	24	78	3.54		0.26
	1.82019	0.08832	0.17631	0.00693	0.32654	0.07496	0.00081	0.05402	0.00378	1052	31	1047	37	1057	22	1	1063	72	53	33	95	2.87		0.35
	1.92030	0.09254	0.17829	0.00699	0.39703	0.07475	0.00081	0.05131	0.00363	1080	32	1063	38	1053	22	3	1011	70	29	19	80	8.97		0.11
AS-3																					
	1.95526	0.09415	0.18565	0.00724	0.58163	0.07605	0.00056	0.05814	0.00405	1100	32	1098	39	1093	15	0	1142	77	367	212	484	2.45		0.41
	2.15085	0.10834	0.20995	0.00823	0.61560	0.07630	0.00058	0.05415	0.00384	1164	34	1212	44	1266	15	-6	1257	86	352	197	411	2.15		0.46
	1.89084	0.09187	0.18329	0.00718	0.71932	0.07606	0.00052	0.05114	0.00366	1077	32	1085	39	1095	14	-1	1008	70	579	368	718	2.01		0.50
	2.05801	0.09888	0.19633	0.00763	0.65999	0.07613	0.00053	0.05460	0.00394	1134	33	1155	41	1197	14	-3	1151	79	793	491	669	1.67		0.60
	2.10406	0.10109	0.20092	0.00782	0.65576	0.07584	0.00057	0.06013	0.00420	1149	33	1180	42	1089	15	-4	1180	80	715	405	587	1.47		0.68
	1.96347	0.09357	0.18923	0.00731	0.58069	0.07567	0.00055	0.05746	0.00395	1103	33	1118	40	1082	14	-2	1130	77	796	450	661	1.52		0.66
Plesovice																					
	0.39299	0.01907	0.05368	0.00309	0.43257	0.05327	0.00351	0.01680	0.00118	337	14	337	13	334	22	0	337	23	39	79	755	9.69		0.10
	0.39401	0.01901	0.05368	0.00308	0.48148	0.05311	0.00348	0.01680	0.00118	337	14	337	13	325	21	0	337	23	39	79	755	9.67		0.10
	0.39426	0.01911	0.05370	0.00311	0.48251	0.05326	0.00346	0.01682	0.00119	337	14	337	13	335	20	0	337	24	39	78	754	9.70		0.10
	0.39399	0.01905	0.05366	0.00309	0.47637	0.05326	0.00350	0.01679	0.00117	337	14	337	13	334	23	0	336	23	39	78	754	9.69		0.10
	0.39461	0.01912	0.05373	0.00311	0.48310	0.05316	0.00352	0.01681	0.00121	337	14	337	13	328	22	0	337	24	39	79	759	9.68		0.10
	0.39357	0.01901	0.05362	0.00307	0.45990	0.05340	0.00349	0.01678	0.00117	337	14	337	13	340	20	0	336	23	39	79	760	9.68		0.10
	0.39440	0.01917	0.05371	0.00309	0.49034	0.05328	0.00353	0.01680	0.00120	337	14	337	13	331	22	0	337	24	39	78	755	9.67		0.10
	0.39398	0.01902	0.05366	0.00307	0.43995	0.05323	0.00350	0.01678	0.00118	337	14	337	13	331	21	0	336	23	39	79	757	9.67		0.10
	0.39358	0.01921	0.05367	0.00310	0.41193	0.05311	0.00355	0.01677	0.00119	337	14	337	13	324	24	0	336	24	39	79	756	9.69		0.10
	0.39432	0.01872	0.05369	0.00304	0.51691	0.05377	0.00349	0.01683	0.00115	338	14	337	13	353	21	0	337	23	39	79	761	9.68		0.10
	0.39469	0.01938	0.05373	0.00315	0.34588	0.05321	0.00354	0.01682	0.00120	338	14	337	13	331	23	0	337	24	40	80	762	9.69		0.10
	0.39327	0.01904	0.05370	0.00309	0.49976	0.05296	0.00351	0.01679	0.00118	337	14	337	13	316	22	0	336	23	39	79	763	9.69		0.10
	0.39427	0.01900	0.05370	0.00309	0.41860	0.05335	0.00348	0.01680	0.00118	337	14	337	13	339	20	0	337	23	39	78	754	9.68		0.10
	0.39373	0.01900	0.05367	0.00308	0.42838	0.05320	0.00347	0.01680	0.00118	337	14	337	13	334	20	0	337	23	39	78	754	9.68		0.10
	0.39417	0.01907	0.05369	0.00308	0.44907	0.05319	0.00349	0.01680	0.00118	337	14	337	13	330	21	0	337	23	39	78	755	9.68		0.10
	0.39386	0.01895	0.05367	0.00308	0.48391	0.05321	0.00345	0.01680	0.00118	337	14	337	13	336	19	0	337	23	39	78	755	9.68		0.10
	0.39418	0.01893	0.05369	0.00307	0.38646	0.05321	0.00348	0.01680	0.00118	337	14	337	13	331	20	0	337	23	39	78	755	9.68		0.10
	0.39375	0.01901	0.05364	0.00305	0.47169	0.05316	0.00352	0.01681	0.00118	337	14	337	13	326	22	0	337	24	39	78	754	9.68		0.10
	0.39394	0.01911	0.05370	0.00313	0.44288	0.05325	0.00350	0.01679	0.00118	337	14	337	13	335	21	0	337	24	39	78	755	9.68		0.10
	0.39408	0.01904	0.05369	0.00309	0.35481	0.05327	0.00353	0.01681	0.00118	337	14	337	13	338	22	0	337	23	39	78	755	9.68		0.10
	0.39365	0.01875	0.05370	0.00312	0.41071	0.05283	0.00349	0.01680	0.00118	337	14	337	13	313	21	0	337	23	39	78	754	9.68		0.10
	0.39402	0.01921	0.05368	0.00311	0.43335	0.05339	0.00352	0.01680	0.00118	337	14	337	13	352	22	0	337	24	39	78	753	9.67		0.10
	0.39452	0.01904	0.05370	0.00306	0.42024	0.05377	0.00355	0.01682	0.00118	338	14	337	13	352	23	0	337	24	39	79	758	9.68		0.10
	0.39363	0.01911	0.05367	0.00308	0.47552	0.05330	0.00349	0.01678	0.00117	337	14	337	13	336	21	0	336	23	39	79	760	9.68		0.10

February 16, 2023

Name	Isotope ratios 207Pb/235U	2 SE	206Pb/238U	2 SE	Rho	207Pb/206Pb	2 SE	Age (Ma) 207Pb/235U	2 SE	206Pb/238U	2 SE	207Pb/206Pb	2 SE	Disc.(%)	208Pb/232Th	2 SE	Elemental data Pb (ppm)	Th (ppm)	U (ppm)	Final U/Th	Th/U
91500																					
	1.8182	0.0424	0.1775	0.0033	0.2818	0.0744	0.0013	0.0546	0.0039	1052	15	1053	18	1052	15	0	1075	75	91	56	131	2.36		0.42
	1.8200	0.0424	0.1756	0.0033	0.3908	0.0751	0.0013	0.0522	0.0038	1052	15	1043	18	1052	15	1	1028	72	84	53	144	2.72		0.37
	1.7610	0.0409	0.1748	0.0033	0.3344	0.0733	0.0012	0.0577	0.0041	1031	15	1038	18	1031	15	-1	1134	79	56	34	118	3.58		0.28
	1.8127	0.0425	0.1756	0.0033	0.3774	0.0747	0.0013	0.0541	0.0039	1049	15	1043	18	1049	15	1	1065	74	68	42	96	2.27		0.44
	1.7927	0.0417	0.1750	0.0033	0.3397	0.0741	0.0013	0.0448	0.0034	1042	15	1040	18	1042	15	0	886	65	63	54	93	2.01		
AS3																					
	2.0031	0.0450	0.1910	0.0036	0.6414	0.0762	0.0012	0.0550	0.0040	1116	15	1127	19	1116	15	-1	1082	76	974	600	1002	1.71		0.59
	2.0182	0.0459	0.1946	0.0036	0.6466	0.0753	0.0012	0.0559	0.0040	1121	15	1146	19	1121	15	-3	1100	77	764	432	857	1.95		0.51
	1.9884	0.0449	0.1887	0.0035	0.7072	0.0763	0.0012	0.0543	0.0039	1111	15	1114	19	1111	15	0	1069	75	701	441	677	1.59		0.63
	1.9777	0.0446	0.1938	0.0036	0.5942	0.0752	0.0012	0.0570	0.0041	1108	15	1126	20	1108	15	-2	1120	77	593	348	616	1.74		0.58
	1.9376	0.0436	0.1863	0.0035	0.6961	0.0755	0.0012	0.0558	0.0039	1094	15	1101	19	1094	15	-1	1098	75	667	411	657	1.62		0.62
Plesovice																					
	0.3942	0.0091	0.0537	0.0010	0.4403	0.0532	0.0009	0.0168	0.0012	337	7	337	6	337	7	0	337	24	39	78	753	9.68		0.10
	0.3938	0.0091	0.0537	0.0010	0.4272	0.0533	0.0009	0.0168	0.0012	337	7	337	6	337	7	0	337	24	39	78	753	9.68		0.10
	0.3944	0.0091	0.0537	0.0010	0.4406	0.0533	0.0009	0.0168	0.0012	337	7	337	6	337	7	0	337	24	39	78	755	9.68		0.10
	0.3936	0.0091	0.0537	0.0010	0.4219	0.0532	0.0009	0.0168	0.0012	337	7	337	6	337	7	0	337	24	39	78	753	9.68		0.10
	0.3938	0.0090	0.0537	0.0010	0.3817	0.0533	0.0009	0.0168	0.0012	337	7	337	6	337	7	0	337	24	39	79	753	9.68		0.10
	0.3942	0.0091	0.0537	0.0010	0.4076	0.0532	0.0009	0.0168	0.0012	337	7	337	6	337	7	0	337	24	39	78	746	9.68		0.10
	0.3943	0.0091	0.0537	0.0010	0.3765	0.0532	0.0009	0.0168	0.0012	337	7	337	6	337	7	0	337	24	39	78	756	9.68		0.10
	0.3937	0.0091	0.0536	0.0010	0.4079	0.0533	0.0009	0.0168	0.0012	337	7	337	6	337	7	0	337	24	39	78	754	9.68		0.10
	0.3933	0.0093	0.0537	0.0010	0.4823	0.0531	0.0009	0.0168	0.0012	337	7	337	6	337	7	0	337	24	39	78	756	9.68		0.10
	0.3945	0.0093	0.0537	0.0010	0.3391	0.0534	0.0009	0.0168	0.0013	338	7	337	6	338	7	0	337	25	39	78	755	9.71		0.10
	0.3942	0.0090	0.0537	0.0010	0.4064	0.0533	0.0009	0.0168	0.0012	337	7	337	6	337	7	0	337	24	39	78	755	9.68		0.10
	0.3938	0.0091	0.0537	0.0010	0.4237	0.0532	0.0009	0.0168	0.0012	337	7	337	6	337	7	0	337	24	39	78	754	9.69		0.10
	0.3940	0.0090	0.0537	0.0010	0.3599	0.0533	0.0009	0.0168	0.0012	337	7	337	6	337	7	0	337	24	39	78	755	9.68		0.10
	0.3941	0.0090	0.0537	0.0010	0.4027	0.0532	0.0009	0.0168	0.0012	337	7	337	6	337	7	0	337	24	39	78	755	9.68		0.10
	0.3939	0.0091	0.0537

U-Th-Pb analyses performed in the used zircon reference materials.

Sample	Isotope ratios									Age (Ma)								Elemental data					
	$^{207}Pb/^{235}U$	±2σ	$^{206}Pb/^{238}U$	±2σ	Rho	$^{207}Pb/^{206}Pb$	±2σ	$^{208}Pb/^{232}Th$	±2σ	$^{207}Pb/^{235}U$	±2σ	$^{206}Pb/^{238}U$	±2σ	$^{207}Pb/^{206}Pb$	±2σ	Disc.(%)	$^{208}Pb/^{232}Th$	±2σ	Pb (ppm)	Th (ppm)	U (ppm)	Final U/Th	Th/U
November 24, 2022																							
Sequence 1																							
91500																							
1065.4 ± 0.3 Ma	1.8498	0.0939	0.1792	0.0090	0.5871	0.0749	0.0030	0.0537	0.0032	1060	33	1062	49	1052	82	0	1058	62	15	30	80	2.67	0.37
Wiedenbeck et al., (1995)	1.8498	0.0940	0.1791	0.0090	0.5295	0.0749	0.0030	0.0537	0.0032	1060	33	1063	50	1054	82	0	1058	62	15	30	80	2.67	0.37
	1.8499	0.0941	0.1792	0.0090	0.4919	0.0749	0.0030	0.0537	0.0032	1060	33	1063	49	1049	83	0	1058	62	15	30	80	2.67	0.37
	1.8497	0.0934	0.1791	0.0089	0.5556	0.0749	0.0030	0.0537	0.0032	1061	33	1062	49	1055	81	0	1058	61	15	30	80	2.67	0.37
	1.8499	0.0935	0.1792	0.0090	0.5222	0.0749	0.0030	0.0537	0.0033	1061	33	1062	49	1052	81	0	1058	62	15	30	80	2.67	0.37
	1.8497	0.0938	0.1792	0.0090	0.4858	0.0749	0.0030	0.0537	0.0033	1061	34	1062	49	1055	83	0	1058	62	15	30	80	2.67	0.37
	1.8611	0.0942	0.1806	0.0092	0.5976	0.0749	0.0030	0.0541	0.0033	1065	34	1071	51	1051	83	0	1066	62	14	28	75	2.67	0.37
	1.8495	0.0944	0.1791	0.0090	0.5634	0.0749	0.0030	0.0537	0.0032	1060	34	1062	49	1050	83	0	1058	62	15	30	80	2.67	0.37
	1.8500	0.0939	0.1792	0.0090	0.4952	0.0749	0.0030	0.0537	0.0032	1062	32	1062	49	1052	83	0	1058	62	15	30	80	2.67	0.37
	1.8498	0.0937	0.1792	0.0090	0.4981	0.0749	0.0030	0.0537	0.0033	1061	34	1062	49	1052	80	0	1058	63	15	30	80	2.67	0.37
	1.8489	0.0938	0.1792	0.0090	0.4982	0.0749	0.0030	0.0538	0.0033	1060	34	1062	49	1053	81	0	1059	63	15	30	81	2.67	0.37
	1.8564	0.0940	0.1802	0.0091	0.4744	0.0747	0.0030	0.0539	0.0033	1064	33	1068	49	1047	80	0	1061	62	16	31	83	2.66	0.38
	1.8479	0.0940	0.1795	0.0090	0.4994	0.0748	0.0030	0.0539	0.0033	1059	34	1064	49	1052	81	0	1060	63	15	31	82	2.67	0.37
	1.8499	0.0945	0.1792	0.0090	0.4438	0.0749	0.0031	0.0537	0.0033	1060	34	1062	49	1046	83	0	1058	63	15	30	80	2.67	0.37
	1.8497	0.0940	0.1792	0.0090	0.5169	0.0749	0.0030	0.0537	0.0033	1060	34	1062	49	1057	83	0	1058	62	15	30	80	2.67	0.37
	1.8498	0.0934	0.1792	0.0090	0.4824	0.0749	0.0030	0.0537	0.0033	1061	33	1062	49	1051	81	0	1058	62	15	30	80	2.67	0.37
AS3																							
1099.1 ± 0.5 Ma	1.9866	0.0997	0.1945	0.0098	0.6581	0.0739	0.0029	0.0577	0.0035	1110	33	1146	54	1031	80	-5	1133	66	111	207	318	1.54	0.65
Paces and Miller (1993)	1.9568	0.0982	0.1834	0.0092	0.6924	0.0776	0.0030	0.0557	0.0033	1100	33	1085	50	1131	78	2	1097	63	88	169	272	1.61	0.62
	2.0272	0.1019	0.1917	0.0096	0.6659	0.0765	0.0030	0.0582	0.0035	1123	35	1130	52	1101	80	-1	1144	67	122	226	363	1.62	0.62
	1.9223	0.0966	0.1866	0.0094	0.7095	0.0746	0.0029	0.0542	0.0033	1088	34	1103	51	1052	81	-2	1067	62	174	353	586	1.66	0.60
Plesovice																							
337.13 ± 0.37 Ma	0.4063	0.0210	0.0558	0.0028	0.6513	0.0531	0.0022	0.0175	0.0011	346	15	350	17	323	92	-2	350	22	9	57	530	9.35	0.11
Sláma et al., (2008)	0.4155	0.0210	0.0560	0.0028	0.6014	0.0539	0.0022	0.0177	0.0011	352	15	351	17	360	88	1	354	21	10	63	655	10.45	0.10
	0.4071	0.0208	0.0551	0.0028	0.5876	0.0534	0.0021	0.0172	0.0011	347	15	346	17	332	93	0	345	21	5	33	395	11.91	0.08
Sequence 2																							
91500	1.8491	0.0733	0.1793	0.0048	0.5319	0.0744	0.0009	0.0538	0.0018	1061	26	1063	26	1046	26	0	1059	35	15	30	80	2.67	0.37
	1.8478	0.0738	0.1790	0.0046	0.5394	0.0747	0.0009	0.0537	0.0018	1060	26	1061	25	1046	24	0	1057	35	15	30	80	2.67	0.37
	1.8527	0.0738	0.1793	0.0046	0.4072	0.0749	0.0010	0.0538	0.0018	1062	26	1063	25	1056	26	0	1059	35	15	30	80	2.67	0.37
	1.8468	0.0741	0.1791	0.0046	0.4820	0.0743	0.0010	0.0537	0.0018	1059	27	1062	26	1034	27	0	1057	35	15	30	80	2.66	0.38
	1.8500	0.0741	0.1792	0.0047	0.4717	0.0751	0.0010	0.0538	0.0018	1062	26	1062	25	1064	25	0	1058	35	15	30	80	2.67	0.37
	1.8500	0.0741	0.1791	0.0046	0.5756	0.0758	0.0009	0.0537	0.0018	1061	26	1062	25	1076	24	0	1058	35	15	30	80	2.67	0.37
	1.8486	0.0738	0.1791	0.0047	0.6274	0.0750	0.0008	0.0537	0.0018	1060	26	1062	25	1058	22	0	1057	35	15	30	80	2.67	0.37
	1.8507	0.0736	0.1792	0.0046	0.5243	0.0751	0.0009	0.0538	0.0018	1062	26	1063	26	1059	24	0	1058	35	15	30	80	2.67	0.37
	1.8518	0.0745	0.1793	0.0047	0.5522	0.0748	0.0009	0.0538	0.0018	1062	27	1064	26	1051	24	0	1059	35	15	30	80	2.67	0.37
	1.8485	0.0731	0.1791	0.0046	0.5714	0.0749	0.0008	0.0537	0.0018	1061	26	1061	25	1057	22	0	1057	34	15	30	80	2.67	0.37
	1.8498	0.0734	0.1791	0.0047	0.5464	0.0748	0.0008	0.0538	0.0018	1061	26	1062	25	1053	23	0	1059	35	15	30	80	2.67	0.37
	1.8494	0.0732	0.1792	0.0046	0.5142	0.0748	0.0009	0.0537	0.0018	1062	26	1062	25	1055	23	0	1057	35	15	30	80	2.67	0.37
	1.8552	0.0743	0.1794	0.0047	0.5335	0.0752	0.0009	0.0538	0.0018	1063	26	1063	25	1064	24	0	1059	35	15	30	80	2.67	0.37
	1.8419	0.0751	0.1790	0.0046	0.4969	0.0746	0.0009	0.0536	0.0018	1059	26	1061	25	1043	25	0	1056	34	15	30	80	2.67	0.37
	1.8551	0.0744	0.1792	0.0046	0.5901	0.0757	0.0009	0.0538	0.0018	1062	26	1063	26	1077	24	0	1058	35	15	30	80	2.67	0.37
	1.8442	0.0742	0.1790	0.0047	0.4664	0.0746	0.0010	0.0537	0.0018	1059	27	1061	26	1046	27	0	1058	35	15	30	80	2.67	0.37
	1.8626	0.0768	0.1799	0.0048	0.6269	0.0746	0.0009	0.0538	0.0018	1065	27	1066	26	1052	24	0	1060	35	15	30	80	2.67	0.37
	1.8400	0.0754	0.1784	0.0048	0.6094	0.0744	0.0009	0.0536	0.0019	1056	27	1058	26	1049	26	0	1056	36	15	30	79	2.67	0.37
	1.8469	0.0753	0.1790	0.0047	0.4874	0.0746	0.0011	0.0538	0.0019	1061	27	1061	26	1046	29	0	1058	36	15	30	80	2.66	0.38
	1.8527	0.0747	0.1793	0.0046	0.4426	0.0750	0.0010	0.0538	0.0018	1061	27	1063	25	1060	26	0	1059	35	15	30	81	2.66	0.38
	1.8564	0.0757	0.1792	0.0047	0.3812	0.0763	0.0012	0.0539	0.0019	1063	27	1062	26	1085	31	0	1061	36	15	31	81	2.67	0.37
	1.8455	0.0736	0.1792	0.0046	0.5241	0.0744	0.0009	0.0537	0.0018	1059	26	1062	25	1044	24	0	1056	35	15	31	81	2.67	0.37
	1.8469	0.0748	0.1789	0.0046	0.6194	0.0746	0.0009	0.0537	0.0018	1059	27	1060	25	1043	25	0	1056	35	15	30	80	2.67	0.37
	1.8527	0.0747	0.1795	0.0047	0.5484	0.0749	0.0010	0.0538	0.0018	1064	27	1064	26	1052	27	0	1059	35	15	30	80	2.67	0.37
	1.8572	0.0751	0.1797	0.0047	0.5134	0.0745	0.0010	0.0539	0.0019	1063	27	1065	26	1039	28	0	1062	36	15	30	80	2.67	0.37
	1.8421	0.0742	0.1786	0.0047	0.5607	0.0747	0.0009	0.0535	0.0018	1058	26	1059	26	1045	26	0	1054	35	15	30	80	2.67	0.37
	1.8506	0.0741	0.1792	0.0047	0.5566	0.0754	0.0009	0.0538	0.0018	1061	26	1062	26	1068	24	0	1058	35	15	30	80	2.67	0.37
AS-3	2.0142	0.0796	0.1896	0.0049	0.6209	0.0759	0.0008	0.0580	0.0019	1118	27	1120	27	1083	21	0	1140	37	78	146	223	1.54	0.65
	2.0374	0.0813	0.1924	0.0051	0.5382	0.0770	0.0010	0.0585	0.0019	1126	27	1134	27	1112	25	-1	1148	37	55	103	165	1.61	0.62
	2.0616	0.0859	0.1943	0.0054	0.5035	0.0766	0.0012	0.0673	0.0023	1134	28	1146	30	1102	31	-1	1316	44	35	58	127	2.21	0.45
	1.9582	0.0769	0.1852	0.0048	0.5231	0.0760	0.0008	0.0563	0.0019	1100	26	1095	26	1088	22	1	1107	36	53	101	166	1.64	0.61
	2.0203	0.0813	0.1951	0.0051	0.6599	0.0754	0.0008	0.0616	0.0021	1120	28	1150	28	1068	22	-4	1209	40	39	67	126	1.84	0.54
	1.9813	0.0792	0.1840	0.0048	0.6355	0.0772	0.0008	0.0548	0.0018	1106	27	1088	26	1117	22	3	1078	35	61	121	198	1.64	0.61
Plesovice	0.4764	0.0201	0.0584	0.0016	0.5094	0.0593	0.0011	0.0199	0.0009	395	14	366	10	561	39	9	399	18	6	31	235	7.58	0.13
	0.3886	0.0154	0.0536	0.0014	0.6506	0.0532	0.0006	0.0168	0.0006	333	11	337	9	329	23	-1	337	11	9	59	575	9.77	0.10
	0.3870	0.0156	0.0531	0.0014	0.5543	0.0529	0.0007	0.0170	0.0006	332	12	333	8	318	29	0	341	12	4	23	312	13.65	0.07
	0.5911	0.0251	0.0597	0.0016	0.5279	0.0710	0.0011	0.0160	0.0006	471	16	374	10	943	34	28	321	11	14	95	329	3.51	0.28

	0.4175	0.0169	0.0565	0.0015	0.5360	0.0537	0.0007	0.0178	0.0006	354	12	354	9	348	30	0	356	12	12	66	606	10.00	0.10
	0.4015	0.0159	0.0542	0.0014	0.5855	0.0532	0.0006	0.0175	0.0006	342	12	340	9	324	26	1	351	12	5	31	360	12.09	0.08
	0.4016	0.0161	0.0545	0.0014	0.6536	0.0534	0.0006	0.0173	0.0006	342	12	342	9	331	26	0	347	12	10	63	640	10.25	0.10
8-Dec-22																								
91500																								
	1.8665	0.0911	0.1793	0.0070	0.3091	0.0758	0.0009	0.0551	0.0038	1068	32	1063	38	1081	22	1	1085	74	49	30	106	3.69	0.27
	1.8799	0.0913	0.1802	0.0070	0.3635	0.0756	0.0008	0.0564	0.0040	1072	32	1068	38	1076	21	1	1108	76	45	28	91	3.38	0.30
	1.9647	0.0948	0.1866	0.0073	0.3381	0.0759	0.0008	0.0565	0.0040	1102	33	1103	40	1086	20	0	1111	76	38	24	78	3.84	0.26
	1.8202	0.0883	0.1763	0.0068	0.3265	0.0750	0.0008	0.0540	0.0038	1052	31	1047	37	1057	22	1	1063	72	53	33	95	2.87	0.35
	1.9020	0.0925	0.1793	0.0070	0.3970	0.0748	0.0008	0.0513	0.0036	1080	32	1063	38	1053	22	3	1011	70	29	19	80	8.97	0.11
AS-3																								
	1.9553	0.0942	0.1857	0.0072	0.5816	0.0761	0.0006	0.0581	0.0040	1100	32	1098	39	1093	15	0	1142	77	367	212	484	2.45	0.41
	2.1508	0.1063	0.2070	0.0082	0.6156	0.0762	0.0006	0.0642	0.0046	1164	34	1212	44	1096	15	-6	1257	88	362	197	411	2.15	0.47
	1.8908	0.0919	0.1833	0.0072	0.7193	0.0761	0.0005	0.0511	0.0037	1077	32	1085	39	1095	14	-1	1008	70	579	368	718	2.01	0.50
	2.0580	0.0989	0.1963	0.0076	0.6600	0.0761	0.0005	0.0586	0.0041	1134	33	1155	41	1097	14	-3	1151	78	700	401	669	1.67	0.60
	2.1041	0.1011	0.2009	0.0078	0.6558	0.0758	0.0006	0.0601	0.0042	1149	33	1180	42	1089	15	-4	1180	80	715	405	587	1.47	0.68
	1.9635	0.0936	0.1892	0.0073	0.5807	0.0757	0.0005	0.0575	0.0040	1103	33	1118	40	1082	14	-2	1130	77	756	450	661	1.52	0.66
Plesovice																								
	0.3940	0.0191	0.0537	0.0021	0.4326	0.0533	0.0005	0.0168	0.0012	337	14	337	13	334	22	0	337	23	39	79	755	9.69	0.10
	0.3940	0.0190	0.0537	0.0021	0.4915	0.0531	0.0005	0.0168	0.0012	337	14	337	13	325	21	0	337	23	39	79	755	9.67	0.10
	0.3943	0.0191	0.0537	0.0021	0.4825	0.0533	0.0005	0.0168	0.0012	337	14	337	13	335	20	0	337	24	39	78	754	9.70	0.10
	0.3937	0.0190	0.0537	0.0021	0.4764	0.0533	0.0005	0.0168	0.0012	337	14	337	13	333	21	0	336	23	39	78	754	9.69	0.10
	0.3946	0.0191	0.0537	0.0021	0.4831	0.0532	0.0005	0.0168	0.0012	337	14	337	13	328	22	0	337	24	39	79	759	9.68	0.10
	0.3936	0.0190	0.0536	0.0021	0.4599	0.0534	0.0005	0.0168	0.0012	337	14	337	13	340	20	0	336	23	39	79	760	9.68	0.10
	0.3944	0.0192	0.0537	0.0021	0.4593	0.0533	0.0005	0.0168	0.0012	337	14	337	13	331	22	0	337	24	39	78	755	9.67	0.10
	0.3937	0.0190	0.0537	0.0021	0.4399	0.0532	0.0005	0.0168	0.0012	337	14	337	13	331	21	0	336	23	39	79	757	9.67	0.10
	0.3936	0.0192	0.0537	0.0021	0.4119	0.0531	0.0005	0.0168	0.0012	337	14	337	13	324	24	0	336	24	39	79	756	9.69	0.10
	0.3943	0.0187	0.0537	0.0020	0.5169	0.0538	0.0005	0.0168	0.0012	338	14	337	12	353	21	0	337	23	39	79	761	9.68	0.10
	0.3947	0.0194	0.0537	0.0022	0.3459	0.0532	0.0005	0.0168	0.0012	338	14	337	13	331	23	0	337	24	40	80	762	9.69	0.10
	0.3933	0.0189	0.0537	0.0021	0.4098	0.0530	0.0005	0.0168	0.0012	337	14	337	13	319	22	0	336	23	39	79	763	9.69	0.10
	0.3943	0.0190	0.0537	0.0021	0.4188	0.0534	0.0005	0.0168	0.0012	337	14	337	13	339	20	0	337	23	39	78	754	9.68	0.10
	0.3937	0.0190	0.0537	0.0021	0.4261	0.0532	0.0005	0.0168	0.0012	337	14	337	13	334	20	0	337	23	39	78	754	9.68	0.10
	0.3942	0.0191	0.0537	0.0021	0.4491	0.0532	0.0005	0.0168	0.0012	337	14	337	13	330	21	0	337	23	39	78	755	9.68	0.10
	0.3939	0.0190	0.0537	0.0021	0.4839	0.0532	0.0004	0.0168	0.0012	337	14	337	13	334	19	0	337	23	39	78	755	9.68	0.10
	0.3942	0.0189	0.0537	0.0021	0.3265	0.0532	0.0005	0.0168	0.0012	337	14	337	13	331	20	0	337	23	39	78	755	9.68	0.10
	0.3938	0.0190	0.0536	0.0020	0.4117	0.0532	0.0005	0.0168	0.0012	337	14	337	13	326	22	0	337	24	39	78	754	9.68	0.10
	0.3939	0.0191	0.0537	0.0021	0.4429	0.0533	0.0005	0.0168	0.0012	337	14	337	13	335	21	0	337	24	39	78	755	9.68	0.10
	0.3941	0.0190	0.0537	0.0021	0.3546	0.0533	0.0005	0.0168	0.0012	337	14	337	13	330	22	0	337	23	39	78	755	9.68	0.10
	0.3936	0.0187	0.0537	0.0021	0.4107	0.0528	0.0005	0.0168	0.0012	337	14	337	13	313	21	0	337	23	39	78	754	9.68	0.10
	0.3940	0.0192	0.0537	0.0021	0.4334	0.0534	0.0005	0.0168	0.0012	337	14	337	13	337	22	0	337	24	39	78	753	9.67	0.10
	0.3945	0.0190	0.0537	0.0021	0.4202	0.0538	0.0006	0.0168	0.0012	338	14	337	13	352	23	0	337	24	39	79	758	9.68	0.10
	0.3936	0.0191	0.0537	0.0021	0.4755	0.0532	0.0005	0.0168	0.0012	337	14	337	13	330	21	0	336	23	39	79	760	9.68	0.10
12-Dec-22																								
91500																								
	1.8572	0.0685	0.1794	0.0072	0.4272	0.0754	0.0008	0.0538	0.0024	1064	24	1063	40	1071	20	0	1060	47	68	43	100	2.33	0.43
	1.8232	0.0674	0.1805	0.0073	0.2709	0.0738	0.0008	0.0534	0.0024	1052	24	1070	40	1025	23	-2	1050	47	115	72	148	2.09	0.48
	1.7380	0.0649	0.1652	0.0067	0.4141	0.0752	0.0009	0.0479	0.0022	1021	24	986	37	1062	24	5	946	42	114	80	164	2.06	0.49
	1.8273	0.0675	0.1746	0.0070	0.3919	0.0755	0.0008	0.0522	0.0024	1054	25	1037	39	1071	22	3	1029	46	64	41	96	2.39	0.42
	1.8303	0.0679	0.1783	0.0072	0.3945	0.0745	0.0008	0.0536	0.0024	1055	24	1057	39	1047	23	0	1055	47	54	34	86	2.51	0.40
	1.8349	0.0678	0.1775	0.0071	0.4192	0.0749	0.0008	0.0523	0.0024	1056	24	1053	39	1057	21	1	1031	46	47	30	82	2.73	0.37
	1.8281	0.0678	0.1771	0.0071	0.4233	0.0747	0.0008	0.0524	0.0024	1054	24	1051	39	1048	22	1	1031	46	126	81	159	2.10	0.48
	1.8247	0.0688	0.1778	0.0072	0.4903	0.0744	0.0009	0.0529	0.0024	1052	25	1054	39	1045	24	0	1042	46	50	32	91	2.87	0.35
	1.7436	0.0648	0.1679	0.0068	0.4057	0.0748	0.0008	0.0494	0.0022	1023	24	1000	37	1052	23	4	975	43	55	37	101	2.71	0.37
AS-3																								
	2.0343	0.0739	0.1931	0.0078	0.6733	0.0764	0.0006	0.0602	0.0027	1126	25	1138	42	1102	15	-2	1182	52	469	263	507	1.93	0.52
	2.2646	0.0831	0.2178	0.0088	0.6607	0.0765	0.0006	0.0683	0.0031	1200	26	1270	47	1101	16	-9	1336	59	572	286	438	1.53	0.65
	2.0652	0.0748	0.1967	0.0079	0.6414	0.0761	0.0005	0.0611	0.0028	1137	24	1157	43	1094	13	-3	1199	53	431	244	530	2.24	0.45
	1.9516	0.0726	0.1836	0.0076	0.7480	0.0769	0.0006	0.0556	0.0026	1098	25	1086	41	1116	15	2	1094	49	474	286	444	1.57	0.64
	1.9832	0.0723	0.1890	0.0076	0.6465	0.0758	0.0006	0.0572	0.0026	1109	25	1116	42	1086	15	-1	1125	50	237	139	292	2.17	0.46
	2.0431	0.0755	0.1945	0.0080	0.7122	0.0756	0.0006	0.0608	0.0028	1128	25	1145	43	1081	16	-2	1192	53	653	358	577	1.61	0.62
	2.1599	0.0791	0.2019	0.0081	0.5500	0.0777	0.0007	0.0669	0.0030	1167	25	1185	44	1135	18	-2	1308	57	234	118	238	2.05	0.49
	2.0533	0.0751	0.1958	0.0079	0.6509	0.0761	0.0006	0.0561	0.0026	1132	25	1152	43	1090	16	-3	1103	49	514	308	512	1.68	0.60
	1.9227	0.0700	0.1820	0.0073	0.6048	0.0762	0.0006	0.0544	0.0025	1088	24	1077	40	1094	16	2	1071	47	238	149	407	2.73	0.37
	2.2351	0.0814	0.2122	0.0085	0.5923	0.0765	0.0006	0.0685	0.0031	1191	25	1240	45	1103	16	-6	1340	58	410	203	348	1.72	0.58
Plesovice																								
	0.3940	0.0143	0.0537	0.0022	0.5177	0.0533	0.0004	0.0168	0.0008	337	10	337	13	334	18	0	337	15	39	78	755	9.68	0.10
	0.3940	0.0144	0.0537	0.0022	0.5895	0.0533	0.0004	0.0168	0.0008	337	11	337	13	337	18	0	337	15	39	78	755	9.68	0.10
	0.3942	0.0144	0.0537	0.0021	0.5330	0.0529	0.0005	0.0168	0.0008	337	10	337	13	318	20	0	337	15	39	78	754	9.68	0.10
	0.3938	0.0144	0.0537	0.0021	0.5849	0.0533	0.0005	0.0168	0.0008	337	10	337	13	335	19	0	336	15	39	78	755	9.68	0.10

	0.3944	0.0145	0.0537	0.0022	0.4263	0.0530	0.0005	0.0168	0.0008	337	11	337	13	318	24	0	337	16	39	78	756	9.68	0.10
	0.3936	0.0146	0.0536	0.0022	0.4585	0.0537	0.0006	0.0168	0.0008	337	11	337	13	345	24	0	336	16	39	78	757	9.68	0.10
	0.3942	0.0145	0.0537	0.0022	0.4597	0.0532	0.0005	0.0168	0.0008	337	11	337	13	326	23	0	337	16	39	78	755	9.68	0.10
	0.3939	0.0146	0.0537	0.0022	0.4663	0.0534	0.0006	0.0168	0.0008	337	11	337	13	335	24	0	336	16	39	78	755	9.68	0.10
	0.3939	0.0144	0.0537	0.0022	0.5499	0.0533	0.0005	0.0168	0.0008	337	11	337	13	335	20	0	336	15	39	78	756	9.68	0.10
	0.3941	0.0144	0.0537	0.0022	0.5142	0.0532	0.0005	0.0168	0.0008	337	10	337	13	331	19	0	337	15	39	78	757	9.68	0.10
	0.3931	0.0143	0.0536	0.0022	0.4544	0.0533	0.0005	0.0168	0.0008	337	10	337	13	334	22	0	336	16	39	78	753	9.68	0.10
	0.3946	0.0145	0.0537	0.0021	0.4577	0.0530	0.0006	0.0168	0.0008	338	11	337	13	322	23	0	337	15	39	77	751	9.69	0.10
	0.3936	0.0144	0.0537	0.0022	0.5436	0.0533	0.0005	0.0168	0.0008	337	11	337	13	334	20	0	336	15	39	78	754	9.67	0.10
	0.3944	0.0142	0.0537	0.0021	0.4847	0.0532	0.0005	0.0168	0.0008	337	10	337	13	331	20	0	337	15	39	77	748	9.69	0.10
	0.3940	0.0144	0.0537	0.0022	0.5064	0.0535	0.0005	0.0168	0.0008	337	10	337	13	341	20	0	337	15	39	78	755	9.67	0.10
	0.3939	0.0144	0.0537	0.0022	0.5682	0.0531	0.0005	0.0168	0.0008	337	11	337	13	326	20	0	337	15	39	78	753	9.68	0.10
	0.3943	0.0145	0.0537	0.0022	0.5135	0.0533	0.0005	0.0168	0.0008	337	11	337	13	330	22	0	337	15	39	79	760	9.68	0.10
	0.3937	0.0144	0.0537	0.0022	0.5070	0.0531	0.0005	0.0168	0.0008	337	10	337	13	324	20	0	337	15	39	79	761	9.68	0.10
	0.3947	0.0146	0.0537	0.0022	0.4688	0.0533	0.0005	0.0168	0.0008	338	11	337	13	335	21	0	337	16	39	78	754	9.68	0.10
	0.3933	0.0142	0.0536	0.0021	0.5405	0.0531	0.0004	0.0168	0.0008	337	10	337	13	329	19	0	336	15	39	78	758	9.68	0.10
	0.3941	0.0144	0.0537	0.0021	0.4687	0.0538	0.0005	0.0168	0.0008	337	11	337	13	353	20	0	337	15	39	78	754	9.68	0.10
	0.3938	0.0145	0.0537	0.0022	0.5067	0.0532	0.0005	0.0168	0.0008	337	11	337	13	329	21	0	337	15	39	78	753	9.67	0.10
	0.3945	0.0145	0.0537	0.0022	0.5036	0.0533	0.0005	0.0168	0.0008	338	11	337	13	331	21	0	337	16	39	78	757	9.69	0.10
	0.3936	0.0144	0.0537	0.0022	0.4883	0.0531	0.0005	0.0168	0.0008	337	10	337	13	324	20	0	337	15	39	79	760	9.68	0.10
	0.3943	0.0146	0.0537	0.0022	0.5421	0.0529	0.0005	0.0168	0.0008	337	11	337	13	316	23	0	337	15	39	78	756	9.68	0.10
	0.3938	0.0144	0.0537	0.0022	0.5392	0.0531	0.0005	0.0168	0.0008	337	11	337	13	328	21	0	337	15	39	78	758	9.68	0.10
	0.3940	0.0145	0.0537	0.0022	0.5430	0.0535	0.0005	0.0168	0.0008	337	11	337	13	341	20	0	337	15	39	78	753	9.67	0.10
	0.3940	0.0145	0.0537	0.0022	0.4473	0.0533	0.0005	0.0168	0.0008	337	11	337	13	328	24	0	337	16	38	76	744	9.69	0.10
	0.3939	0.0146	0.0537	0.0022	0.4025	0.0532	0.0006	0.0168	0.0008	337	11	337	13	328	25	0	336	16	39	78	755	9.67	0.10
	0.3941	0.0147	0.0537	0.0022	0.4206	0.0532	0.0006	0.0168	0.0008	337	11	337	13	325	26	0	337	16	39	78	753	9.68	0.10
	0.3937	0.0144	0.0537	0.0022	0.5244	0.0535	0.0005	0.0168	0.0008	337	10	337	13	342	20	0	336	15	39	78	755	9.68	0.10
	0.3945	0.0145	0.0537	0.0022	0.5804	0.0533	0.0005	0.0168	0.0008	337	11	337	13	333	21	0	337	15	39	78	752	9.67	0.10
	0.3931	0.0145	0.0537	0.0021	0.5743	0.0530	0.0005	0.0168	0.0008	336	11	337	13	326	21	0	336	15	39	78	754	9.69	0.10
	0.3951	0.0146	0.0538	0.0022	0.5791	0.0531	0.0005	0.0168	0.0008	338	11	338	13	324	21	0	338	16	39	77	743	9.67	0.10
	0.3934	0.0144	0.0536	0.0022	0.5473	0.0534	0.0005	0.0168	0.0008	337	10	337	13	337	20	0	336	15	39	78	756	9.68	0.10
	0.3947	0.0145	0.0537	0.0021	0.5993	0.0534	0.0005	0.0168	0.0008	338	11	337	13	335	21	0	337	15	39	78	754	9.68	0.10
	0.3944	0.0146	0.0537	0.0022	0.5478	0.0530	0.0005	0.0168	0.0008	337	11	337	13	321	22	0	337	15	39	78	757	9.68	0.10
	0.3936	0.0144	0.0537	0.0022	0.5513	0.0531	0.0005	0.0168	0.0008	337	11	337	13	326	20	0	336	15	39	79	759	9.68	0.10
	0.3942	0.0145	0.0537	0.0022	0.5024	0.0535	0.0005	0.0168	0.0008	337	11	337	13	339	21	0	337	15	39	78	754	9.68	0.10
	0.3939	0.0145	0.0537	0.0022	0.5415	0.0532	0.0005	0.0168	0.0008	337	11	337	13	333	21	0	337	15	39	78	755	9.68	0.10
15-Dec-22																								
91500																								
	1.8577	0.0694	0.1792	0.0072	0.3824	0.0755	0.0010	0.0536	0.0025	1066	26	1063	39	1074	27	0	1056	49	60	38	98	2.61	0.38
	1.8248	0.0686	0.1778	0.0072	0.3661	0.0755	0.0011	0.0529	0.0025	1053	25	1055	39	1075	27	0	1042	48	54	34	90	2.69	0.37
	1.8394	0.0690	0.1749	0.0070	0.3887	0.0750	0.0010	0.0530	0.0025	1058	25	1040	39	1063	28	3	1044	48	51	32	89	2.83	0.35
	1.8464	0.0694	0.1773	0.0072	0.4259	0.0753	0.0010	0.0538	0.0025	1062	24	1052	39	1071	27	1	1058	49	45	28	79	2.81	0.36
AS-3																								
	2.0910	0.0777	0.2007	0.0081	0.5732	0.0757	0.0009	0.0617	0.0029	1145	25	1179	44	1083	25	-4	1210	55	171	95	188	1.98	0.51
	1.9777	0.0742	0.1873	0.0076	0.6222	0.0770	0.0010	0.0589	0.0028	1107	25	1106	41	1113	26	0	1157	53	137	79	183	2.33	0.43
	2.0462	0.0759	0.1932	0.0078	0.4677	0.0764	0.0010	0.0608	0.0029	1130	25	1138	42	1103	26	-1	1193	55	130	73	185	2.52	0.40
	2.0423	0.0763	0.1936	0.0078	0.5461	0.0762	0.0010	0.0603	0.0028	1128	25	1140	42	1094	26	-2	1183	54	126	71	166	2.43	0.41
Plesovice																								
	0.3941	0.0147	0.0537	0.0022	0.5354	0.0531	0.0007	0.0168	0.0008	337	11	337	13	329	28	0	336	16	39	78	755	9.68	0.10
	0.3938	0.0146	0.0537	0.0022	0.4462	0.0534	0.0007	0.0168	0.0008	337	11	337	13	339	29	0	337	16	39	78	755	9.68	0.10
	0.3945	0.0148	0.0537	0.0022	0.5535	0.0533	0.0007	0.0168	0.0008	338	11	337	13	333	29	0	337	16	39	78	755	9.68	0.10
	0.3937	0.0147	0.0536	0.0022	0.4856	0.0534	0.0007	0.0168	0.0008	337	11	337	13	338	29	0	337	16	39	78	756	9.68	0.10
	0.3933	0.0146	0.0537	0.0021	0.4385	0.0529	0.0007	0.0168	0.0008	337	11	337	13	318	29	0	336	16	39	78	755	9.69	0.10
	0.3950	0.0146	0.0537	0.0021	0.4964	0.0534	0.0007	0.0168	0.0008	338	11	337	13	337	30	0	338	16	39	78	758	9.67	0.10
	0.3932	0.0147	0.0537	0.0022	0.5394	0.0528	0.0007	0.0168	0.0008	337	11	337	13	312	29	0	336	16	39	78	757	9.69	0.10
	0.3948	0.0148	0.0537	0.0022	0.4751	0.0534	0.0007	0.0168	0.0008	338	11	337	13	340	29	0	337	16	39	79	760	9.68	0.10
	0.3934	0.0147	0.0536	0.0022	0.4465	0.0536	0.0007	0.0167	0.0008	337	11	337	13	344	29	0	335	16	39	78	754	9.69	0.10
	0.3946	0.0148	0.0538	0.0022	0.4797	0.0532	0.0007	0.0169	0.0008	337	11	338	13	331	29	0	338	16	39	78	756	9.68	0.10
	0.3941	0.0148	0.0536	0.0022	0.5174	0.0536	0.0007	0.0168	0.0008	337	11	337	13	348	29	0	337	16	39	79	758	9.69	0.10
	0.3938	0.0147	0.0537	0.0022	0.4959	0.0529	0.0007	0.0168	0.0008	337	11	337	13	316	29	0	336	16	39	79	761	9.67	0.10
	0.3942	0.0147	0.0537	0.0022	0.5044	0.0534	0.0007	0.0168	0.0008	337	11	337	13	342	28	0	337	16	39	79	756	9.69	0.10
	0.3938	0.0147	0.0537	0.0022	0.2936	0.0531	0.0007	0.0168	0.0008	337	11	337	13	326	29	0	336	16	39	79	760	9.68	0.10
	0.3942	0.0147	0.0537	0.0022	0.4176	0.0533	0.0007	0.0168	0.0008	337	11	337	13	331	29	0	337	16	39	78	757	9.68	0.10
	0.3938	0.0146	0.0537	0.0021	0.5171	0.0532	0.0007	0.0168	0.0008	337	11	337	13	329	28	0	336	16	39	79	759	9.68	0.10
16-Feb-23																								
91500																								
	1.8182	0.0424	0.1775	0.0033	0.2818	0.0744	0.0013	0.0546	0.0039	1052	15	1053	18	1052	15	0	1075	75	91	56	131	2.36	0.42
	1.8200	0.0424	0.1756	0.0033	0.3908	0.0751	0.0013	0.0522	0.0038	1052	15	1043	18	1052	15	1	1028	72	84	53	144	2.72	0.37
	1.7610	0.0409	0.1748	0.0033	0.3344	0.0733	0.0012	0.0577	0.0041	1031	15	1038	18	1031	15	-1	1134	79	56	34	118	3.59	0.28
	1.8127	0.0425	0.1756	0.0033	0.3774	0.0747	0.0013	0.0541	0.0039	1049	15	1043	18	1049	15	1	1065	74	68	42	96	2.27	0.44
	1.7927	0.0417	0.1750	0.0033	0.3397	0.0741	0.0013	0.0448	0.0034	1042	15	1040	18	1042	15	0	886	65	63	54	93	2.01	0.50

AS3																						
	2.0031	0.0450	0.1910	0.0036	0.6414	0.0762	0.0012	0.0550	0.0040	1116	15	1127	19	1116	15	-1	1082	76	974	600	1002	1.71	0.58
	2.0182	0.0459	0.1946	0.0036	0.6466	0.0753	0.0012	0.0559	0.0040	1121	15	1146	19	1121	15	-3	1100	77	704	432	837	1.95	0.51
	1.9884	0.0449	0.1887	0.0035	0.7072	0.0763	0.0012	0.0543	0.0039	1111	15	1114	19	1111	15	0	1069	75	701	441	677	1.59	0.63
	1.9777	0.0446	0.1908	0.0036	0.5942	0.0752	0.0012	0.0570	0.0040	1108	15	1126	20	1108	15	-2	1120	77	593	348	616	1.74	0.57
	1.9376	0.0436	0.1863	0.0035	0.6961	0.0755	0.0012	0.0558	0.0039	1094	15	1101	19	1094	15	-1	1098	75	667	411	657	1.62	0.62
Plesovice																						
	0.3942	0.0091	0.0537	0.0010	0.4403	0.0532	0.0009	0.0168	0.0012	337	7	337	6	337	7	0	337	24	39	78	753	9.68	0.10
	0.3938	0.0091	0.0537	0.0010	0.4272	0.0533	0.0009	0.0168	0.0012	337	7	337	6	337	7	0	337	24	39	78	753	9.68	0.10
	0.3944	0.0091	0.0537	0.0010	0.4406	0.0533	0.0009	0.0168	0.0012	337	7	337	6	337	7	0	337	24	39	78	755	9.68	0.10
	0.3936	0.0091	0.0537	0.0010	0.4219	0.0532	0.0009	0.0168	0.0012	337	7	337	6	337	7	0	337	24	39	78	753	9.68	0.10
	0.3938	0.0090	0.0537	0.0010	0.3817	0.0533	0.0009	0.0168	0.0012	337	7	337	6	337	7	0	337	24	39	79	763	9.68	0.10
	0.3942	0.0091	0.0537	0.0010	0.4076	0.0532	0.0009	0.0168	0.0012	337	7	337	6	337	7	0	337	24	39	78	746	9.68	0.10
	0.3943	0.0091	0.0537	0.0010	0.3766	0.0532	0.0009	0.0168	0.0012	337	7	337	6	337	7	0	337	24	39	78	756	9.68	0.10
	0.3937	0.0091	0.0536	0.0010	0.4079	0.0533	0.0009	0.0168	0.0012	337	7	337	6	337	7	0	337	24	39	78	754	9.68	0.10
	0.3933	0.0093	0.0537	0.0010	0.4623	0.0531	0.0009	0.0168	0.0012	337	7	337	6	337	7	0	337	24	39	78	756	9.68	0.10
	0.3945	0.0093	0.0537	0.0010	0.3291	0.0534	0.0009	0.0168	0.0013	338	7	337	6	338	7	0	337	25	39	78	755	9.71	0.10
	0.3942	0.0090	0.0537	0.0010	0.4064	0.0533	0.0009	0.0168	0.0012	337	7	337	6	337	7	0	337	24	39	78	755	9.68	0.10
	0.3938	0.0091	0.0537	0.0010	0.4237	0.0532	0.0009	0.0168	0.0012	337	7	337	6	337	7	0	337	24	39	78	754	9.69	0.10
	0.3940	0.0090	0.0537	0.0010	0.3599	0.0533	0.0009	0.0168	0.0012	337	7	337	6	337	7	0	337	24	39	78	755	9.68	0.10
	0.3941	0.0090	0.0537	0.0010	0.4027	0.0532	0.0009	0.0168	0.0012	337	7	337	6	337	7	0	337	24	39	78	755	9.68	0.10
	0.3939	0.0091	0.0537	0.0010	0.5438	0.0532	0.0009	0.0168	0.0012	337	7	337	6	337	7	0	337	24	39	78	755	9.68	0.10
	0.3940	0.0090	0.0537	0.0010	0.6146	0.0533	0.0009	0.0168	0.0012	337	7	337	6	337	7	0	337	24	39	78	756	9.68	0.10
	0.3955	0.0091	0.0537	0.0010	0.5844	0.0533	0.0009	0.0167	0.0011	338	7	337	6	338	7	0	336	21	39	78	755	9.61	0.10
	0.3931	0.0089	0.0536	0.0010	0.3515	0.0532	0.0009	0.0168	0.0013	337	7	337	6	337	7	0	337	27	39	77	753	9.69	0.10
	0.3944	0.0091	0.0537	0.0010	0.4835	0.0532	0.0009	0.0168	0.0012	337	7	337	6	337	7	0	337	24	39	78	756	9.68	0.10
	0.3937	0.0090	0.0536	0.0010	0.4557	0.0533	0.0009	0.0168	0.0012	337	7	337	6	337	7	0	337	24	39	78	755	9.68	0.10

Paces, J.B., Miller Jr., J.D., 1993. Precise U-Pb ages of Duluth Complex and related mafic intrusions, northeastern Minnesota: Geochronological insights to physical, petrogenetic, paleomagnetic, and tectonomagmatic processes associated with the 1.1 Ga Midcontinent Rift System. J. Geophys. Res. Solid Earth 98, 13997–14013. https://doi.org/https://doi.org/10.1029/93JB01159

Sláma, J., Košler, J., Condon, D.J., Crowley, J.L., Gerdes, A., Hanchar, J.M., Horstwood, M.S.A., Morris, G.A., Nasdala, L., Norberg, N., Schaltegger, U., Schoene, B., Tubrett, M.N., Whitehouse, M.J., 2008. Plešovice zircon — A new natural reference material for U–Pb and Hf isotopic microanalysis. Chem. Geol. 249, 1–35. https://doi.org/https://doi.org/10.1016/j.chemgeo.2007.11.005

Wiedenbeck, M., Allé, P., Corfu, F., Griffin, W.L., Meier, M., Oberli, F., Quadt, A. von, Roddick, J.C., Spiegle, W., 1995. Three Natural Zircon Standards for U-Th-Pb, Lu-Hf, Trace Element and REE Analyses. Geostand. Newsl. 19, 1–23. https://doi.org/https://doi.org/10.1111/j.1751-908X.1995.tb00147.x

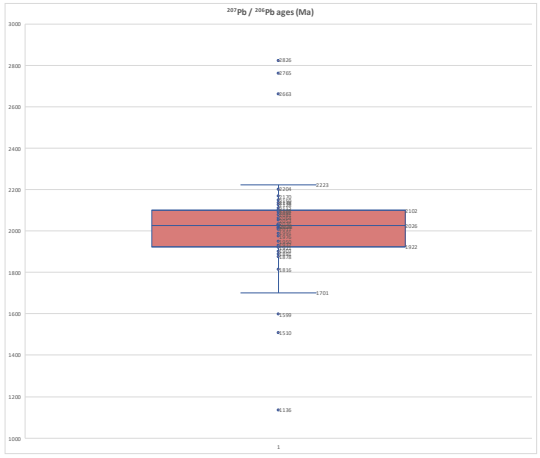
U-Th-Pb analyses of apatite crystals from Cupim Pluton (GC1, GCSA/B, and GC6), and Caatinga-Lamim complex (CM44B).

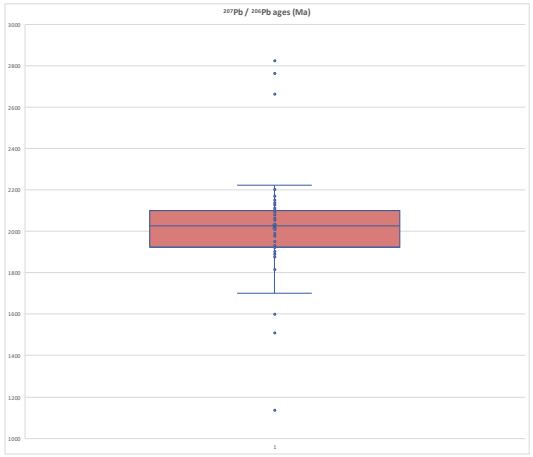
Laboratoire Magmas et Volcans

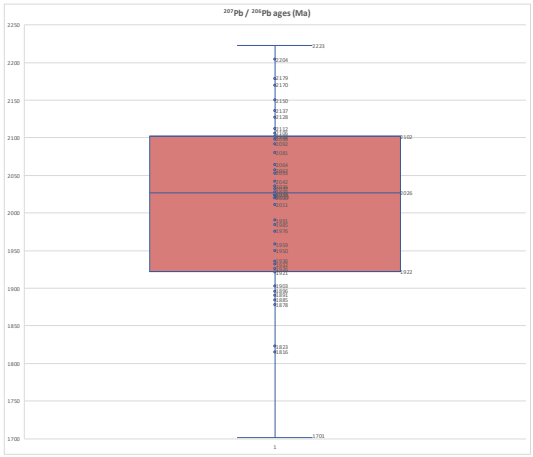
Spot num. analysis	Optical features	Inclusions	Texture BSE	Exolution	Domain BSE	Isotopic ratios $^{207}Pb/^{206}Pb$	±2σ %	$^{206}Pb/^{238}U$	±2σ %	$^{207}Pb/^{235}U$	±2σ %	$^{208}Pb/^{232}Th$	±2σ %	Rho[1]	^{207}Pb correction $^{207}Pb/^{206}Pb$	±2σ %	$^{206}Pb/^{238}U$	±2σ %	$^{207}Pb/^{235}U$	±2σ %	$^{208}Pb/^{232}Th$	±2σ %	f206 (%)	f208 (%)	Ages Pbc age (Ma)	$^{207}Pb/^{206}Pb$	±2σ % (Ma)	$^{206}Pb/^{238}U$	±2σ % (Ma)	$^{208}Pb/^{232}Th$	±2σ % (Ma)	Disc.[2]	Element concentration [3] Age meaning	U ppm	Pb ppm	Th ppm	Th U
GC1																																				
ap#1.1	*Elongated, rounded, incolor*	*none*	*Homogeneous*	*absent*	*Light*	0.5742	0.0053	0.6826	0.0056	53.8932	0.5048	2.8134	0.0263	0.4668	0.1296	0.0023	0.3277	0.0056	5.8547	0.1436	0.0950	0.0013	52%	97%	1827	2092	31	1827	27	1955	21	1835	23	-0.41	Igneous	4.5	8.7	1.3	0.29
ap#1.2	*Elongated, rounded, incolor*	*none*	*Homogeneous*	*absent*	*Light*	0.5252	0.0040	0.6320	0.0043	45.5900	0.3393	2.0824	0.0170	0.4905	0.1311	0.0023	0.3427	0.0059	6.1920	0.1515	0.0986	0.0012	46%	95%	1899	2112	30	1899	28	2003	21	1901	23	-0.08	Igneous	6.5	10.8	2.1	0.33
ap#1.3	*Elongated, rounded, incolor*	*none*	*Homogeneous*	*absent*	*Light*	0.5237	0.0069	0.6566	0.0072	47.3797	0.5898	2.3797	0.0324	0.4825	0.1180	0.0028	0.3537	0.0078	5.7526	0.1852	0.1006	0.0019	46%	96%	1952	1926	41	1952	37	1939	27	1938	34	0.70	Igneous	4.6	8.2	1.4	0.30
ap#2.1	*Stubby, rounded, incolor*	*none*	*Homogeneous*	*absent*	*Light*	0.4898	0.0037	0.6055	0.0043	40.7752	0.3179	1.6822	0.0149	0.4418	0.1276	0.0021	0.3532	0.0058	6.2123	0.1440	0.1016	0.0012	42%	94%	1950	2064	29	1950	27	2006	20	1955	22	-0.26	Igneous	7.3	11.1	2.6	0.36
ap#2.2	*Stubby, rounded, incolor*	*none*	*Homogeneous*	*absent*	*Light*	0.4868	0.0038	0.6137	0.0042	41.1213	0.3415	1.7220	0.0140	0.4020	0.1247	0.0021	0.3599	0.0059	6.1857	0.1451	0.1033	0.0012	41%	94%	1982	2024	29	1982	28	2002	20	1988	22	-0.29	Igneous	7.5	11.6	2.6	0.35
ap#2.3	*Stubby, rounded, incolor*	*none*	*Homogeneous*	*absent*	*Light*	0.5056	0.0042	0.6191	0.0044	42.9883	0.3522	1.8651	0.0154	0.4393	0.1323	0.0021	0.3516	0.0054	6.4097	0.1416	0.1013	0.0012	43%	95%	1942	2128	28	1942	26	2034	19	1950	22	-0.42	Igneous	7.0	11.1	2.4	0.34
ap#3.1	*Stubby, rounded, incolor*	*none*	*Homogeneous*	*absent*	*Light*	0.4744	0.0035	0.5722	0.0037	37.4758	0.3020	1.4641	0.0131	0.3595	0.1355	0.0022	0.3463	0.0054	6.4675	0.1435	0.0995	0.0013	39%	93%	1917	2170	27	1917	26	2041	19	1917	24	-0.04	Igneous	7.8	11.5	2.9	0.37
ap#3.2	*Stubby, rounded, incolor*	*none*	*Homogeneous*	*absent*	*Light*	0.4920	0.0040	0.5978	0.0042	40.4983	0.3167	1.8532	0.0164	0.4775	0.1256	0.0021	0.3453	0.0055	5.9756	0.1368	0.0995	0.0013	29%	95%	1912	2036	29	1912	26	1972	20	1917	23	-0.27	Igneous	7.1	11.1	2.3	0.32
ap#3.3	*Stubby, rounded, incolor*	*none*	*Homogeneous*	*absent*	*Light*	0.4930	0.0042	0.5929	0.0042	40.2607	0.3348	1.8084	0.0142	0.4521	0.1303	0.0024	0.3435	0.0060	6.1700	0.1550	0.0991	0.0012	42%	95%	1903	2102	31	1903	29	2000	22	1909	23	-0.32	Igneous	7.1	11.1	2.3	0.33
ap#4.1	*Stubby, rounded, incolor*	*none*	*Homogeneous*	*absent*	*Light*	0.5191	0.0053	0.6120	0.0049	43.6857	0.4345	2.1617	0.0228	0.3688	0.1271	0.0024	0.3331	0.0058	5.8341	0.1483	0.0963	0.0014	46%	96%	1853	2057	32	1853	28	1951	22	1858	25	-0.23	Igneous	4.9	8.1	1.5	0.30
ap#4.2	*Stubby, rounded, incolor*	*none*	*Homogeneous*	*absent*	*Light*	0.4937	0.0048	0.5609	0.0044	38.1430	0.3548	1.7510	0.0160	0.4300	0.1268	0.0021	0.3200	0.0051	5.5911	0.1295	0.0930	0.0012	43%	95%	1790	2053	29	1790	25	1915	20	1798	22	-0.45	Igneous	5.4	8.0	1.7	0.32
ap#4.3	*Stubby, rounded, incolor*	*none*	*Homogeneous*	*absent*	*Light*	0.5047	0.0038	0.5958	0.0039	41.4108	0.3309	1.8035	0.0162	0.3265	0.1330	0.0020	0.3371	0.0050	6.1778	0.1326	0.0973	0.0012	43%	95%	1873	2137	27	1873	24	2001	19	1877	22	-0.22	Igneous	6.0	9.6	2.0	0.34
ap#5.1	*Stubby, rounded, incolor*	*none*	*Homogeneous*	*absent*	*Light*	0.5390	0.0048	0.6500	0.0046	48.1857	0.4333	2.0044	0.0171	0.3877	0.1382	0.0022	0.3453	0.0051	6.5790	0.1406	0.0996	0.0012	47%	95%	1912	2204	27	1912	24	2057	19	1918	22	-0.31	Igneous	5.4	9.8	1.9	0.36
ap#5.2	*Stubby, rounded, incolor*	*none*	*Homogeneous*	*absent*	*Light*	0.5451	0.0045	0.6817	0.0051	51.3134	0.4175	2.1588	0.0173	0.4940	0.1307	0.0020	0.3562	0.0052	6.4164	0.1347	0.1025	0.0012	48%	95%	1964	2106	26	1964	25	2035	18	1972	21	-0.37	Igneous	5.3	10.3	1.9	0.36
ap#5.3	*Stubby, rounded, incolor*	*none*	*Homogeneous*	*absent*	*Light*	0.5429	0.0047	0.6692	0.0050	49.9955	0.4225	2.1515	0.0179	0.4090	0.1297	0.0021	0.3498	0.0054	6.2537	0.1385	0.1007	0.0012	48%	95%	1934	2093	28	1934	26	2012	19	1939	22	-0.27	Igneous	5.0	9.5	1.8	0.35
ap#7.1	*Elongated, rounded, incolor*	*none*	*Homogeneous*	*absent*	*Light*	0.5506	0.0049	0.6854	0.0057	51.9181	0.4762	2.4047	0.0244	0.4414	0.1301	0.0023	0.3529	0.0062	6.3270	0.1583	0.1018	0.0013	49%	96%	1948	2098	31	1948	29	2022	22	1959	24	-0.54	Igneous	4.9	9.5	1.6	0.33
ap#7.2	*Elongated, rounded, incolor*	*none*	*Homogeneous*	*absent*	*Light*	0.5517	0.0056	0.7346	0.0083	55.9221	0.6750	2.8402	0.0352	0.4246	0.1214	0.0026	0.3787	0.0083	6.3363	0.1930	0.1086	0.0017	48%	96%	2070	1976	37	2070	38	2023	26	2084	31	-0.66	Igneous	4.7	9.7	1.4	0.30
ap#7.3	*Elongated, rounded, incolor*	*none*	*Homogeneous*	*absent*	*Light*	0.5348	0.0053	0.6468	0.0057	47.6467	0.4804	1.9119	0.0212	0.4830	0.1187	0.0024	0.3378	0.0065	5.5258	0.1535	0.0977	0.0014	48%	95%	1876	1936	35	1876	31	1905	24	1885	26	-0.47	Igneous	5.1	9.2	2.0	0.38
ap#8.1	*Stubby, rounded, incolor*	*none*	*Homogeneous*	*absent*	*Light*	0.5596	0.0046	0.6741	0.0049	51.8721	0.4267	2.3725	0.0205	0.4374	0.1302	0.0020	0.3372	0.0050	6.0510	0.1286	0.0973	0.0012	50%	96%	1873	2100	27	1873	24	1983	18	1876	22	-0.15	Igneous	5.0	9.4	1.6	0.33
ap#8.2	*Stubby, rounded, incolor*	*none*	*Homogeneous*	*absent*	*Light*	0.5586	0.0047	0.6689	0.0050	51.3797	0.4635	2.2793	0.0194	0.3999	0.1202	0.0020	0.3301	0.0053	5.4694	0.1270	0.0955	0.0012	51%	96%	1839	1959	29	1839	26	1896	20	1844	21	-0.27	Igneous	5.0	9.4	1.7	0.35
ap#8.3	*Stubby, rounded, incolor*	*none*	*Homogeneous*	*absent*	*Light*	0.5432	0.0044	0.6544	0.0048	48.9314	0.4193	2.0584	0.0184	0.4279	0.1288	0.0021	0.3397	0.0054	6.0291	0.1376	0.0982	0.0012	48%	95%	1885	2081	28	1885	26	1980	20	1893	22	-0.41	Igneous	5.1	9.2	1.8	0.36
ap#9.1	*Stubby, rounded, incolor*	*none*	*Homogeneous*	*absent*	*Light*	0.5342	0.0048	0.6279	0.0046	46.0240	0.4231	2.3521	0.0206	0.3797	0.1245	0.0022	0.3290	0.0056	5.6441	0.1390	0.0953	0.0012	48%	96%	1834	2020	31	1834	27	1923	21	1840	22	-0.34	Igneous	5.4	9.2	1.6	0.29
ap#9.2	*Stubby, rounded, incolor*	*none*	*Homogeneous*	*absent*	*Light*	0.5633	0.0051	0.6491	0.0055	50.2561	0.4765	2.6403	0.0300	0.4372	0.1224	0.0028	0.3148	0.0071	5.3100	0.1704	0.0916	0.0014	52%	97%	1764	1991	40	1764	35	1870	27	1772	27	-0.44	Igneous	4.3	7.8	1.2	0.29
ap#9.3	*Stubby, rounded, incolor*	*none*	*Homogeneous*	*absent*	*Light*	0.5614	0.0080	0.6281	0.0083	48.7430	0.8234	2.3901	0.0437	0.2840	0.0987	0.0029	0.2939	0.0084	3.9975	0.1636	0.0852	0.0021	53%	96%	1661	1599	53	1661	42	1634	33	1652	38	0.54	Igneous	4.0	7.4	1.3	0.32
ap#10.1	*Stubby, rounded, incolor*	*none*	*Homogeneous*	*absent*	*Light*	0.5273	0.0164	0.7646	0.0159	45.9075	0.4768	2.6521	0.0642	0.2533	0.0941	0.0043	0.4084	0.0162	5.2980	0.3221	0.1168	0.0038	47%	96%	2208	1510	84	2208	74	1869	51	2233	68	-1.14	Igneous	4.5	8.6	1.5	0.33
ap#10.2	*Stubby, rounded, incolor*	*none*	*Homogeneous*	*absent*	*Light*	0.6196	0.0050	0.7442	0.0061	62.7741	0.5624	3.3423	0.0362	0.4324	0.1149	0.0023	0.3074	0.0061	4.8681	0.1371	0.0893	0.0012	59%	97%	1728	1878	35	1728	30	1797	23	1729	23	-0.07	Igneous	3.3	7.1	1.0	0.30
ap#10.3	*Stubby, rounded, incolor*	*none*	*Homogeneous*	*absent*	*Light*	0.5590	0.0047	0.6460	0.0051	49.2480	0.4458	2.2592	0.0229	0.4050	0.1158	0.0020	0.3139	0.0052	5.0073	0.1191	0.0911	0.0012	51%	96%	1760	1891	30	1760	26	1821	20	1762	23	-0.16	Igneous	4.4	7.7	1.5	0.34
ap#11.1	*Stubby, rounded, incolor*	*none*	*Homogeneous*	*absent*	*Light*	0.5370	0.0040	0.6376	0.0043	46.7505	0.3726	2.3312	0.0210	0.3885	0.1238	0.0020	0.3324	0.0051	5.6720	0.1253	0.0958	0.0011	48%	96%	1850	2011	28	1850	25	1927	19	1849	20	0.04	Igneous	5.5	9.2	1.7	0.30
ap#11.2	*Stubby, rounded, incolor*	*none*	*Homogeneous*	*absent*	*Light*	0.5087	0.0041	0.5871	0.0041	40.7168	0.3492	2.0234	0.0186	0.3668	0.1177	0.0020	0.3214	0.0052	6.2155	0.1218	0.0932	0.0011	45%	95%	1797	1921	30	1797	25	1855	20	1801	21	-0.22	Igneous	5.9	8.6	1.8	0.31
ap#11.3	*Stubby, rounded, incolor*	*none*	*Homogeneous*	*absent*	*Light*	0.5174	0.0045	0.5804	0.0042	41.0456	0.3818	2.3347	0.0239	0.2861	0.1110	0.0020	0.3073	0.0054	4.7030	0.1193	0.0896	0.0012	47%	96%	1728	1816	33	1728	27	1768	21	1734	22	-0.36	Igneous	5.6	8.3	1.5	0.27
ap#12.1	*Stubby, rounded, incolor*	*none*	*Homogeneous*	*absent*	*Light*	0.5371	0.0051	0.6246	0.0051	45.7090	0.4295	2.7500	0.0299	0.4055	0.1304	0.0023	0.3271	0.0057	5.8783	0.1466	0.0948	0.0014	48%	97%	1824	2102	31	1824	27	1958	21	1830	25	-0.30	Igneous	4.9	8.1	1.2	0.25
ap#12.2	*Stubby, rounded, incolor*	*none*	*Homogeneous*	*absent*	*Light*	0.4997	0.0039	0.6116	0.0047	41.6185	0.3490	2.2812	0.0211	0.4352	0.1196	0.0020	0.3456	0.0056	5.6974	0.1360	0.0995	0.0013	43%	96%	1913	1950	30	1913	28	1931	20	1917	23	-0.21	Igneous	6.2	9.6	1.7	0.27
ap#12.3	*Stubby, rounded, incolor*	*none*	*Homogeneous*	*absent*	*Light*	0.5043	0.0040	0.6080	0.0038	42.3682	0.3392	1.4871	0.0186	0.3618	0.1298	0.0020	0.3490	0.0049	6.1533	0.1278	0.0990	0.0012	43%	96%	1906	2094	26	1906	24	1988	18	1909	21	-0.15	Igneous	6.8	10.5	2.0	0.29
ap#13.1	*Stubby, rounded, incolor*	*none*	*Homogeneous*	*absent*	*Light*	0.4350	0.0033	0.5501	0.0034	32.6519	0.2767	1.2148	0.0096	0.3468	0.1220	0.0018	0.3533	0.0051	5.9403	0.1242	0.1014	0.0011	36%	92%	1951	1985	27	1951	24	1967	18	1952	20	-0.06	Igneous	9.5	12.2	3.8	0.40
ap#13.2	*Stubby, rounded, incolor*	*none*	*Homogeneous*	*absent*	*Light*	0.4954	0.0036	0.6141	0.0038	41.5455	0.3088	1.7719	0.0147	0.4101	0.1340	0.0020	0.3576	0.0051	6.6035	0.1359	0.1027	0.0012	42%	94%	1971	2150	26	1971	24	2060	18	1976	21	-0.25	Igneous	7.6	11.8	2.7	0.35
ap#13.3	*Stubby, rounded, incolor*	*none*	*Homogeneous*	*absent*	*Light*	0.4540	0.0034	0.5373	0.0037	33.3758	0.3105	1.5389	0.0101	0.3181	0.1250	0.0019	0.3322	0.0051	5.7220	0.1250	0.0958	0.0011	38%	92%	1749	2028	27	1849	25	1935	19	1850	20	-0.05	Igneous	9.2	11.8	3.7	0.40
ap#14.1	*Stubby, rounded, incolor, fractured*	*none*	*Homogeneous*	*absent*	*Light*	0.5366	0.0089	0.4994	0.0058	36.4631	0.6552	1.7601	0.0277	0.4915	0.1115	0.0030	0.2445	0.0059	3.7572	0.1352	0.0731	0.0015	51%	96%	1410	1823	48	1410	30	1584	28	1426	28	-1.09	Igneous	5.8	7.8	1.9	0.33
ap#14.2	*Stubby, rounded, incolor, fractured*	*none*	*Homogeneous*	*absent*	*Light*	0.5475	0.0049	0.5756	0.0043	43.5335	0.4065	2.2030	0.0198	0.3581	0.1043	0.0019	0.2777	0.0050	3.9919	0.1032	0.0815	0.0010	52%	96%	1580	1751	30	1580	25	1633	21	1583	19	-0.24	Igneous	5.5	8.9	1.7	0.31
ap#14.3	*Stubby, rounded, incolor, fractured*	*none*	*Homogeneous*	*absent*	*Light*	0.4957	0.0041	0.4798	0.0031	32.8152	0.2619	1.4050	0.0117	0.3867	0.1153	0.0017	0.2619	0.0036	4.1638	0.0837	0.0771	0.0009	45%	95%	1500	1885	28	1500	18	1667	16	1501	16	-0.07	Igneous	7.4	9.5	2.7	0.36
ap#15.1	*Stubby, rounded, incolor*	*none*	*Homogeneous*	*absent*	*Light*	0.5258	0.0043	0.6408	0.0046	46.5864	0.4278	1.9722	0.0159	0.3203	0.1331	0.0021	0.3488	0.0055	6.2986	0.1441	0.1003	0.0012	46%	95%	1909	2138	28	1909	26	2032	20	1933	22	-0.19	Igneous	6.1	10.6	2.1	0.35
ap#15.2	*Stubby, rounded, incolor*	*none*	*Homogeneous*	*absent*	*Light*	0.5140	0.0040	0.6223	0.0044	44.2689	0.4005	2.7810	0.0059	0.3125	0.1811	0.0027	0.3711	0.0055	9.2638	0.1952	0.1057	0.0011	40%	86%	2035	2663	25	2035	26	2364	19	2030	21	0.21	Igneous	6.5	10.8	5.4	0.84
ap#15.3	*Stubby, rounded, incolor*	*none*	*Homogeneous*	*absent*	*Light*	0.5727	0.0057	0.6754	0.0056	53.4268	0.5524	2.2990	0.0250	0.3835	0.1253	0.0023	0.3228	0.0055	5.5750	0.1380	0.0937	0.0013	52%	96%	1804	2032	31	1804	27	1912	21	1811	25	-0.41	Igneous	4.3	8.4	1.5	0.36
ap#16.1	*Stubby, rounded, incolor*	*none*	*Homogeneous*	*absent*	*Light*	0.5660	0.0048	0.6878	0.0053	53.8837	0.4834	2.6333	0.0094	0.4246	0.1927	0.0039	0.3713	0.0073	5.8622	0.2773	0.1064	0.0016	46%	88%	2038	2765	33	2038	34	2422	26	2044	29	-0.39	Igneous	4.5	8.5	4.3	0.96
ap#16.2	*Stubby, rounded, incolor*	*none*	*Homogeneous*	*absent*	*Light*	0.5729	0.0055	0.6913	0.0053	54.5800	0.4729	2.5178	0.0239	0.5122	0.1260	0.0021	0.3324	0.0053	5.7731	0.1345	0.0961	0.0013	52%	96%	1850	2042	30	1850	26	1942	20	1855	23	-0.25	Igneous	4.1	7.7	1.3	0.33
ap#16.3	*Stubby, rounded, incolor*	*none*	*Homogeneous*	*absent*	*Light*	0.5411	0.0049	0.6545	0.0050	48.9014	0.4593	2.1402	0.0196	0.3883	0.1166	0.0020	0.3359	0.0054	5.3964	0.1264	0.0969	0.0012	49%	95%	1867	1903	30	1867	26	1884	20	1870	22	-0.15	Igneous	4.8	8.4	1.7	0.35
ap#17.1	*Elongated, rounded, incolor*	*none*	*Homogeneous*	*absent*	*Light*	0.5180	0.0043	0.6266	0.0049	44.9182	0.3760	1.9815	0.0173	0.5039	0.1167	0.0019	0.3387	0.0053	5.4471	0.1220	0.0980	0.0012	45%	95%	1880	1906	28	1880	26	1892	19	1889	22	-0.46	Igneous	6.3	10.2	2.2	0.34
ap#17.2	*Elongated, rounded, incolor*	*none*	*Homogeneous*	*absent*	*Light*	0.5085	0.0043	0.6025	0.0045	42.4288	0.3937	1.8978	0.0183	0.3547	0.1161	0.0020	0.3308	0.0056	5.5935	0.1288	0.0958	0.0012	45%	95%	1842	1996	31	1842	27	1868	21	1849	21	-0.36	Igneous	6.4	9.9	2.2	0.34
ap#17.3	*Elongated, rounded, incolor*	*none*	*Homogeneous*	*absent*	*Light*	0.5135	0.0045	0.5968	0.0044	42.2637	0.3569	1.7832	0.0143	0.4264	0.1225	0.0022	0.3259	0.0056	5.5038	0.1366	0.0942	0.0012	45%	95%	1919	1993	31	1819	27	1901	21	1820	21	-0.08	Igneous	6.3	9.7	2.3	0.36
ap#18.1	*Stubby, rounded, incolor*	*none*	*Homogeneous*	*absent*	*Light*	0.5013	0.0049	0.4795	0.0039	33.2168	0.3245	0.4851	0.0048	0.4126	0.2001	0.0044	0.2912	0.0062	8.0305	0.2435	0.0850	0.0014	39%	82%	1647	2826	35	1647	31	2234	27	1648	25	-0.07	Igneous	8.1	9.6	8.8	1.09
ap#18.2	*Stubby, rounded, incolor*	*none*	*Homogeneous*	*absent*	*Light*	0.5201	0.0046	0.5173	0.0040	37.1483	0.3768	1.5993	0.0382	0.2268	0.1397	0.0053	0.2775	0.0104	3.4443	0.2836	0.0889	0.0032	46%	92%	1579	2223	64	1579	52	1876	44	1722	59	-0.09	Igneous	6.9	9.0	3.9	0.57
ap#18.3	*Stubby, rounded, incolor*	*none*	*Homogeneous*	*absent*	*Light*	0.5065	0.0042	0.5616	0.0038	39.1439	0.3145	1.6359	0.0144	0.3675	0.1185	0.0019	0.3071	0.0046	5.0129	0.1095	0.0893	0.0011	45%	95%	1726	1932	28	1726	23	1822	18	1729	20	-0.15	Igneous	6.8	9.3	2.5	0.36
ap#19.1	*Stubby, rounded, incolor*	*none*	*Homogeneous*	*absent*	*Light*	0.5725	0.0046	0.7029	0.0052	55.6008	0.4940	2.5278	0.0240	0.3732	0.1362	0.0027	0.3450	0.0067	6.4790	0.1789	0.0996	0.0014	51%	96%	1911	2179	34	1911	32	2043	24	1920	25	-0.46	Igneous	4.9	9.0	1.6	0.33
ap#19.2	*Stubby, rounded, incolor*	*none*	*Homogeneous*	*absent*	*Light*	0.5810	0.0046	0.7340	0.0055	58.8445	0.4896	2.7974	0.0257	0.4084	0.1214	0.0021	0.3476	0.0061	5.8157	0.1445	0.1001	0.0013	53%	96%	1923	1976	31	1923	29	1949	21	1929	23	-0.31	Igneous	4.5	8.8	1.4	0.32
ap#19.3	*Stubby, rounded, incolor*	*none*	*Homogeneous*	*absent*	*Light*	0.5698	0.0050	0.7021	0.0053	55.0335	0.4991	2.4733	0.0265	0.3931	0.1248	0.0022	0.3416	0.0057	5.8740	0.1408	0.0987	0.0013	51%	96%	1894	2025	30	1894	27	1957	21	1903	25	-0.46	Igneous	4.3	8.0	1.4	0.33
ap#20.1	*Elongated, prismatic, incolor, fractured*	*none*	*Homogeneous*	*absent*	*Light*	0.3838	0.0028	0.6812	0.0037	35.8008	0.2721	1.5328	0.0115	0.2748	0.1111	0.0015	0.4857	0.0064	7.4392	0.1424	0.1350	0.0015	29%	91%	2552	1817	25	2552	28	2166	17	2559	26	-0.27	Igneous	9.2	13.1	3.1	0.33
ap#20.2	*Elongated, prismatic, incolor, fractured*	*none*	*Homogeneous*	*absent*	*Light*	0.4661	0.0036	0.5096	0.0039	32.4873	0.3019	1.6510	0.0139	0.2550	0.0776	0.0012	0.2864	0.0043	3.0633	0.0653	0.0840	0.0010	44%	95%	1623	1136	30	1623	22	1424	16	1630	19	-0.43	Igneous	8.3	10.3	2.6	0.31
ap#20.3	*Elongated, prismatic, incolor, fractured*	*none*	*Homogeneous*	*absent*	*Light*	0.5173	0.0046	0.6711	0.0152	47.2801	1.1403	3.0060	0.0880	0.3491	-0.2843	-0.0108	0.2311	0.0100	-9.0524	-0.5219	0.0690	0.0032	66%	98%	1340	na	na	1340	52	na	na	1349	60	-0.67	Igneous	6.3	12.3	2.0	0.33
GCSA/B																																				
ap#1.1	*Elongated, rounded, incolor*	*none*	*Homogeneous*	*absent*	*Light*	0.2832	0.0044	0.0857	0.0007	3.3613	0.0484	0.0198	0.0001	0.4707	0.1208	0.0025	0.3219	0.0069	5.3597	0.1615	0.0934	0.0015	58%	98%	1799	1968	37	1799	34	1878	25	1805	27	-0.33	Igneous	18.2	25.3	1174.2	64.42
ap#1.2	*Elongated, rounded, incolor*	*none*	*Homogeneous*	*absent*	*Light*	0.1203	0.0017	0.1010	0.0006	1.6872	0.0239	0.0290	0.0001	0.2206	0.1133	0.0016	0.3299	0.0046	5.1501	0.1032	0.0952	0.0010	44%	96%	1838	1852	26	1838	22	1844	17	1837	19	0.04	Igneous	37.6	48.4	1518.0	40.39
ap#1.3	*Elongated, rounded, incolor*	*none*	*Homogeneous*	*absent*	*Light*	0.6224	0.0056	0.7709	0.0077	66.1540	0.7715	5.6166	0.0766	0.3103	0.1054	0.0016	0.3326	0.0049	4.8299	0.1014	0.0962	0.0011	44%	95%	1851	1720	27	1851	24	1790	18	1856	20	-0.30	Igneous	4.1	9.3	0.7	0.18
ap#2.1	*Elongated, prismatic, incolor, fractured*	*none*	*Homogeneous*	*absent*

ap#11.3	*Elongated, Rounded, incolor*	*none*	*Core/Rim*	*present*	*Dark Core*	0.3973	0.0045	0.4761	0.0046	25.9415	0.3032	1.6939	0.0232	0.3421	0.1240	0.0025	0.3246	0.0062	5.5461	0.1539	0.0942	0.0017	32%	94%	1812	2013	35	1812	30	1908	24	1820	31	-0.43	Metamorphic	5.0	5.1	1.1	0.21
ap#12.1	*Elongated, Rounded, incolor*	*none*	*Homogeneous*	*absent*	*Dark*	0.3330	0.0037	0.4616	0.0036	21.1387	0.2540	0.7492	0.0091	0.3255	0.1277	0.0038	0.3525	0.0101	6.2044	0.2569	0.1012	0.0020	24%	86%	1947	2066	52	1947	48	2005	36	1948	38	-0.06	Metamorphic	6.4	5.6	2.4	0.38
ap#12.2	*Elongated, Rounded, incolor*	*none*	*Homogeneous*	*absent*	*Dark*	0.3741	0.0045	0.5221	0.0048	26.7877	0.3318	0.8781	0.0121	0.3761	0.1240	0.0033	0.3743	0.0094	6.3939	0.2337	0.1080	0.0021	28%	88%	2049	2013	46	2049	44	2031	32	2073	38	-1.17	Metamorphic	5.3	5.7	2.3	0.44
ap#12.3	*Elongated, Rounded, incolor*	*none*	*Homogeneous*	*absent*	*Dark*	0.3243	0.0039	0.4926	0.0046	22.0819	0.3882	0.6794	0.0137	-0.1221	0.1230	0.0044	0.3809	0.0134	6.4582	0.3255	0.1106	0.0027	23%	84%	2080	2000	63	2080	62	2040	43	2121	49	-1.93	Metamorphic	7.4	6.8	3.4	0.45
ap#13.1	*Elongated, Rounded, incolor*	*none*	*Core/Rim*	*present*	*Light Rim*	0.3141	0.0033	0.4554	0.0032	19.7319	0.2072	0.5040	0.0044	0.3228	0.1238	0.0020	0.3563	0.0049	6.0808	0.1284	0.1021	0.0013	22%	80%	1965	2011	28	1965	23	1987	18	1965	23	-0.03	Metamorphic	8.5	7.4	4.7	0.55
ap#13.2	*Elongated, Rounded, incolor*	*none*	*Core/Rim*	*present*	*Dark Core*	0.2875	0.0030	0.4197	0.0028	16.6236	0.1790	0.5267	0.0046	0.3191	0.1192	0.0022	0.3385	0.0055	5.5598	0.1358	0.0973	0.0013	19%	82%	1880	1943	32	1880	27	1910	21	1876	24	0.19	Metamorphic	9.2	6.9	3.8	0.42
ap#13.3	*Elongated, Rounded, incolor*	*none*	*Core/Rim*	*present*	*Light Rim*	0.2216	0.0028	0.3873	0.0037	11.8177	0.1533	0.2783	0.0029	0.3577	0.1219	0.0026	0.3430	0.0066	5.7638	0.1647	0.0986	0.0017	11%	65%	1901	1984	37	1901	32	1941	24	1901	31	0.00	Metamorphic	20.3	12.6	11.2	0.55
ap#14.1	*Stubby, rounded, incolor*	*none*	*Core/Rim*	*present*	*Dark Core*	0.3667	0.0057	0.4028	0.0050	20.0373	0.2959	1.0742	0.0148	0.4651	0.1154	0.0029	0.2834	0.0066	4.5075	0.1538	0.0832	0.0017	30%	92%	1608	1886	44	1608	33	1732	28	1615	31	-0.43	Metamorphic	4.9	4.0	1.3	0.26
ap#14.2	*Stubby, rounded, incolor*	*none*	*Core/Rim*	*present*	*Dark Core*	0.3748	0.0046	0.4829	0.0044	24.9233	0.2934	1.2291	0.0165	0.4217	0.1209	0.0025	0.3421	0.0066	5.6986	0.1622	0.0989	0.0017	29%	92%	1897	1968	37	1897	32	1931	24	1907	31	-0.55	Metamorphic	4.2	4.2	1.2	0.28
ap#14.3	*Stubby, rounded, incolor*	*none*	*Core/Rim*	*present*	*Dark Core*	0.3470	0.0036	0.4630	0.0036	22.2435	0.2429	1.0012	0.0105	0.3820	0.1175	0.0022	0.3414	0.0060	5.5277	0.1431	0.0985	0.0014	26%	90%	1893	1917	34	1893	29	1905	22	1899	26	-0.29	Metamorphic	5.7	5.2	1.7	0.30
ap#16.1	*Stubby, rounded, incolor*	*none*	*Core/Rim*	*present*	*Dark Core*	0.3680	0.0036	0.5058	0.0041	25.6074	0.2709	0.8811	0.0090	0.3376	0.1222	0.0026	0.3646	0.0074	6.1424	0.1807	0.1044	0.0015	28%	88%	2004	1988	37	2004	35	1996	25	2007	28	-0.17	Metamorphic	6.0	6.3	2.5	0.41
ap#16.2	*Stubby, rounded, incolor*	*none*	*Core/Rim*	*present*	*Dark Core*	0.4226	0.0044	0.5460	0.0043	31.7784	0.3727	1.2827	0.0143	0.3200	0.1245	0.0025	0.3603	0.0069	6.1833	0.1723	0.1031	0.0016	34%	92%	1983	2021	36	1983	33	2002	24	1983	30	0.00	Metamorphic	4.5	5.5	1.6	0.35
ap#16.3	*Stubby, rounded, incolor*	*none*	*Core/Rim*	*present*	*Dark Core*	0.2742	0.0026	0.4263	0.0027	16.1201	0.1408	0.3634	0.0030	0.3978	0.1260	0.0021	0.3538	0.0054	6.1424	0.1406	0.1018	0.0014	17%	72%	1953	2041	30	1953	26	1996	20	1959	25	-0.30	Metamorphic	11.5	8.8	7.2	0.62

[a]corrected for background and instrumental drift and mass bias fractionation based on primary standard (MAD1).
[b] 2 × internal 2SE uncertainties
[c] rho is the $^{207}Pb/^{206}Pb$ / $^{238}Pb/^{206}U$ error correlation coefficient.
[d] degree of discordance: [1-($^{206}Pb/^{238}Pb$ age / $^{207}Pb/^{206}Pb$ age)] x 100
[e] based on primary standard (MKED1).







U-Th-Pb analyses of apatite reference materials. Strikethrough analyses are not used in age calculation. Tera-Wersserburg of before (above) and after (bellow) 208Pb correction diagrams are shown.

Laboratoire Magmas et Volcans

	Isotopic ratios									^{208}Pb correction									Ages								Element concentration [a]			
Standard	$^{207}Pb^*/^{206}Pb$	±2s [b]	$^{206}Pb^*/^{238}U$	±2s [b]	$^{207}Pb^*/^{235}U$	±2s [b]	$^{208}Pb^*/^{232}Th$	±2s [b]	Rho [c]	$^{207}Pb^*/^{206}Pb$	±2s [b]	$^{206}Pb^*/^{238}U$	±2s [b]	$^{207}Pb^*/^{235}U$	±2s [b]	$^{208}Pb^*/^{232}Th$	±2s [b]	f206	f208	Pbc age	$^{207}Pb/^{206}Pb$	±2s [b]	$^{206}Pb/^{238}U$	±2s [b]	$^{207}Pb/^{235}U$	±2s [b]	$^{208}Pb/^{232}Th$	±2s [b]	Disc. [d]	U	Pb	Th	Th/U
MAD 2																		(%)	(%)	(Ma)			(Ma)		(Ma)		(Ma)		ppm	ppm	ppm	
Sequence 1																																
1	0.1007	0.0024	0.0810	0.0006	1.1240	0.0284	0.0240	0.0001	0.0695	0.0566	0.0014	0.0766	0.0019	0.5972	0.0210	0.0236	0.0006	0.0544	0.0147	474	474	53	476	12	475	13	471	5	0%	21.00	14.91	541.83	25.81
2	0.0927	0.0023	0.0796	0.0006	1.0155	0.0259	0.0243	0.0001	0.0886	0.0566	0.0014	0.0760	0.0020	0.5927	0.0211	0.0240	0.0006	0.0445	0.0117	474	474	53	472	12	473	13	482	5	0%	21.17	15.12	545.96	25.78
3	0.0863	0.0023	0.0792	0.0006	0.9416	0.0251	0.0240	0.0001	0.1774	0.0566	0.0015	0.0763	0.0021	0.5949	0.0227	0.0238	0.0007	0.0367	0.0095	474	474	57	474	13	474	14	475	6	0%	20.16	14.54	528.88	26.24
4	0.0802	0.0019	0.0782	0.0006	0.8658	0.0213	0.0236	0.0001	0.1217	0.0566	0.0013	0.0759	0.0019	0.5919	0.0204	0.0234	0.0006	0.0291	0.0075	474	474	52	472	11	472	13	467	5	0%	20.63	14.65	542.21	26.29
5	0.0777	0.0021	0.0780	0.0007	0.8336	0.0215	0.0238	0.0001	0.2538	0.0566	0.0015	0.0760	0.0021	0.5927	0.0228	0.0237	0.0007	0.0260	0.0066	474	474	58	472	13	473	14	474	5	0%	19.57	14.17	521.35	26.64
6	0.0806	0.0022	0.0786	0.0006	0.8744	0.0233	0.0237	0.0001	0.2578	0.0566	0.0016	0.0763	0.0022	0.5948	0.0237	0.0235	0.0007	0.0296	0.0075	474	474	60	474	13	474	15	469	5	0%	19.35	14.20	524.33	27.10
7	0.0795	0.0019	0.0775	0.0007	0.8491	0.0199	0.0239	0.0001	0.2921	0.0566	0.0014	0.0753	0.0019	0.5874	0.0208	0.0238	0.0006	0.0283	0.0071	474	474	53	468	12	469	13	477	5	0%	19.21	13.95	513.27	26.73
8	0.0855	0.0022	0.0790	0.0006	0.9263	0.0222	0.0239	0.0001	0.3513	0.0566	0.0014	0.0762	0.0020	0.5939	0.0217	0.0237	0.0006	0.0357	0.0093	474	474	55	473	12	473	14	473	5	0%	20.89	14.91	548.22	26.15
9	0.1006	0.0034	0.0797	0.0007	1.1031	0.0409	0.0241	0.0001	-0.0857	0.0566	0.0019	0.0754	0.0026	0.5878	0.0284	0.0237	0.0008	0.0542	0.0141	474	474	72	469	16	469	18	475	5	0%	19.97	14.27	525.24	26.30
10	0.0941	0.0024	0.0807	0.0006	1.0340	0.0269	0.0240	0.0001	0.1101	0.0566	0.0015	0.0770	0.0021	0.6000	0.0225	0.0238	0.0007	0.0463	0.0121	474	474	56	478	12	477	14	473	6	0%	20.38	14.67	537.72	26.39
11	0.1241	0.0053	0.0837	0.0009	1.4447	0.0734	0.0244	0.0001	-0.4809	0.0566	0.0024	0.0767	0.0034	0.5983	0.0369	0.0238	0.0011	0.0833	0.0231	474	474	92	477	20	476	23	475	6	0%	21.10	15.18	538.70	25.53
12	0.0855	0.0021	0.0794	0.0007	0.9228	0.0211	0.0240	0.0001	0.1150	0.0566	0.0014	0.0765	0.0020	0.5967	0.0210	0.0238	0.0006	0.0357	0.0096	474	474	53	475	12	475	13	474	5	0%	21.85	15.18	555.03	25.40
13	0.0783	0.0021	0.0790	0.0007	0.8508	0.0221	0.0240	0.0001	0.2756	0.0566	0.0015	0.0769	0.0022	0.5993	0.0237	0.0238	0.0007	0.0267	0.0067	474	474	59	477	13	477	15	475	5	0%	18.50	13.66	501.34	27.10
14	0.0833	0.0022	0.0791	0.0007	0.9087	0.0237	0.0239	0.0001	0.1922	0.0566	0.0015	0.0765	0.0022	0.5968	0.0232	0.0237	0.0007	0.0329	0.0083	474	474	58	475	13	475	15	472	5	0%	19.58	14.43	532.38	27.20
15	0.0905	0.0023	0.0788	0.0006	0.9825	0.0244	0.0239	0.0001	0.3117	0.0566	0.0014	0.0755	0.0020	0.5887	0.0219	0.0237	0.0006	0.0418	0.0107	474	474	56	469	12	470	14	474	5	0%	19.58	14.12	520.88	26.60
16	0.0905	0.0024	0.0792	0.0007	0.9885	0.0263	0.0239	0.0001	0.1188	0.0566	0.0015	0.0759	0.0021	0.5916	0.0226	0.0236	0.0007	0.0419	0.0109	474	474	57	471	13	472	14	472	5	0%	20.58	14.57	537.45	26.12
17	0.1112	0.0030	0.0810	0.0007	1.2354	0.0351	0.0240	0.0001	-0.0733	0.0566	0.0015	0.0755	0.0022	0.5888	0.0232	0.0235	0.0007	0.0673	0.0178	474	474	59	469	13	470	15	470	5	0%	20.08	14.29	529.38	26.37
18	0.1017	0.0027	0.0813	0.0007	1.1332	0.0309	0.0241	0.0001	0.0343	0.0566	0.0015	0.0767	0.0022	0.5984	0.0233	0.0237	0.0007	0.0556	0.0147	474	474	58	477	13	476	15	473	6	0%	20.57	14.70	541.49	26.32
19	0.1462	0.0067	0.0863	0.0011	1.7003	0.0905	0.0247	0.0002	-0.6847	0.0566	0.0026	0.0767	0.0037	0.5983	0.0398	0.0239	0.0012	0.1105	0.0309	474	474	99	477	22	476	25	479	8	0%	20.59	15.03	529.73	25.72
20	0.0944	0.0022	0.0810	0.0007	1.0546	0.0273	0.0241	0.0001	0.0752	0.0566	0.0013	0.0772	0.0019	0.6022	0.0208	0.0238	0.0006	0.0466	0.0126	474	474	52	480	12	479	13	475	5	0%	21.10	14.84	539.98	25.60
21	0.0807	0.0021	0.0776	0.0007	0.8585	0.0224	0.0236	0.0001	0.1419	0.0566	0.0014	0.0753	0.0020	0.5874	0.0218	0.0235	0.0006	0.0297	0.0073	474	474	55	468	12	469	14	469	5	0%	18.42	13.51	507.70	27.56
22	0.0870	0.0023	0.0784	0.0007	0.9345	0.0254	0.0238	0.0001	0.1130	0.0566	0.0015	0.0755	0.0021	0.5885	0.0226	0.0236	0.0007	0.0375	0.0096	474	474	58	469	13	470	14	472	5	0%	20.47	14.59	542.59	26.51
Sequence 2																																
1	0.1000	0.0025	0.0798	0.0007	1.0971	0.0263	0.0238	0.0001	0.1588	0.0566	0.0014	0.0755	0.0020	0.5889	0.0212	0.0235	0.0006	0.0559	0.0145	474	394	62	468	5	456	12	469	5	-3%	20.15	14.51	535.40	26.57
2	0.0966	0.0027	0.0806	0.0007	1.0741	0.0305	0.0242	0.0001	-0.0137	0.0566	0.0016	0.0767	0.0022	0.5978	0.0238	0.0239	0.0007	0.0460	0.0120	474	581	65	478	6	496	13	477	5	4%	20.27	14.65	533.36	26.31
3	0.1001	0.0026	0.0808	0.0007	1.1163	0.0287	0.0241	0.0001	0.1919	0.0566	0.0015	0.0765	0.0021	0.5965	0.0225	0.0238	0.0007	0.0549	0.0145	474	431	63	475	10	467	12	474	5	-2%	19.87	14.27	520.42	26.19
4	0.0931	0.0024	0.0802	0.0007	1.0272	0.0263	0.0239	0.0001	0.2017	0.0566	0.0015	0.0766	0.0021	0.5973	0.0227	0.0236	0.0007	0.0568	0.0149	474	15	68	470	-1	400	11	470	5	-17%	20.52	14.67	540.55	26.35
5	0.1009	0.0031	0.0800	0.0008	1.1107	0.0362	0.0241	0.0001	-0.0845	0.0566	0.0018	0.0756	0.0025	0.5898	0.0265	0.0238	0.0008	0.0384	0.0100	474	938	68	478	13	566	16	477	6	16%	19.63	14.12	513.59	26.16
6	0.0976	0.0024	0.0799	0.0006	1.0786	0.0280	0.0238	0.0001	0.0223	0.0566	0.0014	0.0759	0.0020	0.5916	0.0215	0.0235	0.0006	0.0573	0.0150	474	227	65	468	0	430	12	469	5	-9%	20.49	14.66	540.65	26.38
7	0.0900	0.0023	0.0797	0.0006	0.9891	0.0247	0.0241	0.0001	0.2611	0.0566	0.0015	0.0764	0.0021	0.5960	0.0223	0.0238	0.0007	0.0378	0.0098	474	582	60	476	9	495	12	477	5	4%	19.69	14.15	515.80	26.20
8	0.0908	0.0021	0.0800	0.0006	1.0006	0.0239	0.0240	0.0001	0.1028	0.0566	0.0013	0.0767	0.0019	0.5977	0.0204	0.0238	0.0006	0.0464	0.0120	474	330	59	474	2	450	11	474	5	-5%	20.87	15.10	551.19	26.41
9	0.0899	0.0021	0.0785	0.0006	0.9734	0.0228	0.0239	0.0001	0.2008	0.0566	0.0013	0.0752	0.0019	0.5866	0.0202	0.0237	0.0006	0.0244	0.0063	474	939	53	475	14	564	13	475	4	16%	20.01	14.24	522.28	26.10
10	0.0947	0.0025	0.0812	0.0007	1.0553	0.0279	0.0241	0.0001	0.1181	0.0566	0.0015	0.0774	0.0022	0.6033	0.0235	0.0238	0.0007	0.0613	0.0160	474	-101	74	473	6	387	11	473	5	-22%	20.51	14.91	544.26	26.54
11	0.0929	0.0024	0.0795	0.0006	1.0173	0.0249	0.0241	0.0001	0.2757	0.0566	0.0014	0.0760	0.0020	0.5923	0.0217	0.0239	0.0006	0.0314	0.0082	474	860	58	478	485	550	14	478	5	13%	20.05	14.32	522.82	26.07
12	0.0948	0.0029	0.0805	0.0007	1.0529	0.0350	0.0241	0.0001	-0.1565	0.0566	0.0018	0.0767	0.0025	0.5981	0.0266	0.0238	0.0008	0.0492	0.0128	474	403	76	475	484	463	14	476	6	-3%	20.31	14.72	536.24	26.40
13	0.1072	0.0028	0.0812	0.0007	1.2066	0.0327	0.0242	0.0001	0.0226	0.0566	0.0015	0.0762	0.0021	0.5940	0.0223	0.0238	0.0007	0.0568	0.0149	474	651	61	476	483	507	13	476	5	6%	19.87	14.40	522.53	26.29
14	0.0972	0.0027	0.0804	0.0007	1.0690	0.0292	0.0240	0.0001	0.0585	0.0566	0.0015	0.0764	0.0022	0.5953	0.0236	0.0237	0.0007	0.0507	0.0133	474	451	67	474	482	470	13	473	5	-1%	20.63	14.85	543.74	26.35
15	0.0906	0.0025	0.0798	0.0007	0.9972	0.0285	0.0238	0.0001	-0.0236	0.0566	0.0015	0.0765	0.0022	0.5961	0.0235	0.0235	0.0007	0.0570	0.0149	474	-136	75	468	475	379	11	468	5	-24%	19.84	14.21	525.85	26.50
16	0.0961	0.0024	0.0804	0.0006	1.0627	0.0258	0.0241	0.0001	0.1067	0.0566	0.0014	0.0764	0.0020	0.5960	0.0212	0.0238	0.0006	0.0505	0.0133	474	414	63	474	8	464	12	475	5	-2%	20.64	14.84	542.17	26.27
17	0.1058	0.0029	0.0806	0.0006	1.1735	0.0322	0.0242	0.0001	0.1164	0.0566	0.0016	0.0757	0.0022	0.5905	0.0235	0.0239	0.0007	0.0418	0.0109	474	1001	61	480	485	581	15	479	5	17%	19.84	14.40	519.32	26.17
18	0.0895	0.0022	0.0804	0.0007	0.9906	0.0242	0.0240	0.0001	0.2212	0.0566	0.0014	0.0771	0.0020	0.6015	0.0215	0.0237	0.0006	0.0563	0.0148	474	-165	70	471	473	378	10	472	5	-25%	20.50	14.71	539.61	26.32
19	0.0904	0.0024	0.0792	0.0007	0.9892	0.0262	0.0241	0.0001	0.1216	0.0566	0.0015	0.0759	0.0021	0.5920	0.0225	0.0238	0.0007	0.0304	0.0079	474	805	61	477	485	538	14	477	5	11%	20.10	14.43	528.02	26.28
20	0.0936	0.0025	0.0805	0.0007	1.0358	0.0285	0.0240	0.0001	-0.0099	0.0566	0.0015	0.0769	0.0022	0.5993	0.0232	0.0238	0.0007	0.0533	0.0140	474	192	69	474	481	428	12	474	5	-11%	20.53	14.77	540.47	26.32
21	0.0994	0.0029	0.0802	0.0007	1.0950	0.0321	0.0240	0.0001	0.0717	0.0566	0.0017	0.0760	0.0023	0.5926	0.0253	0.0237	0.0008	0.0499	0.0131	474	566	72	474	482	490	15	473	6	3%	20.08	14.39	527.59	26.27
22	0.0997	0.0032	0.0808	0.0007	1.1129	0.0377	0.0239	0.0001	-0.0700	0.0566	0.0018	0.0765	0.0026	0.5964	0.0277	0.0236	0.0008	0.0620	0.0163	474	139	83	471	479	418	14	470	6	-13%	20.25	14.58	535.79	26.46
23	0.1134	0.0037	0.0819	0.0008	1.2782	0.0459	0.0242	0.0001	-0.2537	0.0566	0.0019	0.0762	0.0026	0.5942	0.0284	0.0238	0.0008	0.0657	0.0175	474	614	77	476	484	500	16	476	6	5%	20.11	14.53	526.71	26.19
24	0.0930	0.0027	0.0808	0.0007	1.0400	0.0315	0.0242	0.0001	0.1039	0.0566	0.0017	0.0771	0.0024	0.6014	0.0255	0.0239	0.0007	0.0488	0.0128	474	339	72	477	485	454	13	477	6	-5%	20.06	14.52	527.67	26.31
25	0.0988	0.0026	0.0794	0.0007	1.0814	0.0292	0.0238	0.0001	0.0908	0.0566	0.0015	0.0753	0.0021	0.5870	0.0223	0.0235	0.0007	0.0460	0.0120	474	662	64	471	479	505	14	470	5	7%	20.01	14.27	527.23	26.35
26	0.0932	0.0027	0.0802	0.0006	1.0248	0.0293	0.0240	0.0001	0.0450	0.0566	0.0017	0.0766	0.0023	0.5970	0.0253	0.0237	0.0008	0.0506	0.0132	474	282	75	473	481	442	14	473	6	-7%	20.40	14.65	538.38	26.39

																												Element concentration			
Standard	$^{207}Pb^*/^{206}Pb$	±2s	$^{206}Pb^*/^{238}U$	±2s	$^{207}Pb^*/^{235}U$	±2s	$^{208}Pb^*/^{232}Th$	±2s [b]	Rho [c]	$^{207}Pb^*/^{206}Pb$	±2s [b]	$^{206}Pb^*/^{238}U$	±2s [b]	$^{207}Pb^*/^{235}U$	±2s [b]	$^{208}Pb^*/^{232}Th$	±2s [b]	f206	f208	Pbc age	$^{207}Pb/^{206}Pb$	±2s	$^{206}Pb/^{238}U$	±2s	$^{207}Pb/^{235}U$	±2s	$^{208}Pb/^{232}Th$	±2s [b]	Disc. [d]	U	Pb	Th	Th/U
Kovdor																		(%)	(%)	(Ma)			(Ma)		(Ma)		(Ma)		ppm	ppm	ppm	
Sequence 1																																
1	0.3514	0.0069	0.1012	0.0013	4.8887	0.0904	0.0209	0.0001	0.4488	0.0524	0.0013	0.0638	0.0012	0.4609	0.0141	0.0198	0.0003	0.3697	0.0539	380	304	54	398	7	385	10	396	5	-4%	12.55	20.06	850.06	67.74
2	0.2883	0.0040	0.0871	0.0007	3.4521	0.0435	0.0197	0.0001	0.3975	0.0310	0.0005	0.0601	0.0008	0.2566	0.0057	0.0188	0.0002	0.3099	0.0439	380	-1063	53	376	5	232	5	377	4	-62%	20.22	28.10	1299.06	64.24
3	0.3586	0.0054	0.0996	0.0008	4.8587	0.0662	0.0201	0.0001	0.4389	0.0436	0.0009	0.0612	0.0011	0.3684	0.0101	0.0191	0.0002	0.3852	0.0516	380	-132	52	383	6	318	7	382	4	-20%	12.39	20.49	936.45	75.58
4	0.3393	0.0048	0.1000	0.0008	4.6905	0.0628	0.0204	0.0001	0.3782	0.0160	0.0003	0.0617	0.0009	0.1359	0.0032	0.0193	0.0002	0.3826	0.0537	380	-3773	108	386	6	129	3	387	4	-198%	14.81	23.95	1064.55	71.87
5	0.4053	0.0097	0.1207	0.0017	6.7310	0.1404	0.0217	0.0001	0.5156	0.0071	0.0002	0.0644	0.0015	0.0633	0.0024	0.0201	0.0003	0.4662	0.0745	380	-268527	240210	403	9	62	2	402	7	-546%	4.82	8.30	343.54	71.25
Sequence 2																																
1	0.2832	0.0044	0.0857	0.0007	3.3613	0.0484	0.0198	0.0001	0.4707	0.0499	0.0009	0.0610	0.0008	0.4197	0.0096	0.0191	0.0002	0.2876	0.0395	380	188	43	382	5	356	7	382	4	-7%	18.23	25.34	1174.22	64.42
2	0.2892	0.0052	0.0879	0.0008	3.5362	0.0553	0.0200	0.0001	0.4922	0.0439	0.0010	0.0615	0.0010	0.3724	0.0101	0.0192	0.0002	0.3001	0.0416	380	-116	54	385	6	321	7	384	4	-20%	19.00	27.31	1233.52	64.93
3	0.4001	0.0064	0.1049	0.0010	5.7782	0.0851	0.0201	0.0001	0.4549	0.0547	0.0014	0.0600	0.0014	0.4523	0.0157	0.0187	0.0003	0.4282	0.0662	380	400	58	375	8	379	11	375	5	1%	8.49	13.02	588.60	69.37
4	0.3742	0.0057	0.1015	0.0010	5.2222	0.0876	0.0202	0.0001	0.1957	0.0556	0.0014	0.0613	0.0014	0.4704	0.0160	0.0191	0.0002	0.3955	0.0541	380	437	56	384	8	391	11	382	5	2%	11.21	18.44	842.69	75.19
5	0.2819	0.0034	0.0856	0.0006	3.3335	0.0421	0.0199	0.0001	0.2629	0.0459	0.0008	0.0608	0.0008	0.3847	0.0082	0.0190	0.0002	0.2895	0.0428	380	-10	40	381	5	330	6	381	3	-15%	21.08	27.52	1263.17	59.93
6	0.2866	0.0039	0.0865	0.0007	3.4093	0.0454	0.0197	0.0001	0.3532	0.0389	0.0007	0.0604	0.0010	0.3241	0.0080	0.0189	0.0002	0.3012	0.0413	380	-423	49	378	6	285	6	378	4	-33%	21.02	29.40	1380.35	65.66

Standard	$^{207}Pb^*/^{206}Pb$	±2s	$^{206}Pb^*/^{238}U$	±2s	$^{207}Pb^*/^{235}U$	±2s	$^{208}Pb^*/^{232}Th$	±2s [b]	Rho [c]	$^{207}Pb^*/^{206}Pb$	±2s [b]	$^{206}Pb^*/^{238}U$	±2s [b]	$^{207}Pb^*/^{235}U$	±2s [b]	$^{208}Pb^*/^{232}Th$	±2s [b]	f206	f208	Pbc age	$^{207}Pb/^{206}Pb$	±2s	$^{206}Pb/^{238}U$	±2s	$^{207}Pb/^{235}U$	±2s	$^{208}Pb/^{232}Th$	±2s [b]	Disc. [d]	U	Pb	Th	Th/U
Sumé 1																		(%)	(%)	(Ma)			(Ma)		(Ma)		(Ma)		ppm	ppm	ppm	
Sequence 1																																
1	0.1129	0.0016	0.0994	0.0006	1.5461	0.0222	0.0290	0.0001	0.2343	0.0542	0.0010	0.0923	0.0013	0.6904	0.0163	0.0286	0.0003	0.0715	0.0133	568	380	42	569	8	533	10	570	5	-7%	36.66	44.84	1403.10	38.27
2	0.1154	0.0016	0.1009	0.0006	1.6067	0.0215	0.0286	0.0001	0.3232	0.0290	0.0006	0.0906	0.0014	0.3615	0.0089	0.0280	0.0003	0.1022	0.0193	568	-1271	61	559	8	313	7	559	5	-78%	38.78	47.68	1503.70	38.78
3	0.1129	0.0016	0.1011	0.0006	1.5575	0.0214	0.0292	0.0001	0.3294	0.0485	0.0009	0.0932	0.0011	0.6229	0.0136	0.0288	0.0002	0.0779	0.0146	568	122	42	575	7	492	9	574	4	-17%	37.24	45.58	1417.64	38.07
4	0.1018	0.0013	0.0987	0.0005	1.3896	0.0175	0.0289	0.0001	0.2517	0.0473	0.0010	0.0922	0.0017	0.6002	0.0172	0.0284	0.0003	0.0659	0.0148	568	61	51	568	10	477	11	567	7	-19%	62.41	63.82	1960.78	31.42
5	0.0993	0.0013	0.0964	0.0005	1.3193	0.0177	0.0286	0.0001	0.2843	0.0597	0.0012	0.0917	0.0015	0.7540	0.0201	0.0284	0.0003	0.0486	0.0098	568	591	44	566	9	571	12	565	6	1%	54.01	58.54	1870.12	34.63
Sequence 2																																
1	0.1203	0.0017	0.1010	0.0006	1.6872	0.0239	0.0290	0.0001	0.2206	0.0469	0.0009	0.0920	0.0013	0.5942	0.0138	0.0285	0.0003	0.0888	0.0159	568	41	44	567	7	474	9	568	5	-20%	37.58	48.36	1517.98	40.39
2	0.1024	0.0013	0.0974	0.0005	1.3816	0.0174	0.0286	0.0001	0.1820	0.0502	0.0009	0.0912	0.0012	0.6305	0.0134	0.0282	0.0003	0.0633	0.0132	568	201	39	563	7	496	8	562	5	-13%	53.90	58.21	1825.46	33.87
3	0.1149	0.0014	0.0992	0.0006	1.5754	0.0197	0.0286	0.0001	0.3423	0.0463	0.0010	0.0909	0.0016	0.5804	0.0159	0.0281	0.0003	0.0828	0.0159	568	13	49	561	10	465	10	561	6	-21%	41.28	48.69	1541.01	37.33
4	0.1316	0.0018	0.1016	0.0006	1.8441	0.0224	0.0287	0.0001	-0.3411	0.0479	0.0009	0.0913	0.0015	0.6023	0.0153	0.0282	0.0003	0.1013	0.0176	568	91	46	563	9	479	10	562	6	-18%	35.38	46.79	1489.62	42.10
5	0.0891	0.0013	0.0996	0.0007	1.2285	0.0222	0.0299	0.0002	-0.1874	0.0569	0.0033	0.0957	0.0054	0.7501	0.0603	0.0296	0.0010	0.0394	0.0079	568	485

6	0.2132	0.0012	0.4141	0.0019	12.0931	0.0707	0.1138	0.0004	0.2192	0.1346	0.0017	0.3770	0.0045	6.9952	0.1200	0.1075	0.0008	0.0897	0.0554	2076	2159	21	2062	21	2111	15	2064	15	2%	50.09	100.41	669.94	13.38
Sequence 2																																	
1	0.2142	0.0012	0.4077	0.0018	12.0553	0.0682	0.1123	0.0004	0.4206	0.1492	0.0019	0.3769	0.0047	7.7523	0.1385	0.1073	0.0009	0.0754	0.0444	2076	2336	22	2062	22	2203	16	2060	16	6%	49.58	102.10	692.26	13.96
2	0.2157	0.0012	0.4105	0.0019	12.2244	0.0692	0.1134	0.0004	0.7050	0.1548	0.0017	0.3813	0.0041	8.1348	0.1250	0.1086	0.0008	0.0712	0.0421	2076	2399	19	2082	19	2246	14	2085	14	7%	47.67	99.02	661.24	13.87
3	0.2142	0.0012	0.4089	0.0018	12.0936	0.0748	0.1137	0.0005	0.3120	0.1682	0.0020	0.3865	0.0045	8.9597	0.1499	0.1100	0.0008	0.0547	0.0324	2076	2539	20	2107	21	2334	15	2109	15	10%	49.30	101.18	677.85	13.75
4	0.2041	0.0010	0.4083	0.0020	11.5239	0.0657	0.1131	0.0005	0.3183	0.1547	0.0018	0.3847	0.0044	8.1992	0.1327	0.1096	0.0008	0.0578	0.0309	2076	2397	19	2098	21	2253	15	2103	14	7%	60.53	134.69	926.93	15.31
5	0.2141	0.0011	0.4217	0.0021	12.4320	0.0766	0.1170	0.0005	0.3652	0.1648	0.0019	0.3970	0.0047	9.0154	0.1502	0.1129	0.0008	0.0584	0.0348	2076	2504	20	2155	21	2340	15	2163	14	8%	52.17	109.97	713.04	13.67
6	0.2149	0.0012	0.4151	0.0020	12.3157	0.0795	0.1140	0.0005	0.2084	0.1495	0.0017	0.3835	0.0044	7.9001	0.1287	0.1091	0.0007	0.0760	0.0434	2076	2339	20	2093	20	2220	15	2093	14	6%	50.44	108.05	727.57	14.42

Standard	$^{207}Pb^*/^{206}Pb$	**±2s**	$^{206}Pb^*/^{238}U$	**±2s**	$^{207}Pb^*/^{235}U$	**±2s**	$^{208}Pb^*/^{232}Th$	**±2s** [b]	**Rho** [c]	$^{207}Pb^*/^{206}Pb$	**±2s** [b]	$^{206}Pb^*/^{238}U$	**±2s** [b]	$^{207}Pb^*/^{206}U$	**±2s** [b]	$^{208}Pb^*/^{232}Th$	**±2s** [b]	**f206**	**f208**	**Pbc age**	$^{207}Pb/^{206}Pb$	**±2s**	$^{206}Pb/^{238}U$	**±2s**	$^{207}Pb/^{235}U$	**±2s**	$^{208}Pb/^{232}Th$	**±2s** [b]	**Disc.** [d]	**U**	**Pb**	**Th**	**Th/U**
Slyudyanka																		**(%)**	**(%)**	**(Ma)**		**(Ma)**		**(Ma)**		**(Ma)**			**ppm**	**ppm**	**ppm**	
Sequence 1																																
1	0.3587	0.0024	0.1085	0.0006	5.3730	0.0414	0.0593	0.0003	0.2675	0.0721	0.0009	0.0693	0.0009	0.6892	0.0122	0.0216	0.0002	0.3609	0.6361	450	988	26	432	5	532	7	431	3	19%	64.72	18.51	138.29	2.14
2	0.3603	0.0025	0.1094	0.0006	5.4261	0.0409	0.0586	0.0003	0.3487	0.0583	0.0008	0.0685	0.0009	0.5500	0.0105	0.0213	0.0002	0.3739	0.6370	450	539	30	427	5	445	7	425	4	4%	60.80	17.40	136.83	2.25
3	0.3554	0.0025	0.1081	0.0005	5.2474	0.0366	0.0586	0.0003	0.3155	0.0625	0.0008	0.0687	0.0008	0.5911	0.0100	0.0214	0.0002	0.3645	0.6353	450	689	26	428	5	472	6	428	4	9%	65.80	18.14	143.59	2.18
4	0.3659	0.0024	0.1093	0.0006	5.5297	0.0351	0.0594	0.0003	0.3881	0.0516	0.0007	0.0671	0.0008	0.4769	0.0084	0.0208	0.0002	0.3859	0.6492	450	265	29	419	5	396	6	417	4	-6%	61.49	17.38	138.07	2.25
5	0.3569	0.0027	0.1081	0.0006	5.2709	0.0355	0.0582	0.0003	0.2055	0.0720	0.0011	0.0693	0.0010	0.6876	0.0139	0.0216	0.0002	0.3588	0.6286	450	984	30	432	6	531	8	432	4	19%	66.86	18.04	146.36	2.19
Sequence 2																																
1	0.3674	0.0028	0.1065	0.0006	5.4086	0.0464	0.0581	0.0003	0.3371	0.0558	0.0008	0.0656	0.0008	0.5047	0.0093	0.0204	0.0002	0.3845	0.6481	450	444	41	410	5	415	6	408	4	1%	59.29	16.30	132.96	2.24
2	0.3618	0.0027	0.1053	0.0006	5.2680	0.0380	0.0564	0.0003	0.4929	0.0577	0.0007	0.0657	0.0007	0.5229	0.0086	0.0205	0.0002	0.3760	0.6375	450	519	32	410	4	427	6	410	4	4%	59.47	16.35	134.72	2.27
3	0.3634	0.0026	0.1075	0.0005	5.3916	0.0379	0.0582	0.0003	0.1897	0.0501	0.0007	0.0662	0.0009	0.4574	0.0088	0.0206	0.0002	0.3839	0.6463	450	200	50	413	5	382	6	412	4	-8%	59.37	16.45	133.87	2.25
4	0.3631	0.0026	0.1070	0.0007	5.3652	0.0472	0.0579	0.0003	0.2789	0.0512	0.0008	0.0660	0.0010	0.4663	0.0101	0.0205	0.0002	0.3827	0.6451	450	252	52	412	6	389	7	410	4	-6%	61.60	16.98	138.91	2.26
5	0.3610	0.0041	0.1070	0.0009	5.2458	0.0615	0.0571	0.0004	0.3921	0.0605	0.0011	0.0671	0.0011	0.5590	0.0134	0.0210	0.0003	0.3730	0.3730	450	619	50	419	7	451	9	420	6	7%	62.09	16.76	141.87	2.28
6	0.3629	0.0030	0.1106	0.0007	5.5605	0.0443	0.0586	0.0003	0.4746	0.0668	0.0011	0.0696	0.0011	0.6409	0.0148	0.0217	0.0002	0.3704	0.3704	450	831	44	434	7	503	9	434	4	14%	59.40	16.88	135.68	2.28

[a] *corrected for background, instrumental drift and mass bias fractionation based on primary stantard (MKED1).*

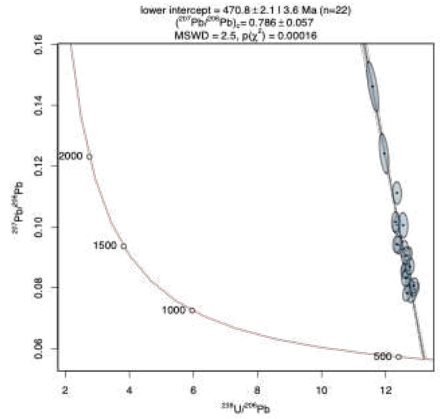
[b] *2 × internal 2SE uncertainities*

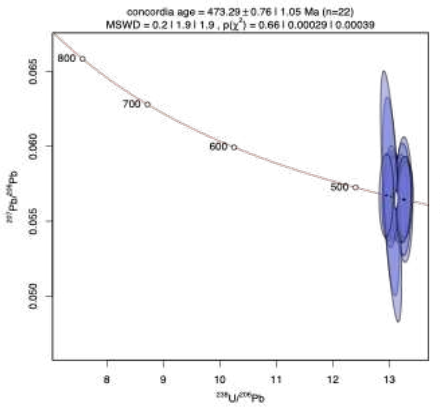
[c] *rho is the $^{207}Pb/^{235}U/^{206}Pb/^{238}U$ error correlation coefficient.*

[d] *degree of discordance: [1-($^{206}Pb/^{238}Pb$ age / $^{207}Pb/^{206}Pb$ age)] x 100*

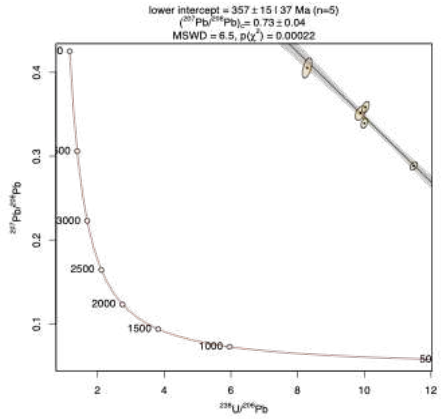
[e] *based on primary standard (MKED1).*

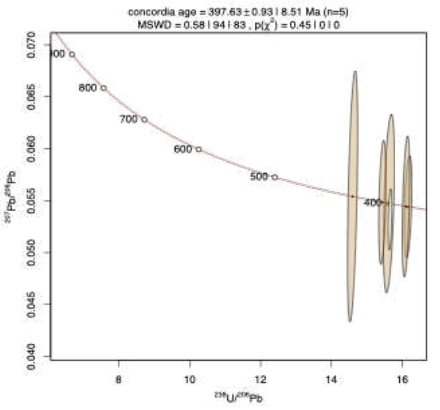
MAD 1



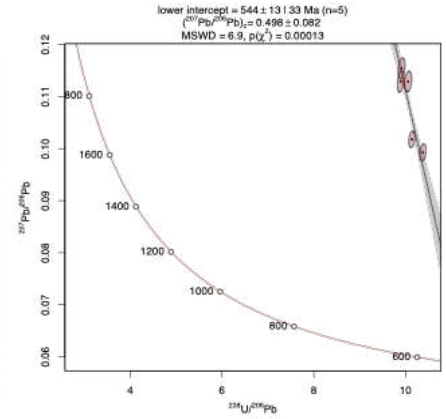


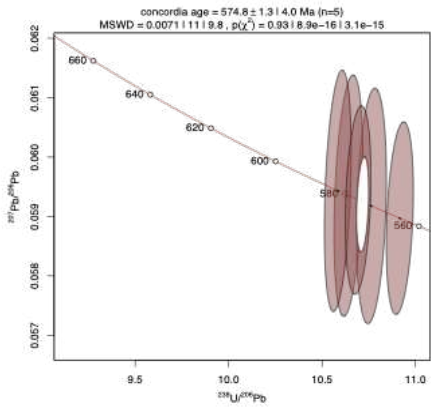
Kovdor



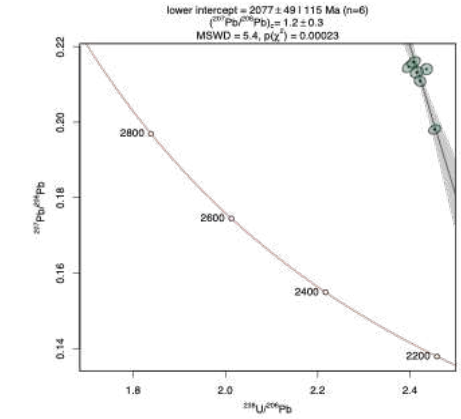


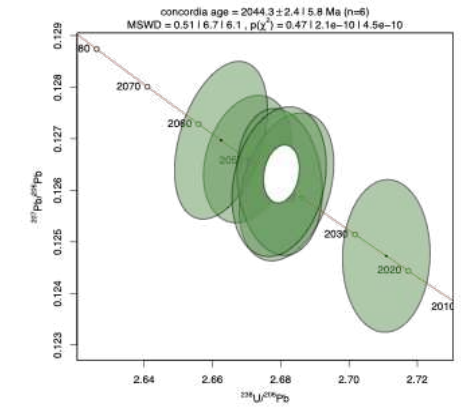
Sumé 1



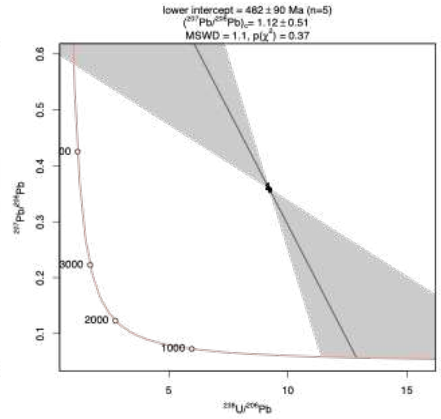


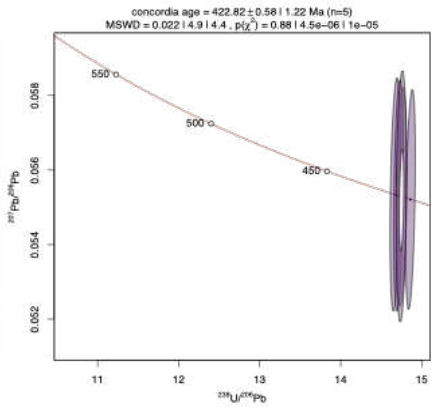
BRZ1



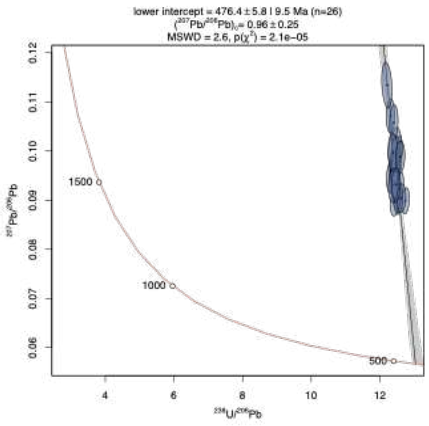


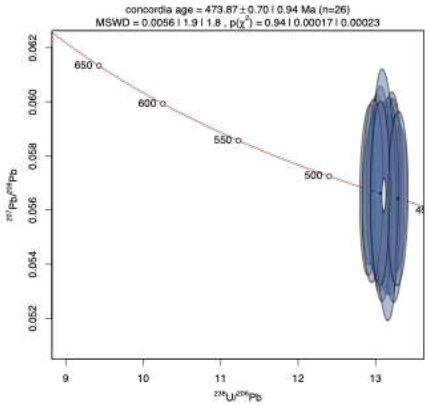
Slyudyanka



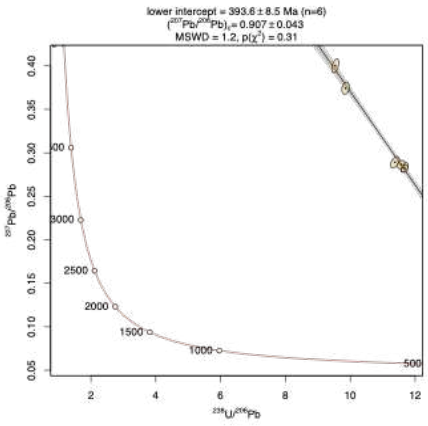


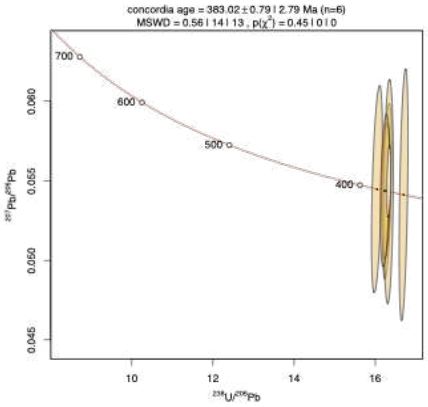
MAD 1



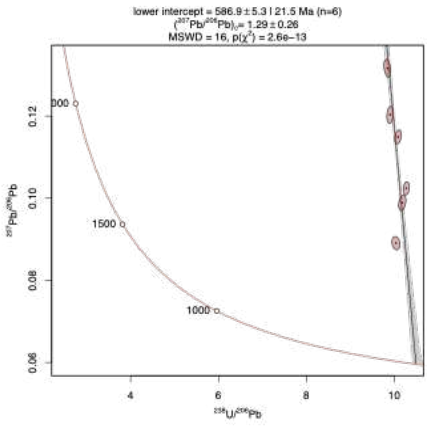


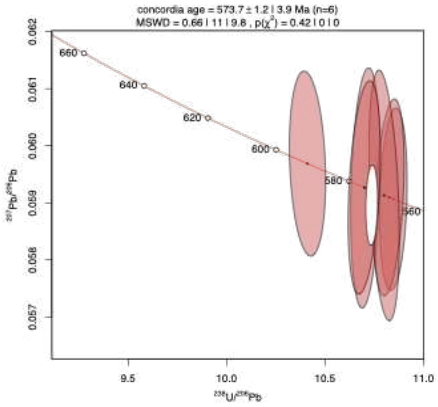
Kovdor



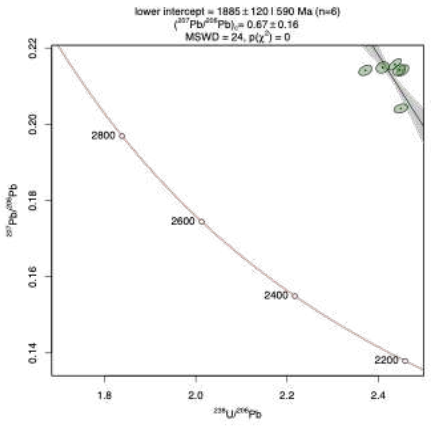


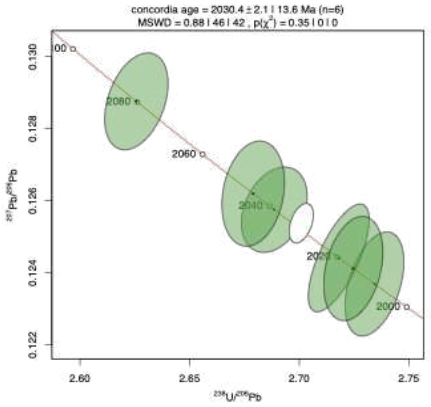
Sumé 1



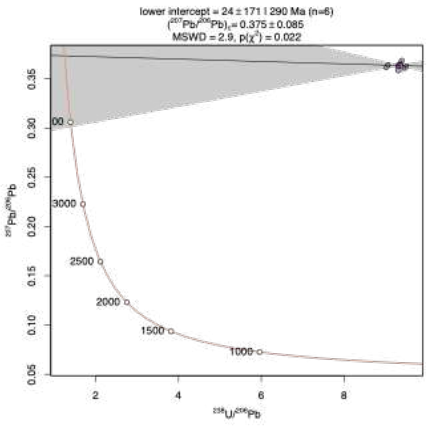


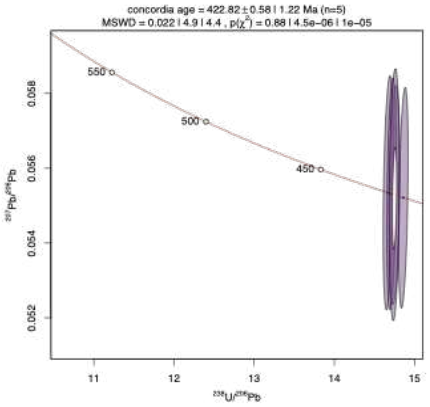
BRZ1





Slyudyanka





U-Th-Pb analyses of titanite grains from Caatinga-Lamim complex (CM44B and CM49). Strikethrough analyses are not used in age calculations due the its texture complexity or small spacial resolution.

Laboratoire Magmas et Volcans

CM44B

Spot num. analysis	Optical features	Inclusions	Texture BSE	Domain BSE	Isotopic ratios $^{207}Pb^*/^{206}Pb$	±2s [b]	$^{206}Pb^*/^{238}U$	±2s [b]	$^{207}Pb^*/^{235}U$	±2s [b]	Rho[c]	Ages $^{207}Pb/^{206}Pb$	±2s [b] (Ma)	$^{206}Pb/^{238}U$	±2s [b] (Ma)	$^{207}Pb/^{235}U$	±2s [b] (Ma)	Disc.[d]	Age meaning	Element concentration [e] U ppm	Pb ppm	Th ppm	Th/U
~~*Ttn#1*~~	~~*Prismatic, incolor, associated with biotie and apatite*~~	~~*none*~~	~~*Homogeneous*~~	~~*Light*~~	~~0.2999~~	~~0.0088~~	~~0.3692~~	~~0.0059~~	~~15.0354~~	~~0.5091~~	~~0.4769~~	~~3454~~	~~45~~	~~1906~~	~~28~~	~~2807~~	~~32~~	42	~~Metamorphic~~	~~0.8~~	~~2.8~~	~~3.1~~	~~0.32~~
Ttn#2	*Prismatic, incolor, associated with biotie and apatite*	*none*	*Homogeneous*	*Light*	0.1340	0.0017	0.3829	0.0036	7.0785	0.0894	0.4174	2147	22	2090	17	2120	11	3	Igneous	45.8	3.7	15.2	0.32
Ttn#3	*Prismatic, incolor, associated with biotie and apatite*	*none*	*Homogeneous*	*Light*	0.1329	0.0017	0.3743	0.0041	6.8711	0.0966	0.4969	2133	22	2049	19	2094	13	4	Igneous	39.2	2.5	9.9	0.24
~~*Ttn#4*~~	~~*Prismatic, incolor, associated with biotie and apatite*~~	~~*none*~~	~~*Homogeneous*~~	~~*Light*~~	~~0.1451~~	~~0.0028~~	~~0.3819~~	~~0.0045~~	~~7.6417~~	~~0.1545~~	~~0.3195~~	~~2282~~	~~34~~	~~2084~~	~~21~~	~~2187~~	~~18~~	9	~~Metamorphic~~	~~15.0~~	~~1.1~~	~~2.7~~	~~0.17~~
Ttn#5	*Prismatic, incolor, associated with biotie and apatite*	*none*	*Homogeneous*	*Light*	0.1309	0.0015	0.3892	0.0041	7.0398	0.0971	0.5956	2106	20	2118	19	2115	12	-1	Igneous	56.0	4.3	19.6	0.32
Ttn#6	*Prismatic, incolor, associated with biotie and apatite*	*none*	*Homogeneous*	*Light*	0.1358	0.0019	0.3399	0.0047	6.3741	0.1181	0.6540	2172	24	1885	22	2026	16	13	Metamorphic	43.8	3.5	15.2	0.32
Ttn#7	*Prismatic, brownish, associated with biotie*	*none*	*Oscilatory zoning*	*Dark*	0.1376	0.0019	0.3643	0.0042	6.8827	0.1055	0.5062	2194	24	2002	20	2095	14	9	Igneous	208.8	22.7	123.1	0.47
Ttn#8	*Prismatic, brownish, associated with biotie*	*none*	*Oscilatory zoning*	*Dark*	0.1374	0.0014	0.3662	0.0041	6.9246	0.0994	0.6951	2192	18	2011	19	2101	13	8	Igneous	153.7	17.1	88.6	0.50
Ttn#9	*Prismatic, brownish, associated with biotie*	*none*	*Oscilatory zoning*	*Light*	0.1459	0.0026	0.3486	0.0042	6.9892	0.1372	0.4173	2293	31	1927	20	2108	18	16	Igneous	43.7	3.3	11.9	0.26
Ttn#10	*Prismatic, brownish, associated with biotie*	*biotite*	*Sector zoned*	*Dark*	0.1379	0.0020	0.3555	0.0041	6.7342	0.1087	0.5139	2196	25	1960	20	2075	14	11	Igneous	67.5	4.9	21.4	0.31
Ttn#11	*Rounded, brownish, isolated*	*none*	*Sector zoned*	*Dark*	0.1375	0.0012	0.3930	0.0039	7.4318	0.0836	0.6768	2194	15	2136	18	2164	10	3	Igneous	214.8	26.3	125.8	0.59
Ttn#12	*Rounded, brownish, isolated*	*none*	*Sector zoned*	*Dark*	0.1333	0.0014	0.3746	0.0037	6.8728	0.0860	0.5796	2139	18	2050	17	2095	11	4	Igneous	151.2	12.9	62.9	0.42
Ttn#13	*Rounded, brownish, isolated*	*none*	*Sector zoned*	*Dark*	0.1355	0.0013	0.3978	0.0056	7.4257	0.1229	0.8219	2169	17	2158	26	2163	15	0	Igneous	152.5	22.0	106.5	0.69
Ttn#14	*Rounded, brownish, isolated*	*none*	*Sector zoned*	*Dark*	0.1342	0.0012	0.3851	0.0041	7.1228	0.0843	0.6548	2151	16	2100	19	2126	11	2	Igneous	152.7	19.1	94.9	0.60
Ttn#15	*Prismatic, brownish, associated with biotie and oxide*	*oxide*	*Homogeneous*	*Dark*	0.1325	0.0016	0.3788	0.0038	6.9227	0.0924	0.5002	2128	21	2070	18	2101	12	3	Igneous	63.5	3.9	16.5	0.25
Ttn#16	*Prismatic, brownish, associated with biotie and oxide*	*oxide*	*Homogeneous*	*Dark*	0.1320	0.0014	0.3872	0.0040	7.0428	0.0945	0.6008	2122	19	2109	19	2115	12	1	Igneous	74.0	5.4	24.5	0.32
Ttn#17	*Prismatic, brownish, associated with biotie and oxide*	*none*	*Homogeneous*	*Dark*	0.1333	0.0016	0.3704	0.0039	6.8046	0.0975	0.5794	2138	22	2031	19	2085	13	5	Igneous	69.2	4.4	19.5	0.27
Ttn#18	*Prismatic, brownish, associated with biotie and oxide*	*none*	*Homogeneous*	*Dark*	0.1343	0.0016	0.3799	0.0040	7.0372	0.0919	0.5063	2153	21	2076	18	2115	12	4	Igneous	80.1	6.5	29.7	0.36
Ttn#19	*Prismatic, brownish, associated with biotie and oxide*	*none*	*Homogeneous*	*Dark*	0.1377	0.0015	0.3709	0.0045	7.0406	0.1036	0.6657	2196	20	2033	21	2115	13	7	Igneous	179.3	19.3	84.6	0.43
Ttn#20	*Prismatic, incolor, associated with biotie*	*none*	*Homogeneous*	*Light*	0.1492	0.0029	0.3555	0.0045	7.3029	0.1445	0.3752	2329	33	1960	22	2146	18	16	Metamorphic	53.9	5.7	19.7	0.34
Ttn#21	*Prismatic, incolor, associated with biotie*	*biotite*	*Homogeneous*	*Light*	0.3041	0.0080	0.5097	0.0115	21.4398	0.8937	0.6908	3479	40	2653	49	3143	40	24	Metamorphic	14.1	5.8	2.8	0.20
Ttn#22	*Prismatic, incolor, associated with biotie*	*none*	*Homogeneous*	*Light*	0.1719	0.0050	0.3905	0.0066	9.1979	0.2680	0.3208	2566	49	2124	31	2353	27	17	Metamorphic	9.6	0.9	1.2	0.12
Ttn#23	*Prismatic, incolor, associated with biotie and apatite*	*none*	*Homogeneous*	*Light*	0.1594	0.0035	0.3709	0.0052	8.1186	0.1888	0.3793	2442	38	2033	24	2242	21	17	Metamorphic	13.9	1.0	1.9	0.14
Ttn#24	*Prismatic, incolor, associated with biotie and apatite*	*none*	*Homogeneous*	*Light*	0.1608	0.0041	0.3444	0.0052	7.6100	0.1973	0.3302	2458	43	1907	25	2184	24	22	Metamorphic	12.4	0.9	3.3	0.27
Ttn#25	*Prismatic, incolor, associated with biotie*	*none*	*Homogeneous*	*Light*	0.1433	0.0030	0.3367	0.0045	6.6510	0.1449	0.3928	2257	37	1870	22	2063	19	17	Metamorphic	17.0	0.8	1.0	0.06
Ttn#26	*Prismatic, incolor, associated with biotie*	*none*	*Homogeneous*	*Light*	0.1554	0.0050	0.3395	0.0057	7.2900	0.2467	0.3189	2397	55	1884	28	2142	30	21	Metamorphic	8.7	0.6	0.5	0.06
~~*Ttn#27*~~	~~*Prismatic, incolor, associated with biotie*~~	~~*none*~~	~~*Homogeneous*~~	~~*Light*~~	~~0.1532~~	~~0.0042~~	~~0.2439~~	~~0.0053~~	~~5.1202~~	~~0.1615~~	~~0.5508~~	~~2359~~	~~47~~	~~1406~~	~~27~~	~~1833~~	~~27~~	40	~~Metamorphic~~	~~13.7~~	~~0.6~~	~~0.7~~	~~0.05~~
Ttn#28	*Prismatic, incolor, associated with biotie*	*biotite*	*Homogeneous*	*Light*	0.1547	0.0038	0.3517	0.0049	7.4955	0.1854	0.1958	2385	43	1942	23	2168	22	19	Metamorphic	11.7	0.8	1.8	0.14
Ttn#29	*Prismatic, incolor, associated with biotie*	*none*	*Homogeneous*	*Light*	0.1573	0.0034	0.3630	0.0052	7.8748	0.1849	0.3988	2421	37	1996	24	2212	21	18	Metamorphic	12.0	0.8	1.4	0.11
Ttn#30	*Prismatic, brownish, associated with biotite*	*none*	*Homogeneous*	*Light*	0.1395	0.0020	0.3788	0.0045	7.2774	0.1168	0.5441	2216	25	2070	21	2145	14	7	Igneous	46.0	3.5	13.9	0.29
Ttn#31	*Prismatic, brownish, associated with biotite*	*none*	*Homogeneous*	*Light*	0.1296	0.0014	0.4045	0.0041	7.2400	0.0955	0.5958	2091	19	2189	19	2141	12	-5	Igneous	150.1	17.7	72.3	0.43
Ttn#32	*Prismatic, brownish, associated with biotite*	*none*	*Homogeneous*	*Light*	0.1312	0.0017	0.4117	0.0049	7.4602	0.1210	0.5876	2111	24	2223	22	2167	15	-5	Igneous	90.3	9.3	34.5	0.36
Ttn#33	*Prismatic, brownish, associated with oxide*	*none*	*Homogeneous*	*Light*	0.1268	0.0014	0.4051	0.0043	7.0935	0.0947	0.5743	2052	20	2192	20	2122	12	-7	Igneous	119.4	11.2	46.9	0.39
Ttn#34	*Rounded, brownish, associated oxide*	*none*	*Sector zoned*	*Light*	0.1270	0.0016	0.4214	0.0046	7.3816	0.1040	0.5936	2056	21	2267	21	2158	13	-10	Igneous	405.0	46.6	220.5	0.55
Ttn#35	*Rounded, brownish, associated oxide*	*none*	*Sector zoned*	*Light*	0.1271	0.0009	0.4250	0.0041	7.4527	0.0738	0.7218	2057	13	2282	19	2167	9	-11	Igneous	335.6	43.8	200.9	0.61
Ttn#36	*Rounded, brownish, associated oxide*	*none*	*Sector zoned*	*Light*	0.1290	0.0010	0.4189	0.0036	7.4633	0.0734	0.6887	2083	13	2255	16	2168	9	-8	Igneous	425.3	63.9	304.5	0.72
Ttn#37	*Rounded, brownish, associated oxide*	*none*	*Sector zoned*	*Light*	0.1319	0.0009	0.3615	0.0030	6.5692	0.0617	0.7004	2122	13	1989	14	2055	8	6	Igneous	421.2	40.9	217.8	0.52
Ttn#38	*Rounded, brownish, associated oxide*	*none*	*Sector zoned*	*Dark*	0.1286	0.0012	0.3777	0.0039	6.7109	0.0748	0.6332	2076	16	2066	18	2073	10	0	Igneous	179.6	12.8	57.0	0.32
Ttn#39	*Rounded, brownish, associated oxide*	*none*	*Sector zoned*	*Light*	0.1252	0.0009	0.3764	0.0032	6.5310	0.0616	0.7023	2030	12	2059	15	2049	8	-1	Recryst.?	445.1	62.7	328.0	0.74
Ttn#40	*Rounded, brownish, associated oxide*	*none*	*Sector zoned*	*Light*	0.1222	0.0009	0.3773	0.0036	6.3945	0.0690	0.7094	1987	14	2063	17	2031	9	-4	Recryst.?	358.7	31.6	161.9	0.45
Ttn#41	*Rounded, brownish, associated oxide*	*none*	*Sector zoned*	*Light*	0.1207	0.0009	0.3863	0.0042	6.4714	0.0752	0.7822	1965	13	2105	19	2041	10	-7	Recryst.?	342.9	34.7	175.9	0.51
Ttn#42	*Prismatic, incolor, associated with biotie and apatite*	*none*	*Homogeneous*	*Light*	0.1692	0.0039	0.3858	0.0059	9.0398	0.2671	0.6344	2538	39	2103	28	2337	27	17	Metamorphic	16.8	2.0	2.2	0.13
Ttn#43	*Prismatic, incolor, associated with biotie and apatite*	*none*	*Homogeneous*	*Light*	0.2445	0.0083	0.4373	0.0093	14.7775	0.6053	0.3088	3134	53	2336	42	2791	37	25	Metamorphic	19.94	6.89	4.77	0.17
~~*Ttn#44*~~	~~*Prismatic, incolor, associated with biotie and apatite*~~	~~*quartz*~~	~~*Homogeneous*~~	~~*Light*~~	~~0.1367~~	~~0.0015~~	~~0.3769~~	~~0.0037~~	~~7.1034~~	~~0.1238~~	~~0.6207~~	~~2182~~	~~19~~	~~2061~~	~~17~~	~~2123~~	~~16~~	6	~~Metamorphic~~	~~166.27~~	~~18.79~~	~~81.93~~	~~0.40~~
Ttn#45	*Rounded, brownish, associated with biotite*	*none*	*Sector zoned*	*Light*	0.1356	0.0014	0.3508	0.0030	6.5609	0.1010	0.4607	2170	18	1938	14	2052	14	11	Igneous	188.48	26.62	132.30	0.63
Ttn#46	*Rounded, brownish, associated with biotite*	*none*	*Sector zoned*	*Light*	0.1325	0.0013	0.3788	0.0036	6.8579	0.1223	0.6336	2129	18	2070	17	2091	16	3	Igneous	304.02	35.48	173.63	0.55
Ttn#47	*Rounded, brownish, associated with biotite*	*none*	*Sector zoned*	*Light*	0.1321	0.0011	0.3742	0.0040	6.8410	0.1116	0.7659	2125	15	2049	19	2089	15	4	Igneous	250.73	31.68	155.22	0.61
~~*Ttn#48*~~	~~*Incolor, associated with biotie and apatite*~~	~~*biotite*~~	~~*Homogeneous*~~	~~*Light*~~	~~0.1896~~	~~0.0046~~	~~0.3215~~	~~0.0049~~	~~8.2693~~	~~0.2454~~	~~0.4545~~	~~2721~~	~~40~~	~~1796~~	~~24~~	~~2255~~	~~27~~	34	~~Metamorphic~~	~~17.00~~	~~2.09~~	~~7.13~~	~~0.40~~
Ttn#49	*Incolor, associated with biotie and apatite*	*biotite*	*Homogeneous*	*Light*	0.1710	0.0039	0.3576	0.0058	8.2920	0.1923	0.3945	2558	39	1970	28	2261	21	23	Metamorphic	20.14	2.17	3.50	0.16
~~*Ttn#50*~~	~~*Incolor, associated with biotie and apatite*~~	~~*none*~~	~~*Homogeneous*~~	~~*Light*~~	~~0.4677~~	~~0.0097~~	~~0.6925~~	~~0.0143~~	~~44.1890~~	~~1.2912~~	~~0.5029~~	~~4134~~	~~31~~	~~3387~~	~~55~~	~~3862~~	~~30~~	18	~~Metamorphic~~	~~7.58~~	~~8.95~~	~~1.47~~	~~0.18~~
~~*Ttn#51*~~	~~*Incolor, associated with biotie and apatite*~~	~~*biotite*~~	~~*Homogeneous*~~	~~*Light*~~	~~0.2207~~	~~0.0055~~	~~0.3698~~	~~0.0057~~	~~11.1419~~	~~0.3662~~	~~0.4706~~	~~2974~~	~~40~~	~~2027~~	~~27~~	~~2525~~	~~31~~	32	~~Metamorphic~~	~~21.25~~	~~5.05~~	~~7.03~~	~~0.32~~
Ttn#52	*Rounded, brownish, associated with biotite*	*none*	*Sector zoned*	*Light*	0.1331	0.0011	0.3868	0.0034	7.0575	0.1091	0.6294	2137	14	2108	16	2117	14	1	Igneous	304.65	45.30	218.41	0.66
Ttn#53	*Rounded, brownish, associated with biotite*	*none*	*Sector zoned*	*Light*	0.1338	0.0011	0.3834	0.0029	7.0192	0.0884	0.3044	2146	14	2092	14	2113	11	3	Igneous	270.85	37.10	182.72	0.65

CM49

Sample	Optical features	Inclusions	Texture BSE	Domain BSE	$^{207}Pb^*/^{206}Pb$	±2s	$^{206}Pb^*/^{238}U$	±2s	$^{207}Pb^*/^{235}U$	±2s	Rho[c]	$^{207}Pb/^{206}Pb$	±2s (Ma)	$^{206}Pb/^{238}U$	±2s (Ma)	$^{207}Pb/^{235}U$	±2s (Ma)	Conc.[d]	Age meaning	Element concentration U ppm	Pb ppm	Th ppm	Th/U
Ttn#1	*Prismatic, incolor, associated with biotite*	*none*	*Patchy zoned*	*Light*	0.1512	0.0033	0.3670	0.0046	7.6449	0.1648	0.1990	2349	18	2014	22	2187	19	14	Metamorphic	24.04	3.28	15.04	0.61
Ttn#2	*Prismatic, incolor, associated with biotite*	*none*	*Patchy zoned*	*Light*	0.1384	0.0020	0.3674	0.0042	7.0123	0.1144	0.2375	2202	13	2017	20	2111	15	8	Metamorphic	75.46	6.86	31.63	0.37
Ttn#3	*Prismatic, incolor, associated with biotite*	*none*	*Patchy zoned*	*Light*	0.1415	0.0024	0.3615	0.0050	7.0470	0.1365	0.1970	2239	14	1988	24	2114	17	11	Metamorphic	73.11	7.07	31.91	0.32
Ttn#4	*Prismatic, incolor, associated with biotite*	*none*	*Patchy zoned*	*Light*	0.1396	0.0020	0.3590	0.0038	6.9017	0.1022	0.2958	2217	12	1978	18	2097	13	11	Metamorphic	109.92	12.82	66.43	0.35
Ttn#5	*Prismatic, incolor, associated with biotite*	*none*	*Patchy zoned*	*Light*	0.1434	0.0024	0.3760	0.0045	7.4227	0.1311	0.2614	2267	14	2057	21	2161	16	9	Metamorphic	75.73	13.94	72.05	0.56
Ttn#6	*Prismatic, incolor, associated with biotite*	*none*	*Patchy zoned*	*Light*	0.1381	0.0021	0.3639	0.0037	6.9266	0.1125	0.2643	2198	13	2000	17	2101	14	9	Metamorphic	93.04	9.53	46.46	0.40
Ttn#7	*Prismatic, incolor, associated with biotite*	*biotite*	*Patchy zoned*	*Light*	0.1454	0.0029	0.3860	0.0056	7.7304	0.1613	0.2950	2285	17	2103	26	2197	19	8	Metamorphic	13.89	1.10	3.86	0.25
Ttn#8	*Prismatic, incolor, associated with biotite*	*biotite*	*Patchy zoned*	*Dark*	0.2111	0.0070	0.4325	0.0080	12.5169	0.4009	0.3039	2894	27	2316	36	2638	31	20	Igneous	3.11	0.75	1.94	0.58
Ttn#9	*Prismatic, incolor, associated with biotite*	*biotite*	*Patchy zoned*	*Dark*	0.2327	0.0105	0.4426	0.0125	14.1570	0.7152	0.1045	3036	36	2360	56	2740	48	22	Igneous	2.20	0.49	0.81	0.35
~~*Ttn#10*~~	~~*Prismatic, incolor, associated with biotite*~~	~~*none*~~	~~*Patchy zoned*~~	~~*Dark*~~	~~0.1632~~	~~0.0053~~	~~0.1450~~	~~0.0109~~	~~10.0327~~	~~0.4360~~	~~0.2873~~	~~2475~~	~~27~~	~~2370~~	~~44~~	~~2427~~	~~40~~	4	~~Inherited?~~	~~0.98~~	~~1.11~~	~~3.10~~	~~0.35~~
Ttn#11	*Prismatic, incolor, associated with biotite*	*none*	*Patchy zoned*	*Light*	0.1367	0.0020	0.3857	0.0040	7.2781	0.1223	0.1959	2185	13	2102	19	2144	15	4	Metamorphic	37.12	2.49	9.78	0.27
Ttn#12	*Prismatic, incolor, associated with biotite and amphibole*	*none*	*Patchy zoned*	*Light*	0.2449	0.0092	0.4360	0.0108	14.6257	0.5385	0.3544	3127	31	2331	49	2781	35	25	Metamorphic	3.19	0.95	1.70	0.54
Ttn#13	*Prismatic, incolor, associated with biotite*	*none*	*Core/Rim*	*Light*	0.1455	0.0026	0.3843	0.0047	7.7044	0.1411	0.3086	2287	15	2096	22	2194	17	8	Metamorphic	36.63	2.23	7.02	0.19
Ttn#14	*Prismatic, incolor, associated with biotite*	*none*	*Core/Rim*	*Dark*	0.1642	0.0036	0.4167	0.0076	9.4173	0.2409	0.2188	2491	19	2245	35	2375	24	10	Igneous	14.05	2.52	8.95	0.64
Ttn#15	*Prismatic, incolor, associated with biotite*	*none*	*Core/Rim*	*Light*	0.1392	0.0018	0.3802	0.0043	7.2865	0.1078	0.2682	2213	11	2077	20	2146	13	6	Metamorphic	66.03	4.87	20.60	0.31

Ttn#16	*Prismatic, incolor, associated with biotite*	*none*	*Patchy zoned*	*Dark*	0.1937	0.0060	0.4310	0.0078	11.4475	0.3311	0.3749	2755	25	2311	35	2554	27	16	Igneous	8.09	2.69	9.19	1.13
Ttn#17	*Prismatic, incolor, associated with biotite*	*none*	*Patchy zoned*	*Light*	0.1418	0.0024	0.3847	0.0051	7.5154	0.1479	0.1886	2243	14	2098	24	2172	17	6	Metamorphic	40.03	3.75	14.83	0.37
Ttn#18	*Prismatic, incolor, associated with biotite*	*none*	*Patchy zoned*	*Dark*	0.1884	0.0056	0.4090	0.0074	10.5766	0.3514	0.1038	2714	25	2209	34	2478	31	19	Igneous	8.64	2.25	7.59	0.89
Ttn#19	*Prismatic, incolor, associated with biotite and amphibole*	*biotite*	*Patchy zoned*	*Light*	0.1695	0.0047	0.3850	0.0068	9.0223	0.2878	0.1762	2539	24	2098	31	2335	28	17	Metamorphic	9.88	1.00	0.51	0.05
Ttn#20	*Prismatic, incolor, associated with biotite and amphibole*	*biotite*	*Patchy zoned*	*Light*	0.1475	0.0040	0.3786	0.0056	7.7128	0.2132	0.2374	2307	24	2069	26	2194	25	10	Metamorphic	14.83	1.11	1.12	0.07
Ttn#21	*Prismatic, incolor, associated with biotite and amphibole*	*none*	*Patchy zoned*	*Light*	0.1140	0.0015	0.3570	0.0041	5.6183	0.0868	0.2292	1861	12	1967	20	1918	14	-6	Metamorphic	61.43	2.55	9.65	0.16
Ttn#22	*Prismatic, incolor, associated with biotite and amphibole*	*none*	*Patchy zoned*	*Light*	0.1265	0.0027	0.3606	0.0052	6.2991	0.1394	0.2759	2043	19	1984	24	2015	20	3	Metamorphic	22.25	1.38	2.26	0.10
Ttn#23	*Prismatic, incolor, associated with biotite and amphibole*	*none*	*Patchy zoned*	*Light*	0.1180	0.0021	0.3657	0.0048	5.9451	0.1091	0.3078	1920	16	2008	22	1965	16	-5	Metamorphic	33.43	1.51	3.50	0.11
Ttn#24	*Prismatic, incolor, associated with biotite and amphibole*	*none*	*Patchy zoned*	*Light/Dark*	0.1335	0.0025	0.3738	0.0051	6.8483	0.1453	0.1962	2136	17	2046	24	2090	19	4	Metamorphic	28.70	2.06	2.98	0.10
Ttn#25	*Prismatic, incolor, associated with biotite and amphibole*	*none*	*Patchy zoned*	*Light*	0.1612	0.0028	0.3727	0.0050	8.3610	0.1691	0.1349	2466	14	2041	23	2268	18	17	Metamorphic	27.18	1.60	3.40	0.12
Ttn#26	*Prismatic, incolor, associated with amphibole*	*none*	*Patchy zoned*	*Dark*	0.1596	0.0030	0.3963	0.0059	8.7747	0.1967	0.0900	2445	15	2151	27	2311	20	12	Igneous	25.60	1.41	2.56	0.10
Ttn#27	*Prismatic, incolor, associated with amphibole*	*none*	*Patchy zoned*	*Dark*	0.1940	0.0044	0.4209	0.0079	11.3112	0.2794	0.2966	2768	19	2264	35	2545	23	18	Igneous	13.22	1.57	0.48	0.03
Ttn#28	*Prismatic, incolor, associated with amphibole*	*none*	*Patchy zoned*	*Light/Dark*	0.1523	0.0034	0.3864	0.0060	8.1388	0.2103	0.0551	2361	19	2105	28	2241	23	11	Metamorphic	21.24	1.11	1.42	0.06
~~***Ttn#29***~~	~~*Prismatic, incolor, associated with amphibole*~~	~~*none*~~	~~*Patchy zoned*~~	~~*Light*~~	~~0.1694~~	~~0.0036~~	~~0.3322~~	~~0.0040~~	~~7.3592~~	~~0.1700~~	~~0.3172~~	~~2450~~	~~19~~	~~1848~~	~~24~~	~~2150~~	~~21~~	25	~~Metamorphic~~	~~18.60~~	~~1.16~~	~~1.24~~	~~0.07~~
Ttn#30	*Prismatic, incolor, associated with biotite and amphibole*	*none*	*Patchy zoned*	*Light*	0.1784	0.0054	0.3910	0.0075	9.6494	0.3133	0.1869	2624	25	2127	35	2394	31	19	Metamorphic	8.17	1.04	1.35	0.16
Ttn#31	*Prismatic, incolor, associated with biotite and amphibole*	*none*	*Patchy zoned*	*Dark*	0.1867	0.0051	0.4000	0.0079	10.2848	0.3138	-0.0531	2698	23	2167	37	2453	28	20	Igneous	11.77	1.32	1.57	0.13
Ttn#32	*Prismatic, incolor, associated with biotite and amphibole*	*none*	*Patchy zoned*	*Dark*	0.1730	0.0045	0.4072	0.0072	9.6746	0.2553	0.3187	2577	21	2200	33	2399	24	15	Igneous	14.23	1.18	1.15	0.08
Ttn#33	*Prismatic, incolor, associated with biotite and amphibole*	*none*	*Core/Rim*	*Dark*	0.1665	0.0041	0.4056	0.0062	9.2824	0.2403	0.1819	2514	20	2194	28	2360	24	13	Igneous	17.90	1.10	0.39	0.02
Ttn#34	*Prismatic, brownish, associated with biotite*	*none*	*Core/Rim*	*Dark*	0.2943	0.0106	0.4618	0.0112	18.6378	0.7173	0.2671	3417	29	2444	49	3013	38	28	Igneous	4.60	1.46	0.28	0.06
Ttn#35	*Prismatic, brownish, associated with biotite*	*none*	*Patchy zoned*	*Dark*	0.2063	0.0066	0.4083	0.0076	11.5406	0.3603	0.3018	2861	26	2205	35	2559	29	23	Igneous	8.54	1.25	0.44	0.05
Ttn#36	*Prismatic, brownish, associated with amphibole*	*none*	*Patchy zoned*	*Dark*	0.1814	0.0049	0.4056	0.0078	10.0681	0.2637	0.3780	2654	22	2193	36	2437	24	17	Igneous	11.28	2.17	5.49	0.50

[a] corrected for background, instrumental drift and mass bias fractionation based on primary stantard (MKED1).

[b] 2 × internal 2SE uncertainities

[c] rho is the $^{207}Pb/^{235}U/^{206}Pb/^{238}U$ error correlation coefficient.

[d] degree of discordance: [1-($^{206}Pb/^{238}Pb$ age / $^{207}Pb/^{206}Pb$ age)] x 100

[e] based on primary standard (MKED1).

U-Th-Pb analyses of titanite reference materials. Strikethrough analyses are not used in 207Pb/206Pb Weighted Mean Age (WMA) calculations.Tera-Wesserburg and 207Pb/206Pb WMA diagrams are shown.

Laboratoire Magmas et Volcans

	Isotopic ratios							Ages							Element concentration			
Standard MKED1	$^{207}Pb/^{206}Pb$[a]	±2s	$^{206}Pb/^{238}U$[a]	±2s	$^{207}Pb/^{235}U$[a]	±2s	Rho[c]	$^{207}Pb/^{206}Pb$	±2s (Ma)	$^{206}Pb/^{238}U$	±2s (Ma)	$^{207}Pb/^{235}U$	±2s (Ma)	Conc.[d] (%)	U ppm	Pb ppm	Th ppm	Th/U
Sequence 1																		
1	0.0960	0.0013	0.2657	0.0023	3.5157	0.0487	0.5398	1543	24	1519	12	1530	11	11	131.0	50.4	368.8	2.82
2	0.0960	0.0013	0.2658	0.0023	3.5166	0.0508	0.3554	1543	26	1519	12	1530	11	11	130.9	50.4	368.7	2.82
3	0.0960	0.0012	0.2658	0.0027	3.5150	0.0459	0.4825	1544	23	1520	14	1530	10	11	130.9	50.4	369.0	2.82
4	0.0960	0.0013	0.2658	0.0023	3.5173	0.0509	0.4165	1542	25	1519	12	1530	12	11	130.5	50.3	367.5	2.82
5	0.0960	0.0012	0.2657	0.0025	3.5145	0.0498	0.4608	1545	24	1519	13	1529	11	11	131.1	50.4	369.3	2.82
6	0.0960	0.0011	0.2658	0.0024	3.5173	0.0430	0.4477	1545	22	1519	12	1531	10	11	131.0	50.4	368.8	2.82
7	0.0960	0.0012	0.2657	0.0026	3.5147	0.0501	0.4662	1544	24	1519	13	1530	11	11	130.8	50.3	368.3	2.82
8	0.0960	0.0013	0.2658	0.0026	3.5173	0.0508	0.3830	1542	27	1519	13	1530	11	11	130.6	50.3	367.7	2.82
9	0.0960	0.0012	0.2657	0.0023	3.5152	0.0453	0.4607	1544	23	1519	12	1530	10	11	131.1	50.4	369.2	2.82
10	0.0960	0.0012	0.2658	0.0023	3.5169	0.0451	0.3775	1544	24	1520	12	1531	10	11	131.0	50.4	368.9	2.82
11	0.0960	0.0012	0.2657	0.0024	3.5156	0.0473	0.4213	1543	24	1519	12	1531	11	11	130.8	50.3	368.3	2.82
12	0.0960	0.0014	0.2658	0.0025	3.5165	0.0510	0.3247	1542	27	1519	13	1530	12	11	130.6	50.3	367.5	2.82
13	0.0961	0.0013	0.2655	0.0031	3.5172	0.0551	0.5412	1544	26	1518	16	1530	12	11	131.1	50.4	369.3	2.82
14	0.0959	0.0011	0.2658	0.0024	3.5143	0.0453	0.4703	1544	22	1519	12	1529	10	11	130.9	50.4	368.8	2.82
15	0.0961	0.0013	0.2657	0.0027	3.5237	0.0537	0.4917	1546	25	1519	14	1531	12	11	131.0	50.4	369.0	2.82
16	0.0960	0.0012	0.2658	0.0025	3.5094	0.0467	0.4696	1544	23	1519	13	1530	10	11	131.0	50.4	369.1	2.82
Sequence 2																		
1	0.0961	0.0011	0.2655	0.0024	3.5081	0.0553	0.1990	1545	22	1518	12	1528	13	11	130.5	50.4	368.2	2.82
2	0.0957	0.0013	0.2661	0.0023	3.5280	0.0651	0.4602	1540	25	1521	12	1532	15	11	130.3	50.2	366.8	2.82
3	0.0962	0.0012	0.2657	0.0023	3.5175	0.0565	0.4441	1546	24	1519	12	1530	13	11	131.2	50.5	369.6	2.82
4	0.0961	0.0013	0.2658	0.0021	3.5143	0.0537	0.3136	1546	25	1519	11	1529	12	11	131.0	50.4	369.1	2.82
5	0.0961	0.0014	0.2656	0.0024	3.5116	0.0584	0.0418	1542	25	1518	12	1527	12	11	131.3	50.6	370.4	2.82
6	0.0958	0.0012	0.2659	0.0022	3.5197	0.0551	0.3469	1540	24	1520	11	1530	12	11	131.5	50.6	371.0	2.82
Sequence 3																		
1	0.0960	0.0012	0.2658	0.0022	3.5161	0.0436	0.2567	1544	23	1519	11	1530	10	11	131.0	50.4	369.1	2.82
2	0.0960	0.0010	0.2657	0.0028	3.5159	0.0473	0.2164	1545	20	1519	14	1530	11	11	131.1	50.4	369.2	2.82
3	0.0960	0.0013	0.2659	0.0027	3.5166	0.0539	0.1431	1543	25	1520	14	1530	12	11	132.1	50.8	374.5	2.81
4	0.0960	0.0011	0.2657	0.0024	3.5158	0.0450	0.3048	1544	22	1519	12	1530	10	11	132.1	50.8	373.2	2.82
5	0.0960	0.0013	0.2657	0.0023	3.5159	0.0514	0.2060	1542	26	1519	12	1529	12	11	130.7	50.3	368.0	2.82
6	0.0960	0.0012	0.2658	0.0026	3.5162	0.0504	0.0850	1544	24	1519	13	1530	11	11	131.1	50.4	369.3	2.82
7	0.0960	0.0014	0.2657	0.0024	3.5133	0.0525	0.2346	1544	27	1519	12	1530	12	11	131.0	50.4	368.9	2.82
8	0.0960	0.0014	0.2658	0.0022	3.5152	0.0562	0.0536	1542	27	1519	11	1529	13	11	131.0	50.4	368.9	2.82
9	0.0961	0.0015	0.2659	0.0022	3.5208	0.0585	0.0369	1544	28	1520	11	1530	13	11	131.0	50.4	369.1	2.82
10	0.0960	0.0013	0.2656	0.0024	3.5126	0.0525	0.2166	1543	26	1518	12	1529	12	11	131.1	50.4	369.2	2.82
11	0.0961	0.0015	0.2659	0.0023	3.5183	0.0566	0.1664	1542	29	1520	12	1530	13	11	131.0	50.4	368.9	2.82
12	0.0960	0.0013	0.2656	0.0022	3.5148	0.0516	0.1126	1543	25	1518	11	1530	12	11	131.0	50.4	368.9	2.82
13	0.0960	0.0013	0.2658	0.0034	3.5166	0.0632	0.1190	1545	26	1520	17	1530	14	11	131.1	50.4	369.1	2.82
14	0.0960	0.0013	0.2657	0.0021	3.5159	0.0490	0.2176	1543	25	1519	11	1530	11	11	131.1	50.4	369.1	2.82

	Isotopic ratios							Ages							Element concentration			
Standard Khan	$^{207}Pb/^{206}Pb$[a]	±2s	$^{206}Pb/^{238}U$[a]	±2s	$^{207}Pb/^{235}U$[a]	±2s	Rho[c]	$^{207}Pb/^{206}Pb$	±2s (Ma)	$^{206}Pb/^{238}U$	±2s (Ma)	$^{207}Pb/^{235}U$	±2s (Ma)	Conc.[d] (%)	U ppm	Pb ppm	Th ppm	Th/U
Sequence 1																		
1	0.0675	0.0012	0.0844	0.0008	0.7878	0.0155	0.3305	848	38	522	5	589	9	7	668.9	23.0	459.9	0.69
2	0.0656	0.0009	0.0831	0.0008	0.7509	0.0108	0.4262	788	28	514	5	568	6	7	918.3	34.5	744.5	0.73
3	0.0994	0.0033	0.0904	0.0011	1.2395	0.0459	0.4717	1598	64	558	6	817	21	12	465.9	19.7	289.9	0.62
4	0.0645	0.0009	0.0840	0.0008	0.7471	0.0117	0.4049	753	30	520	5	566	7	7	774.7	28.2	573.0	0.72
5	0.0635	0.0009	0.0842	0.0008	0.7372	0.0115	0.4447	717	30	521	5	561	7	7	434.5	12.9	265.5	0.61

6	0.0621	0.0009	0.0811	0.0009	0.6946	0.0115	0.4865	670	32	503	5	535	7	7	787.5	28.8	623.3	0.74
~~***7***~~	~~0.0655~~	~~0.0015~~	~~0.0797~~	~~0.0008~~	~~0.7196~~	~~0.0171~~	~~0.2938~~	~~784~~	~~47~~	~~495~~	~~5~~	~~550~~	~~10~~	~~7~~	~~455.0~~	~~13.3~~	~~278.4~~	~~0.61~~
8	0.0790	0.0028	0.0926	0.0014	1.0103	0.0442	0.3310	1147	63	571	8	703	21	9	420.0	15.4	265.9	0.63
Sequence 2																		
1	0.0630	0.0009	0.0838	0.0008	0.7283	0.0146	0.5090	702	29	519	5	555	9	7	898.5	33.5	727.9	0.73
2	0.0626	0.0008	0.0875	0.0008	0.7531	0.0137	0.5409	690	27	540	5	569	8	7	629.2	21.6	436.8	0.69
Sequence 3																		
1	0.0626	0.0009	0.0871	0.0008	0.7527	0.0111	0.2485	692	29	539	5	569	6	7	452.5	14.1	291.5	0.65
2	0.0621	0.0008	0.0880	0.0009	0.7521	0.0111	0.2680	672	28	544	6	569	6	7	363.0	10.6	213.2	0.56
3	0.0630	0.0008	0.0844	0.0008	0.7333	0.0098	0.2566	704	26	523	5	558	6	7	640.1	20.8	433.5	0.68
4	0.0597	0.0007	0.0838	0.0008	0.6900	0.0096	0.3074	588	27	519	5	532	6	6	678.8	21.7	465.3	0.68
5	0.0665	0.0009	0.0868	0.0008	0.8005	0.0114	0.2592	819	28	536	5	597	6	7	625.5	21.3	429.2	0.69
6	0.0646	0.0009	0.0872	0.0009	0.7750	0.0116	0.2802	754	30	539	5	583	7	7	669.8	22.8	468.3	0.70

Standard BLR1	$\frac{^{207}Pb}{^{206}Pb}$[a]	±2s	$\frac{^{206}Pb}{^{238}U}$[a]	±2s	$\frac{^{207}Pb}{^{235}U}$[a]	±2s	Rho[c]	$\frac{^{207}Pb}{^{206}Pb}$	±2s (Ma)	$\frac{^{206}Pb}{^{238}U}$	±2s (Ma)	$\frac{^{207}Pb}{^{235}U}$	±2s (Ma)	Conc.[d] (%)	U ppm	Pb ppm	Th ppm	$\frac{Th}{U}$
Sequence 1																		
1	0.0886	0.0011	0.1801	0.0019	2.2012	0.0327	0.5425	1391	24	1067	10	1181	11	10	251.24	14.41	130.64	0.53
2	0.0862	0.0011	0.1844	0.0020	2.1912	0.0308	0.4794	1338	25	1091	11	1178	10	10	174.69	9.44	83.87	0.48
3	0.0859	0.0011	0.1835	0.0018	2.1730	0.0295	0.4675	1332	25	1086	10	1172	10	10	174.62	9.22	82.66	0.46
~~***4***~~	~~0.0887~~	~~0.0012~~	~~0.1709~~	~~0.0017~~	~~2.0823~~	~~0.0315~~	~~0.4826~~	~~1397~~	~~26~~	~~1017~~	~~9~~	~~1143~~	~~10~~	~~10~~	~~166.55~~	~~8.13~~	~~75.12~~	~~0.45~~
Sequence 2																		
1	0.0884	0.0012	0.1787	0.0017	2.1839	0.0400	0.3511	1385	25	1060	9	1174	13	10	420.00	30.99	294.50	0.55
Sequence 3																		
1	0.0901	0.0014	0.1823	0.0022	2.2666	0.0407	0.1456	1425	28	1079	12	1201	13	10	178.95	10.00	88.88	0.50
2	0.0905	0.0013	0.1791	0.0019	2.2366	0.0347	0.2633	1434	27	1062	11	1192	11	10	222.74	12.71	111.65	0.51
3	0.0976	0.0017	0.1837	0.0019	2.4903	0.0443	0.2893	1572	32	1087	10	1268	13	12	196.72	11.79	103.82	0.53

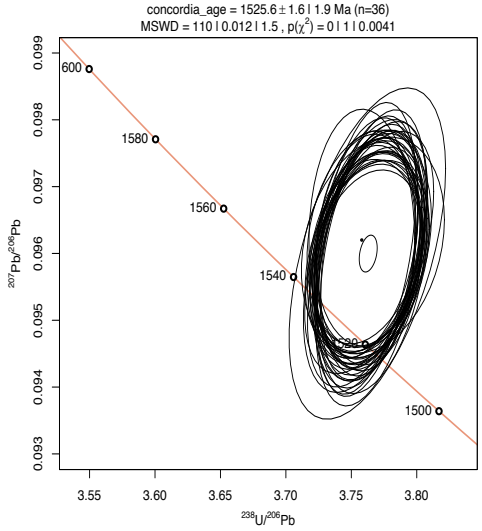
Standard THBL	$\frac{^{207}Pb}{^{206}Pb}$[a]	±2s	$\frac{^{206}Pb}{^{238}U}$[a]	±2s	$\frac{^{207}Pb}{^{235}U}$[a]	±2s	Rho[c]	$\frac{^{207}Pb}{^{206}Pb}$	±2s (Ma)	$\frac{^{206}Pb}{^{238}U}$	±2s (Ma)	$\frac{^{207}Pb}{^{235}U}$	±2s (Ma)	Conc.[d] (%)	U ppm	Pb ppm	Th ppm	$\frac{Th}{U}$
Sequence 1																		
~~***1***~~	~~0.1139~~	~~0.0019~~	~~0.1824~~	~~0.0022~~	~~2.8598~~	~~0.0542~~	~~0.4865~~	~~1856~~	~~31~~	~~1080~~	~~12~~	~~1360~~	~~14~~	~~14~~	~~228.44~~	~~64.07~~	~~726.46~~	~~2.20~~
~~***2***~~	~~0.1138~~	~~0.0018~~	~~0.1867~~	~~0.0019~~	~~2.9256~~	~~0.0484~~	~~0.4187~~	~~1856~~	~~28~~	~~1103~~	~~10~~	~~1387~~	~~13~~	~~14~~	~~161.89~~	~~42.07~~	~~378.66~~	~~2.16~~
3	0.1099	0.0019	0.1922	0.0020	2.9175	0.0492	0.3349	1795	30	1133	11	1385	13	13	158.72	43.62	393.70	2.20
Sequence 2																		
~~***1***~~	~~0.1124~~	~~0.0016~~	~~0.1930~~	~~0.0018~~	~~2.9726~~	~~0.0524~~	~~0.3501~~	~~1833~~	~~26~~	~~1137~~	~~10~~	~~1390~~	~~13~~	~~13~~	~~123.77~~	~~27.83~~	~~251.98~~	~~2.01~~
Sequence 3																		
1	0.1111	0.0015	0.1961	0.0018	2.9963	0.0445	0.2431	1812	25	1154	10	1405	11	13	61.22	11.49	103.03	1.54
2	0.1029	0.0015	0.1819	0.0018	2.5806	0.0379	0.3166	1672	27	1077	10	1295	10	12	130.48	26.42	257.73	1.97
3	0.1175	0.0017	0.1945	0.0019	3.1557	0.0497	0.2709	1916	27	1146	10	1445	12	14	123.58	27.89	246.15	2.00

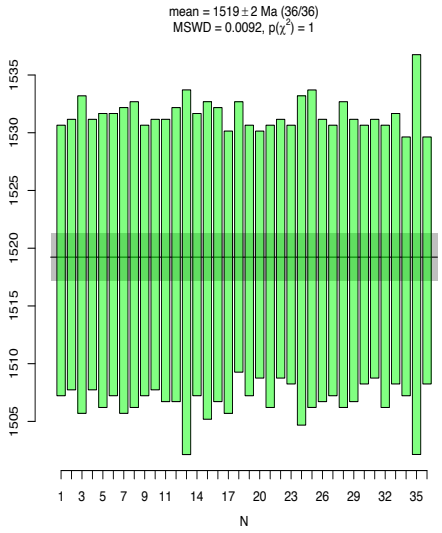
[a] corrected for background, instrumental drift and mass bias fractionation based on primary stantard (MKED1).

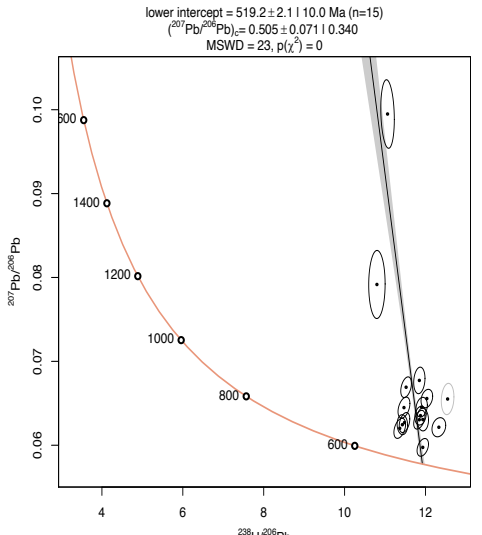
[c] rho is the $^{207}Pb/^{235}U/^{206}Pb/^{238}U$ error correlation coefficient.

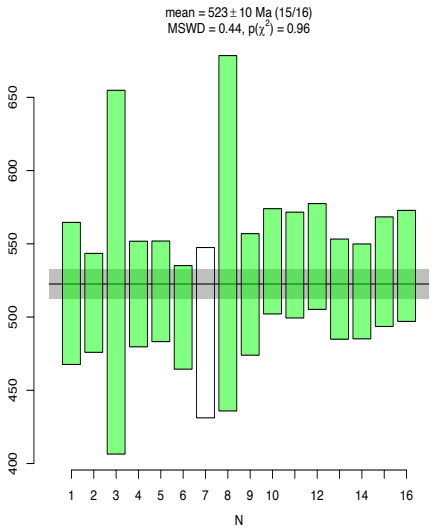
[d] degree of concordance: $(1+((^{206}Pb/^{238}U - ^{207}Pb/^{235}U)/^{206}Pb/^{238}U)) \times 100$

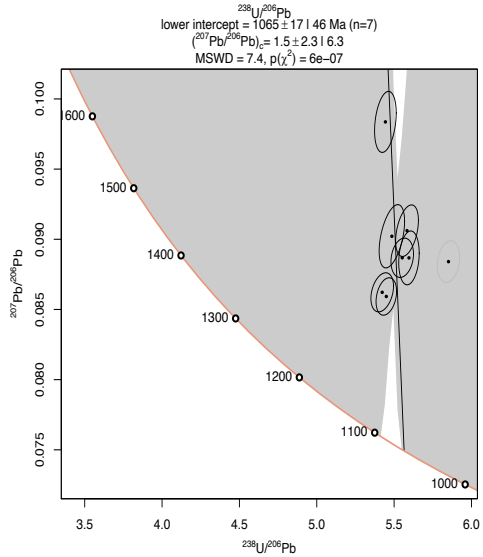
Weighted mean calculations based on $^{206}Pb/^{238}U$ ages.

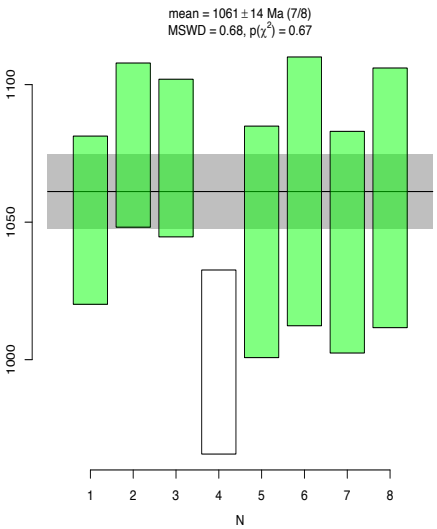

concordia_age = 1525.6 ± 1.6 | 1.9 Ma (n=36)
MSWD = 110 | 0.012 | 1.5 , p(χ²) = 0 | 1 | 0.0041
600
1580
1560
1540
1500
207Pb/206Pb
238U/206Pb

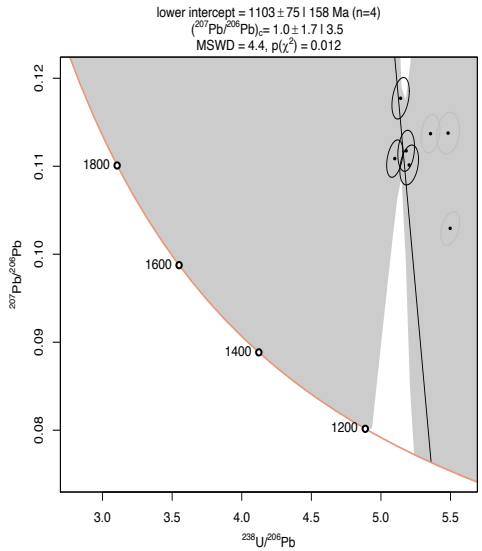

mean = 1519 ± 2 Ma (36/36)
MSWD = 0.0092, p(χ²) = 1
N

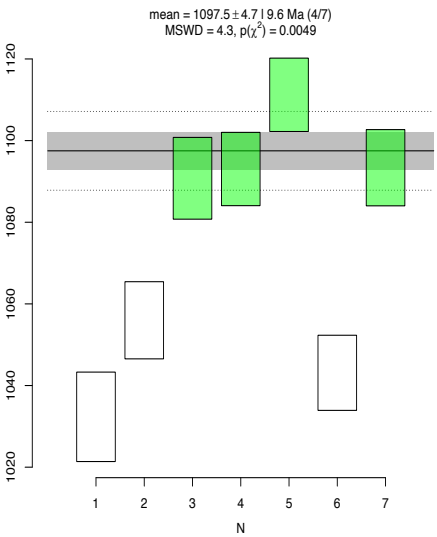

lower intercept = 519.2 ± 2.1 | 10.0 Ma (n=15)
(207Pb/206Pb)c= 0.505 ± 0.071 | 0.340
MSWD = 23, p(χ²) = 0
1400
1200
1000
800
600
207Pb/206Pb
238U/206Pb


mean = 523 ± 10 Ma (15/16)
MSWD = 0.44, p(χ²) = 0.96
N


lower intercept = 1065 ± 17 | 46 Ma (n=7)
(207Pb/206Pb)c= 1.5 ± 2.3 | 6.3
MSWD = 7.4, p(χ²) = 6e−07
1600
1500
1400
1300
1200
1100
1000
207Pb/206Pb
238U/206Pb


mean = 1061 ± 14 Ma (7/8)
MSWD = 0.68, p(χ²) = 0.67
N


lower intercept = 1103 ± 75 | 158 Ma (n=4)
(207Pb/206Pb)c= 1.0 ± 1.7 | 3.5
MSWD = 4.4, p(χ²) = 0.012
1800
1600
1400
1200
207Pb/206Pb
238U/206Pb


mean = 1097.5 ± 4.7 | 9.6 Ma (4/7)
MSWD = 4.3, p(χ²) = 0.0049
N

Lu-Hf isotope composition of Cupim Leucogranites. Italic symbols are inherited domains zircons. Uncertainties correspond to 2σ confidential interval.

Sample	This work	176Hf/177Hf	±2σ	176Lu/177Hf	±2σ	176Yb/177Hf	±2σ	178Hf/177Hf	±2σ	179Hf/177Hf	178Hf (V)	±2σ	176Hf/177Hf(t)	2 STE	EpsHf in	±2σ	EpsHf Age	±2σ	Age (Ma)
GC1																			
GC1-80-120-03.1	**z1**	0.281285	0.000017	0.000976	0.000048	0.04698	0.00237	1.46861	0.00007	0.7325	2	0.6	**0.281248**	0.000017	-10.4	0.6	**-9.4**	**0.6**	**1991**
GC1-80-120-08.2	***z4***	*0.28104*	*0.000029*	*0.00165*	*0.000097*	*0.07368*	*0.00388*	*1.46864*	*0.00008*	*0.7325*	*2.04*	*0.55*	***0.280954***	*0.000029*	*-2.5*	*1*	***-2.5***	***1***	***2733***
GC1-80-120-11.2	***z7***	*0.280881*	*0.000021*	*0.001184*	*0.000046*	*0.0497*	*0.00147*	*1.46864*	*0.00007*	*0.7325*	*2.29*	*0.89*	***0.280808***	*0.000021*	*3*	*0.8*	***3***	***0.8***	***3182***
GC1-80-120-16.3	***z8***	*0.281006*	*0.000018*	*0.000662*	*0.000005*	*0.02949*	*0.00015*	*1.46865*	*0.00007*	*0.7325*	*3.25*	*0.82*	***0.280972***	*0.000018*	*-2.5*	*0.6*	***-2.4***	***0.6***	***2707***
GC1-80-120-17.3	**z10**	0.281233	0.000022	0.000748	0.000009	0.03488	0.00042	1.46856	0.00004	0.7325	2.56	1.13	**0.281206**	0.000022	-12.1	0.8	**-10.9**	**0.8**	**1991**
GC1-120-200-8.3	**z15**	0.281225	0.000018	0.000243	0.000004	0.01193	0.00014	1.46853	0.00005	0.7325	2.34	0.58	**0.281216**	0.000018	-9.5	0.6	**-10.6**	**0.6**	**1991**
GC1-80-120-18.1	**z11**	0.281237	0.000021	0.000991	0.000037	0.04645	0.00152	1.46857	0.00005	0.7325	2.64	1.03	**0.281201**	0.000021	-12.6	0.7	**-11.1**	**0.7**	**1991**
GC1-120-200-14.3	**z23**	0.281274	0.000017	0.000807	0.000046	0.03934	0.00258	1.46851	0.00005	0.7325	2.77	0.89	**0.281244**	0.000017	-10.2	0.6	**-9.6**	**0.6**	**1991**
GC1-120-200-15.3	***z24***	*0.281062*	*0.000027*	*0.001094*	*0.000026*	*0.04598*	*0.00065*	*1.46852*	*0.00011*	*0.7325*	*2.96*	*0.86*	***0.281004***	*0.000027*	*-0.5*	*1*	***-0.5***	***1***	***2739***
GC1-120-200-23.2	***z29***	*0.280994*	*0.000027*	*0.000789*	*0.000032*	*0.03434*	*0.00116*	*1.46845*	*0.00005*	*0.7325*	*2.38*	*0.97*	***0.28096***	*0.000027*	*-13.8*	*1*	***-13.8***	***1***	***2241***
GC1-120-200-23.3	**z31**	0.281078	0.000028	0.000677	0.00001	0.02973	0.00081	1.46849	0.00005	0.7325	2.38	1.05	**0.281051**	0.000028	-14.1	1	**-16.4**	**1**	**1991**
GC2																			
GC2-60-80-02.1	***z37***	*0.28104*	*0.000017*	*0.001051*	*0.00002*	*0.05224*	*0.00121*	*1.46847*	*0.00005*	*0.7325*	*2.65*	*0.77*	***0.280986***	*0.000017*	*-2*	*0.6*	***-2***	***0.6***	***2705***
GC2-60-80-03.3	**z38**	0.28131	0.000029	0.001353	0.000032	0.05958	0.0015	1.46868	0.00016	0.7325	4.39	1.69	**0.281264**	0.000029	-13.5	1	**-8.6**	**1**	**2002**
GC2-60-80-04.2	**z41**	0.281284	0.00002	0.001208	0.000061	0.05781	0.00271	1.46849	0.00005	0.7325	2.95	1.13	**0.281244**	0.00002	-15.3	0.7	**-9.3**	**0.7**	**2002**
GC2-60-80-06.5	**z42**	0.281268	0.00002	0.002168	0.000058	0.10063	0.04789	1.46856	0.00007	0.7325	4.17	2.04	**0.281193**	0.00002	-15.6	0.7	**-11.1**	**0.7**	**2002**
GC2-120-200-09.3	***z32***	*0.281033*	*0.000026*	*0.001004*	*0.000096*	*0.04789*	*0.00505*	*1.46854*	*0.00009*	*0.7325*	*2.47*	*0.87*	***0.280981***	*0.000026*	*-2.2*	*0.9*	***-2.2***	***0.9***	***2703***
GC2-120-200-16.1	**z34**	0.281261	0.00002	0.000138	0.000013	0.00763	0.0008	1.46822	0.00006	0.7325	2.42	0.78	**0.281256**	0.00002	-7.8	0.7	**-8.9**	**0.7**	**2002**
GC2-120-200-18.1	***z36***	*0.281021*	*0.000019*	*0.001117*	*0.000054*	*0.0499*	*0.00285*	*1.46819*	*0.00004*	*0.7325*	*2.83*	*0.93*	***0.280964***	*0.000019*	*-3.3*	*0.7*	***-3.3***	***0.7***	***2682***
GC5A																			
GC5A-60-80-2.2	**z51**	0.281407	0.000017	0.001012	0.000024	0.04598	0.00126	1.46839	0.00007	0.7325	2.83	0.93	**0.281372**	0.000017	-9.2	0.6	**-4.5**	**0.6**	**2012**
GC5A-60-80-8.1	**z55**	0.281484	0.000025	0.001492	0.000078	0.06761	0.0032	1.46838	0.00005	0.7325	2.3	0.99	**0.281433**	0.000025	-7.1	0.9	**-2.4**	**0.9**	**2012**
GC5A-80-120-1.1	**z56**	0.281356	0.000023	0.0008	0.000017	0.03491	0.00061	1.46839	0.00005	0.7325	2.82	0.57	**0.281328**	0.000023	-9.6	0.8	**-6.1**	**0.8**	**2012**
GC5A-80-120-2.3	**z57**	0.281464	0.000019	0.001415	0.000017	0.06406	0.00037	1.46836	0.00006	0.7325	2.29	0.91	**0.281417**	0.000019	-9	0.7	**-2.9**	**0.7**	**2012**
GC5A-80-120-15.1	**z59**	0.281436	0.000014	0.000889	0.000019	0.03973	0.00096	1.46833	0.00007	0.7325	2.14	0.78	**0.281405**	0.000014	-7	0.5	**-3.4**	**0.5**	**2012**
GC5A-120-200-6.2	**z44**	0.281323	0.000018	0.000928	0.000018	0.04313	0.00042	1.46842	0.00005	0.7325	2.61	0.98	**0.281293**	0.000018	-14.2	0.6	**-7.3**	**0.6**	**2012**
GC5A-120-200-7.3	**z46**	0.281415	0.000022	0.00097	0.000015	0.04507	0.00107	1.46841	0.00005	0.7325	2.59	0.97	**0.281385**	0.000022	-12.7	0.8	**-4.1**	**0.8**	**2012**
GC5B																			
GC5B-60-80-3.2	**z67**	0.281385	0.000019	0.000662	0.000018	0.02959	0.00104	1.46836	0.00005	0.7325	2.8	0.8	**0.281361**	0.000019	-8	0.7	**-5.7**	**0.7**	**1977**
GC5B-60-80-5.5	***z70***	*0.281022*	*0.000019*	*0.001161*	*0.000025*	*0.05481*	*0.0011*	*1.46834*	*0.00005*	*0.7325*	*2.83*	*1.04*	***0.280962***	*0.000019*	*-3.3*	*0.7*	***-3.3***	***0.7***	***2688***
GC5B-60-80-6.4	**z72**	0.281351	0.000016	0.00059	0.000001	0.02635	0.00023	1.46832	0.00005	0.7325	2.56	0.97	**0.281331**	0.000016	-11.7	0.6	**-6.8**	**0.6**	**1977**
GC5B-60-80-10.1	**z74**	0.281373	0.000018	0.000876	0.000005	0.04073	0.00046	1.46824	0.00004	0.7325	2.69	0.83	**0.281342**	0.000018	-9.2	0.6	**-6.4**	**0.6**	**1977**
GC5B-80-120-8.2	**z64**	0.28132	0.000016	0.000953	0.000027	0.0422	0.00087	1.46835	0.00006	0.7325	2.63	0.98	**0.281285**	0.000016	-9.4	0.6	**-8.4**	**0.6**	**1977**
GC5B-80-120-10.4	**z65**	0.281361	0.000026	0.000866	0.000013	0.02969	0.0008	1.46749	0.00005	0.7325	2.18	0.75	**0.281334**	0.000026	-14.7	0.9	**-6.7**	**0.9**	**1977**
GC6																			
GC6-80-120-1.2	***z90***	*0.281056*	*0.000026*	*0.001173*	*0.000021*	*0.05466*	*0.00152*	*1.46821*	*0.00005*	*0.7325*	*2.65*	*0.98*	***0.280995***	*0.000026*	*-2.4*	*0.9*	***-2.4***	***0.9***	***2675***
GC6-80-120-3.2	***z91***	*0.280985*	*0.000021*	*0.000822*	*0.000013*	*0.03836*	*0.00085*	*1.46818*	*0.00005*	*0.7325*	*2.17*	*0.73*	***0.280943***	*0.000021*	*-3.7*	*0.8*	***-3.7***	***0.8***	***2697***
GC6-80-120-5.2	**z95**	0.281529	0.00002	0.000668	0.00003	0.03174	0.00128	1.46818	0.00004	0.7325	2.29	0.75	**0.281506**	0.00002	-4.6	0.7	**-0.6**	**0.7**	**1977**
GC6-120-200-2.1	***z79***	*0.280945*	*0.000017*	*0.000949*	*0.000046*	*0.04319*	*0.00171*	*1.46819*	*0.00006*	*0.7325*	*2.36*	*0.81*	***0.280896***	*0.000017*	*-5.1*	*0.6*	***-5.1***	***0.6***	***2709***
GC6-120-200-10.1	***z82***	*0.280998*	*0.000023*	*0.000686*	*0.00002*	*0.03046*	*0.00136*	*1.46828*	*0.00006*	*0.7325*	*2.01*	*1.33*	***0.280962***	*0.000023*	*-2.7*	*0.8*	***-2.7***	***0.8***	***2712***
GC6-120-200-12.1	***z83***	*0.281392*	*0.000019*	*0.000956*	*0.000023*	*0.03559*	*0.00084*	*1.46827*	*0.00007*	*0.7325*	*2.09*	*0.77*	***0.281353***	*0.000019*	*-1.6*	*0.7*	***-1.6***	***0.7***	***2168***
GC6-120-200-13.2	**z85**	0.281411	0.000016	0.001246	0.000007	0.05481	0.00059	1.46829	0.00006	0.7325	2.19	0.73	**0.281363**	0.000016	-4.6	0.6	**-5.7**	**0.6**	**1977**
GC6-120-200-14.3	***z86***	*0.280938*	*0.000019*	*0.00065*	*0.000015*	*0.02965*	*0.0012*	*1.46833*	*0.00005*	*0.7325*	*2.63*	*0.68*	***0.280905***	*0.000019*	*-5.3*	*0.7*	***-5.3***	***0.7***	***2689***
GC6-120-200-20.1	**z87**	0.281342	0.000014	0.001242	0.000085	0.05875	0.00499	1.4683	0.00005	0.7325	2.99	1.05	**0.281299**	0.000014	-12.4	0.5	**-7.9**	**0.5**	**1977**
GC7																			
GC7-80-120-8.1	***z97***	*0.280947*	*0.00002*	*0.000666*	*0.000015*	*0.03049*	*0.00101*	*1.46839*	*0.00005*	*0.7325*	*2.17*	*0.82*	***0.280914***	*0.00002*	*-6.4*	*0.7*	***-6.4***	***0.7***	***2626***
GC7-80-120-10.3	**z98**	0.28124	0.000017	0.000548	0.000037	0.02088	0.00146	1.46843	0.00005	0.7325	2.9	0.72	**0.281222**	0.000017	-14.4	0.6	**-12**	**0.6**	**1918**

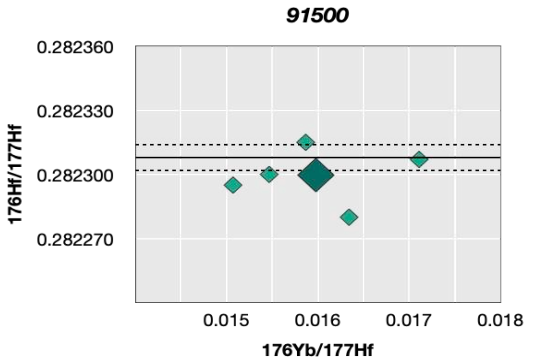
Lu-Hf isotope composition of the studied samples. Italic symbols are inherited domains of zircons.

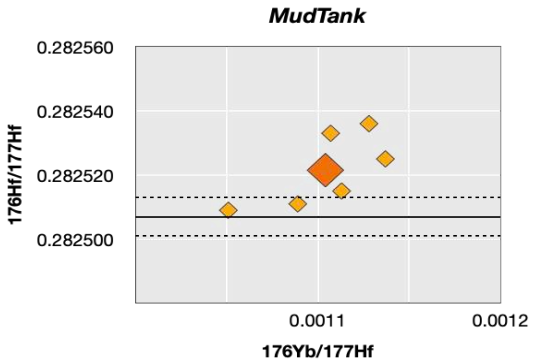
Sample	This work	176Hf/177Hf	±2σ	176Lu/177Hf	±2σ	176Yb/177Hf	±2σ	178Hf/177Hf	±2σ	179Hf/177Hf	178Hf (V)	±2σ	176Hf/177Hf(t)	2 STE	εHf in	±2σ	εHf Age	±2σ	Age (Ma)
CM44A																			
1.2	z1	0.281608	0.000024	0.001086	0.000094	0.049470	0.004847	1.468568	0.000040	0.7325	2.79	0.22	0.281567	0.000024	2.5	0.8	3.0	0.8	2040
4.3	z5	0.281637	0.000026	0.000589	0.000015	0.026621	0.001245	1.468578	0.000054	0.7325	1.96	0.43	0.281614	0.000026	5.3	0.9	4.7	0.9	2040
4.4	z6	0.281557	0.000021	0.000325	0.000010	0.014553	0.000600	1.468611	0.000050	0.7325	3.02	1.04	0.281545	0.000021	0.4	0.8	2.3	0.8	2040
9.1	z7	0.281530	0.000012	0.000232	0.000008	0.009202	0.000401	1.468635	0.000040	0.7325	3.71	1.60	0.281521	0.000012	2.5	0.4	1.4	0.4	2040
9.3	z8	0.281596	0.000020	0.000630	0.000043	0.030433	0.001875	1.468606	0.000042	0.7325	3.62	1.21	0.281572	0.000020	2.2	0.7	3.2	0.7	2040
12.2	*z9*	*0.281556*	*0.000021*	*0.001068*	*0.000075*	*0.047607*	*0.004186*	*1.468627*	*0.000059*	*0.7325*	*2.35*	*0.25*	*0.281509*	*0.000021*	*6.9*	*0.7*	*3.6*	*0.7*	*2152*
17.3	z11	0.281633	0.000019	0.000918	0.000045	0.043764	0.002479	1.468692	0.000045	0.7325	3.00	0.41	0.281597	0.000019	4.3	0.7	4.1	0.7	2040
18.1	z12	0.281625	0.000015	0.000577	0.000007	0.027000	0.000488	1.468750	0.000037	0.7325	2.87	0.82	0.281603	0.000015	5.0	0.5	4.3	0.5	2040
22.2	*z17*	*0.281602*	*0.000012*	*0.000966*	*0.000030*	*0.045241*	*0.001090*	*1.468708*	*0.000054*	*0.7325*	*2.98*	*1.41*	*0.281562*	*0.000012*	*5.4*	*0.4*	*5.5*	*0.4*	*2152*
23.2	*z18*	*0.281570*	*0.000020*	*0.000429*	*0.000009*	*0.017730*	*0.000366*	*1.468943*	*0.000046*	*0.7325*	*3.17*	*1.03*	*0.281553*	*0.000020*	*5.8*	*0.7*	*5.2*	*0.7*	*2152*
24.3	*z20*	*0.281593*	*0.000021*	*0.000369*	*0.000010*	*0.018407*	*0.000477*	*1.468868*	*0.000049*	*0.7325*	*2.02*	*0.59*	*0.281577*	*0.000021*	*6.7*	*0.7*	*6.0*	*0.7*	*2152*
25.3	*z23*	*0.281582*	*0.000022*	*0.000424*	*0.000014*	*0.018787*	*0.000475*	*1.468919*	*0.000046*	*0.7325*	*2.09*	*0.50*	*0.281565*	*0.000022*	*4.8*	*0.8*	*5.6*	*0.8*	*2152*
CM44B																			
5.1	z30	0.281542	0.000022	0.000592	0.000009	0.024113	0.000108	1.468870	0.000040	0.7325	3.25	0.73	0.281520	0.000022	-0.2	0.8	4.0	0.8	2150
5.4	z28	0.281594	0.000018	0.000368	0.000011	0.014941	0.000605	1.468913	0.000039	0.7325	4.68	0.28	0.281580	0.000018	3.8	0.6	6.1	0.6	2150
CM46A																			
1.1	z31	0.281440	0.000019	0.000495	0.000004	0.021204	0.000352	1.468882	0.000061	0.7325	2.39	0.73	0.281420	0.000019	-1.1	0.7	-0.5	0.7	2110
3.2	z33	0.281385	0.000016	0.000511	0.000004	0.020986	0.000120	1.468820	0.000057	0.7325	2.39	0.76	0.281364	0.000016	-2.6	0.6	-2.5	0.6	2110
5.2	z38	0.281389	0.000014	0.000464	0.000018	0.019329	0.000744	1.468878	0.000058	0.7325	2.44	0.82	0.281370	0.000014	-1.4	0.5	-2.3	0.5	2110
9.2	z46	0.281380	0.000011	0.000491	0.000006	0.020438	0.000393	1.468961	0.000050	0.7325	2.30	0.88	0.281360	0.000011	-2.8	0.4	-2.7	0.4	2110
11.3	z48	0.281420	0.000016	0.000453	0.000025	0.018259	0.000917	1.468857	0.000041	0.7325	2.52	1.24	0.281402	0.000016	-1.1	0.6	-1.2	0.6	2110
18.1	z49	0.281382	0.000016	0.000626	0.000021	0.025459	0.000858	1.468625	0.000058	0.7325	2.30	1.02	0.281358	0.000016	-4.1	0.6	-2.7	0.6	2110
18.2	z50	0.281412	0.000028	0.000741	0.000058	0.031771	0.002335	1.468566	0.000058	0.7325	1.87	0.83	0.281382	0.000028	-0.8	1.0	-1.9	1.0	2110
19.3	z52	0.281533	0.000022	0.001396	0.000039	0.057184	0.001826	1.468362	0.000055	0.7325	2.02	0.70	0.281477	0.000022	1.6	0.8	1.5	0.8	2110
20.2	z53	0.281394	0.000017	0.000521	0.000004	0.021656	0.000070	1.468342	0.000047	0.7325	2.45	0.80	0.281373	0.000017	-1.7	0.6	-2.2	0.6	2110
21.3	*z57*	*0.280898*	*0.000023*	*0.000693*	*0.000015*	*0.032124*	*0.000984*	*1.468374*	*0.000053*	*0.7325*	*2.25*	*0.57*	*0.280858*	*0.000023*	*0.8*	*0.8*	*0.8*	*0.8*	*3014*
22.2	z73	0.281417	0.000022	0.000580	0.000001	0.024376	0.000171	1.468445	0.000048	0.7325	2.30	0.84	0.281393	0.000022	-1.3	0.8	-1.5	0.8	2110
23.3	z59	0.281542	0.000018	0.002231	0.000099	0.093047	0.003619	1.468424	0.000074	0.7325	1.84	0.71	0.281451	0.000018	1.5	0.7	0.6	0.7	2110
24.1	z62	0.281360	0.000019	0.000476	0.000008	0.019519	0.000465	1.468422	0.000055	0.7325	2.24	0.75	0.281340	0.000019	-3.1	0.7	-3.4	0.7	2110
25.3	z63	0.281364	0.000019	0.000294	0.000002	0.012020	0.000234	1.468411	0.000050	0.7325	2.30	0.67	0.281352	0.000019	-3.9	0.7	-2.9	0.7	2110
29.1	z67	0.281456	0.000025	0.000641	0.000006	0.026760	0.000184	1.468331	0.000058	0.7325	2.48	0.75	0.281430	0.000025	0.3	0.9	-0.2	0.9	2110
23.1	z60	0.281377	0.000024	0.000517	0.000004	0.017516	0.000074	1.467509	0.000054	0.7325	1.98	0.68	0.281357	0.000024	-4.5	0.9	-2.8	0.9	2110
CM47																			
1.1	z69	0.281219	0.000024	0.000453	0.000003	0.019978	0.000375	1.468364	0.000059	0.7325	2.04	0.54	0.281201	0.000024	-7.5	0.8	-7.3	0.8	2155
2.3	z74	0.281235	0.000018	0.000643	0.000003	0.029040	0.000361	1.468328	0.000054	0.7325	2.02	0.78	0.281208	0.000018	-7.2	0.7	-7.0	0.7	2155
3.4	z80	0.281242	0.000023	0.000576	0.000005	0.025548	0.000241	1.468470	0.000061	0.7325	2.13	0.56	0.281219	0.000023	-6.9	0.8	-6.6	0.8	2155
4.2	z83	0.281235	0.000018	0.000407	0.000006	0.018448	0.000463	1.468654	0.000080	0.7325	2.20	0.63	0.281219	0.000018	-7.4	0.6	-6.6	0.6	2155
5.5	z90	0.281199	0.000022	0.000456	0.000006	0.020223	0.000437	1.468462	0.000061	0.7325	2.11	0.63	0.281180	0.000022	-7.7	0.8	-8.0	0.8	2155
7.1	z91	0.281219	0.000019	0.000507	0.000008	0.022756	0.000176	1.468448	0.000055	0.7325	2.14	0.52	0.281198	0.000019	-7.7	0.7	-7.4	0.7	2155
8.3	z96	0.281229	0.000020	0.000478	0.000009	0.020985	0.000271	1.468501	0.000049	0.7325	2.21	0.44	0.281210	0.000020	-7.4	0.7	-6.9	0.7	2155
10.1	z99	0.281190	0.000019	0.000481	0.000006	0.020642	0.000347	1.468538	0.000060	0.7325	2.48	0.92	0.281171	0.000019	-9.9	0.7	-8.3	0.7	2155
11.1	z101	0.281108	0.000020	0.000314	0.000005	0.013389	0.000388	1.468587	0.000062	0.7325	2.22	0.57	0.281095	0.000020	-11.8	0.7	-11.0	0.7	2155
13.1	z102	0.281194	0.000016	0.000443	0.000005	0.019620	0.000129	1.468506	0.000059	0.7325	2.15	0.53	0.281176	0.000016	-8.6	0.6	-8.1	0.6	2155
17.2	z107	0.281244	0.000024	0.000795	0.000035	0.036092	0.001313	1.468491	0.000051	0.7325	2.09	0.75	0.281213	0.000024	-9.0	0.8	-6.8	0.8	2155
22.3	z112	0.281272	0.000020	0.000458	0.000022	0.019853	0.001023	1.468597	0.000061	0.7325	2.12	0.89	0.281254	0.000020	-5.8	0.7	-5.4	0.7	2155
25.3	z114	0.281261	0.000017	0.000399	0.000005	0.017619	0.000272	1.468644	0.000067	0.7325	2.11	0.45	0.281244	0.000017	-6.0	0.6	-5.7	0.6	2155
26.2	*z115*	*0.280882*	*0.000016*	*0.000620*	*0.000023*	*0.024426*	*0.001235*	*1.468629*	*0.000047*	*0.7325*	*2.41*	*0.63*	*0.280855*	*0.000016*	*-16.3*	*0.6*	*-16.3*	*0.6*	*2295*
31.1	z122	0.281241	0.000021	0.000480	0.000008	0.021375	0.000155	1.468672	0.000061	0.7325	2.19	0.60	0.281221	0.000021	-6.9	0.7	-6.5	0.7	2155
36.3	z126	0.281244	0.000020	0.000454	0.000005	0.020747	0.000331	1.468739	0.000074	0.7325	2.23	0.68	0.281225	0.000020	-7.2	0.7	-6.4	0.7	2155
8.4	z97	0.281201	0.000026	0.000668	0.000034	0.023360	0.000944	1.467595	0.000071	0.7325	1.70	0.66	0.281174	0.000026	-10.3	0.9	-8.2	0.9	2155
10.3	z100	0.280963	0.000023	0.000392	0.000005	0.011907	0.000147	1.467503	0.000058	0.7325	2.05	0.49	0.280947	0.000023	-16.1	0.8	-16.3	0.8	2155
CM49																			
3.4	z132	0.281562	0.000023	0.000825	0.000034	0.031406	0.001104	1.468834	0.000072	0.7325	1.87	0.69	0.281529	0.000023	3.7	0.8	3.8	0.8	2130
4.3	z135	0.281556	0.000022	0.000830	0.000033	0.031791	0.001095	1.468857	0.000070	0.7325	1.89	0.48	0.281522	0.000022	3.8	0.8	3.6	0.8	2130

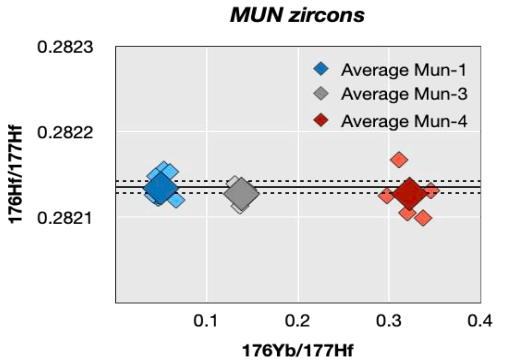
5.4	z138	0.281520	0.000018	0.000332	0.000023	0.012393	0.001072	1.468813	0.000057	0.7325	2.19	0.65	0.281507	0.000018	3.0	0.7	3.0	0.7	2130
7.3	z141	0.281584	0.000026	0.000984	0.000020	0.041865	0.000784	1.468892	0.000051	0.7325	2.18	0.70	0.281545	0.000026	4.0	0.9	4.4	0.9	2130
8.3	z144	0.281580	0.000019	0.000746	0.000037	0.028953	0.001640	1.468929	0.000057	0.7325	2.16	0.74	0.281550	0.000019	4.3	0.7	4.5	0.7	2130
9.3	z146	0.281584	0.000023	0.000889	0.000032	0.035045	0.001194	1.469010	0.000059	0.7325	2.00	0.74	0.281548	0.000023	4.5	0.8	4.5	0.8	2130
10.2	z147	0.281604	0.000020	0.001011	0.000023	0.038744	0.000891	1.469023	0.000055	0.7325	1.87	0.70	0.281563	0.000020	5.2	0.7	5.0	0.7	2130
11.2	z149	0.281642	0.000018	0.000928	0.000030	0.035687	0.001587	1.469028	0.000060	0.7325	1.95	0.50	0.281605	0.000018	5.6	0.6	6.5	0.6	2130
12.1	z152	0.281551	0.000019	0.000326	0.000008	0.012505	0.000278	1.469108	0.000061	0.7325	2.08	0.75	0.281538	0.000019	3.6	0.7	4.1	0.7	2130
12.2	z151	0.281642	0.000028	0.001879	0.000072	0.062607	0.002176	1.467726	0.000054	0.7325	1.97	0.56	0.281565	0.000028	5.7	1.0	5.1	1.0	2130
13.3	z156	0.281550	0.000024	0.000589	0.000098	0.018527	0.003213	1.467681	0.000057	0.7325	1.79	0.67	0.281526	0.000024	3.7	0.9	3.7	0.9	2130
15.3	z158	0.281562	0.000022	0.000528	0.000017	0.016017	0.000558	1.467746	0.000063	0.7325	2.01	0.67	0.281541	0.000022	3.8	0.8	4.2	0.8	2130
16.1	z159	0.281583	0.000024	0.000676	0.000013	0.021108	0.000465	1.467704	0.000055	0.7325	1.79	0.55	0.281556	0.000024	4.2	0.9	4.8	0.9	2130
16.3	z161	0.281613	0.000023	0.001283	0.000028	0.036409	0.001111	1.467689	0.000050	0.7325	2.07	0.64	0.281560	0.000023	5.5	0.8	4.9	0.8	2130
17.3	z164	0.281562	0.000025	0.000665	0.000013	0.020198	0.000273	1.467660	0.000055	0.7325	1.91	0.60	0.281535	0.000025	3.9	0.9	4.0	0.9	2130
18.3	z165	0.281598	0.000024	0.000925	0.000052	0.028431	0.001542	1.467676	0.000057	0.7325	1.67	0.50	0.281560	0.000024	4.5	0.9	4.9	0.9	2130
19.1	z166	0.281600	0.000021	0.000342	0.000008	0.010129	0.000357	1.467712	0.000061	0.7325	1.83	0.56	0.281586	0.000021	5.5	0.7	5.8	0.7	2130
20.3	z168	0.281525	0.000024	0.000312	0.000005	0.008793	0.000210	1.467669	0.000057	0.7325	1.89	0.64	0.281513	0.000024	3.2	0.8	3.2	0.8	2130
23.1	z173	0.281554	0.000021	0.000358	0.000005	0.010897	0.000150	1.467783	0.000054	0.7325	2.00	0.80	0.281540	0.000021	4.0	0.7	4.2	0.7	2130
24.2	z176	0.281510	0.000023	0.000546	0.000068	0.016212	0.001980	1.467626	0.000063	0.7325	1.93	0.87	0.281488	0.000023	2.4	0.8	2.4	0.8	2130
25.3	z178	0.281519	0.000018	0.000347	0.000008	0.010531	0.000310	1.467666	0.000054	0.7325	2.05	0.66	0.281505	0.000018	3.2	0.7	3.0	0.7	2130
26.4	z181	0.281570	0.000023	0.000603	0.000018	0.017942	0.000630	1.467673	0.000061	0.7325	1.79	0.69	0.281546	0.000023	3.8	0.8	4.4	0.8	2130
29.2	z184	0.281553	0.000024	0.000743	0.000059	0.022882	0.002150	1.467579	0.000062	0.7325	1.95	0.15	0.281523	0.000024	3.7	0.9	3.6	0.9	2130
30.4	z187	0.281490	0.000022	0.000421	0.000013	0.012818	0.000407	1.467518	0.000050	0.7325	1.92	0.64	0.281473	0.000022	1.9	0.8	1.8	0.8	2130
31.2	z189	0.281588	0.000024	0.000520	0.000035	0.015354	0.001223	1.467606	0.000050	0.7325	1.71	0.56	0.281567	0.000024	4.7	0.8	5.1	0.8	2130
33.1	z193	0.281573	0.000026	0.000469	0.000008	0.014506	0.000257	1.467528	0.000059	0.7325	1.95	0.76	0.281554	0.000026	4.2	0.9	4.7	0.9	2130
33.2	z194	0.281613	0.000024	0.002812	0.000090	0.101521	0.002496	1.467501	0.000048	0.7325	2.00	0.83	0.281496	0.000024	3.8	0.9	2.6	0.9	2130
34.2	z195	0.281629	0.000024	0.001990	0.000095	0.060644	0.002222	1.467512	0.000055	0.7325	2.54	0.86	0.281546	0.000024	5.5	0.9	4.4	0.9	2130
34.3	z196	0.281596	0.000022	0.000940	0.000020	0.029415	0.000492	1.467500	0.000054	0.7325	1.74	0.50	0.281558	0.000022	4.7	0.8	4.8	0.8	2130
35.2	z198	0.281584	0.000027	0.001320	0.000146	0.043465	0.004884	1.467459	0.000068	0.7325	1.96	0.49	0.281531	0.000027	3.8	1.0	3.9	1.0	2130
36.3	z202	0.281567	0.000024	0.000670	0.000033	0.019902	0.000848	1.467527	0.000063	0.7325	1.86	0.66	0.281540	0.000024	4.2	0.9	4.2	0.9	2130
37.3	z206	0.281573	0.000021	0.000380	0.000022	0.010993	0.000734	1.467707	0.000066	0.7325	1.87	0.56	0.281557	0.000021	4.8	0.7	4.8	0.7	2130
38.2	z208	0.281561	0.000027	0.000646	0.000034	0.019912	0.001048	1.467775	0.000102	0.7325	1.73	0.54	0.281535	0.000027	4.0	1.0	4.0	1.0	2130
25.4	z179	0.281543	0.000025	0.000373	0.000017	0.010988	0.000567	1.467578	0.000048	0.7325	1.84	0.63	0.281528	0.000025	3.8	0.9	3.8	0.9	2130
10.3	z148	0.281538	0.000026	0.000384	0.000007	0.011127	0.000269	1.467573	0.000061	0.7325	1.82	0.66	0.281522	0.000026	2.7	0.9	3.6	0.9	2130
7.2	z140	0.281665	0.000026	0.002737	0.000100	0.095164	0.002440	1.467626	0.000055	0.7325	1.63	0.48	0.281552	0.000026	5.4	0.9	4.6	0.9	2130

Lu-Hf isotope composition for the used zircon reference materials. Uncertainties correspond to 2σ confidential interval.

Standard	176Hf/177Hf	±2σ	176Lu/177Hf	±2σ	176Yb/177Hf	±2σ	178Hf/177Hf	±2σ	179Hf/177Hf	178Hf (V)
91500										
Accepted $^{176}Hf/^{177}Hf$ value	0.282307	0.000038	0.000384	0.000001	0.017109	0.000163	1.468584	0.000080	0.732500	1.300366
0,282308 ± 0,000006	0.282280	0.000029	0.000374	0.000000	0.016342	0.000125	1.468212	0.000076	0.732500	1.534454
Blichert-Toft (2008)	0.282301	0.000019	0.000369	0.000001	0.016014	0.000143	1.468256	0.000083	0.732500	1.538970
	0.282315	0.000025	0.000368	0.000001	0.015867	0.000135	1.468733	0.000069	0.732500	1.518348
	0.282300	0.000024	0.000362	0.000000	0.015467	0.000125	1.468279	0.000061	0.732500	1.539652
	0.282295	0.000024	0.000354	0.000000	0.015071	0.000143	1.468503	0.000081	0.732500	1.537477
Average	***0.282300***	***0.000010***	***0.000369***	***0.000008***	***0.015978***	***0.000578***	***1.468428***	***0.000172***	***0.732500***	***1.494878***
MudTank										
Accepted $^{176}Hf/^{177}Hf$ value	0.282525	0.000016	0.000021	0.000000	0.001137	0.000013	1.468431	0.000058	0.732500	2.778655
0,282507 ± 0,000006	0.282536	0.000015	0.000020	0.000000	0.001128	0.000011	1.468451	0.000041	0.732500	2.829939
Woodhead and Hergt (2005)	0.282533	0.000017	0.000020	0.000000	0.001107	0.000012	1.468465	0.000042	0.732500	2.759139
	0.282509	0.000016	0.000019	0.000000	0.001051	0.000014	1.468840	0.000055	0.732500	2.842585
	0.282511	0.000014	0.000020	0.000000	0.001089	0.000015	1.468344	0.000067	0.732500	2.752857
	0.282515	0.000014	0.000021	0.000000	0.001113	0.000013	1.468804	0.000039	0.732500	2.908363
Average	***0.282522***	***0.000009***	***0.000020***	***0.000001***	***0.001104***	***0.000025***	***1.468556***	***0.000172***	***0.732500***	***2.811923***
Mun-0										
As primary	0.282140	0.000021	0.000000	0.000000	0.000000	0.000000	1.468723	0.000065	0.732500	2.380501
	0.282138	0.000017	0.000000	0.000000	0.000000	0.000000	1.468443	0.000049	0.732500	2.897632
	0.282143	0.000021	0.000000	0.000000	0.000000	0.000000	1.468702	0.000065	0.732500	3.054586
	0.282122	0.000016	0.000000	0.000000	0.000000	0.000000	1.468491	0.000049	0.732500	2.923348
	0.282118	0.000020	0.000000	0.000000	0.000000	0.000000	1.468156	0.000040	0.732500	2.906603
	0.282139	0.000013	0.000000	0.000000	0.000000	0.000000	1.468400	0.000052	0.732500	2.907622
	0.282143	0.000016	0.000000	0.000000	0.000000	0.000000	1.468712	0.000037	0.732500	3.263782
	0.282141	0.000017	0.000000	0.000000	0.000000	0.000000	1.468812	0.000041	0.732500	3.760499
	0.282131	0.000015	0.000000	0.000000	0.000000	0.000000	1.468141	0.000042	0.732500	3.849359
	0.282118	0.000015	0.000000	0.000000	0.000000	0.000000	1.468429	0.000046	0.732500	3.117417
	0.282145	0.000014	0.000000	0.000000	0.000000	0.000000	1.468501	0.000043	0.732500	3.575076
	0.282147	0.000011	0.000000	0.000000	0.000000	0.000000	1.468737	0.000051	0.732500	3.432700
Average	***0.282135***	***0.000006***	***0.000000***	***0.000000***	***0.000000***	***0.000000***	***1.468521***	***0.000129***	***0.732500***	***3.172427***
Mun-1										
Accepted $^{176}Hf/^{177}Hf$ value	0.282125	0.000028	0.000922	0.000008	0.043213	0.000699	1.468769	0.000068	0.732500	1.937280
0,282135 ± 0,000007	0.282137	0.000020	0.000952	0.000011	0.044239	0.000811	1.468406	0.000056	0.732500	2.343854
Fisher et al., (2011)	0.282122	0.000023	0.001010	0.000013	0.047060	0.000991	1.468572	0.000064	0.732500	2.379507
	0.282128	0.000022	0.001064	0.000015	0.049799	0.001100	1.468495	0.000056	0.732500	2.445786
	0.282135	0.000017	0.001102	0.000018	0.051945	0.001315	1.468166	0.000050	0.732500	2.405301
	0.282156	0.000022	0.001124	0.000018	0.053182	0.001308	1.468439	0.000052	0.732500	2.431129
	0.282120	0.000019	0.001399	0.000042	0.066615	0.001679	1.468691	0.000046	0.732500	2.350278
	0.282153	0.000028	0.001273	0.000030	0.059808	0.001038	1.468809	0.000055	0.732500	2.353613
	0.282130	0.000020	0.001113	0.000007	0.051413	0.000487	1.468197	0.000049	0.732500	2.367532
	0.282125	0.000022	0.001023	0.000013	0.046496	0.000976	1.468364	0.000056	0.732500	2.355674
	0.282148	0.000025	0.000977	0.000012	0.044171	0.000916	1.468476	0.000048	0.732500	2.366930
	0.282126	0.000025	0.000930	0.000010	0.041570	0.000738	1.468753	0.000039	0.732500	2.342992
Average	***0.282134***	***0.000007***	***0.001074***	***0.000083***	***0.049959***	***0.004240***	***1.468511***	***0.000124***	***0.732500***	***2.339990***
Mun-3										
Accepted $^{176}Hf/^{177}Hf$ value	0.282132	0.000019	0.002983	0.000030	0.145213	0.000284	1.468633	0.000054	0.732500	3.184264
0,282135 ± 0,000007	0.282139	0.000015	0.002746	0.000001	0.130953	0.001134	1.468462	0.000056	0.732500	3.884325
Fisher et al., (2011)	0.282125	0.000020	0.002778	0.000003	0.133054	0.001097	1.468153	0.000039	0.732500	3.833419
	0.282130	0.000023	0.002883	0.000004	0.138147	0.000922	1.468696	0.000040	0.732500	3.857236
	0.282113	0.000018	0.002957	0.000009	0.136607	0.001057	1.468220	0.000047	0.732500	3.743754
	0.282124	0.000019	0.003109	0.000006	0.145452	0.000993	1.468493	0.000038	0.732500	3.628405
Average	***0.282127***	***0.000007***	***0.002909***	***0.000111***	***0.138238***	***0.004944***	***1.468443***	***0.000178***	***0.732500***	***3.688567***
Mun-4										
Accepted $^{176}Hf/^{177}Hf$ value	0.282131	0.000023	0.006912	0.000045	0.345588	0.000756	1.468408	0.000063	0.732500	3.719945
0,282135 ± 0,000007	0.282099	0.000027	0.006774	0.000051	0.337154	0.001030	1.468409	0.000042	0.732500	3.824003
Fisher et al., (2011)	0.282105	0.000018	0.006506	0.000033	0.320029	0.001355	1.468476	0.000042	0.732500	3.739057
	0.282136	0.000020	0.006630	0.000044	0.322875	0.001230	1.468800	0.000037	0.732500	3.771910
	0.282167	0.000022	0.006468	0.000024	0.310830	0.003415	1.468392	0.000054	0.732500	3.770850
	0.282125	0.000020	0.006189	0.000028	0.297575	0.003936	1.468850	0.000072	0.732500	3.663572
Average	***0.282127***	***0.000020***	***0.006580***	***0.000207***	***0.322342***	***0.014195***	***1.468556***	***0.000172***	***0.732500***	***3.748223***







Blichert-Toft, J., 2008. The Hf isotopic composition of zircon reference material 91500. Chem. Geol. 253, 252–257. https://doi.org/https://doi.org/10.1016/j.chemgeo.2008.05.014

Fisher, C.M., Hanchar, J.M., Samson, S.D., Dhuime, B., Blichert-Toft, J., Vervoort, J.D., Lam, R., 2011. Synthetic zircon doped with hafnium and rare earth elements: A reference material for in situ hafnium isotope analysis. Chem. Geol. 286, 32–47. https://doi.org/10.1016/j.chemgeo.2011.04.013

Woodhead, J.D., Hergt, J.M., 2005. A Preliminary Appraisal of Seven Natural Zircon Reference Materials for In Situ Hf Isotope Determination. Geostand. Geoanalytical Res. 29, 183–195. https://doi.org/https://doi.org/10.1111/j.1751-908X.2005.tb00891.x

LA-MC-ICPMS Cupim leucogranite zircon Si isotopes. Italic symbols are inherited domains zircons. Grey colors are altered composition. Uncertainties correspond to 2σ confidential interval.

Sample	This work	Domain	Composition	Si isotopes								
				δ29Si	±2σ	δ30Si	±2σ	28Si (V)	27Al/28Si	δ30Si calc	±2σ	$\Delta^{30}Si_{Wr-Zrc}$
GC1												
80-120-03.1	z1	Magmatic	Pristine	-0.4	0.08	-0.48	0.15	10.05	0	-0.77	0.15	0.18
80-120-08.2	*z4*	*Inherited*	*Altered*	*-0.46*	*0.08*	*-0.99*	*0.15*	*8.78*	*0*	*-0.88*	*0.16*	*0.69*
80-120-11.1	*z6*	*Inherited*	*Pristine*	*-0.47*	*0.09*	*-0.71*	*0.15*	*10.96*	*0*	*-0.92*	*0.17*	*0.41*
80-120-16.3	*z8*	*Inherited*	*Altered*	*-0.38*	*0.08*	*-0.89*	*0.14*	*10.94*	*0*	*-0.73*	*0.15*	*0.58*
80-120-17.1	z9	Magmatic	Pristine	-0.43	0.07	-1	0.16	7.88	0	-0.83	0.14	0.7
80-120-18.1	z11	Magmatic	Pristine	-0.39	0.08	-1.06	0.14	9.82	0	-0.76	0.16	0.86
120-200-4.1	z13	Magmatic	Altered	-0.47	0.1	-0.88	0.15	9.03	0	-0.9	0.18	0.76
120-200-5.1	z14	Magmatic	Pristine	-0.39	0.09	-0.81	0.14	8.44	0.01	-0.75	0.17	0.44
120-200-8.3	z15	Magmatic	Altered	-0.4	0.09	-0.87	0.13	6.58	0	-0.76	0.18	0.54
120-200-9.1	*z18*	*Inherited*	*Altered*	*-0.39*	*0.09*	*-0.63*	*0.13*	*9.39*	*0.01*	*-0.75*	*0.18*	*0.35*
120-200-9.3	z19	Magmatic	Altered	-0.53	0.09	-1.01	0.13	8.19	0	-1.03	0.17	0.7
120-200-12.3	z22	Magmatic	Pristine	-0.59	0.1	-0.92	0.13	6.94	0	-1.13	0.19	0.65
120-200-12.1	*z21*	*Inherited*	*Altered*	*-0.5*	*0.11*	*-1.04*	*0.14*	*7.71*	*0*	*-0.97*	*0.22*	*0.79*
120-200-14.3	z23	Magmatic	Altered	-0.63	0.08	-0.96	0.14	6.03	0.01	-1.21	0.16	0.7
120-200-15.3	*z24*	*Inherited*	*Altered*	*-0.39*	*0.1*	*-0.66*	*0.16*	*6.17*	*0.03*	*-0.75*	*0.18*	*0.36*
120-200-23.2	z29	Magmatic	Pristine	-0.44	0.09	-0.65	0.16	6.1	0.02	-0.85	0.17	0.36
120-200-23.3	*z31*	*Inherited*	*Pristine*	*-0.5*	*0.11*	*-0.97*	*0.14*	*5.74*	*0*	*-0.96*	*0.2*	*0.6*
GC2												
60-80-2.1	*z37*	*Inherited*	*Altered*	*-0.11*	*0.11*	*-0.27*	*0.16*	*5.18*	*0.03*	*-0.21*	*0.2*	*-0.01*
60-80-4.2	z41	Magmatic	Pristine	-0.39	0.1	-0.77	0.14	6.92	0	-0.76	0.18	0.45
60-80-3.3	z38	Magmatic	Altered	-0.51	0.09	-0.84	0.15	4.92	0.01	-0.98	0.18	0.62
60-80-6.5	z42	Magmatic	Altered	-0.44	0.11	-1.03	0.15	4.67	0.01	-0.85	0.21	0.71
120-200-9.3	*z32*	*Inherited*	*Pristine*	*-0.38*	*0.12*	*-0.54*	*0.16*	*4.77*	*0.01*	*-0.74*	*0.23*	*0.13*
120-200-16.1	z34	Magmatic	Altered	-0.49	0.13	-0.8	0.17	4.29	0.01	-0.95	0.24	0.53
120-200-18.1	*z36*	*Inherited*	*Altered*	*-0.45*	*0.08*	*-0.85*	*0.14*	*7.92*	*0.03*	*-0.88*	*0.16*	*0.56*
GC5A												
60-80-2.2	z52	Magmatic	Altered	-0.37	0.09	-0.58	0.14	8.8	0.02	-0.72	0.18	0.37
60-80-8.1	z55	Magmatic	Pristine	-0.38	0.08	-0.88	0.12	8.92	0	-0.73	0.16	0.63
80-120-1.1	z56	Magmatic	Pristine	-0.55	0.1	-1.09	0.16	5.85	0.01	-1.07	0.2	0.82
80-120-2.3	z57	Magmatic	Altered	-0.4	0.09	-0.79	0.17	5.77	0.01	-0.77	0.18	0.54
80-120-15.1	z59	Magmatic	Altered	-0.57	0.09	-0.96	0.14	5.84	0	-1.09	0.16	0.71
120-200-6.2	z44	Magmatic	Altered	-0.22	0.1	-0.76	0.18	5.54	0	-0.42	0.19	0.73
120-200-7.3	z46	Magmatic	Altered	-0.3	0.1	-0.53	0.16	7.34	0	-0.58	0.19	-0.29

GC5B												
60-80-3.2	z67	Magmatic	Altered	-0.31	0.08	-0.56	0.13	8.98	0	-0.6	0.16	0.28
60-80-5.5	*z70*	*Inherited*	*Pristine*	*-0.35*	*0.08*	*-0.41*	*0.12*	*10.8*	*0.01*	*-0.69*	*0.16*	*0.11*
60-80-10.1	z74	Magmatic	Altered	-0.38	0.08	-0.49	0.14	9.37	0	-0.73	0.16	0.08
60-80-6.4	z72	Magmatic	Altered	-0.43	0.08	-0.99	0.13	8.57	0	-0.83	0.16	0.64
80-120-8.2	z101	Magmatic	Altered	-0.47	0.09	-0.81	0.17	6.53	0	-0.9	0.18	0.45
80-120-10.4	z102	Magmatic	Pristine	-0.4	0.1	-1.11	0.17	6.47	0	-0.77	0.19	0.77
120-200-8.2	z64	Magmatic	Pristine	-0.47	0.09	-0.81	0.17	6.53	0	-0.9	0.18	0.42
GC6												
80-120-1.2	*z90*	*Inherited*	*Altered*	*-0.61*	*0.09*	*-1.41*	*0.13*	*6.95*	*0.24*	*-1.18*	*0.17*	*1.29*
80-120-3.2	*z91*	*Inherited*	*Altered*	*-0.58*	*0.08*	*-1.12*	*0.15*	*6.87*	*0.03*	*-1.12*	*0.15*	*0.84*
80-120-5.2	z95	Magmatic	Pristine	-0.24	0.08	-0.43	0.12	10.97	0	-0.46	0.16	0.15
120-200-2.1	*z79*	*Inherited*	*Altered*	*-0.57*	*0.09*	*-1.01*	*0.13*	*7.15*	*0.01*	*-1.11*	*0.18*	*0.73*
120-200-10.1	*z82*	*Inherited*	*Altered*	*-0.46*	*0.11*	*-0.74*	*0.17*	*7.62*	*0.05*	*-0.89*	*0.21*	*0.45*
120-200-12.1	*z83*	*Inherited*	*Altered*	*-0.49*	*0.09*	*-1.1*	*0.16*	*7.37*	*0*	*-0.94*	*0.17*	*0.8*
120-200-13.2	z85	Magmatic	Altered	-0.4	0.08	-0.86	0.17	7.24	0	-0.77	0.16	0.56
120-200-14.3	*z86*	*Inherited*	*Altered*	*-0.41*	*0.08*	*-0.91*	*0.13*	*10.01*	*0*	*-0.8*	*0.16*	*0.61*
120-200-20.1	z87	Magmatic	Altered	-0.72	0.09	-1.22	0.15	6.41	0	-1.39	0.18	1.01
GC7												
80-120-8.1	*z97*	*Inherited*	*Pristine*	*-0.53*	*0.08*	*-1.25*	*0.16*	*7.1*	*0.01*	*-1.02*	*0.15*	*1.04*
80-120-10.1	z99	Magmatic	Pristine	-0.38	0.09	-0.76	0.13	9.22	0	-0.73	0.17	0.48
Av. Group 1		Magmatic	Pristine	-0.44	0.09	-0.87	0.15	7.63	0.00	-0.85	0.17	0.57
2SD				0.14	0.02	0.39	0.03	2.97	0.01	0.27	0.04	0.43
Av. Group 2		Magmatic	Pristine	-0.31	0.09	-0.60	0.13	10.10	0.00	-0.60	0.17	0.32
2SD				0.20	0.01	0.47	0.01	2.47	0.00	0.38	0.01	0.47
Av. Inherited		*Inherited*	*Pristine*	*-0.45*	*0.10*	*-0.78*	*0.15*	*7.87*	*0.01*	*-0.87*	*0.18*	*0.46*
2SD				***0.16***	***0.04***	***0.68***	***0.03***	***5.73***	***0.01***	***0.29***	***0.07***	***0.77***

LA-MC-ICPMS zircon Si isotopes for the studied samples. Italic symbols are inherited domains zircons. Grey colors refres to zirrcon with altered composition (not used in the calculed average).
Δ30SiWR-Zrc values were calculated as a funtion of the whole-rock SiO2 composition and Ti-in-zircon temperatures, according to Guitreau et al., (2022).

Sample	This work	Domain	Composition	Si isotopes δ29Si	±2σ	δ30Si	±2σ	28Si (V)	27Al/28Si	δ30Si calc	±2σ	Δ30SiWr-Zrc	δ30Si Wr
CM44A													
1.2	z1	Magmatic	Altered	-0.41	0.13	-1.67	0.34	5.38	0.01	-0.78	0.26	0.30	-1.37
12.2	z9	Magmatic	Altered	-0.46	0.08	-0.78	0.13	7.79	0.03	-0.88	0.16	0.28	-0.50
17.3	z11	Magmatic	Pristine	-0.55	0.13	-1.23	0.23	7.16	0.01	-1.05	0.26	0.32	-0.90
18.1	z12	Magmatic	Altered	-0.52	0.11	-1.56	0.24	6.27	0.01	-0.99	0.21	0.25	-1.31
22.2	*z17*	*Inherited*	*Altered*	*-0.35*	*0.11*	*-0.58*	*0.21*	*5.80*	*0.02*	*-0.68*	*0.21*	*0.21*	-0.37
23.2	*z18*	*Inherited*	*Altered*	*-0.41*	*0.09*	*-0.78*	*0.14*	*10.88*	*0.01*	*-0.79*	*0.17*	*0.22*	-0.55
24.3	*z20*	*Inherited*	*Pristine*	*-0.31*	*0.08*	*-0.49*	*0.15*	*11.21*	*0.00*	*-0.61*	*0.15*	*0.32*	-0.17
25.3	*z23*	*Inherited*	*Altered*	*-0.39*	*0.08*	*-0.71*	*0.15*	*10.06*	*0.00*	*-0.76*	*0.16*	*0.28*	-0.43
4.3	z5	Magmatic	Altered	-0.45	0.09	-0.58	0.13	8.35	0.00	-0.87	0.17	0.33	-0.25
4.4	z6	Magmatic	Altered	-0.51	0.09	-0.85	0.18	7.57	0.00	-0.98	0.17	0.33	-0.52
9.1	z7	Magmatic	Altered	-0.33	0.11	-0.58	0.18	5.89	0.01	-0.63	0.22	0.25	-0.33
Average magmatic (2SD)				**-0.55**	**0.13**	**-1.23**	**0.23**	**7.16**	**0.01**	**-1.05**	**0.26**	**0.32**	**-0.90**
Average inheried (2SD)				***-0.31***	***0.08***	***-0.49***	***0.15***	***11.21***	***0.00***	***-0.61***	***0.15***	***0.32***	***-0.17***
CM44B													
5.1	z30	Magmatic	Pristine	-0.66	0.09	-0.66	0.14	6.29	0.00	-1.27	0.17	0.29	-0.37
5.4	z28	Magmatic	Altered	-0.37	0.08	-0.83	0.13	6.94	0.10	-0.71	0.16	0.23	-0.60
Average (2SD)				**-0.66**	**0.09**	**-0.66**	**0.14**	**6.29**	**0.00**	**-1.27**	**0.17**	**0.29**	**-0.37**
CM46A													
1.1	z31	Magmatic	Altered	-0.52	0.09	-1.35	0.13	7.99	0.00	-1.01	0.17	0.35	-1.00
11.3	z48	Magmatic	Altered	-0.38	0.08	-1.58	0.18	7.24	0.01	-0.73	0.16	0.09	-1.48
18.1	z49	Magmatic	Altered	-0.67	0.08	-1.01	0.15	8.97	0.03	-1.30	0.16	0.36	-0.65
18.2	z50	Magmatic	Altered	-0.31	0.08	-1.65	0.17	7.28	0.04	-0.59	0.16	0.23	-1.42
19.3	z52	Magmatic	Altered	-0.41	0.08	-0.65	0.12	11.22	0.00	-0.78	0.16	0.27	-0.37
20.2	z53	Magmatic	Altered	-0.42	0.09	-0.51	0.13	8.19	0.01	-0.81	0.18	0.27	-0.24
21.3	*z57*	*Inherited*	*Pristine*	*-0.35*	*0.08*	*-0.38*	*0.13*	*10.25*	*0.00*	*-0.68*	*0.15*	*0.38*	-0.01
22.2	z73	Magmatic	Pristine	-0.44	0.07	-0.89	0.12	10.85	0.02	-0.86	0.14	0.23	-0.66
23.1	z60	Magmatic	Altered	-0.43	0.09	-0.70	0.13	8.08	0.00	-0.83	0.17	0.19	-0.50
23.3	z59	Magmatic	Altered	-0.34	0.09	-0.65	0.15	7.60	0.00	-0.65	0.18	0.34	-0.31
~~**24.1**~~	~~z62~~	~~Magmatic~~	~~Pristine~~	~~-0.60~~	~~0.09~~	~~-1.43~~	~~0.16~~	~~6.20~~	~~0.00~~	~~-1.16~~	~~0.18~~	~~0.38~~	-1.06
25.3	z63	Magmatic	Altered	-0.39	0.09	-0.98	0.16	10.02	0.01	-0.76	0.17	0.29	-0.70
29.1	z67	Magmatic	Altered	-0.53	0.09	-0.87	0.15	8.46	0.05	-1.03	0.18	0.27	-0.60
~~**3.2**~~	~~z33~~	~~Magmatic~~	~~Pristine~~	~~-0.76~~	~~0.08~~	~~-1.74~~	~~0.14~~	~~6.65~~	~~0.01~~	~~-1.47~~	~~0.16~~	~~0.33~~	-1.41
5.2	z38	Magmatic	Altered	-0.45	0.06	-0.85	0.12	10.90	0.00	-0.87	0.12	0.34	-0.51
7.2	z44	Magmatic	Pristine	-0.49	0.10	-0.77	0.12	7.24	0.00	-0.95	0.19	0.38	-0.39
9.2	z46	Magmatic	Altered	-0.24	0.08	-0.28	0.13	11.27	0.03	-0.46	0.16	0.34	0.06
Average magmatic (2SD)				**-0.47**	**0.09**	**-0.83**	**0.12**	**9.05**	**0.01**	**-0.91**	**0.16**	**0.31**	**-0.52**
CM47													
1.1	z69	Magmatic	Pristine	-0.35	0.10	-0.92	0.16	9.93	0.00	-0.67	0.19	0.35	-0.57
~~**10.1**~~	~~z99~~	~~Magmatic~~	~~Pristine~~	~~-0.76~~	~~0.14~~	~~-1.16~~	~~0.20~~	~~3.81~~	~~0.01~~	~~-1.46~~	~~0.27~~	~~0.36~~	-0.80
~~**10.3**~~	~~z100~~	~~Magmatic~~	~~Pristine~~	~~-0.56~~	~~0.19~~	~~-0.96~~	~~0.22~~	~~3.72~~	~~0.00~~	~~-1.07~~	~~0.36~~	~~0.36~~	-0.60
11.1	z101	Magmatic	Pristine	-0.29	0.11	-0.57	0.16	5.12	0.00	-0.57	0.21	0.32	-0.24

13.1	z102	Magmatic	Altered	-0.55	0.14	-0.82	0.15	5.50	0.00	-1.07	0.27	0.29	-0.53
17.2	z107	Magmatic	Altered	-0.54	0.08	-0.62	0.14	9.13	0.03	-1.04	0.16	0.27	-0.35
2.3	z74	Magmatic	Pristine	-0.44	0.11	-0.68	0.16	6.20	0.00	-0.86	0.21	0.29	-0.39
22.3	z112	Magmatic	Altered	-0.51	0.08	-1.10	0.13	10.31	0.06	-0.98	0.16	0.24	-0.86
25.3	z114	Magmatic	Altered	-0.40	0.09	-0.96	0.13	8.06	0.01	-0.77	0.17	0.24	-0.73
26.2	*z115*	*Inherited?*	*Pristine*	*-0.68*	*0.09*	*-1.44*	*0.14*	*7.52*	*0.00*	*-1.32*	*0.18*	*0.30*	*-1.13*
3.4	z80	Magmatic	Altered	-0.59	0.11	-1.93	0.19	5.55	0.01	-1.13	0.21	0.22	-1.71
31.1	z122	Magmatic	Altered	-0.38	0.09	-0.51	0.12	7.95	0.00	-0.73	0.17	0.18	-0.33
36.3	z126	Magmatic	Pristine	-0.46	0.08	-0.81	0.12	7.80	0.00	-0.89	0.16	0.29	-0.52
4.2	z83	Magmatic	Altered	-0.51	0.12	-0.78	0.17	5.57	0.00	-0.98	0.22	0.29	-0.50
5.5	z90	Magmatic	Altered	-0.53	0.10	-1.11	0.18	5.07	0.01	-1.03	0.20	0.28	-0.83
7.1	z91	Magmatic	Altered	-0.34	0.10	-0.76	0.16	5.07	0.00	-0.66	0.19	0.28	-0.48
8.3	z96	Magmatic	Pristine	-0.47	0.13	-0.76	0.16	4.24	0.01	-0.90	0.25	0.35	-0.41
8.4	z97	Magmatic	Pristine	-0.36	0.13	-0.56	0.15	4.31	0.00	-0.70	0.26	0.33	-0.23
Average magmatic (2SD)				**-0.40**	**0.11**	**-0.72**	**0.15**	**6.27**	**0.00**	**-0.76**	**0.21**	**0.32**	**-0.39**
CM49													
10.2	z147	Magmatic	Altered	-0.33	0.13	-0.81	0.19	3.12	0.01	-0.64	0.26	0.27	-0.54
10.3	z148	Magmatic	Altered	-0.13	0.12	-0.24	0.24	2.99	0.03	-0.26	0.23	0.19	-0.05
11.2	z149	Magmatic	Altered	-0.46	0.16	-1.16	0.24	3.21	0.03	-0.90	0.32	0.31	-0.85
12.1	z152	Magmatic	Pristine	-0.49	0.11	-0.94	0.17	3.54	0.00	-0.95	0.21	0.26	-0.68
12.2	z151	Magmatic	Pristine	-0.30	0.11	-0.64	0.15	3.88	0.00	-0.59	0.21	0.33	-0.30
13.3	z156	Magmatic	Altered	-0.61	0.12	-1.43	0.17	3.90	0.03	-1.18	0.22	0.33	-1.10
16.1	z159	Magmatic	Pristine	-0.54	0.09	-0.84	0.14	6.74	0.01	-1.04	0.18	0.30	-0.54
16.3	z161	Magmatic	Pristine	-0.60	0.10	-0.85	0.14	7.01	0.01	-1.15	0.19	0.35	-0.50
17.3	z164	Magmatic	Altered	-0.60	0.09	-0.95	0.13	7.36	0.01	-1.15	0.17	0.27	-0.68
18.3	z165	Magmatic	Altered	-0.29	0.12	-0.90	0.20	5.53	0.00	-0.56	0.24	0.20	-0.70
19.1	z166	Magmatic	Pristine	-0.53	0.09	-0.77	0.17	7.36	0.00	-1.03	0.17	0.26	-0.50
20.3	z168	Magmatic	Altered	-0.59	0.09	-0.80	0.14	7.23	0.01	-1.13	0.18	0.22	-0.58
23.1	z173	Magmatic	Altered	-0.61	0.15	-0.95	0.20	6.08	0.00	-1.19	0.29	0.30	-0.65
24.2	z176	Magmatic	Pristine	-0.54	0.08	-1.00	0.13	6.64	0.00	-1.04	0.15	0.34	-0.66
3.4	z132	Magmatic	Pristine	-0.50	0.13	-0.21	0.18	5.08	0.02	-0.97	0.25	0.35	0.14
4.3	z135	Magmatic	Pristine	-0.51	0.12	-1.20	0.23	4.41	0.00	-0.99	0.24	0.30	-0.90
5.4	z138	Magmatic	Pristine	-0.46	0.13	-1.15	0.24	3.75	0.02	-0.89	0.25	0.27	-0.88
7.2	z140	Magmatic	Pristine	-0.46	0.09	-0.87	0.16	4.67	0.02	-0.89	0.18	0.24	-0.63
7.3	z141	Magmatic	Pristine	-0.52	0.10	-1.07	0.16	4.72	0.00	-1.00	0.20	0.34	-0.73
8.3	z144	Magmatic	Pristine	-0.55	0.11	-1.03	0.19	4.17	0.02	-1.07	0.21	0.34	-0.69
9.3	z146	Magmatic	Altered	-0.46	0.10	-0.52	0.17	4.08	0.02	-0.88	0.20	0.14	-0.37
Average (2SD)				**-0.50**	**0.11**	**-0.90**	**0.17**	**5.16**	**0.01**	**-0.97**	**0.20**	**0.31**	**-0.57**

Guitreau, M., Gannoun, A., Deng, Z., Chaussidon, M., Moynier, F., Barbarin, B., Marin-Carbonne, J., 2022. Stable isotope geochemistry of silicon in granitoid zircon. Geochim. Cosmochim. Acta 316, 273–294. https://doi.org/10.1016/j.gca.2021.09.029

Silicon isotope composition for the used zircon reference materials. Grey colors are altered composition.

Standard	δ29Si	2 SE	δ30Si	2 SE	28Si (V)	27Al/28Si	δ30Si calc.	2 SE
MudTank	-0.21	0.09	-0.18	0.14	7.3	0	-0.4	0.17
δ^{30}Si = -0.34 ± 0.03‰	-0.17	0.1	-0.23	0.18	7.8	0	-0.33	0.18
Trail et al., (2018)	-0.16	0.08	-0.52	0.15	8	0	-0.32	0.16
δ^{30}Si = -0.47 ± 0.17‰	-0.45	0.1	-0.74	0.16	5.9	0	-0.87	0.18
Guitreau et al., (2020, 2022)	-0.19	0.09	-0.51	0.14	10	0	-0.37	0.17
	-0.3	0.08	-0.79	0.1	11.1	0	-0.58	0.16
	-0.16	0.08	-1.36	0.16	10.8	0	-0.31	0.16
	-0.27	0.09	-0.52	0.12	9.6	0	-0.53	0.17
	-0.21	0.08	-0.37	0.14	10.6	0	-0.4	0.15
	-0.25	0.08	-0.33	0.12	10.4	0	-0.47	0.15
	-0.2	0.08	-0.44	0.12	9.8	0	-0.38	0.15
	-0.23	0.09	-0.32	0.15	11.5	0	-0.45	0.16
	-0.16	0.09	-0.4	0.12	9.1	0	-0.3	0.17
Average (2SD)	***-0.21***	***0.07***	***-0.38***	***0.24***	***9.41***	***0***	***-0.4***	***0.14***
Mun-1	-1.1	0.09	-1.97	0.16	6.5	0.0001	-2.12	0.18
δ^{30}Si ~ -2‰	-0.93	0.1	-1.56	0.16	7.8	0.0001	-1.8	0.19
Guitreau et al., (2020, 2022)	-0.98	0.09	-1.95	0.18	6.7	0.0001	-1.9	0.18
	-0.91	0.08	-1.89	0.12	10.9	0.0001	-1.75	0.16
	-0.98	0.1	-2.31	0.15	7.1	0.0001	-1.89	0.2
	-1.06	0.1	-1.97	0.16	7.2	0.0001	-2.04	0.19
	-0.93	0.07	-1.78	0.11	11.2	0.0001	-1.8	0.14
	-1.01	0.09	-2.12	0.14	8.4	0.0001	-1.96	0.18
	-0.94	0.08	-2.13	0.12	10.8	0.0001	-1.82	0.16
	-0.95	0.09	-1.87	0.14	10.6	0.0001	-1.84	0.17
	-0.92	0.1	-2.2	0.15	6.7	0.0001	-1.77	0.19
	-0.91	0.08	-1.87	0.12	10.2	0.0001	-1.75	0.16
Average (2SD)	***-0.98***	***0.13***	***-1.95***	***0.23***	***9.17***	***0***	***-1.89***	***0.26***
Plesovice	0	0.09	0.24	0.16	8.5	0.0011	0	0.18
δ^{30}Si = -0.38 ± 0.18‰ (2SD)	-0.04	0.09	-0.19	0.17	8.2	0.0011	-0.08	0.17
Guitreau et al., (2020, 2022)	-0.08	0.09	-0.2	0.17	7.7	0.0021	-0.15	0.17
Trail et al., (2018)	-0.36	0.09	-0.61	0.17	7	0.001	-0.69	0.16
	-0.29	0.09	-0.59	0.16	6.6	0.001	-0.57	0.18
	-0.22	0.1	-0.43	0.16	6	0.0009	-0.42	0.19
	-0.15	0.11	-0.4	0.17	5.7	0.001	-0.29	0.22
	-0.31	0.08	-0.64	0.12	10.8	0.0029	-0.6	0.15
	-0.24	0.08	-0.24	0.13	10.8	0.003	-0.46	0.15
	-0.14	0.09	-0.41	0.14	11	0.0025	-0.26	0.17
	-0.18	0.09	-0.35	0.15	11	0.0025	-0.34	0.18
	-0.24	0.08	-0.33	0.12	11.1	0.0025	-0.46	0.16
	-0.02	0.08	-0.17	0.12	11.4	0.0026	-0.03	0.16
	-0.24	0.09	-0.32	0.12	10.8	0.0026	-0.47	0.17
	-0.53	0.11	-0.88	0.16	5.6	0.001	-1.03	0.22
	-0.2	0.08	-0.54	0.14	10.8	0.0017	-0.39	0.16
	-0.23	0.08	-0.31	0.13	10.7	0.0012	-0.45	0.16
	-0.09	0.08	-0.32	0.12	10.8	0.0011	-0.17	0.15
	-0.43	0.1	-0.96	0.17	10.1	0.0025	-0.82	0.19
	-0.57	0.1	-1.02	0.15	8.8	0.0029	-1.09	0.18
	0	0.1	0.04	0.13	8.5	0.0021	0	0.19
	-0.18	0.09	-0.53	0.13	8.1	0.0023	-0.36	0.18
	-0.22	0.1	-0.31	0.14	7.6	0.0024	-0.42	0.19
	-0.35	0.11	-0.66	0.15	5.8	0.0012	-0.68	0.22
	-0.26	0.1	-0.49	0.14	7.4	0.0034	-0.51	0.19
	-0.18	0.1	-0.29	0.13	7.1	0.0024	-0.34	0.2
	-0.17	0.1	-0.42	0.14	6.5	0.0018	-0.33	0.2
	-0.33	0.08	-0.76	0.14	11.9	0.0028	-0.63	0.15
	-0.2	0.08	-0.34	0.15	11.6	0.0007	-0.39	0.15
	-0.11	0.08	-0.25	0.14	11.7	0.0019	-0.21	0.15
	-0.15	0.08	-0.23	0.13	11.9	0.0022	-0.3	0.15
	-0.09	0.08	-0.34	0.12	11.9	0.0023	-0.17	0.15
	-0.25	0.1	-0.32	0.15	6.3	0.0015	-0.49	0.2
	-0.17	0.07	-0.08	0.13	12	0.0255	-0.33	0.14
	-0.03	0.08	-0.13	0.13	11.7	0.0017	-0.06	0.15
	-0.11	0.08	-0.27	0.13	11.6	0.0016	-0.21	0.16
	-0.2	0.09	-0.24	0.12	11.2	0.0018	-0.39	0.16
	-0.24	0.08	-0.57	0.12	10.8	0.0017	-0.46	0.15
	-0.21	0.08	-0.22	0.12	10.7	0.0015	-0.41	0.15
	-0.22	0.08	-0.62	0.11	10.4	0.0015	-0.43	0.16
	-0.15	0.09	-0.21	0.12	10.3	0.0015	-0.29	0.17

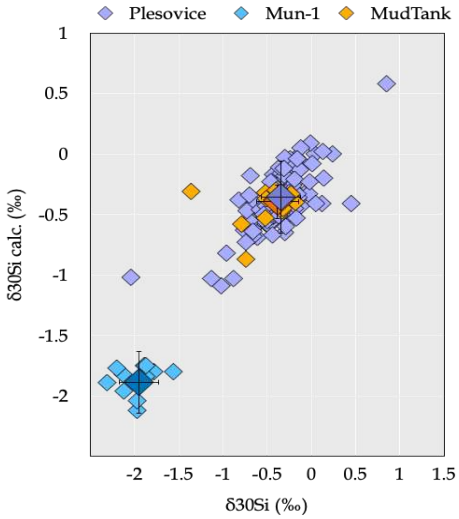
-0.24	0.08	-0.48	0.12	9.9	0.0016	-0.46	0.16
-0.17	0.07	-0.32	0.12	9.7	0.0014	-0.32	0.14
-0.02	0.1	-0.24	0.15	6.8	0.0015	-0.04	0.19
-0.19	0.08	-0.46	0.11	9.6	0.0016	-0.37	0.15
-0.18	0.08	-0.23	0.12	9.6	0.0013	-0.35	0.16
-0.17	0.09	-0.37	0.12	9.4	0.0012	-0.32	0.18
-0.18	0.09	-0.25	0.12	9.2	0.0016	-0.34	0.18
-0.16	0.09	-0.36	0.12	8.9	0.0018	-0.32	0.18
-0.08	0.08	-0.38	0.13	11.5	0.0013	-0.15	0.15
-0.17	0.08	-0.36	0.12	11.4	0.0012	-0.32	0.16
-0.19	0.08	-0.47	0.12	11.5	0.0012	-0.38	0.16
-0.29	0.1	-0.69	0.16	7.8	0.0075	-0.55	0.19
-0.22	0.08	-0.12	0.12	11.1	0.0012	-0.43	0.15
-0.21	0.07	-0.47	0.13	10.8	0.0012	-0.4	0.14
-0.19	0.07	-0.59	0.13	10.9	0.0012	-0.37	0.14
-0.17	0.07	-0.03	0.12	10.8	0.0012	-0.33	0.14
-0.21	0.08	-0.64	0.12	10.5	0.0048	-0.41	0.15
-0.18	0.08	-0.15	0.12	10.7	0.0013	-0.36	0.16
-0.12	0.1	-0.18	0.16	7.6	0.0012	-0.23	0.2
-0.3	0.1	-0.52	0.15	7.3	0.0012	-0.57	0.2
-0.53	0.1	-1.13	0.15	7.1	0.0021	-1.03	0.19
-0.31	0.08	-0.49	0.15	7.4	0.0012	-0.59	0.16
-0.06	0.09	-0.13	0.16	8	0.0012	-0.11	0.17
-0.13	0.09	-0.25	0.16	8.2	0.0012	-0.24	0.18
0.04	0.09	-0.01	0.16	9.2	0.005	0.09	0.18
0.3	0.08	0.85	0.12	10.5	0.0014	0.58	0.15
0.03	0.08	-0.12	0.13	10.5	0.0016	0.05	0.15
-0.34	0.08	-0.3	0.14	9.8	0.0027	-0.65	0.16
-0.2	0.09	-0.82	0.14	9.1	0.0024	-0.38	0.16
-0.23	0.09	-0.19	0.13	8.9	0.0024	-0.45	0.17
-0.09	0.09	-0.31	0.14	8.8	0.0032	-0.17	0.18
-0.3	0.09	-0.48	0.14	8.4	0.0021	-0.59	0.18
-0.28	0.08	-0.59	0.12	11.6	0.0021	-0.53	0.15
-0.17	0.08	-0.16	0.12	11.5	0.0021	-0.33	0.15
-0.17	0.08	-0.7	0.13	11.2	0.0022	-0.34	0.16
-0.21	0.08	0.12	0.13	11.4	0.0022	-0.41	0.15
-0.09	0.07	-0.43	0.15	11.3	0.0022	-0.17	0.14
-0.2	0.07	-0.38	0.14	11.2	0.0021	-0.38	0.14
-0.07	0.07	-0.15	0.14	11.2	0.0016	-0.14	0.14
-0.18	0.07	-0.23	0.13	11.2	0.0017	-0.35	0.14
-0.08	0.07	-0.34	0.13	11.3	0.0016	-0.16	0.14
-0.21	0.07	-0.35	0.12	11.6	0.002	-0.4	0.14
-0.26	0.08	-0.27	0.12	11.3	0.0057	-0.51	0.15
-0.17	0.07	-0.46	0.12	11.1	0.0125	-0.33	0.14
-0.15	0.08	-0.3	0.11	11.4	0.0019	-0.29	0.15
-0.29	0.08	-0.45	0.12	11.2	0.0032	-0.56	0.16
-0.11	0.08	-0.3	0.12	11.1	0.0019	-0.21	0.16
-0.27	0.08	-0.44	0.12	11.2	0.0017	-0.52	0.16
-0.09	0.07	-0.3	0.12	11.3	0.0024	-0.18	0.14
-0.26	0.07	-0.34	0.12	11.1	0.0019	-0.5	0.14
-0.04	0.08	-0.2	0.13	11.2	0.0026	-0.08	0.15
-0.35	0.08	-0.44	0.12	11	0.0025	-0.67	0.15
-0.06	0.08	-0.36	0.12	11	0.0029	-0.11	0.16
-0.24	0.08	-0.4	0.12	10.9	0.0031	-0.45	0.16
-0.26	0.08	-0.42	0.13	10.7	0.0011	-0.51	0.16
-0.28	0.09	-0.5	0.13	9.7	0.0011	-0.55	0.18
-0.29	0.1	-0.67	0.14	9.1	0.0013	-0.55	0.18
-0.06	0.1	-0.13	0.14	8.9	0.0014	-0.13	0.19
-0.26	0.09	-0.45	0.15	8.3	0.0013	-0.5	0.17
-0.15	0.1	-0.27	0.14	7.9	0.0013	-0.29	0.19
-0.18	0.1	-0.32	0.14	7.4	0.0013	-0.34	0.19
-0.28	0.11	-0.55	0.13	7	0.0013	-0.54	0.22
-0.38	0.11	-0.74	0.14	6.7	0.0038	-0.73	0.21
-0.29	0.1	-0.7	0.15	7.2	0.0015	-0.55	0.2
-0.27	0.09	-0.17	0.15	7.3	0.0122	-0.53	0.17
-0.02	0.09	-0.3	0.14	7.6	0.0019	-0.03	0.17
-0.04	0.1	0.01	0.15	7.7	0.0018	-0.08	0.19
-0.23	0.07	-0.37	0.13	12.2	0.002	-0.44	0.13
-0.24	0.08	-0.73	0.12	12.4	0.0021	-0.47	0.15
-0.1	0.08	0.14	0.12	11.7	0.0016	-0.2	0.16
-0.24	0.08	-0.58	0.11	11.4	0.0019	-0.46	0.16
-0.22	0.08	-0.51	0.1	11.3	0.0021	-0.43	0.15
-0.13	0.07	-0.21	0.11	11.6	0.0011	-0.26	0.14
-0.17	0.08	-0.29	0.12	11.6	0.0011	-0.32	0.15
-0.17	0.08	-0.25	0.12	11	0.0012	-0.32	0.15
-0.18	0.07	-0.28	0.12	11.1	0.0023	-0.35	0.14

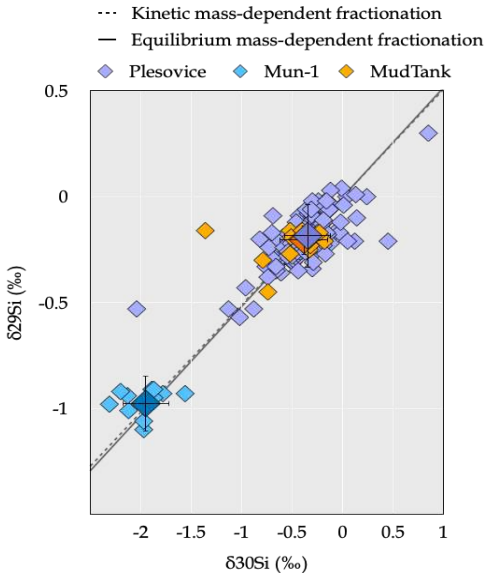
	-0.12	0.07	-0.46	0.12	10.8	0.0012	-0.23	0.14
	-0.31	0.08	-0.29	0.13	10.1	0.0118	-0.6	0.15
	-0.09	0.08	-0.69	0.14	10.1	0.0012	-0.18	0.16
	-0.21	0.08	0.45	0.15	10.2	0.0011	-0.41	0.16
	-0.53	0.08	-2.04	0.14	9.9	0.0022	-1.02	0.16
	-0.21	0.08	0.05	0.14	10.6	0.0017	-0.41	0.16
	0.01	0.08	0.13	0.13	11	0.001	0.02	0.15
	-0.26	0.08	-0.54	0.12	10.8	0.0019	-0.5	0.15
	-0.06	0.08	-0.31	0.12	11.3	0.001	-0.12	0.15
	-0.11	0.07	-0.19	0.11	11.3	0.0028	-0.21	0.14
	-0.12	0.07	-0.02	0.11	11.6	0.0014	-0.23	0.14
	-0.02	0.08	-0.16	0.12	11.6	0.0013	-0.04	0.15
	-0.24	0.08	-0.34	0.13	10.7	0.0014	-0.47	0.16
	-0.17	0.09	-0.41	0.14	10.6	0.0012	-0.33	0.17
	-0.26	0.09	-0.37	0.14	9.7	0.0017	-0.51	0.16
	-0.15	0.09	-0.38	0.14	9.7	0.0019	-0.29	0.17
	-0.33	0.09	-0.66	0.14	9.5	0.0023	-0.64	0.17
Average (2SD)	**-0.18**	**0.15**	**-0.35**	**0.23**	**9.93**	**0**	**-0.36**	**0.3**

Guitreau, M., Gannoun, A., Deng, Z., Chaussidon, M., Moynier, F., Barbarin, B., Marin-Carbonne, J., 2022. Stable isotope geochemistry of silicon in granitoid zircon. Geochim. Cosmochim. Acta 316, 273–294. https://doi.org/10.1016/j.gca.2021.09.029

Guitreau, M., Gannoun, A., Deng, Z., Marin-Carbonne, J., Chaussidon, M., Moynier, F., 2020. Silicon isotope measurement in zircon by laser ablation multiple collector inductively coupled plasma mass spectrometry. J. Anal. At. Spectrom. 35, 1597–1606. https://doi.org/10.1039/d0ja00214c

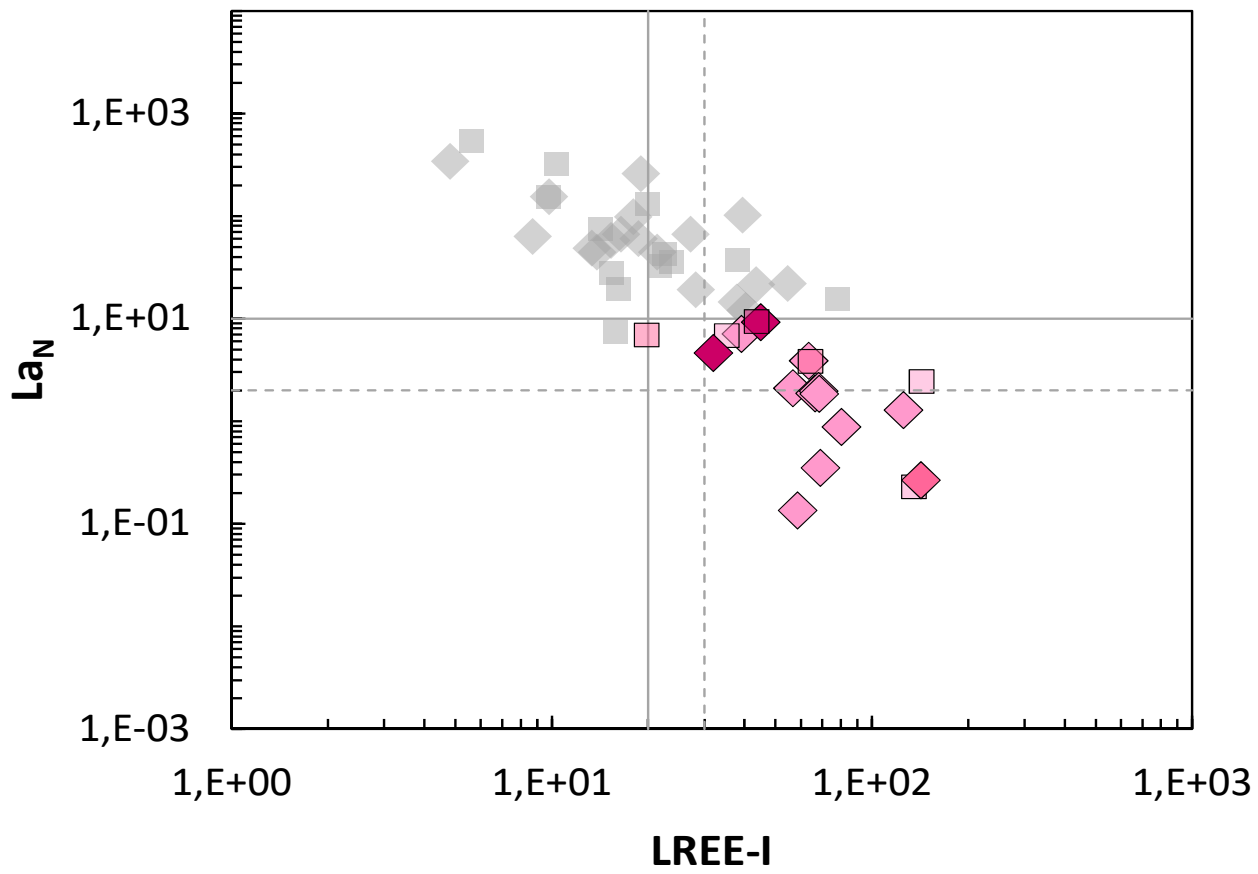
Trail, D., Boehnke, P., Savage, P.S., Liu, M.-C., Miller, M.L., Bindeman, I., 2018. Origin and significance of Si and O isotope heterogeneities in Phanerozoic, Archean, and Hadean zircon. Proc. Natl. Acad. Sci. 115, 10287–10292. https://doi.org/10.1073/pnas.1808335115





LA-ICPMS zircon trace elements (ppm) analyses and Ti in zircon temperatures, equations from Ferry and Watson (2007) for Cupim Pluton samples. Comp. refers to the degree of alteration. Italic symbols are inherited domains zircons. Grey colors are altered composition.

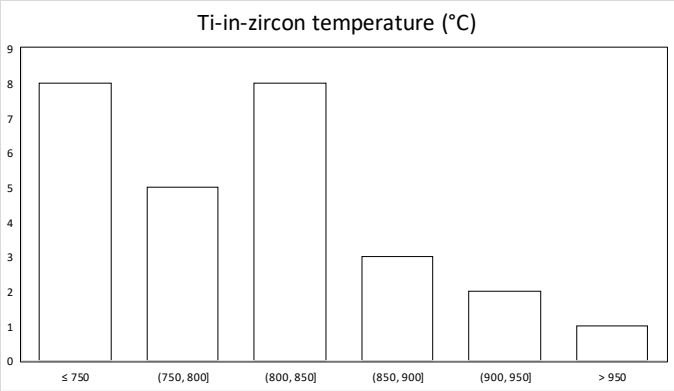
Sample	This work	Domain	Comp.	Elemental concentration																													Ti in zircon		
				Al	P	K	Ca	Ti	V	Zn	Ga	Rb	Sr	Y	Nb	Ba	La	Ce	Pr	Nd	Sm	Eu	Gd	Tb	Dy	Ho	Er	Tm	Yb	Lu	Hf	Ta	Pb	Th	U	T(K)	T(°C)	10^6/T^2
GC1																																					
80-120-3.1	z1	Magmatic	Pristine	37	970	14	885	14	0	8	0	1	2	1820	13	0	1	18	0	4	8	1	43	14	173	59	266	52	445	83	10787	5	2336	608	3036	1135	861	1
80-120-8.2	*z4*	*Inherited*	*Altered*	*332*	*609*	*39*	*2415*	*36*	*0*	*18*	*4*	*1*	*6*	*1724*	*44*	*3*	*76*	*170*	*18*	*72*	*22*	*14*	*59*	*17*	*178*	*57*	*261*	*53*	*490*	*98*	*13166*	*11*	*2107*	*1243*	*2769*	*1256*	*983*	*1*
80-120-11.1	***z6***	***Inherited***	***Pristine***	***44***	***795***	***15***	***637***	***8***	***0***	***6***	***0***	***1***	***1***	***2420***	***18***	***0***	***1***	***12***	***0***	***2***	***4***	***0***	***32***	***14***	***197***	***77***	***389***	***82***	***741***	***144***	***14278***	***11***	***2824***	***316***	***3139***	***1076***	***803***	***1***
80-120-16.3	*z8*	*Inherited*	*Altered*	*82*	*546*	*5*	*453*	*24*	*1*	*7*	*1*	*0*	*1*	*1138*	*63*	*1*	*8*	*35*	*3*	*13*	*9*	*1*	*31*	*10*	*114*	*37*	*168*	*32*	*291*	*58*	*13693*	*3*	*495*	*988*	*933*	*1203*	*930*	*1*
80-120-17.1	z9	Magmatic	Pristine	20	728	8	512	6	0	8	0	0	1	1398	7	0	0	13	0	3	6	0	33	11	131	45	204	39	344	64	10984	4	1788	332	2048	1046	773	1
80-120-18.1	z11	Magmatic	Pristine	16	728	6	423	6	0	5	0	0	1	1301	7	0	0	7	0	1	3	0	23	9	116	42	198	39	357	68	12776	3	1693	149	1500	1051	778	1
120-200-4.1	z13	Magmatic	Altered	84	589	9	614	6	0	6	1	1	1	2091	24	0	5	18	1	7	5	1	24	10	151	60	312	65	586	112	15976	26	2960	156	3375	1044	771	1
120-200-5.1	z14	Magmatic	Pristine	44	1542	12	549	7	0	9	1	1	1	3358	9	0	0	21	1	7	14	1	82	27	320	109	490	93	805	152	10633	5	4532	935	4852	1061	788	1
120-200-8.3	z15	Magmatic	Altered	440	443	12	934	14	0	5	1	0	5	723	16	1	11	28	2	10	8	1	29	9	93	26	98	16	120	20	11608	2	975	577	759	1131	858	1
120-200-9.1	*z18*	*Inherited*	*Altered*	*202*	*614*	*11*	*799*	*36*	*1*	*19*	*2*	*1*	*3*	*2381*	*56*	*6*	*31*	*65*	*6*	*30*	*23*	*3*	*83*	*24*	*256*	*81*	*352*	*66*	*562*	*106*	*8967*	*6*	*1013*	*1296*	*770*	*1258*	*985*	*1*
120-200-9.3	z19	Magmatic	Altered	308	1370	80	3409	8	0	8	1	2	8	2416	45	2	16	17	4	17	13	1	51	16	203	76	391	89	887	186	14605	25	3747	362	4990	1076	803	1
120-200-12.3	z22	Magmatic	Pristine	22	422	7	440	8	0	4	0	0	1	677	3	0	0	10	0	2	3	1	15	5	57	21	105	23	213	45	9746	1	424	100	236	1071	798	1
120-200-12.1	*z21*	*Inherited*	*Altered*	*132*	*1092*	*28*	*1365*	*28*	*0*	*13*	*1*	*1*	*3*	*2093*	*19*	*2*	*4*	*16*	*1*	*4*	*5*	*0*	*35*	*13*	*177*	*66*	*325*	*68*	*637*	*128*	*12170*	*11*	*2537*	*448*	*3564*	*1222*	*949*	*1*
120-200-14.3	z23	Magmatic	Altered	412	1041	23	3314	4	0	10	2	1	6	2945	10	0	24	44	3	15	16	1	80	26	303	96	412	75	620	115	11713	4	2574	587	3989	1012	739	1
120-200-15.3	*z24*	*Inherited*	*Altered*	*174*	*1163*	*24*	*789*	*14*	*0*	*7*	*1*	*1*	*2*	*2387*	*40*	*3*	*9*	*40*	*3*	*13*	*11*	*1*	*51*	*18*	*222*	*78*	*375*	*75*	*666*	*134*	*11804*	*8*	*1568*	*965*	*1265*	*1138*	*865*	*1*
120-200-23.2	z29	Magmatic	Pristine	16	403	8	440	11	0	5	0	0	1	794	3	1	0	6	0	1	3	0	16	5	70	26	128	26	242	51	11938	2	1032	78	641	1111	838	1
120-200-23.3	***z31***	***Inherited***	***Pristine***	***26***	***932***	***8***	***519***	***24***	***0***	***6***	***0***	***1***	***1***	***1836***	***12***	***0***	***0***	***12***	***0***	***2***	***5***	***0***	***34***	***13***	***161***	***59***	***275***	***55***	***479***	***92***	***12092***	***5***	***2571***	***417***	***2812***	***1199***	***926***	***1***
60-80-1.3	z100	Magmatic	Pristine	33	1253	16	717	10	0	7	0	1	1	2236	6	0	0	15	0	4	10	1	58	19	216	73	322	62	535	103	10083	3	2158	597	2428	1098	825	1
GC2																																					
60-80-2.1	*z37*	*Inherited*	*Altered*	*1509*	*1153*	*79*	*5840*	*55*	*1*	*14*	*6*	*2*	*23*	*3107*	*100*	*4*	*37*	*67*	*23*	*90*	*56*	*11*	*93*	*30*	*339*	*109*	*507*	*105*	*957*	*174*	*16290*	*28*	*2833*	*249*	*4937*	*1320*	*1047*	*1*
60-80-4.2	z41	Magmatic	Pristine	27	610	12	777	6	0	9	0	1	1	1639	11	0	0	9	0	1	5	0	32	12	152	51	231	43	366	67	12851	10	5553	639	7487	1038	765	1
60-80-3.3	z38	Magmatic	Altered	153	502	10	495	5	0	7	1	0	1	961	8	0	11	20	4	16	9	1	19	7	83	29	141	30	279	54	13857	6	1952	92	1902	1027	754	1
60-80-6.5	z42	Magmatic	Altered	313	583	31	2246	5	0	6	1	1	6	1260	12	0	5	17	1	6	4	0	21	8	105	38	182	38	343	69	12789	6	2575	231	3392	1031	758	1
120-200-9.3	***z32***	***Inherited***	***Pristine***	***230***	***388***	***13***	***493***	***10***	***1***	***4***	***1***	***0***	***1***	***1144***	***7***	***0***	***2***	***23***	***2***	***12***	***13***	***1***	***31***	***11***	***120***	***40***	***184***	***36***	***308***	***57***	***11665***	***2***	***822***	***178***	***429***	***1093***	***820***	***1***
120-200-16.1	z34	Magmatic	Altered	427	888	99	1339	7	0	10	2	2	4	1609	19	1	16	13	6	24	15	2	35	12	148	50	257	55	535	105	16093	19	2963	258	3672	1066	793	1
120-200-18.1	*z36*	*Inherited*	*Altered*	*1067*	*909*	*40*	*5933*	*20*	*2*	*13*	*3*	*1*	*18*	*2309*	*52*	*2*	*8*	*76*	*5*	*21*	*17*	*2*	*49*	*18*	*220*	*76*	*362*	*74*	*669*	*126*	*13364*	*12*	*2652*	*447*	*3120*	*1176*	*903*	*1*
GC5A																																					
60-80-2.2	z52	Magmatic	Altered	231	699	29	1430	10	1	11	2	1	7	1131	9	1	23	98	6	23	8	5	32	10	111	37	164	31	274	52	10989	2	1769	258	1881	1094	821	1
60-80-8.1	z55	Magmatic	Pristine	59	880	13	5673	15	0	16	1	1	22	2045	19	3	0	20	1	6	11	1	60	19	212	68	292	53	447	83	10244	6	3983	1256	7111	1141	868	1
80-120-1.1	z56	Magmatic	Pristine	48	778	19	1609	15	0	9	0	1	4	1734	10	0	1	15	0	4	8	1	44	15	169	57	252	47	408	80	10330	5	3820	751	5051	1147	874	1
80-120-2.3	z57	Magmatic	Altered	36	641	12	827	10	0	8	0	1	2	1220	6	0	3	10	1	6	7	0	34	11	118	39	178	34	297	58	10969	3	1907	330	2118	1099	825	1
80-120-15.1	z59	Magmatic	Altered	62	620	18	748	10	0	11	1	0	1	1083	6	1	3	25	1	6	4	0	23	8	100	35	165	31	277	54	12256	4	2661	234	3190	1094	821	1
120-200-6.2	z44	Magmatic	Altered	273	670	24	1648	14	0	10	2	1	7	1555	11	1	61	111	10	31	10	0	38	13	147	50	229	44	379	72	11487	5	3224	551	4561	1135	862	1
120-200-7.3	z46	Magmatic	Altered	1509	1153	79	5840	55	1	14	6	2	23	3107	100	4	37	67	23	90	56	11	93	30	339	109	507	105	957	174	16290	28	2833	249	4937	1320	1047	
GC5B																																					
60-80-3.2	z67	Magmatic	Altered	911	529	21	743	7	1	13	4	1	1	783	4	0	11	129	4	16	9	1	24	7	76	25	114	22	198	38	12611	2	1241	142	1104	1061	788	1
60-80-5.5	***z70***	***Inherited***	***Pristine***	***36***	***671***	***5***	***459***	***11***	***0***	***4***	***1***	***1***	***1***	***1470***	***6***		***2***	***57***	***1***	***8***	***9***	***0***	***42***	***13***	***144***	***50***	***222***	***41***	***351***	***68***	***12896***	***2***	***671***	***450***	***383***	***1104***	***831***	***1***
60-80-10.1	z74	Magmatic	Altered	782	665	20	1230	22	2	9	6	1	3	1271	16	1	81	293	32	117	51	5	81	20	172	45	167	28	224	40	11556	2	1262	270	1529	1187	914	1
60-80-6.4	z72	Magmatic	Altered	872	643	57	1307	32	1	29	2	3	2	1334	10	2	14	70	4	19	11	1	37	12	131	43	193	37	321	62	12168	3	2320	286	2863	1241	968	1
80-120-8.2	z101	Magmatic	Altered	296	367	17	776	7	0	7	2	0	2	853	5	0	15	66	7	31	15	2	32	9	88	28	122	23	202	40	12489	2	1202	123	1129	1053	780	1
80-120-10.4	z102	Magmatic	Pristine	99	805	30	3459	14	0	11	1	1	10	1405	10	2	0	10	0	3	5	0	30	11	132	45	211	40	352	69	12224	4	3345	331	4673	1134	861	1
120-200-8.2	z64	Magmatic	Pristine	39	769	18	1866	16	0	9	0	1	3	1065	13	0	2	18	1	5	6	1	34	11	111	34	141	26	222	43	12176	6	2645	418	2873	1147	874	1
GC6																																					
80-120-1.2	*z90*	*Inherited*	*Altered*	*159*	*3105*	*11*	*11151*	*8*	*3*	*8*	*8*	*1*	*4*	*2581*	*11*	*0*	*128*	*302*	*48*	*164*	*60*	*2*	*99*	*24*	*246*	*80*	*363*	*70*	*607*	*114*	*13098*	*4*	*2009*	*516*	*1583*	*1071*	*798*	*1*
80-120-3.2	*z91*	*Inherited*	*Altered*	*1078*	*325*	*23*	*737*	*50*	*5*	*7*	*2*	*1*	*1*	*1284*	*81*	*2*	*5*	*48*	*4*	*18*	*15*	*1*	*39*	*12*	*135*	*44*	*209*	*42*	*388*	*76*	*12202*	*10*	*954*	*535*	*966*	*1305*	*1032*	*1*
80-120-5.2	z95	Magmatic	Pristine	56	144	23	436	15	2	5	1	1	1	746	5	0	1	31	1	4	5	1	22	6	71	23	105	20	175	33	10037	1	205	69	188	1142	868	1
120-200-2.1	*z79*	*Inherited*	*Altered*	*1311*	*361*	*37*	*3536*	*46*	*1*	*11*	*2*	*3*	*4*	*1640*	*64*	*2*	*18*	*43*	*7*	*29*	*17*	*1*	*47*	*15*	*152*	*49*	*234*	*47*	*431*	*83*	*13212*	*22*	*1884*	*428*	*1976*	*1293*	*1020*	*1*
120-200-10.1	*z82*	*Inherited*	*Altered*	*211*	*738*	*27*	*2060*	*12*	*0*	*14*	*1*	*1*	*1*	*785*	*17*	*1*	*7*	*45*	*3*	*13*	*7*	*0*	*22*	*6*	*73*	*25*	*117*	*23*	*203*	*39*	*11034*	*2*	*556*	*272*	*275*	*1116*	*843*	*1*
120-200-12.1	*z83*	*Inherited*	*Altered*	*31*	*1209*	*24*	*3519*	*7*	*0*	*3*	*1*	*0*	*6*	*449*	*2*	*0*	*2*	*18*	*1*	*6*	*4*	*1*	*11*	*3*	*36*	*14*	*71*	*16*	*171*	*39*	*9128*	*1*	*182*	*72*	*123*	*1056*	*783*	*1*
120-200-13.2	z85	Magmatic	Altered	188	318	29	1250	13	1	9	1	1	2	1579	24	1	14	65	5	25	17	2	50	14	152	49	222	45	416	82	12406	11	1550	658	1551	1131	857	1
120-200-14.3	*z86*	*Inherited*	*Altered*	*58*	*461*	*12*	*689*	*7*	*0*	*5*	*1*	*0*	*1*	*1114*	*19*	*0*	*10*	*38*	*3*	*12*	*7*	*1*	*27*	*8*	*99*	*35*	*165*	*32*	*286*	*53*	*11467*	*3*	*717*	*345*	*411*	*1054*	*781*	*1*
120-200-20.1	z87	Magmatic	Altered	428	623	26	1481	40	1	16	1	1	3	1376	43	1	5	19	3	10	9	1	32	12	134	43	194	38	321	59	11632	7	2368	510	3141	1270	997	1
GC7																																					
80-120-8.1	***z97***	***Inherited***	***Pristine***	***68***	***382***	***15***	***400***	***4***	***0***	***6***	***0***	***1***	***1***	***817***	***7***	***0***	***2***	***14***	***1***	***3***	***3***	***0***	***16***	***6***	***70***	***25***	***123***	***25***	***219***	***44***	***10837***	***3***	***463***	***99***	***308***	***1011***	***738***	***1***
80-120-10.1	z99	Magmatic	Pristine	82	395	28	2498	9	0	9	0	1	5	899	17	0	2	4	1	3	3	0	13	5	66	27	143	33	336	75	14132	12	2444	126	2555	1085	812	1
Av. Group 1		Magmatic	Pristine	38	824	13	1446	11	0	8	0	1	4	1623	9	1	1	14	0	3	7	1	39	13	155	53	237	45	395	76	11231	4	2776	516	3495	1098	825	1
2SD				47	642	13	3200	8	0	6	0	1	12	1441	9	2	1	10	0	4	7	1	39	13	143	47	206	38	322	59	2200	5	3014	710	4719			
Av. Group 2		Magmatic	Pristine	69	270	26	1467	12	1	7	0	1	3	823	11	0	2	18	1	4	4	0	17	6	68	25	124	27	256	54	12085	6	1324	98	1371	1113	840	1
2SD				36	354	7	2917	8	2	6	0	1	6	217	17	0	2	38	0	1	3	1	13	2	7	5	53	19	228	59	5792	15	3166	81	3348			
Av. Inherited		*Inherited*	*Pristine*	*81*	*634*	*11*	*502*	*11*	*0*	*5*	*0*	*1*	*1*	*1537*	*10*	*0*	*1*	*24*	*1*	*5*	*7*	*0*	*31*	*11*	*138*	*50*	*239*	*48*	*420*	*81*	*12353*	*5*	*1470*	*292*	*1414*	*1097*	*823*	*1*
2SD				*169*	*490*	*9*	*176*	*15*	*0*	*3*	*0*	*0*	*1*	*1243*	*10*	*0*	*2*	*38*	*2*	*9*	*8*	*1*	*19*	*7*	*95*	*39*	*201*	*44*	*405*	*79*	*2615*	*8*	*2263*	*302*	*2861*			

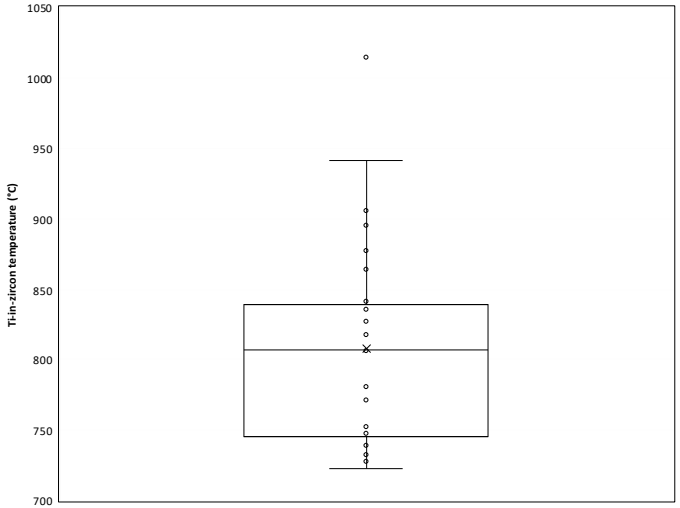

1,E+03
1,E+01
1,E-01
1,E-03
La_N
1,E+00
1,E+01
1,E+02
1,E+03
LREE-I

LA-ICPMS zircon trace elements (ppm) analyses and Ti in zircon temperatures, equations from Ferry and Watson (2007) for the studied samples. Comp. refers to the degree of alteration. Italic symbols are inherited domains zircons. Grey colors are altered composition.

Sample	This work	Domain	Comp.	Elemental concentration																													Ti in zircon temperatures		
				Al	P	K	Ca	Ti	V	Zn	Ga	Rb	Sr	Y	Nb	Ba	La	Ce	Pr	Nd	Sm	Eu	Gd	Tb	Dy	Ho	Er	Tm	Yb	Lu	Hf	Ta	Pb	Th	U	Th/U	T(K)	T(°C)	10^6/T^2
CM44A																																					
1.2	z1	Magmatic	Altered	506	56	32	2100	15	0.40	7.4	4.63	0.43	23.7	792	6.2	2.3	65.6	175	23.2	114.5	60.0	22.4	79.6	13.1	96	26	105	20	181	31	12311	7	1646	127	2229	0.06	1141	868	0.77
4.4	z6	Magmatic	Altered	170	176	8	538	9	0.28	4.7	2.16	0.36	3.1	1255	6.0	0.4	32.9	107	12.6	55.9	30.4	2.3	57.5	13.6	129	36	148	29	246	44	13946	3	1760	59	1678	0.04	1089	815	0.84
4.3	z5	Magmatic	Altered	580	277	24	1230	9	0.52	3.7	4.80	0.55	9.8	3385	2.4	0.6	43.0	182	27.4	142.7	105.7	7.3	216.7	41.5	318	81	263	39	269	49	9819	1	743	99	600	0.17	1080	807	0.86
9.1	z7	Magmatic	Altered	175	147	19	816	35	0.29	5.8	1.17	0.24	4.5	710	50.9	0.9	17.4	48	7.2	38.2	20.3	2.5	33.9	6.9	65	20	93	20	192	43	18163	1	1018	49	1467	0.03	1251	978	0.64
12.2	z9	Magmatic	Altered	1968	6470	406	27316	19	2.25	14.4	3.96	3.70	70.5	3590	20.1	6.7	15.5	75	12.3	84.8	57.1	4.8	159.3	39.0	410	133	567	101	824	154	9555	2	462	96	405	0.24	1172	899	0.73
17.3	z11	Magmatic	Pristine	60	250	6	586	10	1.26	3.7	0.87	0.57	3.2	2018	6.3	0.3	6.4	34	2.0	11.9	13.9	5.8	62.9	18.5	204	67	290	54	444	83	11368	1	1647	167	1339	0.12	1101	828	0.82
18.1	z12	Magmatic	Altered	373	194	66	994	33	0.54	6.6	2.37	0.77	8.2	1435	36.2	2.0	26.3	87	13.2	75.8	56.5	10.3	107.1	18.5	145	40	187	45	519	140	24507	21	3229	497	4182	0.12	1244	971	0.65
22.2	*z17*	*Inherited*	*Altered*	*527*	*227*	*60*	*2601*	*69*	*0.44*	*14.7*	*3.02*	*1.55*	*27.3*	*1655*	*22.8*	*6.8*	*24.4*	*95*	*15.7*	*88.1*	*56.6*	*5.2*	*93.5*	*18.1*	*159*	*44*	*189*	*36*	*323*	*63*	*20588*	*5*	*2326*	*125*	*3593*	*0.03*	*1357*	*1084*	*0.54*
23.2	*z18*	*Inherited*	*Altered*	*240*	*323*	*21*	*1029*	*56*	*0.72*	*6.2*	*2.89*	*0.52*	*7.7*	*1694*	*72.3*	*2.1*	*23.2*	*124*	*14.3*	*77.7*	*42.0*	*8.3*	*91.8*	*21.2*	*196*	*55*	*212*	*37*	*283*	*51*	*9883*	*1*	*1184*	*320*	*1123*	*0.28*	*1324*	*1051*	*0.57*
24.3	*z20*	*Inherited*	*Pristine*	*13*	*226*	*20*	*380*	*11*	*0.19*	*3.2*	*0.32*	*0.11*	*0.7*	*428*	*1.5*	*0.0*	*1.6*	*20*	*0.6*	*3.8*	*5.2*	*3.4*	*29.3*	*6.7*	*57*	*14*	*45*	*7*	*50*	*8*	*9849*	*0*	*341*	*99*	*207*	0.48	*1109*	*836*	*0.81*
25.3	z23	Magmatic	Altered	324	4234	100	17662	21	0.34	5.5	2.04	0.48	38.1	1077	18.5	2.8	10.1	45	6.8	41.4	23.8	4.0	58.5	13.6	127	36	139	24	190	34	10636	0	1067	154	793	0.19	1184	911	0.71
CM44B																																					
5.1	z30	Magmatic	Pristine	178	337	16	538	14	0.76	4.7	1.09	0.32	2.5	661	4.9	1.2	11.5	37	5.0	27.9	20.0	2.7	33.2	5.5	49	18	106	26	279	60	14557	4	1354	21	1105	0.02	1137	864	0.77
5.4	z28	Magmatic	Altered	1288	296	368	2568	40	0.90	10.0	3.43	4.67	20.5	928	6.9	13.7	30.3	97	15.4	84.6	64.2	7.5	103.0	14.2	95	25	114	23	221	44	17586	7	1994	99	2422	0.04	1274	1001	0.62
CM46A																																					
1.1	z31	Magmatic	Altered	361	519	116	548	6	1.20	10.0	1.15	1.18	2.7	1554	4.3	2.9	11.7	43	5.3	31.3	8.7	4.5	24.4	8.2	119	50	267	58	556	120	10506	1	506	109	376	0.29	1044	771	0.92
3.2	z33	Magmatic	Pristine	173	423	42	529	9	0.31	6.1	1.11	0.40	2.5	454	2.1	3.4	2.4	43	5.2	41.3	9.5	7.0	15.2	3.6	42	15	72	15	140	30	10965	1	500	83	466	0.18	1080	807	0.86
5.2	z38	Magmatic	Altered	385	306	28	643	7	0.63	6.7	0.43	0.32	1.9	625	2.3	1.7	1.7	12	1.2	9.0	11.2	5.2	29.2	6.2	62	19	85	20	184	39	10921	1	853	108	602	0.18	1059	786	0.89
7.2	z44	Magmatic	Pristine	29	339	11	459	4	0.09	3.0	0.14	0.25	0.8	682	3.4	0.2	0.0	8	0.0	0.9	2.1	0.3	13.7	4.8	62	23	109	22	196	40	10704	1	649	118	445	0.26	996	723	1.01
9.2	z46	Magmatic	Altered	218	467	42	628	7	0.52	6.1	0.89	0.26	2.2	552	2.3	6.7	6.9	27	3.4	22.6	6.9	3.1	15.9	4.3	49	18	88	18	169	36	10956	1	638	89	526	0.17	1060	787	0.89
11.3	z48	Magmatic	Altered	234	567	54	1480	949	2.41	5.1	0.31	0.41	1.9	606	5.0	1.9	1.3	9	1.2	10.3	6.6	1.3	16.9	4.1	51	19	99	21	201	41	10995	1	377	46	329	0.14	2001	1728	0.25
6.2	z41	Magmatic	Altered	1982	511	463	3916	1986	9.10	20.4	5.68	4.99	20.0	1209	16.2	29.3	55.7	184	29.6	183.7	71.2	34.7	95.5	12.6	110	38	193	41	386	81	12185	3	617	138	955	0.14	2310	2037	0.19
6.4	z42	Magmatic	Altered	386	484	101	1434	21	0.93	7.6	1.55	0.72	14.3	1013	5.3	7.6	12.3	49	6.9	49.8	33.8	19.8	54.8	9.7	96	33	159	32	303	62	12564	2	546	143	747	0.19	1181	908	0.72
18.1	z49	Magmatic	Altered	250	469	15	527	5	0.39	5.5	0.20	0.20	1.1	506	3.6	0.3	0.2	3	0.2	2.0	1.8	0.5	8.6	2.7	37	15	87	20	202	45	12677	3	591	37	550	0.07	1033	760	0.94
18.2	z50	Magmatic	Altered	407	419	131	864	47	0.91	6.9	3.50	0.90	7.5	973	4.2	9.1	28.8	109	20.4	138.1	36.7	9.3	43.1	8.0	88	32	160	33	314	67	10820	1	489	125	580	0.21	1295	1022	0.60
19.3	z52	Magmatic	Altered	483	284	41	640	21	3.86	17.0	2.51	0.49	5.1	797	4.4	13.8	21.8	78	13.4	91.7	28.6	11.5	36.4	6.0	65	25	129	29	300	73	10991	1	235	122	287	0.42	1181	908	0.72
20.2	z53	Magmatic	Altered	279	365	48	475	22	0.39	4.0	0.19	0.27	0.6	440	2.1	2.1	0.2	4	0.2	1.6	2.1	0.3	10.3	3.2	39	14	69	14	131	28	10109	1	485	63	331	0.19	1189	916	0.71
21.3	*z57*	*Inherited*	*Pristine*	*3*	*346*	*7*	*428*	*4*	*0.34*	*3.1*	*0.39*	*0.25*	*0.5*	*929*	*2.0*	*0.1*	*0.1*	*22*	*0.3*	*5.3*	*9.0*	*4.2*	*35.9*	*9.4*	*97*	*30*	*132*	*25*	*215*	*43*	*10339*	*0*	*339*	*101*	*142*	0.72	*1005*	*732*	*0.99*
22.2	z59	Magmatic	Pristine	116	325	25	430	45	0.52	6.2	0.30	0.34	1.0	644	3.0	1.0	1.1	12	0.7	5.3	3.2	1.4	13.9	4.5	57	21	102	21	190	40	10927	1	704	104	487	0.21	1288	1015	0.60
23.3	z62	Magmatic	Altered	213	347	29	629	7	0.35	4.3	1.41	0.48	3.1	799	2.5	0.9	1.1	40	2.8	52.4	20.8	14.6	21.1	4.4	60	25	136	31	304	67	11543	1	478	52	417	0.12	1059	786	0.89
23.1	z60	Magmatic	Altered	120	308	21	384	90	0.35	5.0	0.27	0.33	0.9	616	3.2	0.2	0.8	11	0.7	6.0	3.3	1.0	12.6	4.1	52	20	99	20	187	39	11268	1	625	95	432	0.22	1402	1129	0.51
24.1	z63	Magmatic	Pristine	33	432	17	600	4	0.05	3.3	0.55	0.19	1.4	590	3.0	0.4	0.1	21	0.9	17.7	8.2	15.1	14.9	4.1	51	19	94	19	177	36	11482	1	570	103	467	0.22	1006	733	0.99
25.3	z67	Magmatic	Altered	289	385	50	589	16	0.67	6.7	0.52	0.57	2.1	660	2.8	8.1	1.3	17	1.2	12.7	7.4	3.0	17.7	4.7	58	22	106	21	195	41	10917	1	561	114	577	0.20	1151	878	0.75
29.1	z68	Magmatic	Altered	2526	678	1117	1123	21	9.08	24.1	9.51	3.32	11.4	1014	3.3	135.9	87.2	352	49.6	289.5	57.7	15.7	56.9	9.1	91	33	161	33	311	66	11384	1	616	143	623	0.23	1181	908	0.72
CM47																																					
1.1	z69	Magmatic	Pristine	13	382	7	274	5	0.17	3.9	0.21	0.19	0.5	564	3.0	0.1	0.1	14	0.2	1.7	2.9	0.4	12.7	4.2	54	18	88	18	162	34	11476	1	466	83	303	0.27	1021	748	0.96
2.3	z74	Magmatic	Pristine	37	516	19	1005	11	0.48	4.8	0.28	0.35	3.6	1105	3.4	0.4	0.3	11	0.4	3.5	5.7	1.0	28.1	8.9	106	35	158	30	259	50	10738	1	677	116	581	0.20	1110	836	0.81
3.4	z80	Magmatic	Altered	2527	434	468	956	44	3.11	15.6	1.03	4.61	3.8	967	3.9	8.3	1.7	18	1.7	13.2	9.1	1.7	28.7	8.3	94	31	137	26	223	43	10850	1	616	108	510	0.21	1286	1012	0.61
4.2	z83	Magmatic	Altered	159	463	94	457	12	0.41	4.6	0.26	0.60	1.7	600	3.0	2.2	0.3	9	0.3	2.4	2.9	0.6	14.0	4.5	54	19	83	16	144	29	11171	1	473	66	357	0.19	1116	842	0.80
5.5	z90	Magmatic	Altered	174	409	109	367	15	0.64	4.6	0.28	0.85	1.4	664	3.1	2.0	0.6	12	0.4	3.6	3.5	1.0	16.5	5.1	61	21	97	19	162	33	10382	1	486	75	346	0.22	1141	868	0.77
7.1	z91	Magmatic	Altered	736	322	32	527	15	1.99	8.8	1.28	0.26	0.8	555	3.1	2.0	5.4	51	5.2	38.3	14.5	7.2	23.4	5.1	53	18	83	17	150	31	10762	1	434	85	286	0.30	1140	867	0.77
8.3	z96	Magmatic	Pristine	4	418	6	286	4	0.15	3.6	0.14	0.17	0.5	544	2.7	0.2	0.0	9	0.0	0.8	2.0	0.4	12.3	4.1	50	18	82	17	145	30	10199	1	437	61	277	0.22	1013	739	0.98
8.4	z97	Magmatic	Pristine	13	384	10	312	6	0.16	3.4	0.13	0.20	0.8	668	2.7	0.2	0.0	7	0.1	1.2	2.6	1.2	15.0	5.0	62	21	100	20	172	35	10567	1	533	71	378	0.19	1044	771	0.92
10.1	z99	Magmatic	Pristine	25	345	17	231	4	0.07	3.9	0.12	0.24	1.0	561	2.7	0.7	0.2	9	0.2	2.1	2.9	0.7	13.8	4.4	52	18	83	16	147	30	11198	1	669	80	448	0.18	1001	728	1.00
11.1	z101	Magmatic	Pristine	88	473	43	380	7	1.79	4.5	1.26	0.25	1.1	401	2.5	1.4	1.5	97	1.6	10.0	10.3	3.9	24.1	4.0	38	13	58	11	104	22	10745	1	414	46	335	0.14	1054	781	0.90
13.1	z102	Magmatic	Altered	141	461	37	713	11	0.61	5.7	0.40	0.41	3.7	979	3.3	0.9	0.4	17	0.5	4.7	6.1	0.9	28.3	8.6	96	32	138	26	219	42	10892	1	537	114	511	0.22	1107	834	0.82
17.2	z107	Magmatic	Altered	339	348	71	413	18	0.52	6.1	0.28	0.53	1.0	573	2.7	2.7	1.0	10	0.5	3.8	3.8	0.7	14.5	4.5	53	18	83	16	143	29	10425	1	451	62	303	0.20	1162	889	0.74
22.3	z112	Magmatic	Altered	842	324	149	517	30	1.90	9.3	0.69	1.30	2.0	477	2.7	14.2	4.9	17	1.6	9.4	5.8	1.7	16.6	4.0	45	15	69	14	121	25	10189	1	450	99	304	0.32	1233	960	0.66
25.3	z114	Magmatic	Altered	412	338	218	445	29	3.28	6.1	0.56	1.34	1.3	574	3.0	2.5	1.6	19	1.4	9.7	7.1	1.0	17.9	4.6	51	18	82	16	147	30	10545	1	441	89	309	0.29	1229	955	0.66
26.2	*z115*	*Inherited?*	*Pristine*	*100*	*392*	*36*	*959*	*9*	*0.84*	*5.2*	*0.75*	*0.37*	*4.0*	*800*	*3.2*	*3.5*	*2.2*	*22*	*1.7*	*11.8*	*3.6*	*1.9*	*13.6*	*4.5*	*63*	*25*	*136*	*30*	*297*	*66*	*10993*	*1*	*584*	*100*	*534*	0.19	*1091*	*818*	*0.84*
31.1	z122	Magmatic	Altered	1400	603	372	1490	106	13.79	13.6	5.06	2.90	11.9	1672	6.1	7.0	16.2	235	16.1	108.3	70.7	13.5	116.2	22.0	191	53	215	37	308	59	9669	2	642	273	758	0.36	1432	1159	0.49
36.3	z126	Magmatic	Pristine	71	477	16	1169	12	0.49	4.9	0.65	0.35	4.2	1033	3.1	0.5	2.4	31	2.3	17.6	9.7	2.6	30.7	9.0	103	34	147	27	233	45	10464	1	523	114	505	0.23	1114	841	0.81
CM49																																					
3.4	z132	Magmatic	Pristine	36	291	17	394	4	0.42	3.8	0.19	0.23	0.5	554	1.6	0.3	0.0	12	0.1	1.8	3.0	1.4	13.1	3.9	47	17	85	19	183	42	9756	0	252	73	166	0.44	1013	740	0.98
4.3	z135	Magmatic	Pristine	51	350	11	351	9	1.29	3.3	0.68	0.33	0.8	868	2.7	0.8	1.9	40	1.8	13.8	8.4	2.7	24.5	6.4	74	27	133	28	267	61	8885	1	737	264	513	0.51	1091	818	0.84
5.4	z138	Magmatic	Pristine	22	288	12	420	16	0.57	4.3	0.30	0.16	0.6	550	1.7	0.5	0.7	18	0.6	5.5	4.4	2.5	16.1	4.5	50	18	85	18	170	38	10842	0	328	109	211	0.52	1151	878	0.75
7.2	z140	Magmatic	Pristine	86	353	16	303	27	1.17	3.9	0.25	0.47	0.8	1314	4.5	1.2	0.8	11	0.5	4.0	3.9	1.0	21.2	7.9	110	45	228	47	422	89	10319	1	272	54	165	0.33	1215	942	0.68
7.3	z141	Magmatic	Pristine	9	275	1	327	5	0.45	3.1	0.30	0.28	0.5	839	2.2	0.1	0.3	19	0.3	3.8	5.6	2.2	24.2	6.9	77	27	129	27	255	57	10989	0	736	151	489	0.31	1029	756	0.94
8.3	z144	Magmatic	Pristine	91	266	19	493	5	0.54	3.9	0.28	0.25	0.5	528	1.9	0.3	0.2	18	0.2	1.9	2.4	1.3	11.2	3.4	42	16	84	19	192	47	10760	0	647	128	421	0.30	1023	750	0.95
9.3	z146	Magmatic	Altered	749	362	113	5876	226	4.14	9.7	2.18	2.51	93.8	1959	14.2	47.1	27.0	77	9.2	54.6	17.2	42.5	30.4	8.6	132	60	338	75	720	155	13604	3	2357	14	3640	0.004	1589	1316	0.40
10.2	z147	Magmatic	Altered	545	371	125	428	16	1.36	5.4	1.58	0.72	1.9	714	3.4	9.3	11.9	69	5.8	35.6	17.4	5.3	30.2	5.9	62	22	108	23	228	53	10118	1	1049	439	797	0.55	1154	881	0.75
10.3	z148	Magmatic	Altered	1137	377	268	1856	75	4.76	9.3	4.06	1.87	26.2	571	4.7	43.9	50.4	164	20.7	118.3	46.9	14.1	46.8	5.6	46	16	88	21	228	55	13438	3	1494	51	1940	0.03	1372	1098	0.53
11.2	z149	Magmatic	Altered	240	387	55	418	8	1.13	4.3	1.00	0.73	2.2	736	3.0	1.5	2.6	51	3.4	22.0	10.2	3.3	23.2	5.6	62	22	113	24	239	54	10174	1	892	450	711	0.63	1080	806	0.86
12.2	z151	Magmatic	Altered	151	526	58	322	6	1.90	4.0	0.26	0.73	1.1	1591	3.8	2.2	0.7	9	0.8	6.9	4.1	1.0	23.1	8.4	122	52	282	61	573	125	11920	1	194	35	120	0.29	1039	766	0.93
12.1	z152	Magmatic	Pristine	61	323	16	453	20	0.80	6.5	0.39	0.15	0.6	544	2.5	0.2	0.4	22	0.5	4.1	2.9	1.8	11.4	3.4	42	16	85	19	194	45	10445	1	613	149	400	0.37	1179	906	0.72
13.3	z156	Magmatic	Altered	316	346	83	391	6	0.52	3.9	0.38	0.15	3.2	243	1.7	3.3	3.7	16	1.8	13.0	5.5	2.3	8.6	1.7	18	7	38	9	101	24	10742	0	791	29	510	0.06	1043	770	0.92

16.3	z161	Magmatic	Pristine	22	344	7	192	4	1.59	3.3	0.14	0.33	0.6	877	2.4	0.2	0.3	7	0.4	3.7	3.0	0.8	11.9	4.0	57	25	149	37	409	101	10721	1	282	47	180	0.26	1015	742	0.97
16.1	z159	Magmatic	Pristine	64	252	3	266	10	0.43	3.7	0.23	0.09	0.5	154	1.6	0.3	0.4	11	0.6	4.7	2.2	1.2	4.4	1.0	12	4	24	6	61	15	11015	0	245	38	157	0.24	1100	827	0.83
17.3	z164	Magmatic	Altered	194	315	28	413	17	1.52	4.2	0.51	0.40	0.9	535	2.7	1.3	1.6	26	1.6	11.4	6.6	2.8	15.6	3.7	42	15	80	18	183	42	10591	1	746	163	498	0.33	1155	882	0.75
18.3	z165	Magmatic	Altered	1884	384	230	575	62	3.29	10.6	3.98	3.04	3.1	520	1.9	13.1	25.0	155	20.5	142.7	33.6	46.7	37.5	5.2	46	15	76	17	174	41	9675	0	456	176	368	0.48	1340	1066	0.56
19.1	z166	Magmatic	Pristine	92	426	18	320	19	1.34	4.4	1.14	0.40	0.9	1083	4.0	1.7	3.7	67	3.7	25.1	14.6	4.4	35.2	8.3	91	32	162	34	339	75	9647	1	1275	537	917	0.59	1168	895	0.73
20.3	z168	Magmatic	Altered	853	392	177	378	42	2.64	5.9	2.76	1.06	2.8	725	2.7	18.5	17.6	116	13.6	82.1	24.9	10.9	35.3	6.3	64	22	111	23	235	52	9544	1	672	361	571	0.63	1280	1007	0.61
23.1	z173	Magmatic	Altered	170	473	38	410	10	0.67	4.5	0.52	0.33	0.7	482	1.9	2.3	1.8	25	1.4	10.1	6.4	2.6	14.6	3.4	39	14	72	16	161	37	9980	0	555	151	359	0.42	1102	829	0.82
24.2	z176	Magmatic	Pristine	15	512	9	346	5	0.15	3.9	0.17	0.10	0.5	279	1.6	0.4	0.3	10	0.2	2.0	1.6	0.7	6.1	1.8	22	8	43	9	98	23	9632	0	192	46	123	0.37	1026	753	0.95





Trace element composition for the used zircon reference materails. Grey colors are altered composition. 2SD= 2 × Standard deviation and RSD(%)= | Average - Literature content | ÷ Literature content × 100.

Standard zircon / glass	AS3	AS3	AS3	AS3	AS3	AS3	AS3	AS3	AS3	AS3	AS3	AS3	AS3	AS3	AS3	AS3	AS3	AS3	AS3	AS3	AS3	91500	91500
Element (ppm)	*Pristine*	*Pristine*	*Pristine*	*Pristine*	*Pristine*	*Pristine*	*Pristine*	*Pristine*	*Pristine*	*Pristine*	*Altered*	*Pristine*	*Altered*	*Pristine*	*Altered*	**Average**	**2SD(%)**	**Tekehara et al., 2018**	**RSD(%)**	**Guitreau et al., 2022**	**RSD(%)**	*Pristine*	*Pristine*
Al	0.02	0.63			0.75			3.25	2.17	0.65	688.11	1.82	1533.30	13.41	770.23	**2.84**	**8.80**	1.93	47%	0.10	2740%	9.69	6.69
K	4.64	9.70	8.61	2.23	8.00	7.57	2.46	2.79	5.18	4.86	19.48	4.76	9.05	3.02	42.54	**5.32**	**5.14**	0.16	3225%	6.01	11%	9.96	9.44
Ca	276	436	370	364	359	305	269	328	320	425	565	381	415	328	391	**347**	**105**	1	58681%	350	1%	361	379
Ti	9.38	9.36	9.37	9.53	9.82	9.33	9.56	23.18	21.27	20.92	23.55	18.18	24.11	19.23	22.12	**14.09**	**11.65**	31.00	55%	10.91	29%	5.26	5.75
V	0.47	0.54	0.52	0.42	0.42	0.35	0.39	1.84	0.31	0.23	0.84	0.16	1.38	0.20	0.84	**0.49**	**0.89**			0.42	17%	0.06	0.05
Zn	3.36	3.15	3.38	3.02	3.08	2.80	2.61	3.60	3.80	3.41	7.83	3.02	12.04	3.02	8.01	**3.19**	**0.67**			3.10	3%	9.24	3.55
Ga	0.27	0.27	0.28	0.25	0.22	0.26	0.21	0.24	0.15	0.17	0.56	0.15	0.75	0.20	2.50	**0.22**	**0.09**			0.24	8%	0.05	0.04
Rb	0.69	0.68	0.69	0.77	0.66	0.63	0.62	0.62	0.57	0.43	0.43	0.26	0.33	0.39	0.61	**0.58**	**0.30**			0.65	11%	0.06	0.08
Sr	0.68	0.73	0.70	0.72	0.70	0.70	0.73	0.66	0.64	0.56	1.21	0.49	0.79	0.57	4.11	**0.66**	**0.15**			0.69	4%	0.38	0.38
Y	2247	2403	2341	2627	2348	2120	2142	1673	1464	1060	902	601	793	1000	763	**1835**	**1321**	2421	24%	2161	15%	144	139
Nb	2.27	2.38	2.42	2.67	2.35	2.20	2.09	2.54	2.90	2.94	3.24	2.54	2.70	2.91	2.89	**2.52**	**0.58**			2.41	5%	1.95	1.98
Ba	0.02			0.02	0.01	0.01	0.23	0.00	0.02	0.03	0.88	0.01	0.62	0.02	2.35	**0.04**	**0.13**			0.04	0%	0.02	0.02
La	0.05	0.05	0.05	0.05	0.05	0.05	0.06	0.11	0.06	0.03	1.49		0.74	0.12	57.97	**0.06**	**0.06**	0.22	73%	0.05	20%	0.00	0.00
Ce	11.18	11.72	11.84	11.92	11.34	10.92	11.02	10.44	10.09	8.93	13.22	6.75	8.07	9.06	116.41	**10.43**	**3.05**	10.10	3%	11.11	6%	2.71	2.79
Pr	0.47	0.44	0.46	0.47	0.45	0.44	0.43	0.32	0.17	0.09	1.15	0.04	0.37	0.15	11.36	**0.33**	**0.33**	0.68	51%	0.41	20%	0.01	0.01
Nd	6.41	6.70	6.85	6.74	6.46	6.44	6.26	4.99	2.71	1.61	6.98	0.79	2.54	1.83	40.24	**4.82**	**4.72**	8.14	41%	5.93	19%	0.30	0.25
Sm	11.33	11.41	11.56	11.62	11.05	11.14	10.51	9.32	5.91	4.04	5.61	1.91	2.95	3.76	9.34	**8.63**	**7.29**	11.10	22%	10.33	16%	0.49	0.46
Eu	0.36	0.37	0.40	0.40	0.36	0.34	0.35	0.37	0.23	0.16	0.30	0.07	0.14	0.15	0.99	**0.30**	**0.23**	0.41	27%	0.34	12%	0.22	0.24
Gd	55.88	58.58	57.30	58.13	56.08	54.66	54.62	46.69	35.32	23.56	22.88	11.48	16.65	22.42	22.82	**44.56**	**33.70**	44.40	0%	52.35	15%	2.60	2.33
Tb	17.56	18.48	18.15	18.64	17.83	17.23	17.39	14.60	11.43	8.06	7.33	4.12	5.61	7.45	6.61	**14.24**	**10.27**	17.40	18%	16.67	15%	0.87	0.84
Dy	211.25	220.95	220.74	231.38	217.94	207.34	205.48	171.30	139.15	100.83	87.59	53.16	71.83	92.15	75.14	**172.64**	**122.04**	199.00	13%	201.99	15%	11.68	11.89
Ho	74.84	78.76	80.18	87.23	79.40	72.51	71.09	58.39	50.26	36.43	31.36	20.12	26.31	33.69	25.59	**61.91**	**43.77**	75.60	18%	72.55	15%	4.72	4.69
Er	355	368	375	410	371	335	330	266	233	173	146	98	127	160	116	**290**	**203**	310	7%	340	15%	27	26
Tm	66.79	69.60	69.78	77.55	69.10	63.04	62.94	50.09	44.97	33.52	28.06	19.76	25.30	31.54	23.13	**54.89**	**37.09**	63.50	14%	64.04	14%	6.58	6.46
Yb	554	583	565	626	568	520	517	424	380	293	246	177	223	274	202	**457**	**290**	520	12%	529	14%	67	63
Lu	103	108	109	122	109	97	98	76	68	55	46	34	42	52	38	**86**	**56**	106	19%	100	14%	14	13
Hf	12022	12135	11735	11461	11876	12236	12323	10022	9643	10356	10115	9391	10338	10045	9787	**11104**	**2233**	11031	1%	11768	6%	5630	5792
Ta	2.44	2.50	2.38	2.50	2.36	2.22	2.30	0.78	0.83	0.93	0.89	0.75	0.84	0.88	0.85	**1.74**	**1.61**			2.20	21%	0.49	0.47
Pb	762	871	886	1017	742	537	570	201	188	147	140	102	128	133	118	**513**	**685**			691	26%	65	62
Th	530	607	628	735	559	423	431	184	146	99	102	56	82	93	109	**374**	**489**			502	25%	32	31
U	1044	1159	1158	1324	1018	745	788	278	260	202	192	142	171	186	151	**692**	**901**			930	26%	91	88

Gain, S.E.M., Gréau, Y., Henry, H., Belousova, E., Dainis, I., Griffin, W.L., O'Reilly, S.Y., 2019. Mud Tank Zircon: Long-Term Evaluation of a Reference Material for U-Pb Dating, Hf-Isotope Analysis and Trace Element Analysis. Geostand. Geoanalytical Res. 43, 339–354. https://doi.org/10.1111/ggr.12265

Guitreau, M., Gannoun, A., Deng, Z., Chaussidon, M., Moynier, F., Barbarin, B., Marin-Carbonne, J., 2022. Stable isotope geochemistry of silicon in granitoid zircon. Geochim. Cosmochim. Acta 316, 273–294. https://doi.org/10.1016/j.gca.2021.09.029

Jochum, K.P., Weis, U., Stoll, B., Kuzmin, D., Yang, Q., Raczek, I., Jacob, D.E., Stracke, A., Birbaum, K., Frick, D.A., Günther, D., Enzweiler, J., 2011. Determination of Reference Values for NIST SRM 610–617 Glasses Following ISO Guidelines. Geostand. Geoanalytical Res. 35, 397–429. https://doi.org/https://doi.org/10.1111/j.1751-908X.2011.00120.x

Takehara, M., Horie, K., Hokada, T., Kiyokawa, S., 2018. New insight into disturbance of U-Pb and trace-element systems in hydrothermally altered zircon via SHRIMP analyses of zircon from the Duluth Gabbro. Chem. Geol. 484, 168–178. https://doi.org/10.1016/j.chemgeo.2018.01.028

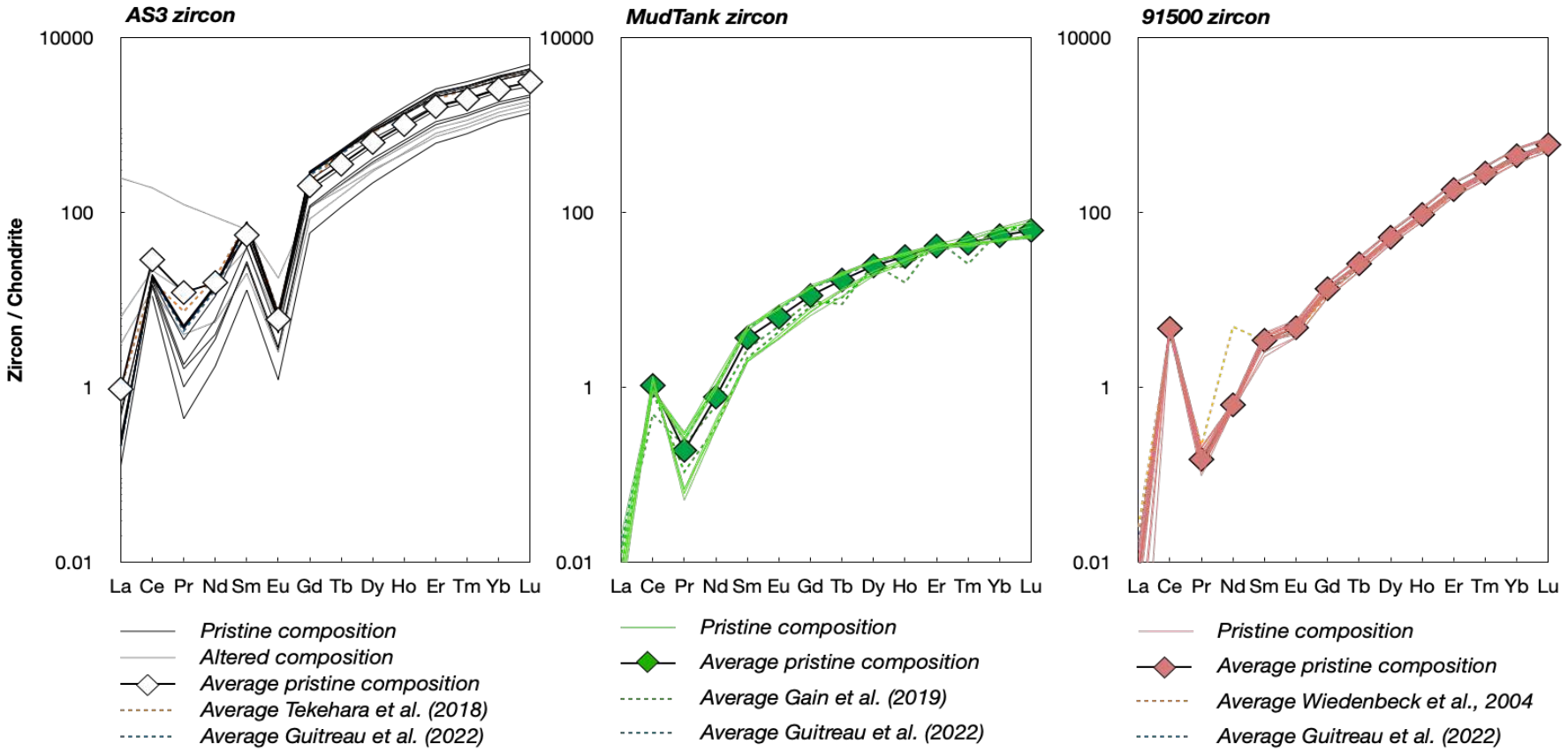
Wiedenbeck, M., Hanchar, J.M., Peck, W.H., Sylvester, P., Valley, J., Whitehouse, M., Kronz, A., Morishita, Y., Nasdala, L., Fiebig, J., Franchi, I., Girard, J.-P., Greenwood, R.C., Hinton, R., Kita, N., Mason, P.R.D., Norman, M., Ogasawara, M., Piccoli, P.M., Rhede, D., Satoh, H., Schulz-Dobrick, B., Skår, O., Spicuzza, M.J., Terada, K., Tindle, A., Togashi, S., Vennemann, T., Xie, Q., Zheng, Y.-F., 2004. Further Characterisation of the 91500 Zircon Crystal. Geostand. Geoanalytical Res. 28, 9–39. https://doi.org/https://doi.org/10.1111/j.1751-908X.2004.tb01041.x

91500	91500	91500	91500	91500	91500	91500	91500	91500	91500	91500	91500	91500	91500	91500	91500	91500	91500	91500	91500	Mudtank	Mudtank	Mudtank
Pristine	*Pristine*	*Pristine*	*Pristine*	*Pristine*	*Pristine*	*Pristine*	*Pristine*	*Pristine*	*Pristine*	*Pristine*	*Pristine*	*Pristine*	*Pristine*	*Pristine*	**Average**	**2SD (%)**	**Wiedenbeck et al., 2004 and Gain et al., 2019**	**RSD(%)**	**Guitreau et al., 2022**	**RSD(%)**	*Pristine*	*Pristine*	*Pristine*
11.58	6.70	3.83	5.22	10.00	7.11	7.42	5.95	5.18	3.95	6.16	4.70	3.23	5.17	4.01	**6.27**	**4.69**			12.60	50%	0.44		1.15
10.23	6.92	8.97	34.95	6.23	3.07	4.72	3.94	7.00		3.55	6.65	6.80	7.14	1.81	**8.21**	**15.12**			1.34	513%	13.88	9.34	6.23
473	360	307	288	340	339	413	284	278	271	223	439	397	546	256	**350**	**170**			64	450%	511	370	364
5.01	5.00	5.20	5.12	5.00	5.26	4.89	5.06	5.14	3.70	5.35	5.22	5.52	5.02	5.29	**5.11**	**0.84**	4.78	7%	4.89	4%	7.21	6.86	6.72
0.11	0.09	0.05	0.09	0.14	0.09	0.08	0.03	0.05	0.08	0.08	0.06	0.06	0.11	0.11	**0.08**	**0.06**			0.10	20%	0.24	0.16	0.20
4.13	3.45	3.79	15.05	5.32	3.03	3.56	2.67	2.57	3.38	3.54	3.54	3.79	3.27	3.34	**4.54**	**6.20**			6.95	35%	3.81	3.39	3.84
0.04	0.04	0.05	0.02	0.03	0.08	0.06	0.07	0.05	0.06	0.02	0.03	0.05	0.07	0.07	**0.05**	**0.04**			0.12	58%	0.02	0.02	0.01
0.04	0.05	0.05	0.02	0.07	0.05	0.07	0.07	0.04	0.05	0.03	0.07	0.08	0.09	0.10	**0.06**	**0.04**			0.09	33%	0.02	0.00	0.03
0.36	0.36	0.38	1.15	0.39	0.37	0.36	0.41	0.39	0.39	0.36	0.40	0.43	0.41	0.40	**0.43**	**0.37**	0.05	760%	0.32	34%	0.39	0.35	0.40
140	131	125	157	151	149	156	153	158	159	159	178	185	181	181	**156**	**35**	140	11%	141	10%	48	48	48
1.95	1.89	1.94	2.06	1.96	1.96	2.00	1.97	2.00	1.99	2.07	2.03	2.08	2.07	2.02	**2.00**	**0.11**	1.03	94%	1.41	42%	1.93	1.99	1.89
0.03	0.01	0.04	0.03		0.02	0.04	0.04		0.03	0.03	0.00	0.02			**0.03**	**0.03**	0.06	50%	0.07	57%			
	0.00		0.00	0.00	0.00	0.00	0.00	0.00		0.00	0.00	0.00	0.00	0.00	**0.00**	**0.00**	0.01	100%	0.00				
2.55	2.45	2.56	2.94	2.83	2.80	2.84	2.85	2.98	2.92	2.99	3.18	3.20	3.10	3.18	**2.87**	**0.45**	2.56	12%	2.59	11%	0.59	0.56	0.53
0.01	0.01	0.01	0.01	0.02	0.01	0.01	0.02	0.01	0.02	0.01	0.01	0.02	0.02	0.02	**0.01**	**0.01**	0.02	50%	0.01	0%	0.03	0.02	0.03
0.26	0.25	0.26	0.29	0.28	0.30	0.32	0.29	0.30	0.29	0.27	0.29	0.31	0.31	0.30	**0.29**	**0.04**	2.24	87%	0.28	4%	0.56	0.49	0.46
0.49	0.38	0.33	0.48	0.57	0.47	0.45	0.52	0.50	0.57	0.57	0.57	0.62	0.61	0.56	**0.51**	**0.16**	0.50	2%	0.49	4%	0.73	0.72	0.73
0.24	0.21	0.21	0.28	0.26	0.25	0.28	0.27	0.27	0.28	0.29	0.31	0.32	0.30	0.30	**0.27**	**0.07**	0.24	13%	0.24	13%	0.45	0.48	0.44
2.39	2.11	2.09	2.72	2.57	2.60	2.61	2.56	2.56	2.71	2.80	3.02	3.10	3.14	3.10	**2.65**	**0.64**	2.21	20%	2.44	9%	2.73	2.68	2.68
0.81	0.76	0.75	0.90	0.90	0.90	0.93	0.90	0.95	0.94	0.95	1.10	1.10	1.09	1.04	**0.93**	**0.22**	0.86	8%	0.84	11%	0.72	0.73	0.73
11.23	10.61	10.55	13.04	12.33	12.20	12.28	12.26	13.20	12.76	12.96	14.59	15.17	14.68	14.47	**12.70**	**2.78**	11.80	8%	11.70	9%	6.85	6.67	6.87
4.56	4.28	4.26	5.19	4.96	4.94	5.17	5.04	5.26	5.33	5.38	5.86	6.24	6.03	6.01	**5.17**	**1.19**	4.84	7%	4.66	11%	1.89	1.84	1.89
25	24	24	29	28	27	29	29	29	29	30	34	35	34	34	**29**	**7**	25	18%	27	9%	7	7	7
6.22	5.88	5.72	6.95	6.68	6.60	6.75	6.71	6.93	7.07	7.09	8.18	8.41	8.30	8.23	**6.99**	**1.65**	6.89	1%	6.29	11%	1.09	1.03	1.06
65	59	58	70	67	67	69	68	71	72	72	84	87	86	84	**71**	**18**	74	4%	67	6%	8	8	8
13	12	12	15	14	14	14	14	15	15	15	17	18	18	18	**15**	**4**	13	13%	13	14%	1	1	1
5513	5465	5751	5736	5618	5525	5684	5531	5655	5591	5824	6244	6270	6250	6203	**5781**	**563**	5940	3%	5969	3%	11466	11190	11090
0.47	0.43	0.43	0.56	0.53	0.52	0.54	0.55	0.57	0.55	0.54	0.62	0.61	0.62	0.62	**0.54**	**0.12**	0.48	13%	0.53	2%	0.97	0.97	0.99
62	57	54	72	71	69	71	72	73	73	76	70	71	71	69	**68**	**12**	N.A.	N.A.	66	4%	4	4	4
30	28	27	37	36	34	35	36	38	38	38	36	35	35	34	**34**	**7**	30	14%	32	9%	5	5	5
86	79	76	101	98	95	99	99	102	103	106	101	101	100	98	**95**	**17**	80	19%	89	7%	9	8	9

Mudtank	Mudtank	MudTank	MudTank	MudTank	MudTank	MudTank	MudTank	MudTank	MudTank	MudTank	MudTank	MudTank	MudTank	MudTank	NIST 612	NIST 612	NIST 612	NIST 612	NIST 612	NIST 612
Pristine	*Pristine*	*Pristine*	*Pristine*	*Pristine*	*Pristine*	*Pristine*	**Average**	**2SD(%)**	Gain et al., 2019 (Av.1)	**RSD(%)**	Gain et al., 2019 (Av. 2)	**RSD(%)**	Guitreau et al., 2022	**RSD(%)**						
0.92	0.42	1.18				0.48	**0.77**	**0.72**	0.89	13%	0.70	10%	0.42	83%	11307	10956	11498	11266	10833	11460
4.55	0.21	1.76	9.36	6.80	6.42	4.75	**6.33**	**7.87**					1.21	423%	66	61	66	67	60	66
237	246	300	526	466	467	426	**391**	**210**	34	1061%	36	987%	58	579%	83047	82188	81453	80520	79887	82813
7.13	6.52	14.47	5.16	4.65	5.21	4.89	**6.88**	**5.68**	5.29	30%	3.75	83%	7.35	6%	41	39	41	39	39	41
0.20	0.19	0.17	0.16	0.17	0.20	0.18	**0.19**	**0.05**	0.08	138%	0.08	138%	0.18	6%	39	38	38	38	37	39
3.02	2.36	2.79	3.61	3.31	3.75	2.87	**3.28**	**1.00**	0.20	1540%	0.68	382%	4.13	21%	40	38	39	39	38	40
	0.04	0.02	0.01	0.02	0.02	0.05	**0.02**	**0.03**	0.01	100%	0.02	0%	0.07	71%	36	36	36	36	36	37
0.05	0.04		0.03	0.00		0.03	**0.03**	**0.03**	0.02	50%	0.01	200%	0.04	25%	31	31	32	31	30	32
0.37	0.36	0.37	0.36	0.36	0.37	0.35	**0.37**	**0.03**	0.21	76%	0.04	825%	0.32	16%	78	78	77	78	75	79
47	47	48	42	39	45	42	**45**	**7**	45	2%	49	8%	47	2%	39	37	39	39	38	39
1.89	1.87	1.97	2.08	2.01	2.13	2.06	**1.98**	**0.18**	1.48	34%	0.74	168%	1.38	43%	38	38	39	38	37	39
													0.07	0%	40	39	39	40	39	40
										0%		0%		0%	36	36	36	36	35	37
0.56	0.55	0.55	0.76	0.71	0.81	0.79	**0.64**	**0.23**	0.54	19%	0.30	113%	0.54	19%	38	38	38	38	37	39
0.03	0.02	0.02	0.01	0.01	0.00	0.01	**0.02**	**0.02**	0.01	100%	0.02	0%	0.02	0%	37	38	38	37	37	38
0.48	0.43	0.42	0.19	0.18	0.15	0.16	**0.35**	**0.32**	0.16	119%	0.28	25%	0.46	24%	35	36	35	35	34	36
0.72	0.66	0.66	0.29	0.31	0.29	0.29	**0.54**	**0.42**	0.32	69%	0.40	35%	0.69	22%	37	38	38	38	37	39
0.43	0.45	0.46	0.20	0.20	0.22	0.20	**0.35**	**0.26**	0.24	46%	0.28	25%	0.43	19%	36	36	36	36	35	36
2.90	2.69	2.70	1.45	1.31	1.58	1.43	**2.22**	**1.35**	1.65	35%	1.91	16%	2.67	17%	39	39	39	38	38	40
0.70	0.69	0.68	0.46	0.39	0.47	0.46	**0.60**	**0.28**	0.38	58%	0.32	88%	0.67	10%	36	37	37	36	36	38
6.84	6.61	6.62	4.73	4.61	5.20	4.86	**5.98**	**1.98**	5.52	8%	6.31	5%	6.58	9%	36	37	36	35	35	37
1.82	1.75	1.83	1.54	1.42	1.59	1.52	**1.71**	**0.34**	1.32	30%	0.86	99%	1.76	3%	38	38	38	37	37	39
7	7	7	6	6	7	6	**7**	**1**	7	3%	8	15%	7	1%	39	39	39	39	38	39
1.05	1.00	1.05	1.19	1.05	1.31	1.20	**1.10**	**0.19**	1.00	10%	0.64	72%	1.03	7%	37	37	37	37	36	38
8	8	8	10	9	11	10	**9**	**3**	10	17%	10	11%	8	10%	39	37	40	39	37	39
1	1	1	2	2	2	2	**2**	**1**	2	9%	2	9%	1	23%	36	36	36	37	35	38
11159	11498	11270	9927	9981	10057	9801	**10744**	**1409**	11800	9%	20000	46%	11124	3%	38	38	37	37	36	38
0.92	0.93	0.98	1.12	1.04	1.15	1.11	**1.02**	**0.16**	1.29	21%	1.02	0%	0.91	12%	37	36	37	37	36	37
4	4	4	10	9	11	9	**6**	**6**	2	292%	2	299%	4	53%	38	39	38	39	38	40
5	5	5	8	7	8	8	**6**	**3**	5	8%	5	11%	5	30%	38	38	38	37	36	39
8	8	8	21	19	22	21	**13**	**13**	15	11%	11	19%	8	63%	37	37	37	37	36	38

NIST 612	NIST 612	NIST 612	NIST 612	NIST 612	NIST 612	NIST 612	NIST 612	NIST 612	NIST 612	NIST 612	NIST 612	NIST 612	NIST 612	NIST 612	NIST 612	NIST 612	NIST 612	NIST610	NIST610	NIST610	NIST610
															Average	2SD(%)	Jochum et al., 2011	RSD(%)			
10926	11020	11433	10984	11023	11464	10919	11035	11283	11275	11126	11458	11204	10943	11035	**11164**	**432**	**10746**	**4%**	10717	10929	10699	10829
54	59	64	60	62	57	64	65	64	63	61	60	62	58	57	**62**	**7**	**62**	**1%**	459	472	460	464
80094	80093	82760	80307	79501	81681	79790	80403	81264	80976	80369	82240	80158	79382	79825	**80893**	**2314**	**85061**	**5%**	80380	85180	81151	82048
39	40	40	40	39	41	39	39	40	39	42	41	39	38	39	**40**	**2**	**44**	**9%**	447	457	447	452
38	38	39	38	38	39	38	38	39	38	39	39	39	38	38	**38**	**1**	**39**	**1%**	447	457	446	452
39	38	40	39	39	41	39	38	40	39	40	39	40	39	40	**39**	**2**	**39**	**1%**	459	464	457	462
36	36	37	36	35	38	36	36	37	36	36	37	36	36	36	**36**	**1**	**37**	**2%**	431	438	429	435
31	31	32	31	31	32	31	31	31	32	31	32	31	31	31	**31**	**1**	**31**	**0%**	415	437	423	423
75	76	77	77	78	79	77	76	77	76	78	79	77	76	76	**77**	**2**	**78**	**2%**	502	536	507	516
38	37	39	38	38	39	38	38	38	38	38	39	38	38	37	**38**	**1**	**38**	**0%**	460	467	458	465
38	37	38	37	37	39	37	37	38	38	38	39	38	37	37	**38**	**1**	**39**	**3%**	461	472	460	465
39	39	40	39	40	41	40	39	39	40	40	40	40	39	39	**40**	**1**	**39**	**1%**	442	466	446	449
35	35	36	35	35	37	36	35	36	36	36	36	36	35	35	**36**	**1**	**36**	**1%**	432	455	434	440
37	38	38	37	38	39	38	38	38	38	37	38	38	37	37	**38**	**1**	**38**	**2%**	443	467	447	452
37	36	38	37	37	37	37	37	38	37	37	37	37	37	37	**37**	**1**	**38**	**2%**	438	463	444	444
34	35	35	35	35	35	35	35	36	35	35	36	35	35	35	**35**	**1**	**36**	**1%**	421	444	424	430
37	37	38	38	38	38	37	38	38	38	37	39	37	37	37	**38**	**1**	**38**	**0%**	442	470	443	451
35	35	35	35	35	36	35	35	35	36	36	36	36	35	35	**35**	**1**	**36**	**1%**	436	465	439	447
37	37	38	38	37	39	37	38	39	38	38	39	38	37	38	**38**	**1**	**37**	**2%**	439	466	441	448
36	36	37	36	36	37	37	36	36	37	37	37	36	36	36	**37**	**1**	**38**	**3%**	428	451	428	437
35	36	37	36	36	37	36	36	36	37	36	36	36	35	36	**36**	**1**	**36**	**1%**	425	451	432	439
37	37	38	37	37	38	37	37	37	38	38	38	37	37	37	**38**	**1**	**38**	**2%**	439	463	442	448
38	38	39	38	38	39	38	39	38	39	39	39	38	37	38	**38**	**1**	**38**	**1%**	446	470	445	453
36	36	37	37	36	38	36	36	37	37	36	37	37	36	36	**37**	**1**	**37**	**0%**	427	449	426	435
38	38	39	37	38	40	38	38	39	38	39	39	39	38	39	**38**	**1**	**39**	**2%**	447	455	446	452
35	36	37	36	36	37	36	36	36	36	36	37	36	35	36	**36**	**1**	**37**	**2%**	428	454	433	436
37	37	38	37	36	38	37	36	37	37	37	38	37	37	37	**37**	**1**	**37**	**1%**	425	453	428	435
37	36	37	36	36	37	36	36	37	36	37	37	37	36	36	**37**	**1**	**38**	**3%**	443	451	442	449
38	38	40	39	39	40	39	38	38	38	38	38	38	37	38	**38**	**2**	**39**	**0%**	415	440	419	426
37	37	38	37	37	38	37	37	37	37	37	38	37	37	37	**37**	**1**	**38**	**1%**	447	472	451	455
36	37	38	36	36	38	37	36	37	37	37	38	36	36	37	**37**	**1**	**37**	**1%**	451	475	456	458

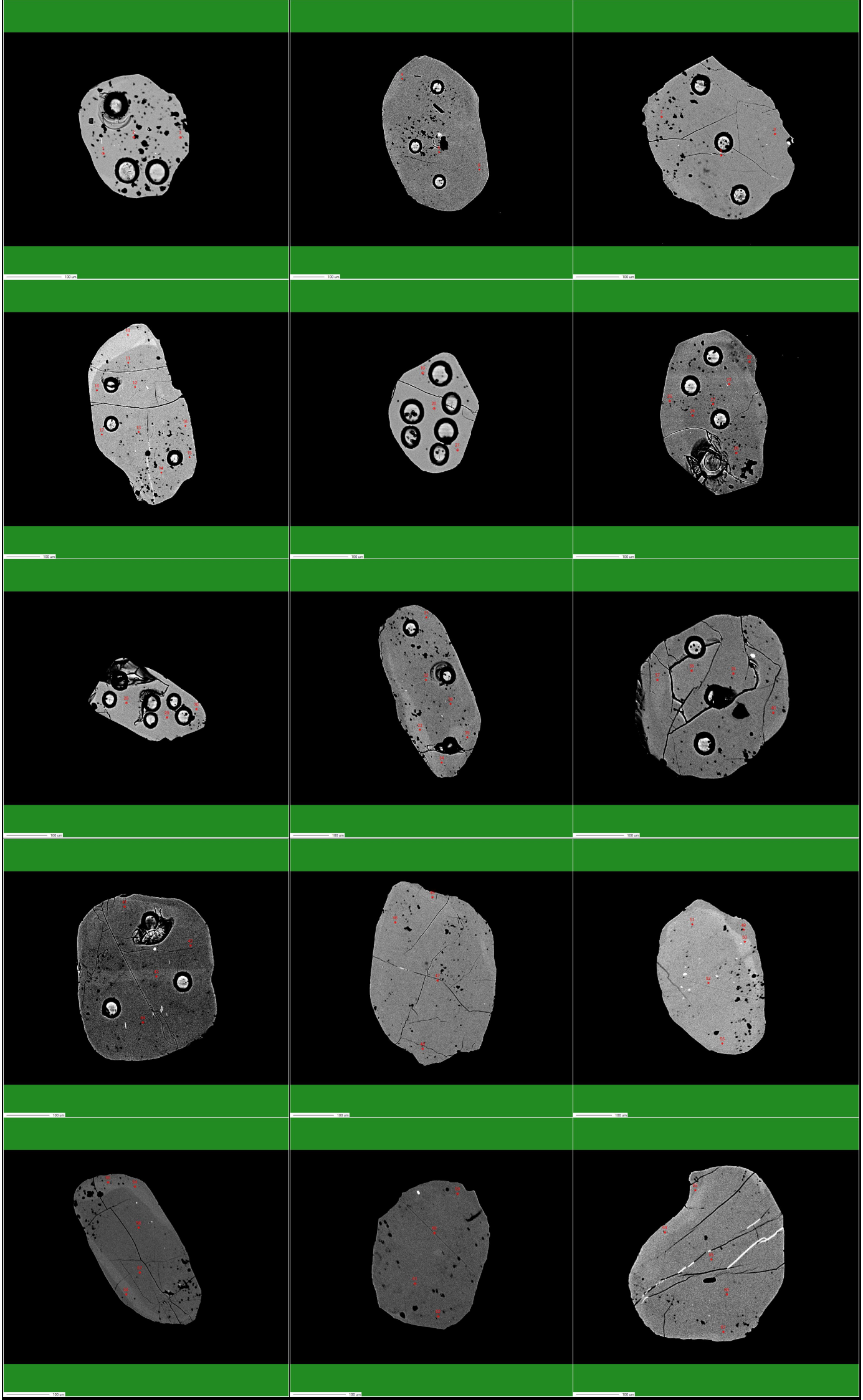
NIST610	NIST610	NIST610	NIST610	NIST610	NIST610	NIST610	NIST610	NIST610	NIST610	NIST610	NIST610	NIST610	NIST610	NIST610	NIST610	NIST610	NIST610	NIST610	NIST610	NIST610	NIST610	NIST610	NIST610
																				Average	2SD(%)	Jochum et al., 2011	RSD(%)
10811	10806	10726	10861	10690	10848	10771	10823	10823	10683	10874	10760	10954	10661	10739	10751	10977	10786	10789	10755	**10794**	**168**	**10320**	**5%**
465	468	458	468	462	470	453	462	466	463	464	464	470	458	460	459	472	464	461	466	**464**	**10**	**464**	**0%**
82447	82858	80971	83083	81485	82914	80825	82338	82229	81561	82576	81742	83432	80937	81329	80984	83533	81841	82666	81944	**82102**	**2171**	**81475**	**1%**
452	453	449	454	447	454	451	450	457	447	455	448	459	448	454	449	455	450	451	453	**452**	**7**	**452**	**0%**
447	453	445	453	447	451	450	451	449	449	451	451	455	444	446	449	454	453	450	447	**450**	**7**	**450**	**0%**
458	463	458	462	457	461	459	459	462	458	461	457	464	458	458	458	464	456	460	460	**460**	**5**	**460**	**0%**
431	435	432	434	431	435	432	433	434	431	435	431	440	426	429	428	438	435	434	431	**433**	**7**	**433**	**0%**
427	431	420	431	420	429	422	425	430	421	428	423	432	422	426	423	428	425	426	425	**426**	**9**	**426**	**0%**
516	521	512	521	509	517	512	516	518	510	520	515	522	507	512	510	519	518	517	515	**515**	**13**	**516**	**0%**
460	464	458	465	458	464	461	461	464	459	463	459	468	456	458	457	467	465	461	461	**462**	**7**	**462**	**0%**
466	467	460	467	462	467	464	465	467	462	466	461	470	463	463	464	468	464	465	464	**465**	**6**	**465**	**0%**
454	460	447	457	447	458	444	452	454	447	456	451	458	444	450	447	457	451	455	450	**452**	**12**	**452**	**0%**
438	445	438	447	433	441	436	442	439	438	444	435	445	435	439	437	444	441	439	439	**440**	**10**	**440**	**0%**
453	457	451	459	444	457	447	454	453	450	456	452	460	447	445	448	459	457	453	453	**453**	**11**	**453**	**0%**
449	454	444	454	440	451	441	447	451	445	449	444	457	444	441	444	452	451	447	448	**448**	**12**	**448**	**0%**
432	435	425	435	425	431	426	430	431	429	431	431	436	426	424	426	433	434	428	432	**430**	**10**	**430**	**0%**
453	458	449	459	449	456	446	450	458	449	455	450	460	451	449	448	457	453	451	458	**453**	**12**	**453**	**0%**
445	453	443	454	440	451	441	447	450	441	451	443	452	445	444	445	453	445	447	446	**447**	**12**	**447**	**0%**
450	457	443	457	441	453	443	449	453	443	452	445	457	441	445	443	454	454	448	449	**449**	**13**	**449**	**0%**
437	444	436	442	428	441	432	437	438	435	438	433	443	430	436	434	442	437	436	437	**437**	**11**	**437**	**0%**
438	444	433	437	433	439	433	437	440	432	441	435	440	432	441	432	440	436	436	438	**437**	**10**	**437**	**0%**
446	459	447	452	441	450	447	449	453	443	453	445	455	443	450	446	453	447	449	449	**449**	**11**	**449**	**0%**
455	464	449	463	447	458	451	455	457	451	457	452	461	451	453	452	460	455	452	457	**455**	**12**	**455**	**0%**
434	443	430	442	429	439	429	436	436	430	439	432	444	429	431	429	440	438	435	434	**435**	**12**	**435**	**0%**
448	452	445	452	446	452	449	449	454	444	453	450	458	444	446	444	456	454	448	451	**450**	**8**	**450**	**0%**
440	445	434	447	431	441	434	438	444	433	441	435	444	432	441	434	443	439	437	440	**438**	**12**	**439**	**0%**
441	440	432	437	428	441	429	435	439	429	439	431	440	430	434	431	438	434	436	434	**435**	**12**	**435**	**0%**
442	449	443	448	442	448	445	446	448	438	451	441	453	443	442	444	451	448	443	448	**446**	**8**	**446**	**0%**
425	432	422	433	421	425	425	425	429	423	428	423	432	421	423	426	429	425	425	426	**426**	**10**	**426**	**0%**
455	464	454	465	449	458	453	457	459	455	459	454	466	453	452	450	459	460	457	460	**457**	**12**	**457**	**0%**
467	468	457	464	457	464	458	461	465	458	464	457	467	458	460	459	465	461	461	462	**461**	**10**	**462**	**0%**

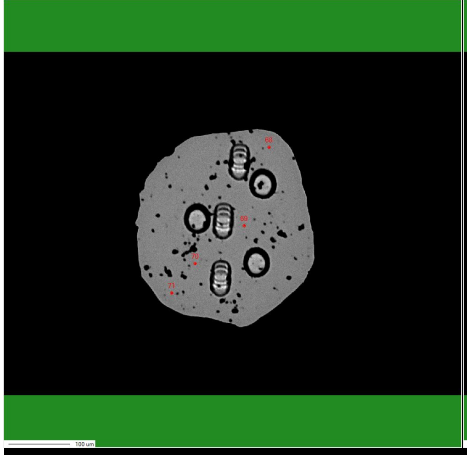
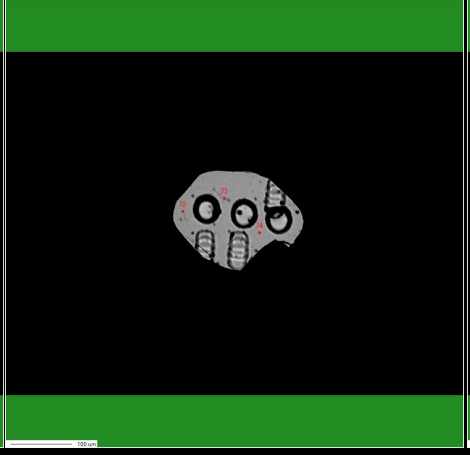
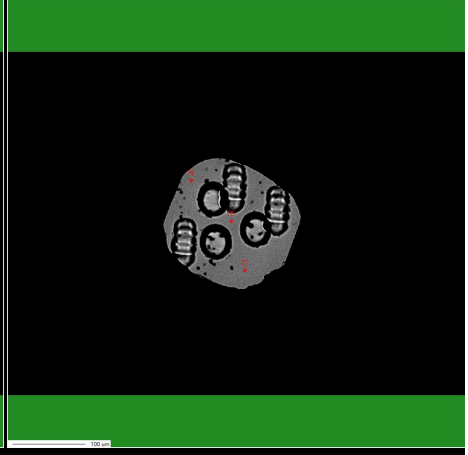
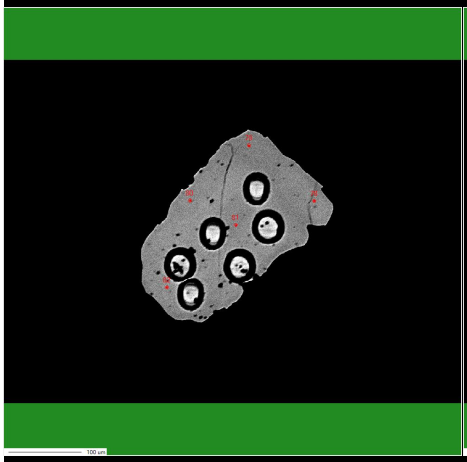

AS3 zircon
MudTank zircon
91500 zircon
Zircon / Chondrite
10000
100
1
0.01
La Ce Pr Nd Sm Eu Gd Tb Dy Ho Er Tm Yb Lu
Pristine composition
Altered composition
Average pristine composition
Average Tekehara et al. (2018)
Average Guitreau et al. (2022)
Pristine composition
Average pristine composition
Average Gain et al. (2019)
Average Guitreau et al. (2022)
Pristine composition
Average pristine composition
Average Wiedenbeck et al., 2004
Average Guitreau et al. (2022)

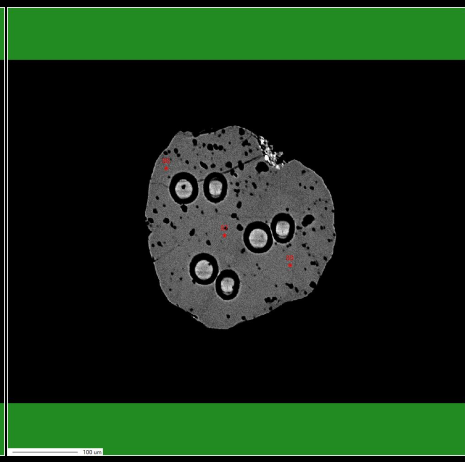
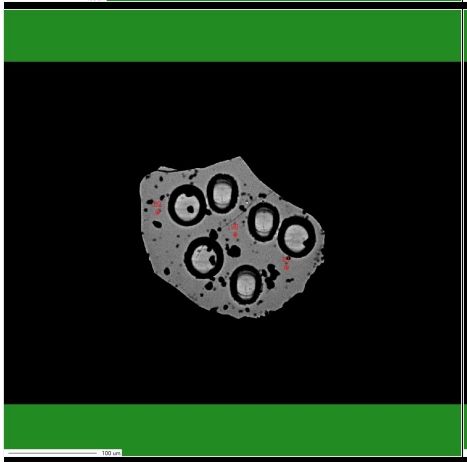
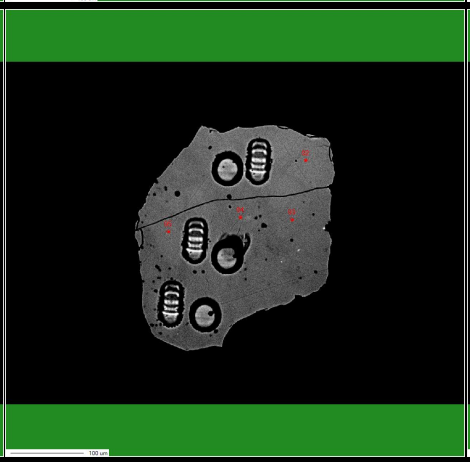
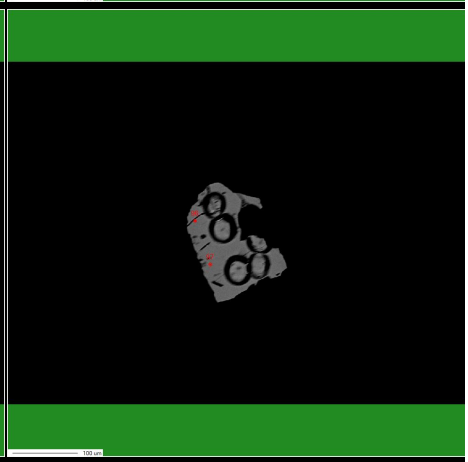
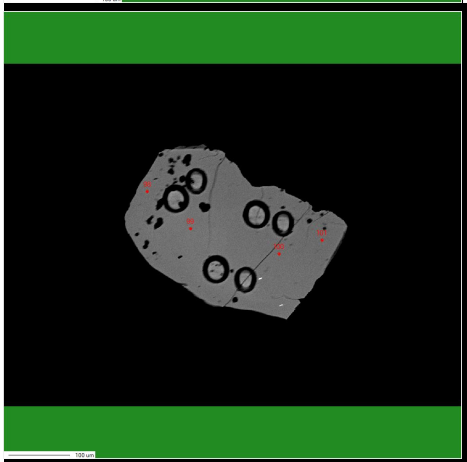
EMPA-WDS analyses of major and minor elements for apatite grains from Caatinga-Lamim Complex (CM44B) and Cupim Pluton (GC1, GC5A/B, GC6).

Sample rock	*Sample apatite*	Texture	CL domain	Element in oxide formula (wt.%)																								p.p.m concentration									
				CaO	P2O5	F	Cl	SO3	SiO2	TiO2	Al2O3	FeO	MnO	MgO	Na2O	K2O	BaO	SrO	V2O3	CuO	La2O3	Ce2O3	Pr2O3	Nd2O3	Sm2O3	Eu2O3	Total	F/Cl	LREE	Mn	Sr	V	La	Ce	Pr	Nd	Sm	Eu	LREE*
Caatinga-Lamim TTG Complex																																					
CM44B - Migmatitic Bt-gneiss																																					
	ap#1	*Homogeneous*	*Border*	54.4	42.1	5.12	0.02	0	0.1	0	0.04	0.01	0.06	0	0.01	0	0.04	0.07	0	0.23	0.03	0.09	0.04	0.01	0	0.07	**100.2**	213	0.17	465	609	0	256	751	359	43	0	596	1409
	ap#1	*Homogeneous*	*Center*	54.6	40.4	4.46	0.03	0.12	0.31	0	0.94	0.01	0	0	0.04	0.03	0	0.1	0	0	0.03	0.15	0.02	0	0	0	**99.4**	179	0.21	0	812	0	230	1281	197	17	26	0	1750
	ap#1	*Homogeneous*	*Border*	55.4	41.2	5.19	0	0	0.07	0.01	0.05	0.04	0.06	0	0	0	0	0.19	0	0.18	0	0.08	0	0	0.01	0	**100.3**	1730	0.09	426	1632	0	0	657	0	0	86	0	744
	ap#2	*Core/Rim*	*Light Rim*	54.5	41.8	4.67	0.01	0	0.21	0.06	0.02	0.03	0.04	0	0	0	0	0.08	0.02	0.08	0.2	0.15	0.01	0.11	0.01	0.09	**100.1**	389	0.48	279	693	163	1697	1315	51	926	121	734	4110
	ap#2	*Core/Rim*	*Dark patchy Core*	56.1	42.2	4.27	0	0	0.07	0	0.02	0	0.07	0	0	0	0	0.05	0	0.1	0.01	0.07	0.1	0.08	0	0.06	**101.4**	2134	0.25	573	389	0	68	572	829	703	0	484	2172
	ap#2	*Core/Rim*	*Light Rim*	56.5	42	4.09	0.01	0	0.06	0.02	0	0.03	0.1	0	0	0	0	0	0.02	0.18	0.09	0.07	0	0	0	0.05	**101.5**	409	0.16	744	0	116	742	581	0	0	0	466	1322
	ap#3	*Core/Rim*	*Dark patchy Core*	55.5	41.2	5.26	0.01	0	0.1	0.04	0	0.01	0.03	0	0	0	0	0	0	0.23	0.02	0.09	0	0.01	0	0.03	**100.3**	657	0.12	248	0	0	128	734	0	120	0	216	982
	ap#3	*Core/Rim*	*Dark patchy Core*	55.5	41.8	4.77	0.02	0.01	0.08	0	0	0	0.01	0	0	0.01	0.01	0	0	0.08	0	0.06	0.04	0.14	0	0.02	**100.6**	298	0.25	62	0	27	34	512	342	1226	0	164	2114
	ap#3	*Core/Rim*	*Dark patchy Core*	55.3	39.8	5	0.01	0	0.04	0	0.03	0.02	0.08	0	0.02	0.01	0	0.01	0	0.05	0.02	0.08	0.04	0.05	0.05	0.07	**98.6**	357	0.24	604	110	0	162	640	299	463	457	639	2021
	ap#5	*Core/Rim*	*Light Rim*	55.2	40.1	4.91	0.02	0.03	0.23	0.02	0	0.03	0.13	0	0.01	0	0.01	0.06	0.03	0.33	0.06	0.12	0.08	0.04	0.12	0.02	**99.4**	234	0.41	1022	507	204	486	999	641	343	1035	155	3504
	ap#5	*Core/Rim*	*Dark patchy Core*	55	39.3	4.86	0.01	0	0.05	0	0	0.02	0.03	0	0.01	0	0	0.22	0.03	0.21	0.09	0.03	0.09	0.16	0	0.09	**98.1**	405	0.36	256	1860	204	759	239	726	1372	0	812	3096
	ap#5	*Core/Rim*	*Dark patchy Core*	54.9	40.2	4.79	0.01	0	0.16	0	0.02	0.01	0.06	0	0	0.01	0.01	0.07	0	0.03	0.06	0.07	0	0	0.04	0.12	**98.5**	399	0.17	472	617	0	546	564	0	0	328	993	1437
	ap#5	*Core/Rim*	*Light Core*	55.3	40.2	4.87	0.01	0.01	0.08	0.02	0	0.01	0.08	0	0	0	0	0.09	0	0.22	0.03	0.09	0	0.01	0.04	0	**99**	487	0.17	627	769	0	239	743	0	120	354	0	1455
	ap#5	*Core/Rim*	*Light Core*	55.6	39.8	5.06	0.01	0	0.13	0.01	0.03	0	0.07	0	0	0.01	0.05	0.12	0	0.13	0.01	0.04	0.06	0.08	0	0.02	**99.1**	421	0.19	534	989	0	43	324	547	712	0	164	1626
	ap#5	*Core/Rim*	*Light Rim*	55.1	40.6	4.97	0.01	0.02	0.07	0.03	0.04	0.01	0.05	0	0	0	0	0.05	0.02	0.22	0.04	0.08	0	0	0.07	0.06	**99.4**	497	0.18	403	406	102	333	657	0	0	561	510	1551
	ap#5	*Core/Rim*	*Light Rim*	55.5	40.4	4.85	0.01	0	0.15	0.02	0.08	0	0.03	0	0	0	0	0.11	0.02	0.17	0.06	0.11	0	0.17	0.07	0	**99.7**	441	0.41	201	964	129	495	965	0	1466	586	0	3512
	ap#5	*Core/Rim*	*Dark patchy Core*	55.4	39.6	5.02	0.03	0	0.06	0.01	0	0.03	0.07	0	0	0	0	0.07	0.01	0	0	0.04	0.03	0	0	0	**98.3**	193	0.07	534	567	61	0	333	256	0	0	0	589
	ap#5	*Core/Rim*	*Dark patchy Core*	54.9	41	4.84	0.03	0.01	0.09	0	0.01	0	0.1	0	0.01	0	0.04	0.05	0	0.12	0	0.04	0	0	0.14	0.06	**99.4**	179	0.18	751	414	0	0	367	0	0	1181	501	1549
	ap#6	*Homogeneous*	*Border*	55.2	40.9	4.9	0.02	0.01	0.12	0	0.03	0.04	0.05	0	0	0	0	0.01	0	0.26	0.02	0.08	0	0	0.02	0.06	**99.6**	258	0.11	372	110	0	136	675	9	0	138	510	957
	ap#6	*Homogeneous*	*Center*	54.8	41.5	5.62	0.01	0.01	0	0	0.02	0.03	0.01	0	0	0.01	0.03	0.05	0.02	0.22	0.02	0.09	0	0.07	0.02	0	**100.2**	468	0.2	62	397	143	196	734	0	583	155	0	1669
	ap#6	*Homogeneous*	*Border*	55.7	39.2	4.93	0	0	0.07	0.01	0.08	0	0.03	0	0	0.01	0	0.07	0	0.14	0.1	0.05	0	0.13	0.08	0.05	**98.6**		0.36	232	575	0	827	444	0	1072	699	406	3041
	ap#8	*Homogeneous*	*Border*	56.5	39.5	4.31	0.01	0.01	0.07	0	0.03	0	0.07	0	0.07	0.01	0	0.03	0.02	0.12	0	0.06	0.02	0.03	0.03	0	**99.1**	332	0.13	550	279	116	34	470	128	257	216	0	1105
	ap#8	*Homogeneous*	*Center*	55.5	41.3	4.34	0.01	0.02	0.17	0	0.03	0.04	0.03	0	0	0	0	0.12	0	0.15	0.02	0.17	0.06	0.02	0	0	**100.1**	482	0.26	248	989	0	128	1443	479	171	0	0	2221
	ap#8	*Homogeneous*	*Center*	55.3	41.4	4.57	0.01	0.01	0.15	0.06	0	0.07	0.02	0	0	0	0.01	0	0	0.18	0.05	0.04	0	0	0.02	0.04	**100**	914	0.12	163	0	0	443	350	0	0	198	320	992
	ap#8	*Homogeneous*	*Border*	55.6	40.6	4.07	0.01	0	0.14	0	0.02	0	0.05	0	0	0	0.01	0.08	0	0.09	0.13	0.11	0	0.08	0.03	0.03	**99.3**	407	0.34	380	685	0	1074	905	0	660	224	294	2864
	ap#8	*Homogeneous*	*Center*	55.9	39.7	4.31	0.01	0.01	0.12	0.06	0.65	0.03	0.08	0	0	0	0	0	0	0.23	0	0.15	0	0	0	0.02	**99.4**	359	0.15	596	25	0	0	1298	0	0	0	190	1298
	ap#8	*Homogeneous*	*Center*	55.4	40.9	4.17	0	0.02	0.15	0	0.02	0.03	0.02	0	0	0.01	0	0.12	0	0.16	0	0.03	0.13	0.12	0.04	0	**99.6**	4168	0.33	132	1049	0	0	290	1094	1029	379	0	2792
	ap#12	*Homogeneous*	*Center*	55.3	41.5	5.06	0.01	0.01	0.1	0	0.03	0	0.13	0	0	0.01	0.02	0.08	0	0	0.06	0.13	0.03	0.1	0.07	0	**100.5**	563	0.39	1015	660	0	495	1076	256	840	638	0	3305
	ap#12	*Homogeneous*	*Center*	55.3	41	4.87	0.01	0.02	0.08	0.02	0.02	0.04	0.05	0	0	0	0.01	0.07	0	0.1	0.02	0.1	0.03	0.02	0	0	**99.7**	405	0.16	395	600	0	128	811	239	206	0	0	1384
	ap#12	*Homogeneous*	*Border*	55.1	40.6	4.59	0.02	0	0.15	0	0.01	0	0.05	0	0	0.01	0.02	0.02	0.02	0.17	0	0.12	0.04	0.05	0	0.08	**99.1**	287	0.21	380	161	143	0	1033	367	403	0	648	1803
	ap#13	*Core/Rim*	*Light Core*	55.1	40.9	4.87	0.01	0.01	0.12	0	0.02	0	0.1	0	0	0	0.04	0.11	0	0.22	0	0.12	0.01	0.08	0.08	0	**99.8**	405	0.28	798	964	0	0	982	68	643	664	35	2357
	ap#13	*Core/Rim*	*Dark Core*	55.4	40.4	5.27	0.01	0.02	0.03	0	0	0.02	0.07	0	0	0	0	0.05	0.01	0.2	0	0.01	0	0.11	0.05	0.12	**99.5**	585	0.17	573	389	41	0	85	0	977	397	1002	1459
	ap#13	*Core/Rim*	*Dark Rim*	54.9	40.4	5.02	0.01	0	0.26	0	0	0.02	0.08	0	0	0	0.01	0.03	0.01	0.23	0.04	0.24	0.02	0	0	0.01	**99.1**	558	0.31	635	279	61	367	2041	205	0	0	121	2612
	ap#13	*Core/Rim*	*Dark Rim*	55.4	39.9	5.42	0.02	0	0.19	0.02	0.02	0.03	0.03	0	0	0	0	0.03	0	0.04	0.06	0.2	0.1	0	0.05	0	**99.3**	339	0.41	201	288	0	495	1725	863	0	414	0	3496
	ap#13	*Core/Rim*	*Light Core*	54.8	40.7	4.9	0.02	0.01	0.13	0	0.01	0.03	0.05	0	0	0	0.02	0.06	0	0.24	0.02	0.21	0	0.04	0	0	**99.2**	306	0.28	356	516	0	188	1802	0	369	0	0	2358
	ap#13	*Core/Rim*	*Light Core*	55.5	39.6	4.91	0.04	0.02	0.07	0	0.01	0.06	0.04	0	0.08	0.02	0.05	0	0	0.16	0.07	0.06	0	0	0.05	0.15	**98.9**	112	0.19	325	0	0	588	521	26	0	448	1269	1583
	ap#14	*Core/Rim*	*Light Rim*	55.1	40.4	5.33	0.01	0.01	0.13	0	0	0.02	0.08	0	0	0	0.04	0.14	0.02	0.24	0.01	0.15	0	0.06	0	0	**99.4**	592	0.22	651	1150	129	119	1247	0	489	0	0	1855
	ap#14	*Core/Rim*	*Dark Core*	55	40.4	5.51	0	0.02	0.03	0.03	0.01	0	0.04	0	0	0	0.01	0.01	0	0.15	0.06	0.06	0.06	0.08	0	0	**99.2**	2757	0.26	341	110	0	495	487	547	660	0	0	2188
	ap#14	*Core/Rim*	*Dark Core*	55.1	40.3	5.32	0.02	0	0.07	0	0.04	0	0.04	0	0	0	0.03	0.04	0.02	0.36	0	0.07	0	0.05	0	0	**99.2**	354	0.11	333	313	143	0	555	0	412	0	0	966
	ap#14	*Core/Rim*	*Dark Core*	55	39.7	6.06	0	0.02	0.06	0.02	0	0	0.05	0	0.01	0.01	0	0	0.06	0.32	0	0.07	0.04	0	0.11	0.06	**99.1**	3031	0.21	364	0	394	0	555	299	0	914	492	1768
	ap#16	*Core/Rim*	*Dark Core*	54.5	40.8	5.35	0.01	0.01	0.18	0.01	0.03	0.08	0.04	0	0	0	0	0.04	0	0.16	0	0.05	0	0.03	0.12	0	**99.1**	594	0.21	333	330	0	0	444	0	283	1052	0	1779
	ap#16	*Core/Rim*	*Dark Core*	55.3	40.5	4.84	0.01	0	0.02	0.03	0.03	0.06	0.08	0	0	0	0.04	0.18	0	0.02	0	0.05	0.06	0.16	0	0.09	**99.4**	346	0.27	620	1556	0	0	401	513	1389	0	751	2303
	ap#16	*Core/Rim*	*Light Rim*	55.1	41	4.55	0.03	0	0.17	0	0.01	0.04	0.06	0	0.04	0.01	0	0.11	0.03	0	0.02	0.15	0.03	0.09	0	0.06	**99.5**	147	0.29	496	956	218	205	1255	248	763	0	527	2471
	ap#16	*Core/Rim*	*Dark Core*	55.2	40.4	5.32	0	0	0.1	0.03	0	0.03	0.05	0	0.04	0	0.01	0	0.02	0.18	0.06	0.09	0	0	0.05	0	**99.4**		0.21	364	0	129	537	794	0	0	457	0	1788
	ap#20	*Core/Rim*	*Light Rim*	55.2	40.4	4.97	0.02	0	0.16	0.01	0.02	0.02	0.04	0	0	0	0	0	0	0	0.1	0.13	0.01	0	0.03	0	**99**	226	0.26	302	8	0	836	1067	60	0	293	0	2256
	ap#20	*Core/Rim*	*Light Rim*	55.7	40	5.1	0.02	0.02	0.14	0.05	0.03	0.01	0.06	0	0	0	0	0.06	0	0.11	0	0.11	0	0.02	0	0.03	**99.3**	255	0.13	480	516	0	0	965	0	146	17	216	1128
	ap#20	*Core/Rim*	*Dark Core*	55.4	40.7	4.73	0	0	0.03	0	0	0.04	0	0	0.01	0.03	0.04	0	0	0.28	0	0.06	0.06	0.14	0	0	**99.5**	2364	0.26	302	321	0	0	546	479	1183	0	0	2208
	ap#20	*Core/Rim*	*Dark Core*	55.2	41	5.05	0.02	0	0.08	0.01	0	0.01	0.07	0	0	0.01	0	0	0	0.17	0	0.08	0.05	0.08	0	0	**99.7**	281	0.22	503	0	0	0	717	427	712	0	0	1856
	ap#21	*Core/Rim*	*Dark Rim*	55.6	40.6	4.97	0.01	0.01	0.04	0	0	0.06	0.06	0	0	0	0	0.1	0	0.03	0.05	0.1	0	0.14	0.06	0	**99.8**	993	0.35	488	854	0	401	854	0	1226	509	0	2989
	ap#21	*Core/Rim*	*Light Rim*	55.3	40.9	5.12	0.01	0	0.25	0	0	0.03	0.08	0	0	0	0.03	0.06	0	0.13	0	0.17	0.07	0.02	0	0.03	**100**	640	0.26	635	465	0	0	1451	590	197	0	285	2238
	ap#21	*Core/Rim*	*Light Rim*	55.4	40.9	4.75	0.01	0.01	0.14	0.03	0.01	0.02	0.09	0	0	0	0.02	0	0.01	0.19	0.04	0.1	0	0.11	0	0.1	**99.9**	475	0.25	705	0	75	315	845	0	934	0	898	2095
	ap#21	*Core/Rim*	*Dark Core*	55.3	40.5	5.01	0.01	0	0.1	0	0.03	0	0	0	0	0	0	0.12	0	0.14	0	0.14	0.06	0	0	0.01	**99.4**	557	0.21	23	972	14	9	1221	521	0	0	121	1751
	ap#21	*Core/Rim*	*Dark Core*	55.5	40	4.85	0.01	0	0.08	0	0.04	0.03	0.05	0	0	0	0	0.18	0.02	0.04	0.03	0.1	0.01	0.08	0.05	0	**99.1**	347	0.26	395	1531	163	247	854	51	643	423	0	2218
	ap#23	*Core/Rim*	*Dark Rim*	54.7	40.4	5	0.01	0	0.22	0.04	0.03	0.05	0.04	0	0.05	0.01	0.04	0.18	0	0	0.01	0.13	0.13	0.15	0.01	0	**99.1**	1000	0.43	271	1556	0	85	1084	1068	1303	95	0	3636
	ap#23	*Core/Rim*	*Dark Rim*	55.1	41.3	4.9	0.02	0	0.25	0	0.02	0	0.04	0	0	0.01	0.02	0.01	0.02	0.08	0.04	0.16	0.06	0.02	0	0	**100**	306	0.28	294	85	156	375	1332	538	137	0	0	2383
	ap#23	*Core/Rim*	*Light Core*	54.9	41	4.95	0.01	0.21	0.04	0	0	0.08	0.12	0	0.01	0	0.02	0.12	0	0.12	0.02	0.05	0	0	0.07	0	**99.6**	495	0.14	906	972	0	128	461	0	0	595	0	1184
	ap#23	*Core/Rim*	*Light Core*	54.6	40.8	5.12	0	0	0.06	0	0	0	0.09	0	0.01	0	0.01	0.11	0	0.25	0	0.07	0.13	0.05	0.03	0.12	**99.3**		0.28	689	888	0	0	615	1094	412	259	1071	2379
	ap#23	*Core/Rim*	*Dark Rim*	54.8	41.3	5.21	0.02	0	0.27	0.04	0	0	0.01	0	0	0.01	0	0.09	0	0.14	0.11	0.1	0	0.09	0	0	**99.9**	274	0.29	101	786	0	904	845	9	754	0	0	2512
	ap#24	*Core/Rim*	*Light Rim*	55.3	40.6	5.25	0.01	0	0.04	0.02	0.01	0.02	0.08	0	0	0	0	0	0	0	0.02	0.06	0	0.05	0.06	0.08	**99.4**	750	0.19	589	0	0	153	538	0	420	517	700	1629
	ap#24	*Core/Rim*	*Dark Core*	55.3	40.8	5.05	0.01	0.01	0.09	0	0.02	0.02	0.09	0	0	0	0	0.06	0	0.08	0.03	0.09	0	0.14	0.08	0	**99.7**	421	0.34	713	490	0	213	777	0	1217	699	0	2906
	ap#24	*Core/Rim*	*Dark Core*	55.3	41	4.74	0.01	0.01	0.04	0	0.01	0.07	0.05	0	0	0	0.04	0.06	0	0.21	0	0.05	0	0.04	0	0.02	**99.6**	527	0.09	380	507	0	0	393	0	369	0	138	761
	ap#24	*Core/Rim*	*Dark Core*	55.2	40.4	5.32	0.02	0.02	0.03	0	0	0.01	0.05	0	0.02	0	0.02	0	0.04	0.2	0	0.09	0	0	0	0.05	**99.3**	332	0.09	418	0	258	0	777	0	0	0	423	777
	ap#29	*Core/Rim*	*Light Rim*	56.6	40.2	4.2	0.01	0	0.08	0.01	0	0	0.08	0	0	0	0	0.04	0.04	0.12	0.04	0.06	0	0	0	0	**99.7**	700	0.1	589	330	272	367	470	0	0	0	0	836
	ap#29	*Core/Rim*	*Light Rim*	55.7	40.5	4.54	0.01	0	0.13	0.03	0.01	0.03	0.04	0	0	0	0	0.13	0	0.11	0.08	0.12	0.08	0.09	0.08	0.12	**99.9**	349	0.44	310	1065	0	648	1059	667	772	655	1010	3800
	ap#29	*Core/Rim*	*Dark Core*	56.2	40.7	4.13	0	0.01	0.04	0	0.01	0.02	0.1	0	0	0	0.02	0.18	0	0.04	0	0.04	0.07	0.15	0.04	0.02	**100**	1033	0.3	759	1539	14	0	316	598	1312	319	147	2545
	ap#29	*Core/Rim*	*Dark Core*	55.4	40.6	5.1	0.01	0	0.08	0.03	0	0.04	0.03	0	0	0.01	0	0.08	0.03	0.2	0.04	0.06	0.02	0.01	0.03	0.08	**99.6**	393	0.17	194	702	190	333	538	171	120	285	665	1446
	ap#29	*Core/Rim*	*Dark Core*	56	40.4	4.15	0.01	0.01	0.1	0	0.03	0	0.01	0	0	0	0	0.1	0.03	0.24	0	0.04	0.04	0.05	0.07	0	**99.6**	377	0.19	93	879	204	0	333	333	394	604	0	1664
		Minimum		54.4	39.2	4.07	0	0	0	0	0	0	0	0	0	0	0	0	0	0	0	0	0	0	0	0	98.1	112	0.07	0	0	0	0	85	0	0	0	0	589
		Maximum		56.6	42.2	6.06	0.04	0.21	0.31	0.06	0.94	0.08	0.13	0	0.08	0.03	0.05	0.22	0.06	0.36	0.2	0.24	0.13	0.17	0.14	0.15	101.5	4168	0.48	1022	1860	394	1697	2041	1094	1466	1181	1269	4110
		Average		***55.3***	***40.6***	***4.89***	***0.01***	***0.01***	***0.11***	***0.01***	***0.04***	***0.02***	***0.06***	***0***	***0.01***	***0***	***0.01***	***0.07***	***0.01***	***0.15***	***0.03***	***0.09***	***0.03***	***0.05***	***0.03***	***0.03***	***99.5***	***648***	***0.23***	***437***	***570***	***58***	***264***	***787***	***242***	***462***	***254***	***279***	***2008***
		1SD		0.5	0.6	0.39	0.01	0.03	0.07	0.02	0.14	0.02	0.03	0	0.02	0	0.02	0.06	0.01	0.09	0.04	0.05	0.04	0.05	0.04	0.04	0.6	733	0.1	229	475	89	324	399	308	458	309	346	827
Cupim S-typre Pluton																																					
GC1 - Two-mica granite																																					
	ap#2	*Homogenoeus*	*Border*	54.8	40.8	5.16	0.01	0	0.06	0	0.01	0.07	0.11	0	0.06	0	0.02	0	0	0.05	0	0.03	0.03	0.17	0.09	0.06	**99.3**	860	0.32	860	0	0	0	231	239	1432	811	553	2712
	ap#2	*Homogenoeus*	*Center*	54.5	40.8	5.24	0.01	0.02	0.01	0	0.03	0.06	0.28	0	0.09	0	0	0.08	0.04	0.12	0.1	0.09	0	0.01	0.05	0	**99.3**	748	0.25	2200	693	258	827	751	0	111	440	0	2130
	ap#2	*Homogenoeus*	*Center*	54.8	41	5.24	0.01	0	0.09	0.03	0.04	0.05	0.2	0	0.06	0	0.02	0.01	0	0.28	0.04	0.08	0	0.08	0.03	0.

| | | |



Trace element analyses of selected apatite grains from the studied rocks.

Spot num. analysis	Texture	P ppm	K ppm	Ca ppm	Ti ppm	V ppm	Fe ppm	Zn ppm	Ga ppm
Cupim Leucogranites									
GC1									
2.1	*Homogeneous*	137790	4.95	398327	0.19	0.16	558	1.24	32
2.2	*Homogeneous*	142878	0.88	400387	0.12	0.10	743	1.94	33
2.3	*Homogeneous*	148103	3.67	398272	0.21	0.13	577	1.66	33
7.1	*Homogeneous*	159467	0.02	403190	0.65	0.18	278	1.52	26
7.2	*Homogeneous*	186232	3.08	400434	0.50	0.07	260	1.34	28
7.3	*Homogeneous*	217572	1.74	399807	0.47	0.15	272	1.40	28
10.3	*Homogeneous*	345793	2.76	404579	0.36	0.17	284	1.91	30
10.1	*Homogeneous*	227077	3.22	404670	0.76	0.13	281	2.05	33
10.2	*Homogeneous*	173275	5.54	404247	0.81	0.13	308	1.48	29
14.1	*Homogeneous*	131565	3.71	402076	0.37	0.09	157	1.56	25
14.2	*Homogeneous*	116308	4.34	407188	0.32	0.08	171	1.67	25
14.3	*Homogeneous*	100004	-5.73	403573	0.80	0.04	206	2.60	28
15.2	*Homogeneous*	236693	3.64	405265	0.19	0.09	295	1.25	29
15.1	*Homogeneous*	389734	4.18	395988	0.20	0.10	439	0.45	31
15.3	*Homogeneous*	1362907	1.69	402295	0.36	0.15	355	0.79	30
16.1	*Homogeneous*	904187	4.87	404408	1.75	0.13	303	1.49	30
16.2	*Homogeneous*	356405	5.52	402400	0.08	0.13	301	0.77	28
16.3	*Homogeneous*	248650	1.84	401412	0.09	0.13	319	0.83	30
20.1	*Homogeneous*	139498	2.21	405095	0.70	0.04	214	0.20	31
20.2	*Homogeneous*	144216	3.02	402810	0.67	0.10	212	0.95	31
20.3	*Homogeneous*	148959	4.85	400283	1.14	0.06	171	1.21	35
GC5A/B									
2.1	*Homogeneous*	160912	4.65	403216	0.18	0.09	387	0.33	31
2.2	*Homogeneous*	172230	19.36	397159	2.24	0.29	900	5.99	30
2.3	*Homogeneous*	183040	1.99	403524	0.04	0.03	115	0.84	26
5.2	*Homogeneous*	269649	86.46	407051	9.97	0.22	514	2.06	37
5.1	*Homogeneous*	278526	20.36	404794	4.01	0.13	560	1.47	31
5.3	*Homogeneous*	284957	65.66	408051	11.90	0.22	239	-0.02	26
GC6									
1.1	*Homogeneous*	292082	3.72	411748	0.60	0.11	142	0.31	19
1.2	*Homogeneous*	292580	3.26	406864	0.28	0.21	153	0.30	20
1.3	*Homogeneous*	291578	13.47	406328	2.14	0.20	183	1.17	33

Caatinga-Lamim gneiss ***CM44B***		P ppm	K ppm	Ca ppm	Ti ppm	V ppm	Fe ppm	Zn ppm	Ga ppm
6.1	*Disturbed dark core*	272406	7.27	407646	1.65	5.86	503	1.58	23
6.2	*Disturbed dark core*	270043	3.95	406191	0.19	4.74	111	0.63	22
6.3	*Disturbed dark core*	272706	0.19	410072	0.24	4.88	120	0.78	22
12.1	*Undisturbed dark core*	261742	4.61	411086	0.32	5.38	319	0.87	34
12.2	*Undisturbed dark core*	254112	3.12	402430	0.04	5.55	327	0.98	35
12.3	*Undisturbed dark core*	257220	0.60	408075	0.16	7.46	511	1.03	31

Rb ppm	Sr ppm	Y ppm	Nb ppm	Ba ppm	La ppm	Ce ppm	Pr ppm	Nd ppm	Sm ppm
0.37	68	2017	0.00	0.02	181.2	612.0	98.7	496.9	256.2
0.43	71	2054	0.00	0.07	194.6	651.0	102.3	510.6	256.0
0.37	70	2127	0.00	0.02	194.2	653.2	102.3	526.3	265.8
0.22	66	1407	0.43	0.67	99.9	361.6	63.0	346.7	184.0
0.26	71	1451	0.07	0.11	115.5	420.7	71.2	381.3	200.2
0.24	69	1575	0.03	0.12	118.7	426.2	73.4	403.6	207.2
0.30	68	1662	0.01	0.04	133.2	468.2	79.1	427.5	228.4
0.33	70	1954	0.01	0.01	156.1	562.8	95.9	513.2	269.0
0.26	67	1578	0.07	0.68	122.8	434.3	72.7	397.0	210.4
0.25	84	1171	0.02	0.01	88.7	305.3	51.3	274.3	141.3
0.23	89	1257	0.03	0.04	86.1	297.3	49.7	266.2	139.1
0.24	80	1467	0.06	0.03	116.9	391.2	62.2	327.2	167.1
0.35	70	1750	0.00	0.03	145.7	486.9	79.1	418.6	217.7
0.37	69	1899	0.00	0.01	168.2	568.1	90.4	463.3	240.0
0.40	70	1850	0.00	0.02	158.0	532.4	86.7	451.8	235.6
0.32	72	1844	0.12	0.05	155.9	543.6	89.5	463.0	234.9
0.28	69	1606	0.00	0.02	124.5	437.5	74.2	385.8	200.6
0.30	74	1757	0.01	0.02	156.1	532.1	86.4	445.5	224.8
0.35	76	1894	0.17	0.08	142.3	509.3	87.7	470.6	247.6
0.33	76	1859	0.00	0.03	142.9	510.4	87.0	461.6	242.4
0.32	82	1702	0.46	0.10	232.7	770.7	117.6	565.5	247.4
0.34	102	1862	0.01	0.04	158.5	528.6	84.5	430.3	206.3
0.52	112	1945	0.04	1.33	137.9	486.5	79.6	416.5	204.4
0.27	122	1454	0.04	0.06	73.3	282.7	49.5	280.3	144.3
2.27	109	2691	0.17	1.68	227.1	763.6	123.7	620.1	289.2
0.82	98	1672	0.04	0.97	155.8	505.1	81.0	408.5	189.9
0.71	120	1166	0.21	2.01	103.7	330.3	55.5	280.7	130.5
0.08	60	727	0.12	0.05	12.3	47.3	9.7	65.7	55.1
0.16	62	851	0.19	0.06	17.4	72.3	15.2	100.7	82.3
0.67	68	2520	0.47	1.27	117.2	507.0	95.2	548.8	364.5

Rb ppm	Sr ppm	Y ppm	Nb ppm	Ba ppm	La ppm	Ce ppm	Pr ppm	Nd ppm	Sm ppm
0.08	548	91	0.03	0.84	90.4	234.4	32.6	158.9	30.8
0.00	559	62	0.01	0.74	87.9	214.0	28.4	132.7	24.3
0.01	553	63	0.01	0.93	95.7	230.3	30.4	139.9	25.7
0.01	610	158	0.04	1.60	370.0	838.2	102.4	440.9	78.4
0.04	610	168	0.03	1.43	403.2	908.1	108.5	466.5	82.6
0.03	580	131	0.03	1.02	283.4	665.5	83.1	368.0	66.1

Eu ppm	Gd ppm	Tb ppm	Dy ppm	Ho ppm	Er ppm	Tm ppm	Yb ppm	Lu ppm	Pb ppm
10.7	389.2	75.5	455.5	74.6	179.8	20.3	110.4	13.2	16.70
9.9	391.1	75.5	462.4	75.7	183.1	20.8	115.8	13.6	17.95
10.7	405.4	78.4	482.5	79.0	186.4	21.7	117.7	13.7	18.51
7.0	284.9	53.5	319.8	51.5	120.0	13.3	72.7	8.4	13.81
8.5	303.4	56.5	340.5	55.0	126.7	14.2	77.7	9.4	12.03
8.2	319.2	61.1	366.7	58.9	137.8	15.4	84.3	10.0	13.16
9.5	351.8	65.3	390.8	62.6	147.7	16.2	87.5	10.1	12.17
11.1	408.6	77.7	472.6	74.7	177.1	19.6	108.8	12.6	19.68
8.7	323.8	60.5	362.1	58.9	137.7	15.6	86.0	10.1	11.67
5.5	226.1	42.4	257.2	43.3	108.6	13.8	85.0	11.8	12.61
5.3	222.8	42.5	263.3	46.0	121.9	15.7	100.7	14.2	13.27
7.4	263.5	50.7	310.5	54.1	141.2	17.9	113.0	15.7	14.78
10.3	342.0	64.9	390.0	64.7	155.1	18.1	102.0	12.1	13.95
10.9	372.8	70.3	425.3	70.4	167.3	19.0	104.7	12.3	14.96
11.0	366.3	70.1	421.8	69.3	164.9	18.9	103.7	12.3	15.53
10.5	366.7	70.4	426.5	69.8	164.7	18.3	100.5	12.1	15.23
9.4	319.0	60.4	367.8	60.0	140.1	15.7	83.4	9.8	12.98
10.7	352.6	66.9	406.1	66.2	153.9	17.3	96.5	11.6	14.53
8.5	380.7	71.7	438.2	71.7	172.7	19.2	104.8	12.3	38.79
8.4	375.9	71.1	437.6	72.0	168.7	19.0	102.2	12.2	21.84
7.8	349.3	64.3	382.1	64.3	151.9	17.3	97.0	12.0	17.14
7.7	321.0	62.3	390.4	68.3	168.7	19.1	103.0	12.1	23.34
7.1	326.7	63.5	401.2	71.5	183.1	21.3	119.9	15.3	46.42
5.6	241.5	46.1	295.6	53.6	140.1	17.5	104.6	14.0	23.95
11.2	446.9	89.9	583.1	99.5	247.9	29.1	162.2	19.0	63.46
8.2	292.8	57.7	364.8	62.3	149.3	16.9	90.3	10.6	21.21
6.5	202.9	39.3	242.5	41.1	98.7	11.3	63.9	7.6	20.78
1.5	119.4	21.6	121.0	18.7	42.0	4.8	27.7	3.4	12.66
1.9	163.5	29.0	159.4	23.6	50.3	5.5	29.8	3.5	14.58
3.7	602.9	112.8	629.0	92.3	207.1	22.6	117.4	13.2	34.47

Eu ppm	Gd ppm	Tb ppm	Dy ppm	Ho ppm	Er ppm	Tm ppm	Yb ppm	Lu ppm	Pb ppm
8.5	29.0	3.0	15.4	2.8	7.1	0.9	5.8	1.0	11.44
5.8	21.9	2.2	10.9	1.9	4.9	0.6	4.0	0.7	10.59
6.0	22.2	2.3	11.3	2.0	5.0	0.6	4.0	0.7	11.23
12.1	64.8	6.5	31.0	5.2	12.9	1.5	9.3	1.5	35.40
11.7	65.9	6.8	32.5	5.5	13.6	1.6	9.6	1.6	41.74
10.4	54.7	5.5	26.6	4.4	10.6	1.2	7.6	1.2	29.06

Th ppm	U ppm	Th/U	Sr/Y	Y/Sr	U/Th	REE	(La/Sm)N	LREE*
2.94	8.06	0.36	0.03	29.52	2.75	2974	0.71	1389
2.80	8.55	0.33	0.03	28.95	3.05	3062	0.76	1459
3.50	9.42	0.37	0.03	30.31	2.69	3137	0.73	1476
5.58	5.53	1.01	0.05	21.17	0.99	1986	0.54	871
1.89	5.23	0.36	0.05	20.50	2.76	2181	0.58	989
3.31	5.37	0.62	0.04	22.78	1.62	2291	0.57	1022
2.07	5.46	0.38	0.04	24.56	2.64	2478	0.58	1108
9.28	15.09	0.62	0.04	27.88	1.63	2960	0.58	1328
3.36	4.87	0.69	0.04	23.53	1.45	2301	0.58	1027
2.00	6.29	0.32	0.07	13.96	3.14	1655	0.63	720
2.75	8.01	0.34	0.07	14.05	2.91	1671	0.62	699
3.45	8.95	0.39	0.05	18.41	2.59	2038	0.70	897
1.98	6.02	0.33	0.04	24.87	3.05	2507	0.67	1130
2.29	6.55	0.35	0.04	27.43	2.86	2783	0.70	1290
2.85	7.68	0.37	0.04	26.60	2.70	2703	0.67	1229
6.60	7.08	0.93	0.04	25.77	1.07	2726	0.66	1252
1.91	5.58	0.34	0.04	23.19	2.93	2288	0.62	1022
2.18	6.33	0.35	0.04	23.74	2.90	2627	0.69	1220
12.65	11.57	1.09	0.04	24.79	0.91	2737	0.57	1210
3.25	10.22	0.32	0.04	24.47	3.14	2712	0.59	1202
17.13	9.58	1.79	0.05	20.77	0.56	3080	0.94	1687
4.45	12.18	0.37	0.05	18.21	2.74	2561		
14.92	26.95	0.55	0.06	17.42	1.81	2535		
6.34	13.73	0.46	0.08	11.95	2.17	1749		
26.30	52.20	0.50	0.04	24.72	1.99	3713		
5.57	10.72	0.52	0.06	17.14	1.92	2393		
3.58	8.94	0.40	0.10	9.74	2.50	1615		
1.24	5.16	0.24	0.08	12.15	0.11	550		
1.45	5.77	0.25	0.07	13.62	0.11	754		
13.21	26.60	0.50	0.03	36.80	0.11	3434		

Th ppm	U ppm	Th/U	Sr/Y	Y/Sr	U/Th	REE	(La/Sm)N	LREE*
4.06	8.00	0.51	6.05	0.17	1.97	621		
1.97	6.95	0.28	9.09	0.11	3.52	540		
2.44	7.14	0.34	8.79	0.11	2.93	576		
13.64	24.68	0.55	3.86	0.26	1.81	1975		
17.98	30.08	0.60	3.64	0.27	1.67	2118		
10.97	20.81	0.53	4.44	0.23	1.90	1588		

Trace element analyses of titanite grains from the studied Caatinga-Lamim rocks.

Spot num. analysis	Optical features	Inclusions	Texture BSE	Domain BSE	Chemistry	Nature	Al ppm	K ppm	Ca ppm	Ti ppm	V ppm	Fe ppm	Zn ppm	Ga ppm	Rb ppm	Sr ppm	Y ppm	Zr ppm
CM44B																		
Ttn#1	*Prismatic, incolor, associated with biotie and apatite*	*none*	*Homogeneous*	*Light*	*Metamorphic*	*Metamorphic*	14771	603.29	208912	215010	440	3605	10	7	11	37	77	57
Ttn#2	*Prismatic, incolor, associated with biotie and apatite*	*none*	*Homogeneous*	*Light*	*Metamorphic*	*Metamorphic*	13641	1.09	206088	217218	439	3391	5	21	0.1	44	1034	111
Ttn#3	*Prismatic, incolor, associated with biotie and apatite*	*none*	*Homogeneous*	*Light*	*Metamorphic*	*Metamorphic*	15239	14.84	206665	210984	464	3504	7	12	0.1	41	267	79
Ttn#4	*Prismatic, incolor, associated with biotie and apatite*	*none*	*Homogeneous*	*Light*	*Metamorphic*	*Metamorphic*	16175	19.02	206175	209394	495	3505	8	9	0.04	38	96	57
Ttn#5.1	*Prismatic, incolor, associated with biotie and apatite*	*none*	*Homogeneous*	*Light*	*Metamorphic*	*Metamorphic*	59324	35030.14	203575	206203	616	61892	251	31	615	33	49	23
Ttn#5	*Prismatic, incolor, associated with biotie and apatite*	*none*	*Homogeneous*	*Light*	*Igneous*	*Metamorphic*	21540	54.48	207090	213247	393	3200	7	26	0.2	139	1709	134
Ttn#7	*Prismatic, brownish, associated with biotie*	*none*	*Oscilatory zoning*	*Dark*	*Igneous*	*Igneous*	11757	12.15	207536	221680	400	3226	6	26	0.2	48	1879	127
Ttn#10	*Prismatic, incolr, associated with biotie*	*biotite*	*Sector zoned*	*Dark*	*Metamorphic*	*Igneous*	17714	2394.14	209010	220154	471	7602	29	12	41	39	247	53
Ttn#11	*Rounded, brownish, isolated*	*none*	*Sector zoned*	*Dark*	*Igneous*	*Igneous*	9714	127.72	205742	225998	534	4724	6	29	3	58	2701	172
Ttn#14	*Rounded, brownish, isolated*	*none*	*Sector zoned*	*Dark*	*Igneous*	*Igneous*	7822	12.46	210234	230878	735	8263	7	37	0.1	67	1164	246
Ttn#16	*Prismatic, brownish, associated with biotie and oxide*	*oxide*	*Homogeneous*	*Dark*	*Igneous*	*Igneous*	14757	11.87	207607	219131	440	3639	8	25	0.1	49	1797	152
Ttn#17	*Prismatic, brownish, associated with biotie and oxide*	*none*	*Homogeneous*	*Dark*	*Igneous*	*Igneous*	14207	129.43	207729	227142	401	3425	8	28	2	76	1863	126
Ttn#18	*Prismatic, brownish, associated with biotie and oxide*	*none*	*Homogeneous*	*Dark*	*Igneous*	*Igneous*	14012	28.63	207082	224498	398	3485	6	37	0.3	76	4042	157
Ttn#21	*Prismatic, incolor, associated with biotie*	*biotite*	*Homogeneous*	*Light*	*Metamorphic*	*Metamorphic*	24889	87.82	208980	216320	446	3303	5	20	0.4	164	726	93
Ttn#22	*Prismatic, incolor, associated with biotie*	*none*	*Homogeneous*	*Light*	*Metamorphic*	*Metamorphic*	17983	26.81	206882	211923	459	2723	6	5	0.1	31	73	20
Ttn#23	*Prismatic, incolor, associated with biotie and apatite*	*none*	*Homogeneous*	*Light*	*Metamorphic*	*Metamorphic*	36284	15201.20	208994	211884	530	29785	99	18	265	93	77	33
Ttn#24	*Prismatic, incolor, associated with biotie and apatite*	*none*	*Homogeneous*	*Light*	*Metamorphic*	*Metamorphic*	14651	8.55	206921	215584	443	2710	5	6	0.01	34	70	36
Ttn#25	*Prismatic, incolor, associated with biotie*	*none*	*Homogeneous*	*Light*	*Metamorphic*	*Metamorphic*	18033	1481.37	208280	213306	402	5533	12	8	23	35	150	23
Ttn#26	*Prismatic, incolor, associated with biotie*	*none*	*Homogeneous*	*Light*	*Metamorphic*	*Metamorphic*	16968	99.64	206864	214178	423	3918	7	6	2	33	62	22
Ttn#27	*Prismatic, incolor, associated with biotie*	*none*	*Homogeneous*	*Light*	*Metamorphic*	*Metamorphic*	21746	4937.87	207609	212661	412	12017	33	11	87	32	157	20
Ttn#28	*Prismatic, incolor, associated with biotie*	*biotite*	*Homogeneous*	*Light*	*Metamorphic*	*Metamorphic*	28495	9737.75	208307	219428	479	19633	63	14	158	40	65	42
Ttn#29	*Prismatic, incolor, associated with biotie*	*none*	*Homogeneous*	*Light*	*Metamorphic*	*Metamorphic*	29565	10716.75	208394	220654	473	20639	74	14	185	34	115	21
Ttn#31	*Prismatic, brownish, associated with biotite*	*none*	*Homogeneous*	*Light*	*Igneous*	*Igneous*	12918	14.48	208880	226603	431	3623	5	36	0.3	53	4476	161
Ttn#35	*Rounded, brownish, associated oxide*	*none*	*Sector zoned*	*Light*	*Igneous*	*Igneous*	9008	123.00	206092	235990	662	8103	6	81	2	73	3632	301
Ttn#36	*Rounded, brownish, associated oxide*	*none*	*Sector zoned*	*Light*	*Igneous*	*Igneous*	9664	16.64	206446	232700	793	11999	6	150	1	86	7107	417
Ttn#37	*Rounded, brownish, associated oxide*	*none*	*Sector zoned*	*Light*	*Igneous*	*Igneous*	10299	121.97	205939	231084	696	8716	5	113	3	71	6159	345
Ttn#38	*Rounded, brownish, associated oxide*	*none*	*Sector zoned*	*Dark*	*Igneous*	*Igneous*	10142	13.08	208542	231658	577	6185	6	59	0.3	61	3839	223
Ttn#39	*Rounded, brownish, associated oxide*	*none*	*Sector zoned*	*Light*	*Igneous*	*Igneous*	10072	10.96	208535	230271	787	10471	6	146	1	80	6807	424
Ttn#42	*Prismatic, incolor, associated with biotie and apatite*	*none*	*Homogeneous*	*Light*	*Recryst.?*	*Recryst.?*	15902	12.07	208134	216007	503	3337	6	9	0.0	37	166	52
Ttn#43	*Prismatic, incolor, associated with biotie and apatite*	*none*	*Homogeneous*	*Light*	*Metamorphic*	*Metamorphic*	16059	15.53	204363	214683	486	3088	6	8	0.0	44	106	43
Ttn#44	*Prismatic, incolor, associated with biotie*	*quartz*	*Homogeneous*	*Light*	*Igneous*	*Metamorphic*	24159	59.73	208602	217691	448	3507	6	29	0.2	161	2429	121
Ttn#45	*Rounded, brownish, associated with biotite*	*none*	*Sector zoned*	*Light*	*Igneous*	*Igneous*	13709	12.00	208349	220314	452	3312	5	24	0.2	46	2334	113
Ttn#46	*Rounded, brownish, associated with biotite*	*none*	*Sector zoned*	*Light*	*Igneous*	*Igneous*	10927	20.77	208462	223886	784	6976	6	37	0.3	58	3074	238
Ttn#52	*Rounded, brownish, associated with biotite*	*none*	*Sector zoned*	*Light*	*Igneous*	*Igneous*	10497	26.50	210060	225138	789	7868	4	41	0.5	60	3251	237
Ttn#49	*Incolor, associated with biotie and apatite*	*biotite*	*Homogeneous*	*Light*	*Metamorphic*	*Metamorphic*	16156	220.19	205942	213116	470	3544	5	8	4	36	236	39
Ttn#50	*Incolor, associated with biotie and apatite*	*none*	*Homogeneous*	*Light*	*Metamorphic*	*Metamorphic*	75605	48221.43	212378	219869	774	89407	359	44	811	37	239	49
Ttn#48	*Incolor, associated with biotie and apatite*	*biotite*	*Homogeneous*	*Light*	*Metamorphic*	*Metamorphic*	15747	14.20	208719	218797	451	3114	4	8	0.1	35	562	25
Ttn#51	*Incolor, associated with biotie and apatite*	*biotite*	*Homogeneous*	*Light*	*Metamorphic*	*Metamorphic*	39285	19244.92	206938	217966	566	35909	138	22	323	33	310	24
CM49																		
Ttn#3	*Prismatic, incolor, associated with biotite*	*none*	*Patchy zoned*	*Dark*		*Metamorphic*	7480	4	209241	232661	576	5836	11	66	0.33	65	1582	170
Ttn#6	*Prismatic, incolor, associated with biotite*	*none*	*Patchy zoned*	*Light*		*Metamorphic*	7875	4	204136	226029	618	5295	11	31	0.18	58	896	136
Ttn#8	*Prismatic, incolor, associated with biotite*	*biotite*	*Patchy zoned*	*Dark*		*Igneous*	8040	5	202256	224189	574	4842	12	45	0.28	61	1250	130
Ttn#10	*Prismatic, incolor, associated with biotite*	*none*	*Patchy zoned*	*Light*		*Inherited?*	10834	65	207932	230363	472	5973	12	20	1.59	63	498	82
Ttn#12	*Prismatic, incolor, associated with biotite and amphibole*	*none*	*Patchy zoned*	*Light*		*Metamorphic*	8535	9	209143	236582	438	4243	10	24	0.14	52	729	93
Ttn#15	*Prismatic, incolor, associated with biotite*	*none*	*Core/Rim*	*Light*		*Metamorphic*	8018	7	207963	231682	765	5859	11	14	0.17	57	733	171
Ttn#17	*Prismatic, incolor, associated with biotite*	*none*	*Patchy zoned*	*Dark*		*Metamorphic*	8492	95	210981	250845	624	10169	17	71	1.87	74	1729	208
Ttn#19	*Prismatic, incolor, associated with biotite and amphibole*	*biotite*	*Patchy zoned*	*Light*		*Metamorphic*	11067	1	208609	229070	770	6546	9	7	0.11	54	296	103
Ttn#22	*Prismatic, incolor, associated with biotite and amphibole*	*none*	*Patchy zoned*	*Light*		*Metamorphic*	10690	73	210333	234442	566	6564	11	8	1.37	58	410	574
Ttn#24	*Prismatic, incolor, associated with biotite and amphibole*	*none*	*Patchy zoned*	*Light/Dark*		*Metamorphic*	9210	3	206121	231708	626	5144	8	35	0.28	61	1305	117
Ttn#27	*Prismatic, incolor, associated with amphibole*	*none*	*Patchy zoned*	*Dark*		*Igneous*	9349	8	208632	234726	619	5556	7	30	0.24	68	1116	318
Ttn#28	*Prismatic, incolor, associated with amphibole*	*none*	*Patchy zoned*	*Light/Dark*		*Metamorphic*	8706	10	208161	233859	529	4066	7	22	0.28	56	1398	124
Ttn#31	Prismatic, incolor, associated with biotite and amphibole	none	Patchy zoned	Dark		Igneous	8167	11	203216	230043	560	6622	6	39	0.30	57	1348	124
Ttn#32	*Prismatic, incolor, associated with biotite and amphibole*	*none*	*Patchy zoned*	*Dark*		*Igneous*	*9337*	*12*	*204910*	*227358*	*411*	*4451*	*7*	*25*	*0.32*	*49*	*1064*	*81*
Ttn#33	Prismatic, incolor, associated with biotite and amphibole	none	Core/Rim	Dark		Igneous	9486	28	208413	229276	619	7222	9	22	0.66	59	1235	123
Ttn#34	Prismatic, brownish, associated with biotite	none	Core/Rim	Dark		Igneous	8115	7	202390	226762	606	5445	6	34	0.27	58	1331	132
Ttn#36	Prismatic, brownish, associated with amphibole	none	Patchy zoned	Dark		Igneous	7478	348	203680	230946	558	5724	7	29	1.23	57	1012	109

Nb ppm	Ba ppm	La ppm	Ce ppm	Pr ppm	Nd ppm	Sm ppm	Eu ppm	Gd ppm	Tb ppm	Dy ppm	Ho ppm	Er ppm	Tm ppm	Yb ppm	Lu ppm	Hf ppm	Ta ppm	Pb ppm	Th ppm	U ppm	Th/U	Sr+U	REE	Eu/Eu*	Nb/Ta	Y/Sr	Sr/Y	LREE
659	20	34	166	31	146	30	43	21	2	13	2	7	1	5	1	2	7	33	38	80	0.48	118	501	3.4	99.6	2.06	0.4851	376.8
997	0.3	156	797	159	886	266	85	244	33	178	32	86	11	72	11	10	53	124	34	94	0.36	138	3016	0.7	18.7	23.41	0.0427	1998.5
756	1	91	414	73	347	79	67	64	8	42	8	21	3	19	3	6	28	73	22	57	0.38	98	1237	1.9	27.3	6.54	0.1529	924.1
715	1	51	240	42	189	39	50	27	3	15	3	7	1	6	1	4	12	44	10	34	0.30	71	675	3.0	58.6	2.55	0.3926	522.6
370	1378	9	51	11	56	15	30	13	2	8	2	4	1	3	1	2	5	16	2	13	0.13	46	205	4.4	76.1	1.50	0.6651	127.0
1576	12	221	983	191	1013	338	89	365	52	297	53	145	19	122	17	12	174	171	53	124	0.43	263	3905	0.5	9.1	12.32	0.0812	2407.3
1471	0	198	1005	212	1210	428	97	456	64	364	64	172	22	130	18	11	137	150	43	112	0.38	160	4440	0.5	10.8	39.16	0.0255	2624.5
691	71	60	283	52	257	69	65	64	8	46	8	21	3	17	3	4	11	58	13	44	0.30	82	956	2.0	61.6	6.42	0.1558	652.1
1197	2	197	1057	240	1470	612	113	661	101	591	101	265	36	221	27	16	182	372	48	269	0.18	327	5694	0.4	6.6	46.87	0.0213	2965.1
2314	1	710	2210	324	1475	365	152	310	40	215	37	98	13	86	12	14	134	432	225	308	0.73	375	6047	0.9	17.3	17.26	0.0579	4719.1
1149	1	213	983	189	1027	342	86	368	53	302	57	155	21	134	19	13	204	191	53	138	0.38	187	3951	0.5	5.6	36.71	0.0272	2413.4
1373	5	196	1030	226	1321	473	90	480	68	377	66	167	22	128	17	12	137	167	41	121	0.34	196	4663	0.4	10.0	24.63	0.0406	2774.1
1593	3	276	1403	309	1849	780	93	889	138	814	147	377	49	298	37	14	191	201	65	144	0.45	220	7457	0.2	8.3	53.27	0.0188	3836.4
1120	14	128	650	130	679	196	81	181	23	124	22	60	8	50	7	8	80	101	36	83	0.44	247	2339	0.9	14.0	4.41	0.2267	1587.0
701	1	7	43	9	55	18	33	18	2	12	2	6	1	5	1	2	12	13	1	10	0.10	42	212	3.9	57.3	2.33	0.4298	113.9
562	541	18	101	21	109	29	40	23	3	14	2	6	1	5	1	2	12	26	3	21	0.14	113	372	3.1	46.2	0.83	1.2095	249.1
594	0.1	24	128	25	123	29	44	22	2	12	2	5	1	4	1	2	6	30	4	23	0.17	58	422	3.5	102.1	2.02	0.4953	300.6
563	61	14	84	19	112	39	61	38	5	27	5	12	2	10	2	2	27	35	2	29	0.08	64	430	3.3	20.8	4.28	0.2335	229.5
357	8	10	54	11	56	15	37	14	2	10	2	5	1	5	1	2	8	22	2	20	0.08	53	220	5.2	46.0	1.85	0.5401	129.8
488	128	13	77	18	104	36	61	37	5	27	5	14	2	11	2	2	24	34	2	28	0.06	61	411	3.5	20.7	4.88	0.2049	211.6
672	315	29	143	26	121	25	41	18	2	11	2	5	1	4	1	2	11	32	10	54	0.18	95	427	3.9	63.0	1.61	0.6223	318.2
561	357	13	70	16	89	30	47	29	4	20	4	10	1	8	1	2	14	26	2	22	0.09	57	340	3.3	39.3	3.35	0.2987	187.0
1425	1	263	1343	293	1764	788	93	916	149	897	159	431	57	347	43	14	224	180	60	142	0.42	195	7543	0.2	6.4	84.45	0.0118	3662.7
2275	3	930	3978	758	3958	1170	232	1009	139	763	128	331	45	284	35	24	212	597	289	411	0.70	484	13760	0.4	10.7	50.08	0.0200	9624.2
3159	1	1423	6640	1396	7932	2601	382	2241	306	1665	270	664	81	460	49	33	604	1140	555	776	0.72	862	26109	0.3	5.2	82.75	0.0121	17391.0
2641	2	1053	4852	1009	5710	1956	282	1821	256	1419	235	580	74	422	48	28	497	746	367	533	0.69	604	19717	0.3	5.3	86.36	0.0116	12624.6
1689	1	448	2330	514	3162	1201	144	1171	165	908	149	363	45	255	29	21	378	449	125	317	0.39	379	10882	0.3	4.5	62.49	0.0160	6453.4
3139	1	1429	6477	1359	7607	2426	380	2130	288	1535	255	633	81	457	50	33	495	1114	583	774	0.75	854	25107	0.3	6.3	84.94	0.0118	16872.1
1032	1	45	219	40	201	52	95	44	5	29	5	13	2	11	2	4	24	53	9	40	0.23	77	764	4.1	43.8	4.51	0.2219	505.1
1096	1	27	141	28	141	38	87	32	4	21	3	9	1	7	1	3	39	39	5	30	0.17	74	540	5.1	27.8	2.38	0.4201	336.6
1396	9	210	988	210	1234	488	96	545	79	460	83	213	29	176	24	12	126	145	66	105	0.63	266	4835	0.4	11.1	15.13	0.0661	2642.2
1420	1	178	879	186	1049	412	101	475	75	447	79	213	29	178	23	10	87	134	46	102	0.45	148	4321	0.5	16.4	50.52	0.0198	2290.6
1366	1	533	1898	305	1482	456	171	482	79	518	100	306	50	362	48	15	144	371	188	271	0.69	329	6791	0.8	9.5	53.14	0.0188	4217.9
1454	1	533	1995	341	1719	536	184	544	89	565	107	322	52	364	47	16	178	389	188	280	0.67	340	7396	0.7	8.2	53.76	0.0186	4587.4
736	6	27	133	26	142	47	133	48	7	39	7	19	3	17	3	2	32	23	7	18	0.35	55	651	5.9	22.7	6.53	0.1531	328.1
610	1574	32	145	27	142	49	127	51	7	41	7	20	3	18	3	3	26	21	12	21	0.54	59	669	5.4	23.5	6.40	0.1562	345.6
845	1	22	133	33	211	102	188	126	19	110	19	50	6	37	5	2	82	32	3	25	0.10	60	1061	3.6	10.3	16.12	0.0620	398.5
678	579	17	90	21	126	54	169	64	10	54	10	26	3	22	3	2	48	24	5	21	0.22	54	670	6.2	14.2	9.31	0.1074	254.0
734	0.08	336	1982	453	2569	670	207	486	62	325	58	152	20	128	16	15	40	87	25	64	0.39	129	7464	0.72	18	24.5	0.04	5340
484	0.05	135	857	205	1167	336	100	254	33	182	32	86	12	75	10	10	28	46	9	31	0.30	89	3484	0.69	17	15.4	0.07	2364
519	0.05	213	1298	294	1687	461	149	338	45	247	45	122	17	115	15	11	27	61	15	45	0.34	106	5044	0.75	19	20.6	0.05	3492
278	15.05	102	548	115	643	162	93	121	16	91	17	48	7	51	7	7	6	14	16	10	1.62	73	2021	1.33	44	7.9	0.13	1409
361	0.02	106	641	152	896	260	109	204	26	146	26	71	10	63	9	9	10	17	5	12	0.40	64	2720	0.96	36	14.1	0.07	1796
359	0.00	52	335	82	485	158	105	138	20	120	24	72	11	78	11	10	5	24	1	16	0.08	74	1691	1.47	66	12.8	0.08	954
942	58.56	341	2093	476	2738	763	203	563	71	380	65	166	22	131	16	15	78	91	35	75	0.47	149	8027	0.62	12	23.3	0.04	5648
156	0.01	19	115	27	162	55	26	51	8	48	10	31	5	36	6	6	8	9	0	6	0.09	59	596	1.04	21	5.5	0.18	322
315	6.08	19	127	35	236	89	34	81	11	66	13	41	6	48	8	25	12	9	27	6	4.51	64	815	0.84	27	7.1	0.14	417
541	0.17	139	914	228	1344	409	133	308	43	246	45	126	19	130	17	9	22	47	4	34	0.11	96	4102	0.75	24	21.3	0.05	2626
1197	0.14	126	782	186	1120	353	116	295	39	219	40	108	15	103	14	24	55	62	5	44	0.10	112	3517	0.74	22	16.4	0.06	2213
503	1.07	59	438	130	911	371	142	341	48	278	51	140	20	124	16	13	27	24	1	19	0.05	75	3068	0.83	19	25.1	0.04	1539
535	0.05	128	949	253	1570	477	168	380	49	273	49	132	18	119	15	11	12	20	2	14	0.15	71	4581	0.80	43	23.6	0.04	2900
397	*3.37*	*60*	*491*	*151*	*1024*	*348*	*129*	*288*	*38*	*213*	*38*	*104*	*14*	*94*	*12*	*9*	*9*	*14*	2	10	0.18	59	3004	0.84	46	21.8	0.05	1725
375	8.46	55	434	124	830	330	136	302	43	246	45	124	17	112	15	10	21	23	3	15	0.17	74	2814	0.90	18	21.0	0.05	1444
512	1.65	119	806	209	1310	446	138	361	49	275	48	129	18	111	14	11	39	44	2	31	0.08	89	4032	0.70	13	22.8	0.04	2444
581	17.92	132	771	183	1082	322	143	263	34	195	35	100	14	95	13	10	13	14	4	10	0.43	67	3384	1.01	45	17.8	0.06	2169

Trace element analyses performed on glass and apatite reference materials.

Glass / apatite reference material	Spot num. analysis	P ppm	K ppm	Ca ppm	Ti ppm	V ppm	Fe ppm	Zn ppm	Ga ppm	Rb ppm	Sr ppm	Y ppm	Nb ppm	Ba ppm	La ppm	Ce ppm	Pr ppm	Nd ppm	Sm ppm	Eu ppm	Gd ppm	Tb ppm	Dy ppm	Ho ppm
NIST 610																								
	1	412	464	81739	452	449	459	460	432	423	515	461	464	451	438	450	447	429	450	446	448	435	436	448
	2	437	463	82530	453	454	454	460	438	428	514	464	468	451	442	458	451	433	455	449	450	439	440	451
	3	420	466	81857	452	447	461	459	429	427	521	462	463	456	441	452	448	429	454	446	448	439	436	447
	4	417	462	82232	451	448	457	461	431	423	514	457	461	449	441	453	443	425	450	449	444	433	436	448
	5	411	464	83086	454	450	453	460	436	427	520	467	466	451	443	458	450	433	458	454	452	439	441	453
	6	413	464	81842	451	454	466	460	432	426	513	462	465	453	438	450	448	430	451	448	451	433	436	448
	7	413	464	82052	453	448	446	460	434	424	514	461	465	451	439	453	448	430	452	446	448	438	437	449
	Average	418	464	82191	452	450	457	460	433	426	516	462	465	452	440	453	448	430	453	448	449	436	437	449
	2SD(%)	19	2	957	2	6	13	1	6	4	6	6	4	5	4	7	5	5	6	6	5	5	4	4
Jochum et al., 2011	*Literature*	413	464	81475	452	450	458	460	433	426	516	462	465	452	440	453	448	430	453	447	449	437	437	449
	Average/Lit	**1.01**	**1.00**	**1.01**	**1.00**	**1.00**	**1.00**	**1.00**	**1.00**	**1.00**	**1.00**	**1.00**	**1.00**	**1.00**	**1.00**	**1.00**	**1.00**	**1.00**	**1.00**	**1.00**	**1.00**	**1.00**	**1.00**	**1.00**
NIST 612																								
	1		67	88799	42	41	59	42	38	34	82	41	40	42	38	40	40	38	41	38	41	39	38	40
	2		71	87167	43	40	44	42	38	33	81	40	40	41	37	40	39	37	40	37	40	39	38	39
	3	322	77	87314	43	40	68	44	38	33	82	40	40	41	38	39	39	37	40	37	39	39	38	39
	4		65	86879	41	40	84	41	38	33	81	40	40	40	37	39	38	37	39	37	40	38	37	39
	5		65	87537	41	40	62	40	38	33	81	40	39	41	37	39	39	37	40	37	40	38	38	40
	6		65	87948	43	41	47	42	39	34	82	40	40	42	38	40	39	37	40	37	40	39	38	40
	Average	322	68	87607	42	40	61	42	38	33	82	40	40	41	38	40	39	37	40	37	40	39	38	40
	2SD(%)		10	1371	2	1	29	3	1	1	2	1	1	1	1	1	1	0	1	1	1	1	1	0
Jochum et al., 2011	*Literature*	47	62	85061	44	39	51	39	37	31	78	38	39	39	36	38	38	36	38	36	37	38	36	38
	Average/Lit	**6.90**	**1.10**	**1.03**	**0.96**	**1.04**	**1.19**	**1.07**	**1.04**	**1.06**	**1.04**	**1.04**	**1.03**	**1.05**	**1.04**	**1.04**	**1.03**	**1.05**	**1.06**	**1.04**	**1.07**	**1.03**	**1.06**	**1.03**
Apatite reference materials																								
Durango																								
	1	136112	5	396235	0.00	51	365	0.93	104	0.21	509	996	0.04	2.12	4482	5809	505	1677	244	19	221	28	163	32
	2	1346733	5	404095	0.51	51	377	0.82	106	0.17	524	992	0.03	2.09	4552	5860	512	1676	248	20	218	28	165	32
	3	-105907	8	403997	0.54	52	390	0.66	103	0.18	524	996	0.04	2.14	4612	5882	511	1706	249	20	220	28	164	32
	4	145499	4	402245	0.26	52	342	1.08	106	0.18	524	1001	0.04	2.24	4512	5840	503	1691	247	20	220	28	162	32
	5	232250	7	401105	0.83	51	358	0.62	109	0.18	521	999	0.03	2.13	4577	5910	507	1705	252	20	221	28	164	33
	6	278936	5	404506	0.29	51	439	0.08	108	0.19	520	999	0.03	2.20	4521	5782	504	1689	243	20	217	27	165	32
	Average	338937	6	402030	0.40	51	379	0.70	106	0.18	520	997	0.04	2.15	4543	5847	507	1691	247	20	219	28	164	32
	2SD(%)	1022576	3	6245	0.57	1	68	0.69	4	0.03	11	6	0.01	0.11	95	94	7	26	6	1	3	0	2	1
Chew et al. 2016	*Literature*					34					475	1069			4404	5659	495	1751	262	21	237	31	174	35
	Average/Lit					**1.52**					**1.09**	**0.93**			**1.03**	**1.03**	**1.02**	**0.97**	**0.94**	**0.92**	**0.92**	**0.90**	**0.94**	**0.92**
Kovdor																								
	1	-2207132	10	398584	0.73	129	344	1.75	142	0.06	2471	239	3.17	16.57	3279	7165	834	3015	392	91	224	20	84	11
	2	135787	9	396585	0.61	139	330	1.44	155	0.03	2479	268	4.31	16.72	3591	7876	912	3313	427	100	244	23	92	12
	Average	-1035672	9	397584	0.67	134	337	1.60	149	0.05	2475	254	3.74	16.65	3435	7520	873	3164	410	96	234	22	88	11
	2SD(%)	3313387	1	2827	0.18	14	20	0.43	18	0.04	12	41	1.61	0.21	442	1005	110	421	50	11	27	3	12	2
Arzamastsev et al., 2	*Literature*					151		2.00	1	0.10	3051	304	1.40	62.00	1524	2680	295	1167	173	46	121	14	67	12
	Average/Lit					**0.89**		**0.80**	**148.70**	**0.46**	**0.81**	**0.83**	**2.67**	**0.27**	**2.25**	**2.81**	**2.96**	**2.71**	**2.37**	**2.08**	**1.93**	**1.55**	**1.32**	**0.95**
Sumé 1																								
	1	124654	6	401842	0.49	38	81	0.81	72	0.04	799	278	2.05	0.99	1509	3367	374	1320	172	24	105	11	55	10
	2	-117339	5	413063	1.31	38	118	0.55	72	0.07	818	280	1.86	1.35	1572	3453	385	1354	177	25	106	11	56	10
	3	229264	7	410248	0.48	38	108	0.59	77	0.04	832	288	1.89	1.31	1581	3516	391	1367	180	25	109	11	57	10
	4	53326	2	84135	0.05	8	26	0.04	15	0.01	175	57	0.52	0.31	311	692	76	272	36	5	21	2	11	2
	Average	72476	5	327322	0.58	31	83	0.50	59	0.04	656	226	1.58	0.99	1243	2757	307	1078	141	20	85	9	45	8
	2SD(%)	291437	4	324389	1.06	30	83	0.65	59	0.05	641	226	1.42	0.96	1245	2756	308	1076	141	20	85	9	45	8
Lana et al. 2022	*Literature*	163117		396226		18	70	1.10			749	202	0.80	1.00	1415	3440	358	1055	129	20	131	10	42	7
	Average/Lit	**0.44**		**0.83**		**1.70**	**1.19**	**0.45**			**0.88**	**1.12**	**1.97**	**0.99**	**0.88**	**0.80**	**0.86**	**1.02**	**1.09**	**1.00**	**0.65**	**0.89**	**1.07**	**1.08**

Arzamastsev, A.A., Arzamastseva, L. V., Bea, F., Montero, P., 2009. Trace elements in minerals as indicators of the evolution of alkaline ultrabasic dike series: LA-ICP-MS data for the magmatic provinces of northeastern Fennoscandia and Germany. Petrology 17, 46–72. https://doi.org/10.1134/S0869591109010032

Chew, D.M., Babechuk, M.G., Cogné, N., Mark, C., O'Sullivan, G.J., Henrichs, I.A., Doepke, D., McKenna, C.A., 2016. (LA,Q)-ICPMS trace-element analyses of Durango and McClure Mountain apatite and implications for making natural LA-ICPMS mineral standards. Chem. Geol. 435, 35–48. https://doi.org/10.1016/j.chemgeo.2016.03.028

Jochum, K.P., Weis, U., Stoll, B., Kuzmin, D., Yang, Q., Raczek, I., Jacob, D.E., Stracke, A., Birbaum, K., Frick, D.A., Günther, D., Enzweiler, J., 2011. Determination of Reference Values for NIST SRM 610–617 Glasses Following ISO Guidelines. Geostand. Geoanalytical Res. 35, 397–429. https://doi.org/https://doi.org/10.1111/j.1751-908X.2011.00120.x

Lana, C., Gonçalves, G.O., Mazoz, A., Buick, I., Kamo, S., Scholz, R., Wang, H., Moreira, H., Babinski, M., Queiroga, G., 2022. Assessing the U-Pb, Sm-Nd and Sr-Sr Isotopic Compositions of the Sumé Apatite as a Reference Material for LA-ICP-MS Analysis. Geostand. Geoanalytical Res. 46, 71–95. https://doi.org/10.1111/ggr.12413

Er ppm	Tm ppm	Yb ppm	Lu ppm	Pb ppm	Th ppm	U ppm	Th/U
451	433	448	439	424	456	460	0.99
458	437	452	439	430	458	464	0.99
455	435	449	440	425	458	461	0.99
453	430	450	440	423	454	456	0.99
462	439	458	444	427	459	464	0.99
454	433	449	441	424	459	462	0.99
454	435	449	438	426	457	461	0.99
455	435	451	440	425	457	461	0.99
7	6	7	4	5	4	6	0.77
455	435	450	439	426	457	462	0.99
1.00	**1.00**	**1.00**	**1.00**	**1.00**	**1.00**	**1.00**	**1.00**
41	38	41	39	41	39	39	1.00
40	38	40	38	41	40	39	1.02
40	38	40	38	41	39	38	1.01
40	38	40	38	40	39	38	1.01
40	38	41	38	41	39	39	1.02
40	39	41	39	41	39	39	1.01
40	38	41	38	41	39	39	1.01
1	1	1	1	1	1	1	0.96
38	37	39	37	39	38	37	1.01
1.06	**1.04**	**1.04**	**1.03**	**1.06**	**1.04**	**1.04**	**1.00**
89	11	59	6.9	0.4	402.4	16.7	24.1
91	11	61	7.0	0.4	406.3	16.9	24.1
90	11	61	7.0	0.4	409.1	16.8	24.3
90	11	60	7.0	0.4	402.9	16.6	24.2
90	11	61	7.0	0.4	402.9	16.9	23.8
88	11	60	7.0	0.4	401.8	16.9	23.8
90	11	60	7.0	0.4	404.2	16.8	24.1
1	0	2	0.1	0.0	5.7	0.2	0.4
91	11	61	6.8	1.0	350.1	17.7	19.8
0.99	**0.96**	**0.99**	**1.03**	**0.38**	**1.15**	**0.95**	**1.22**
20	1.8	8	0.8	6.9	1706.8	25.9	65.9
22	1.9	9	1.0	7.6	1772.7	27.0	65.8
21	1.8	9	0.9	7.3	1739.7	26.4	65.8
3	0.3	1	0.2	0.9	93.1	1.5	61.5
27	3.1	15	2.0	0.6	133.0	12.0	11.1
0.79	**0.59**	**0.57**	**0.45**	**12.09**	**13.08**	**2.20**	**5.94**
25	2.9	17	2.1	31.5	2822.8	91.9	30.7
25	3.0	18	2.2	32.9	2945.3	94.7	31.1
26	3.0	18	2.2	34.2	2995.1	97.6	30.7
5	0.6	3	0.4	7.2	603.5	19.5	30.9
20	2.4	14	1.7	26.4	2341.7	75.9	30.8
20	2.4	14	1.7	25.8	2322.1	75.3	30.8
20	2.2	13	1.6		1960.0	54.0	36.3
1.01	**1.08**	**1.07**	**1.09**		**1.19**	**1.41**	**0.85**

Durango apatite

Standard zircon	Durango	Durango	Durango	Durango	Durango	Durango	Durango	Durango	Durango	Durango
Element (ppm)							Average	2SD(%)	Chew et al. 2016	Av. / Lit.
Al										
28 Si	4421.54			29.39			2225.47	6211.44		
29 Si	2257.19	1884.44			772.40		1638.01	1544.93		
P	136111.75	1346732.70		145499.23	232250.27	278935.82	427905.95	1034221.08		
K	4.51	4.81	7.90	4.21	7.36	5.48	5.71	3.11		
Ca	396234.91	404094.55	403997.08	402244.57	401105.11	404505.79	402030.33	6244.73		
Ti		0.51	0.54	0.26	0.83	0.29	0.49	0.46		
V	51.01	51.05	51.58	51.53	51.26	51.01	51.24	0.52	33.81	1.52
Fe	365.15	376.94	390.15	342.02	357.87	439.18	378.55	67.85		
Zn	0.93	0.82	0.66	1.08	0.62	0.08	0.70	0.69		
Ga	104.13	105.97	102.98	105.78	108.64	107.63	105.86	4.21		
Rb	0.21	0.17	0.18	0.18	0.18	0.19	0.18	0.03		
Sr	509.27	524.04	524.23	523.66	520.84	519.79	520.30	11.42	475.40	1.09
Y	995.94	992.48	996.08	1000.93	998.87	998.87	997.19	5.97	1069.00	0.93
90 Zr	2.49	1.92	1.48	1.64	2.36	1.56	1.91	0.86		
91 Zr	2.44	2.29	2.42	1.96	1.46	2.40	2.16	0.78		
96 Zr	0.32	0.69	0.14	0.27	0.80	0.44	0.44	0.51		
Nb	0.04	0.03	0.04	0.04	0.03	0.03	0.04	0.01		
Ba	2.12	2.09	2.14	2.24	2.13	2.20	2.15	0.11		
La	4481.84	4552.01	4612.20	4511.51	4577.45	4520.58	4542.60	95.03	4404.00	1.03
Ce	5809.22	5860.00	5881.64	5839.52	5909.92	5781.78	5847.01	94.08	5659.00	1.03
Pr	504.72	511.96	510.73	503.49	506.53	504.35	506.96	7.11	494.80	1.02
Nd	1677.40	1675.96	1705.97	1691.44	1704.59	1688.50	1690.64	25.70	1751.00	0.97
Sm	244.10	247.59	248.90	246.72	251.80	243.37	247.08	6.24	261.60	0.94
Eu	19.28	19.72	19.90	19.86	20.01	19.51	19.71	0.55	21.31	0.92
Gd	220.86	218.29	219.59	219.65	221.08	216.54	219.33	3.40	237.20	0.92
Tb	27.63	27.91	28.00	27.66	27.79	27.45	27.74	0.41	30.88	0.90
Dy	162.56	164.62	163.61	161.99	164.16	164.59	163.59	2.19	173.70	0.94
Ho	32.06	32.11	32.44	32.31	32.67	31.89	32.24	0.57	35.12	0.92
Er	89.37	90.59	89.88	89.83	89.83	88.42	89.65	1.44	90.91	0.99
Tm	10.77	10.89	10.97	10.87	10.84	10.71	10.84	0.19	11.25	0.96
Yb	58.82	60.74	60.95	59.76	61.45	60.27	60.33	1.88	60.87	0.99
Lu	6.93	6.97	7.03	7.03	6.96	6.98	6.98	0.08	6.75	1.03
Hf	0.01	0.02	0.02	0.01	0.01	0.01	0.01	0.01		
Ta	0.00	0.01	0.01	0.00	0.01	0.00	0.00	0.00		
Pb	0.37	0.37	0.37	0.37	0.36	0.36	0.37	0.01	0.95	0.38
Th	402.43	406.28	409.11	402.87	402.89	401.78	404.23	5.72	350.10	1.15
U	16.68	16.88	16.81	16.63	16.92	16.85	16.80	0.23	17.71	0.95

Kovdor apatite

Standard zircon Element (ppm)	Kovdor	Kovdor	Kovdor Average	Kovdor 2SD(%)	Kovdor Arzamastsev et al., 2009	Kovdor Av. / Lit.
Al						
28 Si	2881.57	2459.19	**2670.38**	**597.33**		
29 Si	4130.15	4762.77	**4446.46**	**894.66**		
P		135786.88	**135786.88**			
K	9.50	8.76	**9.13**	**1.05**		
Ca	398583.81	396585.02	**397584.42**	**2826.72**		
Ti	0.73	0.61	**0.67**	**0.18**		
V	129.38	139.23	**134.31**	**13.94**	**151.00**	**0.89**
Fe	344.30	329.91	**337.11**	**20.36**		
Zn	1.75	1.44	**1.60**	**0.43**	**2.00**	**0.80**
Ga	142.45	154.95	**148.70**	**17.68**	**1.00**	**148.70**
Rb	0.06	0.03	**0.05**	**0.04**	**0.10**	**0.46**
Sr	2470.63	2479.35	**2474.99**	**12.34**	**3051.00**	**0.81**
Y	239.16	268.44	**253.80**	**41.41**	**304.00**	**0.83**
90 Zr	35.33	50.51	**42.92**	**21.47**	**14.00**	**3.07**
91 Zr	36.47	51.39	**43.93**	**21.10**	**14.00**	**3.14**
96 Zr	6.00	8.33	**7.17**	**3.30**	**14.00**	**0.51**
Nb	3.17	4.31	**3.74**	**1.61**	**1.40**	**2.67**
Ba	16.57	16.72	**16.65**	**0.21**	**62.00**	**0.27**
La	3278.83	3591.35	**3435.09**	**441.98**	**1524.00**	**2.25**
Ce	7165.22	7875.60	**7520.41**	**1004.64**	**2680.00**	**2.81**
Pr	833.93	911.78	**872.85**	**110.10**	**295.00**	**2.96**
Nd	3015.42	3313.29	**3164.36**	**421.26**	**1167.00**	**2.71**
Sm	391.98	427.35	**409.66**	**50.02**	**173.00**	**2.37**
Eu	91.49	99.58	**95.54**	**11.44**	**46.00**	**2.08**
Gd	224.48	243.75	**234.12**	**27.25**	**121.00**	**1.93**
Tb	20.50	22.77	**21.63**	**3.21**	**14.00**	**1.55**
Dy	83.79	92.46	**88.13**	**12.26**	**67.00**	**1.32**
Ho	10.85	11.93	**11.39**	**1.54**	**12.00**	**0.95**
Er	20.41	22.35	**21.38**	**2.74**	**27.00**	**0.79**
Tm	1.76	1.93	**1.84**	**0.25**	**3.10**	**0.59**
Yb	8.13	8.91	**8.52**	**1.10**	**15.00**	**0.57**
Lu	0.83	0.98	**0.90**	**0.21**	**2.00**	**0.45**
Hf	0.07	0.15	**0.11**	**0.11**		
Ta	0.04	0.06	**0.05**	**0.03**		
Pb	6.95	7.56	**7.25**	**0.86**	**0.60**	**12.09**
Th	1706.81	1772.65	**1739.73**	**93.12**	**133.00**	**13.08**
U	25.89	26.96	**26.42**	**1.51**	**12.00**	**2.20**

Sumé 1 apatite

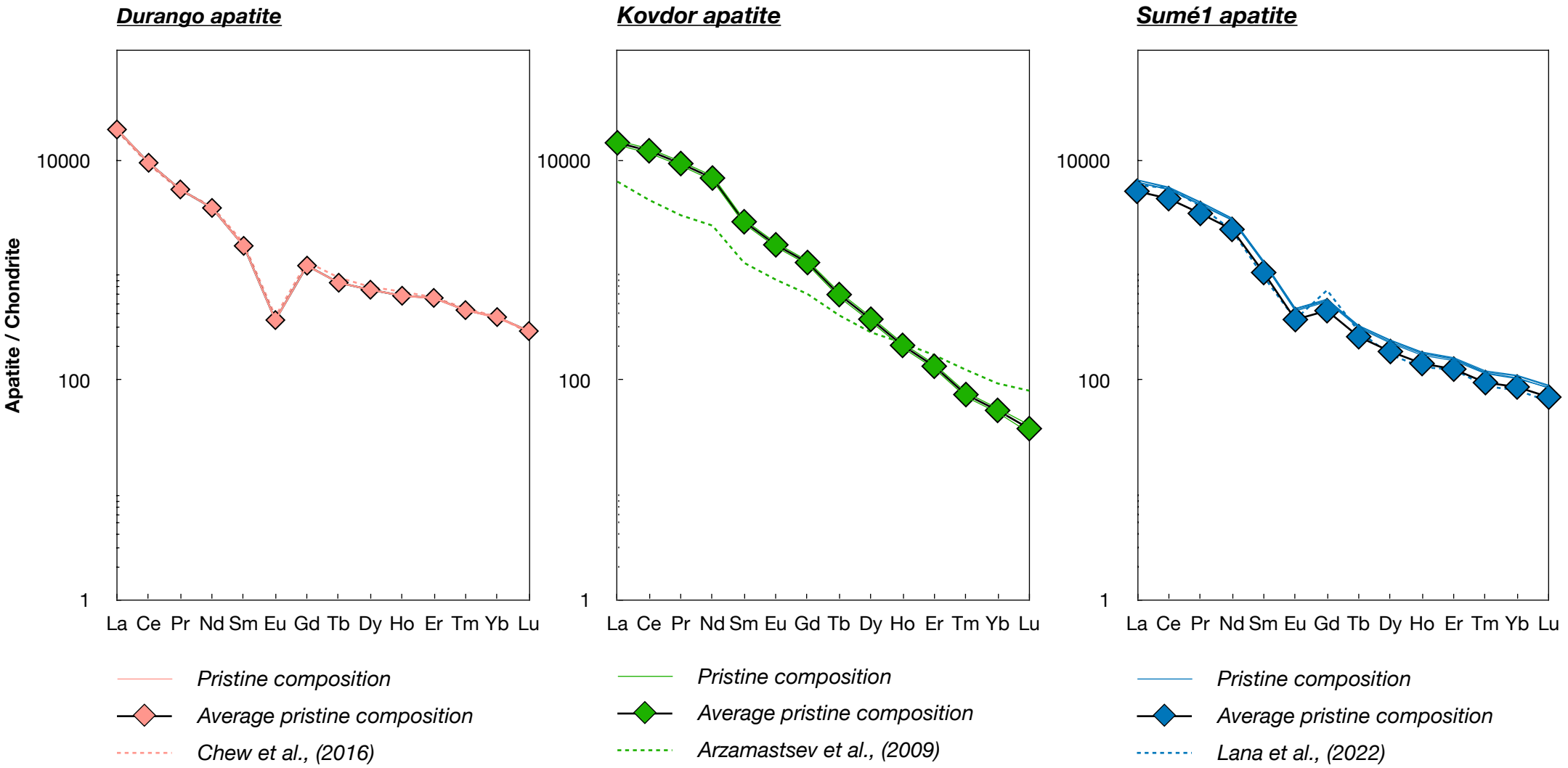
Standard zircon Element (ppm)	Sumé1	Sumé1	Sumé1	Sumé1	Sumé1 Average	Sumé1 2SD(%)	Sumé1 Lana et al. 2022	Sumé1 Av. / Lit.
Al							**52.92**	
28 Si	7352.67	9607.63	5698.75	1391.15	**6012.55**	**6945.15**	**7432.69**	**0.81**
29 Si	10553.19	6697.76	6987.22	1148.78	**6346.74**	**7767.14**	**5308.00**	**1.20**
P	124654.41		229263.92	53326.26	**135748.20**	**176983.82**	**163117.47**	**0.83**
K	5.87	4.91	6.61	1.74	**4.78**	**4.29**		
Ca	401841.50	413063.29	410247.93	84135.22	**327321.99**	**324389.16**	**396226.42**	**0.83**
Ti	0.49	1.31	0.48	0.05	**0.58**	**1.06**		
V	37.93	38.45	38.14	8.03	**30.64**	**30.15**	**18.00**	**1.70**
Fe	81.06	118.46	107.93	25.75	**83.30**	**82.94**	**69.94**	**1.19**
Zn	0.81	0.55	0.59	0.04	**0.50**	**0.65**	**1.10**	**0.45**
Ga	72.00	72.15	77.20	15.48	**59.21**	**58.50**		
Rb	0.04	0.07	0.04	0.01	**0.04**	**0.05**		
Sr	798.59	817.86	832.10	175.47	**656.01**	**641.30**	**749.00**	**0.88**
Y	277.79	280.21	288.50	56.80	**225.82**	**225.56**	**202.00**	**1.12**
90 Zr	18.66	19.74	19.88	4.69	**15.74**	**14.78**	**12.00**	**1.31**
91 Zr	18.62	20.52	20.26	4.68	**16.02**	**15.21**	**12.00**	**1.33**
96 Zr	2.99	3.57	3.71	0.75	**2.76**	**2.74**		
Nb	2.05	1.86	1.89	0.52	**1.58**	**1.42**	**0.80**	**1.97**
Ba	0.99	1.35	1.31	0.31	**0.99**	**0.96**	**1.00**	**0.99**
La	1509.37	1571.73	1581.34	310.79	**1243.31**	**1245.00**	**1415.00**	**0.88**
Ce	3366.88	3453.26	3515.82	691.65	**2756.90**	**2756.37**	**3440.00**	**0.80**
Pr	374.41	385.46	390.56	76.05	**306.62**	**307.72**	**358.00**	**0.86**
Nd	1320.40	1353.56	1366.83	271.51	**1078.08**	**1076.13**	**1055.00**	**1.02**
Sm	171.78	177.46	179.89	35.81	**141.23**	**140.73**	**129.00**	**1.09**
Eu	24.44	25.15	25.13	4.95	**19.92**	**19.97**	**20.00**	**1.00**
Gd	105.27	105.78	108.66	21.40	**85.28**	**85.22**	**131.00**	**0.65**
Tb	10.98	11.23	11.29	2.23	**8.94**	**8.94**	**10.00**	**0.89**
Dy	54.70	56.32	56.98	11.09	**44.77**	**44.95**	**42.00**	**1.07**
Ho	9.55	9.75	9.90	1.92	**7.78**	**7.82**	**7.20**	**1.08**
Er	24.76	25.15	25.59	5.00	**20.12**	**20.18**	**20.00**	**1.01**
Tm	2.90	2.96	3.03	0.59	**2.37**	**2.37**	**2.20**	**1.08**
Yb	16.90	17.58	17.78	3.44	**13.92**	**14.00**	**13.00**	**1.07**
Lu	2.11	2.19	2.25	0.44	**1.75**	**1.74**	**1.60**	**1.09**
Hf	0.11	0.11	0.12	0.02	**0.09**	**0.09**	**0.10**	**0.89**
Ta	0.04	0.04	0.04	0.01	**0.03**	**0.03**		
Pb	31.48	32.90	34.19	7.15	**26.43**	**25.80**		
Th	2822.84	2945.33	2995.06	603.54	**2341.69**	**2322.05**	**1960.00**	**1.19**
U	91.86	94.74	97.61	19.55	**75.94**	**75.33**	**54.00**	**1.41**

NIST 610 Glass

Standard zircon	NIST 610	NIST 610	NIST 610	NIST 610	NIST 610	NIST 610	NIST 610	NIST610	NIST610	NIST610	NIST610
Element (ppm)								Average	2SD(%)	Jochum et al., 2011	Av. / Lit.
Al	10864.32	10725.28	10775.03	10802.27	10792.22	10881.78	10692.61	**10790.50**	**136.62**	**10320.19**	**1.05**
28 Si	328658.43	322383.93	330680.87	331905.26	326074.41	325933.91	326112.58	**327392.77**	**6499.73**	**325822.74**	**1.00**
29 Si	323518.56	331856.50	327667.46	324884.76	327858.85	329430.66	325406.75	**327231.93**	**5740.70**	**325822.74**	**1.00**
P	411.94	437.34	419.83	417.30	410.70	413.18	412.82	**417.59**	**18.56**	**413.00**	**1.01**
K	464.24	463.33	466.29	462.27	464.36	464.41	463.80	**464.10**	**2.45**	**464.00**	**1.00**
Ca	81738.65	82529.90	81857.32	82232.18	83085.91	81841.58	82051.53	**82191.01**	**957.40**	**81475.13**	**1.01**
Ti	451.63	453.00	451.66	450.64	453.75	450.60	452.80	**452.01**	**2.41**	**452.00**	**1.00**
V	448.78	454.26	447.01	447.77	450.45	454.21	447.68	**450.02**	**6.15**	**450.00**	**1.00**
Fe	459.47	453.67	461.36	456.85	452.64	465.66	446.06	**456.53**	**12.87**	**458.00**	**1.00**
Zn	459.90	460.41	459.48	460.83	459.83	460.01	459.99	**460.07**	**0.87**	**460.00**	**1.00**
Ga	432.13	437.59	428.65	430.61	436.15	432.04	434.43	**433.08**	**6.29**	**433.00**	**1.00**
Rb	423.36	428.15	426.71	423.20	427.33	425.64	424.41	**425.54**	**3.90**	**425.70**	**1.00**
Sr	515.09	513.94	520.65	513.65	520.26	513.19	514.32	**515.87**	**6.38**	**515.50**	**1.00**
Y	460.75	464.28	461.63	457.35	466.84	461.51	461.50	**461.98**	**5.91**	**462.00**	**1.00**
90 Zr	447.68	449.36	447.54	445.65	449.23	448.37	447.88	**447.96**	**2.50**	**448.00**	**1.00**
91 Zr	446.69	450.47	446.48	448.13	448.91	448.57	447.39	**448.09**	**2.78**	**448.00**	**1.00**
96 Zr	447.02	451.12	443.86	444.79	451.64	447.92	448.68	**447.86**	**5.87**	**448.00**	**1.00**
Nb	463.85	467.89	463.36	460.86	465.87	465.44	465.27	**464.65**	**4.44**	**465.00**	**1.00**
Ba	450.60	451.43	456.04	448.71	451.29	452.62	451.05	**451.68**	**4.51**	**452.00**	**1.00**
La	437.98	441.69	441.17	440.87	443.33	438.04	438.90	**440.28**	**4.05**	**440.00**	**1.00**
Ce	450.28	457.73	452.45	452.65	458.19	449.78	452.75	**453.40**	**6.65**	**453.00**	**1.00**
Pr	446.54	450.99	448.15	442.63	450.32	448.08	447.96	**447.81**	**5.48**	**448.00**	**1.00**
Nd	428.68	432.57	429.03	425.44	433.36	430.40	429.95	**429.92**	**5.26**	**430.00**	**1.00**
Sm	449.53	455.01	453.58	450.40	458.36	451.10	452.10	**452.87**	**6.12**	**453.00**	**1.00**
Eu	446.14	448.59	445.94	448.58	454.11	448.28	445.77	**448.20**	**5.80**	**447.00**	**1.00**
Gd	448.26	450.07	448.27	443.90	452.21	450.73	448.47	**448.85**	**5.27**	**449.00**	**1.00**
Tb	434.92	438.67	439.08	432.73	438.96	433.43	437.66	**436.49**	**5.47**	**437.00**	**1.00**
Dy	435.52	439.77	435.98	436.14	441.33	436.27	436.75	**437.39**	**4.47**	**437.00**	**1.00**
Ho	447.70	450.89	446.81	447.69	452.85	447.81	448.97	**448.96**	**4.32**	**449.00**	**1.00**
Er	451.19	457.67	455.34	452.75	461.96	454.46	453.91	**455.33**	**7.12**	**455.00**	**1.00**
Tm	433.31	437.35	434.65	429.79	438.55	432.97	435.12	**434.53**	**5.82**	**435.00**	**1.00**
Yb	448.38	451.90	449.17	450.01	457.86	449.30	449.23	**450.83**	**6.58**	**450.00**	**1.00**
Lu	438.61	438.62	440.41	440.27	444.04	440.75	437.56	**440.04**	**4.23**	**439.00**	**1.00**
Hf	433.31	437.18	433.61	434.44	441.60	436.05	434.16	**435.77**	**5.84**	**435.00**	**1.00**
Ta	443.35	449.97	445.21	440.73	450.10	446.87	445.25	**445.93**	**6.80**	**446.00**	**1.00**
Pb	423.69	430.02	424.72	422.72	427.11	423.86	426.14	**425.47**	**5.01**	**426.00**	**1.00**
Th	455.64	458.32	458.19	453.54	459.43	459.47	456.50	**457.30**	**4.37**	**457.20**	**1.00**
U	459.72	464.20	460.63	456.05	464.24	461.83	461.38	**461.15**	**5.64**	**461.50**	**1.00**

NIST 612 Glass

Standard zircon	NIST 612	NIST 612	NIST 612	NIST 612	NIST 612	NIST 612	NIST 612	NIST 612	NIST 612	NIST 612
Element (ppm)							Average	2SD(%)	Jochum et al., 2011	Av. / Lit.
Al	11826.93	11766.36	11717.26	11691.50	11591.91	11751.52	**11724.24**	**159.24**	**10746.00**	**1.09**
28 Si	361839.02	349236.73	350346.81	355089.93	353089.59	363732.01	**355555.68**	**11989.75**	**337041.88**	**1.05**
29 Si	357276.53	350804.11	353322.63	351187.20	344973.35	354434.07	**351999.65**	**8341.72**	**337041.88**	**1.04**
P			321.71				**321.71**		**46.60**	**6.90**
K	66.95	70.83	77.04	64.99	65.40	65.10	**68.38**	**9.56**	**62.30**	**1.10**
Ca	88798.98	87166.99	87313.81	86879.46	87536.87	87948.01	**87607.35**	**1371.39**	**85061.00**	**1.03**
Ti	42.04	42.62	43.16	40.98	40.90	43.42	**42.19**	**2.15**	**44.00**	**0.96**
V	41.07	40.26	40.31	40.28	39.82	40.56	**40.38**	**0.83**	**38.80**	**1.04**
Fe	59.20	43.89	68.32	84.48	61.58	47.48	**60.83**	**29.44**	**51.00**	**1.19**
Zn	41.56	41.63	44.29	41.40	39.78	42.13	**41.80**	**2.92**	**39.10**	**1.07**
Ga	38.44	38.20	38.14	38.16	38.40	39.30	**38.44**	**0.88**	**36.90**	**1.04**
Rb	33.86	33.41	33.05	32.63	32.58	33.62	**33.19**	**1.05**	**31.40**	**1.06**
Sr	82.42	81.39	81.81	80.56	80.84	82.40	**81.57**	**1.57**	**78.40**	**1.04**
Y	40.96	39.76	39.94	39.52	39.91	40.02	**40.02**	**0.98**	**38.30**	**1.04**
90 Zr	40.54	39.46	39.77	39.68	40.05	39.87	**39.90**	**0.74**	**37.90**	**1.05**
91 Zr	40.87	40.35	41.10	40.26	39.91	41.44	**40.66**	**1.15**	**37.90**	**1.07**
96 Zr	41.21	40.80	40.03	41.37	40.53	40.55	**40.75**	**0.98**	**37.90**	**1.08**
Nb	40.31	40.01	39.56	39.92	39.19	40.42	**39.90**	**0.92**	**38.90**	**1.03**
Ba	42.07	41.05	41.36	40.42	40.73	41.53	**41.19**	**1.18**	**39.30**	**1.05**
La	37.55	37.13	37.60	37.39	37.36	38.10	**37.52**	**0.66**	**36.00**	**1.04**
Ce	40.32	39.98	39.46	39.37	39.44	40.03	**39.77**	**0.79**	**38.40**	**1.04**
Pr	39.60	39.27	39.14	38.31	38.64	39.19	**39.03**	**0.94**	**37.90**	**1.03**
Nd	37.51	37.03	37.13	37.16	37.24	37.17	**37.21**	**0.33**	**35.50**	**1.05**
Sm	40.61	39.71	40.12	39.10	39.75	39.66	**39.82**	**1.01**	**37.70**	**1.06**
Eu	37.51	37.23	36.80	36.82	37.18	37.19	**37.12**	**0.54**	**35.60**	**1.04**
Gd	40.63	39.76	38.95	40.18	40.16	40.12	**39.97**	**1.14**	**37.30**	**1.07**
Tb	38.90	38.79	38.59	38.22	38.10	38.65	**38.54**	**0.63**	**37.60**	**1.03**
Dy	38.23	37.74	37.90	37.09	37.63	38.13	**37.79**	**0.82**	**35.50**	**1.06**
Ho	39.90	39.41	39.40	39.43	39.64	39.76	**39.59**	**0.42**	**38.30**	**1.03**
Er	41.06	40.38	40.46	40.11	39.73	40.32	**40.34**	**0.88**	**38.00**	**1.06**
Tm	38.49	38.33	38.15	37.87	38.14	38.73	**38.29**	**0.60**	**36.80**	**1.04**
Yb	40.93	40.39	40.17	39.87	40.74	41.37	**40.58**	**1.09**	**39.20**	**1.04**
Lu	38.58	38.07	38.10	37.78	38.23	38.73	**38.25**	**0.71**	**37.00**	**1.03**
Hf	39.56	39.60	38.93	38.66	38.86	39.02	**39.11**	**0.77**	**36.70**	**1.07**
Ta	38.66	38.79	38.40	38.07	38.34	38.84	**38.52**	**0.60**	**37.60**	**1.02**
Pb	41.32	40.79	40.56	40.31	40.86	40.98	**40.80**	**0.69**	**38.60**	**1.06**
Th	39.43	39.70	38.98	38.83	39.24	39.38	**39.26**	**0.63**	**37.80**	**1.04**
U	39.34	38.75	38.47	38.45	38.56	38.81	**38.73**	**0.66**	**37.40**	**1.04**


Durango apatite
Kovdor apatite
Sumé1 apatite
Apatite / Chondrite
10000
100
1
La Ce Pr Nd Sm Eu Gd Tb Dy Ho Er Tm Yb Lu
Pristine composition
Average pristine composition
Chew et al., (2016)
Arzamastsev et al., (2009)
Lana et al., (2022)

Trace element analyses of titanite grains from the studied Caatinga-Lamim rocks.

Spot num. analysis	Optical features	Inclusions	Texture BSE	Domain BSE	Chemistry	Nature	Al ppm	K ppm	Ca ppm	Ti ppm	V ppm	Fe ppm	Zn ppm	Ga ppm	Rb ppm	Sr ppm	Y ppm	Zr ppm
CM44B																		
Ttn#1	*Prismatic, incolor, associated with biotie and apatite*	*none*	*Homogeneous*	*Light*	*Metamorphic*	*Metamorphic*	14771	603.29	208912	215010	440	3605	10	7	11	37	77	57
Ttn#2	*Prismatic, incolor, associated with biotie and apatite*	*none*	*Homogeneous*	*Light*	*Metamorphic*	*Metamorphic*	13641	1.09	206088	217218	439	3391	5	21	0.1	44	1034	111
Ttn#3	*Prismatic, incolor, associated with biotie and apatite*	*none*	*Homogeneous*	*Light*	*Metamorphic*	*Metamorphic*	15239	14.84	206665	210984	464	3504	7	12	0.1	41	267	79
Ttn#4	*Prismatic, incolor, associated with biotie and apatite*	*none*	*Homogeneous*	*Light*	*Metamorphic*	*Metamorphic*	16175	19.02	206175	209394	495	3505	8	9	0.04	38	96	57
Ttn#5.1	*Prismatic, incolor, associated with biotie and apatite*	*none*	*Homogeneous*	*Light*	*Metamorphic*	*Metamorphic*	59324	35030.14	203575	206203	616	61892	251	31	615	33	49	23
Ttn#5	*Prismatic, incolor, associated with biotie and apatite*	*none*	*Homogeneous*	*Light*	*Igneous*	*Metamorphic*	21540	54.48	207090	213247	393	3200	7	26	0.2	139	1709	134
Ttn#7	*Prismatic, brownish, associated with biotie*	*none*	*Oscilatory zoning*	*Dark*	*Igneous*	*Igneous*	11757	12.15	207536	221680	400	3226	6	26	0.2	48	1879	127
Ttn#10	*Prismatic, incolr, associated with biotie*	*biotite*	*Sector zoned*	*Dark*	*Metamorphic*	*Igneous*	17714	2394.14	209010	220154	471	7602	29	12	41	39	247	53
Ttn#11	*Rounded, brownish, isolated*	*none*	*Sector zoned*	*Dark*	*Igneous*	*Igneous*	9714	127.72	205742	225998	534	4724	6	29	3	58	2701	172
Ttn#14	*Rounded, brownish, isolated*	*none*	*Sector zoned*	*Dark*	*Igneous*	*Igneous*	7822	12.46	210234	230878	735	8263	7	37	0.1	67	1164	246
Ttn#16	*Prismatic, brownish, associated with biotie and oxide*	*oxide*	*Homogeneous*	*Dark*	*Igneous*	*Igneous*	14757	11.87	207607	219131	440	3639	8	25	0.1	49	1797	152
Ttn#17	*Prismatic, brownish, associated with biotie and oxide*	*none*	*Homogeneous*	*Dark*	*Igneous*	*Igneous*	14207	129.43	207729	227142	401	3425	8	28	2	76	1863	126
Ttn#18	*Prismatic, brownish, associated with biotie and oxide*	*none*	*Homogeneous*	*Dark*	*Igneous*	*Igneous*	14012	28.63	207082	224498	398	3485	6	37	0.3	76	4042	157
Ttn#21	*Prismatic, incolor, associated with biotie*	*biotite*	*Homogeneous*	*Light*	*Metamorphic*	*Metamorphic*	24889	87.82	208980	216320	446	3303	5	20	0.4	164	726	93
Ttn#22	*Prismatic, incolor, associated with biotie*	*none*	*Homogeneous*	*Light*	*Metamorphic*	*Metamorphic*	17983	26.81	206882	211923	459	2723	6	5	0.1	31	73	20
Ttn#23	*Prismatic, incolor, associated with biotie and apatite*	*none*	*Homogeneous*	*Light*	*Metamorphic*	*Metamorphic*	36284	15201.20	208994	211884	530	29785	99	18	265	93	77	33
Ttn#24	*Prismatic, incolor, associated with biotie and apatite*	*none*	*Homogeneous*	*Light*	*Metamorphic*	*Metamorphic*	14651	8.55	206921	215584	443	2710	5	6	0.01	34	70	36
Ttn#25	*Prismatic, incolor, associated with biotie*	*none*	*Homogeneous*	*Light*	*Metamorphic*	*Metamorphic*	18033	1481.37	208280	213306	402	5533	12	8	23	35	150	23
Ttn#26	*Prismatic, incolor, associated with biotie*	*none*	*Homogeneous*	*Light*	*Metamorphic*	*Metamorphic*	16968	99.64	206864	214178	423	3918	7	6	2	33	62	22
Ttn#27	*Prismatic, incolor, associated with biotie*	*none*	*Homogeneous*	*Light*	*Metamorphic*	*Metamorphic*	21746	4937.87	207609	212661	412	12017	33	11	87	32	157	20
Ttn#28	*Prismatic, incolor, associated with biotie*	*biotite*	*Homogeneous*	*Light*	*Metamorphic*	*Metamorphic*	28495	9737.75	208307	219428	479	19633	63	14	158	40	65	42
Ttn#29	*Prismatic, incolor, associated with biotie*	*none*	*Homogeneous*	*Light*	*Metamorphic*	*Metamorphic*	29565	10716.75	208394	220654	473	20639	74	14	185	34	115	21
Ttn#31	*Prismatic, brownish, associated with biotite*	*none*	*Homogeneous*	*Light*	*Igneous*	*Igneous*	12918	14.48	208880	226603	431	3623	5	36	0.3	53	4476	161
Ttn#35	*Rounded, brownish, associated oxide*	*none*	*Sector zoned*	*Light*	*Igneous*	*Igneous*	9008	123.00	206092	235990	662	8103	6	81	2	73	3632	301
Ttn#36	*Rounded, brownish, associated oxide*	*none*	*Sector zoned*	*Light*	*Igneous*	*Igneous*	9664	16.64	206446	232700	793	11999	6	150	1	86	7107	417
Ttn#37	*Rounded, brownish, associated oxide*	*none*	*Sector zoned*	*Light*	*Igneous*	*Igneous*	10299	121.97	205939	231084	696	8716	5	113	3	71	6159	345
Ttn#38	*Rounded, brownish, associated oxide*	*none*	*Sector zoned*	*Dark*	*Igneous*	*Igneous*	10142	13.08	208542	231658	577	6185	6	59	0.3	61	3839	223
Ttn#39	*Rounded, brownish, associated oxide*	*none*	*Sector zoned*	*Light*	*Igneous*	*Igneous*	10072	10.96	208535	230271	787	10471	6	146	1	80	6807	424
Ttn#42	*Prismatic, incolor, associated with biotie and apatite*	*none*	*Homogeneous*	*Light*	*Recryst.?*	*Recryst.?*	15902	12.07	208134	216007	503	3337	6	9	0.0	37	166	52
Ttn#43	*Prismatic, incolor, associated with biotie and apatite*	*none*	*Homogeneous*	*Light*	*Metamorphic*	*Metamorphic*	16059	15.53	204363	214683	486	3088	6	8	0.0	44	106	43
Ttn#44	*Prismatic, incolor, associated with biotie*	*quartz*	*Homogeneous*	*Light*	*Igneous*	*Metamorphic*	24159	59.73	208602	217691	448	3507	6	29	0.2	161	2429	121
Ttn#45	*Rounded, brownish, associated with biotite*	*none*	*Sector zoned*	*Light*	*Igneous*	*Igneous*	13709	12.00	208349	220314	452	3312	5	24	0.2	46	2334	113
Ttn#46	*Rounded, brownish, associated with biotite*	*none*	*Sector zoned*	*Light*	*Igneous*	*Igneous*	10927	20.77	208462	223886	784	6976	6	37	0.3	58	3074	238
Ttn#52	*Rounded, brownish, associated with biotite*	*none*	*Sector zoned*	*Light*	*Igneous*	*Igneous*	10497	26.50	210060	225138	789	7868	4	41	0.5	60	3251	237
Ttn#49	*Incolor, associated with biotie and apatite*	*biotite*	*Homogeneous*	*Light*	*Metamorphic*	*Metamorphic*	16156	220.19	205942	213116	470	3544	5	8	4	36	236	39
Ttn#50	*Incolor, associated with biotie and apatite*	*none*	*Homogeneous*	*Light*	*Metamorphic*	*Metamorphic*	75605	48221.43	212378	219869	774	89407	359	44	811	37	239	49
Ttn#48	*Incolor, associated with biotie and apatite*	*biotite*	*Homogeneous*	*Light*	*Metamorphic*	*Metamorphic*	15747	14.20	208719	218797	451	3114	4	8	0.1	35	562	25
Ttn#51	*Incolor, associated with biotie and apatite*	*biotite*	*Homogeneous*	*Light*	*Metamorphic*	*Metamorphic*	39285	19244.92	206938	217966	566	35909	138	22	323	33	310	24
CM49																		
Ttn#3	*Prismatic, incolor, associated with biotite*	*none*	*Patchy zoned*	*Dark*		*Metamorphic*	7480	4	209241	232661	576	5836	11	66	0.33	65	1582	170
Ttn#6	*Prismatic, incolor, associated with biotite*	*none*	*Patchy zoned*	*Light*		*Metamorphic*	7875	4	204136	226029	618	5295	11	31	0.18	58	896	136
Ttn#8	*Prismatic, incolor, associated with biotite*	*biotite*	*Patchy zoned*	*Dark*		*Igneous*	8040	5	202256	224189	574	4842	12	45	0.28	61	1250	130
Ttn#10	*Prismatic, incolor, associated with biotite*	*none*	*Patchy zoned*	*Light*		*Inherited?*	10834	65	207932	230363	472	5973	12	20	1.59	63	498	82
Ttn#12	*Prismatic, incolor, associated with biotite and amphibole*	*none*	*Patchy zoned*	*Light*		*Metamorphic*	8535	9	209143	236582	438	4243	10	24	0.14	52	729	93
Ttn#15	*Prismatic, incolor, associated with biotite*	*none*	*Core/Rim*	*Light*		*Metamorphic*	8018	7	207963	231682	765	5859	11	14	0.17	57	733	171
Ttn#17	*Prismatic, incolor, associated with biotite*	*none*	*Patchy zoned*	*Dark*		*Metamorphic*	8492	95	210981	250845	624	10169	17	71	1.87	74	1729	208
Ttn#19	*Prismatic, incolor, associated with biotite and amphibole*	*biotite*	*Patchy zoned*	*Light*		*Metamorphic*	11067	1	208609	229070	770	6546	9	7	0.11	54	296	103
Ttn#22	*Prismatic, incolor, associated with biotite and amphibole*	*none*	*Patchy zoned*	*Light*		*Metamorphic*	10690	73	210333	234442	566	6564	11	8	1.37	58	410	574
Ttn#24	*Prismatic, incolor, associated with biotite and amphibole*	*none*	*Patchy zoned*	*Light/Dark*		*Metamorphic*	9210	3	206121	231708	626	5144	8	35	0.28	61	1305	117
Ttn#27	*Prismatic, incolor, associated with amphibole*	*none*	*Patchy zoned*	*Dark*		*Igneous*	9349	8	208632	234726	619	5556	7	30	0.24	68	1116	318
Ttn#28	*Prismatic, incolor, associated with amphibole*	*none*	*Patchy zoned*	*Light/Dark*		*Metamorphic*	8706	10	208161	233859	529	4066	7	22	0.28	56	1398	124
Ttn#31	Prismatic, incolor, associated with biotite and amphibole	none	Patchy zoned	Dark		Igneous	8167	11	203216	230043	560	6622	6	39	0.30	57	1348	124
Ttn#32	*Prismatic, incolor, associated with biotite and amphibole*	*none*	*Patchy zoned*	*Dark*		*Igneous*	*9337*	*12*	*204910*	*227358*	*411*	*4451*	*7*	*25*	*0.32*	*49*	*1064*	*81*
Ttn#33	Prismatic, incolor, associated with biotite and amphibole	none	Core/Rim	Dark		Igneous	9486	28	208413	229276	619	7222	9	22	0.66	59	1235	123
Ttn#34	Prismatic, brownish, associated with biotite	none	Core/Rim	Dark		Igneous	8115	7	202390	226762	606	5445	6	34	0.27	58	1331	132
Ttn#36	Prismatic, brownish, associated with amphibole	none	Patchy zoned	Dark		Igneous	7478	348	203680	230946	558	5724	7	29	1.23	57	1012	109

Nb ppm	Ba ppm	La ppm	Ce ppm	Pr ppm	Nd ppm	Sm ppm	Eu ppm	Gd ppm	Tb ppm	Dy ppm	Ho ppm	Er ppm	Tm ppm	Yb ppm	Lu ppm	Hf ppm	Ta ppm	Pb ppm	Th ppm	U ppm	Th/U	Sr+U	REE	Eu/Eu*	Nb/Ta	Y/Sr	Sr/Y	LREE
659	20	34	166	31	146	30	43	21	2	13	2	7	1	5	1	2	7	33	38	80	0.48	118	501	3.4	99.6	2.06	0.4851	376.8
997	0.3	156	797	159	886	266	85	244	33	178	32	86	11	72	11	10	53	124	34	94	0.36	138	3016	0.7	18.7	23.41	0.0427	1998.5
756	1	91	414	73	347	79	67	64	8	42	8	21	3	19	3	6	28	73	22	57	0.38	98	1237	1.9	27.3	6.54	0.1529	924.1
715	1	51	240	42	189	39	50	27	3	15	3	7	1	6	1	4	12	44	10	34	0.30	71	675	3.0	58.6	2.55	0.3926	522.6
370	1378	9	51	11	56	15	30	13	2	8	2	4	1	3	1	2	5	16	2	13	0.13	46	205	4.4	76.1	1.50	0.6651	127.0
1576	12	221	983	191	1013	338	89	365	52	297	53	145	19	122	17	12	174	171	53	124	0.43	263	3905	0.5	9.1	12.32	0.0812	2407.3
1471	0	198	1005	212	1210	428	97	456	64	364	64	172	22	130	18	11	137	150	43	112	0.38	160	4440	0.5	10.8	39.16	0.0255	2624.5
691	71	60	283	52	257	69	65	64	8	46	8	21	3	17	3	4	11	58	13	44	0.30	82	956	2.0	61.6	6.42	0.1558	652.1
1197	2	197	1057	240	1470	612	113	661	101	591	101	265	36	221	27	16	182	372	48	269	0.18	327	5694	0.4	6.6	46.87	0.0213	2965.1
2314	1	710	2210	324	1475	365	152	310	40	215	37	98	13	86	12	14	134	432	225	308	0.73	375	6047	0.9	17.3	17.26	0.0579	4719.1
1149	1	213	983	189	1027	342	86	368	53	302	57	155	21	134	19	13	204	191	53	138	0.38	187	3951	0.5	5.6	36.71	0.0272	2413.4
1373	5	196	1030	226	1321	473	90	480	68	377	66	167	22	128	17	12	137	167	41	121	0.34	196	4663	0.4	10.0	24.63	0.0406	2774.1
1593	3	276	1403	309	1849	780	93	889	138	814	147	377	49	298	37	14	191	201	65	144	0.45	220	7457	0.2	8.3	53.27	0.0188	3836.4
1120	14	128	650	130	679	196	81	181	23	124	22	60	8	50	7	8	80	101	36	83	0.44	247	2339	0.9	14.0	4.41	0.2267	1587.0
701	1	7	43	9	55	18	33	18	2	12	2	6	1	5	1	2	12	13	1	10	0.10	42	212	3.9	57.3	2.33	0.4298	113.9
562	541	18	101	21	109	29	40	23	3	14	2	6	1	5	1	2	12	26	3	21	0.14	113	372	3.1	46.2	0.83	1.2095	249.1
594	0.1	24	128	25	123	29	44	22	2	12	2	5	1	4	1	2	6	30	4	23	0.17	58	422	3.5	102.1	2.02	0.4953	300.6
563	61	14	84	19	112	39	61	38	5	27	5	12	2	10	2	2	27	35	2	29	0.08	64	430	3.3	20.8	4.28	0.2335	229.5
357	8	10	54	11	56	15	37	14	2	10	2	5	1	5	1	2	8	22	2	20	0.08	53	220	5.2	46.0	1.85	0.5401	129.8
488	128	13	77	18	104	36	61	37	5	27	5	14	2	11	2	2	24	34	2	28	0.06	61	411	3.5	20.7	4.88	0.2049	211.6
672	315	29	143	26	121	25	41	18	2	11	2	5	1	4	1	2	11	32	10	54	0.18	95	427	3.9	63.0	1.61	0.6223	318.2
561	357	13	70	16	89	30	47	29	4	20	4	10	1	8	1	2	14	26	2	22	0.09	57	340	3.3	39.3	3.35	0.2987	187.0
1425	1	263	1343	293	1764	788	93	916	149	897	159	431	57	347	43	14	224	180	60	142	0.42	195	7543	0.2	6.4	84.45	0.0118	3662.7
2275	3	930	3978	758	3958	1170	232	1009	139	763	128	331	45	284	35	24	212	597	289	411	0.70	484	13760	0.4	10.7	50.08	0.0200	9624.2
3159	1	1423	6640	1396	7932	2601	382	2241	306	1665	270	664	81	460	49	33	604	1140	555	776	0.72	862	26109	0.3	5.2	82.75	0.0121	17391.0
2641	2	1053	4852	1009	5710	1956	282	1821	256	1419	235	580	74	422	48	28	497	746	367	533	0.69	604	19717	0.3	5.3	86.36	0.0116	12624.6
1689	1	448	2330	514	3162	1201	144	1171	165	908	149	363	45	255	29	21	378	449	125	317	0.39	379	10882	0.3	4.5	62.49	0.0160	6453.4
3139	1	1429	6477	1359	7607	2426	380	2130	288	1535	255	633	81	457	50	33	495	1114	583	774	0.75	854	25107	0.3	6.3	84.94	0.0118	16872.1
1032	1	45	219	40	201	52	95	44	5	29	5	13	2	11	2	4	24	53	9	40	0.23	77	764	4.1	43.8	4.51	0.2219	505.1
1096	1	27	141	28	141	38	87	32	4	21	3	9	1	7	1	3	39	39	5	30	0.17	74	540	5.1	27.8	2.38	0.4201	336.6
1396	9	210	988	210	1234	488	96	545	79	460	83	213	29	176	24	12	126	145	66	105	0.63	266	4835	0.4	11.1	15.13	0.0661	2642.2
1420	1	178	879	186	1049	412	101	475	75	447	79	213	29	178	23	10	87	134	46	102	0.45	148	4321	0.5	16.4	50.52	0.0198	2290.6
1366	1	533	1898	305	1482	456	171	482	79	518	100	306	50	362	48	15	144	371	188	271	0.69	329	6791	0.8	9.5	53.14	0.0188	4217.9
1454	1	533	1995	341	1719	536	184	544	89	565	107	322	52	364	47	16	178	389	188	280	0.67	340	7396	0.7	8.2	53.76	0.0186	4587.4
736	6	27	133	26	142	47	133	48	7	39	7	19	3	17	3	2	32	23	7	18	0.35	55	651	5.9	22.7	6.53	0.1531	328.1
610	1574	32	145	27	142	49	127	51	7	41	7	20	3	18	3	3	26	21	12	21	0.54	59	669	5.4	23.5	6.40	0.1562	345.6
845	1	22	133	33	211	102	188	126	19	110	19	50	6	37	5	2	82	32	3	25	0.10	60	1061	3.6	10.3	16.12	0.0620	398.5
678	579	17	90	21	126	54	169	64	10	54	10	26	3	22	3	2	48	24	5	21	0.22	54	670	6.2	14.2	9.31	0.1074	254.0
734	0.08	336	1982	453	2569	670	207	486	62	325	58	152	20	128	16	15	40	87	25	64	0.39	129	7464	0.72	18	24.5	0.04	5340
484	0.05	135	857	205	1167	336	100	254	33	182	32	86	12	75	10	10	28	46	9	31	0.30	89	3484	0.69	17	15.4	0.07	2364
519	0.05	213	1298	294	1687	461	149	338	45	247	45	122	17	115	15	11	27	61	15	45	0.34	106	5044	0.75	19	20.6	0.05	3492
278	15.05	102	548	115	643	162	93	121	16	91	17	48	7	51	7	7	6	14	16	10	1.62	73	2021	1.33	44	7.9	0.13	1409
361	0.02	106	641	152	896	260	109	204	26	146	26	71	10	63	9	9	10	17	5	12	0.40	64	2720	0.96	36	14.1	0.07	1796
359	0.00	52	335	82	485	158	105	138	20	120	24	72	11	78	11	10	5	24	1	16	0.08	74	1691	1.47	66	12.8	0.08	954
942	58.56	341	2093	476	2738	763	203	563	71	380	65	166	22	131	16	15	78	91	35	75	0.47	149	8027	0.62	12	23.3	0.04	5648
156	0.01	19	115	27	162	55	26	51	8	48	10	31	5	36	6	6	8	9	0	6	0.09	59	596	1.04	21	5.5	0.18	322
315	6.08	19	127	35	236	89	34	81	11	66	13	41	6	48	8	25	12	9	27	6	4.51	64	815	0.84	27	7.1	0.14	417
541	0.17	139	914	228	1344	409	133	308	43	246	45	126	19	130	17	9	22	47	4	34	0.11	96	4102	0.75	24	21.3	0.05	2626
1197	0.14	126	782	186	1120	353	116	295	39	219	40	108	15	103	14	24	55	62	5	44	0.10	112	3517	0.74	22	16.4	0.06	2213
503	1.07	59	438	130	911	371	142	341	48	278	51	140	20	124	16	13	27	24	1	19	0.05	75	3068	0.83	19	25.1	0.04	1539
535	0.05	128	949	253	1570	477	168	380	49	273	49	132	18	119	15	11	12	20	2	14	0.15	71	4581	0.80	43	23.6	0.04	2900
397	*3.37*	*60*	*491*	*151*	*1024*	*348*	*129*	*288*	*38*	*213*	*38*	*104*	*14*	*94*	*12*	*9*	*9*	*14*	2	10	0.18	59	3004	0.84	46	21.8	0.05	1725
375	8.46	55	434	124	830	330	136	302	43	246	45	124	17	112	15	10	21	23	3	15	0.17	74	2814	0.90	18	21.0	0.05	1444
512	1.65	119	806	209	1310	446	138	361	49	275	48	129	18	111	14	11	39	44	2	31	0.08	89	4032	0.70	13	22.8	0.04	2444
581	17.92	132	771	183	1082	322	143	263	34	195	35	100	14	95	13	10	13	14	4	10	0.43	67	3384	1.01	45	17.8	0.06	2169

Trace element analyses of glass and titanite reference materials.

Glass / titanite reference material	Spot num. analysis	Al ppm	K ppm	Ca ppm	Ti ppm	V ppm	Fe ppm	Zn ppm	Ga ppm	Rb ppm	Sr ppm	Y ppm	Nb ppm	Ba ppm	La ppm	Ce ppm	Pr ppm	Nd ppm	Sm ppm	Eu ppm	Gd ppm	Tb ppm	Dy ppm	Ho ppm	Er ppm	Tm ppm	Yb ppm	Lu ppm	Hf ppm	Ta ppm	Pb ppm	Th ppm	U ppm	Th/U
Sequence 1																																	
NIST610	*1*	10812	462	82140	452	450	454	460	433	425	516	461	466	450	439	450	448	430	450	446	448	434	435	447	451	435	448	437	434	443	426	456	461	1.0
	2	10738	462	81506	453	449	460	461	434	427	515	461	463	456	442	454	447	432	454	448	452	440	439	449	458	436	452	440	435	448	427	461	463	1.0
	3	10723	464	82502	451	447	457	457	429	424	515	462	464	451	438	451	449	426	453	447	446	434	438	453	453	433	448	440	438	444	424	454	457	1.0
	4	10842	470	82696	453	456	460	462	437	428	517	466	468	452	439	454	450	432	457	449	450	439	437	449	457	436	453	440	437	452	427	459	463	1.0
	5	10809	455	81548	450	448	463	458	430	423	514	460	463	455	442	455	448	427	452	447	451	438	438	453	457	433	447	441	434	442	426	457	460	1.0
	6	10880	469	82502	453	451	461	460	433	427	516	463	465	452	438	450	447	430	450	443	446	435	434	445	454	436	449	436	433	447	426	455	463	1.0
	7	10706	455	81534	452	445	455	459	431	424	517	461	464	448	439	451	446	431	453	446	447	432	432	446	449	431	446	435	431	448	422	455	459	1.0
	8	10788	466	82498	452	451	455	460	435	426	514	461	466	453	440	456	450	429	453	449	450	440	440	452	456	436	453	442	438	446	429	460	462	1.0
	Average	**10787**	**463**	**82116**	**452**	**450**		**460**	**433**	**426**	**516**	**462**	**465**	**452**	**440**	**453**	**448**	**430**	**453**	**447**	**449**	**437**	**437**	**449**	**454**	**434**	**450**	**439**	**435**	**446**	**426**	**457**	**461**	**1.0**
	Jochum et al., 2011	**10320**	**464**	**81475**	**452**	**450**		**460**	**433**	**426**	**516**	**462**	**465**	**452**	**440**	**453**	**448**	**430**	**453**	**447**	**449**	**437**	**437**	**449**	**455**	**435**	**450**	**439**	**435**	**446**	**426**	**457**	**462**	**1.0**
	Av. / Lit.	**1.05**	**1.00**	**1.01**	**1.00**	**1.00**		**1.00**	**1.00**	**1.00**	**1.00**	**1.00**	**1.00**	**1.00**	**1.00**	**1.00**	**1.00**	**1.00**	**1.00**	**1.00**	**1.00**	**1.00**	**1.00**	**1.00**	**1.00**	**1.00**	**1.00**	**1.00**	**1.00**	**1.00**	**1.00**	**1.00**	**1.00**	**1.00**
NIST612	*1*	11411	67	87711	40	40	60	41	37	32	81	40	40	41	37	40	39	37	40	37	40	39	37	40	41	39	41	39	39	39	41	40	39	1.0
	2	11427	64	86509	37	40	70	39	37	33	82	40	40	41	37	40	40	37	39	36	41	39	38	40	41	39	40	38	39	40	40	40	40	1.0
	3	11180	71	86466	42	40	58	40	38	32	81	40	40	41	37	39	39	37	39	36	41	39	38	40	40	39	40	39	38	39	41	39	39	1.0
	4	11418	66	85940	38	40	57	40	38	32	81	40	40	41	37	40	40	37	39	38	40	39	38	40	41	39	39	38	39	39	40	39	39	1.0
	5	11415	63	86401	41	39	60	39	37	33	82	40	40	42	37	39	40	37	39	37	40	39	38	40	40	39	40	38	39	39	40	39	39	1.0
	6	11638	73	85993	35	40	52	37	38	33	80	40	40	41	37	39	39	37	39	37	39	39	37	39	40	38	39	38	38	39	41	40	39	1.0
	7	11669	69	87049	37	40	41	41	38	33	82	40	40	42	38	40	39	37	40	37	40	39	39	41	41	39	40	39	39	39	42	40	39	1.0
	Average	**11451**	**68**	**86581**	**39**	**40**	**57**	**40**	**38**	**33**	**81**	**40**	**40**	**41**	**37**	**40**	**40**	**37**	**39**	**37**	**40**	**39**	**38**	**40**	**40**	**39**	**40**	**39**	**39**	**39**	**41**	**40**	**39**	**1.0**
	Jochum et al., 2011	**10746**	**62**	**85061**	**44**	**39**		**39**	**37**	**31**	**78**	**38**	**39**	**39**	**36**	**38**	**38**	**36**	**38**	**36**	**37**	**38**	**36**	**38**	**38**	**37**	**39**	**37**	**37**	**38**	**39**	**38**	**37**	**1.0**
	Av. / Lit	**1.07**	**1.08**	**1.02**	**0.88**	**1.03**		**1.01**	**1.02**	**1.04**	**1.04**	**1.05**	**1.03**	**1.05**	**1.04**	**1.03**	**1.04**	**1.05**	**1.05**	**1.04**	**1.07**	**1.03**	**1.07**	**1.04**	**1.06**	**1.06**	**1.02**	**1.04**	**1.06**	**1.04**	**1.05**	**1.05**	**1.05**	**1.00**
Titanite reference materials																																	
BLR1	*1*	18865	16	207497	202083	171	20143	4	39	0	64	3418	3963	0	337	1593	300	1472	497	80	562	115	829	173	504	66	338	29	59	220	176	151	272	0.6
	2	19096	5	206415	209212	173	20274	5	39	0	65	3466	4007	0	337	1618	303	1496	496	80	576	115	820	171	501	66	336	30	59	225	172	154	281	0.5
	3	19734	9	210167	201737	183	20074	5	42	0	72	3786	3852	0	402	1799	331	1642	533	83	631	125	910	188	554	74	387	33	57	190	224	192	327	0.6
	4	19555	21	207136	204587	183	20203	15	42	1	71	3813	3883	1	392	1828	330	1632	537	83	610	125	903	190	561	74	379	33	57	189	226	193	328	0.6
	Average	**19312**	**13**	**207804**	**204405**	**178**	**20173**	**7**	**40**	**0**	**68**	**3621**	**3926**	**0**	**367**	**1710**	**316**	**1560**	**516**	**82**	**595**	**120**	**866**	**181**	**530**	**70**	**360**	**31**	**58**	**206**	**199**	**173**	**302**	**0.6**
	Ma et al. 2019	**16567**		**195542**	**197895**					**1**	**54**	**3652**	**3797**	**<2,96**	**403**	**1799**	**321**	**1646**	**527**	**86**	**473**	**125**	**873**	**186**	**516**	**70**	**379**	**31**	**57**	**174**	**67**	**219**	**334**	**0.7**
	Av./Lit	**1.17**		**1.06**	**1.03**					**0.38**	**1.25**	**0.99**	**1.03**		**0.91**	**0.95**	**0.98**	**0.95**	**0.98**	**0.95**	**1.26**	**0.96**	**0.99**	**0.97**	**1.03**	**1.01**	**0.95**	**1.01**	**1.01**	**1.18**	**3.00**	**0.79**	**0.90**	**0.87**
CKHB	*1*	8602	14	205310	224281	724	10392	6	45	0	45	808	415	0	758	2719	408	1720	325	75	238	29	155	28	77	10	68	10	25	19	8	282	129	2.2
	2	8562	13	210009	222880	734	10230	6	45	0	45	822	444	0	772	2779	414	1765	330	78	238	30	158	29	77	11	70	11	24	20	8	293	135	2.2
	3	8294	10	204812	229076	719	10454	7	44	0	45	829	474	0	773	2780	416	1776	337	77	244	30	161	29	78	11	69	11	25	21	9	295	133	2.2
	Average	**8486**	**12**	**206711**	**225412**	**725**	**10359**	**6**	**45**	**0**	**45**	**820**	**444**	**0**	**768**	**2759**	**413**	**1754**	**331**	**77**	**240**	**30**	**158**	**29**	**77**	**11**	**69**	**10**	**25**	**20**	**8**	**290**	**133**	**2.2**
	2SE	**193**	**3**	**3311**	**3752**	**9**	**133**	**1**	**1**	**0**	**0**	**12**	**34**	**0**	**10**	**41**	**5**	**34**	**7**	**2**	**4**	**1**	**3**	**1**	**1**	**0**	**2**	**0**	**0**	**1**	**0**	**8**	**4**	**0.03**
MKED1	*1*	7893	8	206310	224318	377	11187	6	43	0	19	1089	1034	0	574	2494	414	1796	389	70	309	45	257	44	116	14	74	7	16	77	135	426	142	3.0
	2	7656	15	207607	223092	365	11469	5	59	0	20	1360	1562	1	867	3596	578	2439	515	91	395	56	319	57	144	17	94	9	28	152	211	729	217	3.4
	3	8014	13	208086	228394	378	11472	6	45	0	19	1135	1111	0	611	2626	434	1869	401	72	317	46	266	46	118	15	76	7	18	85	149	465	152	3.1
	4	7765	8	208479	226856	371	11761	4	61	0	20	1377	1585	0	875	3614	588	2461	519	91	391	57	326	56	142	18	93	9	28	154	211	753	214	3.5
	5	7878	9	205134	226953	371	11366	5	44	0	18	1071	1031	0	553	2433	401	1790	386	70	305	44	255	45	111	14	75	7	16	74	138	404	141	2.9
	6	8090	13	210494	226136	375	11478	4	45	0	18	1096	965	0	564	2449	407	1804	393	72	310	44	261	45	113	14	75	7	15	66	134	381	134	2.8
	7	8400	9	209125	230940	390	11381	6	60	0	19	1507	1381	0	801	3466	567	2471	532	95	413	60	354	62	155	19	104	10	23	125	229	768	236	3.3
	Average	**7957**	**11**	**207891**	**226670**	**375**	**11445**	**5**	**51**	**0**	**19**	**1234**	**1238**	**0**	**692**	**2954**	**484**	**2090**	**448**	**80**	**348**	**50**	**291**	**51**	**129**	**16**	**84**	**8**	**21**	**105**	**172**	**561**	**177**	**3.2**
	Ma et al. 2019	**7146**		**195971**	**216360**					**<0,56**	**8**	**947**	**747**	**<1,51**	**509**	**2067**	**339**	**1559**	**336**	**64**	**211**	**40**	**218**	**39**	**93**	**12**	**68**	**6**	**12**	**42**	**49**	**321**	**106**	**3.0**
	Av./Lit	**1.11**		**1.06**	**1.05**						**2.37**	**1.30**	**1.66**		**1.36**	**1.43**	**1.43**	**1.34**	**1.33**	**1.26**	**1.65**	**1.27**	**1.34**	**1.29**	**1.38**	**1.33**	**1.25**	**1.34**	**1.67**	**2.49**	**3.54**	**1.75**	**1.67**	**1.05**
Sequence 2																																	
NIST610		10980	475	83345	460	457	442	462	443	432	525	470	471	459	444	459	453	436	460	453	454	444	441	456	460	440	455	445	441	452	432	462	466	1.0
		10633	449	80898	443	438	494	459	423	419	505	454	459	440	434	445	440	422	446	438	438	429	431	443	444	426	441	431	428	437	418	448	456	1.0
		10674	463	81580	445	446	462	454	429	421	510	457	461	448	435	448	441	426	450	442	446	433	431	441	450	428	446	435	430	441	422	455	458	1.0
		10926	468	82740	456	453	450	464	438	429	519	466	467	455	444	456	452	434	456	451	453	440	441	452	458	439	452	441	438	449	428	460	465	1.0
	Average	**10804**	**464**	**82140**	**451**	**449**	**462**	**460**	**433**	**425**	**515**	**461**	**465**	**450**	**439**	**452**	**447**	**430**	**453**	**446**	**448**	**436**	**436**	**448**	**453**	**433**	**449**	**438**	**434**	**445**	**425**	**456**	**461**	
	Jochum et al., 2011	**10320**	**464**	**81475**	**452**	**450**	**458**	**460**	**433**	**426**	**516**	**462**	**465**	**452**	**440**	**453**	**448**	**430**	**453**	**447**	**449**	**437**	**437**	**449**	**455**	**435**	**450**	**439**	**435**	**446**	**426**	**457**	**462**	
	Av. / Lit.	**1.05**	**1.00**	**1.01**	**1.00**	**1.00**	**1.01**	**1.00**	**1.00**	**1.00**	**1.00**	**1.00**	**1.00**	**1.00**	**1.00**	**1.00**	**1.00**	**1.00**	**1.00**	**1.00**	**1.00**	**1.00**	**1.00**	**1.00**	**1.00**	**1.00**	**1.00**	**1.00**	**1.00**	**1.00**	**1.00**	**1.00**	**1.00**	
G_NIST612		11995	65	90096	39	41	6	38	39	34	83	41	41	42	38	41	40	38	41	38	40	40	38	41	41	39	41	39	40	39	41	40	40	1.0
		11123	68	82728	31	39	113	43	36	31	77	38	38	39	35	38	37	35	37	35	37	37	35	38	37	37	38	36	37	37	39	37	37	1.0
		11197	62	83983	34	39	74	43	37	33	79	39	39	39	36	39	38	36	38	36	38	38	37	39	39	37	39	37	38	37	39	38	38	1.0

	Average	**11438**	**65**	**85602**	**35**	**40**	**64**	**42**	**37**	**33**	**80**	**39**	**39**	**40**	**36**	**39**	**39**	**36**	**39**	**36**	**39**	**38**	**37**	**39**	**39**	**38**	**40**	**37**	**38**	**38**	**40**	**38**	**38**	**1.0**
	Jochum et al., 2011	**10746**	**62**	**85061**	**44**	**39**		**39**	**37**	**31**	**78**	**38**	**39**	**39**	**36**	**38**	**38**	**36**	**38**	**36**	**37**	**38**	**36**	**38**	**38**	**37**	**39**	**37**	**37**	**38**	**39**	**38**	**37**	
	Av. / Lit.	**1.06**	**1.04**	**1.01**	**0.79**	**1.02**		**1.06**	**1.02**	**1.04**	**1.02**	**1.03**	**1.01**	**1.02**	**1.01**	**1.02**	**1.02**	**1.02**	**1.03**	**1.02**	**1.04**	**1.01**	**1.04**	**1.02**	**1.03**	**1.03**	**1.01**	**1.01**	**1.04**	**1.01**	**1.03**	**1.01**	**1.02**	
Titanite reference materials																																	
BLR1		19850	5	208148	206249	184	19777	9	52	1	74	3787	3954	0	377	1757	325	1609	535	82	608	122	892	189	535	71	369	32	58	187	217	194	325	0.6
		20578	14	209446	210903	190	19590	9	53	1	71	3753	3864	0	350	1686	317	1586	524	83	598	122	887	188	548	73	376	32	56	182	224	195	333	0.6
		20008	9	205007	204198	183	20003	8	53	1	69	3662	3863	0	349	1676	313	1560	517	81	600	120	881	185	540	72	366	32	55	179	218	191	324	0.6
	Average	20145	9	207534	207116	186		9	53	1	71	3734	3894	0	359	1706	318	1585	526	82	602	121	886	188	541	72	370	32	56	183	220	193	327	
	Ma et al. 2019	16567		195542	197895					1	54	3652	3797	<2,96	403	1799	321	1646	527	86	473	125	873	186	516	70	379	31	57	174	67	219	334	
	Av. / Lit.	**1.22**		**1.06**	**1.05**					**0.90**	**1.31**	**1.02**	**1.03**		**0.89**	**0.95**	**0.99**	**0.96**	**1.00**	**0.95**	**1.27**	**0.97**	**1.02**	**1.01**	**1.05**	**1.03**	**0.98**	**1.04**	**0.99**	**1.05**	**3.30**	**0.88**	**0.98**	
MKED1		8110	3	207525	228856	380	11144	9	60	0	21	1117	1030	0	581	2555	417	1831	397	72	314	46	264	46	116	15	76	7	16	72	143	423	146	2.9
		7928	3	204943	227996	372	11120	8	84	0	22	1384	1598	0	896	3658	588	2474	512	91	395	56	323	56	143	17	94	9	27	151	213	759	217	3.5
		7798	11	203096	228535	368	11929	8	83	0	24	1372	1595	6	890	3640	583	2463	509	90	397	56	326	56	142	17	93	9	27	148	216	752	217	3.5
	Average	**7945**	**6**	**205188**	**228462**	**373**	**11398**	**9**	**76**	**0**	**22**	**1291**	**1408**	**2**	**789**	**3284**	**529**	**2256**	**473**	**85**	**369**	**53**	**305**	**53**	**133**	**16**	**88**	**8**	**24**	**123**	**191**	**645**	**193**	
	Ma et al. 2019	**7146**		**195971**	**216360**					**<0,56**	**8**	**947**	**747**	**<1,51**	**509**	**2067**	**339**	**1559**	**336**	**64**	**211**	**40**	**218**	**39**	**93**	**12**	**68**	**6**	**12**	**42**	**49**	**321**	**106**	
	Av. / Lit.	**1.11**		**1.05**	**1.06**						**2.82**	**1.36**	**1.88**		**1.55**	**1.59**	**1.56**	**1.45**	**1.41**	**1.33**	**1.75**	**1.33**	**1.40**	**1.35**	**1.43**	**1.38**	**1.30**	**1.35**	**1.92**	**2.94**	**3.91**	**2.01**	**1.82**	
Kola	*In house*	1618	6	191544	208407	397	9455	5	30	0	3911	228	1723	2	576	1496	194	764	136	39	101	13	66	10	22	2	10	1	71	181	0	6	2	4.2

Jochum, K.P., Weis, U., Stoll, B., Kuzmin, D., Yang, Q., Raczek, I., Jacob, D.E., Stracke, A., Birbaum, K., Frick, D.A., Günther, D., Enzweiler, J., 2011. Determination of Reference Values for NIST SRM 610–617 Glasses Following ISO Guidelines. Geostand. Geoanalytical Res. 35, 397–429. https://doi.org/https://doi.org/10.1111/j.1751-908X.2011.00120.x

Ma, Q., Evans, N.J., Ling, X.X., Yang, J.H., Wu, F.Y., Zhao, Z.D., Yang, Y.H., 2019. Natural Titanite Reference Materials for In Situ U-Pb and Sm-Nd Isotopic Measurements by LA-(MC)-ICP-MS. Geostand. Geoanalytical Res. 43, 355–384. https://doi.org/10.1111/ggr.12264

NIST610 glass

Standard glass	G_NIST610	G_NIST610	G_NIST610	G_NIST610	G_NIST610	G_NIST610	G_NIST610	G_NIST610	G_NIST610	G_NIST610	G_NIST610	G_NIST610	G_NIST610	G_NIST610	G_NIST610	G_NIST610
Element (ppm)													**Average**	**2SD (%)**	**Jochum et al., 2011**	**Av. / Lit.**
Al	10980.29	10633.48	10674.36	10926.27	10812.33	10737.56	10723.23	10842.06	10809.41	10880.37	10705.99	10788.06	10793.21	207.65	10320.19	**1.05**
K	475.05	448.68	462.91	467.75	462.15	462.13	464.47	469.82	454.97	469.27	454.85	466.41	462.91	14.82	464.00	**1.00**
Ca	83344.76	80897.64	81579.54	82740.00	82139.78	81506.30	82501.72	82695.92	81548.40	82501.86	81534.30	82497.94	82090.02	1412.07	81475.13	**1.01**
Ti	460.45	442.80	444.75	456.09	451.58	452.88	451.14	453.08	450.10	452.78	452.38	451.68	451.64	9.16	452.00	**1.00**
Fe	442.17	494.23	462.26	449.80	453.55	459.61	457.06	459.62	463.14	461.29	454.59	455.23	459.76	24.92		
V	457.44	438.08	445.78	453.20	450.31	448.80	446.99	455.91	448.36	451.47	444.99	451.31	449.21	10.41	450.00	**1.00**
Zn	461.51	459.19	453.91	463.68	460.08	461.10	457.36	462.37	457.88	460.18	458.98	460.40	459.66	5.12	460.00	**1.00**
Ga	442.82	422.91	429.06	437.88	432.85	433.91	428.64	437.34	429.84	433.24	430.72	435.11	432.66	10.37	433.00	**1.00**
Rb	432.26	418.92	421.23	428.78	425.43	426.97	423.82	427.93	423.17	426.81	424.40	426.35	425.43	7.08	425.70	**1.00**
Sr	524.71	504.77	509.52	519.40	515.55	514.67	515.42	517.45	514.03	516.01	516.97	514.34	515.32	9.73	515.50	**1.00**
Y	469.85	453.99	456.59	465.53	460.72	461.35	461.91	466.27	459.96	462.66	461.14	461.21	461.81	8.38	462.00	**1.00**
Nb	471.28	459.21	461.13	467.45	465.88	462.86	464.03	467.81	462.85	464.86	464.27	465.79	464.69	6.42	465.00	**1.00**
Ba	458.67	440.07	447.80	455.25	449.72	455.72	450.83	451.68	455.11	452.24	447.79	452.50	451.35	9.72	452.00	**1.00**
La	444.30	434.44	434.81	443.52	439.45	441.57	438.46	439.31	441.61	437.66	439.20	440.43	439.49	6.06	440.00	**1.00**
Ce	459.31	444.59	447.70	456.42	450.00	454.35	451.00	454.45	455.11	450.19	450.78	455.71	452.17	8.28	453.00	**1.00**
Pr	453.35	440.35	440.90	452.19	447.72	446.56	448.95	449.92	447.84	446.57	445.65	449.74	447.27	7.85	448.00	**1.00**
Nd	435.89	422.12	425.79	434.30	429.57	431.54	425.99	432.03	427.06	430.25	431.26	429.39	429.62	7.74	430.00	**1.00**
Sm	459.91	445.52	450.17	456.28	450.44	453.80	452.82	456.92	451.59	450.31	452.60	453.16	452.76	7.48	453.00	**1.00**
Eu	452.95	438.33	441.65	450.89	446.02	447.52	447.19	448.72	446.98	443.11	445.92	448.89	446.30	7.99	447.00	**1.00**
Gd	453.62	437.70	445.74	453.38	447.81	451.86	446.08	450.29	451.01	446.12	447.45	450.21	448.28	8.76	449.00	**1.00**
Tb	443.56	429.28	432.57	439.57	433.57	440.03	434.34	438.92	438.11	435.47	431.59	440.26	436.09	8.54	437.00	**1.00**
Dy	441.46	430.94	431.24	440.65	435.26	439.16	437.87	437.35	437.73	433.52	432.09	440.18	436.12	7.51	437.00	**1.00**
Ho	456.39	442.93	441.15	451.68	447.16	448.67	452.85	448.58	453.25	445.25	446.22	451.51	448.56	9.03	449.00	**1.00**
Er	459.62	443.92	449.62	457.91	451.10	457.89	452.89	457.44	456.75	453.52	449.33	456.34	453.63	9.32	455.00	**1.00**
Tm	440.04	426.16	427.53	439.09	434.57	435.89	432.54	436.38	433.16	436.17	430.76	436.27	433.84	8.50	435.00	**1.00**
Yb	455.00	440.91	446.43	452.46	448.27	451.63	448.47	453.36	447.35	448.60	445.70	453.45	448.93	8.07	450.00	**1.00**
Lu	444.84	431.21	434.50	441.03	436.88	439.68	440.46	440.42	441.00	435.75	434.67	442.48	438.22	7.90	439.00	**1.00**
Hf	441.45	427.67	429.71	437.59	433.56	434.63	437.98	437.22	433.82	433.45	431.40	437.64	434.41	7.83	435.00	**1.00**
Ta	452.47	436.54	441.30	448.98	443.17	447.87	444.20	451.60	441.89	446.66	447.52	445.61	445.65	9.08	446.00	**1.00**
Pb	432.24	417.79	422.13	428.05	425.64	427.33	424.36	426.98	426.32	426.19	422.43	429.39	425.41	7.50	426.00	**1.00**
Th	462.39	448.20	454.87	459.57	456.14	460.70	453.99	459.37	457.21	455.32	454.52	459.54	456.57	7.67	457.20	**1.00**
U	465.98	455.79	457.52	464.50	460.59	463.20	457.09	463.24	459.60	462.91	459.49	462.11	460.90	6.35	461.50	**1.00**

NIST612 glass

Standard glass	G_NIST612	G_NIST612	G_NIST612	G_NIST612	G_NIST612	G_NIST612	G_NIST612	G_NIST612	G_NIST612	G_NIST612	G_NIST612	G_NIST612	G_NIST612	G_NIST612
Element (ppm)											**Average**	**2SD (%)**	**Jochum et al., 2011**	**Av. / Lit.**
Al	11995.07	11123.38	11196.63	11410.72	11427.31	11180.06	11418.14	11414.69	11637.60	11668.51	11447.21	528.32	10746.00	**1.07**
K	65.03	67.72	61.91	66.83	63.64	71.43	65.63	62.77	73.25	69.47	66.77	7.47	62.30	**1.07**
Ca	90096.23	82727.97	83982.96	87711.02	86508.79	86465.76	85939.89	86400.88	85992.53	87049.12	86287.51	3966.28	85061.00	**1.01**
Ti	39.19	31.15	33.60	40.22	37.00	42.20	37.53	40.76	35.48	37.04	37.42	6.76	44.00	**0.85**
Fe	5.91	112.72	74.35	60.13	70.43	58.33	56.62	59.64	52.47	40.90	64.32	53.53		
V	41.28	38.56	38.88	40.25	39.63	39.65	40.27	39.13	39.88	40.00	39.75	1.57	38.80	**1.02**
Zn	38.40	43.04	43.09	40.81	39.42	39.50	39.51	39.05	37.38	40.89	40.11	3.73	39.10	**1.03**
Ga	39.02	36.37	37.00	37.41	37.49	37.77	37.55	37.14	38.37	37.83	37.60	1.46	36.90	**1.02**
Rb	34.02	31.32	32.57	32.24	32.71	32.08	31.98	32.63	32.92	33.08	32.55	1.46	31.40	**1.04**
Sr	82.77	77.41	78.69	81.15	82.17	80.80	81.30	82.36	80.47	82.03	80.92	3.40	78.40	**1.03**
Y	41.49	37.99	38.66	40.02	40.24	39.99	40.47	40.49	40.47	40.36	40.02	1.99	38.30	**1.04**
Nb	40.62	38.29	38.82	39.90	39.94	39.56	39.64	39.74	40.14	40.40	39.70	1.40	38.90	**1.02**
Ba	41.77	39.06	39.43	41.09	41.49	40.73	40.68	41.58	40.86	41.91	40.86	1.91	39.30	**1.04**
La	37.87	34.97	36.31	37.26	37.39	37.02	37.27	36.80	37.49	38.02	37.04	1.76	36.00	**1.03**
Ce	40.61	37.89	38.53	39.79	39.75	39.47	39.75	39.25	39.45	40.21	39.47	1.57	38.40	**1.03**
Pr	40.44	37.31	37.99	39.39	39.58	39.45	39.61	39.55	39.45	39.50	39.23	1.79	37.90	**1.03**
Nd	37.88	34.64	36.05	37.38	36.59	37.36	37.27	37.38	36.76	37.43	36.87	1.88	35.50	**1.04**
Sm	40.78	37.46	37.87	40.02	39.20	39.28	39.26	39.21	39.15	39.66	39.19	1.91	37.70	**1.04**
Eu	37.55	35.37	35.63	37.11	36.27	36.48	37.57	36.82	36.94	37.40	36.71	1.54	35.60	**1.03**
Gd	40.38	37.28	38.45	40.34	40.52	40.56	39.64	39.96	39.50	39.77	39.64	2.08	37.30	**1.06**
Tb	39.82	36.88	37.51	39.01	39.02	38.71	38.94	38.93	38.62	38.91	38.64	1.67	37.60	**1.03**
Dy	38.45	35.36	36.72	37.26	37.93	38.10	37.98	38.31	37.49	38.59	37.62	1.96	35.50	**1.06**
Ho	40.69	37.99	38.75	39.80	40.17	39.95	40.35	39.84	39.25	40.70	39.75	1.73	38.30	**1.04**
Er	40.95	37.38	39.46	40.52	40.76	40.22	41.01	40.29	39.80	40.59	40.10	2.15	38.00	**1.06**
Tm	39.37	37.03	37.11	38.85	38.69	39.19	39.02	39.43	38.27	38.74	38.57	1.72	36.80	**1.05**
Yb	41.18	38.06	39.50	41.19	39.88	40.11	38.96	40.30	39.31	40.11	39.86	1.92	39.20	**1.02**
Lu	39.06	36.10	36.55	39.20	38.38	38.51	38.39	38.44	38.13	39.03	38.18	2.08	37.00	**1.03**
Hf	39.87	37.20	37.50	39.02	39.05	38.45	38.75	39.43	37.79	39.37	38.64	1.78	36.70	**1.05**
Ta	38.96	36.97	37.45	38.68	39.59	38.65	38.98	39.30	38.71	39.03	38.63	1.62	37.60	**1.03**
Pb	41.45	38.64	39.35	40.83	40.39	40.70	40.36	39.86	41.05	41.69	40.43	1.88	38.60	**1.05**
Th	39.66	36.79	37.93	39.93	40.37	39.03	39.13	39.34	39.64	39.74	39.16	2.11	37.80	**1.04**
U	40.00	36.97	37.86	39.37	39.55	39.35	38.84	39.17	39.07	39.16	38.93	1.77	37.40	**1.04**

Bear Lake (BRL1) titanite

Standard titanite	T_BLR1	T_BLR1	T_BLR1	T_BLR1	T_BLR1	T_BLR1	T_BLR1	T_BLR1	T_BLR1	T_BLR1	T_BLR1
Element (ppm)								**Average**	**2SD (%)**	**Ma et al. 2019**	**Av. / Lit.**
Al	19849.68	20577.88	20007.93	18864.89	19095.91	19733.79	19555.18	19669.32	1144.77	16567.09	**1.19**
K	5.33	13.75	9.34	16.05	4.54	8.94	20.95	11.27	11.90		
Ca	208148.41	209446.13	205006.87	207497.37	206415.42	210167.03	207136.48	207688.25	3521.08	195541.92	**1.06**
Ti	206248.72	210902.86	204197.89	202083.33	209212.31	201737.37	204586.86	205567.05	6921.54	197894.95	**1.04**
Fe	19777.06	19589.87	20002.77	20142.66	20274.14	20073.58	20203.25	20009.05	489.61		
V	184.20	190.27	182.94	171.47	172.54	183.30	182.76	181.07	13.43		
Zn	8.85	8.95	8.48	4.48	5.04	4.95	14.67	7.92	7.16		
Ga	52.33	53.04	52.62	38.51	38.56	42.24	42.20	45.64	13.48		
Rb	1.13	1.09	1.19	0.39	0.46	0.39	0.68	0.76	0.73	1.26	**0.60**
Sr	73.76	70.75	69.29	64.18	64.81	71.81	70.92	69.36	7.18	54.20	**1.28**
Y	3787.26	3753.10	3662.21	3417.84	3465.70	3785.90	3812.67	3669.24	326.42	3652.00	**1.00**
Nb	3954.48	3863.72	3863.45	3962.63	4007.11	3851.73	3883.14	3912.32	122.66	3797.00	**1.03**
Ba	0.02	0.07	0.09	0.03	0.14	0.13	0.51	0.14	0.34	<2,96	
La	377.22	349.86	348.66	337.09	336.61	401.81	392.50	363.39	53.69	403.00	**0.90**
Ce	1756.95	1686.40	1675.82	1593.17	1618.15	1799.12	1827.57	1708.17	178.43	1799.00	**0.95**
Pr	324.79	317.13	312.69	300.18	302.63	330.93	330.03	316.91	24.93	321.00	**0.99**
Nd	1608.95	1586.38	1559.51	1471.99	1495.68	1642.30	1631.65	1570.93	131.78	1646.00	**0.95**
Sm	535.07	524.48	517.19	496.53	496.30	533.13	536.63	519.90	34.80	527.00	**0.99**
Eu	82.15	82.53	80.69	80.04	80.39	82.81	83.05	81.67	2.51	86.00	**0.95**
Gd	607.74	597.97	600.11	562.07	576.37	631.19	609.81	597.89	45.45	473.00	**1.26**
Tb	121.87	121.66	120.48	114.54	115.43	125.40	125.26	120.66	8.60	125.00	**0.97**
Dy	891.91	886.63	880.59	828.83	820.24	910.16	902.80	874.45	71.13	873.00	**1.00**
Ho	189.25	188.49	185.05	173.49	171.39	188.00	189.81	183.64	15.65	186.00	**0.99**
Er	535.47	548.34	540.25	504.06	501.49	554.40	560.79	534.97	47.10	516.00	**1.04**
Tm	71.45	72.52	71.98	66.35	65.98	74.28	73.85	70.92	6.79	69.60	**1.02**
Yb	369.42	375.93	366.03	338.15	335.94	386.81	378.57	364.41	39.69	379.00	**0.96**
Lu	32.12	32.27	31.57	29.25	29.68	32.75	33.05	31.53	2.98	30.90	**1.02**
Hf	58.26	55.76	55.17	58.62	59.01	56.60	56.59	57.14	2.98	57.20	**1.00**
Ta	186.62	182.44	178.62	219.77	224.78	190.27	188.66	195.88	37.00	174.00	**1.13**
Pb	216.73	224.10	218.12	176.15	171.66	224.18	225.50	208.06	47.20	66.50	**3.13**
Th	193.83	194.83	191.37	151.29	153.93	191.88	192.96	181.44	39.49	219.00	**0.83**
U	324.61	332.55	324.50	271.94	281.08	327.11	327.79	312.80	50.15	334.00	**0.94**

MKED1 titanite

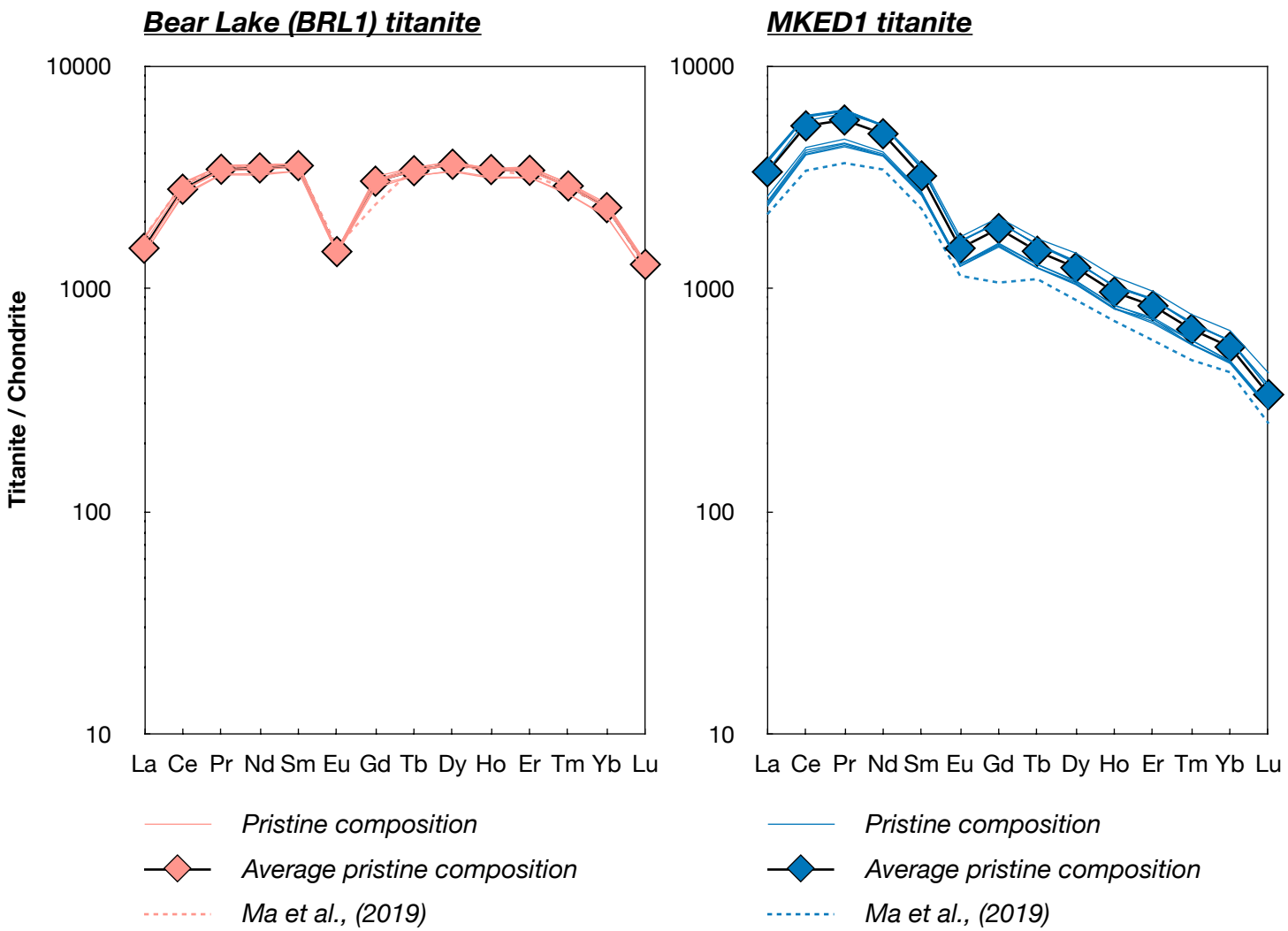
Standard titanite	T_MKED1	T_MKED1	T_MKED1	T_MKED1	T_MKED1	T_MKED1	T_MKED1	T_MKED1	T_MKED1	T_MKED1	T_MKED1	T_MKED1	T_MKED1	T_MKED1
Element (ppm)											**Average**	**S2D (%)**	**Ma et al. 2019**	**Av. / Lit.**
Al	8109.79	7927.58	7798.46	7892.72	7656.20	8014.18	7764.90	7877.64	8090.43	8399.84	7953.17	211.92	7145.55	**1.11**
K	2.94	3.04	11.22	8.49	14.63	13.00	7.51	9.45	13.30	8.59	9.22	4.02		
Ca	207524.87	204942.74	203096.01	206309.52	207606.53	208086.23	208479.17	205133.70	210493.56	209125.12	207079.75	2213.65	195970.74	**1.06**
Ti	228855.76	227996.33	228534.74	224317.81	223091.54	228393.74	226856.24	226952.56	226135.62	230939.85	227207.42	2286.84	216359.55	**1.05**
Fe	11144.34	11119.93	11928.59	11186.66	11469.11	11471.83	11760.82	11366.33	11478.07	11380.73	11430.64	259.71		
V	379.56	372.30	367.70	376.81	365.41	377.76	371.23	371.06	375.50	390.34	374.77	7.06		
Zn	9.16	8.37	8.04	6.11	5.08	6.26	4.33	4.58	4.41	5.73	6.21	1.75		
Ga	59.67	84.03	83.06	43.44	59.47	45.32	60.82	43.74	45.25	59.51	58.43	15.12		
Rb	0.21	0.32	0.34	0.05	0.10	0.11	0.14	0.13	0.12	0.14	0.17	0.09	<0,56	
Sr	20.94	22.43	24.12	18.55	20.41	18.68	20.18	18.16	18.12	18.66	20.02	2.02	7.99	**2.51**
Y	1116.86	1384.24	1372.28	1088.85	1360.33	1134.56	1377.01	1071.22	1096.47	1507.42	1250.92	163.33	947.00	**1.32**
Nb	1029.81	1598.18	1595.13	1033.88	1561.61	1110.87	1584.85	1031.01	965.48	1381.45	1289.23	277.87	747.00	**1.73**
Ba	0.44	0.07	5.79	0.14	1.06	0.23	0.35	0.14	0.31	0.32	0.88	1.75	<1,51	
La	580.68	895.83	890.46	573.84	867.27	611.20	874.51	552.72	563.65	800.89	721.11	155.31	509.00	**1.42**
Ce	2555.11	3657.66	3640.38	2494.23	3595.51	2625.79	3614.04	2433.24	2449.18	3466.24	3053.14	575.60	2067.00	**1.48**
Pr	417.00	587.56	582.89	414.02	577.66	434.35	588.10	401.19	406.82	566.59	497.62	88.03	339.00	**1.47**
Nd	1830.63	2474.24	2462.81	1796.18	2438.75	1869.22	2460.83	1789.78	1803.72	2471.19	2139.73	340.06	1559.00	**1.37**
Sm	397.20	511.76	508.90	389.28	515.34	400.57	518.77	385.95	392.54	532.34	455.27	65.92	336.00	**1.35**
Eu	72.10	91.50	90.48	70.43	90.54	71.87	91.05	70.19	71.78	95.18	81.51	10.89	63.70	**1.28**
Gd	314.02	394.84	397.34	308.99	394.70	317.07	390.68	304.80	309.96	413.22	354.56	46.43	211.00	**1.68**
Tb	45.95	56.27	56.13	44.59	56.35	46.11	56.98	44.35	44.46	60.15	51.13	6.49	39.60	**1.29**
Dy	264.44	323.45	325.67	257.27	318.88	266.12	326.01	255.49	260.98	353.91	295.22	37.51	218.00	**1.35**
Ho	46.30	56.38	56.01	44.35	56.54	45.91	55.62	44.50	44.84	62.12	51.26	6.68	39.20	**1.31**
Er	115.74	142.98	141.71	116.34	143.79	118.17	142.36	111.37	113.36	155.08	130.09	16.44	93.40	**1.39**
Tm	14.56	17.23	17.33	13.98	17.33	14.64	17.64	13.96	14.08	19.06	15.98	1.91	11.90	**1.34**
Yb	75.81	94.35	93.17	74.03	94.13	76.03	93.31	74.98	74.99	103.95	85.47	11.30	67.60	**1.26**
Lu	7.33	8.82	8.85	7.19	9.14	7.45	9.22	7.19	7.37	10.40	8.29	1.13	6.18	**1.34**
Hf	15.93	27.45	27.31	16.35	27.75	17.78	27.69	16.07	15.16	23.06	21.45	5.68	12.30	**1.74**
Ta	71.90	150.91	147.58	76.72	151.73	85.24	154.31	73.96	65.64	124.81	110.28	38.65	42.00	**2.63**
Pb	142.74	213.48	215.74	135.34	211.36	148.88	211.43	137.56	133.60	228.65	177.88	40.82	48.70	**3.65**
Th	422.83	759.30	751.88	426.12	729.24	465.31	753.25	403.50	381.48	767.91	586.08	176.70	321.00	**1.83**
U	146.20	216.87	216.76	141.83	216.61	152.38	213.87	140.83	134.13	236.10	181.56	41.26	106.00	**1.71**

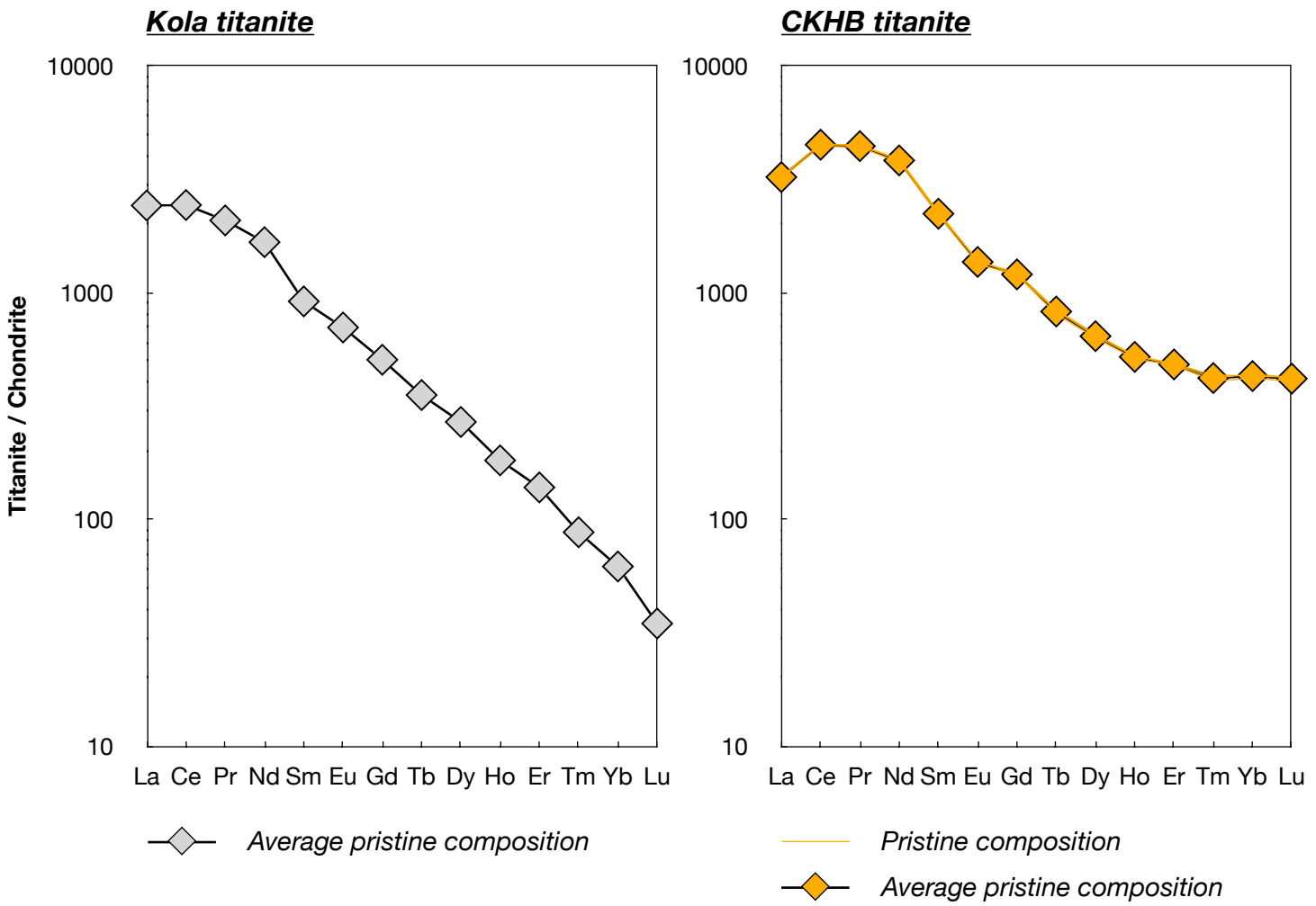
CKHB titanite

Standard titanite	T-CKHB	T-CKHB	T-CKHB	T-CKHB	T-CKHB
Element (ppm)				Average	2SE
Al	8601.60	8562.40	8294.22	8486.08	193.18
K	14.06	13.18	9.57	12.27	2.75
Ca	205310.27	210009.34	204812.29	206710.63	3311.21
Ti	224281.04	222879.72	229075.66	225412.14	3751.79
Fe	10391.86	10230.35	10453.61	10358.61	133.12
V	723.68	733.85	718.66	725.39	8.94
Zn	5.68	5.60	6.77	6.02	0.75
Ga	44.64	45.46	44.43	44.84	0.63
Rb	0.01	0.07	0.04	0.04	0.03
Sr	45.23	45.15	45.15	45.18	0.06
Y	808.38	822.24	828.90	819.84	12.09
Nb	414.94	444.14	473.67	444.25	33.91
Ba	0.06	0.08	0.37	0.17	0.20
La	758.05	771.61	773.38	767.68	9.68
Ce	2718.86	2779.37	2780.25	2759.50	40.63
Pr	407.57	413.90	416.41	412.63	5.26
Nd	1720.03	1764.57	1776.22	1753.60	34.24
Sm	325.15	329.82	336.70	330.56	6.71
Eu	75.03	77.74	77.12	76.63	1.64
Gd	238.42	238.03	243.72	240.06	3.67
Tb	28.95	30.08	30.34	29.79	0.85
Dy	155.40	158.48	161.45	158.45	3.49
Ho	28.14	28.89	29.09	28.71	0.58
Er	76.75	77.48	77.80	77.35	0.62
Tm	10.20	10.53	10.84	10.52	0.37
Yb	67.61	70.49	69.34	69.15	1.67
Lu	10.20	10.59	10.58	10.46	0.26
Hf	24.78	24.33	24.63	24.58	0.26
Ta	18.56	19.62	20.70	19.63	1.23
Pb	8.42	8.44	8.55	8.47	0.08
Th	282.34	292.71	295.30	290.12	7.92
U	128.85	135.44	133.50	132.59	3.91

Kola titanite

Standard titanite	Kola
Element (ppm)	
Al	1618.19
K	6.27
Ca	191543.69
Ti	208407.15
Fe	9454.60
V	397.17
Zn	5.21
Ga	29.99
Rb	0.02
Sr	3911.09
Y	227.84
Nb	1723.48
Ba	2.13
La	575.63
Ce	1495.78
Pr	194.09
Nd	764.48
Sm	135.69
Eu	39.40
Gd	100.87
Tb	12.75
Dy	66.31
Ho	10.04
Er	22.18
Tm	2.20
Yb	10.00
Lu	0.87
Hf	70.76
Ta	180.85
Pb	0.48
Th	6.33
U	1.52


Bear Lake (BRL1) titanite
MKED1 titanite
Titanite / Chondrite
10000
1000
100
10
La Ce Pr Nd Sm Eu Gd Tb Dy Ho Er Tm Yb Lu
Pristine composition
Average pristine composition
Ma et al., (2019)


Kola titanite
CKHB titanite
Titanite / Chondrite
10000
1000
100
10
La Ce Pr Nd Sm Eu Gd Tb Dy Ho Er Tm Yb Lu
Average pristine composition
Pristine composition
Average pristine composition